PACIFIC EARTHQUAKE ENGINEERING RESEARCH CENTER

Performance of Circular Reinforced Concrete Bridge Columns under Bidirectional Earthquake Loading

Mahmoud M. Hachem
Stephen A. Mahin
Jack P. Moehle
University of California, Berkeley

Technical Report Documentation Page

1. Report No. PEER 2003/06	2. Government Accession No.	3. Recipient's Catalog No.
4. Title and Subtitle Performance of Circular Reinforced Concrete Bridge Columns under Bidirectional Earthquake Loading		5. Report Date February 2003
		6. Performing Organization Code UCB/ENG-9374
7. Author(s) Mahmoud M. Hachem, Stephen A. Mahin, and Jack P. Moehle		8. Performing Organization Report No. UCB/PEER
9. Performing Organization Name and Address Pacific Earthquake Engineering Research Center 1301 South 46th Street Richmond, CA 94804		10. Work Unit No. (TRAIS)
		11. Contract or Grant No. Contract No. 59 A 131
12. Sponsoring Agency Name and Address California Department of Transportation Engineering Service Center 1801 30th Street MS#9 Sacramento, CA 95816		13. Type of Report and Period Covered Research Report 1996-2001
		14. Sponsoring Agency Code National Science Foundation

15. Supplementary Notes

16. Abstract

The behavior of ductile reinforced concrete bridge columns subjected to cyclic loading has been the subject of extensive research. However, some areas of uncertainty remain, including the response of such columns when subjected to one or more components of intense earthquake ground motions, and the ability of current analytical models to predict response. As such, an integrated series of experimental and analytical studies were undertaken.

This report describes the dynamic testing of four circular reinforced concrete bridge columns on the earthquake simulator of the Earthquake Engineering Research Center (EERC) of the University of California at Berkeley. The specimens were divided into two pairs, with each pair subjected to a different ground motion. Within each pair, one specimen was subjected to one component of the ground motion, while the other specimen was subjected to two components. The four columns exhibited stable ductile behavior under several repetitions of the targeted ground motions. The bidirectionally loaded columns behaved similar to the unidirectionally loaded columns under the design earthquake, and were in fact able to sustain more repetitions of loading before failure was reached.

A number of elastic and inelastic analytical models were evaluated in terms of their ability to predict the local and global behavior of the tested columns. While simple numerical models such as the stiffness degrading Clough/Takeda model generally give satisfactory results, refined fiber-based elements provide more accurate prediction of both global and local forces and deformations.

Finally, two analytical studies were carried out for a wide array of column heights, diameters, and axial load intensities. The columns were subjected to large suites of ground motions scaled to match on average the design response spectrum. Results indicate that columns detailed according to modern seismic design criteria generally behave well. These studies show that certain design approaches used today might lead to excessive displacement demands for columns with short periods, and that some columns might be susceptible to low-cycle fatigue failure. It was also found that peak response under bidirectional excitation was similar to that predicted unidirectionally, but that increased demands might occur in the short period range, including increased residual displacements.

17. Key Word Reinforced concrete, bridges, circular columns, shaking table, experiments, bidirectional loading, modeling, finite element analysis	18. Distribution Statement No restrictions		
19. Security Classification (of this report) Unclassified	20. Security Classification (of this page) Unclassified	21. No. of Pages 490	22. Price

Form DOT F 1700.7 (8-72)   Reproduction of completed page authorized

Performance of Circular Reinforced Concrete Bridge Columns under Bidirectional Earthquake Loading

Mahmoud M. Hachem

Stephen A. Mahin

Jack P. Moehle

Department of Civil and Environmental Engineering
University of California, Berkeley

ABSTRACT

The behavior of ductile reinforced concrete bridge columns subjected to cyclic loading has been the subject of extensive research. It is now possible to predict with fair accuracy the strength and deformation capacities of those columns given a variety of parameters that include the section geometry, amounts of longitudinal and transverse reinforcement, slenderness ratio, axial load and material strengths. Nonetheless, some areas of uncertainty remain, including the response of such columns when subjected to one or more components of intense earthquake ground motions, and the ability of current analytical models to predict performance.

As such, an integrated series of experimental and analytical studies were undertaken. This report describes the dynamic testing of four circular reinforced concrete bridge columns on the earthquake simulator of the Earthquake Engineering Research Center (EERC) of the University of California at Berkeley. The specimens were divided into two pairs, with each pair subjected to a different ground motion. Within each pair, one specimen was subjected to one component of the ground motion, while the other specimen was subjected to two components.

The four columns exhibited stable ductile behavior under several repetitions of the targeted ground motions. The bidirectionally loaded columns behaved similarly to the unidirectionally loaded columns under the design earthquake, and were able to sustain more repetitions of loading before failure was reached.

A number of elastic and inelastic analytical models were evaluated in terms of their ability to predict the local and global behavior of the tested columns. While simple models such as the stiffness degrading Clough/Takeda model give satisfactory results, the use of refined fiber elements results in better prediction of both global and local forces and deformations. Use of bilinear hysteretic models proved inadequate. Properly calibrated elastic models were able to provide good predictions of maximum displacements.

Finally, two large analytical studies were carried out on a wide array of column heights, diameters, and axial load intensities. The columns were subjected to large suites of ground motions scaled to match on average the design response spectrum. Results indicate that columns detailed according to modern seismic criteria generally behave satisfactorily. The first portion of the parametric investigations examined the effect of three alternative design methodologies on performance under unidirectional loading. These studies demonstrated that certain design approaches used today might lead to excessive displacement demands for columns with short periods, and that

some columns might be susceptible to low-cycle fatigue failure. The second phase of the parametric studies examined the effects of bidirectional motions. It was found that peak bidirectional response was similar to that predicted unidirectionally, but that increased demands might be observed in the short period range. Bidirectional loading also tended to increase residual displacements. Elastic analysis methods were able to provide adequate predictions of displacement demands for moderate and long period structures, but often substantially underestimated demands in the short period range.

ACKNOWLEDGMENTS

CONTENTS

LIST OF FIGURES

xx

xxi

LIST OF TABLES

1   Introduction

1.1   BACKGROUND

In recent years, moderate to large magnitude earthquakes have caused significant damage to bridges around the world. The 1989 Loma Prieta and the 1994 Northridge earthquake in California and the 1995 Hyogo-ken Nanbu earthquake in Kobe, Japan are but a few examples. These earthquakes subjected a large number of bridges of various types to intense ground shaking. Damage resulting from these earthquakes ranged form none to moderate, with some older bridges completely collapsing. Even though modern bridges generally performed well, these earthquakes prompted worldwide re-evaluation of many of the design procedures, analysis methods and construction details used for bridges located in regions of high seismic hazard. This scrutiny has been motivated by a number of factors, including the severity and unusual dynamic characteristics seen in some of the recorded accelerograms, and increasing public expectations for the seismic performance of important bridges.

In particular, the California Department of Transportation (Caltrans) has undertaken a wide array of experimental and analytical research to improve capabilities for evaluating and retrofitting existing older bridges and for designing and analyzing new structures (e.g. [109]). Most of the experimental research to date has subjected components and simple bents to prescribed histories of cyclic displacement reversals. These studies have:

1. Improved or validated detailing requirements.

2. Provided information necessary to develop basic numerical models for simulating seismic response.

3. Identified factors influencing the capacity of the elements or systems in question.

4. Allowed the development of methods for estimating element and system capacity.

However, few experiments and analyses have focused on identifying the factors that influence seismic demand, and the ability of design criteria to achieve targeted seismic performance. To do this, highly accurate computer models could be used to simulate the response of a bridge structure to the range of seismic excitations anticipated at a particular site. Unfortunately, little experimental or field data exist to validate such computer simulations, especially under the intense and complex three-dimensional dynamic loading conditions expected during major earthquakes in California and elsewhere. Without this validation, computer-based predictions may not be as reliable as desired.

While the results of experimental and computational predictions have been compared for quasi-static tests for many types of bridge column, several concerns remain when such models are used to predict dynamic response:

1. The standard cyclic displacement histories used in quasi-static tests may not capture behavior that may occur under certain earthquake loading conditions, such as (a) intense, large velocity pulses observed in accelerograms recorded in the immediate vicinity of a fault rupture, (b) long duration, harmonic-like motions recorded on soft soils, or (c) severe long duration motions that may be associated with great earthquakes. Standard cyclic loading tests, where the amplitude of displacement increases in successive cycles, are very useful in comparing behavior of different design details since they subject specimens to identical loading histories. However, they may not produce the same damage occurring during more erratic seismic loading conditions, and they may not provide information needed to define analytical models that are required to simulate these more complex response histories.

2. Few tests have studied the response of elements and systems under three-dimensional actions that would be expected during earthquakes. Limited results suggest that behavior under bidirectional loading may differ from that obtained during unidirectional testing. However, little data is available to assess the ability of computer models to predict the response of columns and systems to three-dimensional input motions.

3. Rate of loading effects may change failure or other behavior modes. For instance, a column might fail in flexure when tested quasi-statically, but fail in shear when loaded dynamically.

4. The effect of various strength deterioration modes, such as spalling, bar buckling and loss of confinement, on seismic demands has not been studied in any detail either analytically or experimentally. For instance, the loss of strength and stiffness associated with bar buckling

and fracture might increase demands, but the ability of computer analyses to predict the resulting redistribution of loads within a system, and the increased local or global demands remains uncertain.

Tests employing more complex cyclic or pseudo-dynamic displacement histories can be used to obtain information on some of these issues. However, such tests do not account for the effects of the observed behavioral characteristics on dynamic response.

As a result, increasing interest has been directed towards dynamic testing of components and simple bridge systems using earthquake simulators (shaking tables). Comparison of shaking table test results with results of quasi-static tests and numerical simulations can be used to identify differences between static and dynamic behavior, assess current design methods, deduce factors influencing seismic demands and evaluate design-oriented as well as more refined analytical models and assumptions.

A wide range of problems could be addressed in such investigations. For new construction representative of current California construction practices, issues could be investigated regarding cross-sectional shape, detailing, aspect ratio, axial load, and model scale. An even wider array of issues arises for existing and retrofit conditions. With respect to ground motions, differences in response under unidirectional versus multi-directional motions are of interest. Considerable concern has also been raised regarding performance under near-fault excitations containing severe velocity pulses associated with the rupture process as well as the response of bridge columns under long duration motions associated with large magnitude but more distant events. Similarly of interest would be the response of damaged bridges during aftershocks and of columns that have been repaired following a damaging earthquake.

1.2   RESEARCH PROGRAM OBJECTIVES

Based on discussions with Caltrans engineers, it was decided to focus initial investigations on specimens representative of new construction found in single column bents. As such, a simple, fixed-base cantilever column idealization was used. In these initial studies, only well confined, spirally reinforced circular cross-sections were considered. The main objectives of the research reported herein are the investigation of:

1. The effects of different ground motion characteristics, specifically intense, but relatively short duration, near-fault ground motions and longer duration motions representative of large magnitude events recorded at moderate distances to the fault.

2. The effects of a second component of horizontal seismic loading on response.

3. The ability of various simple and refined analysis methods to predict measured response.

4. The effectiveness of current design assumptions.

5. The performance of a wide range of bridge columns with various dimensions and loading conditions.

1.3   REPORT SCOPE AND ORGANIZATION

Four identical reinforced concrete bridge columns, with spirally reinforced circular cross-sections were tested in this investigation. The prototype column was designed according to the 1991 Caltrans Bridge Design Specifications (BDS) [97]. Two ground motions were used in the testing: a near-fault motion from the 1994 Northridge earthquake and a longer duration record from the 1985 Chile earthquake. Two specimens were tested using each of the motions: one under one component of horizontal excitation, and the other under both components of the recorded excitations (Table 1-1). Various analyses are conducted to interpret the results and access the adequacy of design assumptions and analysis models and procedures.

Table 1-1 Specimen test matrix

Test Matrix	Unidirectional	Bidirectional
Earthquake 1 Olive View (Northridge, 1994)	Specimen A1	Specimen A2
Earthquake 2 Llolleo (Chile, 1985)	Specimen B1	Specimen B2

Chapter 2 contains a literature review and an overview of current bridge design methodology. The design and construction of the test specimens are described in Chapter 3, along with issues related to geometric and material similitude. The experimental program, physical test setup, instrumentation and loading (ground motion records) are described in Chapter 4. The global response and the damage experienced by the specimens are summarized in Chapter 5. A compari-

son of experimental and analytical results is presented in Chapter 6. Simplified methods similar to those used in design are considered, and compared with results of more refined elastic and inelastic dynamic analyses. Based on the assessment of analytical models in Chapter 6, a suite of parametric and sensitivity analyses are presented in Chapter 7 to evaluate the performance of bridge columns considering a wide range of physical properties, loading conditions and design criteria. Conclusions and recommendations are summarized in Chapter 8.

A number of Appendices are attached to the report to provide more detailed information on various aspects of the research. Appendix A lists the details of all the instruments used in the test, as well as all the shaking table runs performed for each specimen. Appendix B summarizes certain hand calculations used in the process of proportioning and detailing the test specimens. Appendix C documents the performance and damage of each specimen during individual test runs corresponding to various excitation levels. Appendix D presents plots of the global response of the specimens for some selected runs. Appendix E shows comparisons of measured experimental responses to analytical results obtained using various linear and nonlinear models to represent the column.

2   Literature Review and Design Philosophy

2.1   INTRODUCTION

This report focuses on the seismic response of columns in new bridge structures having single column bents. The columns are assumed to have a circular cross-section. Spiral transverse reinforcement is used to provide confinement and shear resistance. Such columns are usually fixed to the foundation at the base. At the top, columns are usually free to rotate in the transverse direction of the roadway. In cases where the bridge deck is continuous, the column will frequently be connected monolithically to the deck by means of a transverse bent cap. In other cases, the deck may be simply supported on the bent cap. As such, the columns are often idealized in the transverse direction as being cantilevers with pin connections at their top; while in the longitudinal direction, the conditions at the top range from being nearly fixed to being nearly pinned. Because the focus of this investigation is the comparison of behavior under one and two components of excitation, and for different ground motions, the column is simplified and idealized as being pin connected in all directions at its top. Because the column is to be representative of new construction, flexure is intended to be the primary mode of inelastic behavior, so precautions were taken as in design to preclude premature failure modes due to shear, or lack of anchorage. An axial load representative of typical practice was also selected. In this case, the axial load was taken to be 10% of the gross cross-sectional area of the column times the nominal strength of the concrete. However, the effective axial load ratio based on actual concrete strength at the time of testing was around 6%.

        Section 2.2 presents a summary previous shaking table tests performed on reinforced concrete columns. A short discussion on the behavior of reinforced concrete columns under reversed cyclic loading is presented in Section 2.3. In Section 2.4, some of the fundamental procedures and assumptions used in the seismic-resistant design of reinforced concrete columns are outlined; the reliability of these assumptions will be assessed in the testing program and subsequent analyses.

Section 2.5 discusses the principals of *Capacity Design* typically employed to ensure that damage is concentrated at intended locations and that undesirable failure modes are prevented.

2.2   PREVIOUS RESEARCH

In the last two decades, a significant amount of research on reinforced concrete bridge piers has been performed. Most of the research was undertaken in the United States, Japan, and New Zealand, with the majority of the tests performed under quasi-static loading. A comprehensive summary of this research is beyond the scope of this report, but the interested reader is referred to Lehman et al. [50].

2.2.1   Shaking Table Tests

Shaking table tests on columns or specimens containing columns are becoming more common, despite some practical limitations imposed by available shaking tables. These restrictions include physical limits on the peak displacement, velocity and acceleration that can be imposed, the size and weight of the specimen that can be tested, and the number of directions of table motion that can be applied. Only recently, with the development of new tables in Japan has it become feasible to test columns approaching full size.

Generally, shaking table test specimens utilize large scale factors (i.e., small size columns), and vary considerably in the realism of the test setup. Table 2-1 provides a brief summary of shaking table tests to date involving yielding columns. Only two test programs have utilized circular spirally reinforced sections representative of current Caltrans construction. The remainder have generally utilized rectangular sections with hoop reinforcement. Only two test programs have examined the effect of bidirectional motion on seismic response, using small sized rectangular columns with fixed-fixed boundary conditions. Some of these test programs are described below for reference.

Dodd and Cook [22] tested fourteen small-scale bridge piers under unidirectional input. They investigated 200 mm (7.9 in.) diameter circular columns to assess the effects of pier slenderness, axial-load intensity, ground motion characteristics and base flexibility conditions. These test columns were based on a 1/6th-scale factor. The specimens tested had aspect ratios of 4, 7 and 10. The axial loads considered were 0.05 and $0.4 A_g f_c'$. In order to achieve the higher axial load intensity, the inertial mass was not changed, but external post-tensioning was used to apply the axial

load in a manner that underestimated the P-Δ effects, due to the restoring component of the pre-stressing mechanism. Unidirectional base accelerations, consisting mainly of the north-south component of the 1940 Imperial Valley (El Centro) record and simple sine waves, were applied to all specimens. Flexural behavior controlled the behavior of the specimens tested. Overall trends in the dynamic response could be roughly approximated using simple nonlinear analysis models, but both nonlinear and elastic models erred significantly in predicting peak response. The researchers found that key modeling parameters that controlled response, such as initial stiffness, yield curvature and yield displacement, could be predicted with little accuracy using conventional design methods even when the member configuration and material properties were known.

Gutierrez et al. [31] compared the unidirectional response of a square column obtained using shaking table and pseudo-dynamic testing. The pseudo-dynamic test method used hydraulic actuators to quasi-statically apply the displacements computed during the test for a specified ground motion based on measured hysteretic response of the test specimen. The test specimens considered in this program had a 250 mm (9.8 in.) square section and a length of 1500 mm (59 in.). The experiment resulted in good correlation between the displacement histories obtained in both tests, suggesting that rate of loading effects are not significant.

Inoue et al. [35] conducted a study to evaluate the effect of ground motion duration on the dynamic response of concrete columns. One static and two unidirectional shaking table tests were conducted. Two artificial ground motions generated to match the same spectrum were used for the two dynamic tests. Strengths recorded in the dynamic tests were 10% to 20% higher than those of the static test. All specimens showed similar crack patterns, and both dynamic tests resulted in very similar peak displacements. The investigators also noted that the peak displacement's occurrence coincided with the peak energy input rates of the input motions.

Kitajima et al. ([39] and [40]) tested 1/9th-scale square columns with a size of 80 mm (3.2 in.). Column responses under both unidirectional and bidirectional dynamic excitations were compared. The investigators observed a reduction in stiffness and strength of the columns tested under bidirectional excitations compared to the unidirectional excitations. They also found that the effects of shear and bond slip on the response could not be ignored in predicting response, especially for the bidirectional loading cases.

Kogoma et al. [42] tested four 1/3rd-scale one-story concrete frames with four columns each. All columns were 850 mm (33.5 in.) high, with a 130 mm (5 in.) square section. Hoop spacings ranged from 50 mm (2 in.) to 285 mm (11.2 in.). Displacement and strength capacities from

shake table tests compared well with static tests. The failure modes were very brittle, and damage patterns varied with both the hoop spacing and the testing method (static vs. dynamic).

Kowalsky et al. [43] evaluated the dynamic response of light-weight concrete bridge bents. Two specimens were subjected to one component of the 1978 Tabas earthquake. The two specimens had the same circular column sections, and differed in the beam details. The tests focused on the usability and repairability of light-weight concrete in bridges, and the validity of conventional analysis and design models.

MacRae et al. [53] tested one as-built and one retrofit 1/6th-scale two-column bent. The rectangular column sections considered were 200 by 250 mm (8 in. by 10 in.). The retrofitted specimen showed great improvement of the as-built specimen that suffered a brittle shear failure in the column.

Minowa and Obgawa [64] tested 1/3rd-scale 130 mm (5.1 in.) square columns, with a height of 850 mm (33.5 in.). Columns were tested to collapse with the shear reinforcement spacing being the main parameter changing among the different specimens. The results agreed with static test results. P-Δ effects were found to be significant.

Minowa et al. [65] tested two actual size one-story reinforced concrete frames, and one three-story frame. The one-story frames had four columns each, with the hoop reinforcement spacing being the parameter of interest. Columns had a 350 mm (13.8 in.) square section, and aspect ratio of 5.7. The specimen with closer hoop spacing of 100 mm (4 in.) failed at a displacement three times larger than the other specimen with hoop spacing of 400 mm (16 in.).

Nakayama et al. [72] compared the unidirectional and bidirectional behavior of two identical one-story structures with five columns with square cross-sections. Each column was reinforced with four longitudinal bars (ρ_l=1.1%), and with closely spaced stirrups. The specimens were subjected to four levels of motion: Elastic, Cracking, Yield, and Failure. An artificial ground motion was used. The motion was 10 seconds long, with both components having similar spectra. The bidirectional specimen experienced a significant reduction in strength and stiffness following the third level (yield) compared to the unidirectional specimen, and could not be subjected to the fourth level due to excessive damage, while the unidirectional specimen survived all four levels.
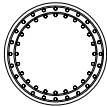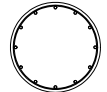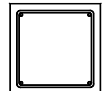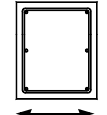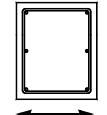
Sanders et al. [90] tested two circular columns on a shaking table. Those columns were similar to columns tested at NIST [47]. However, they used a scale of 3 while NIST used a scale of 4. The two identical columns had a diameter of 406 mm (16 in.), and an aspect ratio of 4.5. The first column was subjected to nine runs of the El Centro ground motion. The ground motion was incre-

Table 2-1 Summary of R/C column shaking table tests

Program	Section	Aspect Ratio	ρ,%	$\dfrac{P}{f_c'A_g}$ (%)	Scale Factor	Dimensions	Directions	Earthquake	Comments
New Zealand [22]		4, 7 & 10	1.6	5 & 40	6	8"	1	El Centro	Axial load consists of supported mass + pre-tensioning.
ISMES Italy [31]		6	2.6	10	1	10"x10"	1	Artificial	Comparison with pseudo-dynamic test.
Nihon Japan [39], [40]		2 & 3	2	14	9	3"x3"	2	Hachinoche record of the 1968 Toka-chi-Oki	Small scale. Fixed-fixed conditions.
NIED Japan [42] & [64]		3.3	4.75	15	3	5"x5"	1	Hachinoche record of the 1968 Toka-chi-Oki (EW)	1-story RC frame with 4 columns. Effect of hoop spacing. Small scale.
UCSD [53]		2.2	4.2	10	6	8"x10"	1	El Centro 1940	Axial load consists of supported mass + pre-tensioning. Two-column Bent.
NIED Japan [65]		2.9	2.5	6	1	13.8" x 13.8"	1	Hachinoche record of the 1968 Toka-chi-Oki (EW)	1-story RC frame with 4 columns. Effect of hoop spacing.
UNR [90]		4.5	2	10	3	16"	1	El Centro	Matches NIST specimens. Off-table mass.

Table 2-1 Summary of R/C column shaking table tests

Program	Section	Aspect Ratio	ρ,%	$\dfrac{P}{f_c'A_g}$ (%)	Scale Factor	Dimensions	Directions	Earthquake	Comments
PWRI Japan [111]		4.6, 5.5 & 7	1.6, 3.8 & 4.0	2.5, 3 & 10	6	14", 18" & 21"	1	Kaihokubashi	Comparison of US and Japan column designs
UCSD [43]		3.7	2.62	5	6	8"	1	Tabas	LWC 2-column bent
Kajima Japan [72]		3	1.1	13	?	4"x4"	2	Artificial	1-story RC frame with 5 columns.
Tohoku Japan [35]		3	0.8	3	?	4.7"x4"	1	Artificial	2-column bent. Effect of motion duration.
China [108]		9 to 12	1.7 to 5	1	1	24"x7" & 7"x9"	1	Harmonic	Effect of sudden cracking on dynamic behavior.

mentally increased from 1/3 to 4 times El Centro by the final run. The second specimen was brought immediately to a level of 3.5 El Centro. The columns performed well overall. It was found that the first specimen became vulnerable to P-Δ effects once permanent offset occurred. However, P-Δ effects were not realistically simulated in these tests. It was also found that although the second specimen experienced less damage and permanent set in the first application of the 3.5 El Centro record, significant additional damage occurred during the repetition of the record.

Wu and Liu [108] investigated the effect of sudden cracking on the dynamic response of RC columns. They tested eight specimens with rectangular sections and varying dimensions and test setups. The shaking table tests used unidirectional harmonic motions to excite single column specimens, and two-column bent specimens (along transverse direction). The authors concluded that dynamic testing reveals effects of sudden cracking that cannot be captured by static or pseudo-dynamic tests. This results in a sudden change of section rigidity and a slight change in the force-displacement curve of the column.

Yen et al. [111] compared the dynamic behavior of three bridge columns designed according to the US and Japanese codes, and tested at the laboratory of the Public works Research Institute (PWRI) in Japan. One column was designed according to AASHTO, and had a diameter of 356 mm (14 in.), while the other two columns were designed according to the JRA specifications, and had diameters of 450 mm (17.7 in.) and 533 mm (21 in.). All three columns had a height of 2442 mm (96 in.), and a scale factor of 6 was assumed. All specimens performed well in the design level test. However, the US specimen showed more resistance to bar fracture due to its spiral reinforcement design, but sustained a larger residual displacement than the Japanese specimens.

The results of the limited shaking table testing to date suggest that dynamic test results contain many features that cannot be detected in quasi-static tests utilizing prescribed displacement histories. Few of the shaking table tests have been performed using specimens applicable to conditions found in California. For example, few specimens to date had spirally reinforced circular sections (and none had non-circular sections reinforced transversely with interlocking spiral reinforcement). Most tests have been conducted utilizing very small size specimens. Results suggest that standard analysis procedures have difficulty in predicting the response of some specimens and that bidirectional loading and fracture of bars can have a significant effect on dynamic response. Most ground motions considered have not been representative of excitations utilized in the design of major bridges in California.

2.3   BEHAVIOR OF CIRCULAR REINFORCED CONCRETE COLUMNS

A brief overview of the behavior of reinforced concrete columns under unidirectional and bidirectional lateral loads is provided in this section. Because of the extent of research on unidirectional loading, emphasis is placed on bidirectional loading. The reader is referred to Ref. [50] for more information on unidirectional testing.

2.3.1   Behavior of Reinforced Concrete Columns under Quasi-Static Loading

Ductile columns tested cyclically under progressively increasing displacements typically undergo the following stages before failure is reached:

1. For small displacement cycles, cracks are observed at locations of maximum bending moment.

2. Further increasing the displacement amplitude results in spalling of the concrete cover.

3. The cover eventually spalls over the height of the plastic hinge, but the core remains confined by the spiral reinforcement.

4. Continued cycling to large displacements causes erosion of the confined core through arching action and yielding of the spiral reinforcement, which reduces the confinement of both the core concrete and the longitudinal reinforcement bars.

5. This is usually followed by buckling of the longitudinal reinforcement and eventually after repeated cycles of buckling and straightening, their fracture.

6. The buckling of the longitudinal bars increases the tensile strains in the spiral reinforcement leading to their fracture, which may occur before or after the fracture of the longitudinal reinforcement depending on the amount of confinement.

7. In ductile columns, failure is usually indicated by a *significant loss of capacity*, that is typically caused by the fracture of some of the longitudinal reinforcement as well as the spiral reinforcement.

   This hierarchy of behavior may not be representative of more complex displacement loading histories experienced during actual earthquakes. For example, the progressive increase in cyclic amplitude is not typical of actual earthquake response. This is especially true for near fault ground motions, in which the largest displacements typically occur in the first few cycles, posing

14

very large demands on the column in a very short period of time. Similarly, the inclusion of more than one component may result in a significantly different behavior.

2.3.2   Biaxial Behavior of Reinforced Concrete Columns

Some of the experimental work on bidirectional testing of columns is presented below, followed by analytical research on the effects of bidirectional ground motions. Most researchers observe loss of strength and stiffness under bidirectional loading as compared to unidirectional loading. Very little is reported however on the effect of bidirectional loading on the ultimate displacement capacity and fatigue resistance of a column.

Otani et al. [78] tested three pairs of column under quasi-static unidirectional and bidirectional loading. The tested columns had square cross-sections typical of ground level columns in reinforced concrete buildings. The three sets of columns had varying amounts of lateral reinforcement, and different concrete compressive strengths. The researchers concluded that the hysteretic behavior was similar for the unidirectional and bidirectional tests and that the failure modes were generally the same. They also noted a reduction in a column's stiffness in one direction after it had been loaded in the other direction. The bidirectional tests showed flexural and diagonal cracking as well as crushing on all four sides while the unidirectional tests predominantly showed this type of damage on two sides only.

Ogawa et al. ([75], [76], [77]) conducted a series of tests involving unidirectional and bidirectional quasi-static loading of square columns. The columns had an axial load ratio of 25% in most tests. Ogawa et al. [75] found that the biaxial loading causes more severe damage and more degradation in strength and stiffness than the unidirectional loading, especially for columns loaded with circular loading paths. Ogawa et al. [77] found that while biaxial effects on restoring force and stiffness are significant, those effects tend to decrease significantly with higher amounts of transverse reinforcement. Ogawa et al. [76] observed that the strains in the column section are significantly higher in the biaxial case at the same drift level. They also observed that columns that were bidirectionally loaded along lines parallel to the two principal directions, had about 2/3 the unidirectional displacement capacity, while columns with a circular loading path only had 1/2 of the displacement capacity, under the 25% axial load level.

Saatcioglu and Ozcebe [88] tested square columns under unidirectional and bidirectional loading following elliptical paths. The authors noted a decrease in ductility and an increase in

strength and stiffness degradation with increasing axial load. They noted that deformations larger than yield in one direction have a significant effect on the response in the second direction.

From the above, it appears that lower axial load and better confinement reduce the effects of biaxial loading. Although it is clear that the biaxial interaction leads to more strength and stiffness degradation, it is not apparent whether the displacement capacity is adversely affected, especially for well confined columns with low axial load intensities.

Several analytical studies have been carried out on bidirectional response. Nigam [74] conducted a series of analyses using a coupled bilinear plasticity model. He found that stiff structures with periods less than 0.5 seconds experience a significant increase in ductility demands due to bidirectional loading, while flexible structures (T > 1 second) were virtually unaffected. Pecknold [83] performed analytical studies using a coupled bilinear hysteretic model. He observed that biaxial ground motion input almost doubles ductility demands for stiff structures (T ≤ 0.3 seconds), but has little effects for longer periods. Aktan et al. [3] compared the analytical response of a reinforced concrete member to one and two horizontal components. They found that relying on unidirectional analysis results in unconservative estimates of displacement when compared to bidirectional analysis.

2.4   SEISMIC DESIGN OF REINFORCED CONCRETE COLUMNS

This section presents a discussion of the seismic design practice of reinforced concrete bridges in California. Because of the time frame during which the specimens were designed, emphasis is placed on the Caltrans Bridge Design Specifications [97]. Basic issues related to performance goals, seismic design forces, and proportioning and detailing are also discussed.

2.4.1   Design Philosophy

Historically, ordinary bridges have been designed for a collapse prevention criteria. That is, under the design basis earthquake, the bridge should not collapse. Recently, Caltrans design procedures such as the new Seismic Design Criteria [99], and the ATC-32 recommendations[5] have suggested two performance goals for bridges based on service level and repairability of damage, and two levels of seismic hazard (Table 2-2).

The seismic hazard levels consist of a *Functional-Level Design Earthquake* corresponding to a smaller event with a relatively large probability of occurrence, and a larger *Safety-Level Design*

Table 2-2 Seismic performance criteria in ATC-32 [5].

Ground Motion at Site	Ordinary Bridges	Important Bridges
Functional-Evaluation Ground Motion	Service Level - Immediate Repairable Damage	Service Level - Immediate Minimal Damage
Safety-Evaluation Ground Motion	Service Level - Limited Significant Damage	Service Level - Immediate Repairable Damage

Earthquake with a return period of about 1000-2000 years. For special or critical bridges (Important Bridges), the bridge is expected to be operable immediately after the design seismic event. As such, it is expected that structural damage should be limited, even under the larger *Safety-Level Design Earthquake*, which is often referred to as *Maximum Credible Earthquake* (MCE). The second service level is for ordinary bridges where the bridge may sustain significant damage but preserve life safety by not collapsing under the larger *Safety-Design Event*. As such, considerable damage may be anticipated and the damaged portions of the bridge may have to be demolished and rebuilt prior to restoration of traffic. Both types of bridges would be required to be operational immediately following a more frequent and less severe ground motion corresponding to the *Functional-Design Earthquake*.

2.4.2   Design Seismic Loads

Generally, seismic-resistant design of bridges is based on elastic modal analysis procedures. These procedures generally utilize an elastic response spectrum that accounts for the type and magnitude of earthquake expected on faults near the bridge, the distance to the fault rupture and the local soil conditions. An example of such a spectrum is the Caltrans ARS spectrum shown in Figure 2-1.

As indicated above, most bridges are not expected to remain elastic during earthquakes. This is based on the high cost of constructing a structure strong enough to remain elastic under the very rare design earthquake, and the fact that excellent response can be achieved by structures designed to sustain deformations in the inelastic range of behavior. However, in conventional reinforced concrete bridges, inelastic deformations are associated with damage, such as permanent cracking and spalling of concrete, residual displacements, fracture or buckling of reinforcement and, for sufficiently large inelastic deformations, loss of structural integrity. Thus, care must be exercised to limit inelastic deformations to levels appropriate for the intended performance.
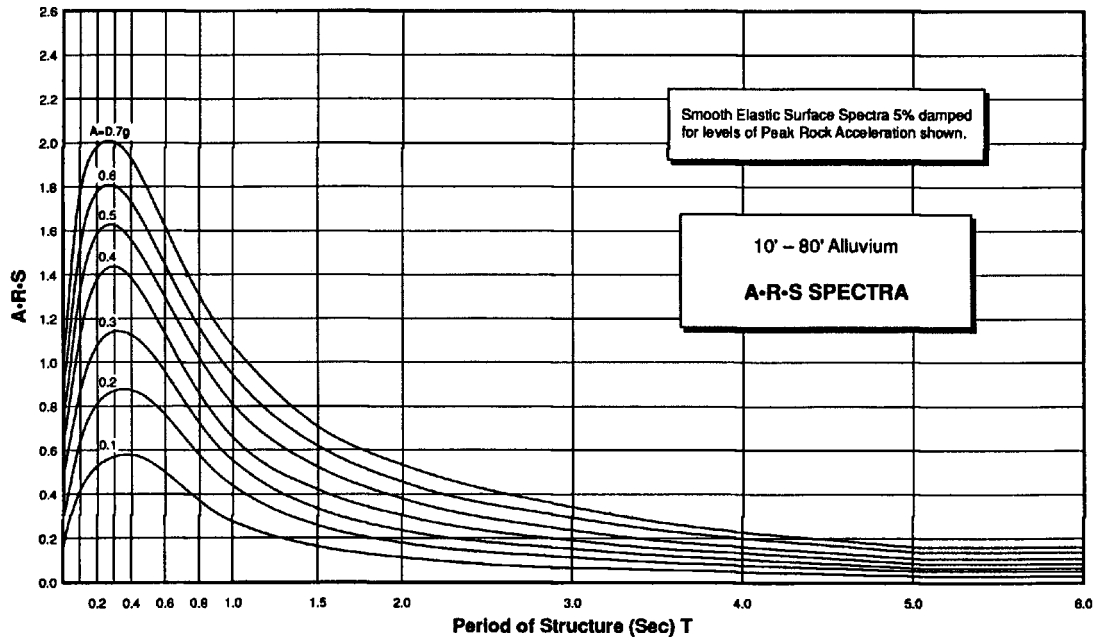
Figure 2-1. ARS spectra for 10-80 ft of alluvium soil (Figure 3.21.4.3B in BDS [97]).

To achieve this ductile response, a response modification factor has historically been used to reduce seismic design forces relative to those expected in a bridge if it remained elastic. In the 1991 Bridge Design Specifications [97], the modification factor is called a Risk and Ductility Factor, Z. It is also referred to as a Force Reduction Coefficient in ATC-32. A variety of studies have examined the reliably of such factors (e.g. Miranda and Bertero [66], Mahin and Bertero [55], Nassar and Krawinkler [73]). Such studies indicate that the factor ideally depends on the period of the structure, and to a lesser extent on its hysteretic and damping characteristics. Historically, values of Z have ranged from 3 to 6 for ordinary bridges depending on the type of structure, fundamental period, the component being designed and detailing provided, and from 1 to 2 for important bridges.

As implemented in the BDS, this force reduction factor approach suggests that the global earthquake-induced displacements in the bridge are similar to those predicted assuming elastic response under the design level earthquake. This has been shown to be reasonable for intermediate to long period structures, but near-fault and soft soil ground motions may cause larger than elastic displacements for intermediate period range structures. Additionally, yielding structures with short periods are generally expected to have displacements significantly larger than predicted elastically [66]. ATC-32 has recognized this fact by incorporating a displacement amplification factor that

18

Full Ductility Structures
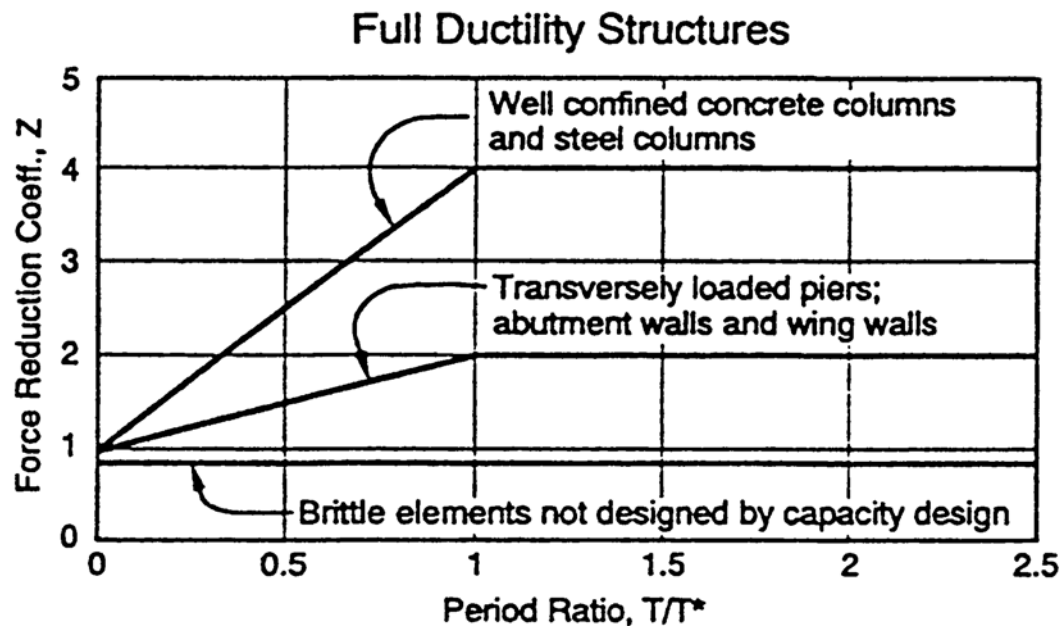
Figure 2-2. ATC-32 Force Reduction Coefficient [5].

increases deformations for short period bridges (ATC-32 Section 3.21.10.1). More recent Caltrans recommendations in the 1999 Seismic Design Criteria [98] have implemented a more direct approach where designers are required to develop a force-deformation relation for a bridge based on material, geometric and other nonlinearities, and demonstrate by means of such a static "push-over" analysis that the bridge has adequate displacement capacity, both locally and globally (SDC 3.1.2). The largest uncertainty in both the response modification factor approach and the static pushover analysis approach is the displacement demand that the structure must be designed to withstand.

A further complication regarding predicting the lateral displacement demand arises when considering two horizontal components of input motion. Bidirectional seismic effects have been considered in Caltrans and other bridge design specifications for many years. For dynamic analysis, the full response spectrum or acceleration record is imposed along both principal axes of the bridge. Equivalent static approaches typically try to approximate the results of such analyses by simultaneously imposing 100% of the equivalent static seismic design load along one principal direction of the bridge, and 30% of the design load along the perpendicular direction (and vice versa). While this approach would be expected to work reasonably well for systems that respond elastically, previous research has suggested that the maximum displacements of ideal elasto-plastic

19

systems may be much larger than predicted by the maximum unidirectional or SRSS combined bidirectional elastic responses ([3], [83]). Strength and stiffness degradation add further uncertainties regarding these predictions of inelastic displacement demands, and correspondingly, on the local inelastic deformations in yielding elements.

2.4.3 Proportioning and Detailing Considerations

Generally, earthquake damage to bridge structures is intended to concentrate in specially designed, ductile columns. Flexure is the preferred mode of behavior, and various provisions are stipulated in design standards to delay more brittle failure modes, such as shear, axial load or anchorage. Thus, a cantilever column would be expected to develop the most severe damage near its fixed end(s), where moments are largest. Conservative estimates of the flexural strength of columns are used to size adjacent elements to insure that they are stronger than the column.

Under monotonically increasing lateral loading, a column would be expected to crack when stresses, due to bending, axial load, shrinkage, temperature and other factors, exceed the tensile strength of the concrete. In a properly designed column, subsequent lateral loading will increase bending stresses in the cracked section, leading to tensile yielding in some of the longitudinal reinforcement. For columns with ductile detailing, or low axial loads, typical reinforced concrete columns should be able to sustain significant inelastic behavior (evidenced by disproportionate increases in lateral displacement with additional loading, widening flexural cracks and yielding of longitudinal reinforcement) prior to crushing and spalling of the concrete cover on the compression side of the member. Prior to crushing, residual damage observable after removal of the applied lateral loads may be small, and well-documented principles of mechanics can be used to predict the flexural strength and lateral displacement of the column. Under load reversal, the same basic behavior is expected, but the column will exhibit various forms of stiffness degradation due to cracks remaining open across the entire section during portions of the loading cycle, Bauschinger effects in previously yielded steel, and intermittent yielding of the compression steel (in columns with significant axial load), as well as the possibility of increased deformations due to the accumulating effects of shear and bond deterioration. Most design-oriented models for predicting strength and deformation capacity only consider monotonic loading conditions.

For circular columns with confinement provided by closely spaced spiral reinforcement, significantly larger inelastic deformations can occur beyond crushing of the cover concrete before the column begins to lose substantial strength. The ultimate failure mode depends on a number of

factors including the quantity and distribution of transverse and longitudinal reinforcement, the aspect ratio, the axial load, the strength of the concrete and steel, the intensity of applied shear, and the loading history. Under monotonic loading, failure can be precipitated by a number of phenomena, including buckling of the longitudinal reinforcement acting in compression, fracture of the spiral reinforcement, and fracture of the tensile reinforcement (due to excessive strains). In the case of repeated cycles of load reversal, failure can also result from fracture of the tensile or compressive reinforcement due to low cycle fatigue as a rebar repeatedly yields or buckles in compression and then straightens and yields in tension. The shear and anchorage resistance of columns deteriorates under cyclic loading, leading to the possibilities of this mode of failure even though they might not occur under monotonic loading. Behavior near failure is quite complex and influenced by many factors. Predictive models for column displacement capacity have been developed based on the constitutive properties of confined concrete [85]. Methods to incorporate buckling and low cycle fatigue failures of reinforcing bars are currently an active area of research ([25], [28], [34], [102]).

Many of the basic analytical methods used to predict inelastic column response in flexure (i.e., fiber models) can be directly extended to predict response under bidirectional loading. However, there is some concern that additional phenomena may be introduced. For instance, torsion may be present in columns with a displacement imposed in the direction with loading applied in the perpendicular direction. This torsion may affect shear response, and change the buckling mode of the longitudinal reinforcement. Furthermore, under bidirectional loading, the cover concrete may spall entirely around the section, possibly affecting the stress distribution in the spiral reinforcement, and the plastic hinge length. Under unidirectional loading, the cover generally only spalls over a short region where the maximum compression strains develop in the concrete. If the cover spalls completely around the section during bidirectional loading, the effectiveness of spiral reinforcement in providing confinement to the concrete core and buckling restraint for the longitudinal reinforcement may be reduced (due to increased flexibility of the spirals) and the effect of fracture of a spiral would have a much more immediate adverse consequence.

2.4.4 Summary

Based on the above comments, it will be desirable to design the test specimens consistent with current design methods and assumptions. If possible, testing should obtain information regarding response: (1) near the onset of yielding (before spalling) in order to evaluate modeling

assumptions that may be used for important bridges, as well as at the functional-level earthquake for ordinary bridges, (2) under unidirectional and bidirectional input motions, and (3) considering ground motion excitations representative of intense near-field sites as well as of longer duration motions. These objectives can be achieved by comparing the ultimate failure mode observed in the shaking table tests with those anticipated from quasi-statically tested specimens, identifying the effect on overall seismic demands of the deterioration in strength and stiffness that occurs near failure, and reconciling experimental results with analytical predictions.

In order to achieve all of the above, four identical circular columns with spiral transverse reinforcement were constructed. These columns were divided into pairs. One column of each pair was subjected to a single component of excitation while the second column was subjected to both horizontal components of ground shaking. For the first pair (Specimens A1 and A2), a near fault ground motion was considered, whereas a longer duration motion was employed for the second pair (Specimens B1 and B2).

2.5   CAPACITY DESIGN

Because the intended inelastic behavior mode of the column is flexure, the prototype column and test specimen were designed so that other failure modes would occur after the formation of a plastic hinge at the base of the column. Thus, efforts were made to prevent premature failure due to loss of confinement, shear, anchorage, and foundation failure. At the time of design of the columns of this study, the SDC requirements were not finalized yet, and the BDS requirements were followed. Hence, the following discussion is focused on the BDS requirements. The SDC requirements are visited in Chapter 7.

2.5.1   Confinement

In order to withstand high ductility demands, circular columns are reinforced with closely spaced continuous spiral reinforcement or welded circular hoops. This transverse reinforcement increases toughness and ductility, and increases the shear capacity of the column. Several equations are in use to determine the minimum amount of spiral reinforcement needed to confine spirally reinforced columns. This is determined in terms of a volumetric spiral reinforcement ratio which is defined as the ratio of spiral reinforcement volume to the volume of the concrete core. The

volumetric spiral reinforcement ratio for a column with core diameter D_c, and spiral reinforcement having an area A_{sp} and pitch s is given by Equation 2-1:

$$\rho_{sp} = \frac{V_{sp}}{V_{core}} = \frac{4A_{sp}}{D_c s} \tag{2-1}$$

Equation 2-2 indicates the requirement stipulated in the 1991 Caltrans Bridge Design Specification (Section 8.18.2.2.2),

$$\rho_{sp} = 0.45\left(\frac{A_g}{A_c} - 1\right)\frac{f_c'}{f_{yh}} \tag{2-2}$$

where f_{yh} is the nominal yield strength of the spiral and is not to exceed 60,000 psi (414 MPa). Furthermore, for potential plastic hinge regions, the spiral reinforcement ratio should not be less than:

$$\rho_{sp} = 0.45\left(\frac{A_g}{A_c} - 1\right)\frac{f_c'}{f_{yh}}\left(0.5 + \frac{1.25P}{f_c'A_g}\right) \tag{2-3}$$

for columns less than 3 ft (914 mm) in diameter, and:

$$\rho_{sp} = 0.12\frac{f_c'}{f_{yh}}\left(0.5 + \frac{1.25P}{f_c'A_g}\right) \tag{2-4}$$

for columns larger than 3 ft in diameter. In these equations, ρ_{sp} is the volumetric spiral reinforcement ratio, f_c' is the concrete compressive strength, A_g and A_c are the gross and core areas of the section, while P is the axial load on the column (See Figure B-1 for more details). Within the plastic hinge region, the maximum spiral pitch is 4 in. (100 mm).

2.5.2   Shear

To prevent a premature shear failure, BDS stipulates the column must be designed for the maximum probable shear in the column when the full flexural plastic moment, M_p, develops. ATC-32 recommends using 1.4 times the design flexural strength corresponding to a maximum concrete compressive strain of 0.004, and using expected materials strengths of $f_{ce}' = 1.3f_c'$ and $f_{ye} = 1.1f_y$ for concrete and steel, respectively. Alternatively, M_p may be obtained from a pushover analysis up to the expected design displacement, where maximum possible material properties of $f_{co}' = 1.7f_c'$ and $f_{yo} = 1.7f_y$ are assumed. This amplified moment accounts for actual material strengths being higher than minimum specified values, as well as for strain hardening in the steel and confinement and aging effects in the concrete.

23

For a pin ended cantilever column, such as considered for the prototype, the design shear force is usually taken as M_p/L, where L is the length from the plastic hinge to the center of the applied lateral load. In actuality, a column will have some fixity at the top due to higher mode effects and to inherent rigidity of the connection to the superstructure. Any moments developed at the top will increase the column shear. The ultimate shear design force is usually taken in the range of M_p/L to $2M_p/L$.

Shear capacity is estimated using standard procedures. The American Concrete Institute Committee 318 [2] and ATC-32 [5] contain similar provisions for estimating shear capacity, while the SDC uses somewhat different equations (see Section 7.3.2.2 for the SDC procedure). A reduction factor (ϕ) for shear capacity may or may not be used depending on the design provisions being followed.

2.5.3   Bar Anchorage

In addition to checking the transverse reinforcement and shear capacity, the anchorage of the bars should be checked at locations of extreme actions. Splice lengths should also be checked for adequacy. In general, splicing should be avoided in plastic hinge regions. Design guidelines must be followed in order to prevent undesirable anchorage and bond failures in seismic components. For example, the BDS requires that the basic development length in tension for #11 bars and smaller be computed using Equation 2-5, and that Equation 2-6 be used to compute the basic development length in compression. Hooks may be used for bar development in tension to reduce development length requirements; the development length for hooks in tension, is given in Equation 2-6 for bars having a yield strength of 60,000 psi (414 MPa).

$$\text{Tension: } l_{db} = \frac{0.04 A_b f_y}{\sqrt{f_c'}} \text{ (psi units)} \tag{2-5}$$

$$\text{Compression: } l_{db} = \frac{0.02 d_b f_y}{\sqrt{f_c'}} \text{ (psi units)} \tag{2-6}$$

$$\text{Standard hook: } l_{dh} = \frac{1200 d_b}{\sqrt{f_c'}} \text{ (psi units)} \tag{2-7}$$

Additional factors may be applied to the above expressions to obtain the final lengths (see BDS Section 8.25). Similar expressions are provided by other codes and recommendations such as ACI-318 [2] and ATC-32 [5].

2.5.4 Summary

These capacity design concepts were considered and used in the design of the test speci-
mens. The design developed was representative of Caltrans construction practices in effect during
the early-to-mid 1990's.

3 Specimen Design and Construction

3.1 INTRODUCTION

The prototype column used as the basis of the test specimens is described in Section 3.2. Section 3.3 discusses the design procedure including specimen detailing and similitude scaling. The properties of the materials used are reported in Section 3.4, and the construction process is briefly documented in Section 3.5.

3.2 PROTOTYPE COLUMN

For simplicity in achieving the objectives of this investigation, the specimens are assumed fixed at the base and pinned at the top. The prototype column has a circular cross-section with a diameter of 6 ft (1.83 m). The prototype column diameter was selected in accordance with previous research performed at UC Berkeley ([34], [50], [51] and [52]). The length of the column was initially undefined ($L = a_r D$), in order to assess the effect of aspect ratio a_r (column length to diameter) on dynamic response.

The axial load in the prototype column was taken to be $0.1 A_g f_c'$ based on the nominal strength specified for the concrete (3250 psi or 22.4 MPa). The inertial mass tributary to the column was then taken to be a multiple α of the weight supported by the column (divided by g). That is $m = \alpha(0.1 A_g f_c'/g)$. The period of the column was then estimated for design purposes as $T = (2\pi)^{-1}\sqrt{m/k}$, where $k = 3EI_{eff}/(a_r D)^3$ corresponding to a fixed ended cantilever. While methods that are more precise are possible, EI_{eff} was initially taken to be $EI_{gross}/2$ [8]. Columns having a variety of aspect ratios ($a_r = 4$, 6, 8 and 10) and mass effectiveness ratios ($\alpha = 1$, 2 and 3) were designed. Each column was designed to withstand demands estimated using the ARS response spectrum (Figure 2-1) corresponding to stiff soil sites representing alluvium with depth of 10 ft to 80 ft (3.05 m to 24.4 m), with 0.7g peak acceleration, and 5% structural damping. Con-
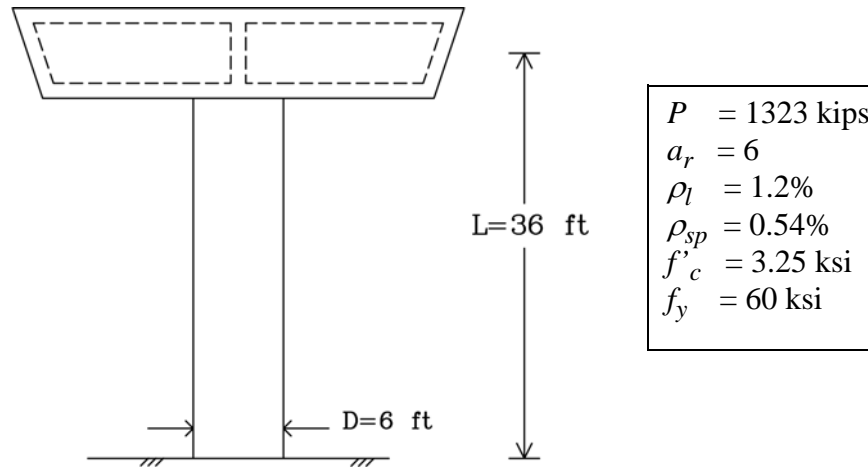
Figure 3-1. Prototype Column (1 ft = 0.3048 m).

sistent with practices in the early 1990's, a Z factor of 4 was assumed. The required yield strength F_y of the column was determined from the spectral acceleration Sa at the structural period and the supported mass m as follows:

$$F_y = \frac{Sa \cdot m}{Z} \tag{3-1}$$

When the percentage of longitudinal reinforcement required fell below 1% for a particular combination of parameters considered, a longitudinal reinforcement ratio of 1% was provided. When the required amount of longitudinal reinforcement exceeded 3.0%, the design was considered infeasible. The feasible columns were subjected to detailed nonlinear dynamic analyses using a single component of 10 near-fault ground motion records. More than 500 time history analyses were performed and interpreted to identify feasible designs for testing. Based on an interpretation of these results, consultation with Caltrans, and a review of aspect ratios used in practice, an aspect ratio a_r of 6 and a mass effectiveness ratio α of unity were selected for the test program.

Once the overall dimensions and general properties of the prototype column were known, and the column design was completed, a second analytical study was subsequently undertaken. About 300 unidirectional and bidirectional time-history analyses using detailed fiber element models were performed to finalize dimensions and select appropriate ground motions for consideration in the tests. This has resulted in the selection of the Olive View record of the 1994 Northridge earthquake and the Llolleo record of the 1985 Chile earthquake.

3.3   SPECIMEN DESIGN

Due to the limitations of testing equipment and cost considerations, tests are not usually carried out at full scale. This is especially true for shaking table tests, where limitations arise from the physical size of the table, as well as from limits on the displacements, accelerations and velocities that can be imposed by the table. Thus, most test specimens need to be constructed at a reduced scale.

As a result of these considerations, the diameter of the model column was set at 16 in. (406 mm) which corresponds to a prototype to model length scale factor of 4.5. This scale factor was used to compute the other quantities and dimensions. Detailed calculations may be found in Appendix B.

3.3.1   Model Scaling

Dimensional analysis provides guidance on how to scale the dimensions, material properties, and loads for the model specimen. Scaling rules are relatively straight-forward for statically loaded specimens. For dynamic tests, time and time-dependant parameters (such as acceleration, velocity and strain rate) must also be considered. Table 3-1 summarizes dimensional similitude require-ments for dynamic tests for the condition that the acceleration of gravity is maintained. In this case, strains developed in the test specimen and prototype are identical, and by using the same materials in the model and prototype, the same stresses would be anticipated in both. For a more complete treatment of similitude requirements, the reader is referred to Krawinkler and Moncarz [45].

It should be noted that it is not always practical or physically possible to scale all quantities properly. For instance, if a very small-scale model is used, scaling concrete material becomes prob-lematic. Microconcrete, in which the aggregate and sand dimensions have been scaled, does not have the same mechanical properties as the full sized material. Generally, the tensile strength of microconcrete is too large, affecting cracking, shear, bond and other aspects of element behavior. When such phenomena have a significant impact on overall behavior, it is desirable that specimens be constructed as near to full-scale as possible. For large reduced-scale test specimens, a regular concrete mix design having slightly reduced-size aggregates is usually employed.

In this project, nearly all of the properties of the test specimen were modeled in accordance to the relations contained in Table 3-1. The only exception was the mass density of the concrete, which was not changed. The required density to preserve similitude would have been higher than practical to achieve. However, since the mass of the column is small in comparison to the total iner-

Table 3-1 Similitude requirements and scaling factors for the tested columns [45].

Quantity	Scale Symbol	Target Scale Factor	Scale Factor Value Used
Length	S_d	S_d	4.50
Time	S_t	$S_d^{1/2}$	2.12
Frequency	S_ω	$S_d^{-1/2}$	0.47
Displacement	S_d	S_d	4.50
Velocity	S_v	$S_d^{1/2}$	2.12
Acceleration	S_a	1	1
Mass Density	S_ρ	S_E / S_d	1.0 (0.22 target)
Strain	S_ε	1	1
Stress	S_σ	S_E	1
Modulus of Elasticity	S_E	S_E	1
Force	S_F	$S_E S_d^2$	20.25
Moment	S_M	$S_E S_d^3$	91.13
Energy	S_W	$S_E S_d^3$	91.13

tial mass being considered for the specimen, the error in using regular concrete for the column is considered negligible. However, since the supporting mass block was also constructed from normal weight concrete, its dimensions were made larger. This resulted in a larger mass moment of inertial than expected if the mass block were constructed from a denser material. However, the resulting mass moment of inertia was still consistent with one that might be encountered in an actual bridge (See Section B.6).

3.3.2 Design of the Test Specimen

Four identical 16 in. (406 mm) diameter model columns were designed. The clear cover to the spiral reinforcement was set to 1/2 in. (13 mm). See Figure B-1 for section dimensions and notations.

The aspect ratio selected for the specimens was 6. As a result, the height from the base of the column to the center of mass was 96 in. (2.44 m). However, because of the finite size of the inertial mass block, the actual clear distance from the base of the column to the bottom of the mass block was 64 in. (1.63 m). The design axial load was 65 kips (289.1 kN) or 10% of $A_g f_c'$ (assuming a typical Caltrans design strength of 3250 psi or 22.4 MPa). Since the actual concrete strength was about 5700 psi (39.3 MPa) on average at the time of testing, the real axial load ratio was about 6%

of $A_g f_c'$. The column details are illustrated in Figure 3-2. Figure 3-3 shows the details of the column-footing connection. Figure 3-4 shows the steel layout in the whole specimen.

3.3.2.1   Column Longitudinal Reinforcement

The longitudinal reinforcement of the column consisted of 12 #4 deformed grade 60 (A706) reinforcing bars. This resulted in a reinforcement ratio of about 1.20%. A moment capacity of about 1500 kip.in (170 kN.m) was calculated at the design axial load. The amount of steel reinforcement was chosen to provide enough strength according to the Caltrans ARS spectra (Figure 2-1). The development length of the #4 bars into the top slab was checked for both tension and compression using the requirements of the BDS. The bars were developed into the footing using 90 hooks, bent outwards with a bend diameter of 6 d_b as shown in Figure 3-3, and a development length conforming to BDS (Equation 2-7).

3.3.2.2   Column Spiral Reinforcement

Since the prototype column had a diameter of 6 ft, Equation 2-4 was used to size the column spiral reinforcement. The spiral reinforcement consisted of W2.5 undeformed wire, which has a cross-sectional area A_{sp} of 0.025 in.^{2} and a diameter d_{sp} of 0.178 in. A continuous spiral with a pitch of 1.25 in. was built for each column. The resulting volumetric ratio of the spiral reinforcement was 0.54% (See Appendix B). The provided transverse reinforcement was also found to be satisfactory for shear resistance. The column's shear capacity was computed using both the BDS and ATC-32 shear equations. Using the BDS equations, the designed column was found to have a factor of safety against shear failure of 5.3 assuming cantilever action ($V_u = M_p/L$), and 2.65 for fixed conditions ($V_u = 2M_p/L$). The ATC-32 equations yielded slightly higher factors of safety equal to 6.8 and 3.4, respectively.

3.3.3   Footing and Top Slab

The column was connected to a square slab at each end as show in Figures 3-2 to 3-4. The slabs will be designated *footing* and *top slab* in the remainder of the report. The footing and top slab were both 8 ft x 8 ft (2.44 m x 2.44 m) in plan and 16 in. (406 mm) thick. The footing was cast first with a cold joint at the column-footing interface, while the top slab was cast monolithically with the column. The footing and top slab were designed to remain elastic during the test; both used identical reinforcement consisting of #5 longitudinal bars top and bottom and #2 deformed stirrups. Design forces on the footing included bending and shear due to the full development of the plastic moment capacity of the column at the base, while the upper slab was checked for bending and shear due the

Elevation

Notes:

1. Four identical specimens to be constructed
2. No splices will be allowed in column longitudinal reinforcement or spiral
3. Cross section shown below
4. Transverse Reinforcement in Footing and Top Block not shown

Cross Section (A-A)

$\frac{1}{2}''$ Clear Cover to Spiral

12 No. 4

16''

W2.5 Continuous Spiral @ 1.25''

16''

16''

64''

40''

36''

2''

16''

SYMM.

96''
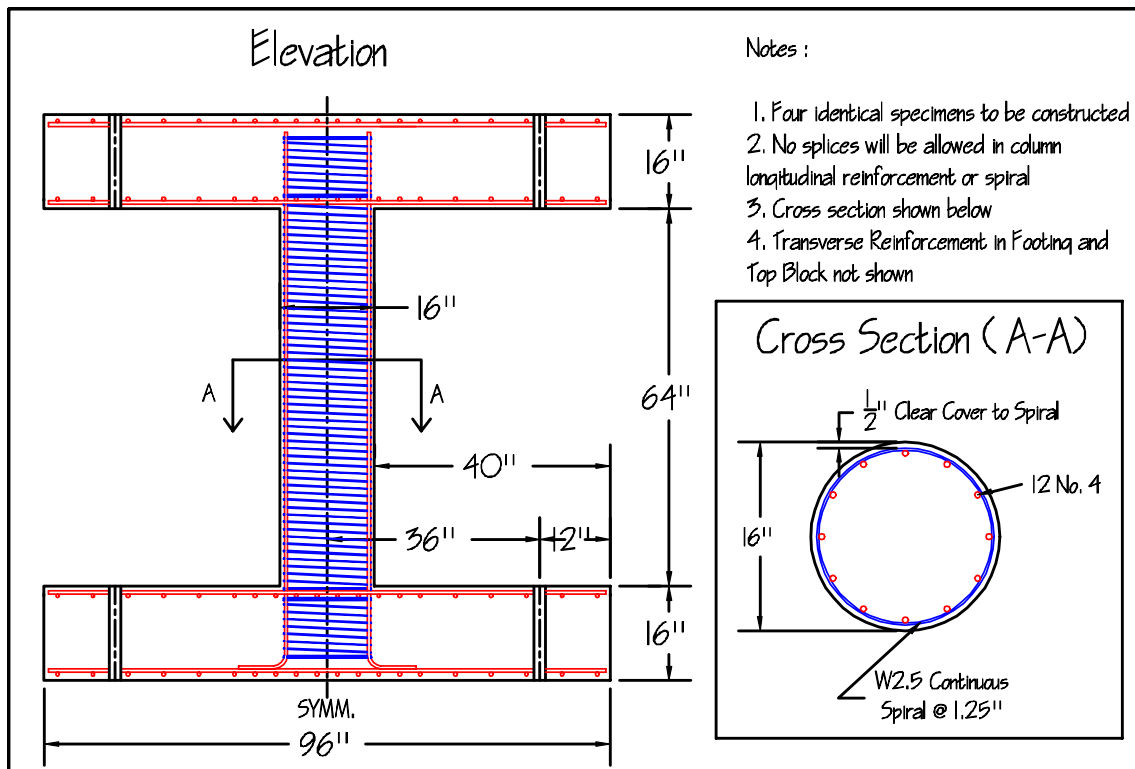
Figure 3-2. Specimen dimensions and reinforcement details.

12'' 28'' 16'' 28'' 12''

May be absent in some sections (Typical)

W2.5 Spiral @ 1.25''

No. 5 Bars

1''

5 spacings @ 6''

4 x 3$\frac{1}{2}''$

$\frac{3}{4}''$

SYMM

$\frac{1}{2}''$ Clear Cover

2'' PVC Pipe

No. 2 stirrup ties in both directions

Bent Bar Detail

R1$\frac{1}{2}''$

6''
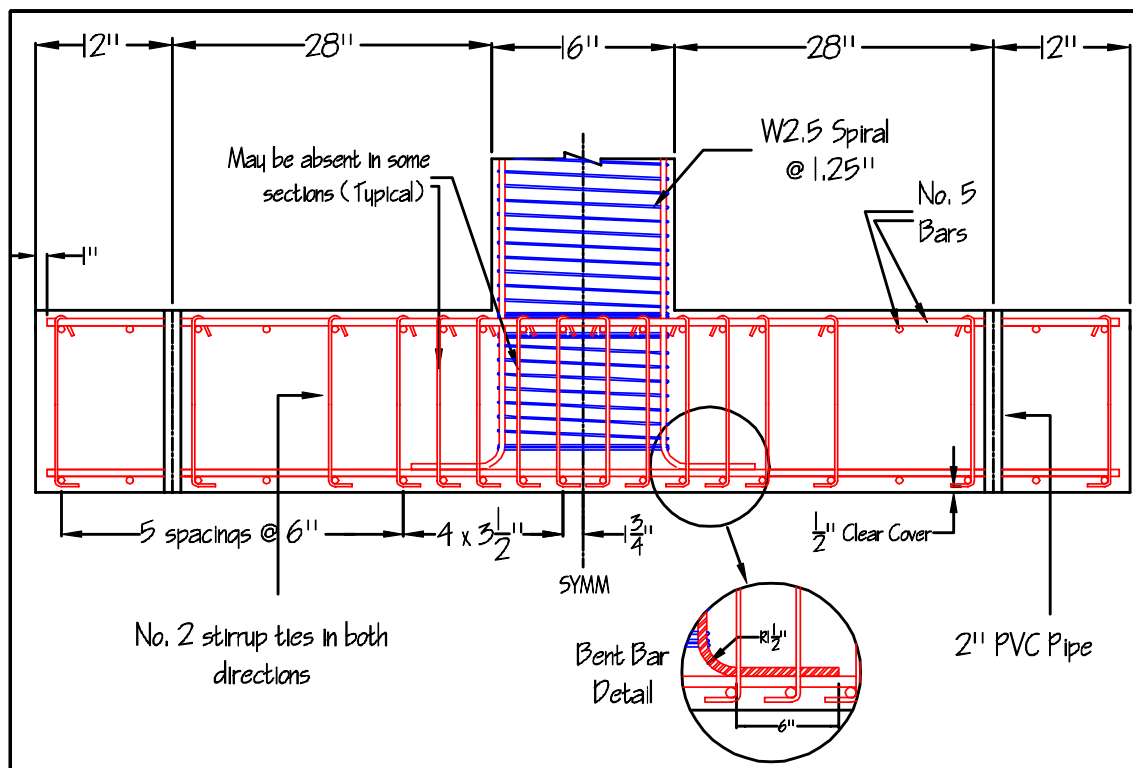
Figure 3-3. Footing details.
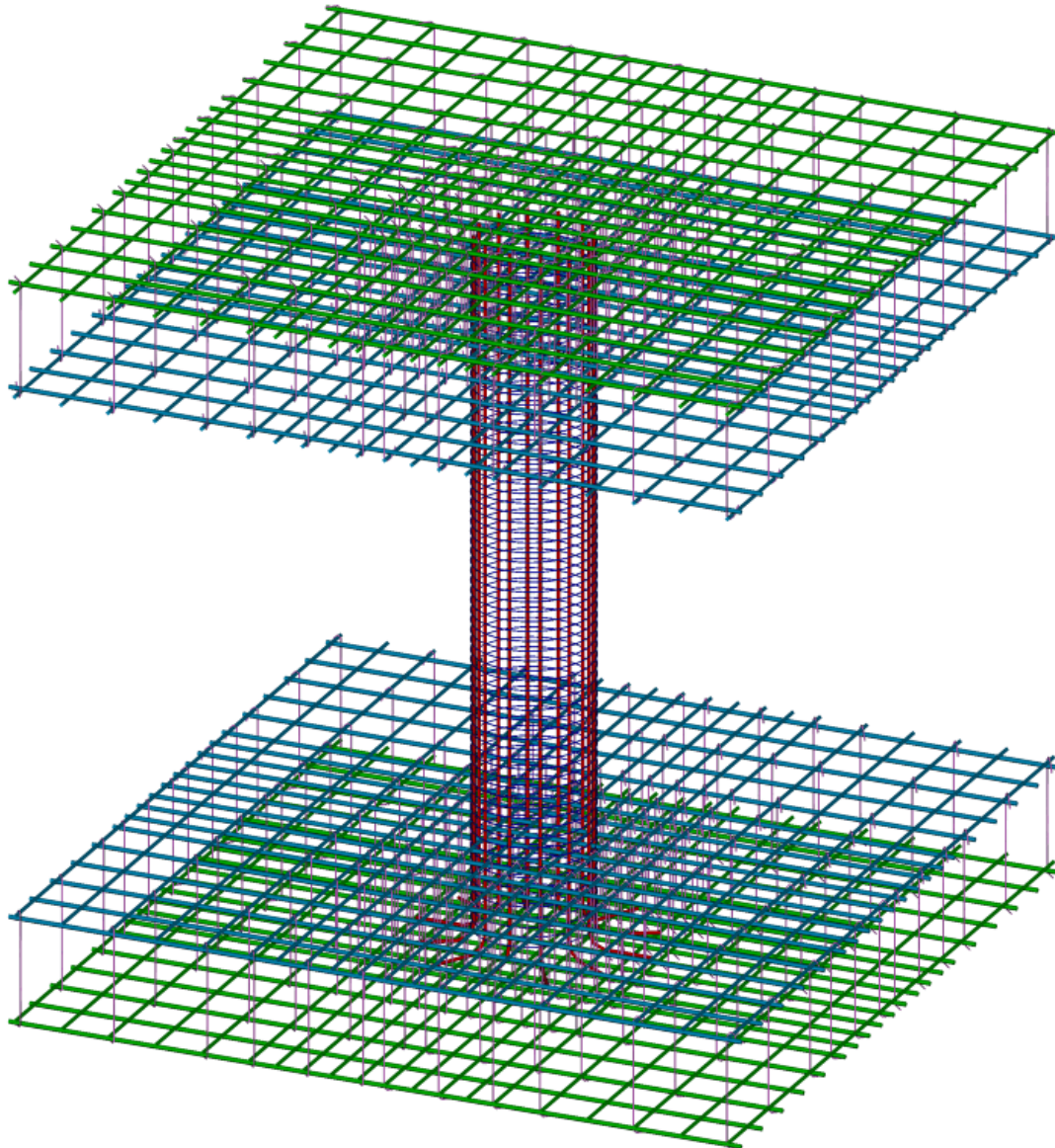
Figure 3-4. Steel layout of the column, footing and top slab.

supported load of 65 kips. The specimen was symmetric in the vertical direction, except that the column bars were developed into the footing with a standard 90° hook turned to the outside of the column (Figure 3-2), but straight anchorage was provided in the top slab, in order to facilitate construction. The column bars were checked for development length in the top slab. The anchorage length of 13 in. (330 mm) was sufficient for full development of the #4 bars. The footing had 8 holes that were used for prestressing the footing to tie-down holes on the shaking table. The top slab had similar holes that were used for attaching the remainder of the mass block.

The footing was detailed with #5 reinforcing bars. The bar spacing was 3.5 in. (89 mm) in the middle strip of the footing and was changed to 6 in. (152 mm) near the corners. Single stirrups were used every 3.5 in. (89 mm) near the center of the column, and that was progressively relaxed to 6 in. (152 mm) and 12 in. (305 mm) towards the outer sides of the footing. The footing stirrups had a 90° bend at the bottom and a 135° bend at the top. The top slab stirrups were similar but upside down. At least one stirrup was provided next to each prestressing hole to help reduce creep at locations of high stress.

3.3.4   Weight Blocks

The mass at the top of the specimen consisted of the top slab plus three square slabs with a thickness of 14 in. (356 mm) each (Figure 3-5). The weight blocks were 10 ft x 10 ft (3.05 m x 3.05 m) and weighed about 17.1 kips (76 kN) each. That resulted in a total weight of 65 kips (289 kN) supported by the column, including the weight of the top slab. Figure 3-5 shows the specimen with the weight blocks on top.

3.4   MEASURED MATERIALS PROPERTIES

3.4.1   Steel Reinforcement Properties

The column longitudinal steel was specified as grade 60 ASTM 706 steel. It was also required that all the longitudinal steel be taken from the same batch to assure uniformity. Four samples from the #4 bars were tested and the resulting stress-strain relations are shown in Figure 3-6. For the spiral steel, W2.5 plain wire grade 80 ASTM 82 was specified, and four samples were tested (Figure 3-7). The main rebar in the footing and top slab was all #5 grade 60, while the rebar used in the weight blocks consisted mainly of #4 grade 60 steel.

3.4.2   Concrete Properties

In order to represent the actual properties of concrete found in reinforced concrete bridges, the concrete was specified as normal weight (NWC) with a 28-day design strength of no less than 4000 psi (27.6 MPa) and no more than 5500 psi (37.9 MPa). Two batches of concrete were used: one for specimens A1 and A2, and the other for specimens B1 and B2. Compressive and tensile tests were performed on cylinders taken while casting the specimens. The cylinders had a length to diameter ratio of 2:1, with a 12 in. (300 mm) length.
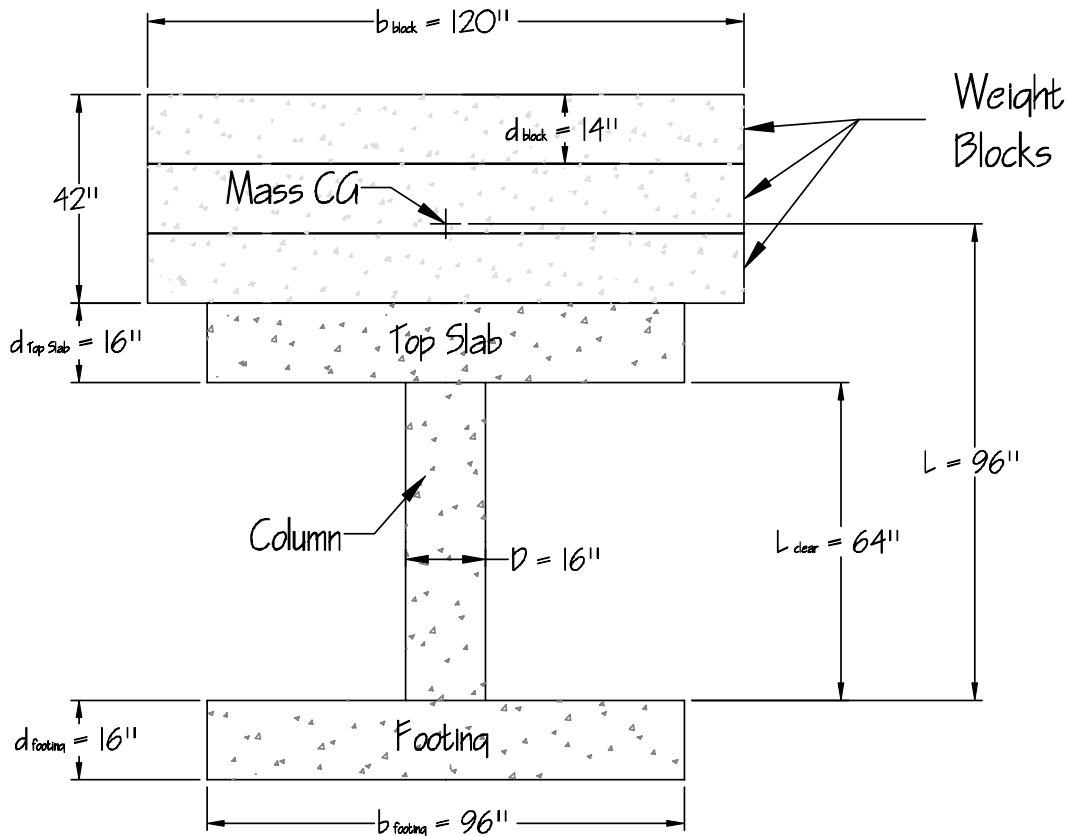
Figure 3-5. Column Dimensions.

Compressive strength tests were performed for each batch of concrete at 7, 14, 24 and 28 days after casting, and additional cylinders were tested at the time of testing. In each case, three cylinders were tested, and the results were used to compute mean and standard deviation compressive strengths (Table 3-2 and Figures 3-10 and 3-11).

The 28-day concrete strength averaged 4400 psi (30.3 MPa) for specimens A1 and A2, and 4950 psi (34.1 MPa) for specimens B1 and B2.

Additional cylinders were tested within a week of the actual shaking table test for each of the specimen sets (A and B). For each set, three cylinders were tested under compression, three under splitting tension, and five more loading tests were performed to obtain the concrete's stress-strain relation in compression. At the time of testing, the strength of the first set of columns (A1 and A2) averaged 5707 psi (39.3 MPa) with a standard deviation of 309 psi (2.13 MPa), while the second set (B1 and B2) averaged 5664 psi (39.1 MPa) with a standard deviation of 132 psi (0.91

MPa). The compressive stress-strain curves are provided in Figure 3-8 for the A1/A2 set and in Figure 3-11 for the B1/B2 set.

Splitting tension tests performed around the time of the shaking table tests, gave the following results: σ_{mean} = 414 psi (2.85 MPa), and σ_{sd} = 19 psi (0.13 MPa) for set A; and σ_{mean} = 440 psi (3.0 MPa), and σ_{sd} = 33 psi (0.23 MPa) for set B.

Table 3-2 Concrete cylinder test results for different specimens at various time intervals

	Specimens A1 and A2		Specimens B1 and B2	
Day	**Mean (psi)**	**St. Dev. (psi)**	**Mean (psi)**	**St. Dev. (psi)**
7	3020	87	3321	187
14	3783	131	4425	298
24	4429	191	4542	131
28	4397	199	4941	185
158	5707	309	-	-
184	-	-	5664	132

3.5   CONSTRUCTION

Different ways of supporting the mass were considered before deciding to prestress the mass to the top of specimen. The choice was dictated by various factors the most important being cost of construction, safety, and ease of attaching and removing.

The construction site was prepared by cleaning and leveling the ground, and setting up the wooden forms for the four specimen footings and three mass blocks. Meanwhile, part of the longitudinal reinforcement was instrumented using strain gages.

The lower layer of the footing steel was first laid in the forms. The column steel cages were next constructed with each cage consisting of 12 longitudinal #4 bars, 4 of which had strain gages attached over the height (7 strain gages on each of four bars, one on each side of the column). The continuous spiral reinforcement was then tied around the cage with a spacing of 1.25 in. (32 mm). Those cages were then installed in the middle of the footings, and tied down to the bottom steel layer (Figure 3-12). At the same time, the weight blocks were formed, and the steel layers were placed (Figure 3-15). PVC pipes were installed to provide holes extending through the footings and weight blocks. These holes were needed for attaching the weight blocks to the specimen and the footing to the simulator platform. Special inserts were installed in footings (and later in the top
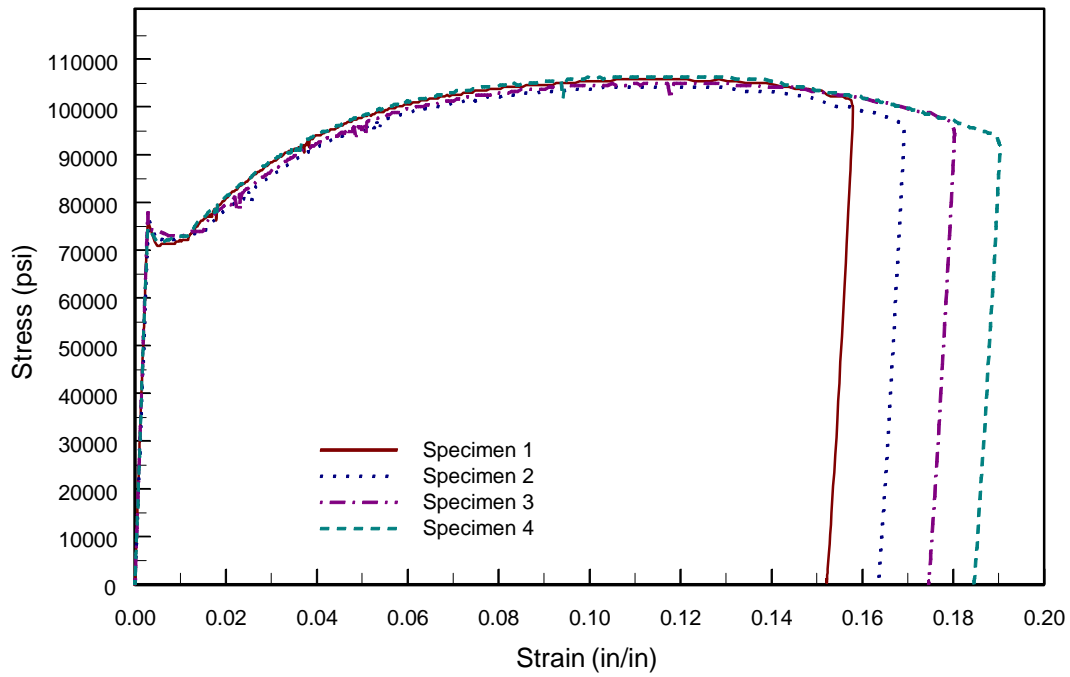
Figure 3-6. Stress-strain curve of grade 60 A706 #4 bars.
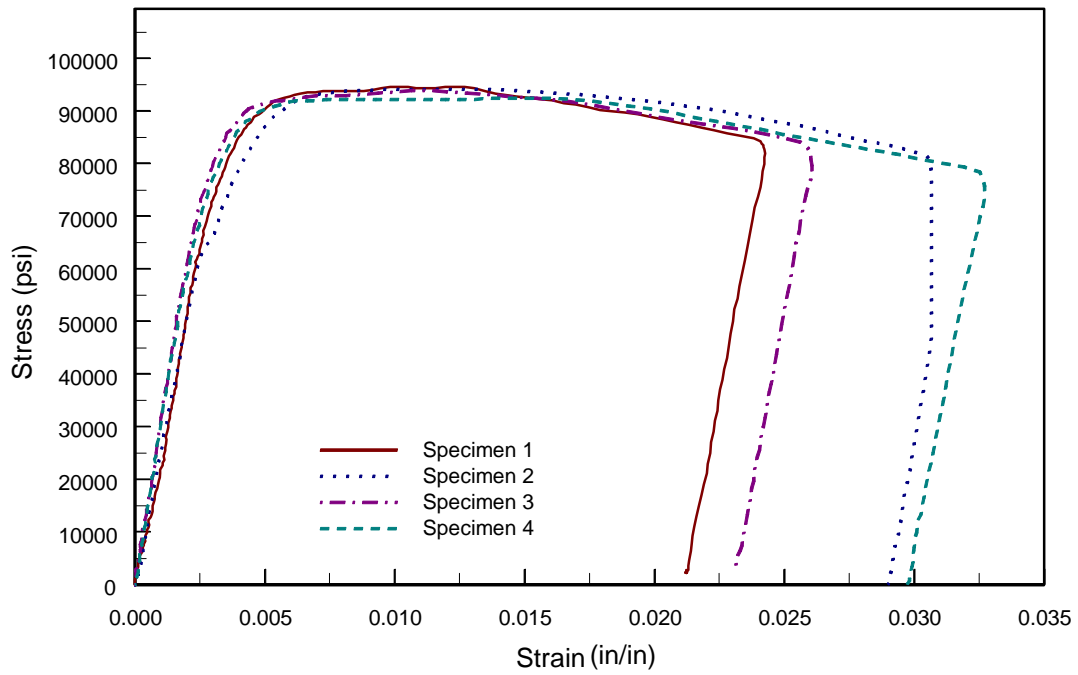
Figure 3-7. Stress-strain curve of grade 80 W2.5 spiral steel.
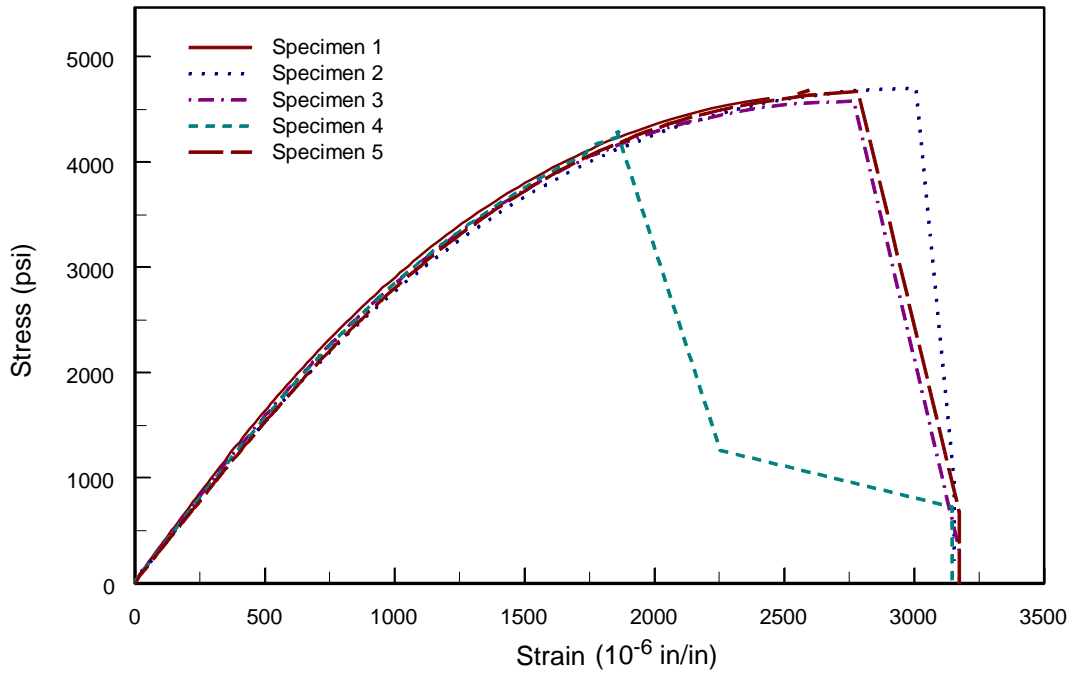
Figure 3-8. Stress-strain curve of concrete cylinders from specimens A1 and A2.
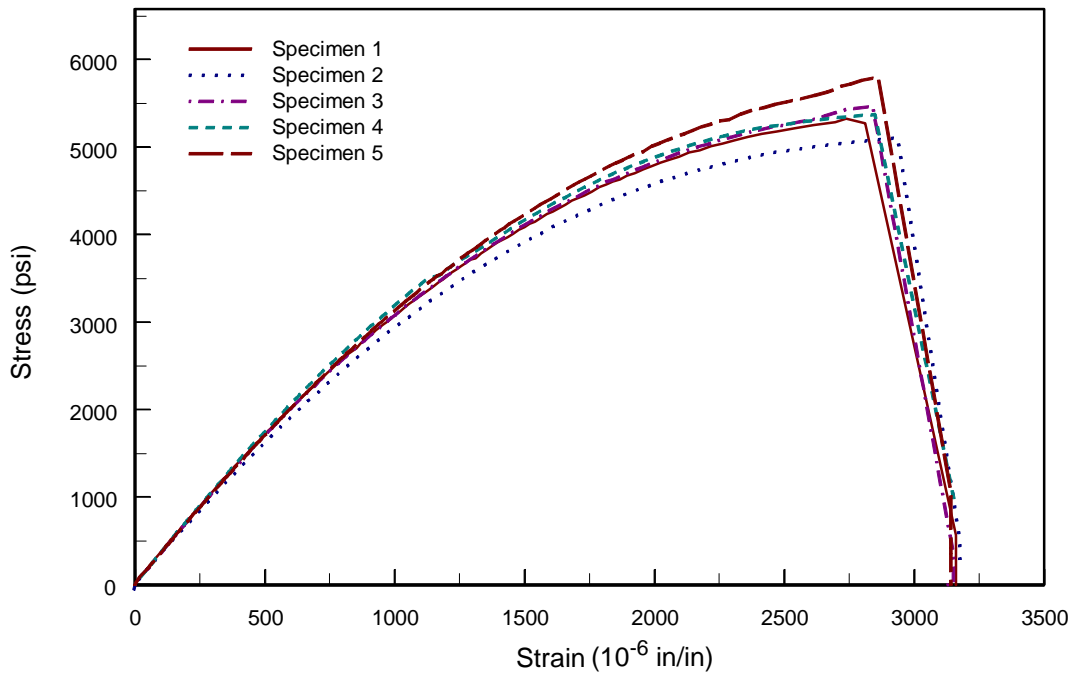
Figure 3-9. Stress-strain curve of concrete cylinders from specimens B1 and B2.
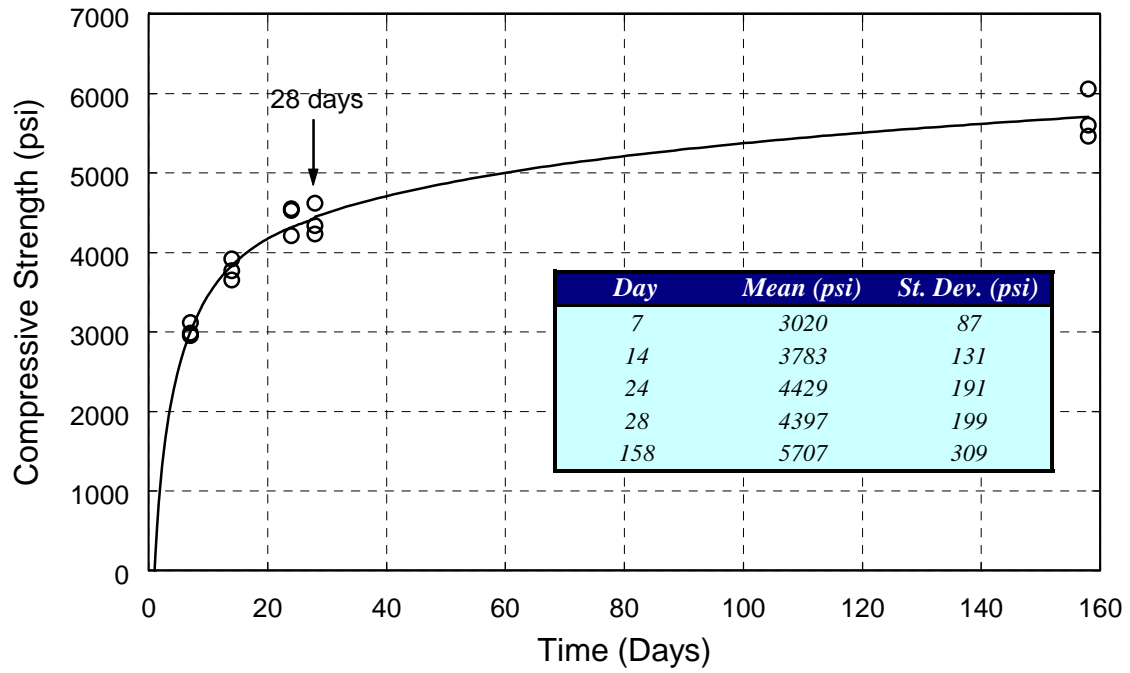
Figure 3-10. Concrete compressive strengths of specimens A1 and A2 at 7, 14, 24, 28 and 158 days.

Day	Mean (psi)	St. Dev. (psi)
7	3020	87
14	3783	131
24	4429	191
28	4397	199
158	5707	309
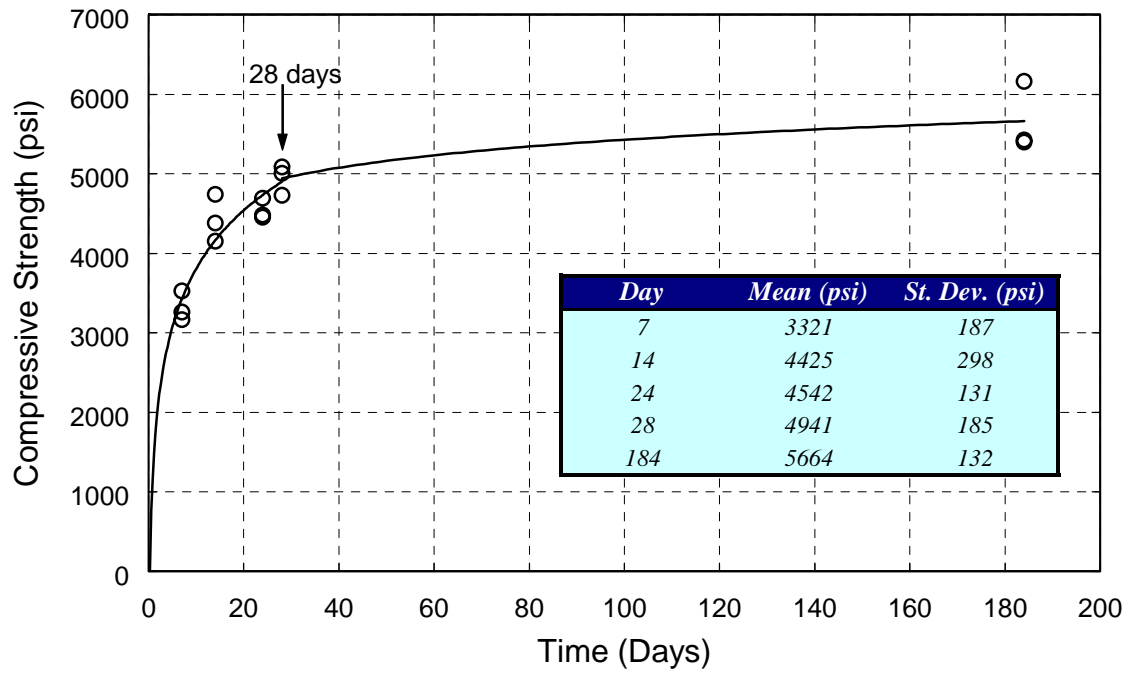
Figure 3-11. Concrete compressive strengths of specimens B1 and B2 at 7, 14, 24, 28 and 184 days.

Day	Mean (psi)	St. Dev. (psi)
7	3321	187
14	4425	298
24	4542	131
28	4941	185
184	5664	132

slab) as well as the mass blocks to allow lifting of the specimens and weights. The top layers of reinforcing steel were then placed in the footing, #2 stirrups were placed and tied, and the specimens were ready to be cast (Figures 3-13 and 3-14). Each pair of specimens (A1/A2 and B1/B2) was cast from the same concrete truck. The recorded slump was 4.5 in. (114 mm) and 2.5 in. (64 mm), respectively, for the two trucks. The weight blocks were cast from different trucks (Figure 3-16). Test cylinders that measured 6 in. (152 mm) in diameter and 12 in. (305 mm) in height were taken from all trucks. The footings were then covered with burlap and cured for seven days.

The spiral reinforcement was then strain gaged at the 4 sides of each column. A scaffolding system was next built to support the top slabs (Figure 3-17). The joint area at the column-footing interface was sand blasted and cleaned in preparation for casting the columns. Column forms were then put in place, followed by the installation of 1/2 in. (13 mm) threaded rods that were inserted transversely through the column form in order to provide a means for measuring the curvature distribution along the height of the column especially in the plastic hinge zone (Figure 3-19). Finally, the steel layers of the top slab were placed and the specimens were ready for casting (Figure 3-21). The footing forms were removed and used to form the sides of the top slabs.

The columns and the top slab were then cast monolithically. Two trucks were needed for casting the columns and top slabs. Columns in the same set (A or B) were cast from the same truck in order to be able to compare the unidirectional to the bidirectional response.

The columns and top slabs were then cured for 10 days before the formwork was removed.

Throughout the construction sequence, special care was taken to properly label and protect strain gage cables. Strain gages were also protected by applying coatings, and were tested at various stages to ensure that they were not damaged by the construction process.

Figure 3-12. The column steel cage set on the bottom steel of the footing.
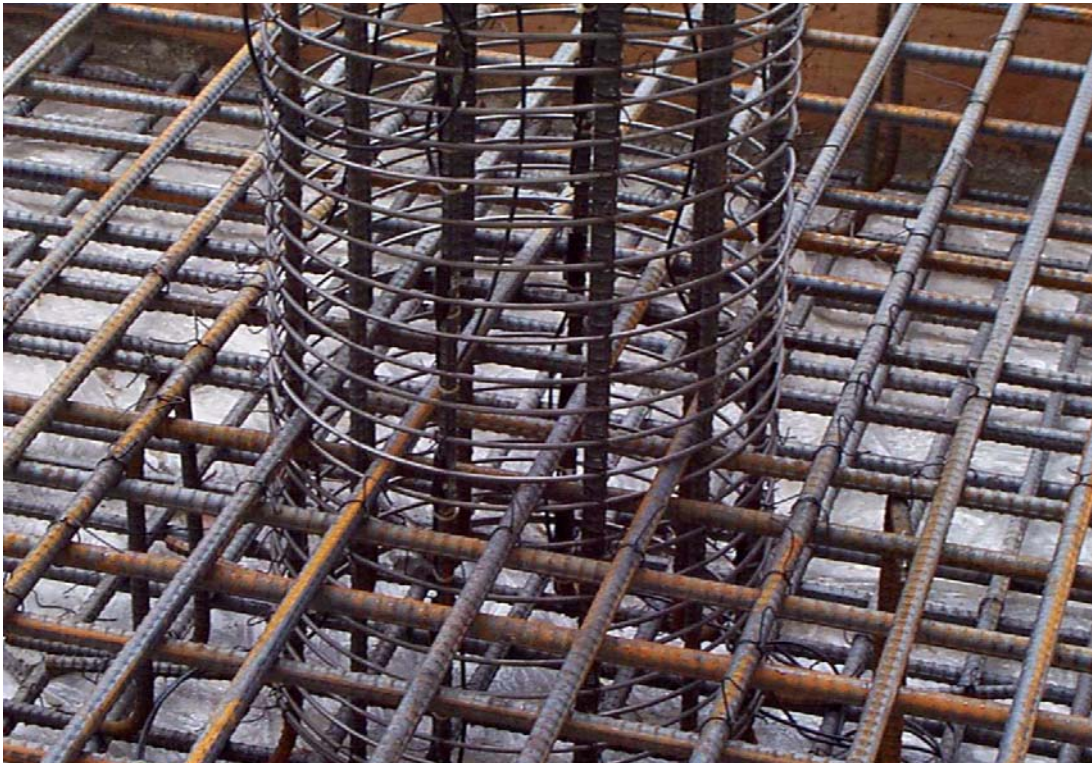
Figure 3-13. Column footing connection steel.
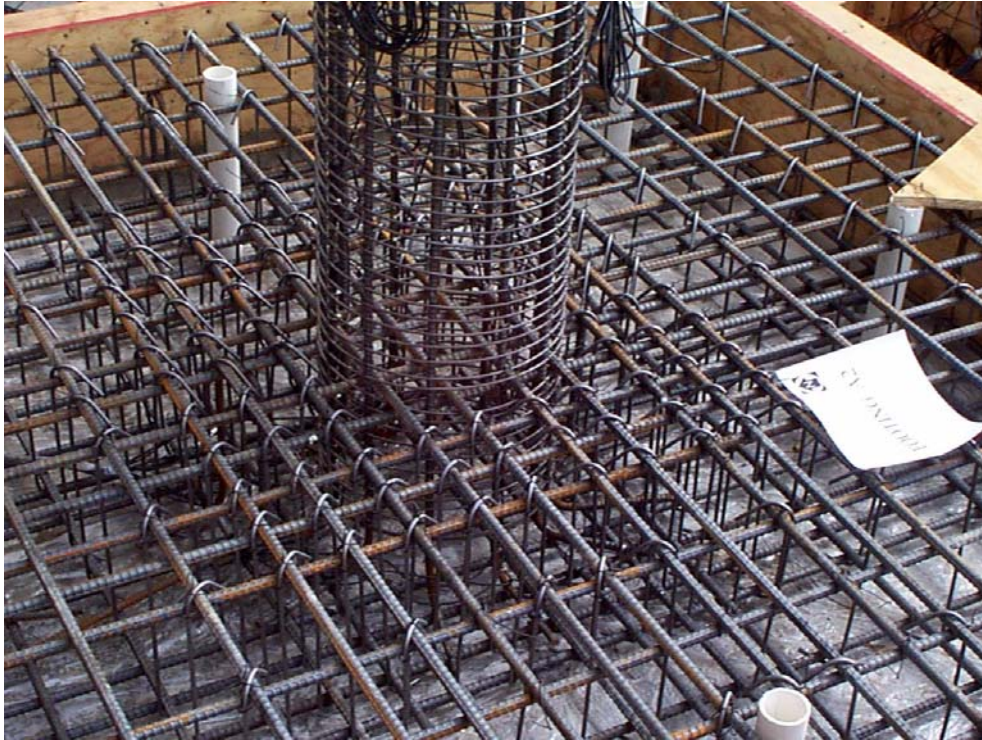
Figure 3-14. Column footing connection, with footing stirrups in place.

Figure 3-15. Steel details for one of the three similar weight blocks.

Figure 3-16. Casting the weight blocks.

Figure 3-17. Construction of formwork to support the top slabs, while curing the footings.
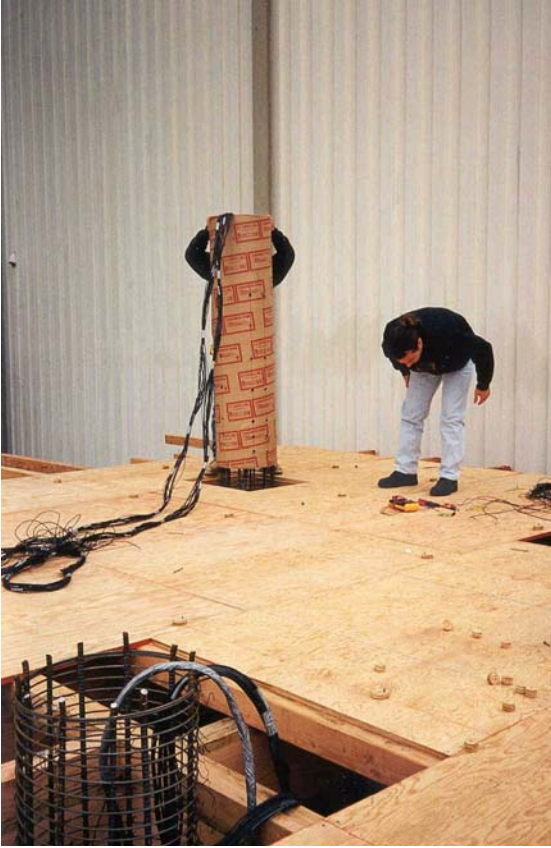
Figure 3-18. Forming the column.

Figure 3-19. Column form.
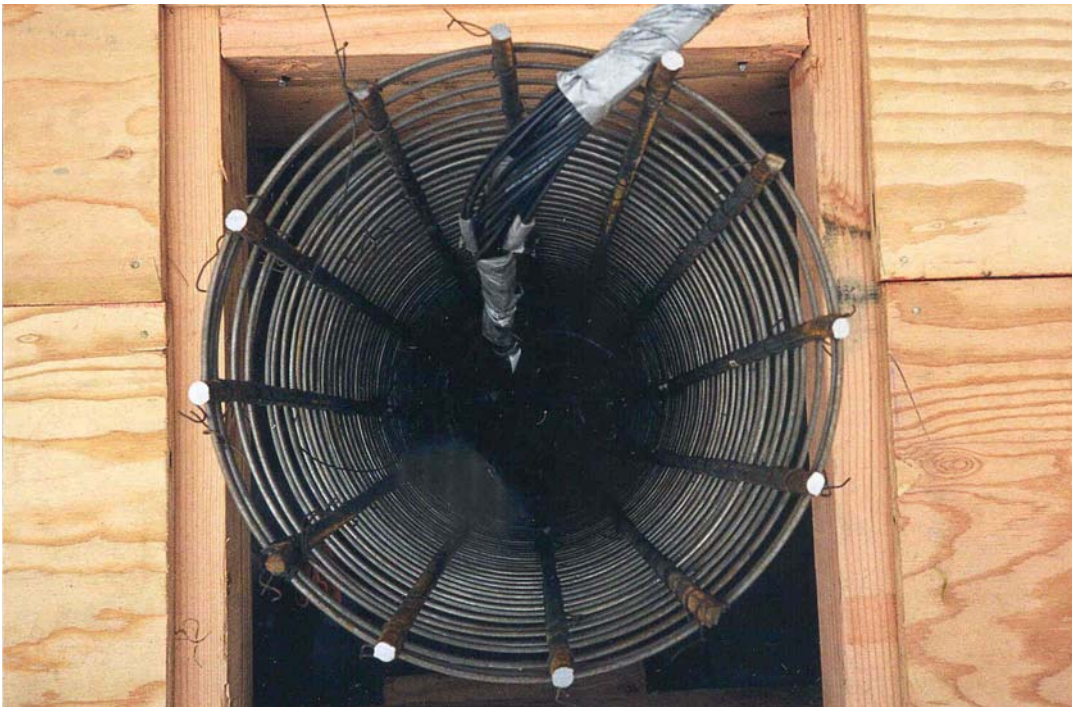
Figure 3-20. Top view of the column cage.

Figure 3-21. View of the top slab steel layout.

Figure 3-22. The four specimens after form removal.

4   Experimental Setup and Test Program

This chapter discusses the test setup of the shaking table experiments, the details of the instrumentation used to collect data, and the test program. Section 4.1 describes the test setup. The purpose and location of various instruments used to monitor the tests are discussed in Section 4.2. The purpose and location of those instruments are indicated. Table A-1 in Appendix A provides a list of all the instruments and their location. Section 4.3 discusses data acquisition procedures, and briefly discusses the process of reducing and correcting the data. The ground motions used in the tests are presented in Section 4.4, while Section 4.5 describes the performance of the shaking table. The testing sequence used for the four specimens is discussed in Section 4.6.

4.1   TEST SETUP

In order to simulate a fixed support at the base of the column, the footing was rigidly attached to the simulator platform using prestressing rods. The weight blocks were similarly prestressed to the top slab in order to represent a rigid supported mass. The specimen footing had 8 prestressing holes matching the locations of the tie-down holes in the shaking table, which form a 7 x 7 square grid with a spacing of 36 in. (914 mm). The top slab had similar holes for prestressing the weight blocks to the specimen. A layer of hydrostone was placed between the footing and the shaking table platform to provide a uniform contact surface in order to ensure a uniform distribution of bearing stresses. The footing was then attached to the shaking table with 8 smooth prestressing rods with a diameter of 1 in. (25.4 mm) each, using 10 in. x 10 in. x 2 in. (254 mm x 254 mm x 50.8 mm) steel plates at the location of prestressing to keep the bearing stresses on the concrete below approximately 1.5 ksi (10 MPa). Hydrostone was also used between the weight blocks and between the weight blocks and the top slab. The three weights were then prestressed to the top slab using four threaded prestressing rods. Figure 4-1 shows the top and side views of the test setup.
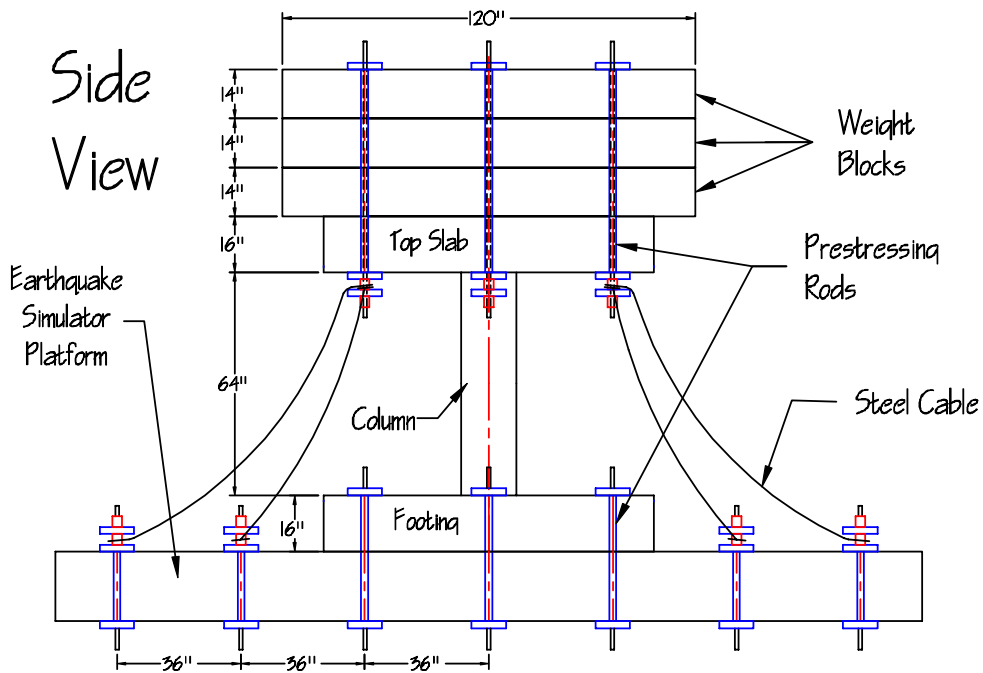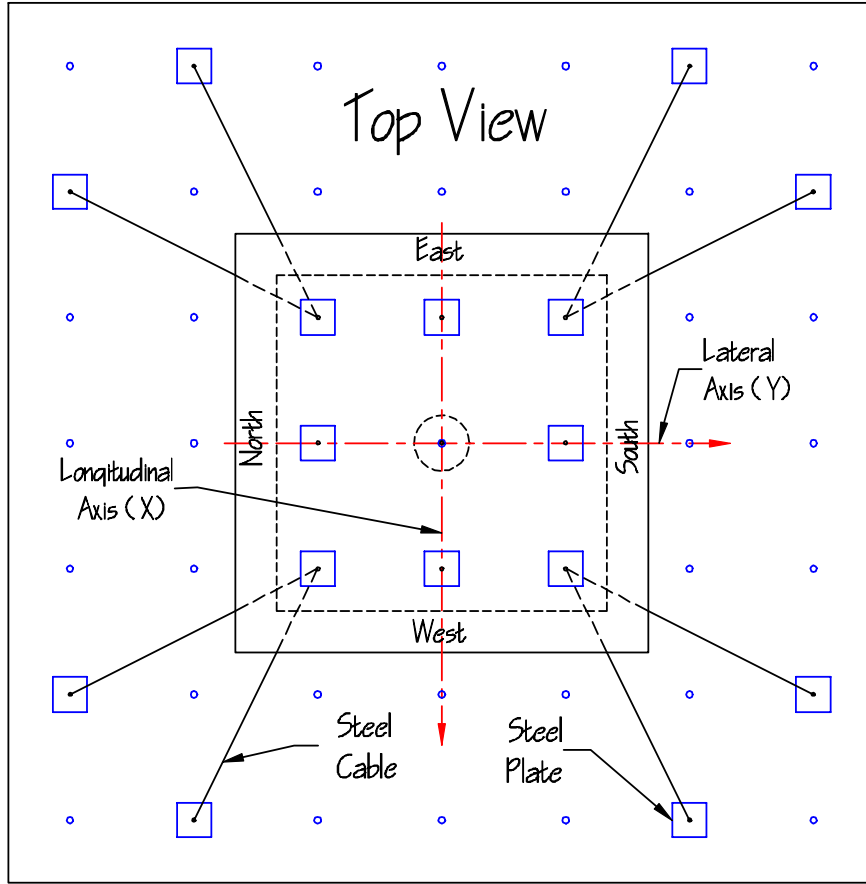
Figure 4-1. Top and side views of the test setup.

In order to prevent catastrophic collapse during testing, the corners of the top slab were connected with 8 one-inch (25.4 mm) diameter steel cables to the shaking table. Each of the cables had a breaking strengths of 51.7 tons (460 kN). This was however a safety precaution, and the specimen was not expected to reach a displacement that would cause the cables to go into tension. The cables were designed to accommodate a displacement of the specimen of at least 10 in. (250 mm), which corresponded to a displacement ductility of about 10. The safety system was not triggered during any of tests.
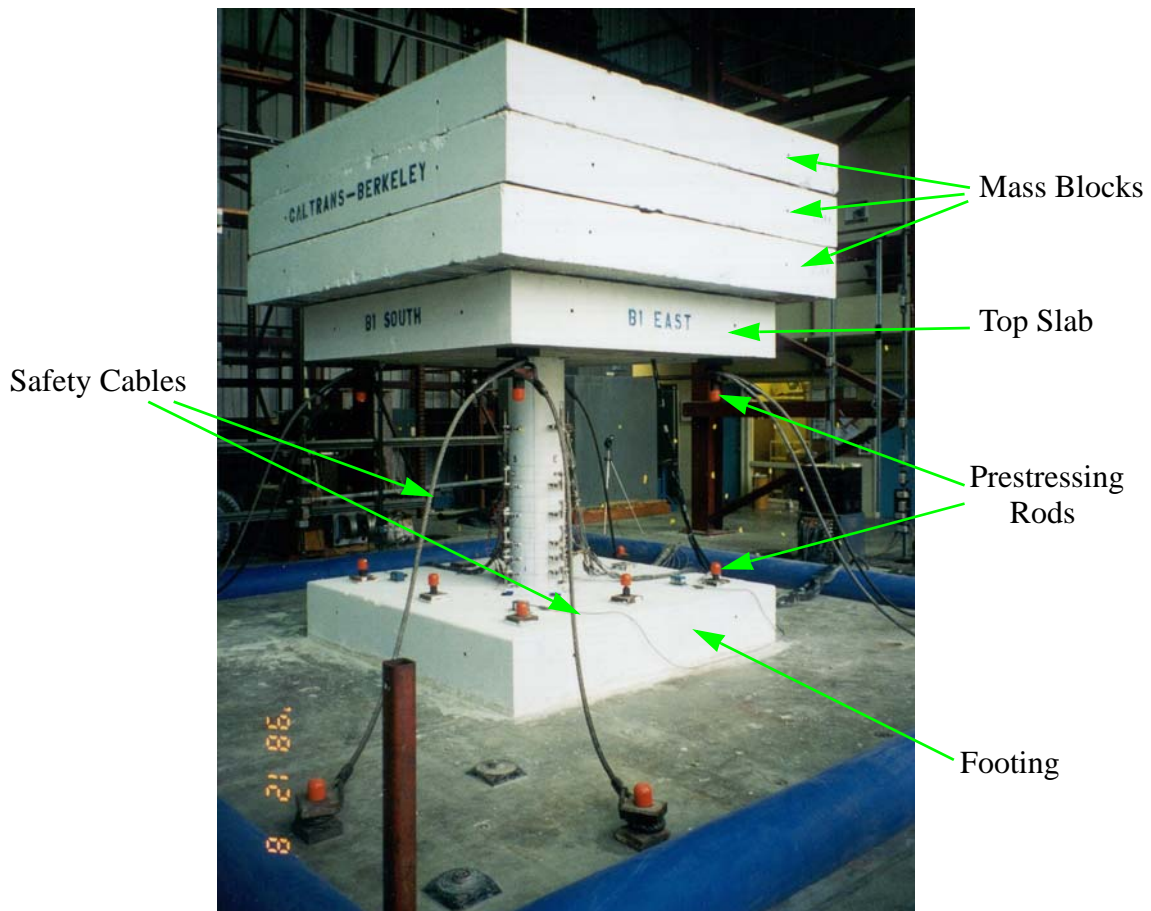
Figure 4-2. Specimen B1 with footing attached to the shaking table, and mass blocks prestressed to the top slab. Safety cables are also shown.

Care was exercised in moving the specimens onto the table and in installing the mass blocks to avoid cracking the column. A steel column was temporarily attached to the shaking table at the start of each test sequence. The column was used as a support to perform pull-back tests. Three to

five pullback tests were performed in each direction before testing each specimen to measure the fundamental period and damping ratio of the undamaged specimen under free vibration.

4.2   INSTRUMENTATION

4.2.1   Overview

An extensive instrumentation scheme was used to monitor the global response of the column, and the local deformations and strains at selected locations. A total of 144 data channels were used in each of the shaking table tests. Those channels corresponded to several types of instruments, including Direct Current Displacement Transducers (DCDT), Linear Displacement Potentiometers (LP), accelerometers and strain gages. The 144 channels were distributed as follows:

- 16 channels for monitoring the displacements and accelerations of the shaking table

- 48 channels for strain gages: 28 for measuring strains on the longitudinal rebar and 20 for measuring strains the spiral rebar

- 19 accelerometer channels for measuring accelerations at different locations on the specimen

- 32 channels for DCDT instruments measuring relative deformations between different points over the height of the specimen

- 29 channels for linear potentiometers measuring global displacements at various points on the specimen

The data was sampled at a rate of 0.01 seconds multiplexed at 500 kHz. More detailed information on the instrumentation is presented below. A complete listing of all the instruments used, their location and name, and the corresponding channel number is provided in Table A-1 in Appendix A. The global coordinates of each instrument are also provided in the table. The convention for the global coordinate system is provided in Figure 4-3. The origin of the xy-plane of the coordinate system was taken at the center of the column. The origin of the z-axis was assumed at the top of footing.

4.2.2   Shaking Table Instrumentation

The Earthquake Engineering Research Center (EERC) shaking table at the University of California at Berkeley was used to conduct the column tests. The EERC shaking table measures 20 ft by 20 ft (6.1 m by 6.1 m) in dimensions, and is equipped with a six-degree of freedom control system.
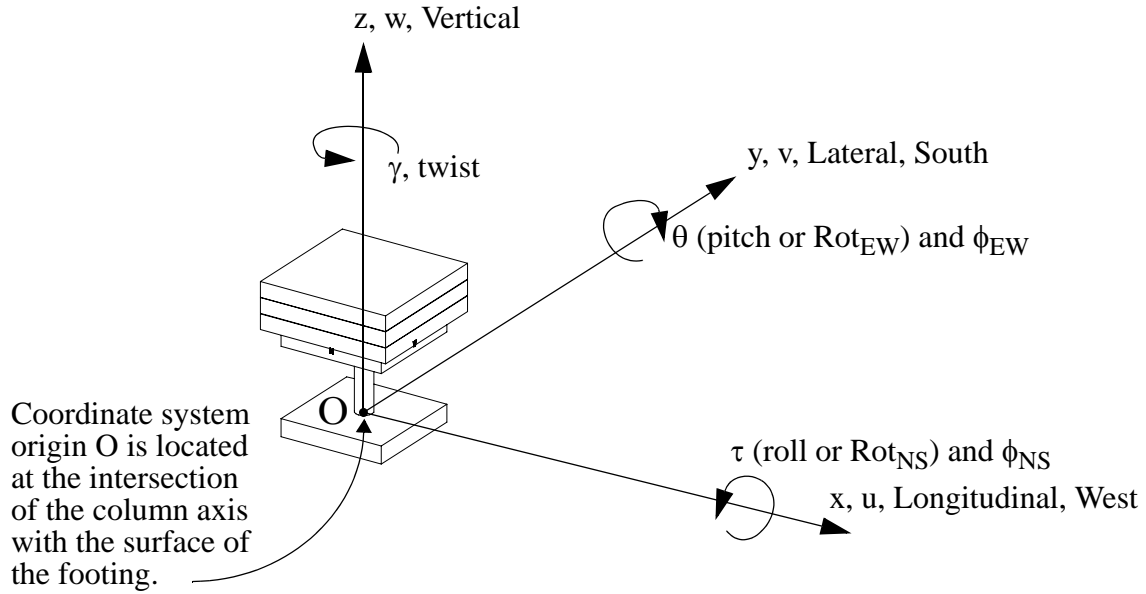
Figure 4-3. Conventions of the coordinate system used.

Figure 4-4 shows the mechanical system of the table and the locations of the instruments used to monitor the table displacements and accelerations. Four accelerometers (v1a, v2a, v3a and v4a) and four displacement transducers (V1od, V2od, V3od and V4od) measure vertical accelerations and displacements near the four corners of the table. Horizontal accelerations and displacements are monitored through four accelerometers (h12a, h23a, h34a and h41a) placed at the four sides of the table, and four displacement transducers (H1od, H2od, H3od and H4od) acting along the outer horizontal actuators (two in each direction). Those measurements allow the computation of acceleration and displacement components in all six degrees of freedom. The type, designation and orientation of each instrument are shown in Table A-1.

4.2.3   External Instrumentation

A total of 80 external instruments were used to monitor the motion and deformation of the specimen throughout each experiment. External instruments consisted of accelerometers, and DCDT and LP instruments. Figures 4-5 and 4-6 show the approximate locations of most external instruments.

4.2.3.1   Accelerometers

Accelerations were directly read by accelerometers mounted at critical locations on the specimen. Groups of three accelerometers were placed on the west face, south face and the top of the mass

51
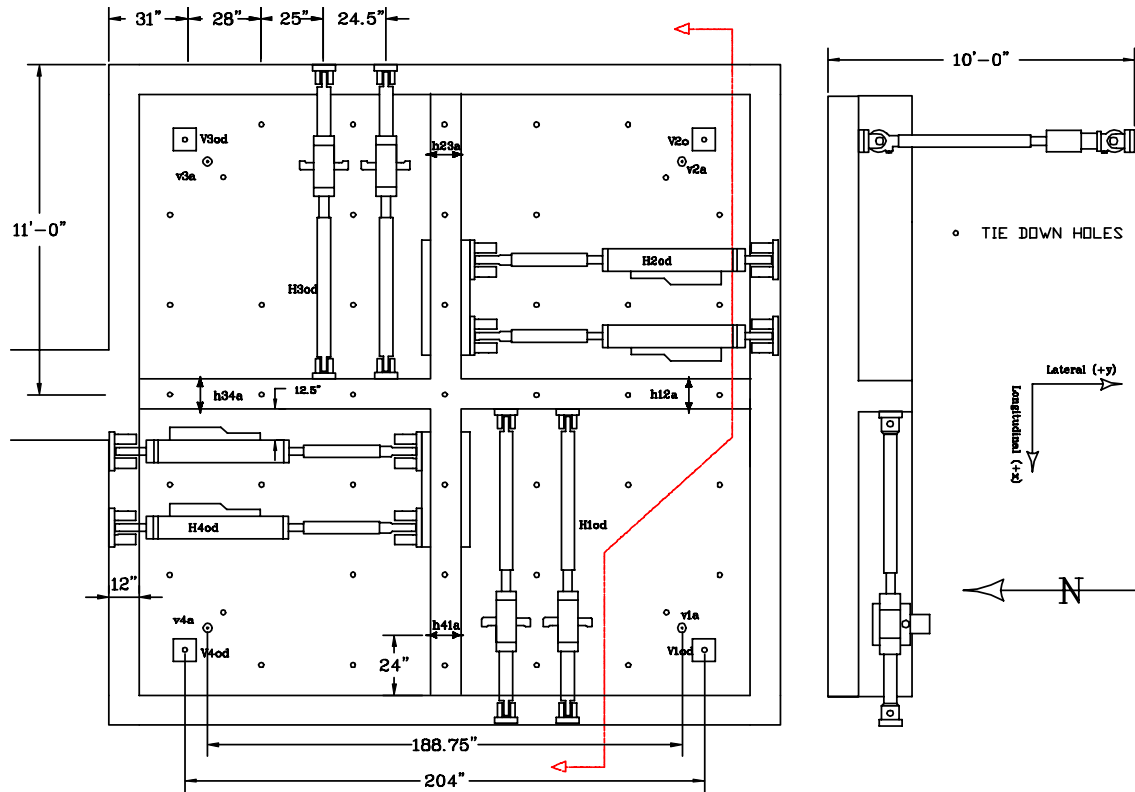
Figure 4-4. Shaking table instrumentation.

block and oriented along the three major axes. Each group measured accelerations in 3 directions: longitudinal, lateral and vertical. Using the data from the accelerometers, all six components of the block acceleration could be computed assuming rigid body motion. Three components of acceleration were also measured at the west and north faces of the footing. Accelerations in the longitudinal (x) and lateral (y) directions were also measured on the column face at a height of 32 in. (813 mm) above the footing. The locations of accelerometers are shown in Figures 4-5 and 4-9.

4.2.3.2   Displacement Transducers

Direct Current Displacement Transducers (DCDT) were used to measure relative displacements between different sections along the height of the column. The DCDT instruments measured the displacements between special rods crossing the section from end to end that were placed during construction. The 1/2 in. (13 mm) diameter rods were located at the following elevations from the top of the footing: 4 in., 8 in., 12 in., 20 in., 28 in. and 44 in. (102 mm, 203 mm, 305 mm, 508 mm, 711 mm, and 1118 mm) along the transverse (North-South) direction, and were 0.75 in. (19 mm) higher along the Longitudinal (East-West) direction. Those measurements were taken at all four

52
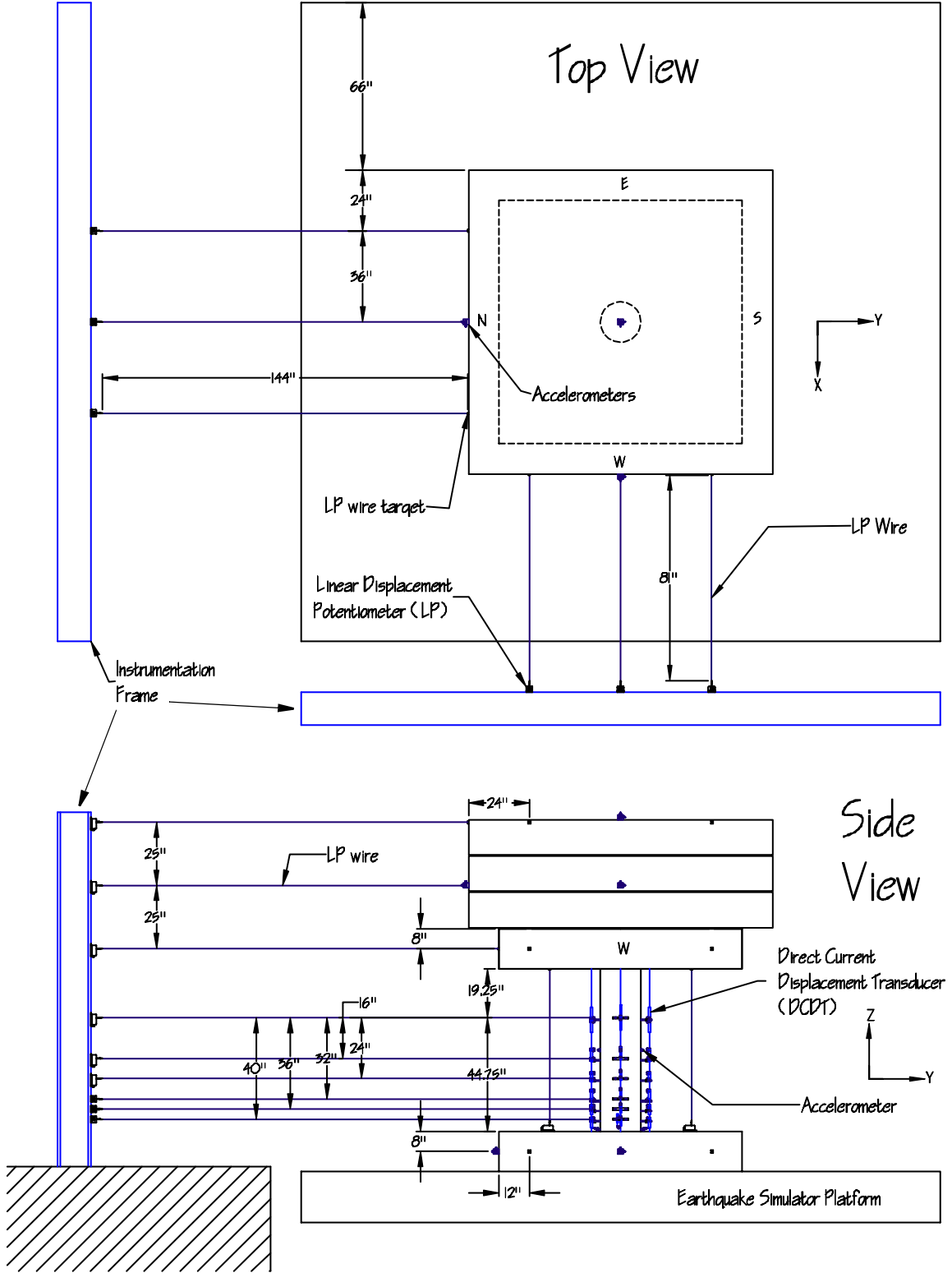
Figure 4-5. Top and side views of the instrumentation scheme.
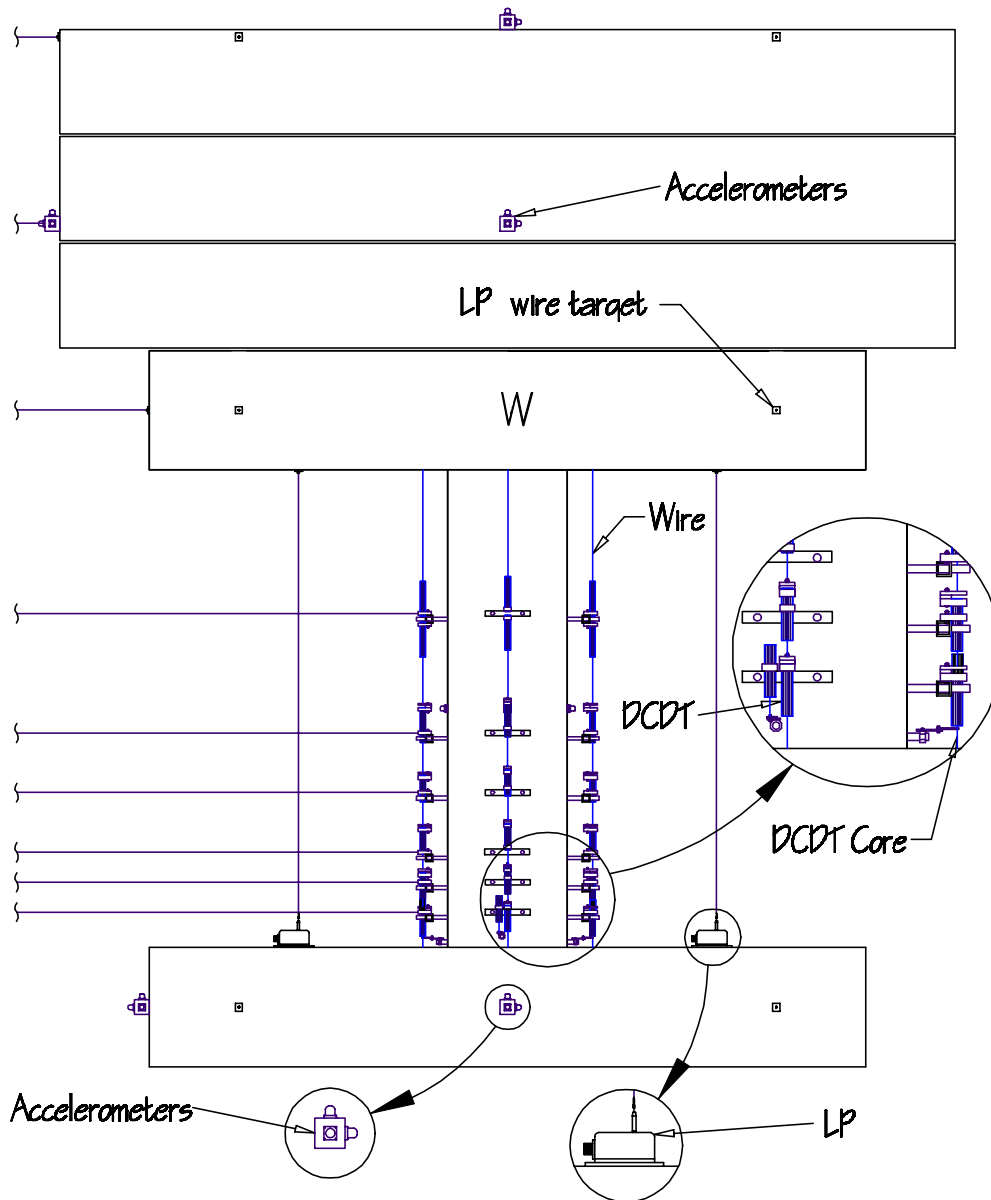
Figure 4-6. Details of the instrumentation along the elevation of the specimen.

faces, and were used to estimate the average curvatures and axial deformations along the height of the column. Additional rods were placed just above the footing surface; the deformation between that point and the footing was used to estimate the slippage of the longitudinal rebar in the footing. Those rods were located at about 0.75 in. (19 mm) and 1.5 in. (38 mm) above the footing surface along the lateral and longitudinal directions, respectively. The location and names of all the DCDT instruments used are shown in Figures 4-7 and 4-8.

Figure 4-7. Instrument locations on the North face of the column.

Figure 4-8. Instrument locations on the West face of the column.
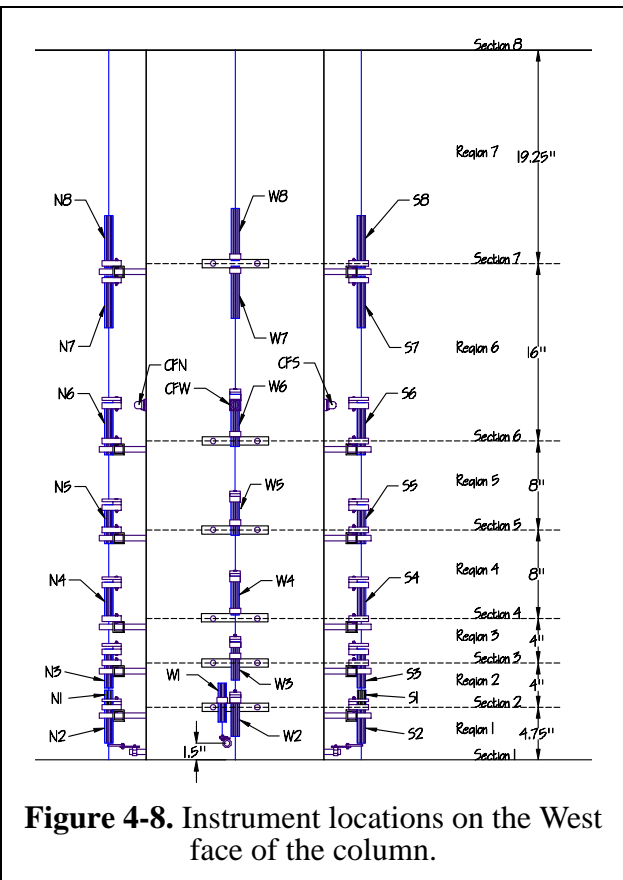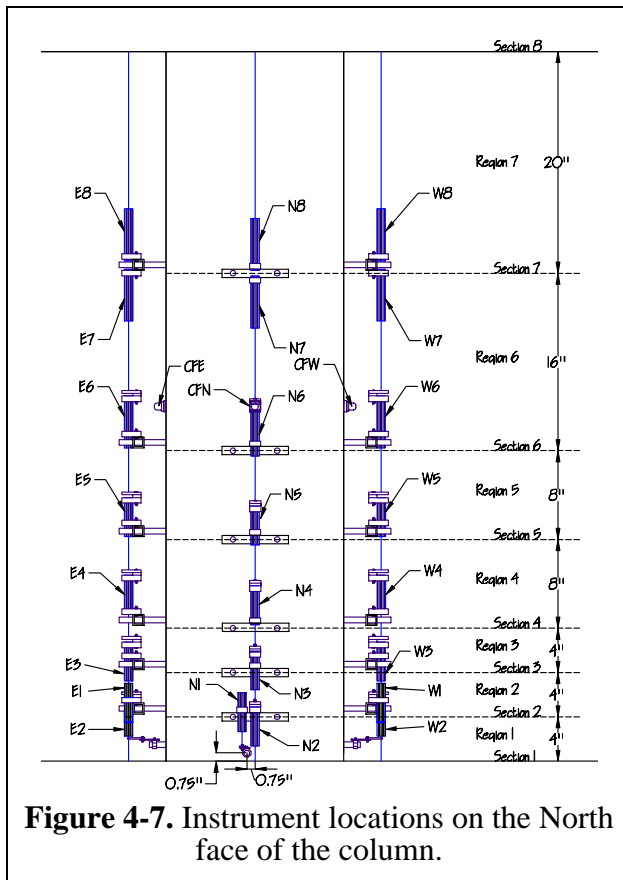
Global displacements were directly measured by linear potentiometers (LP) that were installed on stiff instrumentation frames located off the shaking table. Multiple potentiometers measured displacements at various points on the mass block including the center of gravity of the mass block. Other potentiometers monitored the longitudinal and lateral displacements at several locations along the column height. Those locations corresponded to the rods used for curvature measurements. These measurements were used to compute the relative displacements and rotations of the specimen and the deflected shape of the column. Shear deformations could also be estimated by subtracting estimates of the flexural deformations obtained through curvature readings using the DCDT instruments at the face of the column.

The displacement of the shaking table was measured through displacement transducers located along the actuators as discussed in Section 4.2.2. The displacement of the footing was also monitored by additional displacement potentiometers in the event of slip of the specimen relative to the table. Four potentiometers were used to measure the vertical displacements between the footing and top slab at the four corners. The locations and names of the various LP instruments are shown in Figures 4-5 and 4-9.

55
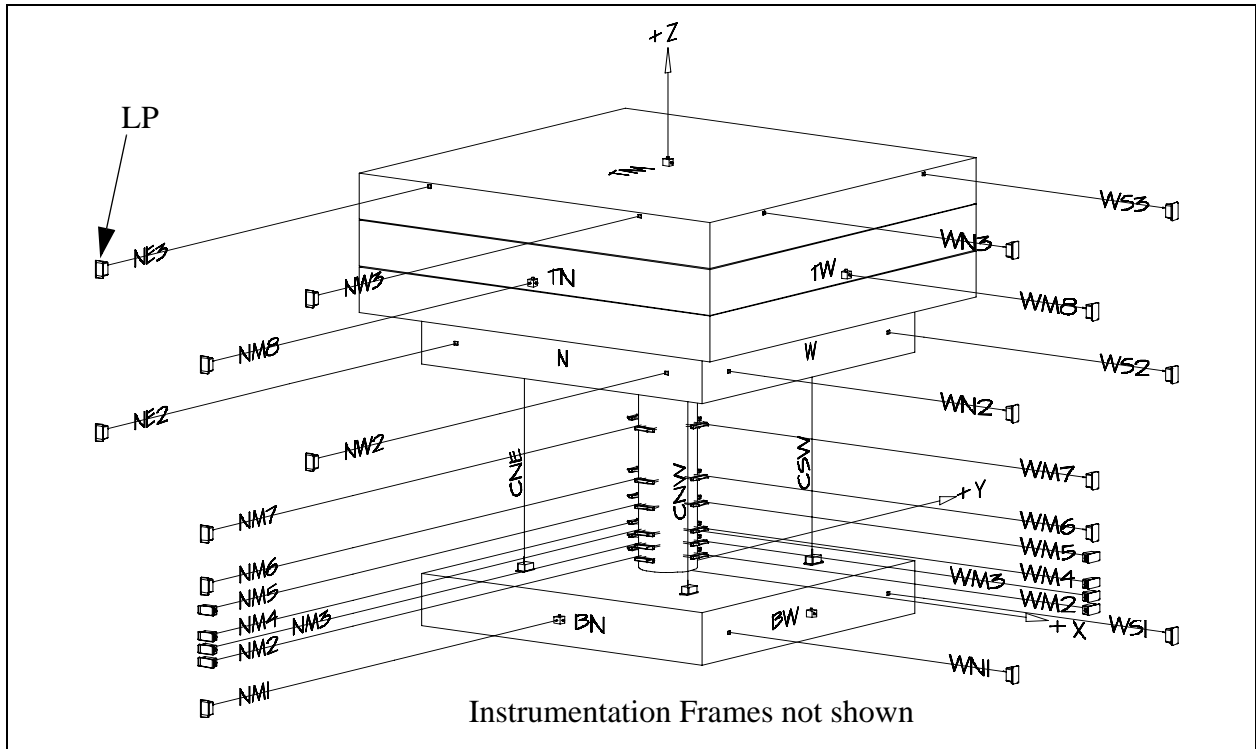
Figure 4-9. Locations of various accelerometers and linear potentiometers.

4.2.4 Strain Gages

A total of 48 strain gages were used in each specimen. Strain gages were used to monitor strain histories in both longitudinal and transverse reinforcement.

4.2.4.1 Strain Gages on Longitudinal Reinforcement

Each specimen had 28 strain gages distributed over four longitudinal bars (7 gages per bar). The bars were gaged prior to construction and one bar was placed on each side of the column (East, North, West and South). In each bar, the gages were placed at the following distances from the column-footing interface: -10 in., -5 in., 0 in., 6 in., 12 in., 24 in., 48 in. (-254 mm, -127 mm, 0 mm, 152 mm, 305 mm, 610 mm, 1219 mm); or in terms of bar diameter: -20 d_b, -10 d_b, 0, 12 d_b, 24 d_b, 48 d_b, and 96 d_b (negative values correspond to gages within the footing).

4.2.4.2 Strain Gages on Spiral Reinforcement

The spiral reinforcement was instrumented with 20 strain gages per specimen, distributed over the four faces of the specimen. Each face had 5 strain gages on the spiral reinforcement. The spacings varied slightly from specimen to specimen and from side to side on the same specimen due to variations of the actual spiral layout, but the average heights of the gages from the surface of the footing

56

were: 2.5 in., 5 in., 7.5 in., 10 in. and 12.5 in. (64 mm, 127 mm, 191 mm, 254 mm and 318 mm) as shown in Figure 4-10.
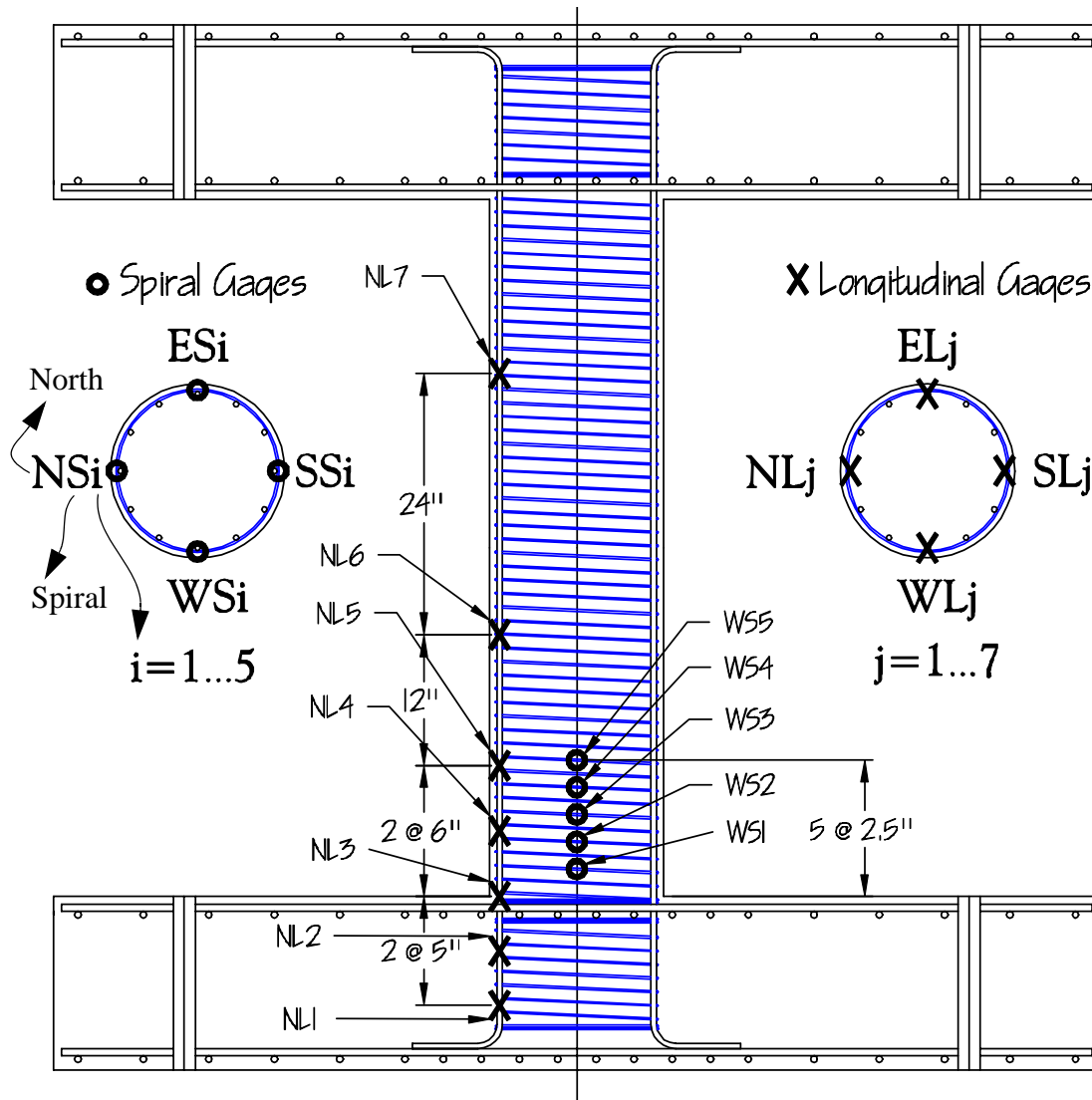
Figure 4-10. Strain gage locations for longitudinal and spiral reinforcement.

4.3   DATA ACQUISITION

All four specimens had the same instrumentation scheme. Hence, the same procedures for collecting and reducing data were followed. Furthermore, most instruments needed to be calibrated only once prior to the first test. However, since each instrument usually has a different calibration, care was exercised to place instruments at the same location in each of the specimens. Instruments that needed to be removed were marked, and were placed at the same location on the next specimen,

and then connected to the same cable. All channels were double-checked before and after the test to ensure proper connection, and to correct the data in the case errors were found.

Different procedures were used to extract and reduce data. The external displacements were used to monitor and draw a deflected shape of the column at each instant of the test (at 0.01 second increments) as shown in Figure 4-12, as well as to monitor the movements including translations and rotations of the top block (assumed rigid). The DCDT readings were used to compute the average curvature distribution over the length of the column and to estimate the amount of rebar pullout at the base.

Accelerometers were placed at the base of the column to record the input acceleration, and in various locations at the top of the column to record accelerations allowing computation of amplification factors and estimates of the inertial forces which are in turn used to estimate the shear force and moment at the base of the column. The strain gage data are useful for following the strain histories in the reinforcement bars and to evaluate the amount of energy absorbed before buckling and fracture. However, some strain gages located on longitudinal reinforcement in the plastic hinge region failed during the first or second large earthquake run, because of high strains and damage due to nearby cracking and spalling.

The various stages of each test were documented using photographs, slides and analog video which was later digitized. Three video cameras were used simultaneously: two cameras were focused on the plastic hinge region at the East-South and the North-West faces of the column, while the third camera was used to obtain a global view of the specimen. The video footage, especially the close-ups to the plastic hinge area, were extremely helpful in further understanding the column behavior.

4.3.1   Data Correction

Data was read from the channels once every 0.01 seconds and appended to the data file. The data was recorded in a text file with each channel occupying one column. The first two columns contained the date and time; channel one was stored in column three and so on.

All computations involving data correction, processing, and evaluation were performed using MATLAB [105]. An interactive program was written in MATLAB to allow immediate access to results after each test. The program allowed the plotting of a single or a collection of instruments (e.g. strain gages or DCDT instruments) or derived quantities (e.g. relative displacement or base moments) as shown in Figure 4-11. Figure 4-12 shows a module of the program, capable of replay-

ing an animation of the experiment including column deformations and curvatures along height from recorded data. The results could be replayed immediately after the test, which allowed a quick inspection of the instrument connections and data collection system, and reduced the potential for instrumentation errors.

In spite of the good quality of data obtained, further correction and manipulation was needed. Correction procedures included filtering the data to remove noise, improving noisy signals or handling channels that were mistakenly switched.

In most of the test runs, the data recording was initiated a few seconds prior to the beginning of the earthquake signal. That leading time was eliminated in the data correction phase to allow for comparison of the test data between different runs, and to compare input and output ground motion signals. A list of all runs performed and their descriptions is provided in Appendix A (Table A-2).

Another aspect of data reduction was to ensure continuity between the data of the different runs, in order to follow residual deformations and strains. This was complicated by the sensitivity of some instruments (e.g. strain gages), and by other factors such as having to stop and restart the data acquisition system due to test continuation over more than one day. In general, displacement potentiometers and DCDT instruments were corrected by subtracting an initial value corresponding to the reading of the instrument at the initial undeformed state of the specimen. This undeformed state was obtained by taking a snapshot of the instrument readings at or before the first run of each specimen. Accelerometer readings were assumed to start at zero in each run. A different approach was followed with strain gages. Strain gage data was assumed to start at the cumulative value that was reached at the end of the previous run. Only major runs were considered in this process; white noise excitations that were conducted to characterize the dynamic properties of the column between major runs were ignored.

The data was then filtered using a sixth-order high-pass Butterworth filter with a cut-off frequency of 20 Hz. The filtering was performed to remove high-frequency noise, and smooth some of the data that were exhibiting sharp variations.

Overall, the data correction was performed in the following order:

1. Account for switched or misconnected channels by switching the corresponding columns in the data array, and multiplying by the corresponding calibration factors (when applicable). Filtering of some very noisy instruments is also performed at this stage.
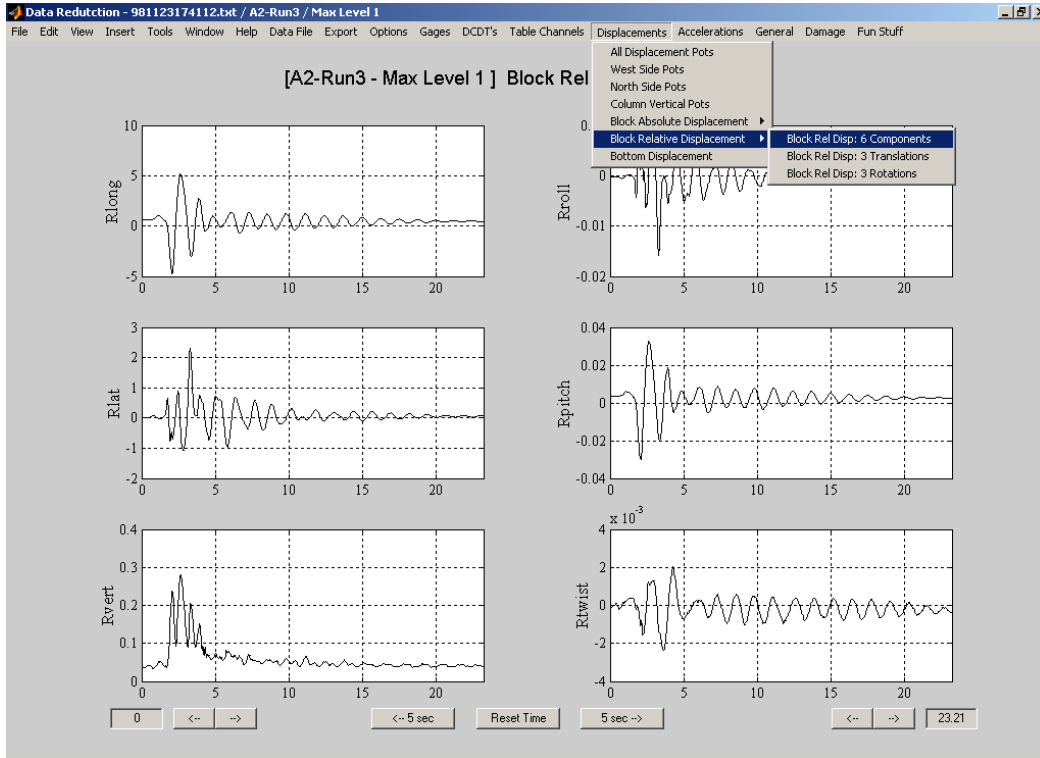
Figure 4-11. MATLAB program used for data reduction, processing, and presentation.
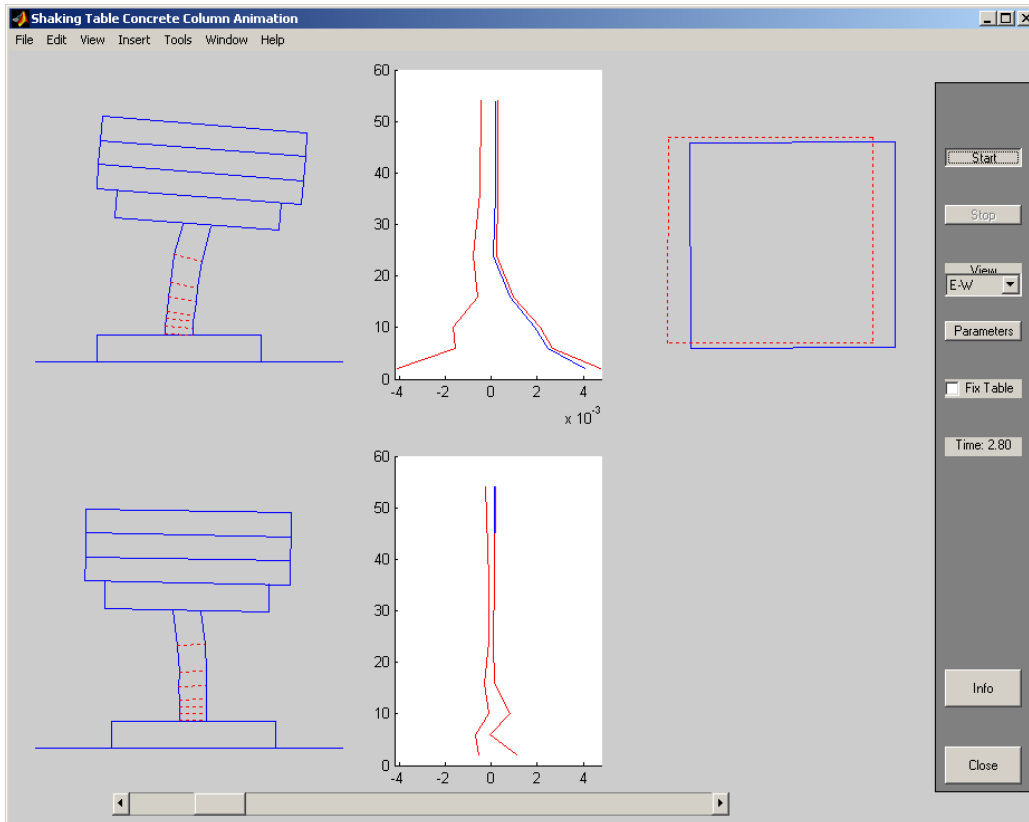
Figure 4-12. Animation module for replaying response from recorded data.

60

2. Shift the time scale by eliminating the first portion of the record to synchronize the data between the different runs and the input.

3. Correct the instrumentation data by subtracting an initial value or ensuring data continuity from a previous run.

4. Filter all data with a high-pass filter at 20 Hz.

5. Perform some minor corrections that could not be performed in step 1.

4.3.2   Data Reduction

After correcting the data, the various data channels were used to compute time histories of strains, displacements, accelerations and forces at various locations in the specimen. The following sections provide a brief discussion on how various instrument data was used to obtain those quantities.

4.3.2.1   Accelerations

The components of interest were the horizontal components as well as the two rotational components (about the horizontal axes). The rotational component of the acceleration was computed by taking the difference between the acceleration at the middle and the top of the block, and dividing by the appropriate distance.

4.3.2.2   Forces and Moments

The shear force in each direction was approximated by the inertia force obtained as the product of the acceleration and the mass, thereby neglecting the damping forces. Using rotational accelerations and the moment inertia of the block, the rotational inertial force was similarly estimated as a function of time. Considering equilibrium by summing moments about the base, and neglecting damping again, the moment at the base of the column is obtained as a function of both the translational and rotational accelerations. The following illustrates computations in the x-direction. Computations along the y-direction are similar. The equations of motion in the longitudinal direction are:

$$m\ddot{u} + F_{dx} + F_{sx} = -ma_{gx} \tag{4-1}$$

$$m_R\ddot{\theta} + M_{d\theta} + M_{s\theta} = 0 \tag{4-2}$$

where the variables are defined below (see Figure 4-3 for conventions):

- m: supported mass,

- m_R: Rotational mass of inertia of the block,

- u: Longitudinal relative displacement of the center of mass,

- θ: Rotation of the center of mass about the y-axis,

- a_{gx}: Table acceleration in the x-direction,

- F_{dx}: Damping force in the x-direction,

- F_{sx}: Hysteretic force in the x-direction,

- $M_{d\theta}$: Damping moment about the y-axis,

- $M_{s\theta}$: Hysteretic moment about the y-axis,

If u_t is the total displacement of the center of mass then: $u_t = u + d_{gx}$, where d_{gx} is the table displacement in the x-direction, and $\ddot{u}_t = \ddot{u} + a_{gx}$. Equations 4-1 and 4-2 become:

$$F_{sx} = -m\ddot{u}_t - F_{dx} \approx -m\ddot{u}_t \qquad (4\text{-}3)$$

$$M_{s\theta} = -m_R\ddot{\theta} - M_{d\theta} \approx -m_R\ddot{\theta} \qquad (4\text{-}4)$$

The above equations were used to approximate the bending moment and shear force at the center of mass. Assuming that the damping force is small compared to the hysteretic force, this approximation is expected to yield good results. The approximation is best at displacement peaks, since they correspond to zero velocities and hence zero damping forces (assuming pure viscous damping). Having the shear and moment at the center of mass, and using equilibrium, the moment can be determined at every other point along the height, using equilibrium as shown in Figure 4-13. For example, the moment at the base of the column can be obtained as follows:

$$M_b = (m\ddot{u}_t + F_{dx})L - M_{d\theta} - m_R\ddot{\theta}_t + Pu_r \approx m\ddot{u}_t L - m_R\ddot{\theta}_t + Pu_r \qquad (4\text{-}5)$$

4.3.2.3   External Displacements

External linear potentiometers directly measured the global displacement of a given point along the specimen's exterior. Multiple measurements were made on the North and West faces of the mass block. Those measurements were used to compute all displacement components of the rigid body motion of the block. Looking at Figures 4-5 and 4-9, and using the assumption that all instrument readings were corrected such that displacements are positive along +x, +y and +z, the following quantities can be computed:

$$\tau_{t,block} = \left(\frac{NW2 + NE2}{2} - \frac{NW3 + NE3}{2}\right) \bigg/ D_\tau \qquad (4\text{-}6)$$
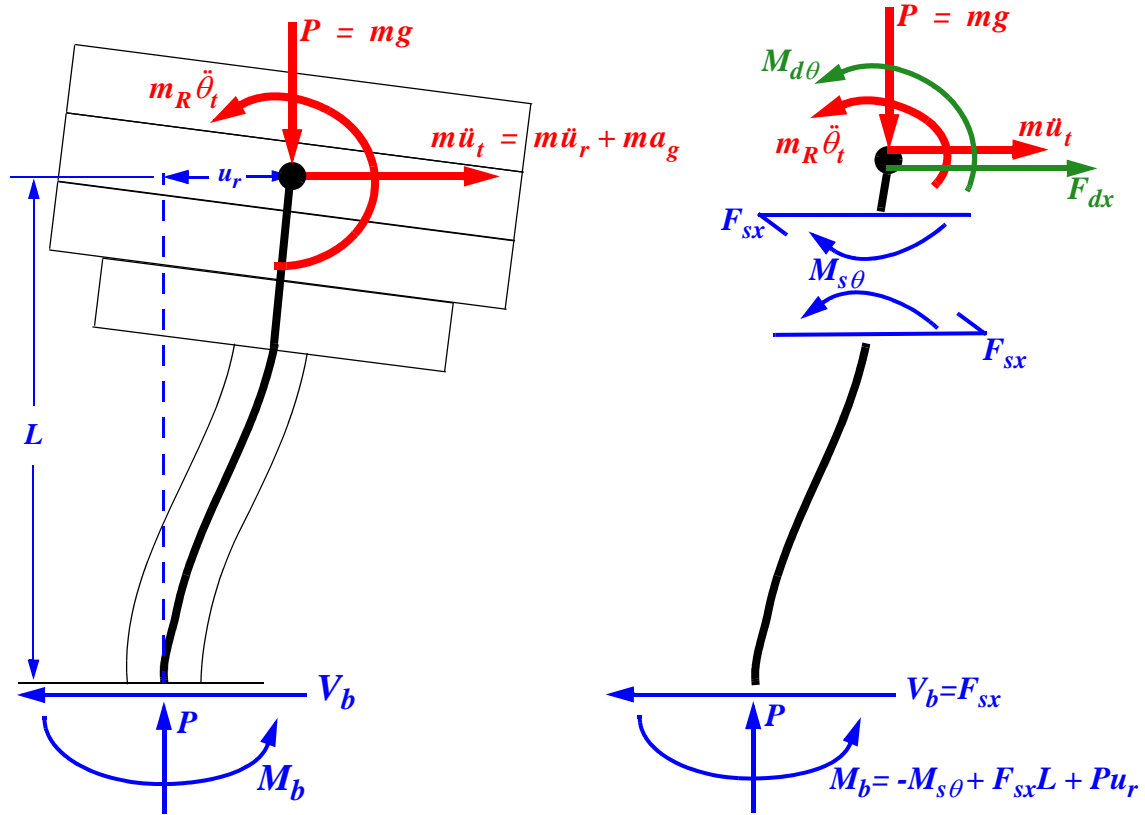
Figure 4-13. Free body diagram.

$$\gamma_{t,\,block} \;=\; \left(\frac{WS2 + WS3}{2} - \frac{WN2 + WN3}{2} \right) \Big/ D_\gamma \tag{4-7}$$

where τ_t and γ_t are the total rotations about the x and z axes. D_τ and D_γ are the corresponding distances between the various instruments, and can be obtained from Figure 4-5 as 50 in. (1.27 m) and 72 in. (1.83 m) respectively. This gives an example of how the global measurements are used to compute global displacements. Relative displacements between the specimen and the footing can then be obtained by subtracting the appropriate footing (or shaking table) displacement from the total displacement, as illustrated in Equation 4-8:

$$u_{r,\,block} \;=\; u_{t,\,block} - u_{footing} \;=\; WM8 - (WN1 + WS1)\big/2 \tag{4-8}$$

where u_r is the relative displacement of the block in the longitudinal direction. Likewise, the relative displacement of other locations on the column can be obtained by subtracting the footing displacement from the measured total displacement at those points. Other quantities are relative by definition such as the vertical displacement between the top slab and the footing, which is also equal to the column elongation:

$$w_{r,block} = (CNW + CSW + CSE + CNE)/4 \qquad (4\text{-}9)$$

4.3.2.4   *Curvature Measurements along the Column's Elevation*

The DCDT instruments measure deformations at the face of the column on all four sides (East, West, North and South). There are eight DCDT instruments on each face of the column measuring deformations over seven regions along the column height, and the slip deformation at the interface between the column and the footing. The instruments are labeled from 1 to 8 on each face as shown in Figures 4-7 and 4-8. The measurements are used to estimate the rotations at several sections along the height. Average curvatures and axial deformations are calculated over the different regions. Using the sign conventions of Figure 4-3, the average axial strain over region i, $[\varepsilon_{axial}]_i$, is calculated as the average of the readings on all four sides divided by the height h_i of the region (Equation 4-10). The rotation at a section i (θ_i for EW direction and τ_i for NS direction) is approximated as the sum of the rotation at section $(i\text{-}1)$ plus the rotation contribution of the region in between (Equation 4-11). The average curvature over a region i ($[\phi_{EW}]_i$ for EW direction and $[\phi_{NS}]_i$ for NS direction) can be calculated as the rotation over the region, divided by the region height h_i (Equation 4-12).

$$[\varepsilon_{axial}]_i = \frac{(E[i+1] + W[i+1] + N[i+1] + S[i+1])}{4h_i}, \quad i = 1 .. 7 \qquad (4\text{-}10)$$

$$\theta_i = \theta_{i-1} + \frac{(E[i] - W[i])}{S_{horizontal}} \qquad , i = 2 .. 8, \text{ and } \theta_1 = 0 \qquad (4\text{-}11)$$

$$[\phi_{EW}]_i = \frac{\theta_{i+1} - \theta_i}{h_i} \qquad , i = 1 .. 7 \qquad (4\text{-}12)$$

In the above, $S_{horizontal}$ is the horizontal separation between DCDT instruments on opposite sides of the specimen, and is equal to 22.75 in. (578 mm) in both the EW and NS directions. $E[i]$ and $W[i]$ refer to instruments *Ei* and *Wi* in Figures 4-7 and 4-8. For example for $i = 3$, $N[i+1]$ refers to instrument *N4*, and so on. If Equation 4-12 is used to compute the average curvature, the computed curvature over the first region will include the effect of slip in $[\phi_{EW}]_1$, the slip contribution can be estimated from instruments E1 and W1 and subtracted from $[\phi_{EW}]_1$.

Knowing the distribution of curvatures and rotations over the height of the column, the horizontal relative deformations due to flexure at each section level i (u_i) can be approximated using Equation 4-13:

$$u_i = u_{i-1} + \frac{(\theta_i + \theta_{i-1})}{2} h_{i-1}, \, i = 2 \, .. \, 8, \text{ and } u_1 = 0 \qquad (4\text{-}13)$$

The above quantities can be compared to the relative lateral deformations measured using the linear potentiometers (LP).

4.4 GROUND MOTIONS

As mentioned, two ground motion time histories were used in the tests. Specimens A1 and B1 were subjected to one component of motion, while Specimens A2 and B2 were subjected to both horizontal components of motion. For simplicity in these tests, no vertical accelerations were considered.

4.4.1 Preprocessing of the Records

Some preprocessing was performed on each record before the record was used as input to the shaking table. The two components of each record were processed in the same manner. The first step was to scale the record in time using a time scale factor equal to the square root of the length scale (see Table 3-1). The magnitude of the acceleration was left unchanged. The record was then band pass filtered to remove unwanted frequency components. The filter was characterized using two cutoff frequencies and two corner frequencies. The final step was to scale the acceleration record to the desired testing level. In particular, the design level was determined by scaling the record such that its spectral acceleration matches the design spectrum at the period of the specimen.

4.4.2 The 1994 Northridge Earthquake (Olive View record)

Columns A1 and A2 were subjected to modified version of the Olive View record of the 1994 Northridge earthquake. This record was intended to be representative of a near-fault ground motion containing a high velocity pulse. The specific records used were the NF15 and NF16 records that were developed as part of the SAC Steel Project [95]. The Northridge earthquake had a moment magnitude of 6.7 and the base record used was recorded at Sylmar, at a distance of 6.4 km (4 miles) from fault rupture. The base record was scaled to correspond to firm soil conditions, as defined by the ARS spectrum for soil type B (Figure 2-1). The two components used for the earthquake simulator tests correspond to the fault normal and fault parallel directions. The fault-normal component (NF15) was used in test A1, while both components were used in test A2. The records were

scaled assuming a length scale factor of 4.5 which is consistent with the scale of the specimen. Hence, the time duration of the record was reduced by 2.12 ($\sqrt{4.5}$) while the acceleration was kept the same. After scaling, the original records were pass band filtered, then scaled up by a factor of 1.09 to obtain the design level earthquake. The filter used had cutoff frequencies of 0.1 Hz and 15 Hz with corner frequencies at 0.15 Hz and 13 Hz.

Figures 4-14 and 4-15 compare the processed records used (input) to the actual shaking table recorded motions (output) corresponding to the first design level run of specimen A2. Each figure includes plots of the Fourier spectrum and of the acceleration, velocity and displacement time histories of the records. The elastic response spectra of the longitudinal and lateral shaking table accelerations measured during Run 5 of tests A1 and A2 are shown in Figure 4-16.

4.4.3 The 1985 Chile Earthquake (Llolleo record)

Columns B1 and B2 were subjected to the 1985 Chile earthquake recorded at the Llolleo station. The Llolleo site was located 64 km (40 miles) from the epicenter of the event. This record had a very long duration (nearly 2 minutes), with peak accelerations of 0.70g and 0.45g in the two horizontal components. The frequency content of this earthquake was scaled down by 1.5 before being used in tests B1 and B2 by increasing the apparent digitization interval from 0.005 sec. to 0.0075 sec. This factor was chosen because the ground motion as recorded had small ground displacements and high frequency content. By shifting the frequency content of the ground motions, the spectral acceleration demands at the expected fundamental period of the test specimen are closer to the design spectrum (ARS). Otherwise, the amplitude of the record would have had to be amplified to unrealistic levels. Since the intent of these particular tests were to assess duration effects, and not the specific response of a structure during the Chilean earthquake, this modification was viewed as acceptable. The time duration of the record was then reduced by 2.12 ($\sqrt{4.5}$) similar to the processing of the Olive View record. The record was scaled up to the ARS spectrum at the estimated column period by multiplying it by 1.29, in order to obtain the design record, and then filtered using a passband filter similar to that used to filter the Olive View record. A comparison of the specified (input) and recorded (output) shaking table motions is shown in Figures 4-17 and 4-18. The elastic response spectra of the longitudinal and lateral shaking table accelerations measured during Run 8 of tests B1 and B2 are shown in Figure 4-19.

66
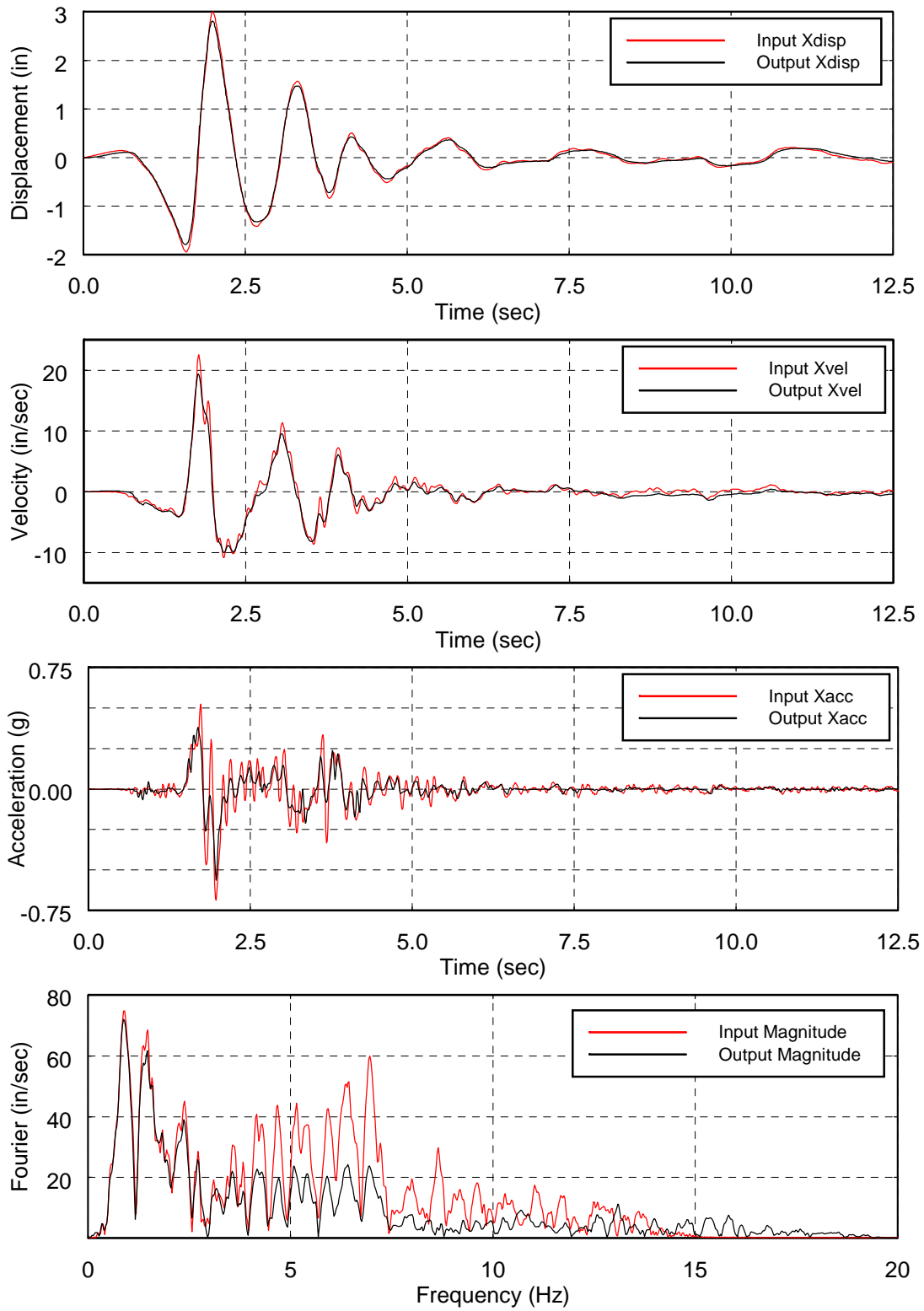
Figure 4-14. Shaking table input and output time histories due to the NF15 record applied in the longitudinal direction (Northridge Olive View fault-normal component).
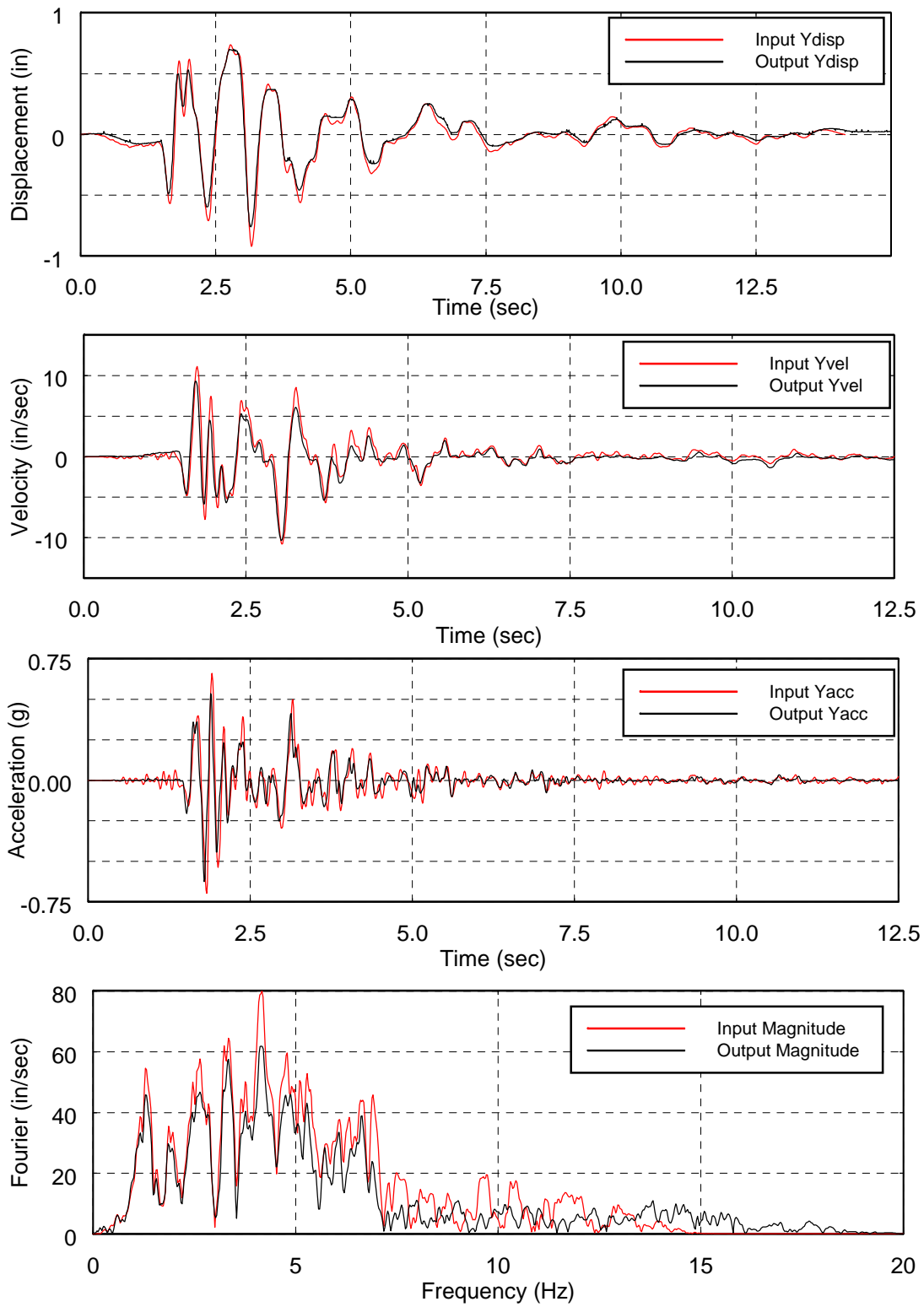
Figure 4-15. Shaking table input and output time histories due to the NF16 record applied in the lateral direction (Northridge Olive View fault-parallel component).

68
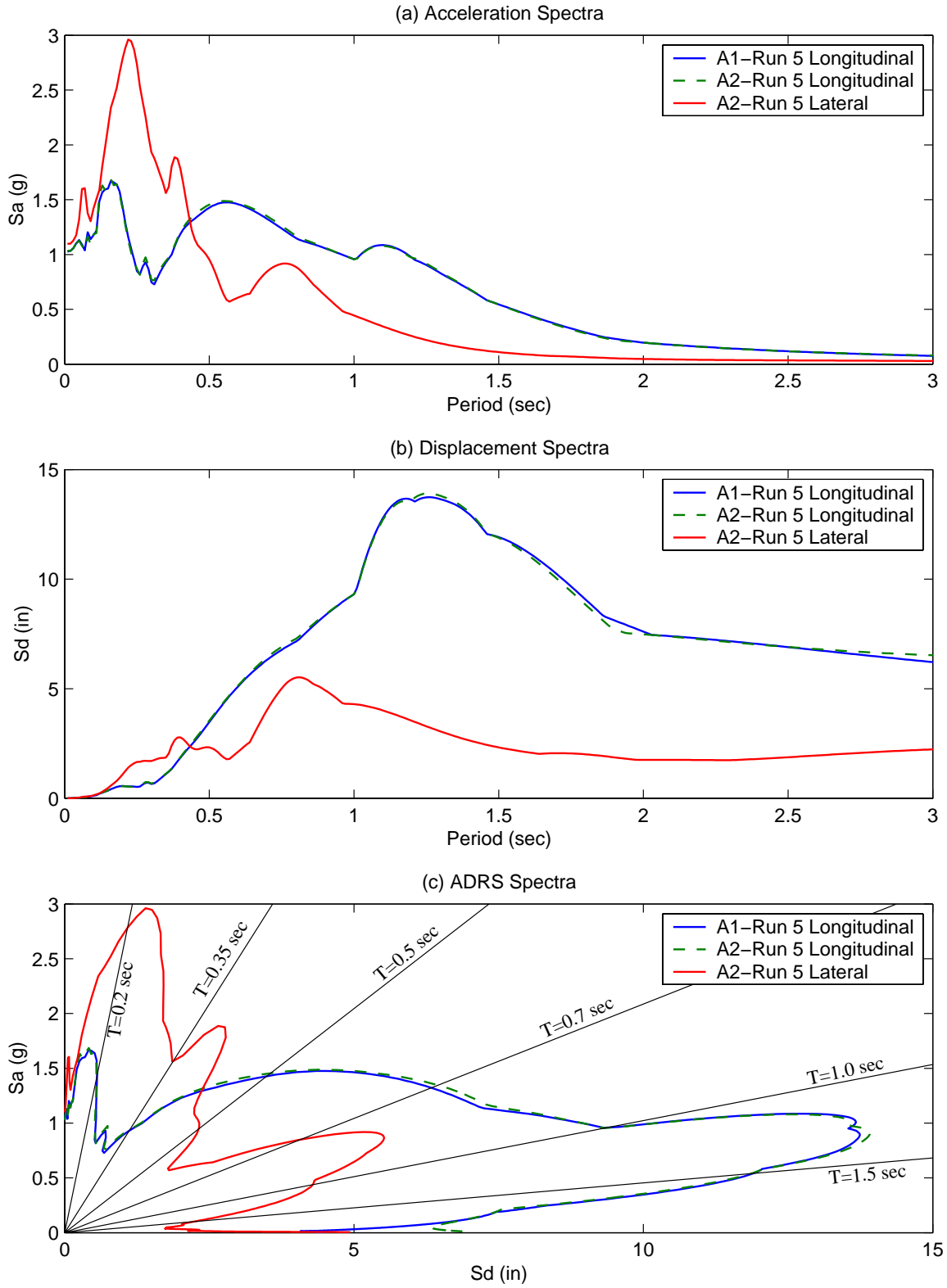
Figure 4-16. Response spectra of the longitudinal and lateral shaking table acceleration time histories recorded during Run 5 (maximum level earthquake) of tests A1 and A2.
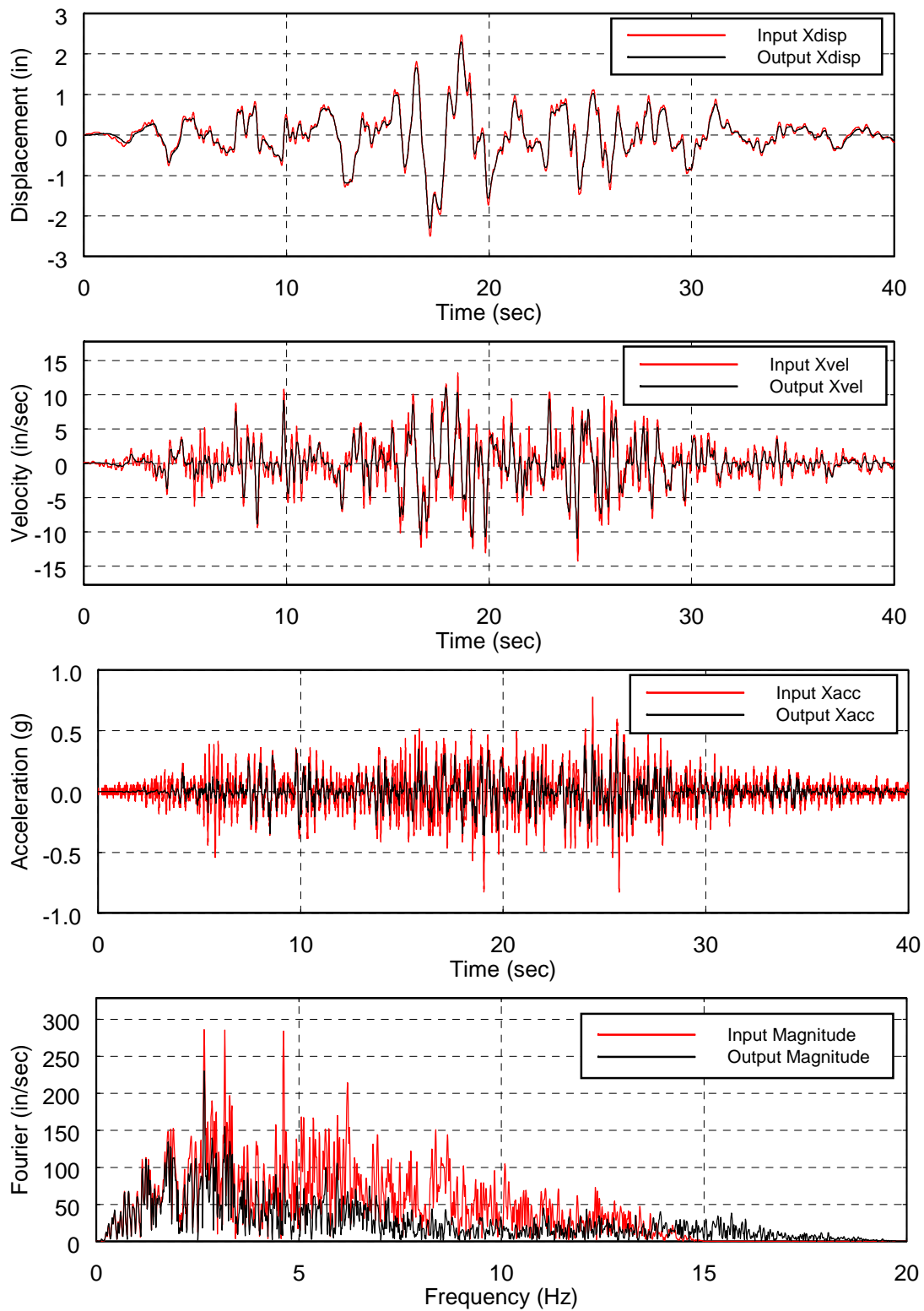
Figure 4-17. Shaking table input and recorded time histories of the record Llolleo 10°
(Longitudinal).
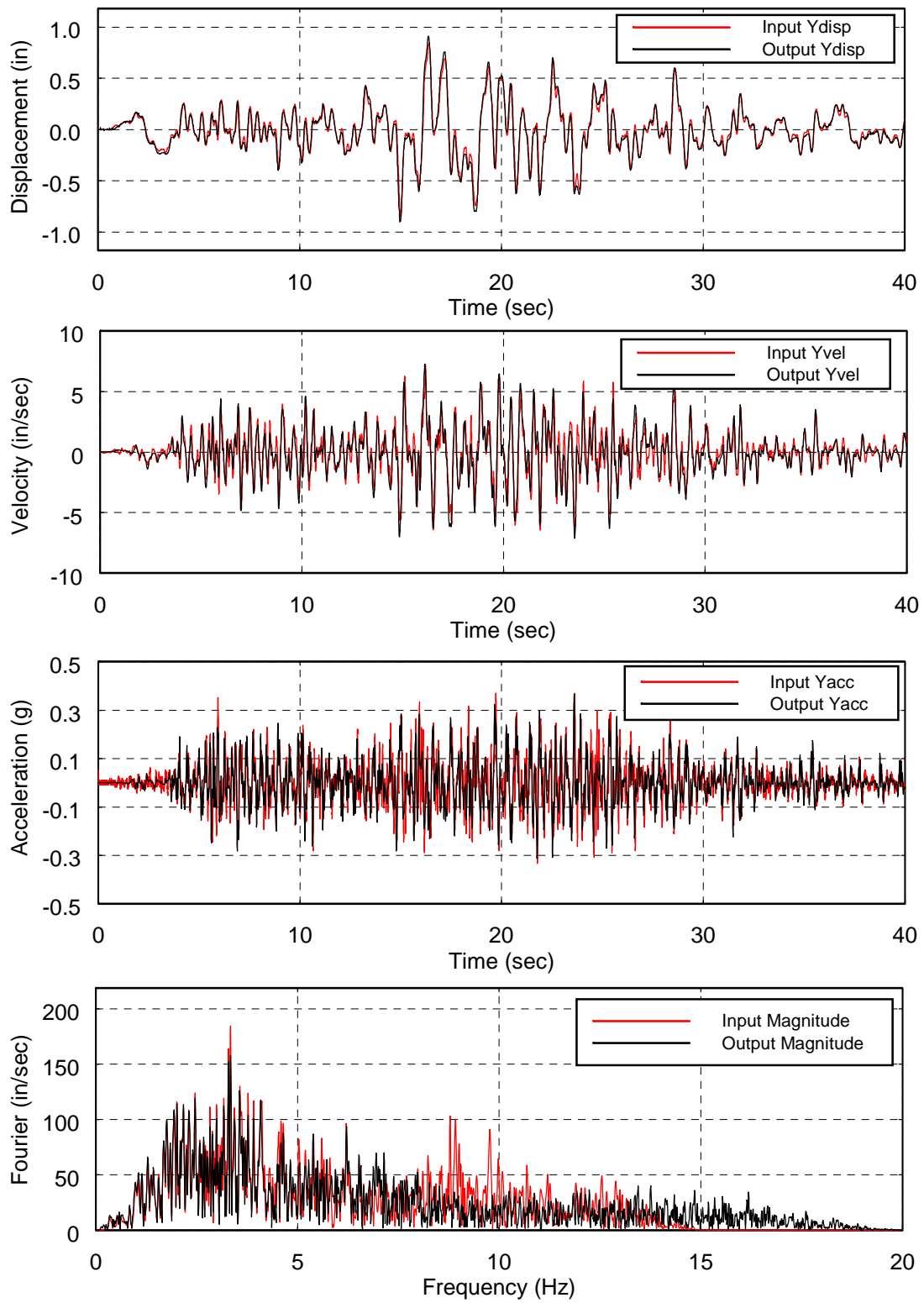
Figure 4-18. Shaking table input and recorded time histories of the record Llolleo 100° (Lateral).

71
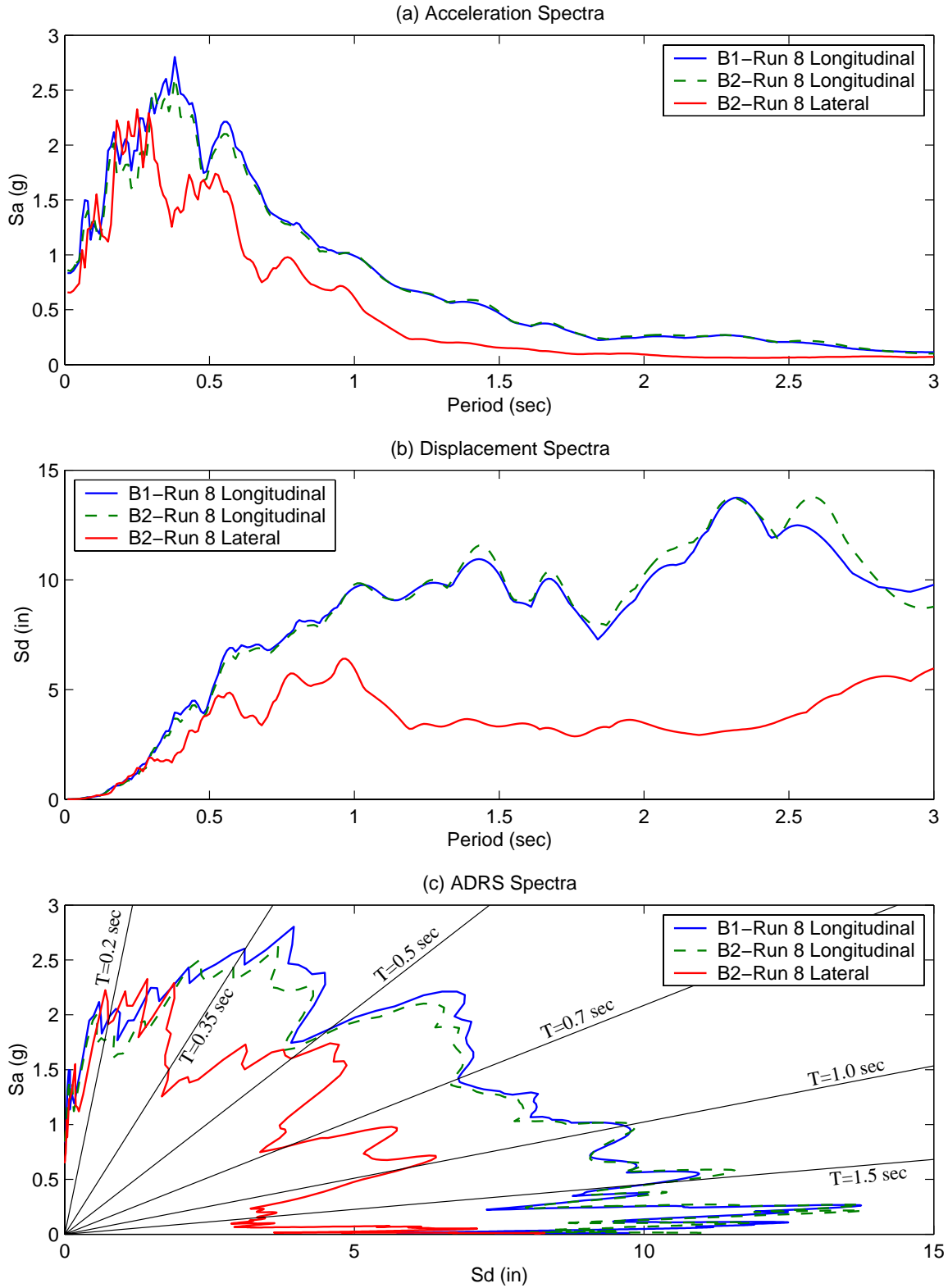
Figure 4-19. Response spectra of the longitudinal and lateral shaking table acceleration time histories recorded during Run 8 (maximum level earthquake) of tests B1 and B2.

4.5   SHAKING TABLE PERFORMANCE

Before studying the effects of the ground motions excitations on the specimens, it is desirable to investigate the performance of the shaking table. Performance is defined as the ability of the shaking table to accurately reproduce the input signal. This is illustrated in Figures 4-14 to 4-18, in which it is shown that the input signals are reproduced with a fair degree of accuracy for a selected run. Another aspect of performance is the repeatability of a certain signal, i.e. whether the repetitive application of an input signal results in small variations of the output signal. This is important when comparing the response of a specimen to two different runs of the same magnitude or when comparing the response of two specimens subjected to unidirectional and bidirectional excitations respectively.

Figures 4-20 to 4-23 illustrate the performance by comparing the recorded acceleration and displacement time histories during the maximum level runs for each of the four tests. Spectral accelerations and displacements are also compared. The data recorded during various runs matches well. The displacements are particularly close, while the accelerations are slightly less accurate. The spectral accelerations and displacements seem to agree well, in general. The only exception was Run 8 of Test B1. In that run, the shaking table did not behave as expected in the initial few seconds of the test. However, the remaining part of the excitation matches well with the other runs.

4.6   TESTING SEQUENCE

Each of the tests started with a series of pullback tests to estimate the natural period and the damping ratio of each of the specimens. A steel column was temporarily attached to the shaking table, and a turn-buckle was used to statically load the specimen with a force of 1-2 kips (4.45 to 8.9 kN) through a cable that was wrapped around the top of the column. The cable had a calibrated load cell to measure the exerted force at one end and a machined bolt to be cut at the other end. A bolt cutter was used to cut the bolt and initiate the free vibration of the specimen. The table was supported during these tests on its static rests to avoid significant movement of the table during vibration. The displacement and acceleration time histories of the mass block were recorded.

A series of very low level shaking tests were then performed that consisted of a small fraction of the record or white noise as input to the shaking table. The Fourier amplitude spectra from these tests were computed to identify the frequency and damping of the specimens at small deformations. The white noise tests were repeated between different runs to detect changes in the effec-
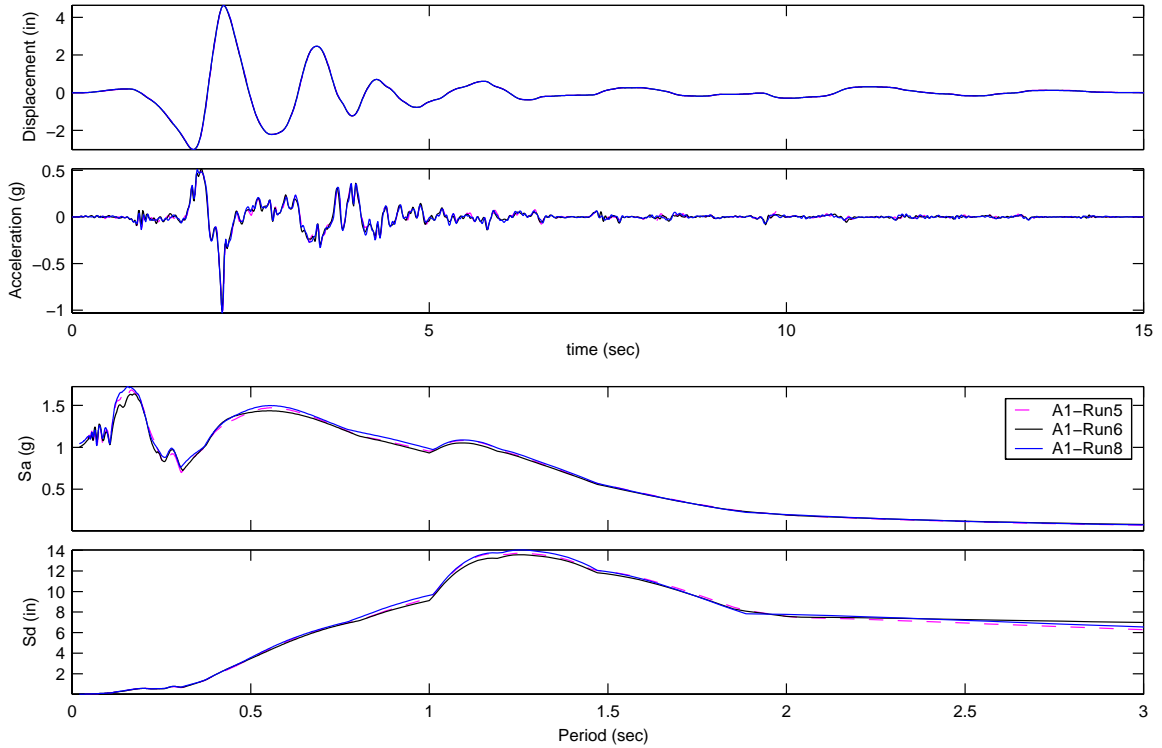
Figure 4-20. Shaking table performance during three runs of test A1.
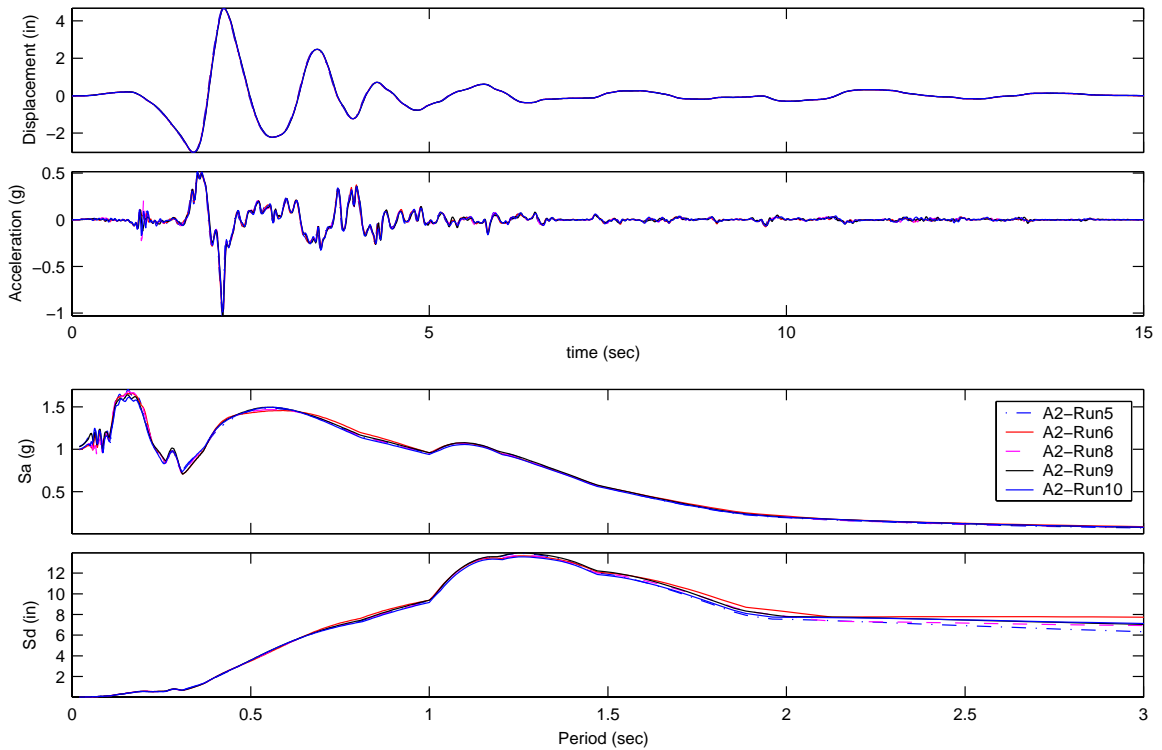
Figure 4-21. Shaking table performance during five runs of test A2.
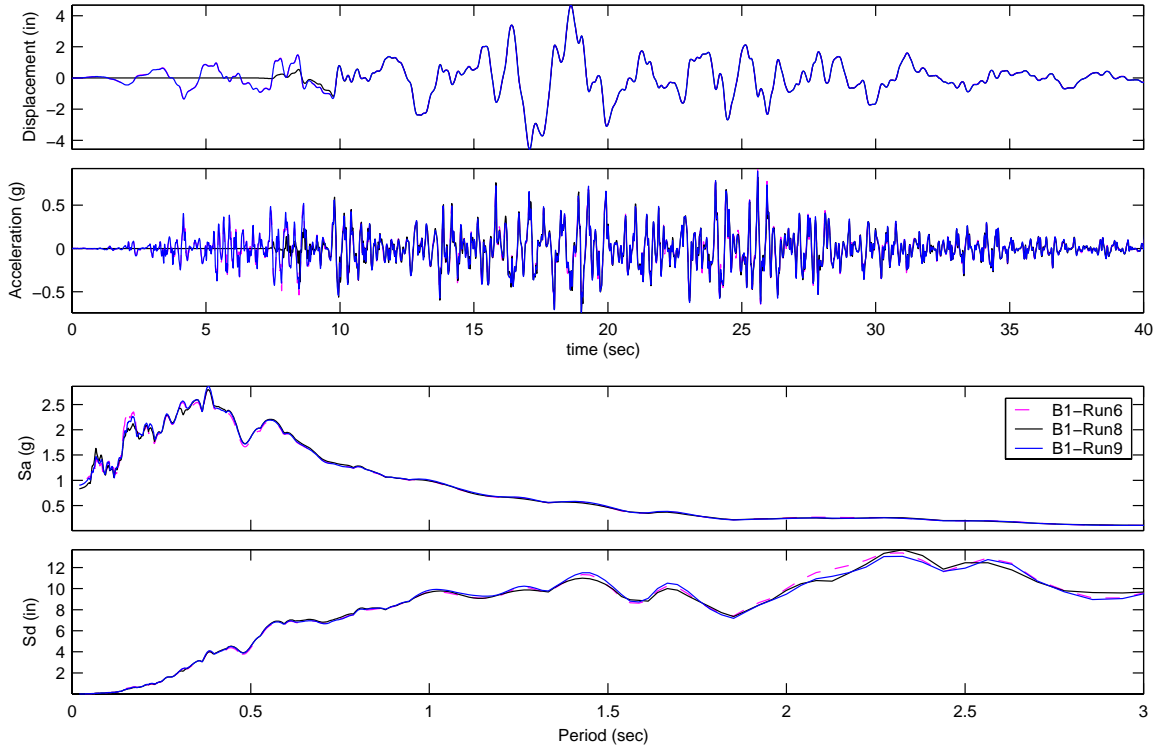
Figure 4-22. Shaking table performance during three runs of test B1.
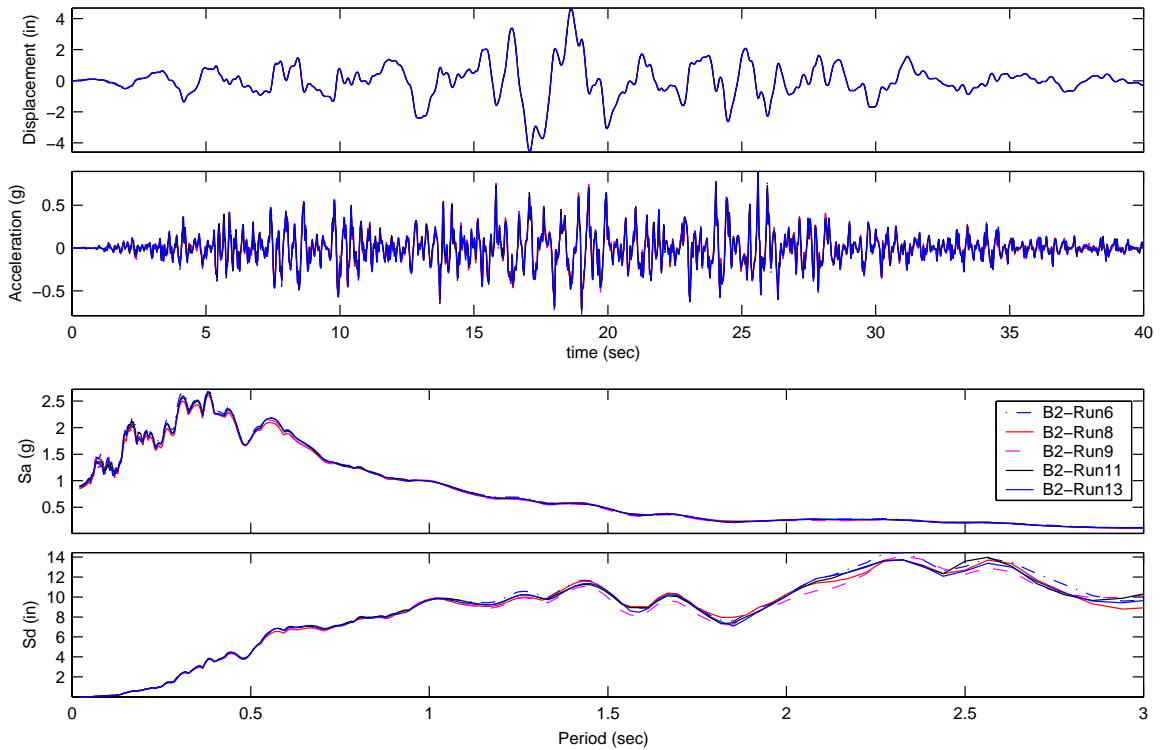
Figure 4-23. Shaking table performance during five runs of test B2.

75

tive period of the specimen after each run. Each specimen was subjected to several runs in which the earthquake record selected for a particular specimen was run at different amplitudes. The runs considered for each specimen are shown in Tables 4-1 and 4-2. Note that exactly the same amplitude sequences were used for the corresponding runs for specimen pairs A1/A2 and for B1/B2. In this way, the effect of bidirectional motion could be assessed by comparing the response of the two specimens in each pair.

Each specimen was initially subjected to one or more runs at or below the expected yield level. These tests help identify the response in the elastic range and the column behavior under a small frequent earthquake. The level was then raised to the *design level* which was selected such that the record's spectral acceleration measured at the specimen's period matched the spectral acceleration of the ARS spectra (at the prototype period). Following the design level, the *maximum level* earthquake was imposed. The amplitude of this record corresponded to about 1.5 to 2 times the design level earthquake. This level matched the capacity of the simulator. In the next run, the shaking level was taken back to the design level, which would be similar to the effect of a major aftershock on a bridge that has been previously subjected to a very strong motion. The comparison of the two design level tests would help assess the effect of cumulative damage on specimen response. These runs constituted the portions of the program to assess the behavior of the bridge columns designed according to BDS.

Since none of the specimens were severely damaged at this stage, additional tests were run to assess and compare the damage and failure characteristics of the columns under repeated dynamic loading. The maximum and design level runs were repeated until the column lost significant strength due to bar buckling and fracture as well as concrete crushing and fracture of confining spirals. The number of additional repetitions at maximum level excitation needed to reach failure ranged between 3 and 6 for all of the four columns. Testing was stopped when the lateral resistance of the column degraded significantly or laboratory safety became a concern.

For each of the runs, the peak acceleration, peak displacement, and longitudinal and lateral span settings for the table controllers are shown in Tables 4-1 and 4-2. The span is a measure of the peak displacement of the record proportional to the limit displacement of the table. A maximum possible span of 1000 corresponds to a table peak displacement of about 5.0 in. (127 mm).

Table 4-1 Summary of measured peak displacement and acceleration for specimens A1 and A2.

Run #	Description	Specimen A1			Specimen A2		
		Span	**PGA**[a]	**PGD**[b]	**Span**	**PGA**	**PGD**
Run 1	Yield	164	0.17g	0.91"	[164 , 184][c]	[0.18g,0.21g]	[0.75",0.18"]
Run 2	Design 1	600	0.55g	2.75"	[600 , 277]	[0.55g,0.67g]	[2.85",0.78"]
Run 3	Max 1	900	0.88g	4.17"	[900 , 184]	[0.93g,1.02g]	[4.3", 1.2"]
Run 4	Design 2	600	0.55g	2.79"	[600 , 277]	[0.55g,0.66g]	[2.81",0.79"]
Run 5	Max 2	1000	1.0g	4.7"	[1000 , 307]	[1.03g,1.14g]	[4.7", 1.3"]
Run 6	Max 3	1000	1.0g	4.7"	[1000 , 307]	[0.99g,1.04g]	[4.74", 1.3"]
Run 7	Design 3	600	0.53g	2.78"	[600 , 277]	[0.54g,0.62g]	[2.82",0.77"]
Run 8	Max 4	1000	1.02	4.7"	[1000 , 307]	[1.02g,1.09g]	[4.76", 1.3"]
Run 9	Max 5				[1000 , 307]	[1.02g,1.07g]	[4.77", 1.3"]
Run 10	Max 6				[1000 , 307]	[1.04g,1.11g]	[4.77", 1.29"]

a. PGA = Peak Ground (Table) Acceleration

b. PGD = Peak Ground (Table) Displacement

c. [longitudinal,lateral] : notation is used to imply components (displacement, acceleration, span) along longitudinal and lateral directions.

Table 4-2 Summary of measured peak displacement and acceleration for specimens B1 and B2.

Run #	Description	Specimen B1			Specimen B2		
		Span	PGA[a]	PGD[b]	Span	PGA	PGD
Run 1	Low Level 1	50	0.05g	0.19"	[50 , 20][c]	[0.04g,0.05g]	[0.20",0.08"]
Run 2	Low Level 2	100	0.10g	0.42"	[100 , 40]]	[0.08g,0.15g]	[0.43",0.20"]
Run 3	Yield 1	150	0.15g	0.66"	[150 , 60]	[0.13g,0.21g]	[0.69",0.28"]
Run 4	Yield 2	200	0.19g	0.90"	[200 , 80]	[0.19g,0.26g]	[0.94",0.35"]
Run 5	Design 1	500	0.50g	2.30"	[500 , 200]	[0.52g,0.37g]	[2.32",0.92"]
Run 6	Max 1	1000	0.99g	4.70"	[1000 , 400]	[0.93g,0.73g]	[4.73",1.83"]
Run 7	Design 2	500	0.50g	2.32"	[1000 , 400]	[0.47g,0.37g]	[2.32",0.90"]
Run 8	Max 2	1000	0.91g	4.71"	[1000 , 400]	[0.96g,0.69g]	[4.65", 1.86"]
Run 9	Max 3	1000	1.02g	4.73"	[1000 , 400]	[0.90g,0.71g]	[4.67", 1.83"]
Run 10	Max 4				[1000 , 400]	[0.95g,0.73g]	[4.67", 1.82"]
Run 11	Max 5				[1000 , 400]	[0.97g,0.61g]	[4.69", 1.83"]
Run 12	Max 6				[1000 , 400]	[0.96g,0.70g]	[4.69",1.83"]
Run 13	Max 7				[1000 , 400]	[0.96g,0.73g]	[4.69",1.85"]

a. PGA = Peak Ground (Table) Acceleration

b. PGD = Peak Ground (Table) Displacement

c. [longitudinal,lateral] : notation is used to imply components (displacement, acceleration, span) along longitudinal and lateral directions.

5 Experimental Results

5.1 INTRODUCTION

This chapter describes the basic results obtained from the tests of the four column specimens. For each specimen, the response and damage occurring during each run are described (Sections 5.2 and 5.3). Global response measures (e.g. relative displacement, base shear, and overturning moment) are discussed in Section 5.4, and local response measures (e.g. strains, curvature) are discussed in Section 5.5. Section 5.6 presents a correlation of damage indices to the recorded response and the observed damage progression. Information is also presented in Section 5.7 on the change of dynamic properties of the specimens throughout the test program.

As indicated previously, Specimens A1 and A2 were subjected to a modified version of the Olive View record obtained during the 1994 Northridge earthquake. The NF15 (fault normal) component was imposed in the longitudinal direction of both Specimens A1 and A2. Specimen A2 was simultaneously subjected to the fault parallel component NF16, whereas Specimen A1 was only subjected to the unidirectional excitation. Specimens B1 and B2 were both subjected to modified versions of the Llolleo record obtained during the 1985 Chilean earthquake. The 10° component was imposed along the longitudinal axis of both Specimens B1 and B2. The 100° component was simultaneously imposed along the lateral axis of Specimen B2. The orientation of the columns principal axes can be identified in Figure 4-3.

To help identify the location of damage, longitudinal bars are numbered as shown in Figure 5-1. Moreover, in the photographs presented later, the compass orientations shown in this figure are stenciled on the specimen, and a grid has been painted on the specimen. The grid lines are spaced at 4 in. vertically along the column near its base, and horizontally at 30° increments around the perimeter. These orientations and designations are used to describe the type and location of physical damage in the test specimens, including cracking and spalling of concrete, buckling and fracture of longitudinal reinforcing bars, kinking and fracture of spirals reinforcement, etc.

Tables 5-2 through 5-5 present the physical damage observed following each run and other derived global response data for Specimens A1 through B2. Information is also provided regarding the peak and residual relative displacements, column shears, and base moments.

Figure 5-1. Bar Numbering.

To compute the maximum relative displacement of a specimen occurring along one of its principal axes, the difference is computed for that direction between the measured horizontal displacement at mid-height of the mass block and the horizontal displacement at the shaking table level. In Tables 5-2 to 5-5, the cumulative residual relative displacements remaining in each specimen following a particular run are noted as *Residual Relative Displacements*. However, for the purpose of computing the *Peak Relative Displacement*, those residual displacements are assumed zero at the beginning of each run.

Since load cells were not used to support the test specimen, peak horizontal column shears are estimated using Newton's second law. Thus, the peak column shear is approximated as the value of the mass of the top mass block times the peak measured horizontal acceleration at the mid-height of mass block in the direction of interest. Time histories of this product are used subsequently as estimates of the time history of column shear, and to make plots of column force versus relative displacement. However, it must be recognized that these time histories of mass times acceleration only approximate the variation of column shear, as the product also includes any viscous damping forces that may be present. At the point of maximum relative displacement, these errors should be small.

In viewing the time histories of horizontal acceleration at the top of the test specimens, it is apparent that there are significant higher frequency components to the response. This is principally due to higher modes of response introduced by the significant rotation (about a horizontal axis) of the large supported mass block.

The overturning moment at the base of the column is calculated as the sum of three components due to the lateral and rotational inertia forces in addition to the P-Δ secondary moment as given by Equation 4-5 and illustrated in Figure 4-13.

To illustrate second order effects, base moment values with and without P-Δ effects will be presented. The sum of these components will give the overturning moment at the base of the specimen. Dividing this overturning moment by the height from the base to the center of mass will pro-

vide the equivalent lateral force to be applied to the tip of a single degree of freedom, cantilever column to produce the same base moment. It is expected that the time history of this force will have far less higher mode contribution [14].
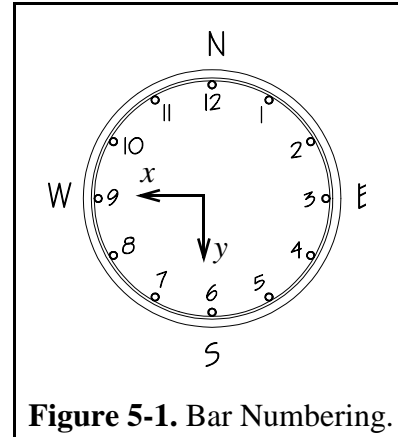
In addition to the data summarized in Tables 5-2 to 5-5, sketches of crack patterns on all column sides and photographs of the damage to each specimen following various runs are shown in Appendix C.

Histories of relative displacement, column shear, overturning moment as well as hysteretic loops of column shear versus relative displacement are included in Appendix D. To facilitate comparison of relative displacement, column shear and base moment between different runs and specimens, Figures 5-9 to 5-20 summarize those quantities for each specimen. Figures 5-39 and 5-40 compare response quantities for Specimens A1 and A2, while Figures 5-44 and 5-45 compare the same quantities for Specimens B1 and B2.

5.2   OBSERVED COLUMN RESPONSE

This section describes the physical behavior of the four specimens. Each of the four tests was started by subjecting the column to pull back tests to determine the period and damping, followed by low level testing consisting of a low percentage of the ground motion record and random white noise. This was followed by a number of higher level runs consisting of the respective records scaled to levels corresponding to the nominal yield level, design level, or maximum level. Low level white noise tests were performed in both directions between successive runs to characterize the effect of shaking on the specimen dynamic properties. Table A-2 summarizes all the runs performed for each of the specimens.

Generally, the testing sequence of the bidirectional specimens followed the testing histories of the corresponding unidirectionally loaded specimen. In the bidirectional case, the second component was scaled similar to the first component in all runs. Table 5-1 presents a quick test summary for each of the specimens, while Tables 5-2 through 5-5 describe the damage evolution for each specimen in detail.

The most immediate objective of the tests was to evaluate the adequacy of the column design in response to an event corresponding to the design level, and to a possibly higher event. Hence, more focus will be placed on the first few runs, including the first design and maximum levels, and the second design level which may represent a significant aftershock. Further experi-

Table 5-1 Test summary information for each specimen.

	Specimen A1	Specimen A2	Specimen B1	Specimen B2
Type of Excitation	Unidirectional	Bidirectional	Unidirectional	Bidirectional
Earthquake Record	Olive View, Northridge 1994	Olive View, Northridge 1994	Llolleo, Chile 1985	Llolleo, Chile 1985
Component	Normal (NF15)	Parallel (NF14)	Llolleo 10°	Llolleo 100°
Major Runs	3 Design/4 Max	3 Design/6 Max	2 Design/3 Max	2 Design/7 Max
First Fractured Bar	Spiral	Longitudinal	Spiral	Longitudinal
Failure Run	Run 6 (Max 3)	Run 9(Max 5)	Run 8(Max 2)	Run 12 (Max 6)
Fractured Long. Bars	#3 & #9	#9	#3, #4 and #9	#3 and #9
Buckled Long. Bars	#10	#10	#2, #5 and #10	#4
Fractured Spirals	1 spiral (West Side)	1 spiral (West Side)	2 spirals (East and West sides)	1 spiral (East Side)
Detailed Description of Performance	Table 5-2	Table 5-3	Table 5-4	Table 5-5
Crack Maps Figures	C-2 to C-6	C-7 to C-13	C-14 to C-17	C-18 to C-24
Pictures of Damage	C-25 to C-36	C-37 to C-54	C-55 to C-66	C-67 to C-82
Measured Response Plots	D-1 to D-4	D-5 to D-14	D-15 to D-18	D-19 to D-28

mental data from repetitive testing are used subsequently to estimate the toughness of such columns, and validate available failure models and indices.

Overall, no permanent damage was observed in any of the specimens prior to the design level earthquake. Only minor cracking was observed up to that level, and most cracks closed completely by the end of shaking to the point where they could not be distinguished. This shows that the columns would exhibit an excellent performance during a functional-evaluation level earthquake.

The design level record resulted in significant cracking throughout the height of the column. This cracking pattern of the entire height is a result of the higher mode effects due to the rotational inertia of the mass block, which resulted in a non-zero moment diagram throughout the height of the column. However, the cracking was more concentrated at the bottom of the column near the footing as would be expected, which is also where most of the subsequent damage to the reinforcement was observed. Minor spalling was observed near the base of the column during the design level event. The performance of the columns through the design level run was deemed very satisfactory. Damage mainly consisted of minor spalling of the concrete cover, and the measured permanent deformation was generally small.

The application of the maximum level earthquake caused an increase in displacement demand, and resulted in more spalling in the plastic hinge region. A complete plastic hinge eventually formed as additional spalling occurred at the base during the maximum level event. Most of the cover spalled over a height of about 12 in. (305 mm) from the top of the footing. The overall behavior was still deemed satisfactory since there was no apparent distress in the column's reinforcement, and since the residual deformations were still acceptable. Specimen B1 (which showed some signs of bar buckling at this level, and sustained a permanent lateral deformation of about 1 in.) was the only exception to the above.

After the application of the first maximum level earthquake, a second design level run was performed, which is representative of a large aftershock. This repetition of the design level caused minor additional damage consisting of the spalling of small pieces of concrete.

After several (1 to 4) applications of the maximum level earthquake, the longitudinal reinforcement started to buckle. This was typically followed by fracture of spiral reinforcement near the buckled longitudinal bar, and fracture of the longitudinal reinforcement itself. Even though longitudinal reinforcement fracture was associated with loss of strength capacity, the specimens were in general able to sustain additional repetitions of the maximum level earthquake. This additional excitation ranged from one to several applications of the whole record. The tests were usually stopped after the specimen had sustained significant damage and it was deemed unsafe to subject it to additional excitations. The ability of the tested columns to sustain several repetitions of the maximum level earthquake, which exceeds the seismic demands expected during the lifetime of a bridge, illustrates the ductile behavior of those columns. Furthermore, the residual capacity remaining even after some longitudinal reinforcement has fractured indicates that a column that

Table 5-2 Summary of response for Specimen A1.

Run #	Performance Level	Table Displacement and Acceleration		Relative Displacement[a]		Base Shear and Moment		Observations
		PGA[b] (g)	PGD[c] (in)	Peak[d] (in)	Residual[e] (in)	Shear[f] (kip)	Moment[g] (kip·in)	
		Long[h]	Long	Long	Long	Long	Long	
1	Yield Level 30% NF15	0.16	0.72	1.25	0.01	11.7	1304	No cracks or visible signs of damage.
2	Design Level 1 110% NF15	0.58	2.76	4.87	0.48	21.6	1777	Some spalling appeared at the west face of the column. Cracks developed over the full height of the column on both east and west sides, with more cracks near the bottom; a large crack formed at the interface with the footing. Cracks were also developed near the top slab especially on the east side. Cracks closed after the end of the test.
3	Maximum Level 1 165% NF15	0.90	4.19	5.24	0.40	17.6	1737	Additional concrete spalled on the west side, and the first spalling occurred on the east side. More cracks appeared over the height of the column.
4	Design Level 2 110% NF15	0.60	2.80	3.79	0.47	16.7	1501	Minor additional spalling was observed.
5	Maximum Level 2 180% NF15	1.04	4.70	6.67	0.11	17.1	1751	More spalling was observed, and the middle bar on the west side (bar #9) started to buckle.
6	Maximum Level 3 180% NF15	1.02	4.70	6.83	0.59	16.6	1701	On the west side, significant new spalling occurred with two bars buckling (#9 and #10), and one spiral (third spiral from face of footing) fractured at the point of contact with bar #9. Less damage occurred on the east side.
7	Design Level 3 110% NF15	0.57	2.79	3.84	0.45	15.1	1315	No new damage but predominant period of response increased.
8	Maximum Level 4 180% NF15	1.03	4.71	7.49	1.62	14.4	1474	One longitudinal reinforcement bar broke in tension at each face (first bar #9 on the west face then bar #3 on the east face). This happened during one big cycle in which the center of mass experienced a large lateral displacement. A significant residual displacement was observed.

a. Relative Displacement is the difference between the displacement of the center of mass and the table displacement = Block Disp - Table Disp

b. PGA: Peak Ground (Table) Acceleration

c. PGD: Peak Ground (Table) Displacement

d. Peak Relative Displacement assuming zero residual displacement at the beginning of the run

e. Cumulative Residual Relative Displacement at the end of the run

f. The shear force is estimated as the mass of the block times the acceleration at the center of the block, ignoring damping forces

g. Base moment is estimated using Newton's second law accounting for translational and rotational inertia forces and ignoring damping forces

h. Long: Measurements in the longitudinal direction

Table 5-3 Summary of response for Specimen A2.

Run #	Performance Level	Table Displacement and Acceleration				Relative Displacement[a]				Base Shear and Moment				Observations
		PGA[b] (g)		PGD[c] (in)		Peak[d] (in)		Residual[e] (in)		Shear[f] (kip)		Moment[g] (kip·in)		
		Long[h]	Lat[i]	Long	Lat	Long	Lat	Long	Lat	Long	Lat	Long	Lat	
1	Yield Level 30% NF15/16	0.16	0.19	0.75	0.18	1.33	0.69	0.02	0	11.8	7.4	1298	723	Some horizontal cracks opened during the test but they were closed by the end of the test. No visible signs of damage.
2	Design Level 1 110% NF15/16	0.58	0.65	2.85	0.78	4.76	1.61	0.62	0.02	19.8	15.1	1719	658	Some spalling mostly at the west side of the column, with no signs of bar buckling. Cracks were formed during the shaking at both the east and west faces partly extending to the south and north faces. Cracks also formed at the column-footing interface.
3	Maximum Level 1 165% NF15/16	0.91	0.95	4.27	1.17	5.4	2.29	0.47	0.06	15.8	24.5	1701	756	More damage was observed, especially on east side face where a 4 in. tall piece of concrete spalled. More crushing occurred on the west face. The spalling extended about 8 in. from the base. The cover was severely cracked up to a height of 12 in. (0.75 x Diameter).
4	Design Level 2 110% NF15/16	0.57	0.61	2.81	0.79	3.63	1.65	0.61	0.06	15.8	18.8	1503	681	More crushing was observed, but without signs of bar buckling. On the west face, some spalling occurred in the already cracked region.
5	Maximum Level 2 180% NF15/16	1.03	1.06	4.74	1.31	6.8	2.45	0.08	0.06	15.5	28.1	1694	830	More spalling occurred around the base. Spalling at the top of the column was also observed. Bar pullout seems to increase at the base making the specimen more flexible.
6	Maximum Level 3 180% NF15/16	1.03	1.08	4.74	1.3	6.94	2.43	0.39	0.01	14.9	27.1	1671	824	Little additional damage was observed on the east side. Small pieces of concrete spalled at the west side near the base up to a height of about 12 in.
7	Design Level 3 110% NF15/16	0.57	0.61	2.82	0.77	3.82	1.5	0.3	0	14.9	20.4	1352	607	Minor additional spalling.
8	Maximum Level 4 180% NF15/16	1.02	1.05	4.76	1.3	7.2	2.41	0.87	0.02	15	26.9	1656	814	Bar #9 (See Figure 4-1) on the west side buckled. Increased Spalling occurred on east and west sides especially in the east-south area near the base.

Table 5-3 Summary of response for Specimen A2.

Run #	Performance Level	Table Displacement and Acceleration				Relative Displacement[a]				Base Shear and Moment				Observations
		PGA[b] (g)		PGD[c] (in)		Peak[d] (in)		Residual[e] (in)		Shear[f] (kip)		Moment[g] (kip·in)		
		Long[h]	Lat[i]	Long	Lat	Long	Lat	Long	Lat	Long	Lat	Long	Lat	
9	Maximum Level 5 180% NF15/16	1.03	1.07	4.77	1.3	7.34	2.52	2.05	0.13	13.8	27	1420	789	Bar #9 on the west side fractured in tension. Bar #10 buckled slightly causing the remaining cover around it to spall. The third spiral on the west side fractured at the end of the run.
10	Maximum Level 6 180% NF15/16	1.05	1.1	4.77	1.29	7.93	2.37	6.07	0.54	12.3	29.2	1360	825	Very large peak and residual displacements were observed. Buckling of bar #10 becomes more pronounced.

a. Relative Displacement is the difference between the displacement of the center of mass and the table displacement = Block Disp - Table Disp

b. PGA: Peak Ground (Table) Acceleration

c. PGD: Peak Ground (Table) Displacement

d. Peak Relative Displacement assuming zero residual displacement at the beginning of the run

e. Cumulative Residual Relative Displacement at the end of the run

f. The shear force is estimated as the mass of the block times the acceleration at the center of the block, ignoring damping forces

g. Base moment is estimated using Newton's second law accounting for translational and rotational inertia forces and ignoring damping forces

h. Long: Measurements in the longitudinal direction

i. Lat: Measurements in the lateral direction

Table 5-4 Summary of response for Specimen B1.

Run #	Performance Level	Table Displacement and Acceleration		Relative Displacement[a]		Base Shear and Moment		Observations
		PGA[b] (g)	PGD[c] (in)	Peak[d] (in)	Residual[e] (in)	Shear[f] (kip)	Moment[g] (kip·in)	
		Long[h]	Long	Long	Long	Long	Long	
1	Low Level 1 13% Llolleo	0.03	0.19	0.23	0.00	4.6	509	No visible signs of damage.
2	Low Level 2 26% Llolleo	0.08	0.42	0.50	0.00	7.5	840	No visible signs of damage.
3	Yield Level 1 39% Llolleo	0.14	0.66	0.79	0.00	10.1	1106	This level was slightly under yield. The observed displacement of the column was about 0.8 in. which is slightly less than the yield displacement of 1 in.
4	Yield Level 2 52% Llolleo	0.19	0.90	1.48	0.00	15.0	1493	Slightly above yield. No visible damage.
5	Design Level 1 130% Llolleo	0.48	2.30	3.42	0.04	17.6	1717	Some spalling occurred at the column base. Major flexural cracks were observed over a height of about 20 in. (1.25 D), with other cracks distributed over the height of the column.
6	Maximum Level 1 260% Llolleo	0.87	4.70	5.81	1.00	27.5	1788	Spalled concrete fell off the base of the column. Bar #4 on the east side buckled and bars #2 and #3 were starting to buckle.
7	Design Level 2 130% Llolleo	0.46	2.32	3.10	0.89	18.1	1383	Additional concrete damage due to this run was not significant. Smaller pieces of concrete were spalled. During each cycle, buckled bar #4 on the east side was pressing on the third spiral from the footing which was starting to kink at that location (observed in video replay).
8	Maximum Level 2 260% Llolleo	0.89	4.71	5.25	0.74	30.0	1715	Two longitudinal bars and one spiral fractured. Bar #4 on the east-south side buckled more causing the spiral to fracture at that location. The middle longitudinal bar at the east side (#3) fractured in the tension part of the same cycle. The middle longitudinal bar at the west side (#9) fractured later in the run.

Table 5-4 Summary of response for Specimen B1.

Run #	Performance Level	Table Displacement and Acceleration		Relative Displacement[a]		Base Shear and Moment		Observations
		PGA[b] (g)	PGD[c] (in)	Peak[d] (in)	Residual[e] (in)	Shear[f] (kip)	Moment[g] (kip·in)	
		Long[h]	Long	Long	Long	Long	Long	
9	Maximum Level 3 260% Llolleo	0.91	4.73	5.09	0.66	26.0	1525	On the west side, the north-west bar (#10) buckled, causing more crushing and fracturing a spiral. On the east side, the buckled bar (#4) fractured after losing confinement from the spiral which fractured in the previous run. The neighboring bar (#5) also buckled, extending the spalling well into the south face.

a. Relative Displacement is the difference between the displacement of the center of mass and the table displacement = Block Disp - Table Disp

b. PGA: Peak Ground (Table) Acceleration

c. PGD: Peak Ground (Table) Displacement

d. Peak Relative Displacement assuming zero residual displacement at the beginning of the run

e. Cumulative Residual Relative Displacement at the end of the run

f. The shear force is estimated as the mass of the block times the acceleration at the center of the block, ignoring damping forces

g. Base moment is estimated using Newton's second law accounting for translational and rotational inertia forces and ignoring damping forces

h. Long: Measurements in the longitudinal direction

Table 5-5 Summary of response for Specimen B2.

Run #	Performance Level	Table Displacement and Acceleration				Relative Displacement[a]				Base Shear and Moment				Observations
		PGA[b] (g)		PGD[c] (in)		Peak[d] (in)		Residual[e] (in)		Shear[f] (kip)		Moment[g] (kip·in)		
		Long[h]	Lat[i]	Long	Lat	Long	Lat	Long	Lat	Long	Lat	Long	Lat	
1	Low Level 1 13% Llolleo	0.02	0.05	0.20	0.08	0.15	0.20	0.00	0.00	2.5	3.3	288	355	A small fraction of the motion was applied. No observed cracks.
2	Low Level 2 26% Llolleo	0.07	0.15	0.43	0.20	0.42	0.49	0.01	0.03	6.0	7.9	667	661	A small fraction of the motion was applied. No observed cracks.
3	Yield Level 1 39% Llolleo	0.12	0.19	0.69	0.28	1.32	0.76	0.02	0.03	11.8	9.7	1333	911	This run caused slight yielding in the column. No observable damage.
4	Yield Level 2 52% Llolleo	0.17	0.21	0.94	0.35	1.73	1.03	0.02	0.17	14.3	11.9	1462	934	This run was slightly larger than yield. Some cracks were observed all around the base.
5	Design Level 1 130% Llolleo	0.47	0.36	2.32	0.92	2.85	1.81	0.08	0.07	15.7	15.5	1482	1094	Some minor spalling was observed on the east and west faces.
6	Maximum Level 1 260% Llolleo	0.90	0.67	4.73	1.83	5.20	2.67	0.18	0.05	25.5	20.3	1649	1166	More spalling was observed especially on the east face.
7	Design Level 2 130% Llolleo	0.43	0.36	2.32	0.90	2.94	1.62	0.16	0.21	19.0	14.2	1332	818	Little additional damage.
8	Maximum Level 2 260% Llolleo	0.88	0.65	4.65	1.86	5.59	2.66	0.29	0.07	23.7	19.3	1644	1128	Spalling on the north-east side.
9	Maximum Level 3 260% Llolleo	0.87	0.69	4.67	1.83	5.52	2.69	0.39	0.02	24.7	19.7	1609	1081	More crushing was seen at the north-west and south-east sides. Spalled area reached about 12 in. on the south-east side.
10	Maximum Level 4 260% Llolleo	0.91	0.67	4.67	1.82	5.45	2.62	0.51	0.03	25.0	18.2	1576	1047	Some minor crushing.

Table 5-5 Summary of response for Specimen B2.

Run #	Performance Level	Table Displacement and Acceleration				Relative Displacement[a]				Base Shear and Moment				Observations
		PGA[b] (g)		PGD[c] (in)		Peak[d] (in)		Residual[e] (in)		Shear[f] (kip)		Moment[g] (kip·in)		
		Long[h]	Lat[i]	Long	Lat	Long	Lat	Long	Lat	Long	Lat	Long	Lat	
11	Maximum Level 5 260% Llolleo	0.89	0.67	4.69	1.83	5.34	2.61	0.66	0.05	25.0	18.0	1557	1025	More concrete crushing. Bar #9 starts to buckle.
12	Maximum Level 6 260% Llolleo	0.90	0.65	4.69	1.83	4.66	2.51	0.80	0.06	25.8	18.1	1392	1008	The middle longitudinal bar on the East side (bar #3) fractured. The middle longitudinal bar on the West side (bar #9) fractured.
13	Maximum Level 7 260% Llolleo	0.89	0.66	4.69	1.85	4.80	2.47	0.96	0.18	24.8	18.4	1351	948	The south-east longitudinal bar (#4) buckled, and a spiral fractured on the east side.

a. Relative Displacement is the difference between the displacement of the center of mass and the table displacement = Block Disp - Table Disp

b. PGA: Peak Ground (Table) Acceleration

c. PGD: Peak Ground (Table) Displacement

d. Peak Relative Displacement assuming zero residual displacement at the beginning of the run

e. Cumulative Residual Relative Displacement at the end of the run

f. The shear force is estimated as the mass of the block times the acceleration at the center of the block, ignoring damping forces

g. Base moment is estimated using Newton's second law accounting for translational and rotational inertia forces and ignoring damping forces

h. Long: Measurements in the longitudinal direction

i. Lat: Measurements in the lateral direction

has been severely damaged in an earthquake might still be able to undergo several cycles without collapsing.

The progress of damage generally agreed well with reported tests on well-confined circular reinforced concrete columns (See for example [50], [47], [51]).

5.3   RECORDED RESULTS

The response histories of selected runs are presented in Appendix D. For each specimen, figures illustrating variables of interest are provided for the following runs: yield level, first design level, first maximum level run and last maximum level run, in addition to some other test runs during which the column experienced significant damage. Each figure includes a number of plots labeled (a) to (q) showing: (a) relative displacement, (b) shear force, and (c) base moment histories. Moment-curvature behavior at the middle of regions 1 to 7 (defined in Figures 4-7 and 4-8) along the column height appear in plots (d), (e), (f), (g), (h), (i) and (j). Hysteretic behavior is presented in plots: (k) base bending moment-displacement and (l) shear force-displacement. Bidirectional displacement and moment interaction are illustrated in plot (m). Plot (m) shows displacement inter-action in the longitudinal direction figure and moment interaction in the lateral direction figure (e.g. see Figures D-7 and D-8). The rest of the plots are: (n) curvature variation against height, (o) moment along height, and (p) deformation along height. Plot (q) shows the elevation of the specimen scaled to the height (elevation) of plots (n), (o) and (p). For each of the figures, a number of peak displacements are identified in plot (a), and identified by numbers 1, 2, 3, etc. The occurrences of those peaks are identified in plots (k), (l) and (m). For plots (n), (o) and (p), only values corresponding to the peaks are presented.

The above response quantities were obtained either directly from collected data or by simple computations, as illustrated in Section 4.3.2.

5.4   GLOBAL RESPONSE MEASURES

The peak displacements and forces are tracked over each run of each specimen test. This information is later used to compare the response of a specimen under different runs, or the response of two specimens during the same run. The complete relative displacement histories of each specimen are plotted in Figures 5-3 through 5-8. Those plots provide a global view of all the shaking runs performed on each specimen, including the offset of the displacement baseline because of residual dis-

placements. Note that the vertical lines in each plot correspond to the end of a run after which the testing was stopped for observation.

Tables 5-2 to 5-5 list values of peak relative and residual displacements and peak shear forces and base moments. Those quantities are also plotted in Figures 5-9 to 5-20 to illustrate the variation of peak displacements and forces throughout the various runs for each test. For each direction of each test, two plots are provided: a displacement plot and a force plot.

5.4.1 Displacements

A comparison of the peak ground displacement, peak relative displacement, cumulative peak relative displacement and cumulative residual displacement is plotted in a displacement plot for each specimen (Figures 5-9, 5-11, 5-13, 5-15, 5-17 and 5-19). The peak relative displacement is the peak relative displacement for each run assuming the specimen started with an initial displacement of zero at the beginning of the run. The cumulative peak relative displacement measures the actual peak deformation during a given run including the residual deformation at the end of the previous run. Figure 5-2 illustrates the different terminology for the peak and residual relative displacements. The figure shows the longitudinal relative displacement history (displacement at center of mass - footing displacement) during the last two runs of Specimen A2.

5.4.2 Forces and Moments

Figures 5-10, 5-12, 5-14, 5-16, 5-18, and 5-20 show the peak shear and base moment experienced during each run for the four tested specimens. Since no forces were directly measured during the tests, those quantities were estimated using Newton's second law. The shear is computed from measured total acceleration at the center of mass using Newton's second law (See Section 4.3.2.2). Base moments are computed by adding contributions from the shear force along the column, and from the applied inertia moment at the center of mass. To obtain the peak base moment, the P-Δ contribution, which is equal to the weight of the block times the relative deformation of the block with respect to the base, is also added. Peak base moments with and without P-Δ contribution are reported in the figures. Note that in the shear plots, the ordinates of the moment axis are equal to 96 times the ordinates of the shear axis. The factor 96 is equal to the height of the column in inches, which is used to convert the base moment into an effective shear force and vice versa.

93
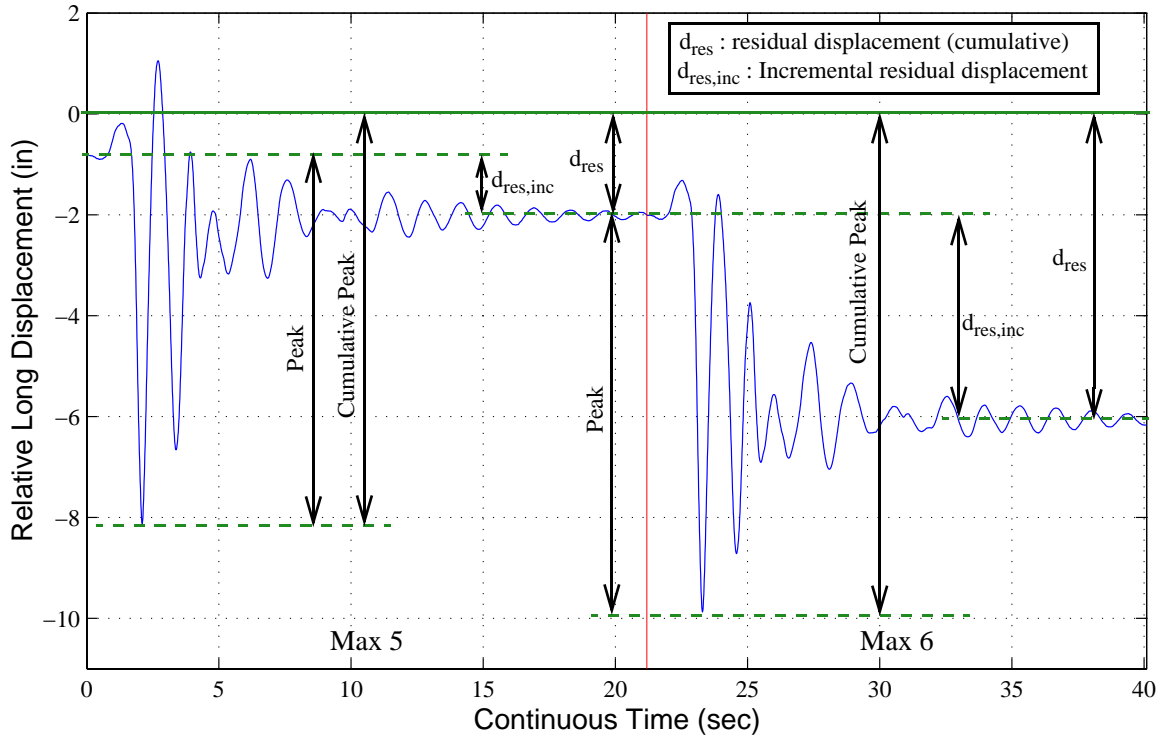
Figure 5-2. Illustration of terminology used for peak and residual relative displacement.

5.4.3 Higher Mode Contribution to Forces and Displacements

The shear values are decomposed into the contributions of the first and second mode to the peak shear value. The shown contribution is only valid at the peak however, and may not necessarily reflect the whole record. It is generally observed that the lateral direction of Specimen A2 has a significant second mode shear contribution. This is mainly due to high spectral accelerations in the short period range (0.1-0.4 seconds) of the lateral Olive View record (NF16), which at the maximum earthquake level, reach about $3g$ assuming 5% damping (Figure 4-16). The longitudinal direction shows significantly smaller spectral accelerations in that range. Figure 5-21 shows the longitudinal shear history for Specimen A2 during Run 5. As discussed before, the shear is obtained by multiplying the total acceleration at the center of the mass by the total supported mass. Also shown in Figure 5-21 is the Fourier spectrum of the shear history, and the identified first and second mode periods, which were generally found to be in the neighborhood of 1.2 seconds and 0.17 seconds respectively. In order to separate the first and second mode contributions, the signal was filtered using high and low pass filters with a corner frequency at 2 Hz. The separated mode components are shown in the top plot of Figure 5-22. The lower plot shows the ratio of the 2nd mode contribution to the total shear at all peaks exceeding 25% of the largest peak. The contribu-
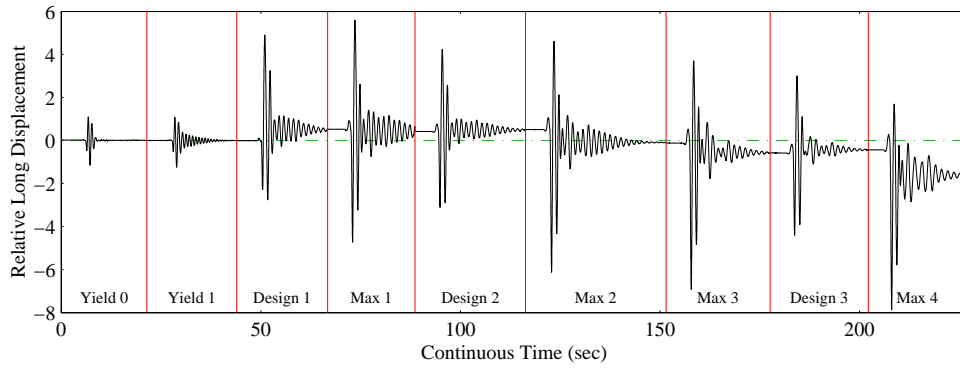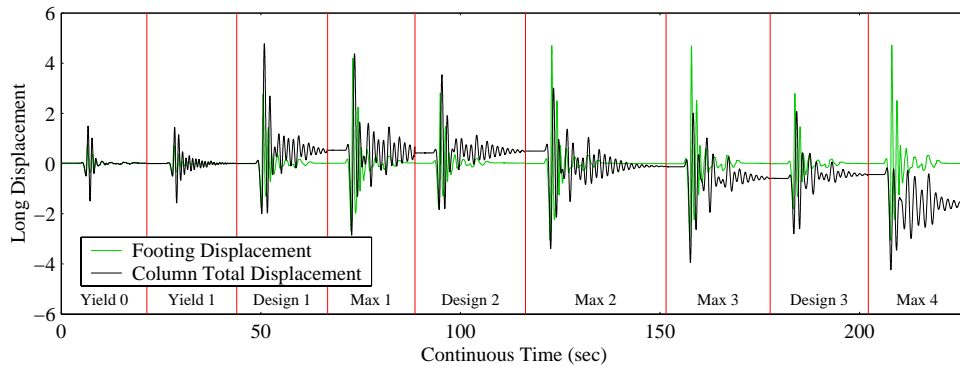
Figure 5-3. Longitudinal displacement history for all runs of Specimen A1.
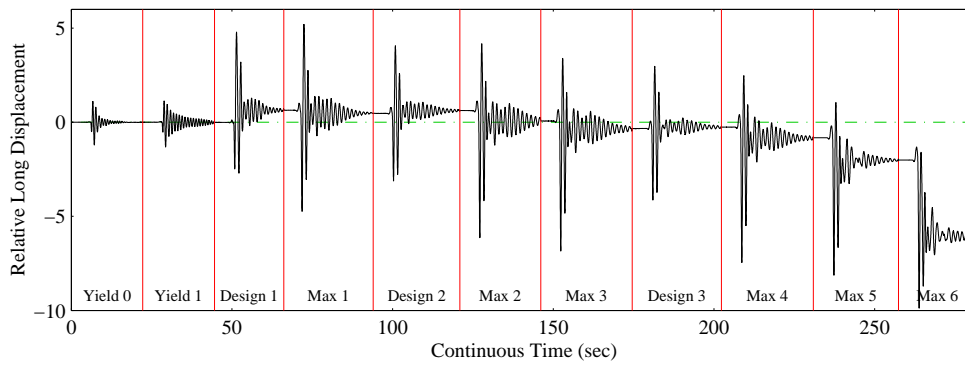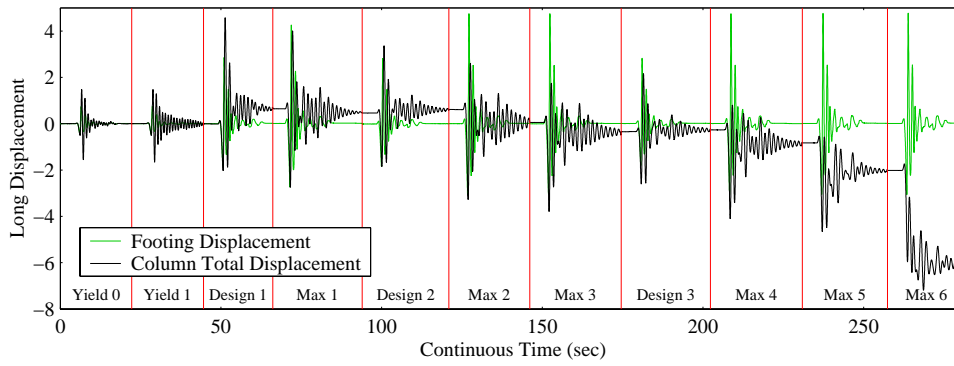
Figure 5-4. Longitudinal displacement history for all runs of Specimen A2.
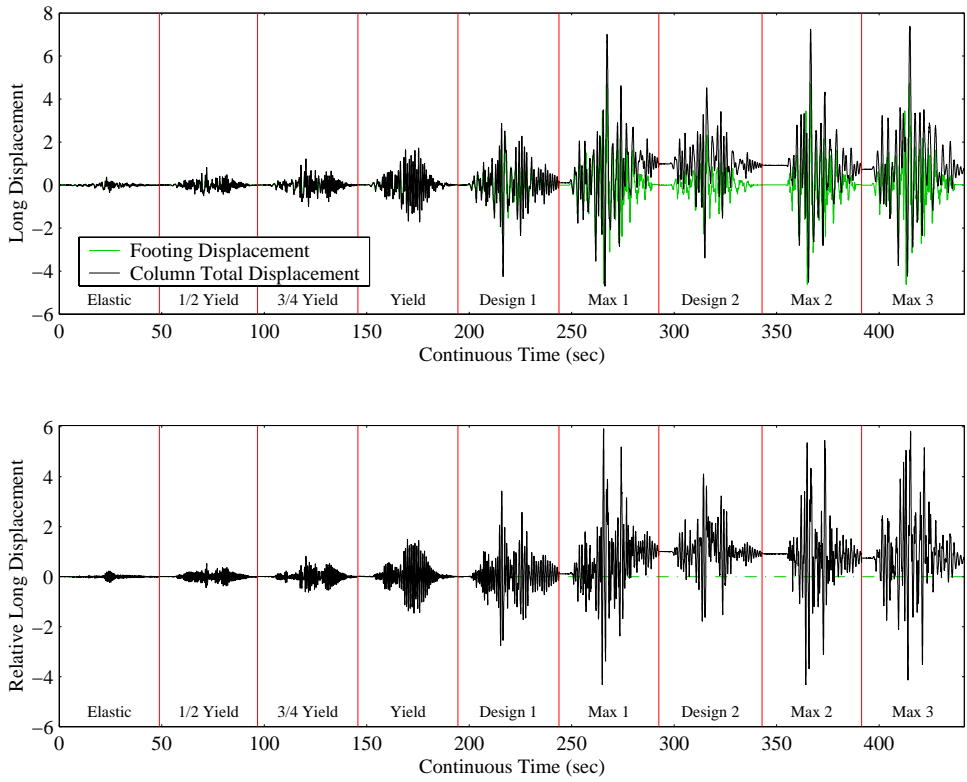
Figure 5-5. Longitudinal displacement history for all runs of Specimen B1.
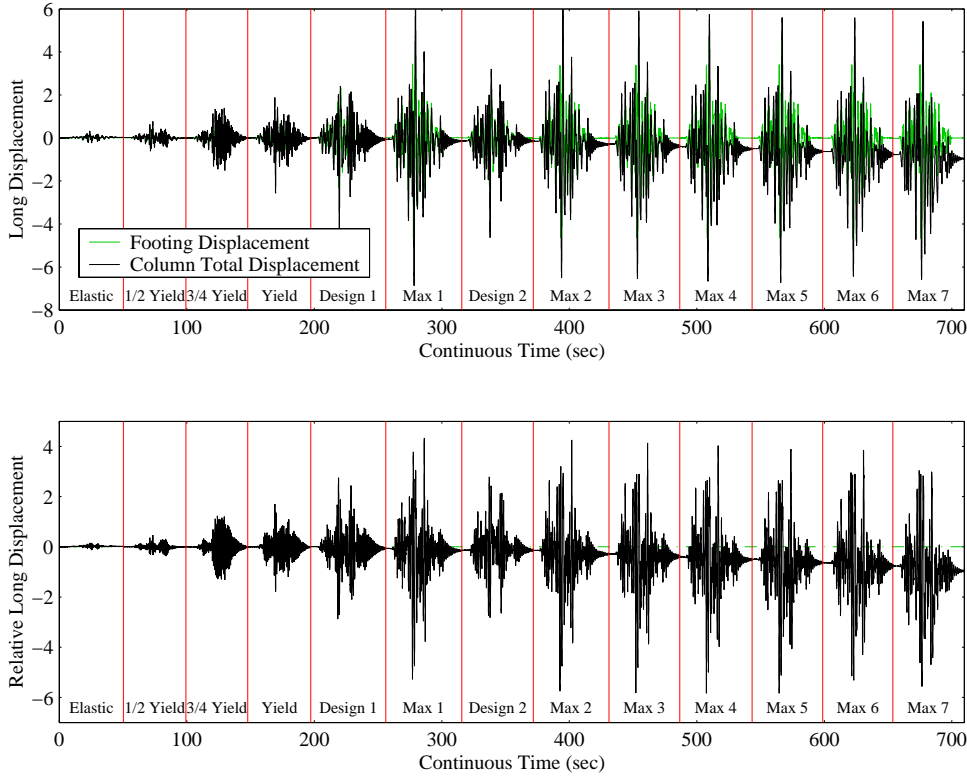
Figure 5-6. Longitudinal displacement history for all runs of Specimen B2.
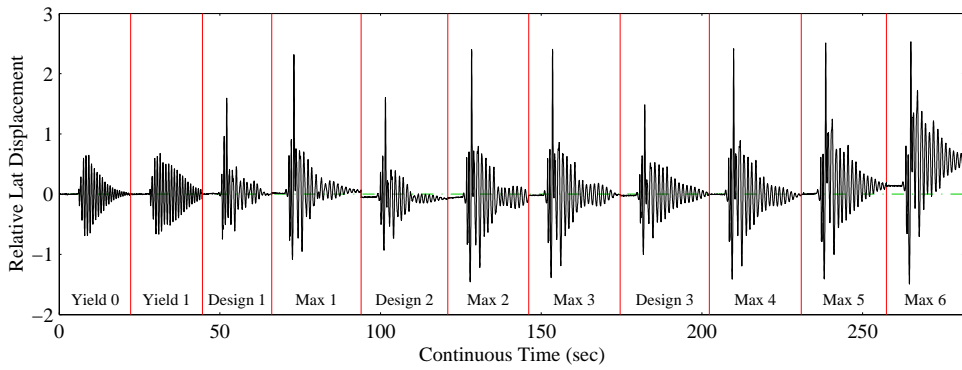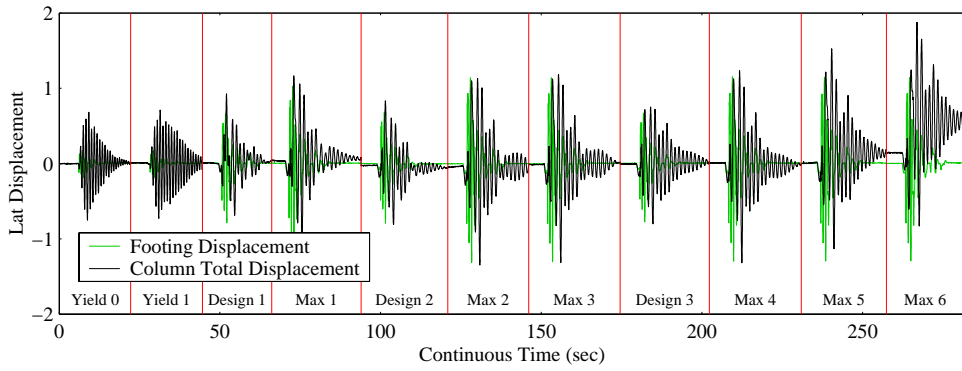
Figure 5-7. Lateral displacement history for all runs of Specimen A2.
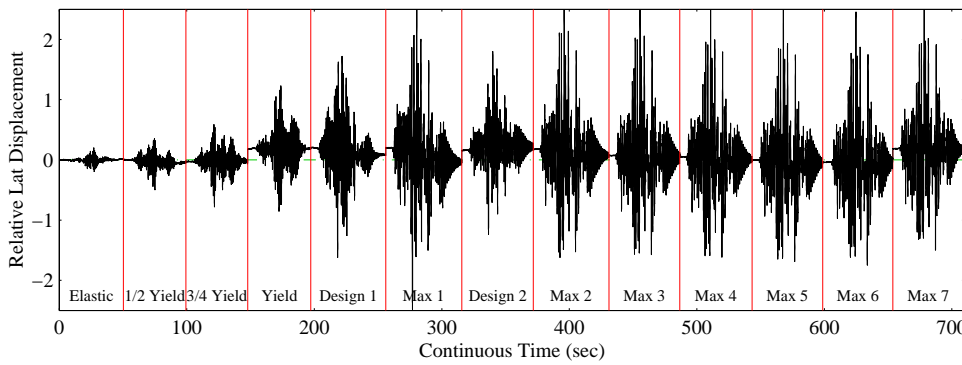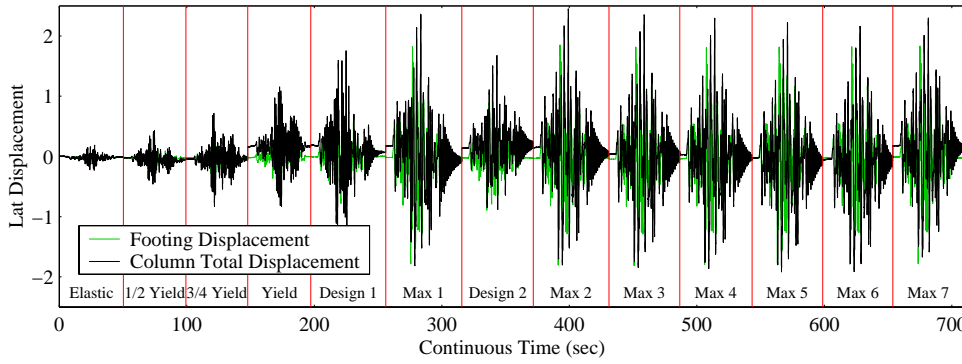
Figure 5-8. Lateral displacement history for all runs of Specimen B2.

Figure 5-9. Peak displacement values for Specimen A1 in the longitudinal direction.
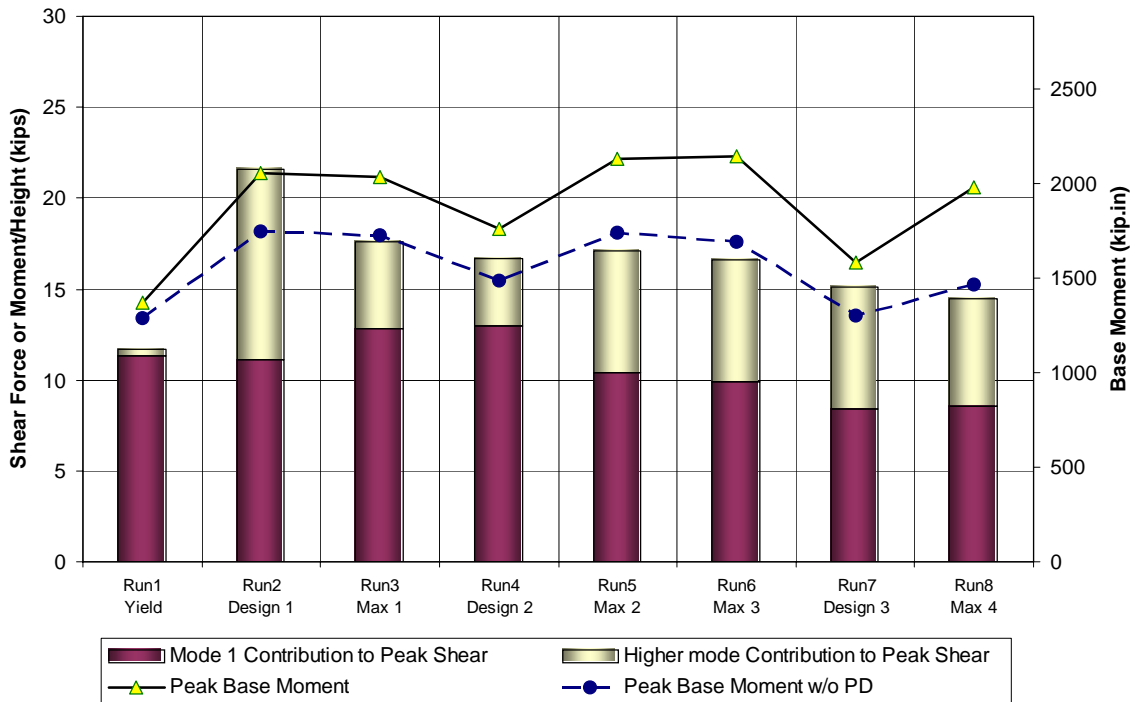
Figure 5-10. Peak shear and base moment for Specimen A1 in the longitudinal direction.

Figure 5-11. Peak displacement values for Specimen A2 in the longitudinal direction.
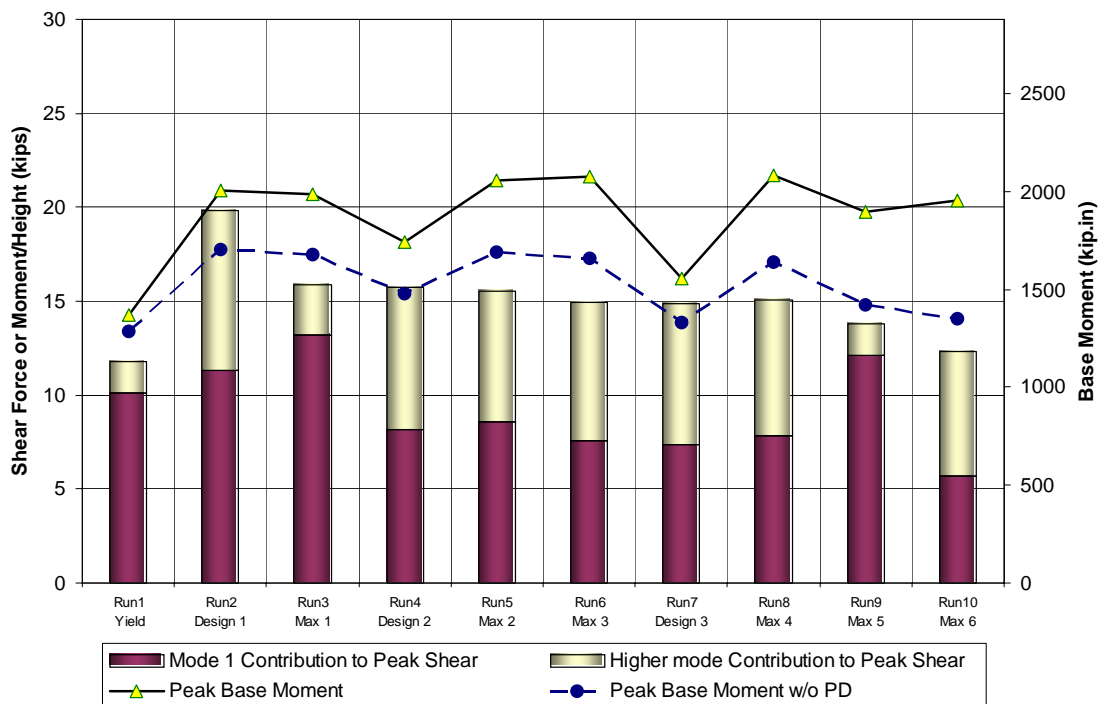
Figure 5-12. Peak shear and base moment for Specimen A2 in the longitudinal direction.

Figure 5-13. Peak displacement values for Specimen A2 in the lateral direction.
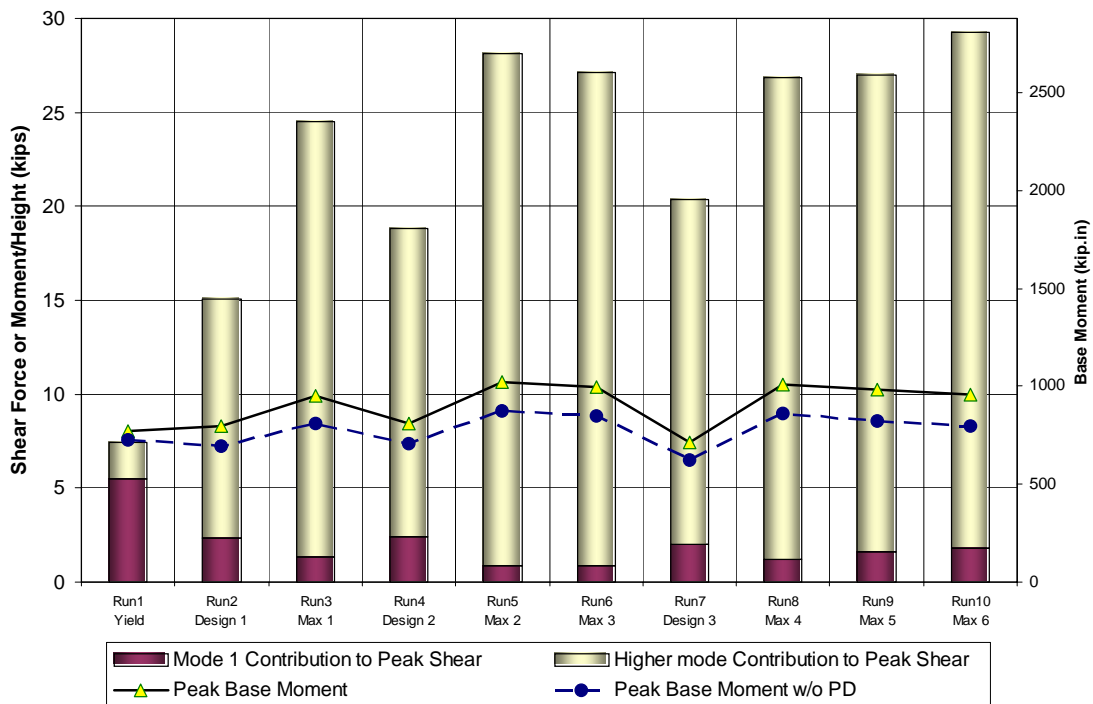
Figure 5-14. Peak shear and base moment for Specimen A2 in the lateral direction.

100
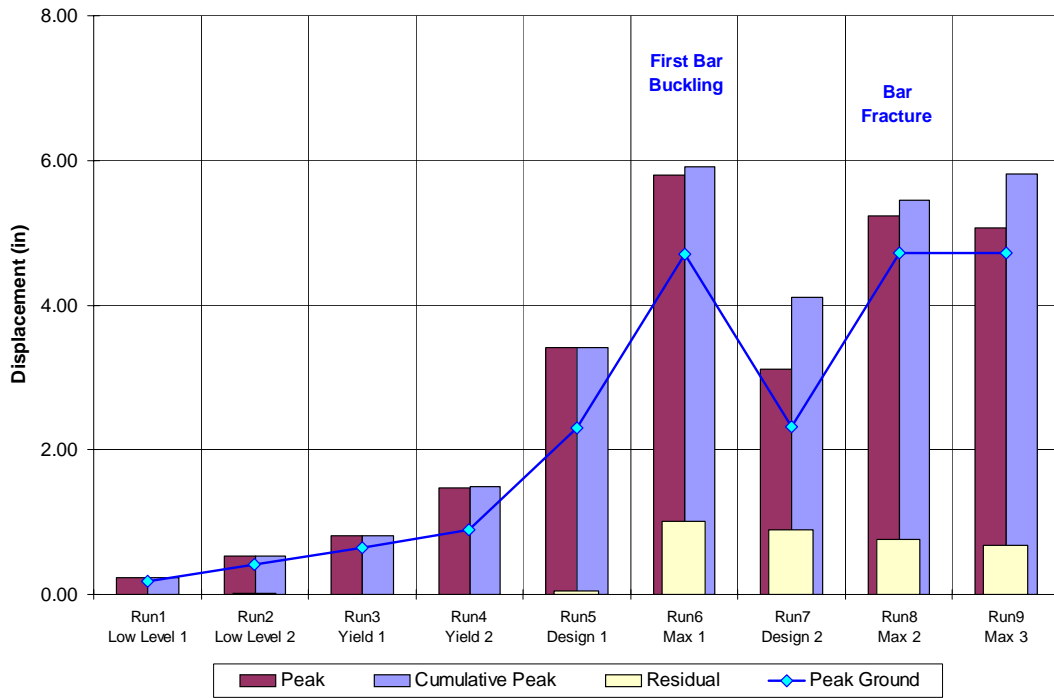
Figure 5-15. Peak displacement values for Specimen B1 in the longitudinal direction.
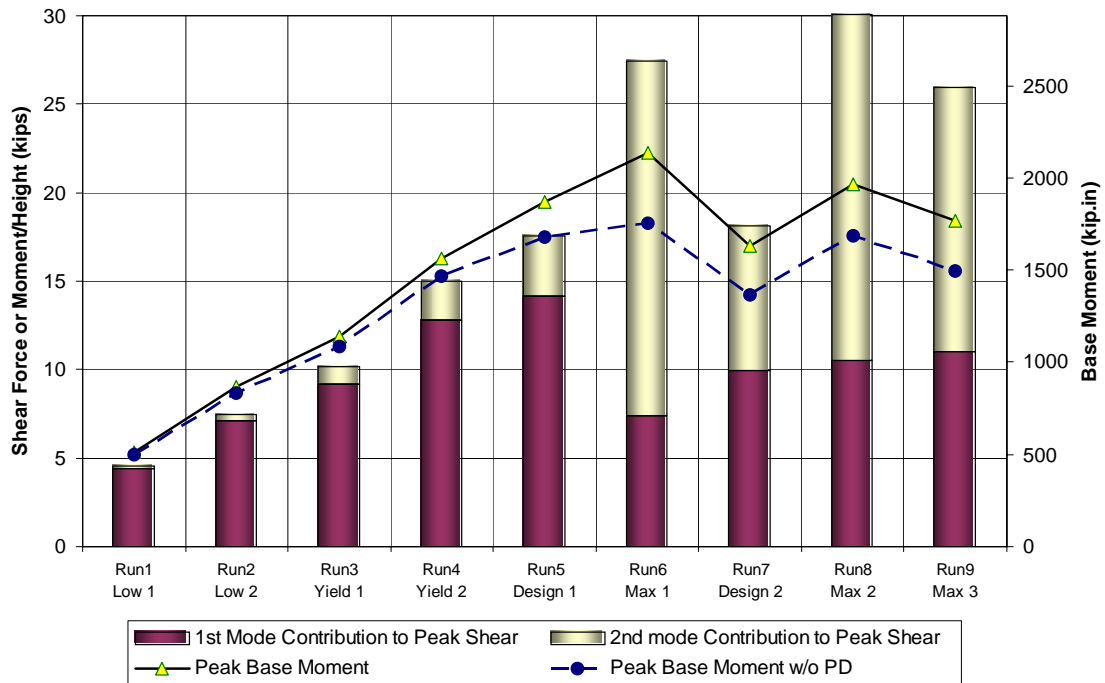
Figure 5-16. Peak shear and base moment for Specimen B1 in the longitudinal direction.
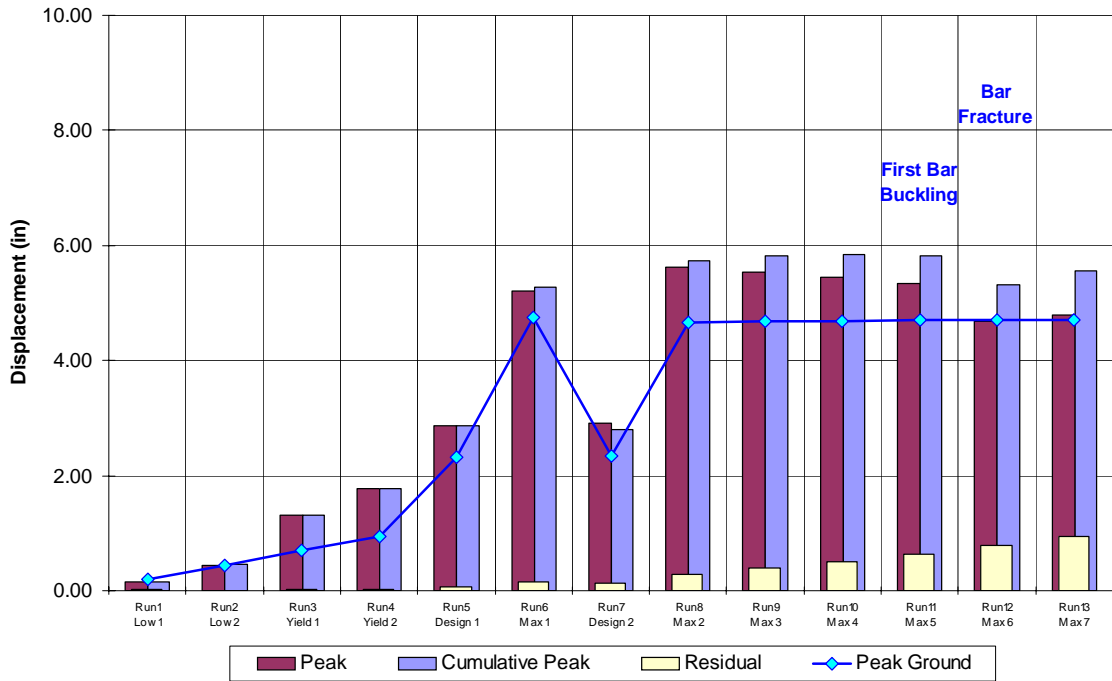
Figure 5-17. Peak displacement values for Specimen B2 in the longitudinal direction.
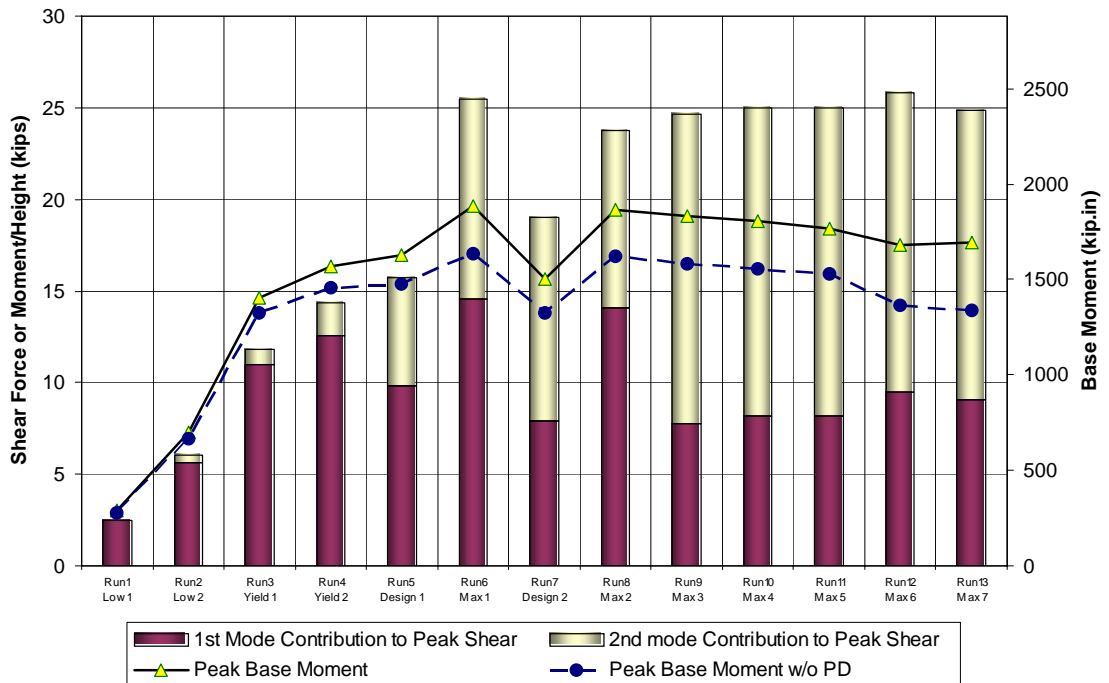
Figure 5-18. Peak shear and base moment for Specimen B2 in the longitudinal direction.
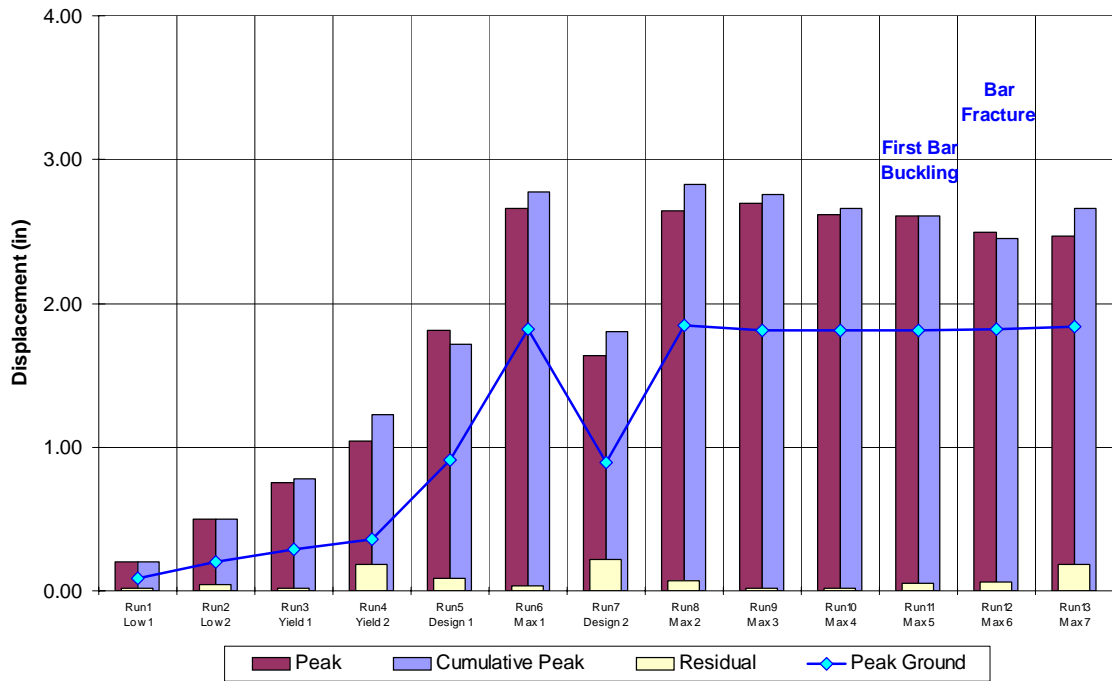
Figure 5-19. Peak displacement values for Specimen B2 in the lateral direction.
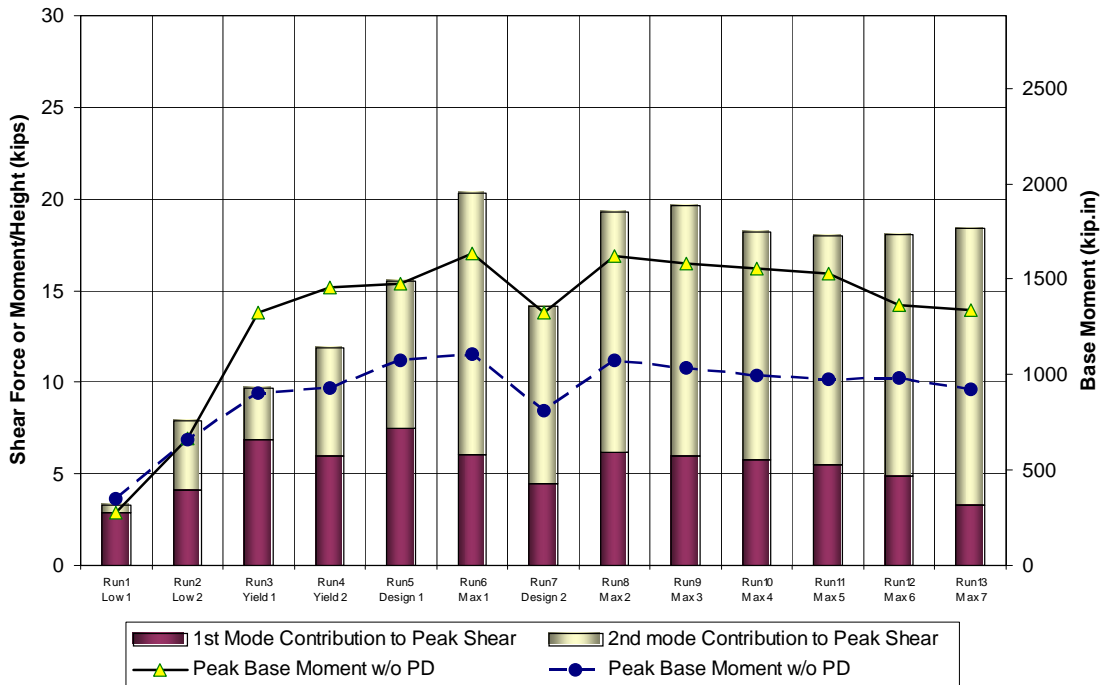
Figure 5-20. Peak shear and base moment for Specimen B2 in the lateral direction

103

tion of the largest peak is marked with a circle. Similar to Figures 5-21 and 5-22, Figures 5-23 through 5-36 show a similar decomposition of shear and displacement histories in the longitudinal and lateral directions of Specimens A2 and B2. Figures 5-23 and 5-24 demonstrate the high second mode contributions to the shear in the lateral direction of Specimen A2. In fact, the second mode is so significant in that case that it contributes significantly to the peak relative displacement in the lateral direction, while this is not the case for the longitudinal direction of Specimen A2, and for both directions of Specimen B2.

The higher mode contribution also has the adverse effect of causing the peak shear in the column to significantly exceed the maximum shear expected in a cantilever situation. This can be shown by comparing the shear to the moment divided by the height (M_{base}/L). Since the moment scale is equal to the shear scale multiplied by the cantilever height (96 in.), the shear and moment would be expected to be the same in the shear and moment plots (Figures 5-10, 5-12, 5-14, 5-16, 5-18 and 5-20). This is almost never the case. In the case of Specimen A1, the peak shear is actually less than M_{base}/L. This is mainly attributed to a small second mode contribution. Another factor that reduces the peak shear as compared to the peak moment is the effect of nonlinear geometry (P–Δ). Figure 5-14 offers another interesting observation. The shear experienced in the lateral direction of Specimen A2 is up to around 3 times the shear that would be expected from a cantilever action, i.e. M_{base}/L, where L is the height to the center of mass or 96 in. Even when the column is deformed under double curvature, the shear would not be expected to exceed $2M_{base}/L$. However, since the top 32 in. of the height L are embedded in the rigid block, this creates a shorter column with an effective height of 64 in. This effectively brings the maximum theoretical shear in the column to $2M_{base}/L_{eff}$, or $3M_{base}/L$, since in this case $L_{eff}=2L/3$. This shows that neglecting higher mode effects and the rigidity of the deck might lead to a significant underestimation of the maximum shear in the column of up to three times, depending on the second mode contribution and the relative heights of the deck and column.

The longitudinal and lateral ground motions components in Specimen B2 both have a frequency rich acceleration response spectrum that exhibits high spectral accelerations in the period range of 0.1-0.5 seconds (Figure 4-19). This, along with the longer duration of the Llolleo record, result in generally high shears and high second mode contributions in Specimens B1 and B2.

In contrast to the higher mode contribution to acceleration and shear, the displacement response shows no significant contribution from higher modes, as would be expected from elementary dynamics theory [14]. This can be observed in Figures 5-25 to 5-28 and 5-33 to 5-36.
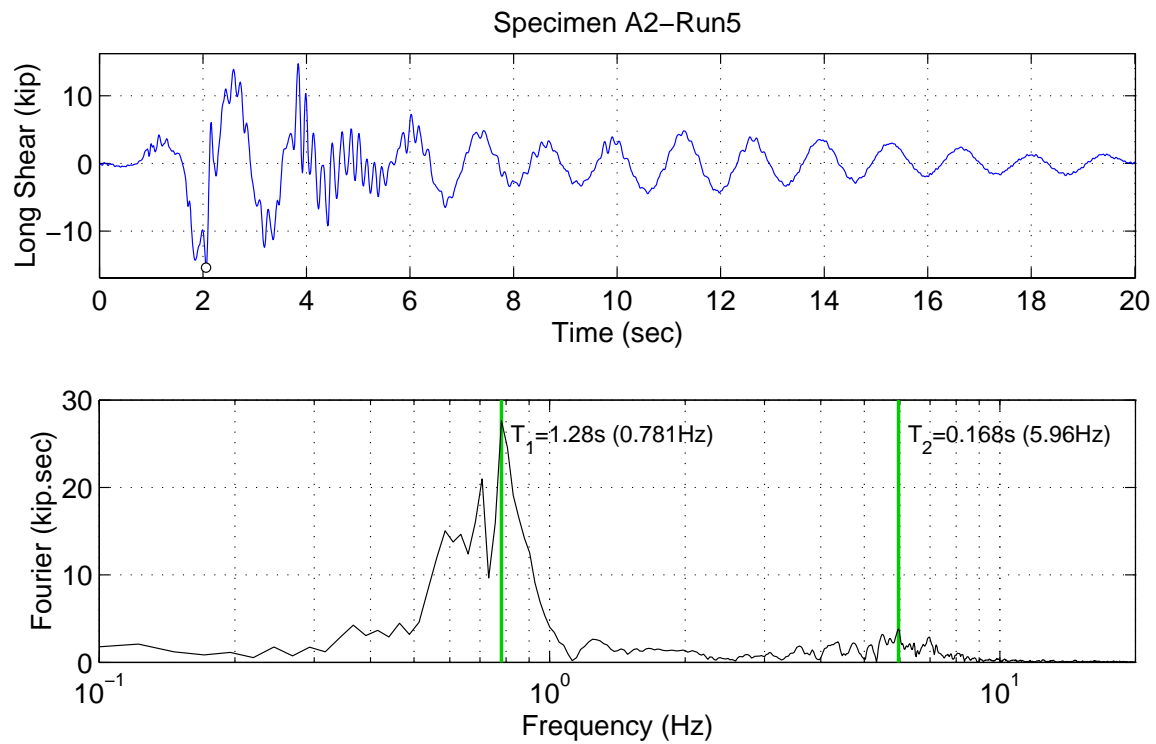
Figure 5-21. History and Fourier spectrum of the longitudinal shear force (Specimen A2 - Run 5).
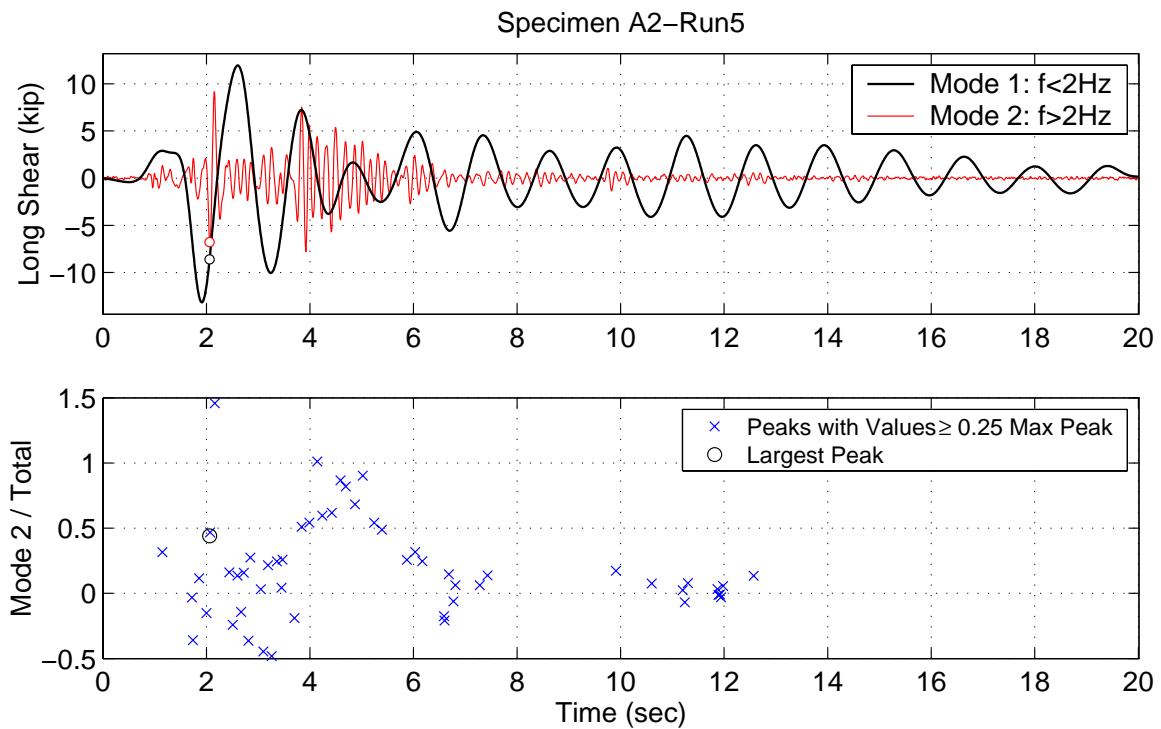
Figure 5-22. Mode decomposition and ratio of second mode contribution to the mode sum of the longitudinal shear force (Specimen A2 - Run 5).
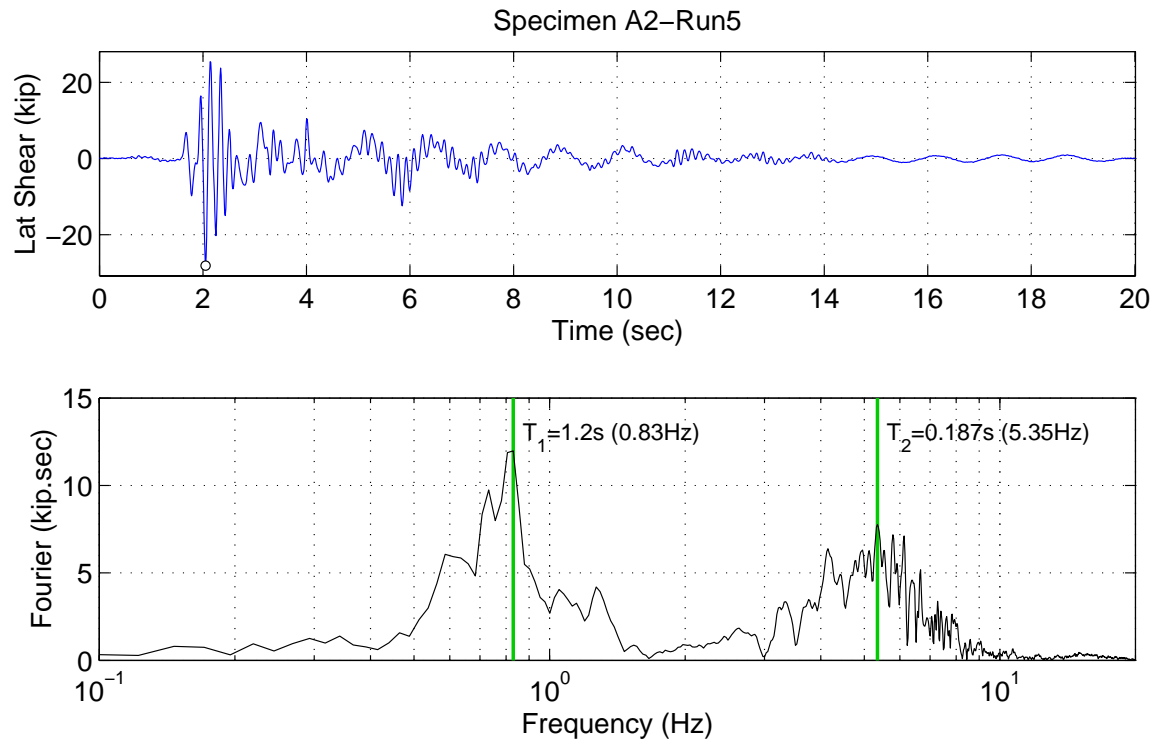
Figure 5-23. History and Fourier spectrum of the lateral shear force (Specimen A2 - Run 5).
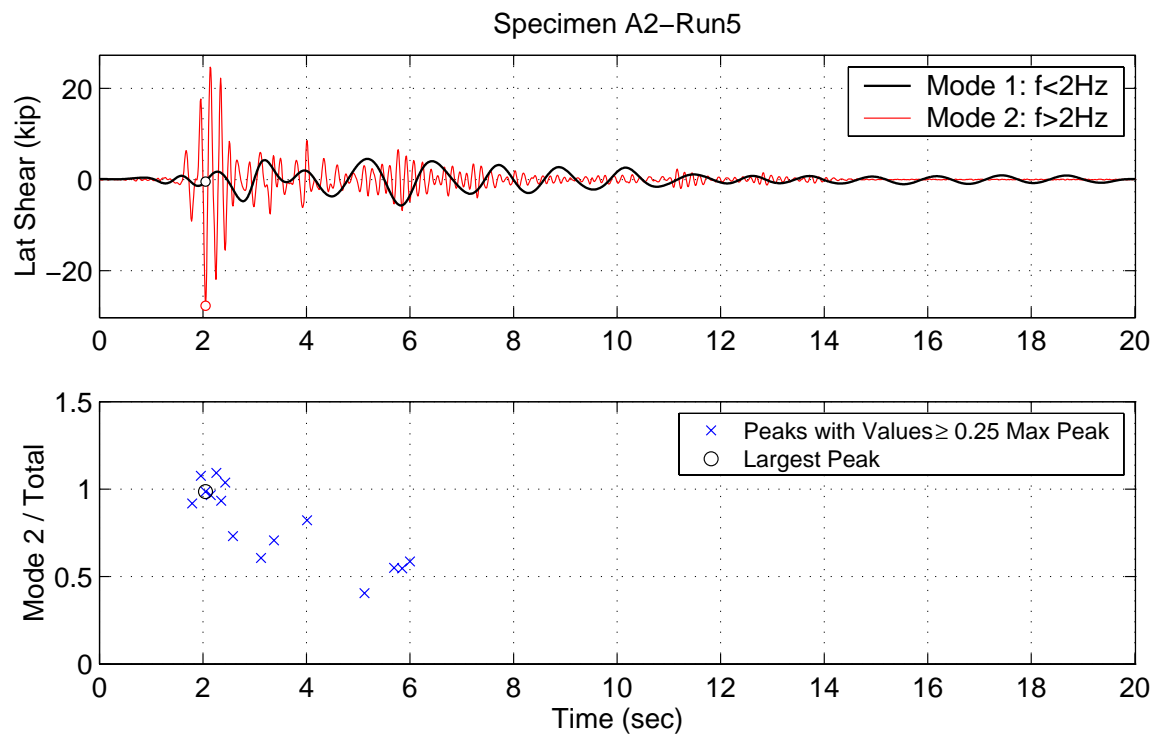
Figure 5-24. Mode decomposition and ratio of second mode contribution to the mode sum of the lateral shear force (Specimen A2 - Run 5).
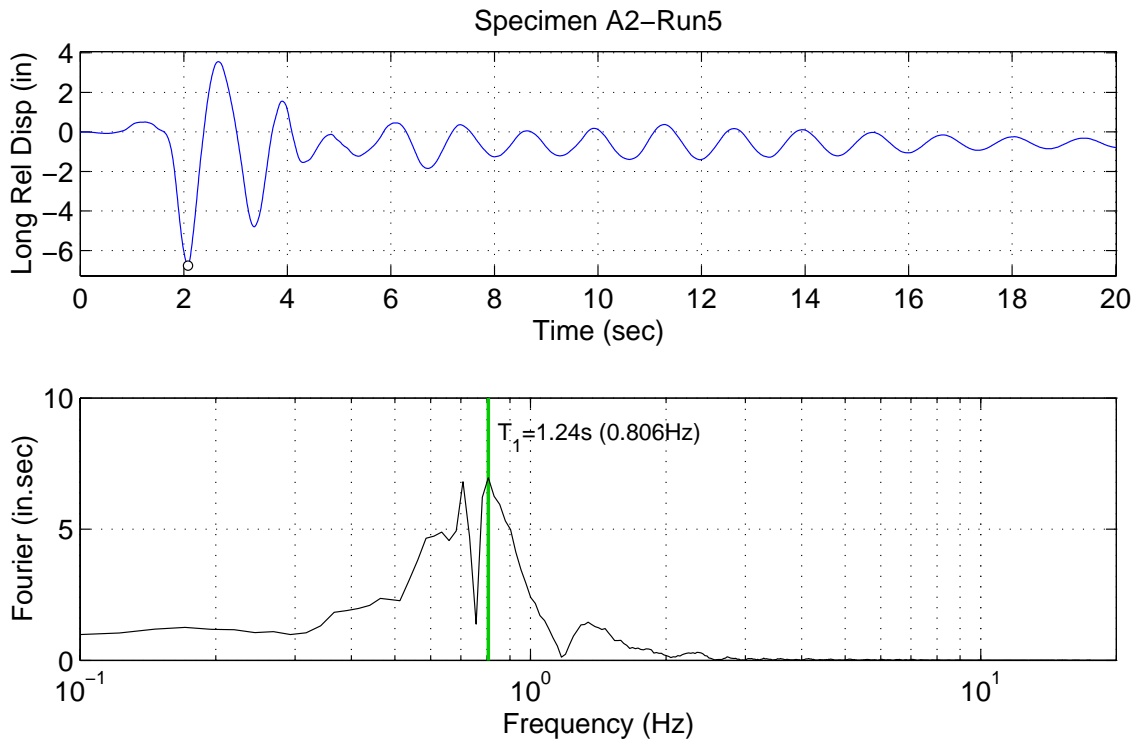
Figure 5-25. History and Fourier spectrum of the longitudinal relative displacement (Specimen A2 - Run 5).
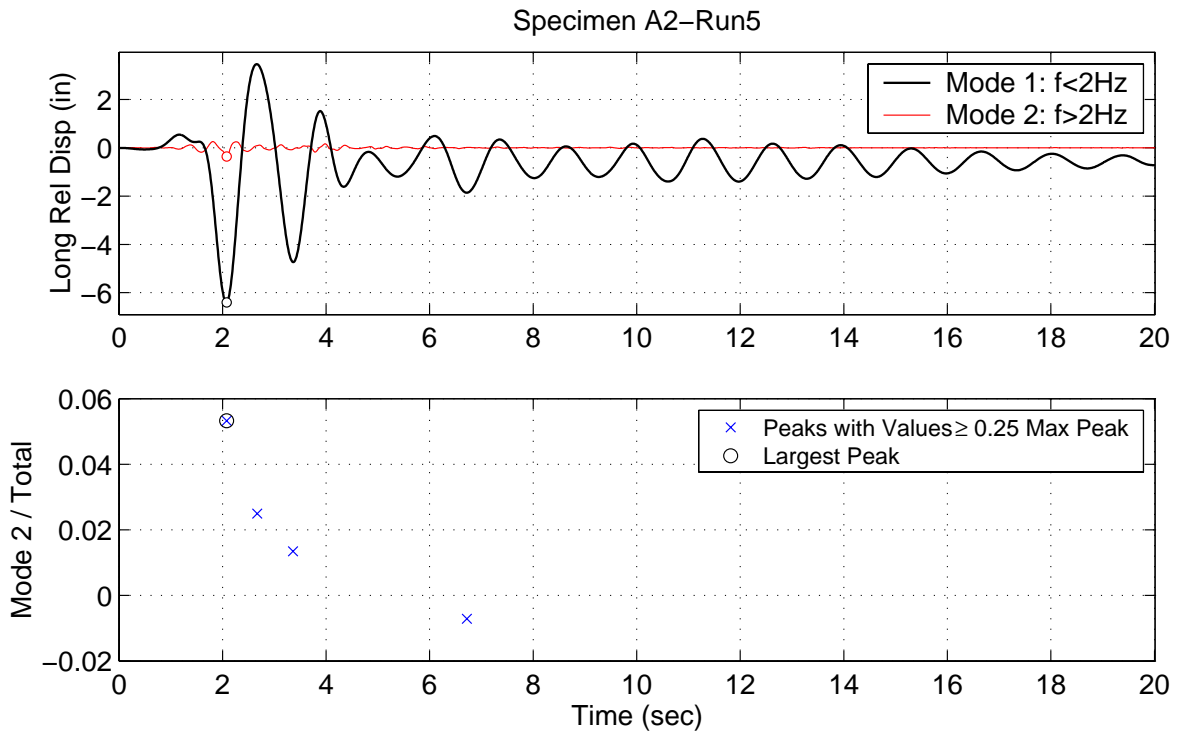
Figure 5-26. Mode decomposition and ratio of second mode contribution to the mode sum of the longitudinal relative displacement (Specimen A2 - Run 5).
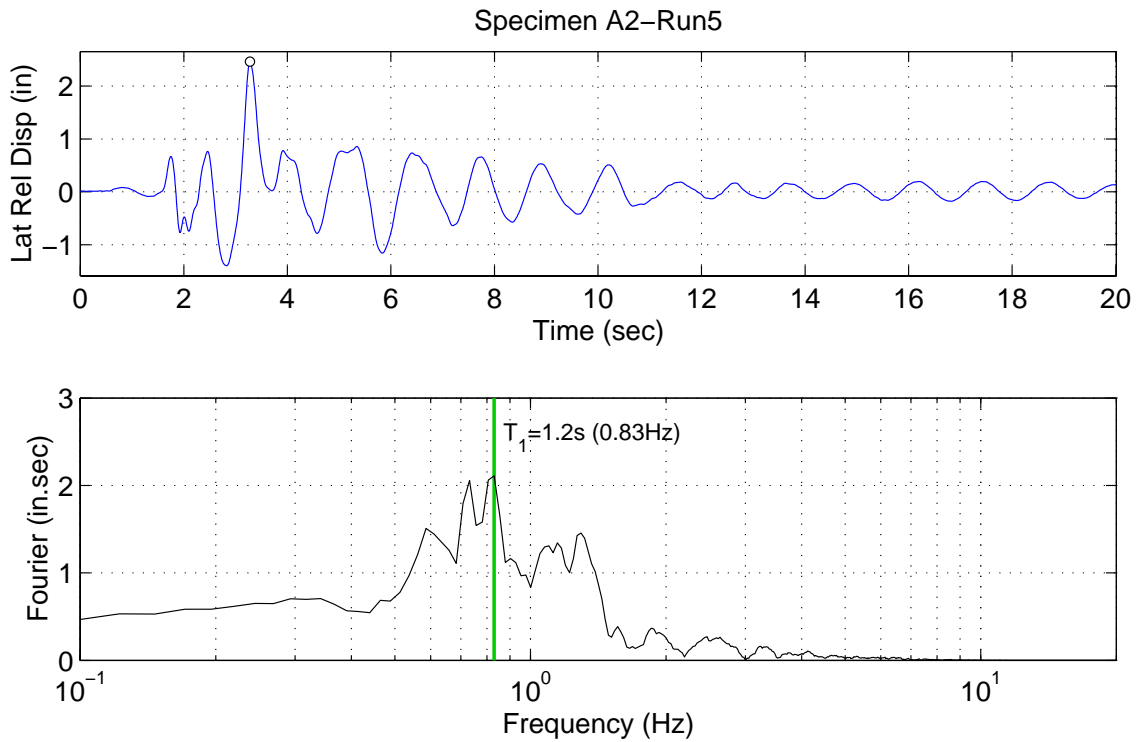
Figure 5-27. History and Fourier spectrum of the lateral relative displacement (Specimen A2 - Run 5).
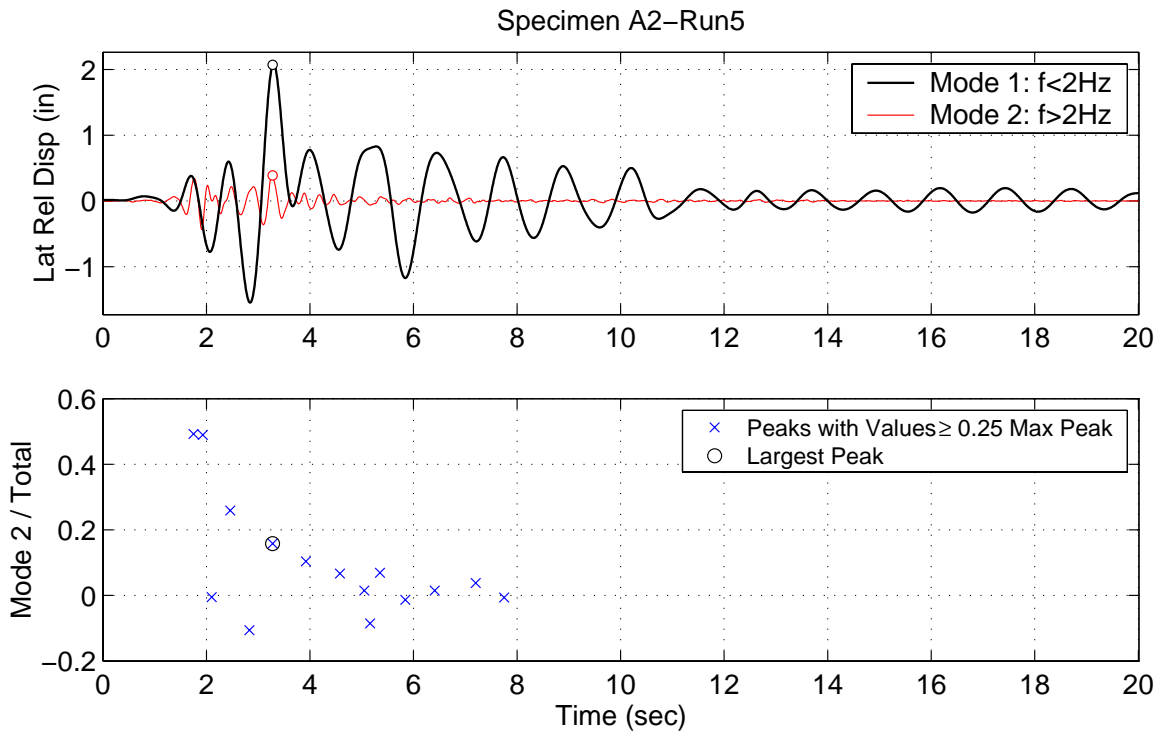
Figure 5-28. Mode decomposition and ratio of second mode contribution to the mode sum of the lateral relative displacement (Specimen A2 - Run 5).
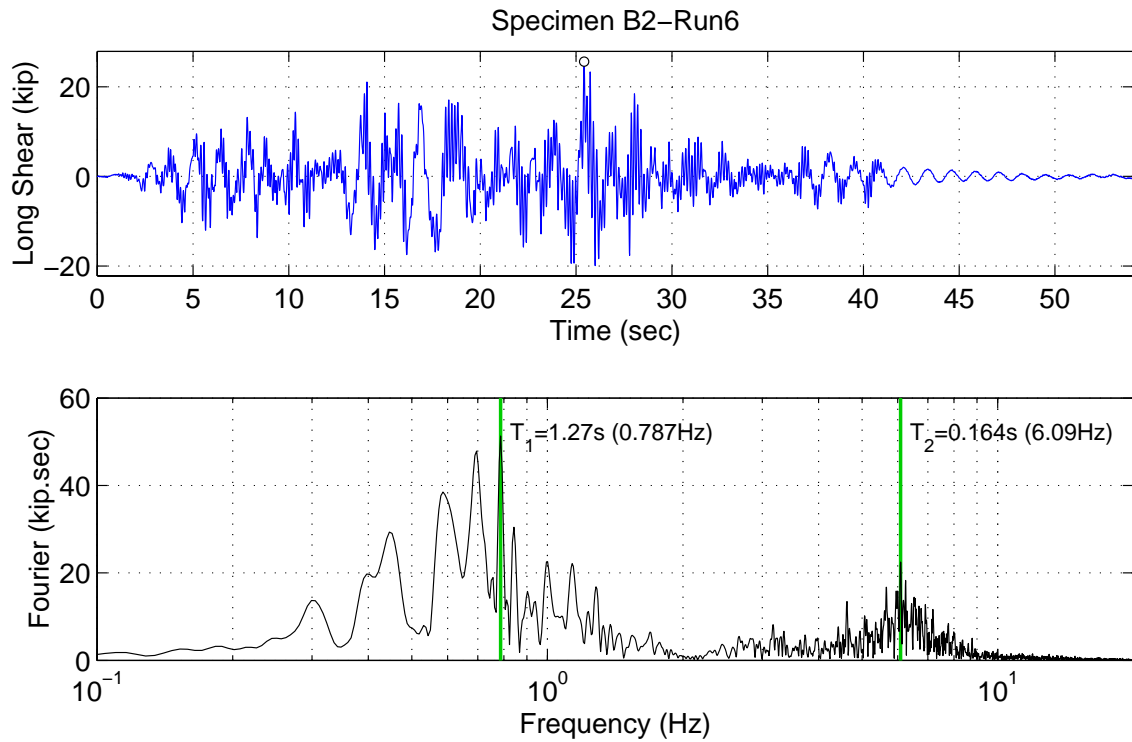
Figure 5-29. History and Fourier spectrum of the longitudinal shear force (Specimen B2 - Run 6).
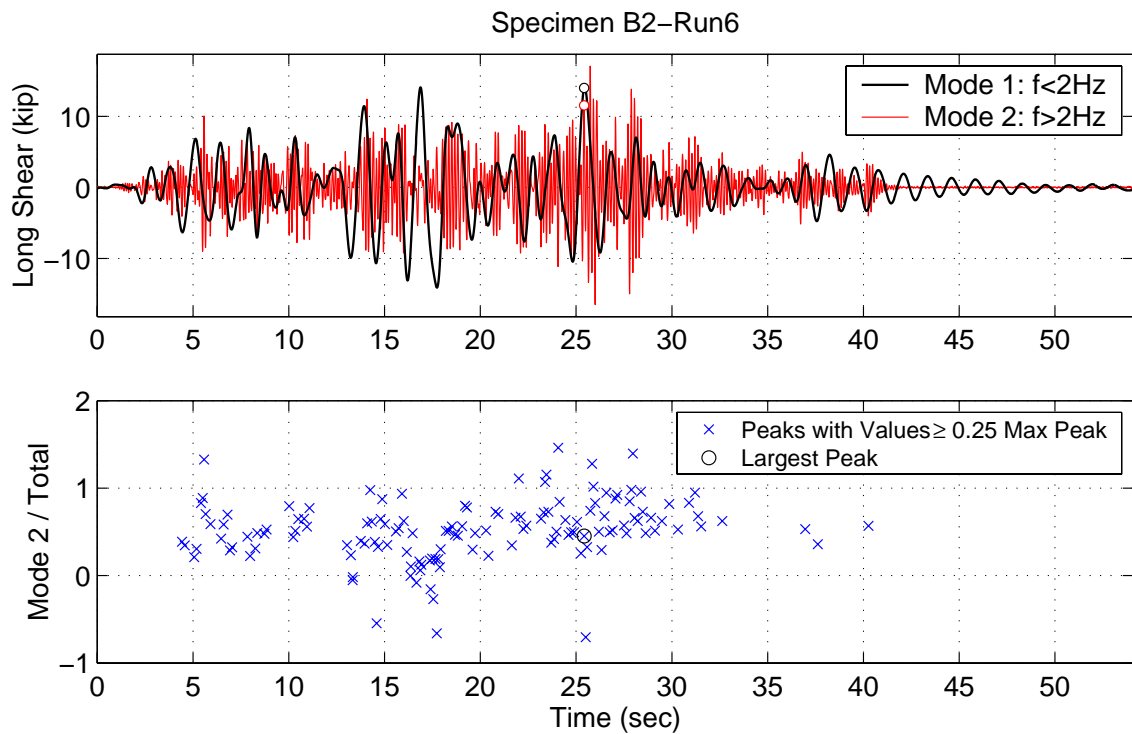
Figure 5-30. Mode decomposition and ratio of second mode contribution to the mode sum of the longitudinal shear force (Specimen B2 - Run 6).
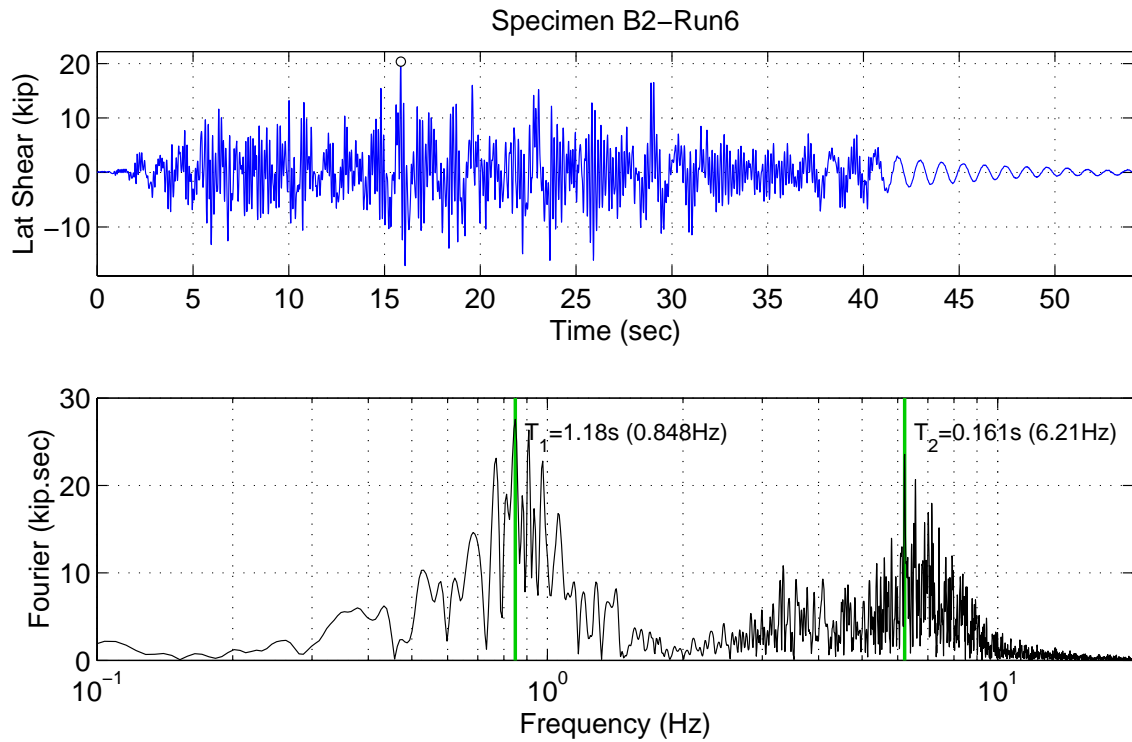
Figure 5-31. History and Fourier spectrum of the lateral shear force (Specimen B2 - Run 6).
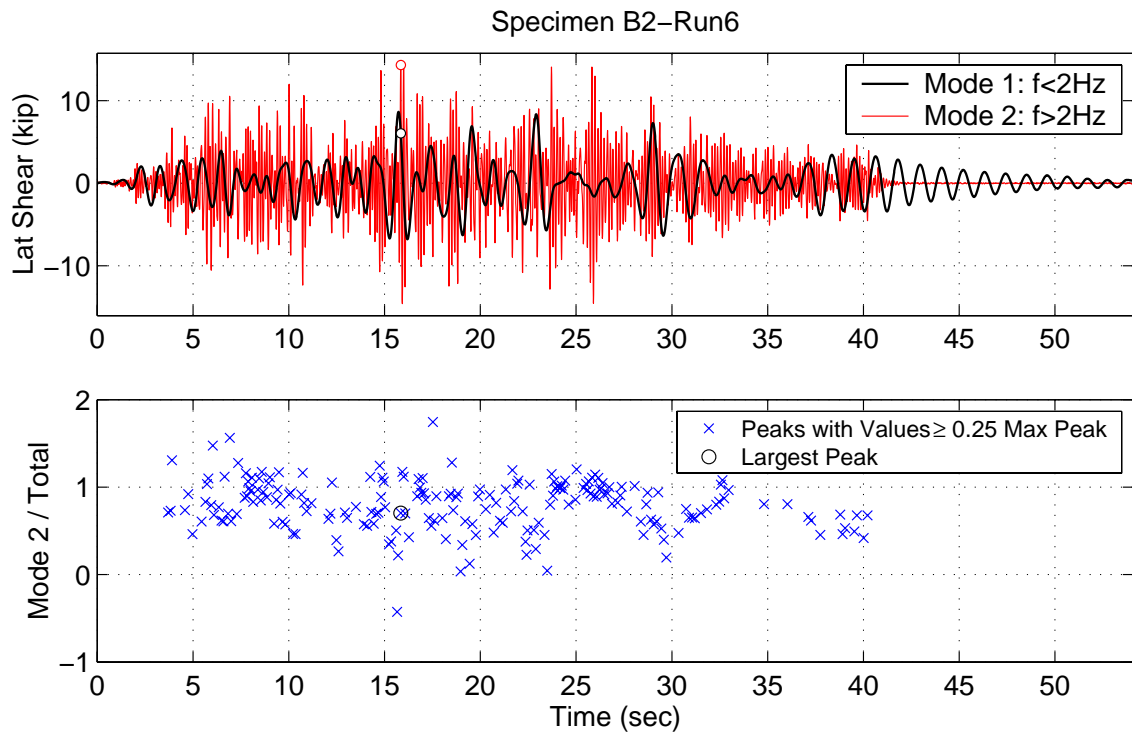
Figure 5-32. Mode decomposition and ratio of second mode contribution to the mode sum of the lateral shear force (Specimen B2 - Run 6).
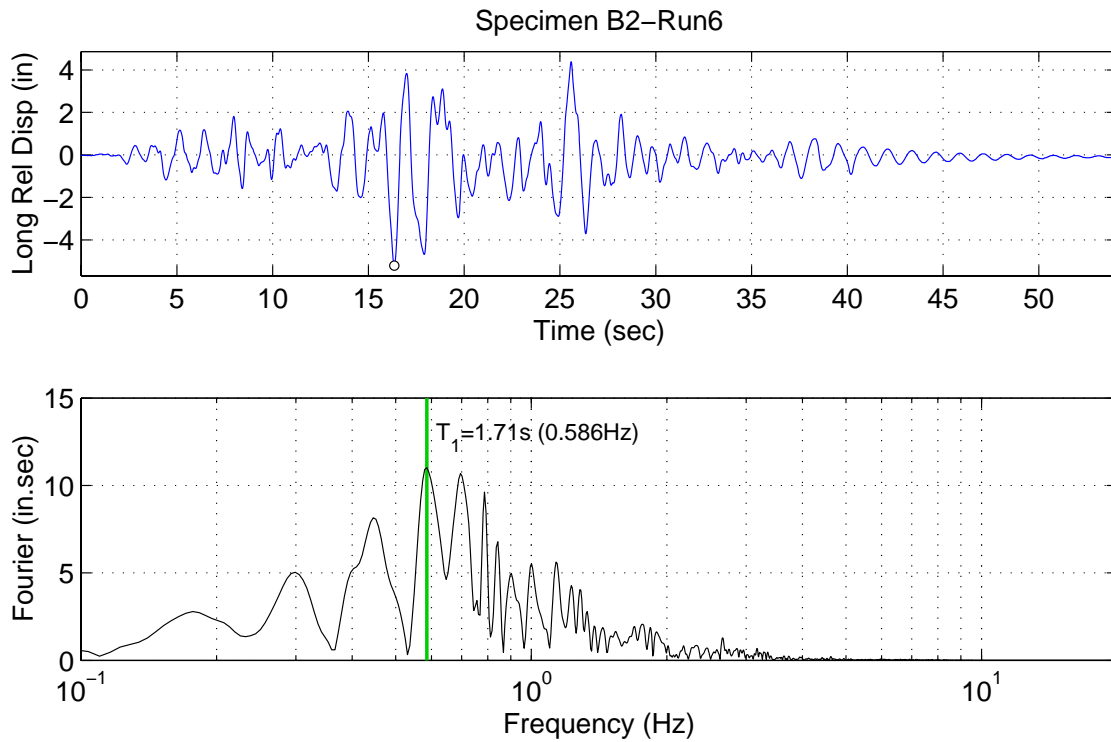
Figure 5-33. History and Fourier spectrum of the longitudinal relative displacement (Specimen B2 - Run 6).
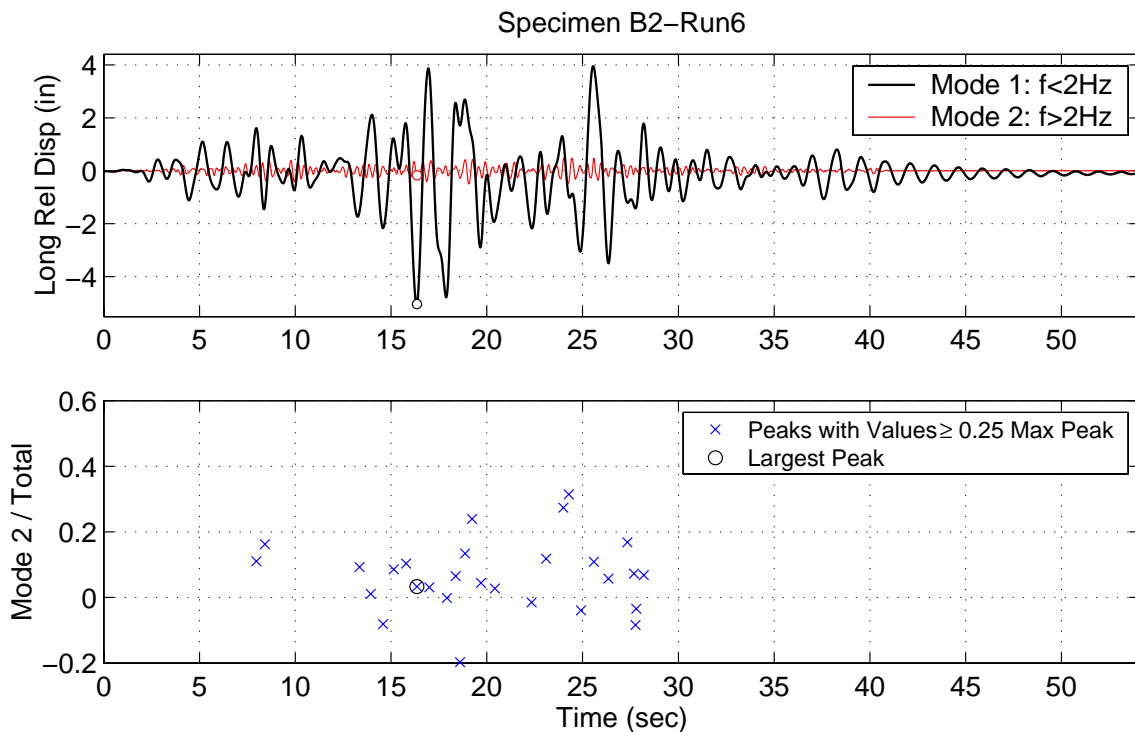
Figure 5-34. Mode decomposition and ratio of second mode contribution to the mode sum of the longitudinal relative displacement (Specimen B2 - Run 6).

111
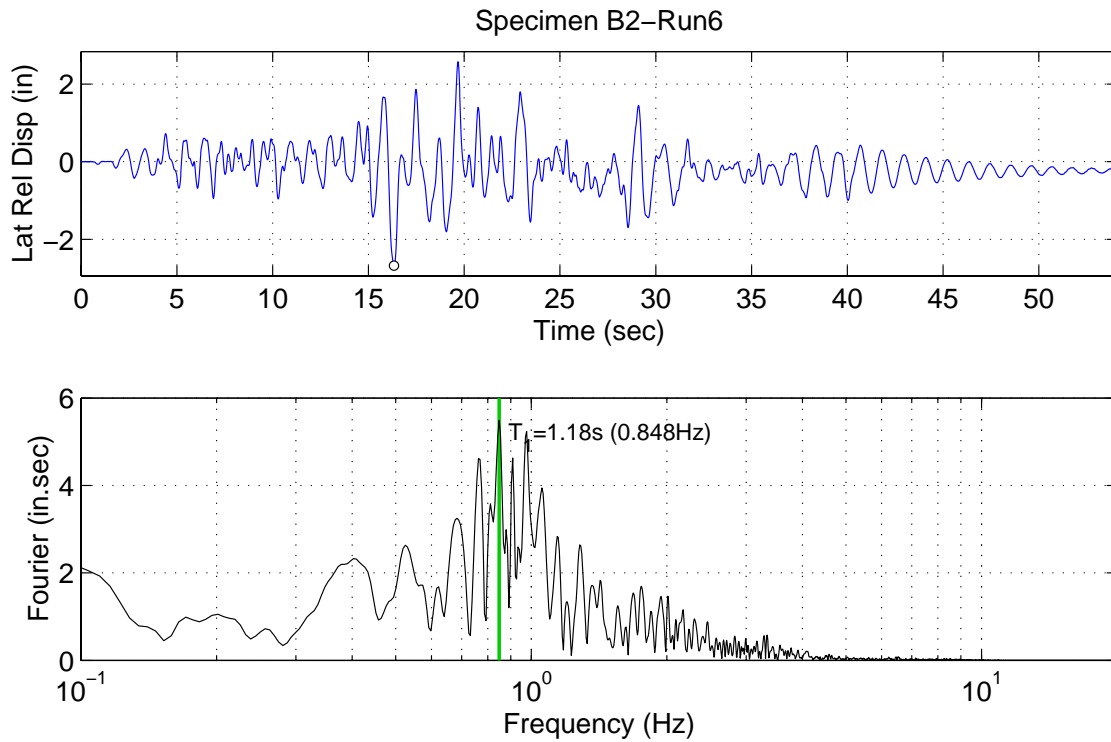
Figure 5-35. History and Fourier spectrum of the lateral relative displacement (Specimen B2 - Run 6).
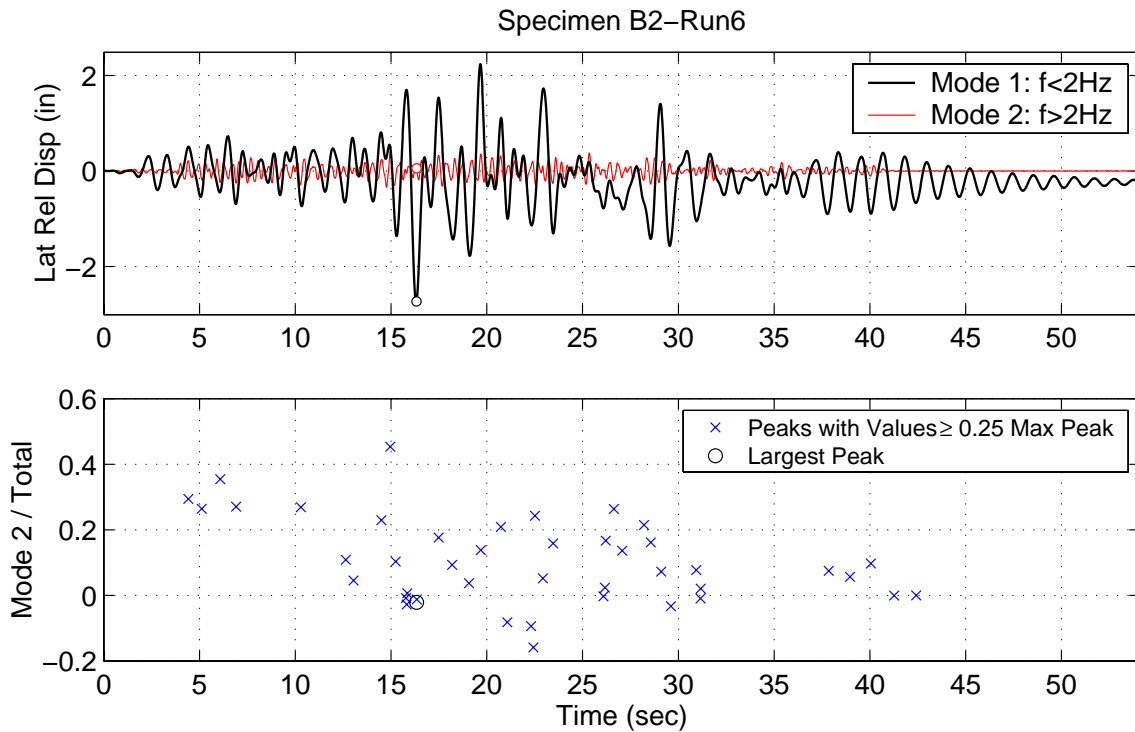
Figure 5-36. Mode decomposition and ratio of second mode contribution to the mode sum of the lateral relative displacement (Specimen B2 - Run 6).

5.4.4 Energy

The force and moment equilibrium equations (Equations 4-1 and 4-2) can be written in matrix form as follows:

$$\begin{bmatrix} m & 0 \\ 0 & m_R \end{bmatrix} \begin{bmatrix} \ddot{u} \\ \ddot{\theta} \end{bmatrix} + \begin{bmatrix} F_{dx} \\ M_{d\theta} \end{bmatrix} + \begin{bmatrix} F_{sx} \\ M_{s\theta} \end{bmatrix} = \begin{bmatrix} -ma_{gx} \\ 0 \end{bmatrix} \tag{5-1}$$

Pre-multiplying the above equation by $\begin{bmatrix} \dot{u} & \dot{\theta} \end{bmatrix}$ yields Equation 5-2. The terms of Equation 5-2 represent the rate of energy change, i.e. power. The power equation can be integrated to obtain Equation 5-3 which represents the sum of energy components.

$$\underbrace{(\dot{u}m\ddot{u} + \dot{\theta}m_R\ddot{\theta})}_{\text{Kinetic Power}} + \underbrace{(\dot{u}F_{dx} + \dot{\theta}M_{d\theta})}_{\text{Damping Power}} + \underbrace{(\dot{u}F_{sx} + \dot{\theta}M_{s\theta})}_{\text{Hysteretic Power}} = \underbrace{-\dot{u}ma_{gx}}_{\text{Input Power}} \tag{5-2}$$

$$E_K + E_D + E_H = E_I \tag{5-3}$$

The kinetic energy (E_K), damping energy (E_D), hysteretic energy (E_H) and input energy (E_I) are defined in Equations 5-4 to 5-7.

$$E_K = \int (\dot{u}m\ddot{u} + \dot{\theta}m_R\ddot{\theta})dt = \frac{m\dot{u}^2}{2} + \frac{m_R\dot{\theta}^2}{2} \tag{5-4}$$

$$E_D = \int (\dot{u}F_{dx} + \dot{\theta}M_{d\theta})dt \tag{5-5}$$

$$E_H = \int (\dot{u}F_{sx} + \dot{\theta}M_{s\theta})dt \tag{5-6}$$

$$E_I = \int (-\dot{u}ma_{gx})dt \tag{5-7}$$

The hysteretic energy part includes the energy dissipated by hysteresis, and the elastic recoverable energy in the column. Since the damping and hysteretic forces are not known independently, we consider the sum of E_D and E_H:

$$\begin{aligned} E_D + E_H &= \int (\dot{u}(F_{dx} + F_{sx}) + \dot{\theta}(M_{d\theta} + M_{s\theta}))dt \\ &= \int (\dot{u}(-m\ddot{u}_t) + \dot{\theta}(-m_R\ddot{\theta}))dt \\ &= \int (-\dot{u}ma_{gx})dt + \int (-\dot{u}m\ddot{u} - \dot{\theta}m_R\ddot{\theta})dt \\ &= E_I - E_K \end{aligned} \tag{5-8}$$

E_K, $E_D + E_H$ and the Error defined as $E_I - (E_K + E_D + E_H)$ are plotted in Figures 5-37 and 5-38 for sample runs corresponding to Specimens A2 and B1. It can be seen that for Specimen A2, most of the energy dissipation occurs during one large pulse lasting around one second, and almost all of the energy is dissipated in about two seconds, during which the rate of energy dissipation, or power, reaches its peak value. In the case of Specimen B2, the energy history shows a gradual increase of dissipated energy over about 15 seconds, consisting of a region of steep increase with a length of approximately 5 seconds, followed by another region with a smaller amount of energy dissipation. Considering total dissipated energy, the energy dissipated by Specimen B2 during the maximum level run was almost 2.5 times that dissipated by Specimen A2. This is mainly due to the longer duration of the Llolleo earthquake used with Specimens B1 and B2 as compared with the Olive View record used with Specimens A1 and A2.

5.4.5   Comparison of Bidirectional and Unidirectional Tests

In each pair of specimens, one specimen was subjected to unidirectional shaking while the other specimen was subjected to bidirectional shaking. In general, no deterioration in column response was observed in the bidirectional tests when compared to the unidirectional tests. In fact, in both pairs of specimens, the bidirectional test survived more runs than the unidirectional test, even though the damage in the plastic hinge zone spread more around the base of the column, due to biaxial bending. The following sections compare the response of the columns in each pair, and describe the similarities and differences between unidirectional and bidirectional response.

5.4.5.1   Specimens A1 and A2

Comparing the results of Specimens A1 and A2, it is first noted that Specimen A2 survived two maximum level runs more than Specimen A1. The results look very similar however during the first eight runs for the longitudinal component, which is the fault-normal and dominant earthquake component in the test of Specimen A2. Figure 5-39 compares the peak relative and peak ground displacements in the longitudinal direction of tests A1 and A2. The peak displacement presented is the relative displacement occurring during the test, with the displacement at the beginning of each run assumed to be zero. Figure 5-40 compares peak shear and base moment values.

Time history results from Specimen A1 are presented in Figures D-1 to D-4 in Appendix D. It's notable that the base moment has a smoother variation with time compared to the base shear response, with less contribution from the higher modes of vibration. The base moment plot shows a clear reduction in strength towards the end of the test. This is evident in the 8th run of the test
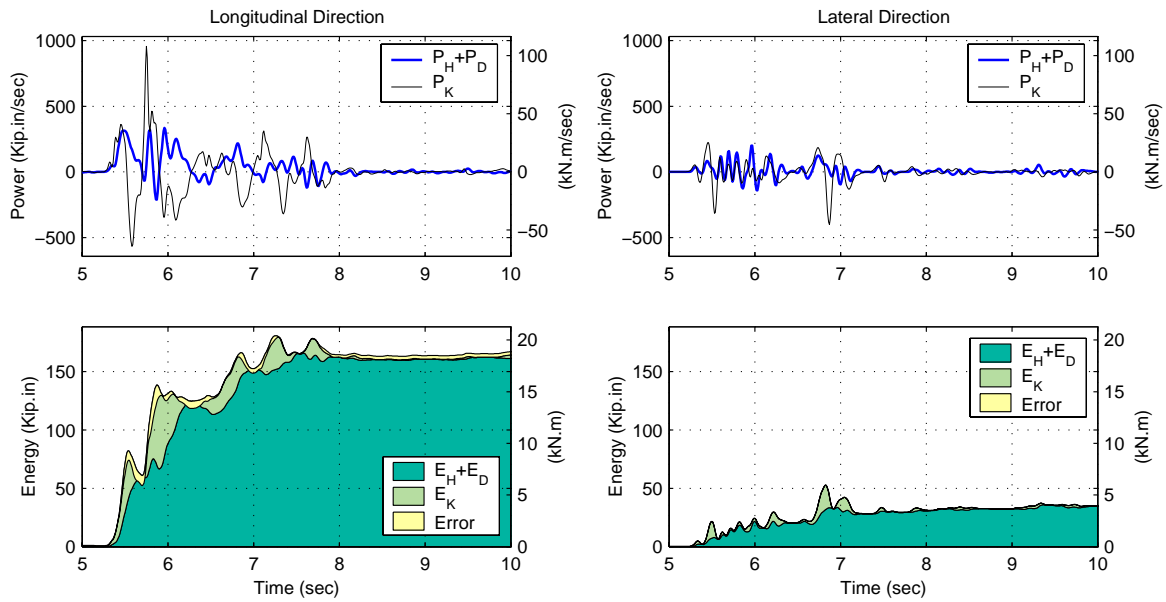
Figure 5-37. Power and energy components in the longitudinal and lateral directions during Run 3 of Specimen A2 (Maximum Level 1).
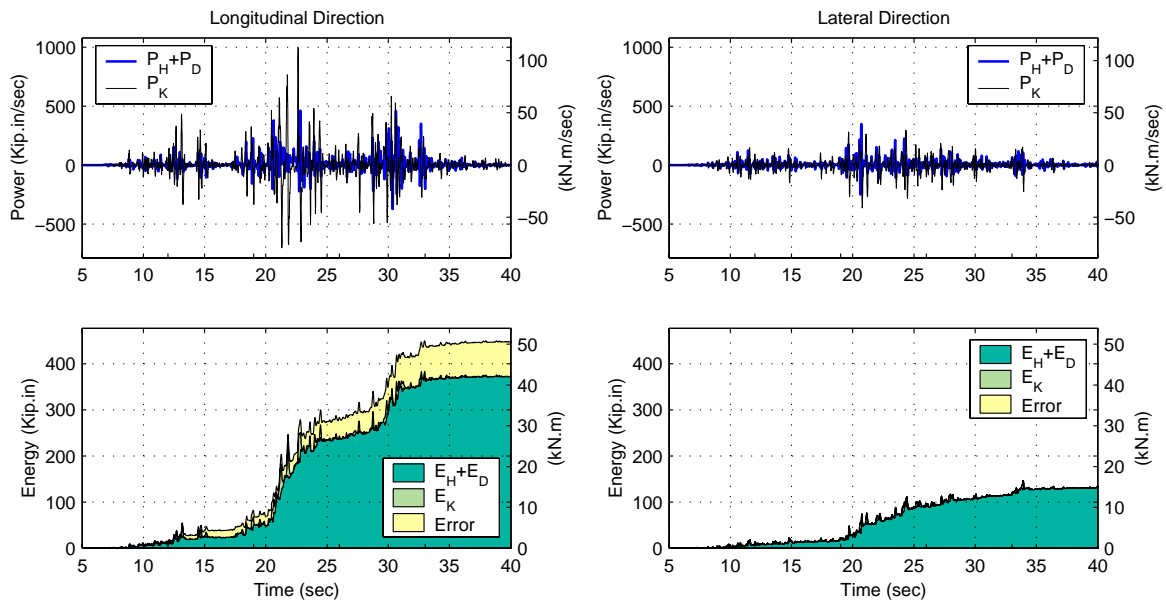
Figure 5-38. Power and energy components in the longitudinal and lateral directions during Run 6 of Specimen B2 (Maximum Level 1).

(Figure D-4) in which the bar fracture occurred. The strength capacity (in terms of equivalent shear strength) was reduced from more than 15 kips (67 kN) to about 10 kips (45 kN).

Specimen A2 data are presented in a similar way to those of A1 in Figures D-5 to D-14. Each page corresponds to one direction of one run. Since test A2 was bidirectional, the response in both directions is presented. As in Specimen A1, strength reduction in the positive direction is observed in the last two runs especially Run 10. This corresponds to severe damage in the plastic hinge region.

The peak relative displacements for Specimens A1 and A2 were very close in all of the first eight runs. There is a small increase in peak displacement from one maximum run to the next with the maximum relative displacement reaching about 8 in. ($\approx$200 mm) corresponding to a displacement ductility $\mu \approx 8.0$ by the last run (for both Specimens A1 and A2). The peak displacement is relatively constant even in the last run of Specimen A2 in which the column developed a very large residual displacement of 6 in. ($\approx$150 mm). When residual deformations at the beginning of the run are accounted for (See Figure 5-11), the peak relative displacement of Specimen A2 during the last run is about 10 in. ($\approx$250 mm) corresponding to a displacement ductility $\mu \approx 10.0$.

Residual displacements were relatively constant until the last run. The last runs typically had large residual displacements, which was associated with at least one fractured bar. It is worth noting that the residual displacements had some fluctuations between positive and negative values in the first few runs as can be seen in Figure 5-3, but those values were generally small. However, once a large enough residual displacement occurred in one direction, there was a tendency for that residual displacement to continue increasing in the same direction following repetitions of the earthquake. Although this would depend on the characteristics and scaling of the earthquake, and on the properties of the column (which are continuously changing due to increased damage), it can be simply attributed to an increase of P-Δ effects which tend to cause an incremental type of collapse.

Displacements in the lateral direction of Specimen A2 were significantly smaller than the longitudinal direction. Peak displacements of about 2.5 in. ($\approx$60 mm, $\mu\approx$2.5) were observed in the lateral direction (compared to 8 in. in the longitudinal direction). The effect of the lateral displacement on the maximum relative displacement in the xy-plane is negligible, since the lateral (y) relative displacement happens to be very small when the peak longitudinal (x) relative displacement occurs. In general, the demand in the lateral direction was significantly smaller than that in the lon-

gitudinal direction, and so was the damage. The concrete did not completely spall on the North and South faces of Specimen A2, and the cracking was more moderate along the column height.

The peak shear forces in Specimens A1 and A2 follow similar trends (in the longitudinal direction). At yield level, the force roughly corresponds to the theoretical shear force required to yield the longitudinal steel. The shear force reached its highest value during the design level. After that, the peak longitudinal shear force gradually decreased in each successive run. A closer look at Figure 5-40 shows that the largest decrease in shear force occurs between Run 2 (Design Level 1) and Run 3 (Maximum Level 1). However, the base moment (including P-Δ) does not seem to change much between those two runs, which suggests that the shear variation could be attributed more to higher mode contribution than to actual strength degradation, and that the higher mode effects were reduced by the softening of the column in the later runs.

In the plots showing the peak shear and base moment during various runs, the shear and moment are plotted against different scales (left and right of the plot). The moment scale is obtained by multiplying the shear scale by 96, the height (in inches) to the center of mass. This means that when the shear and moment (without P-Δ) values fall on top of each other, the column is more dominated by the first mode. This seems to be the case in most of the runs for Specimens A1 and A2 in the longitudinal direction (Figures 5-10 and 5-12). In the lateral direction however, there is a significant difference between the moment and shear lines (Figure 5-16). The recorded maximum base moment is less than two-thirds of that recorded in the longitudinal direction of both A1 and A2, while the shear is up to two times larger. This may be due to two factors:

1. The bidirectional interaction causes a reduced moment capacity in the lateral direction because of substantial movement in the longitudinal direction. As the column yields in the longitudinal direction, the capacity is reduced in the other direction. Since the interaction surface of a circular column in circular in shape, the strength reduction is more significant in the direction with less deformation (Figure 5-41).

2. The response in the lateral direction has large contributions from the second mode of vibration (Figure 5-23), and hence the shear force is significantly larger than would be expected from a column behaving in single curvature.

For Specimen A1, the shear force measured at failure (Run 8) was 67% of the peak shear capacity measured during Run 2. For Specimen A2, the shear force during the same run (Run 8)
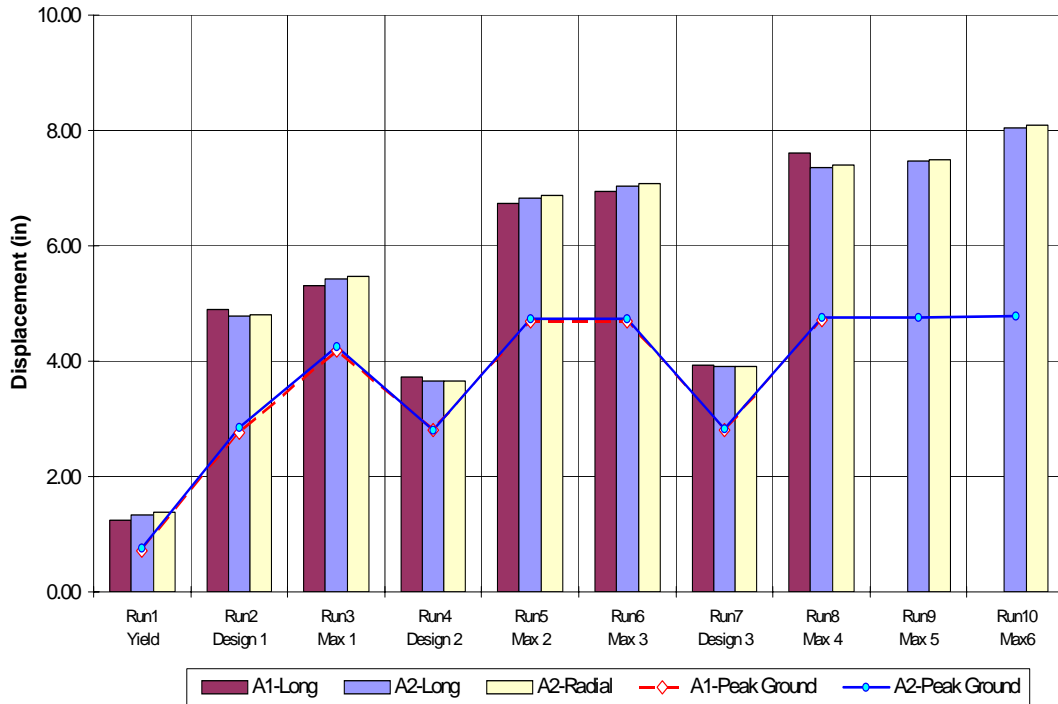
Figure 5-39. Peak displacement values for Specimens A1 and A2 in the longitudinal direction.
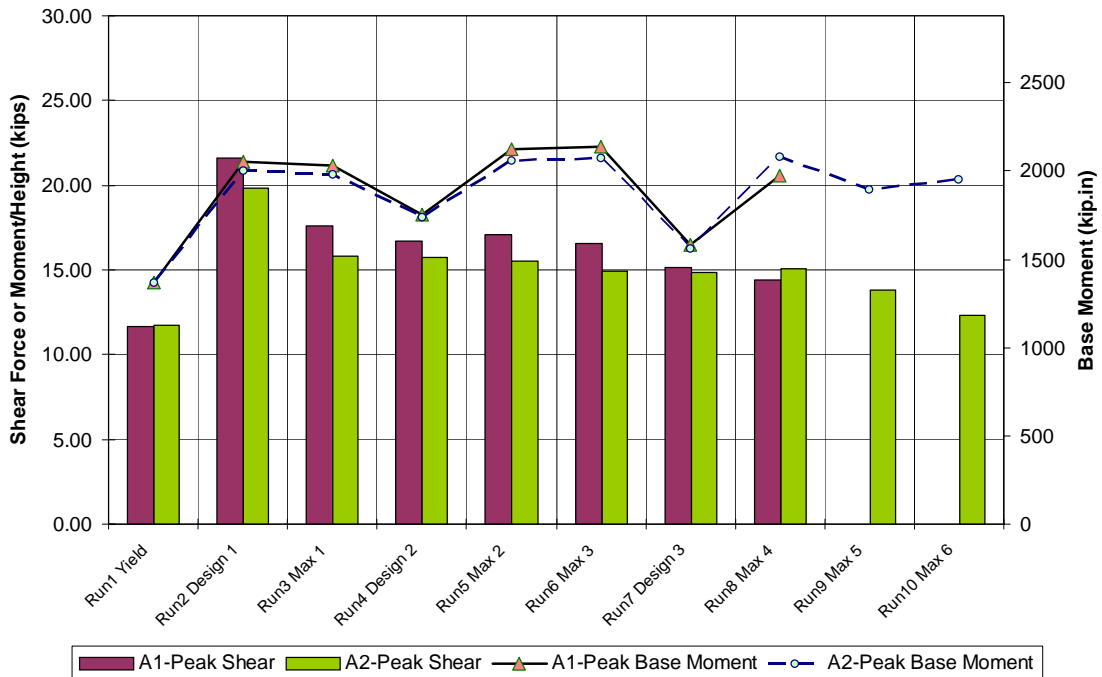
Figure 5-40. Peak shear and base moment for Specimens A1 and A2 in the longitudinal direction.

was 76% of the peak shear capacity measured during Run 2, but at failure of Specimen A2 (Run 10) the ratio was 62%.

Comparing the measured moment in Specimens A1 and A2 also shows that peak base moments measured in Specimen A1 tend to be higher than those measured in Specimen A2 (in the longitudinal direction). The lower moment capacity for Specimen A2 can be attributed to bidirectional interaction between the two components of Specimen A2. While the reduction in base moment in the longitudinal direction may be attributed to bidirectional interaction, the moments in the lateral direction are significantly more affected. This can be observed in Figure 5-41 which shows the bidirectional moment interaction for Specimen pairs A1/A2 and B1/B2. For example, for Specimen A2, the moments in the lateral directions are so reduced that they never exceed the yield moment M_y. The bidirectional interaction of the displacements and curvatures (Figures 5-42 and 5-43) also shows that the longitudinal direction dominates the response of Specimens A1/A2 and to a lesser degree in the case Specimens B1/B2.

Despite the good agreement in displacements and forces between Specimens A1 and A2 (until Run 8), the progression of damage in the two Specimens was different. Specimen A1 experienced more damage at an earlier stage, and consequently could not sustain as many test repetitions as Specimen A2. Both specimens however behaved extremely well until Run 5. This corresponds to being subjected to one design level earthquake, a second much larger record, and then the design level earthquake again (representing an aftershock) without any significant damage other than spalling.

5.4.5.2   Specimens B1 and B2

As with Specimens A1 and A2, Specimen B2 survived four more runs than Specimen B1 did. In test B2, the maximum level earthquake was applied four times beyond what was applied by the end of test B1. Another related observation was the delay in the occurrence of bar buckling and fracture in B2 compared to B1. The results are fairly comparable during the first nine runs which are common between the two tests (in the longitudinal direction). Figure 5-44 compares the peak relative and peak ground displacements in the longitudinal direction of tests B1 and B2. As in Figure 5-39, the peak displacement compared is non-cumulative, i.e. the residual displacement is assumed zero at the beginning of each run. Figure 5-45 compares peak shear and base moment values. The moments compared are total base moments including nonlinear geometric effects (P-Δ).
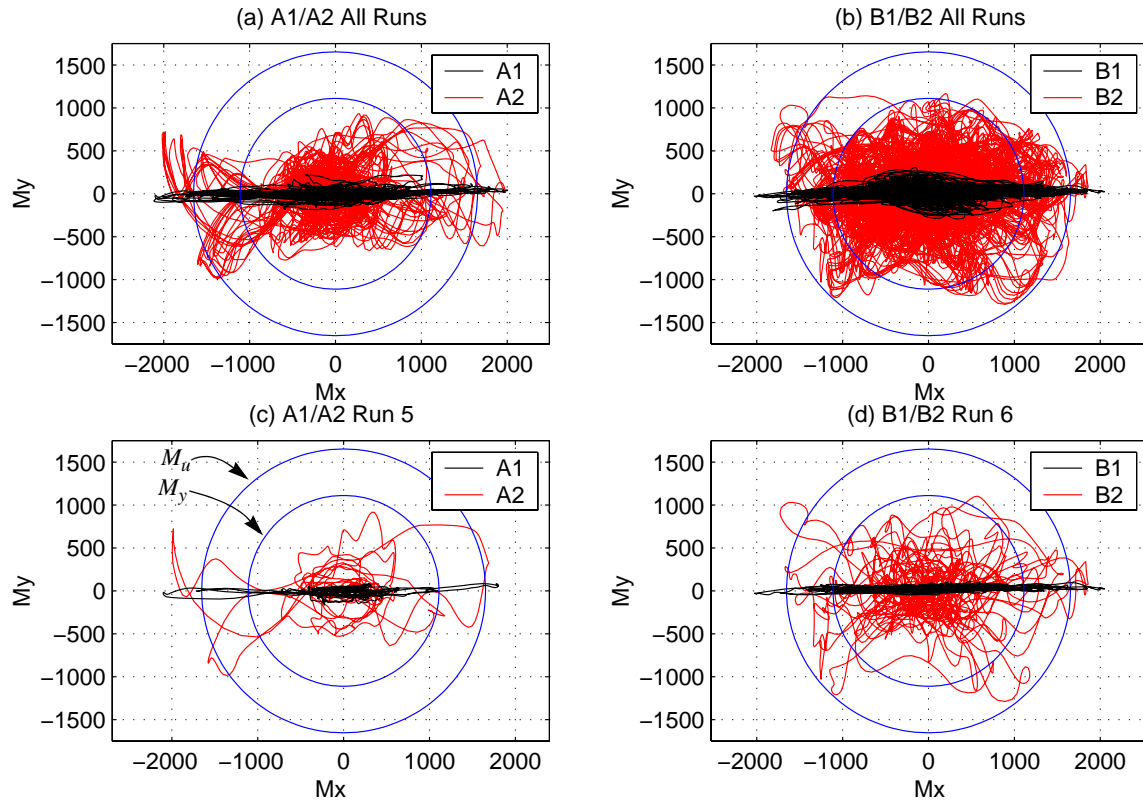
Figure 5-41. Bidirectional moment interaction for Specimens A1/A2 and B1/B2.
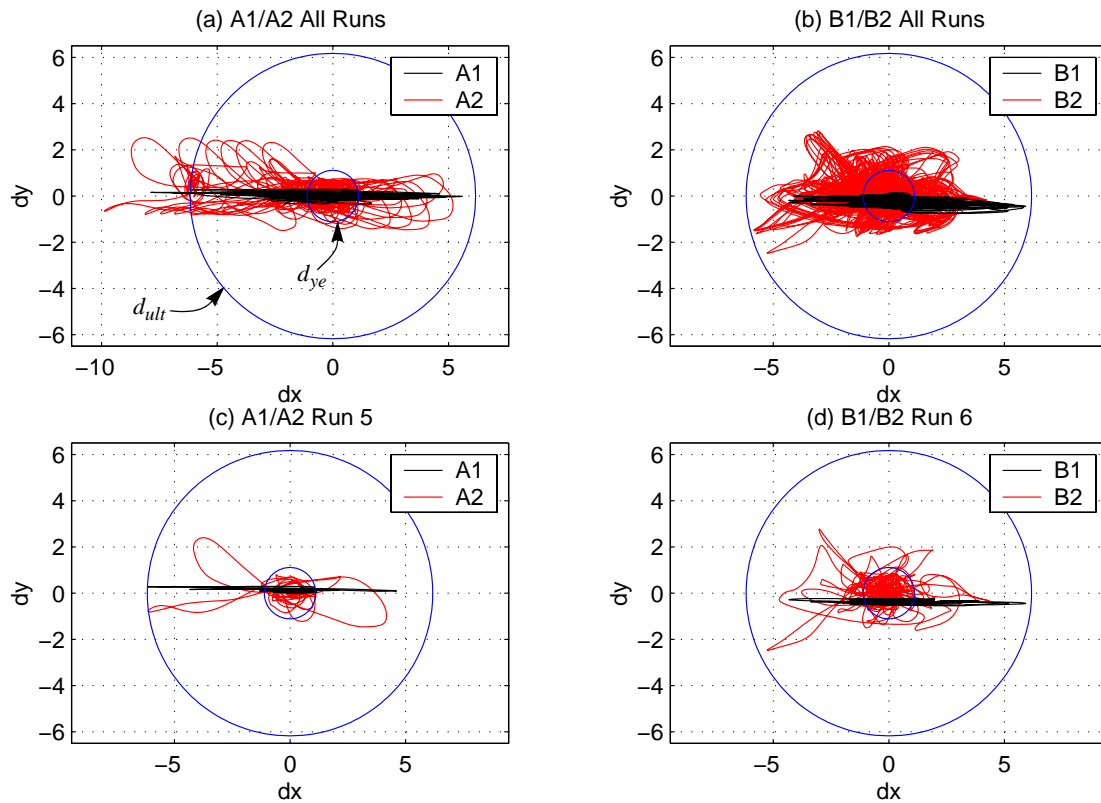
Figure 5-42. Bidirectional displacement interaction for Specimens A1/A2 and B1/B2.
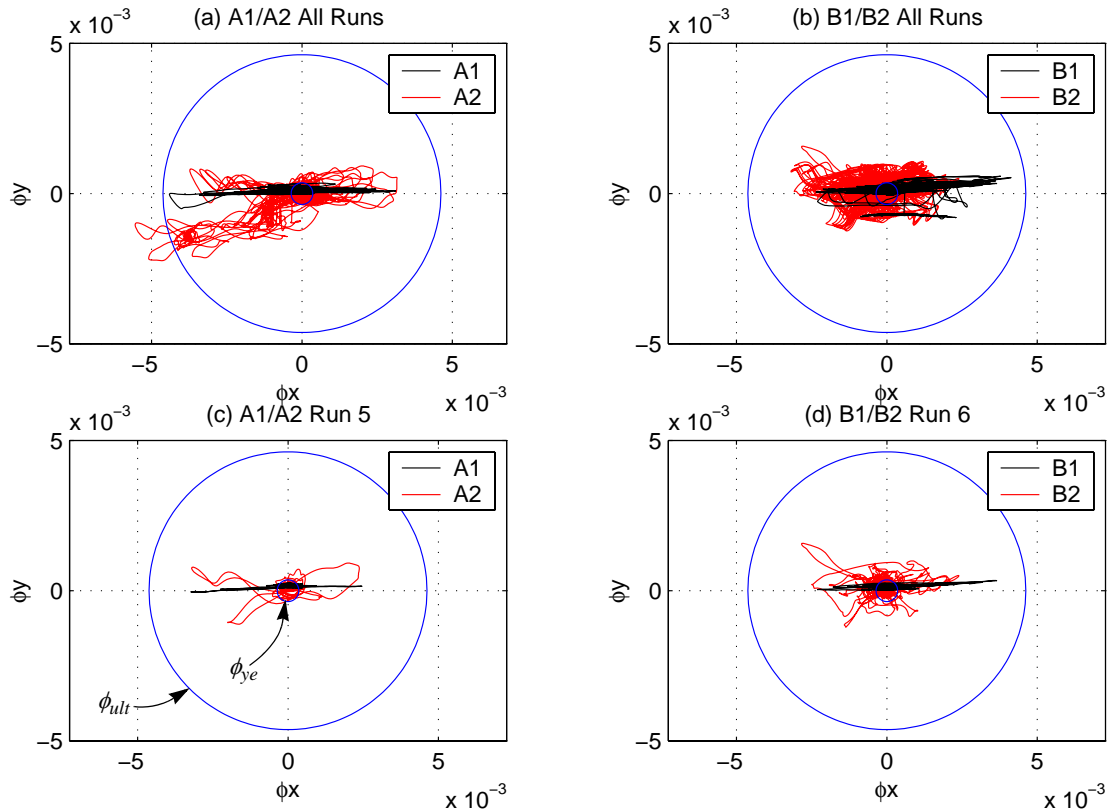
Figure 5-43. Bidirectional curvature interaction for Specimens A1/A2 and B1/B2.

Time history results from specimen B1 are presented in Figures D-15 to D-18 in Appendix D. A large number of cycles was observed as opposed to only two or three cycles in the near fault case (A1 and A2). Failure occurred at a smaller maximum displacement, but with more cycles.

Specimen B2 data are presented in a similar way to those of B1 in Figures D-19 to D-28. In addition to the 10 degree Llolleo main component, this specimen was also subjected to the 100 degree lateral component. Comparing the two components, the lateral component had less energy in the 0-2 Hz region of main interest, and hence had smaller ground displacement while the peak acceleration was comparable to the longitudinal direction. Hence, the response in the lateral direction has more higher frequency contribution, which explains the smaller displacements in this direction. At the end of the test, the specimen had retained most of its strength despite the fact that one longitudinal bar had fractured.

The measured peak relative displacements in the first nine runs for Specimens B1 and B2 were slightly different but followed the same trend. Displacements of Specimen B1 were larger in the first three large runs (Runs 5, 6 and 7), but they were smaller for Runs 8 and 9. Peak displacements that ranged from 5 to 6 in. (120 mm to 150 mm, $\mu \approx 5.0$ to 6.0) were observed during the max-

imum level runs in the longitudinal direction of both B1 and B2. Peak displacements observed in the design level runs were about 50% smaller.

Residual displacements increased gradually in test B2 to 0.94 in. (24 mm) in Run 13. Those residual displacements were all in the same direction (negative direction). In test B1 however, a residual displacement of one inch was experienced as early as Run 6, in the positive direction. Further runs resulted in gradually decreasing residual displacements ending with 0.67 in. (17 mm) in Run 9.

Displacements in the lateral direction of Specimen B2 were about one-half of those observed in the longitudinal direction of B2. Peak relative displacements were about 2.6 in. (66 mm, $\mu \approx 2.6$) on average, and decreased slightly from Runs 8 to 13. Residual displacements were not significant (<0.20 in. or 5 mm), and hence the cumulative peak relative displacements were very close to the non-cumulative peak relative displacements. The demand in the lateral direction was less than that in the longitudinal direction. That was reflected in the damage to the North and South faces of Specimen B2, which although severely cracked, did not completely spall. Hence, the cover confined the longitudinal steel, and prevented premature buckling of rebar along the lateral direction.

Specimen B1 experienced larger shears and moments than specimen B2. As with the A1/A2 pair, this can be attributed to bidirectional interaction, which was more significant in the B1/B2 pair, since the ratio of lateral to longitudinal deformation was larger in this case (0.50 for B2 vs. 0.35 for A2 on average). Bending moments in Specimen B2 over Runs 8 to 13 (all at maximum level) showed some strength degradation. Shear forces were generally much higher in the B1/B2 pair than the A1/A2 pair in the longitudinal direction (compare Figures 5-40 and 5-45), while the shear forces in the lateral direction of B2 were smaller than those of A2 (compare Figures 5-14 and 5-20). This is mainly attributed to the second mode contribution to inertia and shear forces.

Another distinction between this pair and the A1/A2 pair was the difference of the response to the design and maximum levels. For both B1 and B2, the response to the maximum level was much larger. Displacements in the design level were up to 45% smaller, while moments were up to 24% smaller than those experienced during the maximum level earthquake. This is partly due to the fact that the maximum level is twice as large as the design level earthquake (the ratio is 1.67 for A1/A2). The moment difference can be attributed to strain hardening, although 24% appears to be somewhat high.

Damage progression differed significantly between Specimens B1 and B2, with B1 failing much earlier than B2. Specimen B1 experienced more damage at an earlier stage, and consequently was not able to sustain as many test repetitions as Specimen B2. The behavior of both specimens however until Run 8 was very satisfactory. This corresponds to being subjected to one design level earthquake, a second much larger record, and then the design level earthquake again (representing an aftershock) without any significant damage other than spalling, and some minor buckling during Run 6 in Specimen B1.

5.5   LOCAL RESPONSE MEASURES

The measurement of curvatures and strains in critical locations, and their correlation to global measures and observed damage are inherent to the understanding and development of performance-based design criteria. Low-cycle fatigue models, for example, which are discussed later in the chapter, greatly depend on a good estimate of the strain history of the steel reinforcement. This estimate, in turn, depends on several factors including but not limited to the plastic hinge length, the curvature distribution inside the plastic hinge length, and the relation between curvature and strain, which is complicated by reinforcement slip and by severe distortions in the plastic hinge zone at high curvature demands.

5.5.1   Section Deformations

Curvatures and elongations are estimated over regions of the column extending between the location of DCDT instruments attached to the face of the column. As shown in Section 4.3.2.4, the measurements from those instruments can be used to estimate axial elongations and biaxial curvatures. The integration of curvatures along the height of the columns yields the rotations and horizontal deformation at different heights. As an example, the curvatures, rotations and deformations are plotted at the different regions and sections in Figure 5-46 for the DCDT data obtained from the fifth run of Specimen A2 in the longitudinal direction. Figure 5-47 compares two different measures of horizontal longitudinal deformations at the different sections along the column height, and at the center of mass block. The first measure is directly obtained from external displacement measurements and hence represents the measured relative deformation, while the second is obtained by integrating curvatures from DCDT measurements along the height of the column. The plot clearly shows a good match between the two measures which indicates that the shear contribution
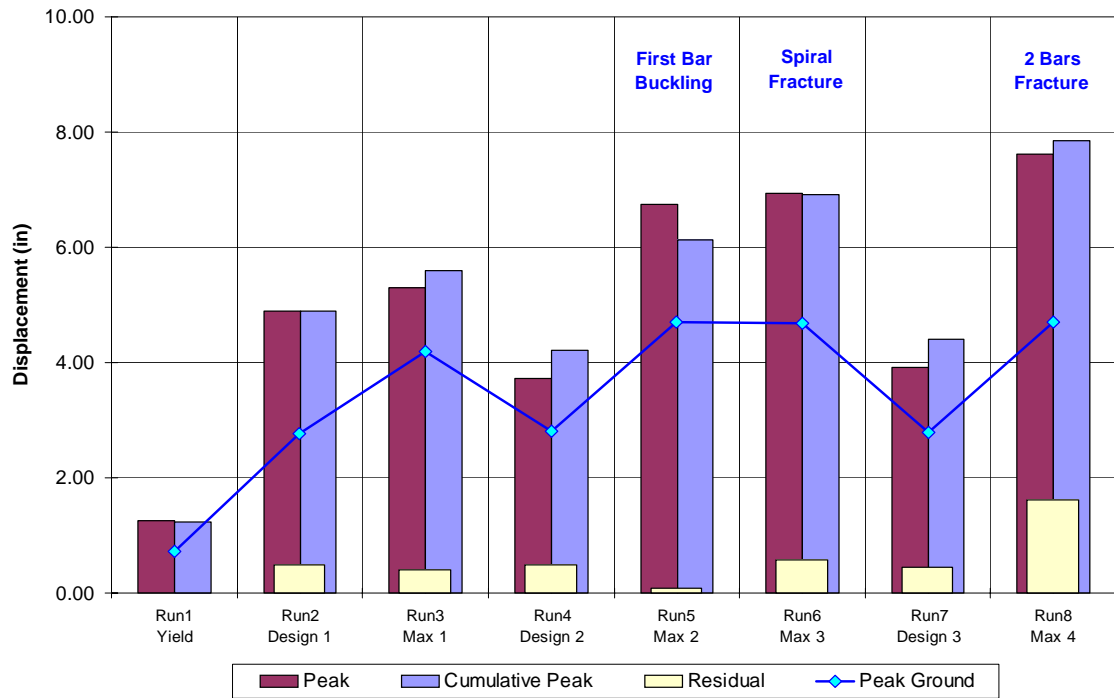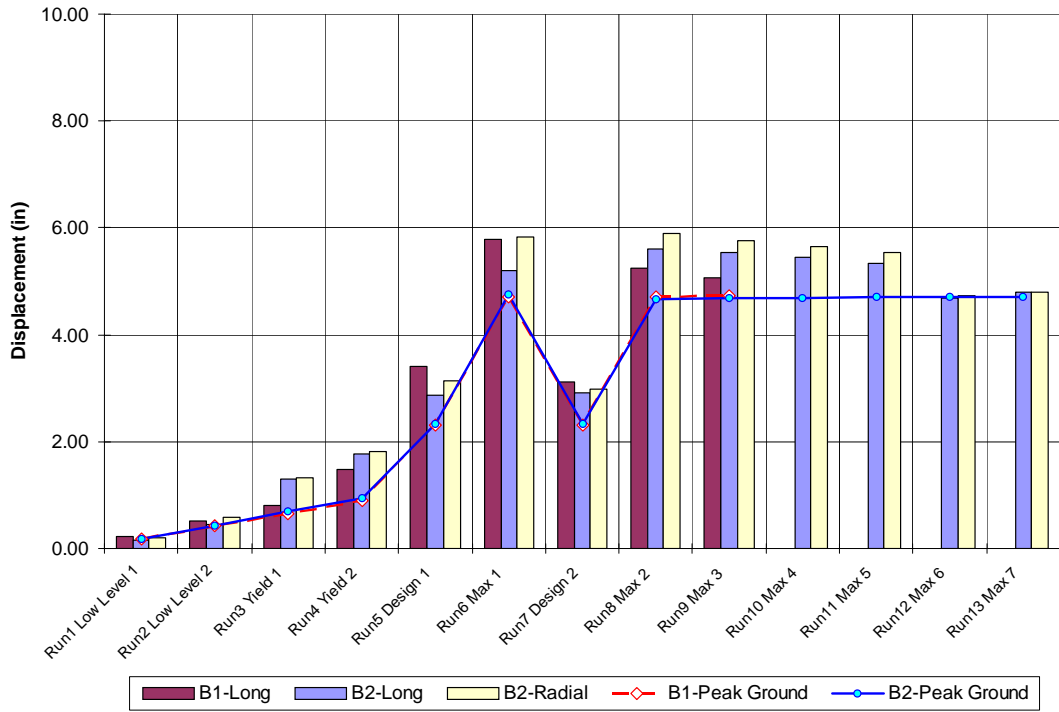
Figure 5-44. Peak displacement values for Specimens B1 and B2 in the longitudinal direction.
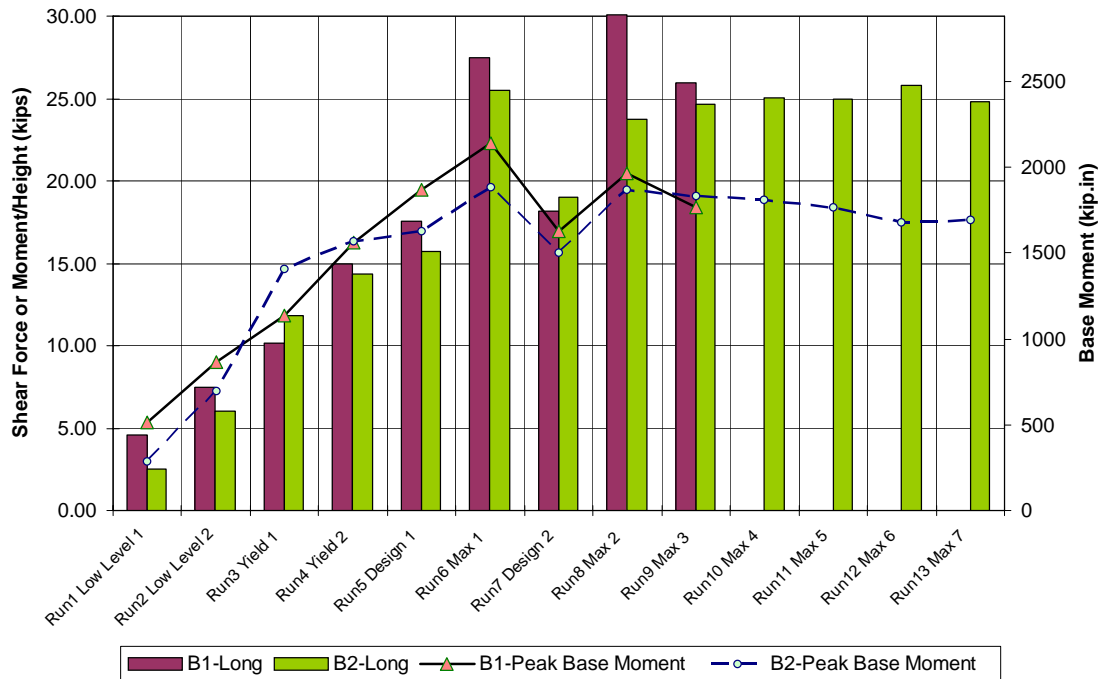
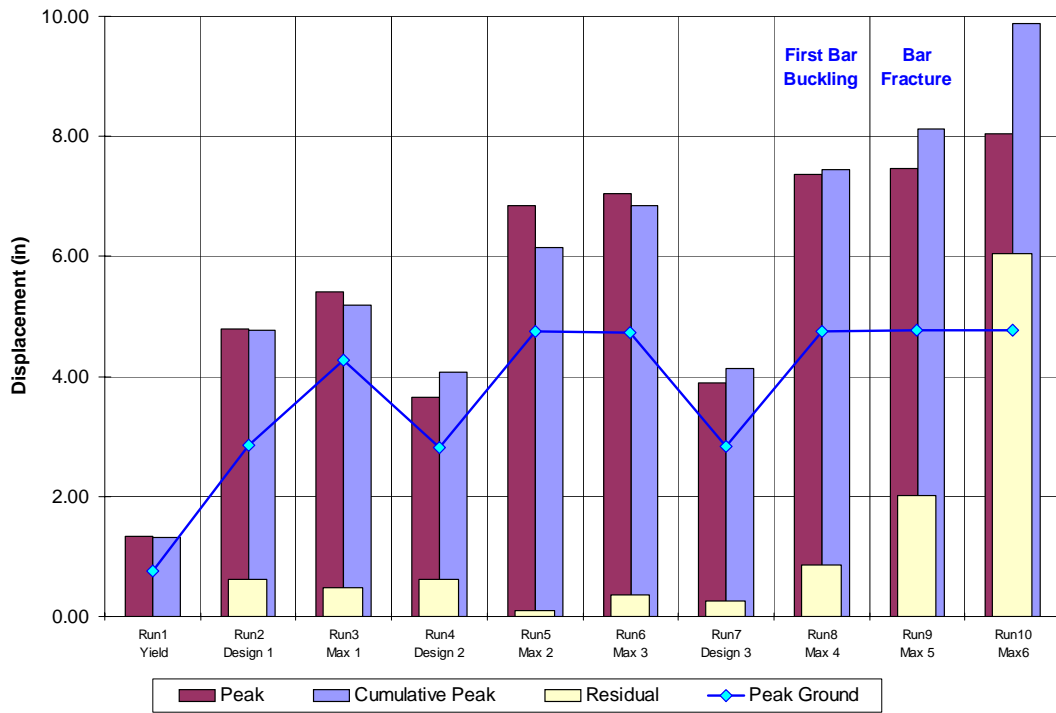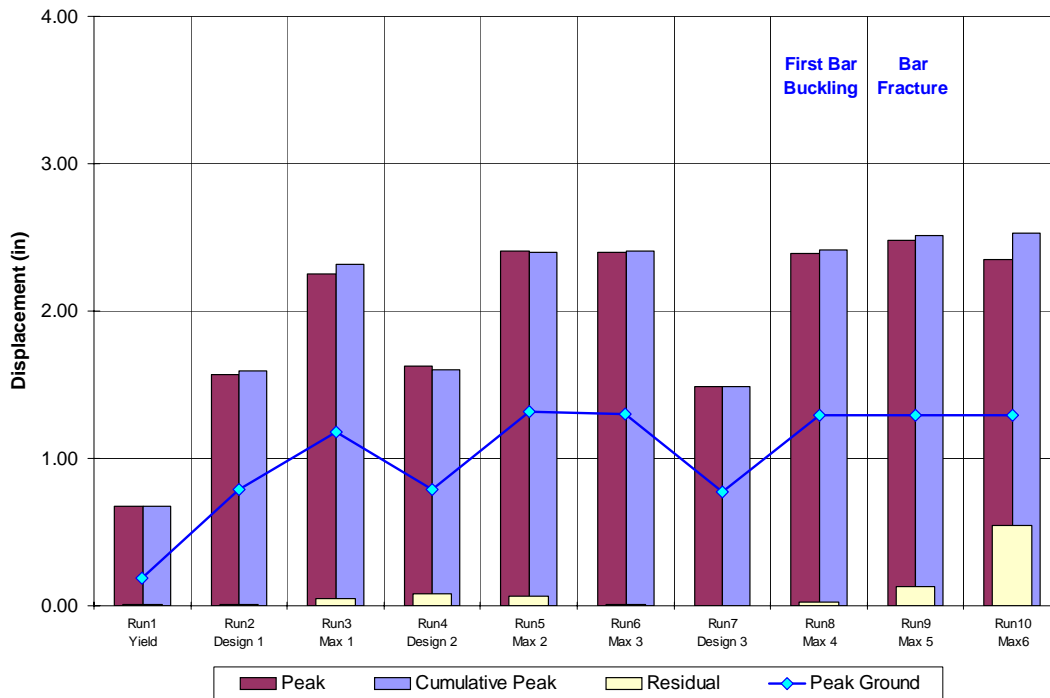**Figure 5-45.** Peak shear and base moment for Specimens B1 and B2 in the longitudinal direction.

to total deformation is negligible, since the integration of curvature only includes the effects of flexural and slip deformations.

The pullout of the longitudinal reinforcement from the footing was measured using DCDT instruments mounted on rods located at 0.75 in. (19 mm) and 1.5 in. (38 mm) from the footing surface (Figure 4-7). By using the measurement at opposing faces of the column, a slip rotation can be calculated similar to the calculations in Section 4.3.2.4. The product of that rotation by the distance to the center of mass yields the slip contribution to total deformation. The amount of this contribution as a fraction of total deformation is shown in the lower portion of Figures 5-48 to 5-51 for all the runs of each of the Specimens. Only peaks larger than 1.5 in. (38 mm) were considered. It is observed for all the specimens that, on average, slip accounts for about 20% of total deformation, and may be as high as 30% or more. In the upper portion of each figure, the slip deformation time history is superimposed on top of the total displacement history.[1]

5.5.2 Strains

Strain gages mounted on longitudinal and spiral steel bars provide valuable data, that can be used to trace the strain history at various locations in the specimen, and to correlate internal strains to observed damage and bar buckling or fracture. However, because strain gages on longitudinal reinforcement in the plastic hinge region may fail following a cycle occurring during one of the initial design or maximum level runs, their usefulness in tracing strain demands due to repeated excitations may be lost. This is contrasted to quasi-static testing with standard increasing cycles under which peak strains are reached at the end of the test, and the life of strain gages is fully utilized. To overcome this problem, strains in the plastic hinge zone are estimated from the external measurements recorded at the face of the column. This approach assumes strain compatibility between steel and concrete, i.e. little or no slip occurs between the reinforcement and the concrete, which yields an average strain over the height between the instruments. For a bar with coordinates (b_x, b_y) from the center of the section, the strain ε_{bar} is obtained from the measured values for the curvatures ϕ_{EW} and ϕ_{NS} (according to the conventions of Figure 4-3) and the average section elongation ε_a as shown in Equation 5-9:

$$\varepsilon_{bar} = \varepsilon_a - b_x \phi_{EW} + b_y \phi_{NS} \tag{5-9}$$

---

1. The displacement histories shown in Figures 5-48 to 5-51 consist of all displacement peaks connected by straight lines. Peaks used in the calculations are marked with a circle.
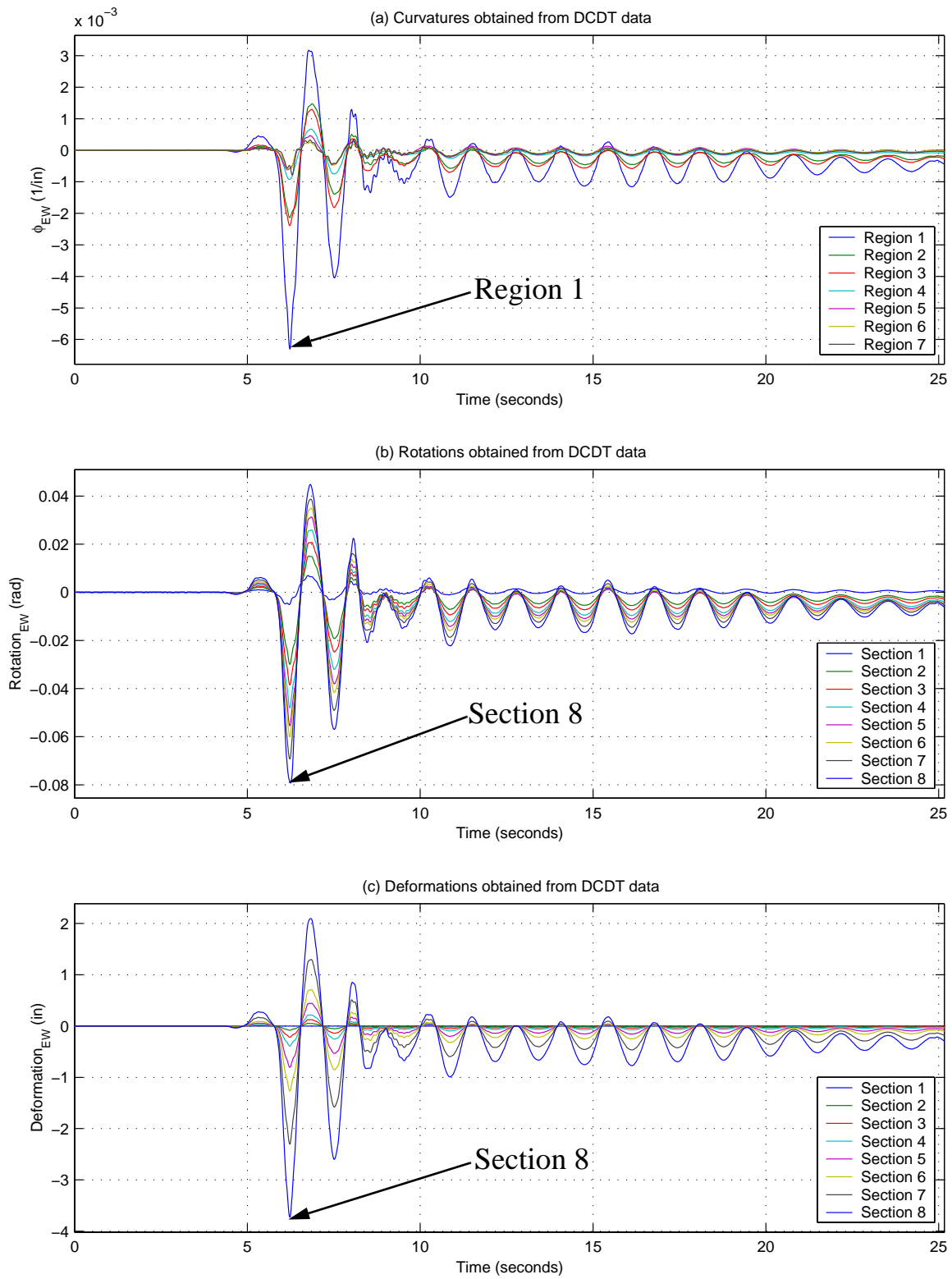
Figure 5-46. Curvatures, Rotations and Deformations along the height of Specimen A2 during Run 5.
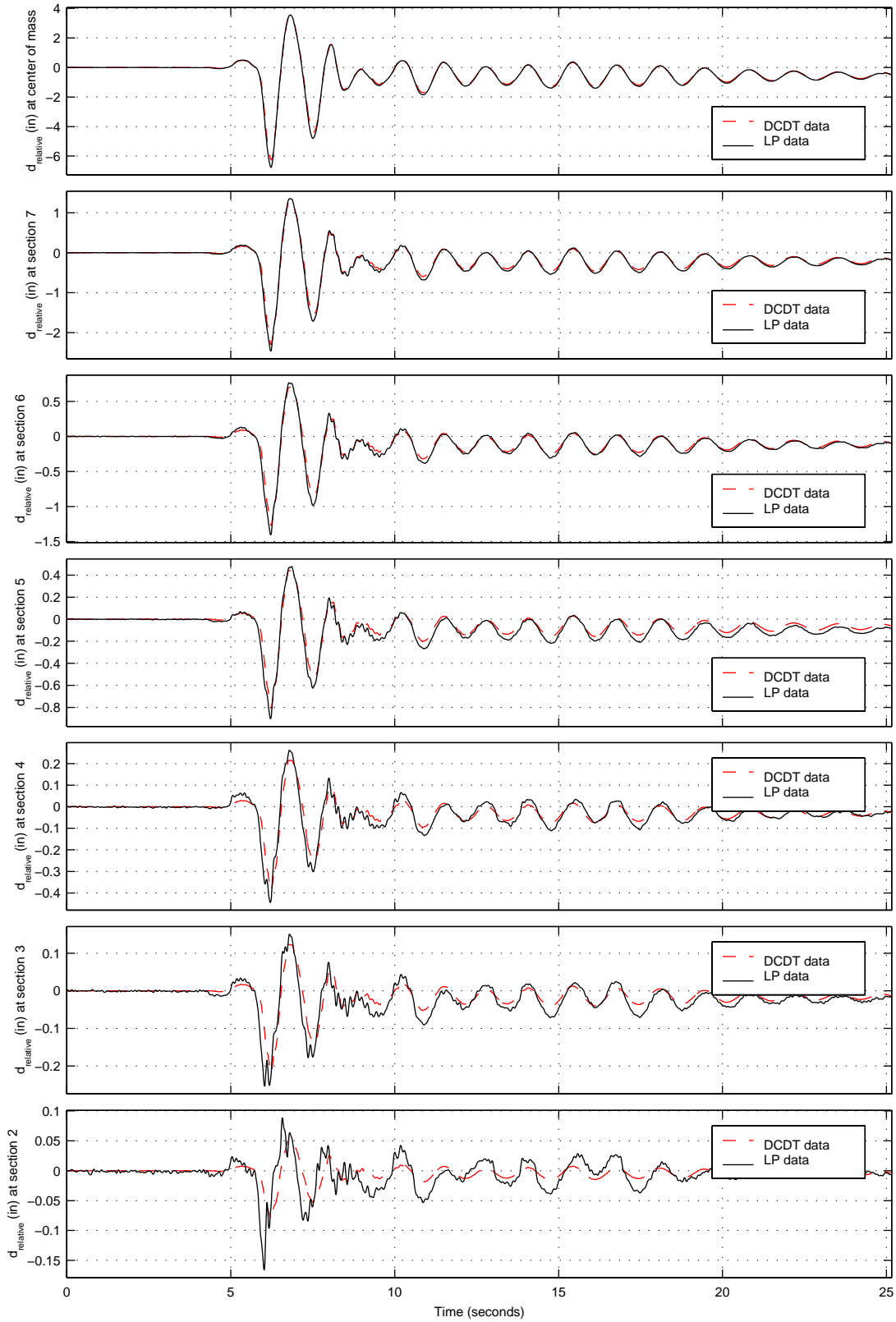
Figure 5-47. Longitudinal relative displacements for Specimen A2-Run 5, from DCDT and LP data.

127
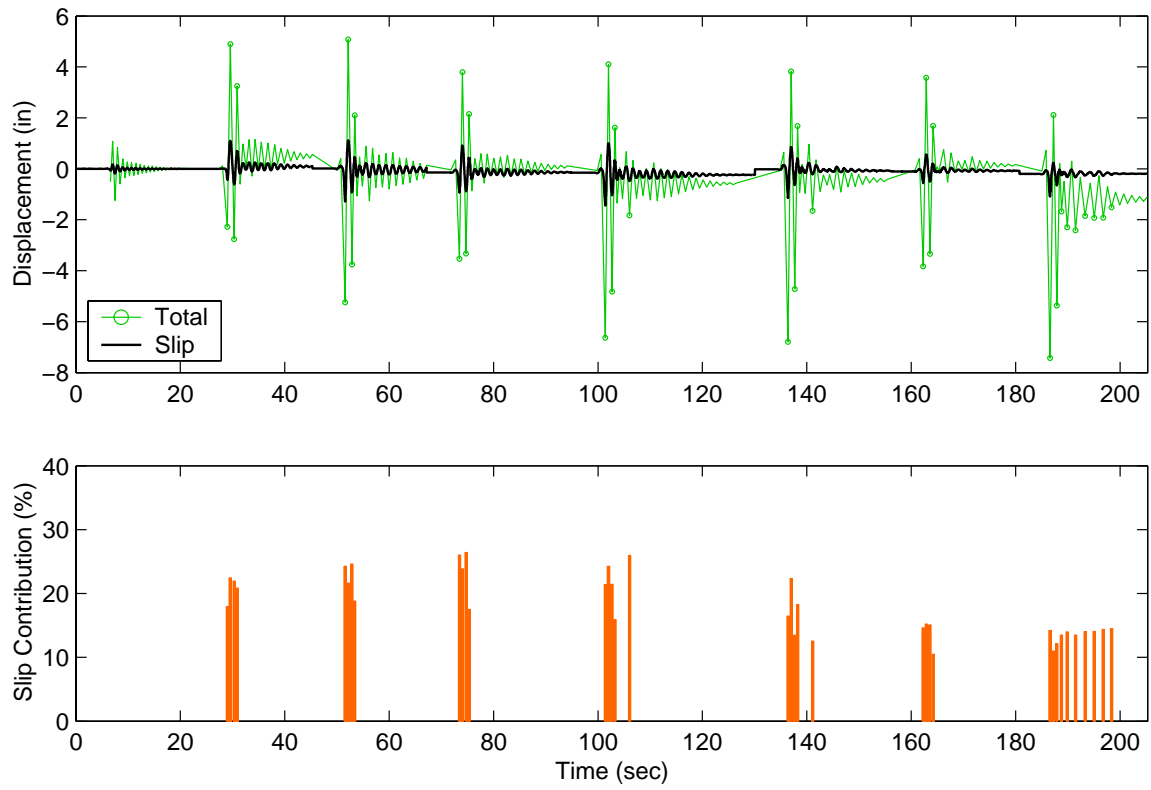
Figure 5-48. Slip contribution to total displacement for all runs of Specimen A1.
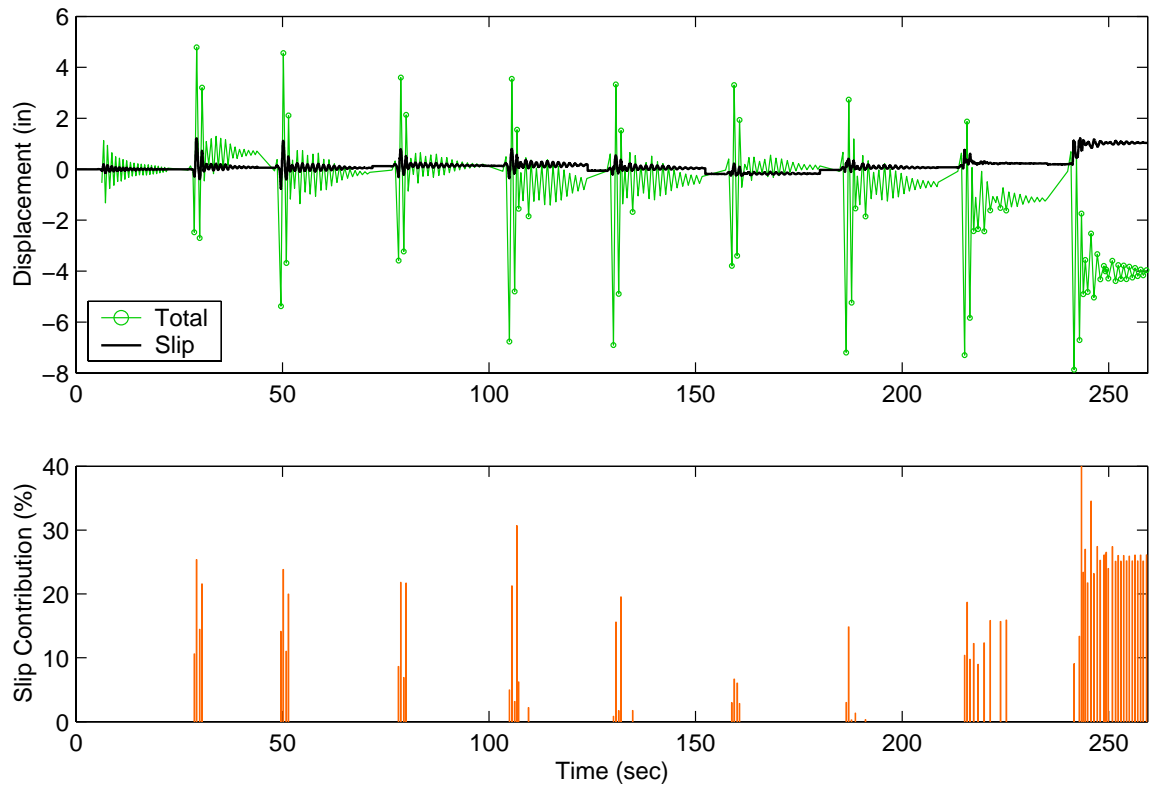
Figure 5-49. Slip contribution to total displacement for all runs of Specimen A2.

128
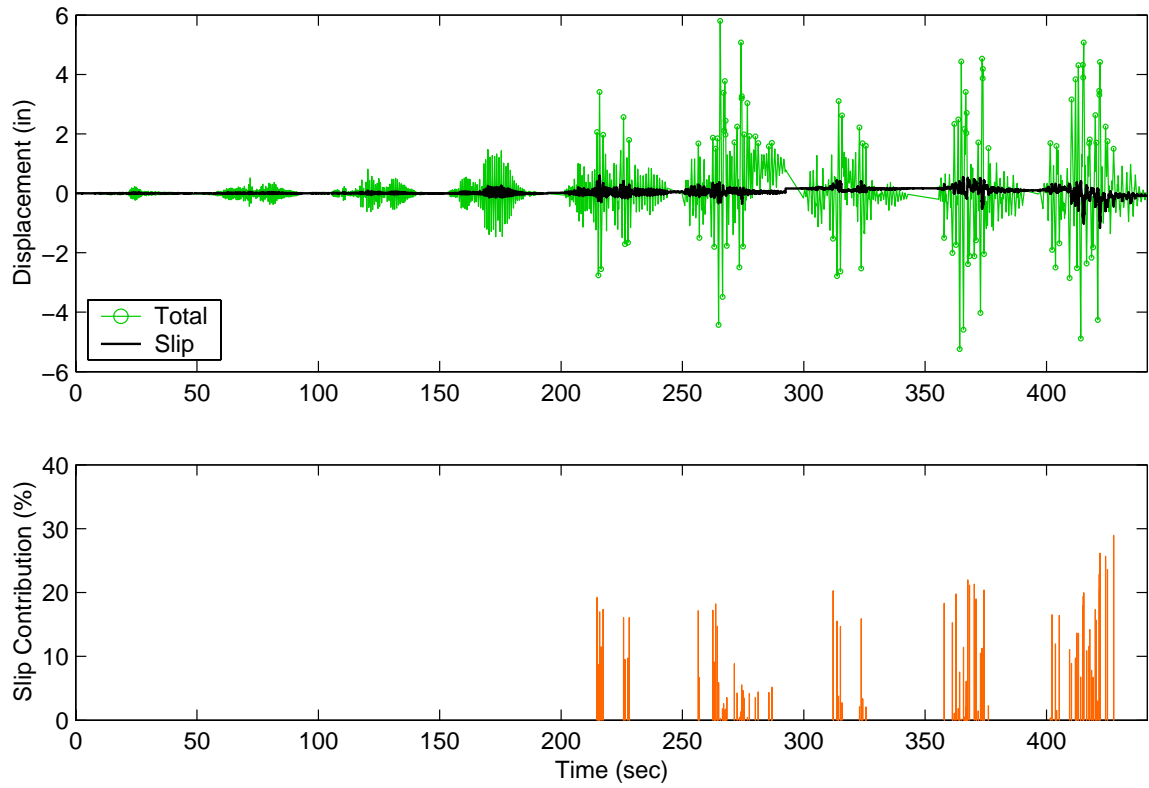
Figure 5-50. Slip contribution to total displacement for all runs of Specimen B1.
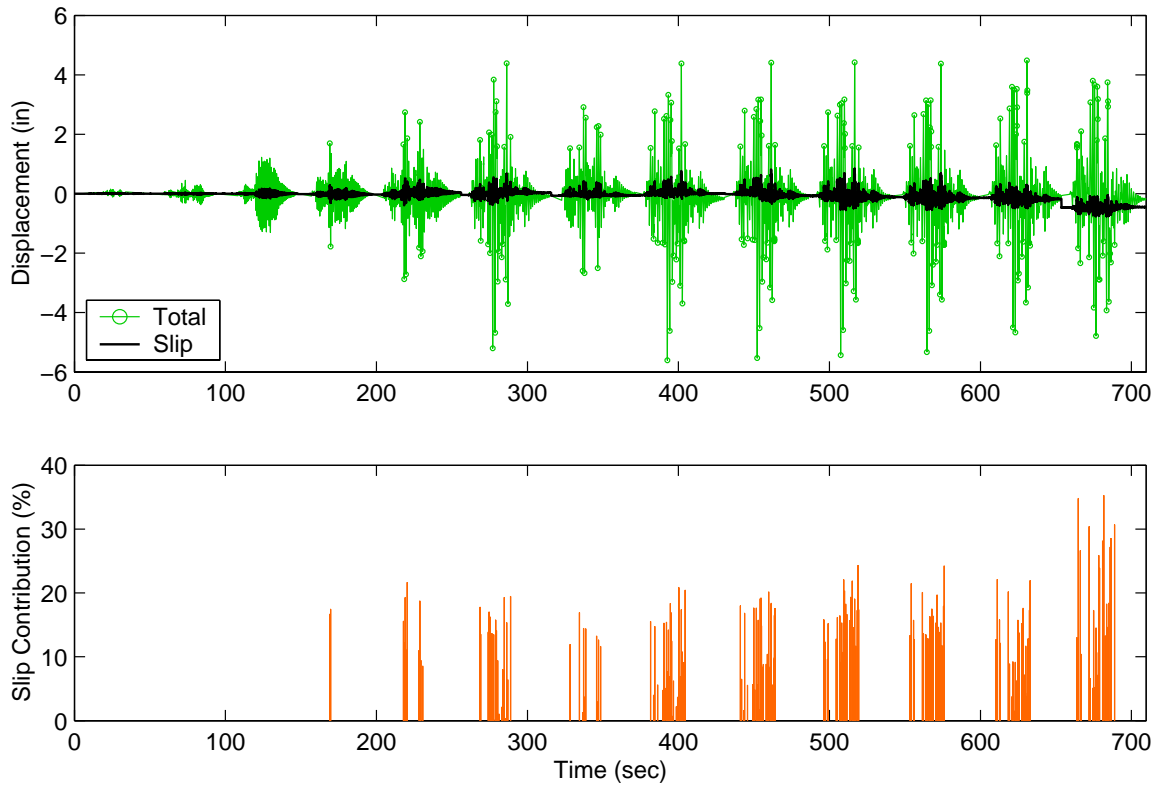
Figure 5-51. Slip contribution to total displacement for all runs of Specimen B2.

129

This approach was used to estimate the strain in the longitudinal reinforcement at the base of the column where the strains are expected to be highest. It was found that the directly measured gage strains at that location can be well predicted using Equation 5-9 where ε_a, ϕ_{EW} and ϕ_{NS} are averaged over the first three regions. Those three regions span a height totalling 12 in. to 12.75 in. (305 mm to 324 mm) in the East-West and North-South directions, respectively, which is roughly equal to the observed plastic hinge length. A comparison between the measured and computed strain histories is shown in Figures 5-52 to 5-54 for longitudinal bars with different locations under the yield level, design level and maximum level excitations. Strain values were zeroed at the beginning of each run in order to allow for a better comparison. This estimate seems to work surprisingly well suggesting that the curvatures are in fact uniform in the plastic hinge zone. However, Figure 5-46 (a) clearly shows that the average curvature over the first region is significantly larger than the curvature in regions 2 and 3 (See Figure 4-7 for definition of regions). The reason for this is that the curvature in the first region includes the effect of the bar pullout from the footing, which increases the effective curvature in the plastic hinge zone without significantly affecting the strain in the longitudinal reinforcement.

The peak longitudinal bar strains experienced during the various runs are summarized in Figure 5-55. The figure contains 16 (4 x 4) subplots each corresponding to one side of one of the four specimens. The rows correspond to the four specimens A1, A2, B1 and B2, while the columns correspond to the four sides of the specimens (North, South, East and West). The peaks measured are plotted along the x-axis, while the y-axis denotes the location of the gage along the height of the column (the footing base has zero height; negative values correspond to gages inside the footing). Each plot contains peak data from all the runs that the specimen was subjected to. Data from gages that failed or were unstable were discarded. As a result, strains taken from Specimen A1 seem smaller than the other specimens because the gains of some the gages were set incorrectly, which resulted in discarding the data from those gages. Despite these irregularities, the results are still very useful in showing the peak strains experienced in some of the early runs, and the progression of those peak values with repetitive loading. Figure 5-56 shows the variation of measured longitudinal strains (on each column side) with the level of excitation. Since the measured peak strains varied along the height, the maximum of those peaks was used in Figure 5-56.

The distribution of peak spiral strains along height for various runs is shown in Figure 5-57. The plots follow the same conventions as Figure 5-55. Figure 5-58 shows the variation of the
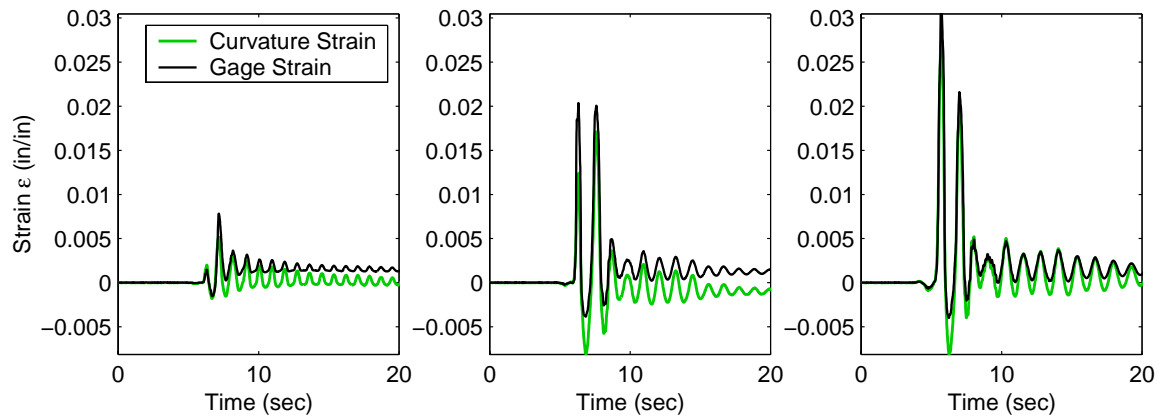
Figure 5-52. Comparison of measured strains and estimated strains for Runs 1, 2, and 3 of Specimen A2 for the west bar (0° from the x-axis) at the base of the column.
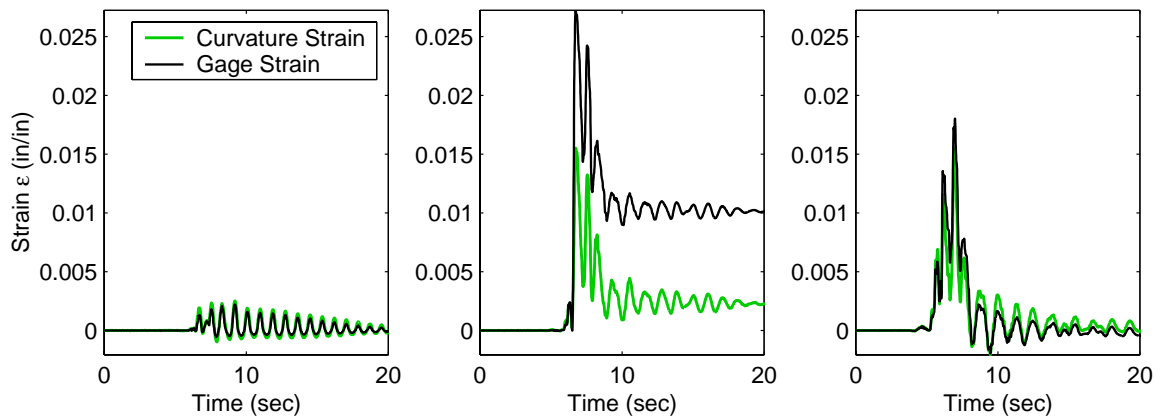
Figure 5-53. Comparison of measured strains and estimated strains for Runs 1, 2, and 3 of Specimen A2 for the south bar (90° from the x-axis) at the base of the column.
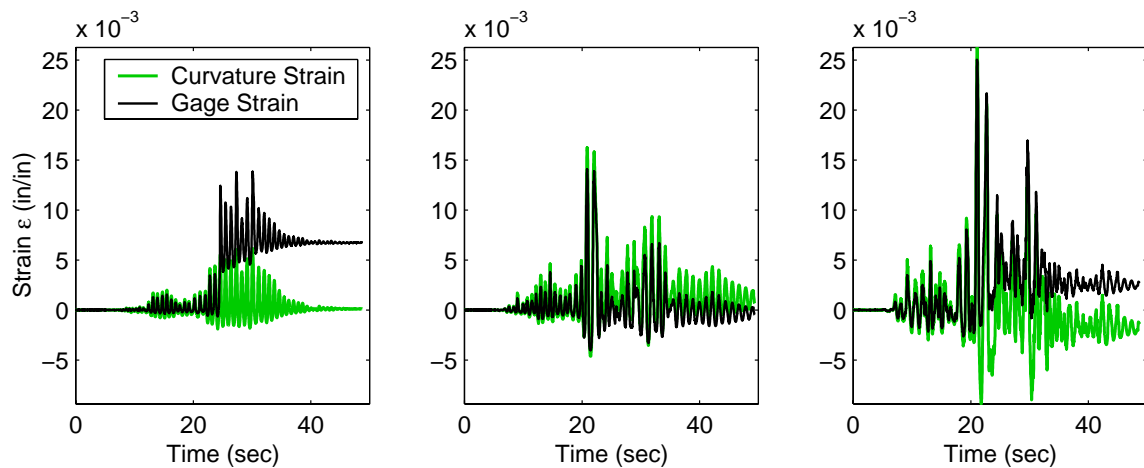
Figure 5-54. Comparison of measured strains and estimated strains for Runs 4, 5 and 6 of Specimen B1 for the west bar (0° from the x-axis) at the base of the column.

peak spiral strain with the excitation level. Since the peak spiral strains were almost constant along the height in the plastic hinge zone, the average value over height was used.

5.6   CORRELATION WITH DAMAGE INDICES

Damage indices are mathematical expressions that are used to predict the failure of a structure or structural member under a given loading history. Those mathematical predictors are generally divided into two categories: local and global. Local indices are calibrated for a specific type of structural member. Global indices, on the other hand, are used to predict the failure of a complete structure, and are usually computed as a weighted combination of local damage indices of individual members. Working with damage indices presents some difficulties such as determining calibration constants for a particular member, and the computational complexity of some indices. Nonetheless, they are perfectly suited for performance evaluation and constitute a tremendous aid in retrofit decisions.

A number of damage indices have been proposed for predicting the damage of reinforced concrete members. An extensive review of those indices is beyond the scope of this report. Williams and Sexsmith [107] and Chung et al. [15] present a critical review of damage indices for reinforced concrete structures. Those indices are classified into cumulative and non-cumulative. Non-cumulative indices relate the state of damage to peak response quantities such as displacement, ductility, rotation, drift or other physical quantity like stiffness, and do not account for cyclic loading effects. Cumulative indices include part or all of the loading history to predict the capacity reduction due to cyclic repetitive loading. Such indices are computed cumulatively using various measures such as energy, total or plastic deformation, or a combination [79]. Some other models attempt to predict low-cycle fatigue by applying the Coffin-Manson [18] and Miner rules [62], either directly to global member behavior or to the behavior of the underlying materials ([47], [58]).

Damage indices are usually normalized such that a value of zero indicates an undamaged state while a value of one indicates failure.

5.6.1   Ductility Index

One of the simplest and most widely used indices is the ductility index. A structure is often presumed to fail at a certain ductility μ_{ult}. The underlying damage index is given by Equation 5-10,
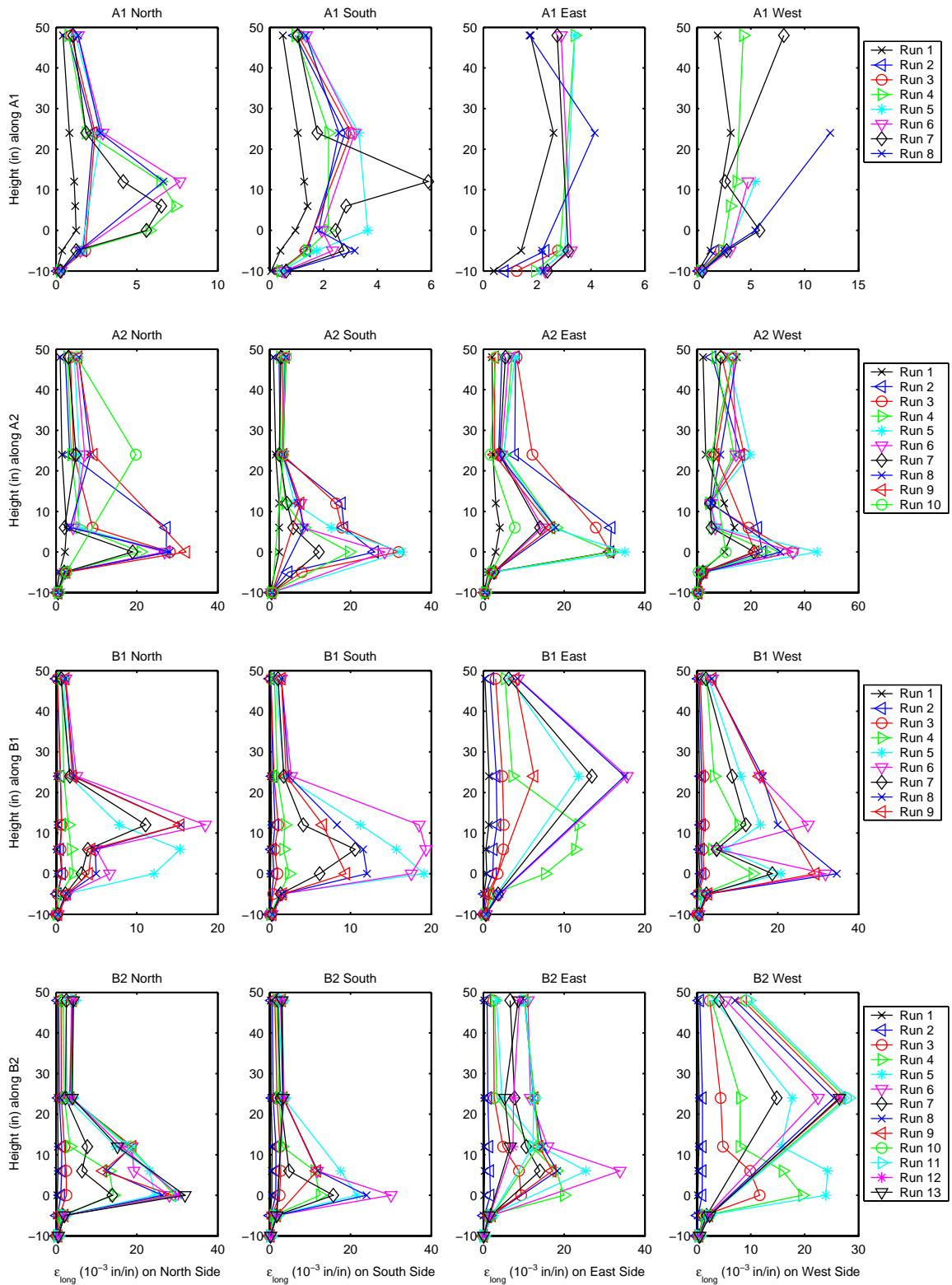
Figure 5-55. Distribution of *peak* longitudinal strains over height with level of excitation.

133
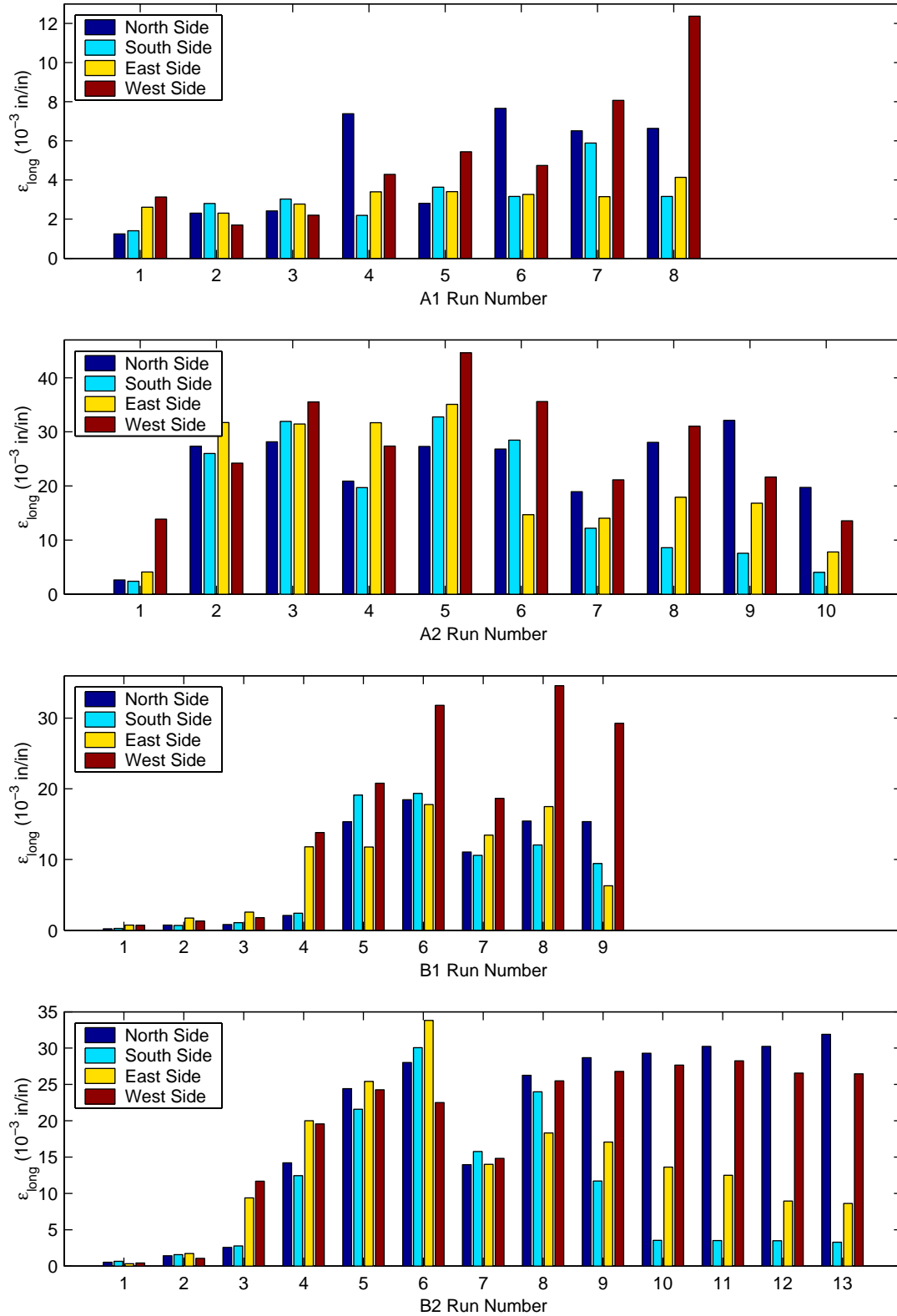
Figure 5-56. Variation of *peak* longitudinal strain (taking largest peak over height) with level of excitation.

134
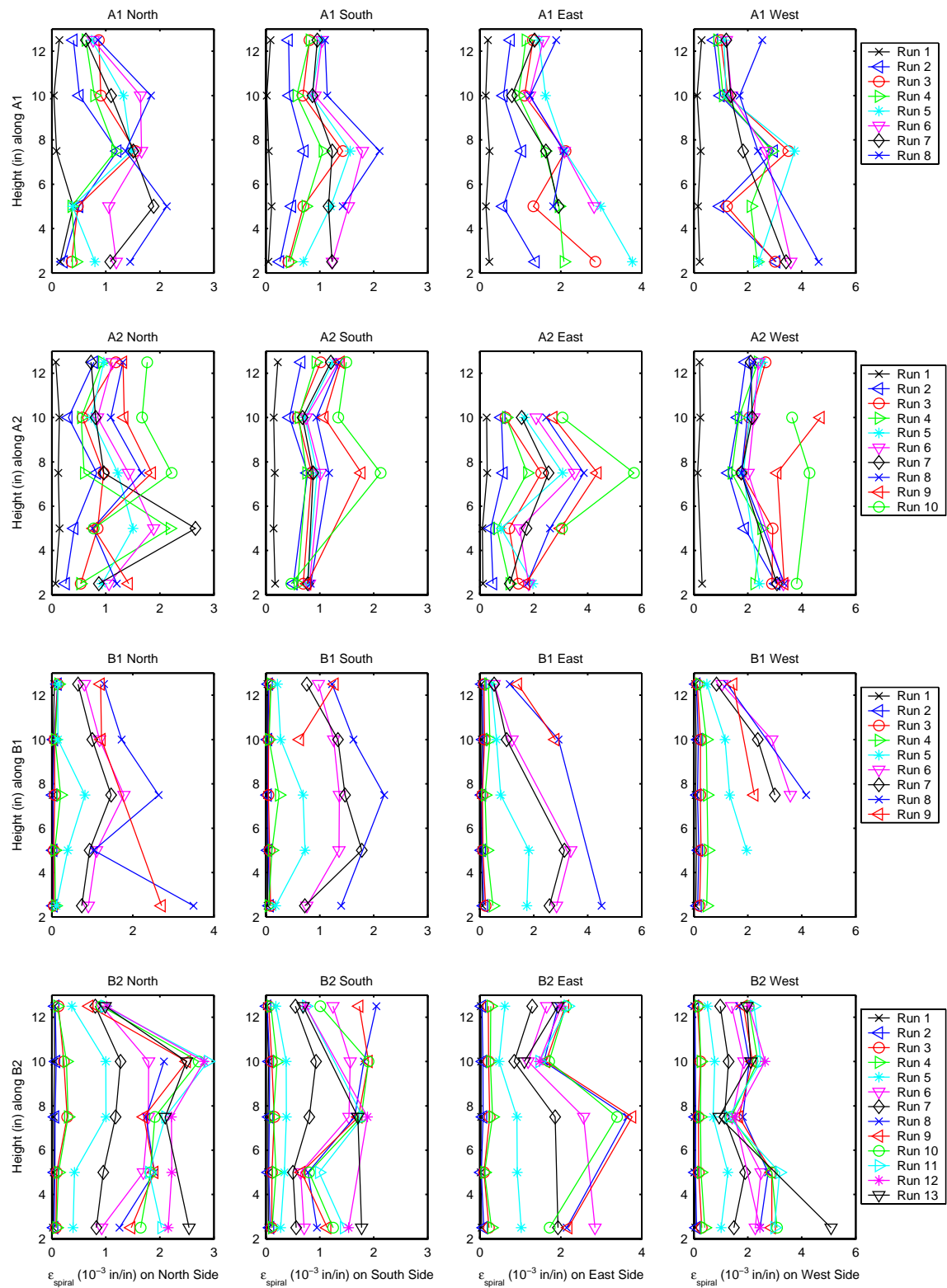
Figure 5-57. Distribution of *peak* spiral strains over height with level of excitation.
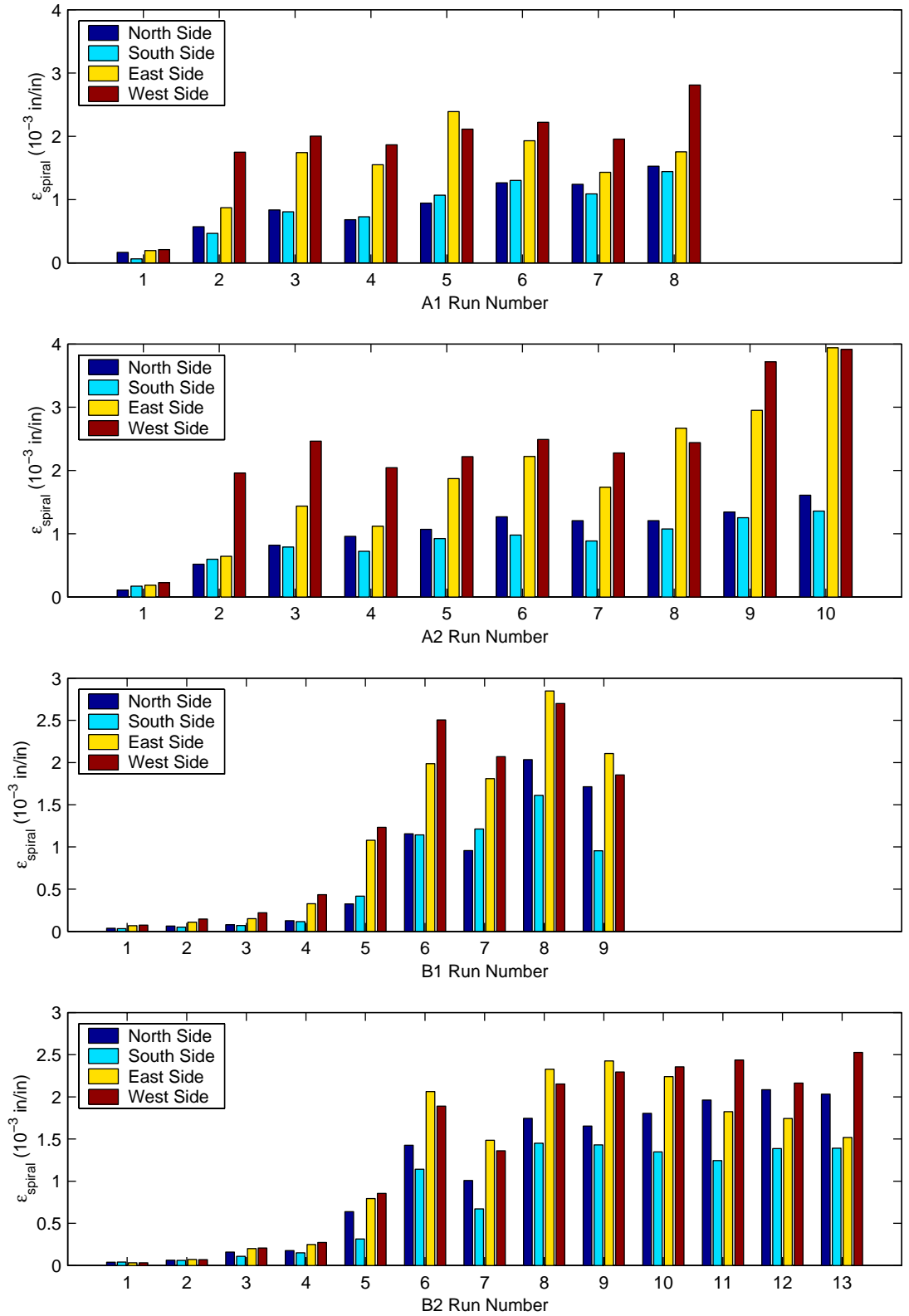
Figure 5-58. Variation of *average* spiral strains (averaging peaks over height) with level of excitation.

or alternatively by Equation 5-11. Equation 5-11 was used to measure the performance of the test specimens.

$$D = \frac{d_{max}}{d_{ult}} = \frac{\mu_{max}}{\mu_{ult}} \qquad (5\text{-}10)$$

$$D = \frac{d_{max} - d_y}{d_{ult} - d_y} = \frac{\mu_{max} - 1}{\mu_{ult} - 1} \qquad (5\text{-}11)$$

The ductility index is a non-cumulative damage index. It assumes that failure occurs at a certain displacement (or ductility) regardless of the loading history and energy dissipated.

5.6.2 Energy Index

The energy index is often defined as the ratio of the dissipated energy to the monotonic energy capacity of the member. While useful in evaluating brittle members, the energy index generally underestimates the energy dissipation capacity of most ductile members.

$$D = \frac{\int dE}{F_y d_{ult}} \qquad (5\text{-}12)$$

5.6.3 Park and Ang Damage Index

A widely used damage index is the Park and Ang index ([79], [81]), which is shown in its original form in Equation 5-13. The index is considered a hybrid index since it is a combination of a ductility index and an energy index. Failure is assumed to occur when the damage D reaches 1.0, while a value of 0 represents an undamaged state.

$$D = \frac{d_{max}}{d_{ult}} + \beta \frac{\int dE}{F_y d_{ult}} \qquad (5\text{-}13)$$

With proper calibration of this model, a wide range of failure modes can be predicted. For example, setting β close to zero turns the index into a ductility index, which means that failure is reached when a certain displacement is exceeded regardless of the amount of dissipated energy. It is observed [20] that low values of β are typical of well confined members while larger values are more suitable for shear critical members.

Park [79] suggested Equation 5-14 to calculate β based on regression analysis using experimental data from 261 beam and column cyclic tests. However, there was a large scatter between

the equation and the observed values of β, and some observed β values were negative (Figure 5-59).
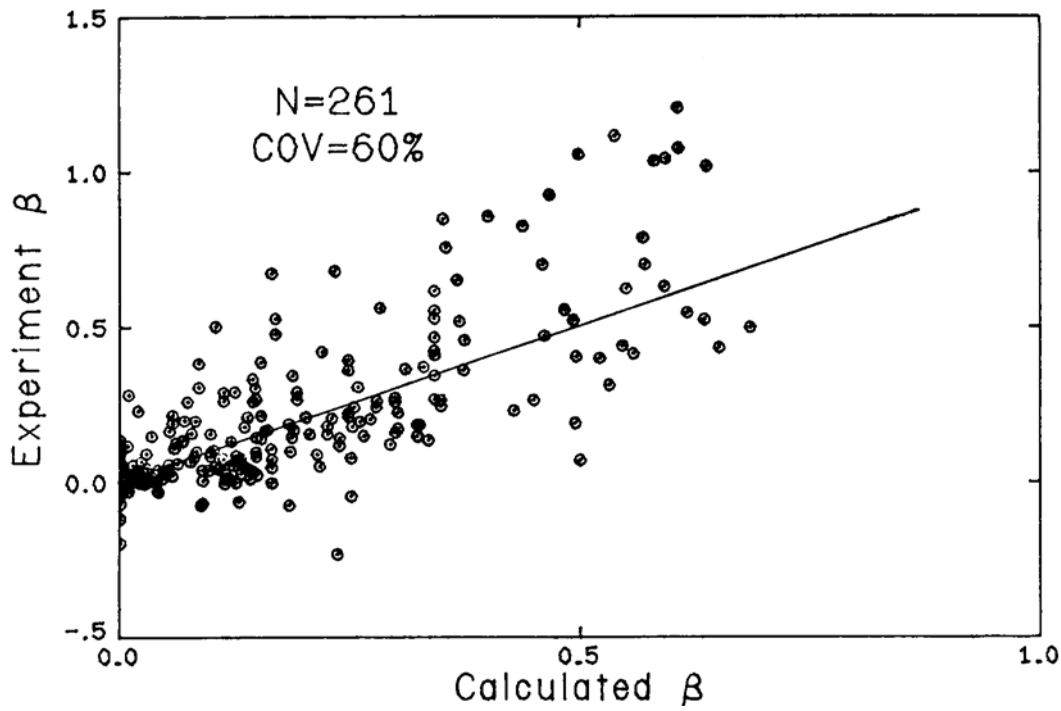
Figure 5-59. Observed values of β vs. values calculated from Equation 5-14 [81].

$$\beta = \left(-0.447 + 0.073\frac{L}{D} + 0.24\frac{P}{A_g f_c'} + 0.314\rho_l\right)0.7^{\rho_{sp}} \qquad (5\text{-}14)$$

Another expression for β was later proposed by Kunnath et al. ([49]), as shown in Equation 5-15:

$$\beta = \left(0.37\frac{P}{A_g f_c'} + 0.36\left(\frac{\rho_l f_y}{0.85 f_c'} - 0.2\right)^2\right)0.9^{\rho_{sp}} \qquad (5\text{-}15)$$

Stone and Taylor ([100], [101] and [104]) proposed a statistical expression for β based on test data from 65 tests of lightly reinforced circular bridge columns. The resulting equations consist of a large number of terms, and is highly complex. When the equation in Ref. [104] was used to compute β for the column tested in this study, a value of -0.27 was obtained for both the model and prototype columns, even though all parameters were within the specified ranges. This highlights a major problem with the Park and Ang index; that is, the difficulty of properly estimating β, especially in the absence of experimental data. The index also requires a good estimate of the mono-

tonic ultimate displacement, which may be difficult to obtain. This is due to several reasons including the absence of consistent definition among researchers of what constitutes failure.

From the studies of Stone and Taylor on circular columns, it appears that β generally varies from 0 to 0.30. In general, a value of 0.05 to 0.15 is recommended for well detailed members ([11], [48] and [80]).

The Park and Ang index has been extensively used and calibrated by several researchers, and some modifications were suggested by a number of researchers. For example, Kunnath et al. [49] modified the deformation term of the index by subtracting a recoverable deformation from both the numerator and denominator as shown in Equation 5-16. Chai et al. [12] modified the model by subtracting the plastic energy dissipated under monotonic loading from the numerator of the energy term. The modification was motivated by the fact that the original model predicted $D > 1$ for monotonic failure. The modified model used a modified β^* which is a function of β and $\mu_{ult}=d_{ult}/d_y$. Equation 5-16 was used to estimate the damage experienced by the columns tested on the shaking table.

$$D \ = \ \frac{d_{max} - d_y}{d_{ult} - d_y} + \beta \frac{\int dE}{F_y d_{ult}} \tag{5-16}$$

The first term in Equation 5-16 is very close to d_{max}/d_{ult} when the latter ratio is close to 1.0, but can be different for other values. Hence, Equations 5-13 and 5-16 should yield similar results when the displacement demand is close to the ultimate displacement capacity.

When a low value of β is used, the above damage index essentially computes the quantity $(d_{max} - d_y)/(d_{ult} - d_y)$, and the energy contribution of the damage is generally small. Typically, this contribution is found to be about 5% of the total damage for $\beta=0.05$, and tends to increase proportionally with β [38]. d_{ult} is the monotonic displacement capacity of the column, which is usually reached when the strain in the confined concrete region exceeds ε_{cu}. This failure mode may be delayed by supplying a larger amount of spiral reinforcement. Other forms of failure may not be preventable, however, such as fatigue failure of the longitudinal reinforcement. Low-cycle fatigue failure can be predicted using a fatigue index as shown next.

5.6.4   Low-Cycle Fatigue Indices

Different models have been proposed for predicting the fatigue capacity of reinforced concrete members. In general, these models rely on the Coffin and Manson law to estimate the damage con-

tributed by each cycle, and then use Miner's rule to accumulate the damage for different loading cycles. Some of these models are based empirically on global measures such as ductility, while others are derived from the fatigue behavior of the material, namely that of the reinforcing steel.

Jeong and Iwan [36] proposed a damage model based on the Coffin [18] and Manson [61] law as shown in Equation 5-17, where N_f is the number of cycles of ductility μ required to cause fatigue failure, and c and s are constants. The damage is then found by adding the damage contribution from each cycle using Miner's rule [62] as shown in Equation 5-18. N_f is generally used to represent the number of complete reversals or full cycles to failure, but may be occasionally used to imply the number of half-cycles. Any consistent definition may be used in Equations 5-17 and 5-18.

$$N_f \, \mu^s = c \tag{5-17}$$

$$D = \sum_{\text{all cycles}} D_i = \sum_{\text{all cycles}} \frac{1}{N_{f,i}} = \sum_i \frac{\mu_i^s}{c} \tag{5-18}$$

Krawinkler and Zohrei [46] proposed a similar model which used plastic deformations instead of ductility. Cosenza [36] also used a similar model that uses plastic ductility as shown in Equation 5-19, where μ_{ult} is the ultimate monotonic displacement ductility, and b is an experimentally determined constant, usually around 1.6 to 1.8.

$$\frac{1}{N_{f,i}} = \left(\frac{\mu_i - 1}{\mu_{ult} - 1} \right)^b \tag{5-19}$$

Chung et al. [15] proposed another fatigue based model that imposes at every cycle a strength loss ΔM_i, as a fraction of the total moment reduction at failure ΔM_f, to the moment-curvature curve, proportional to the plastic curvature (Equation 5-20). The member reaches failure when the moment-curvature curve degrades below a defined failure criteria. An attractive property of this model is that it relates strength degradation to the damage index. But despite good agreement with some test results, the method itself is not well calibrated against experimental observations [107].

$$\Delta M_i = \Delta M_f \left(\frac{\phi_i - \phi_y}{\phi_f - \phi_y} \right)^{1.5} \tag{5-20}$$

Other researchers studied the fatigue behavior of reinforcing bars ([9], [58]). Since the strain history in the reinforcing bars can be determined from the column displacement history using

assumptions about curvature and strain distributions, it suffices to calibrate the fatigue models for reinforcing steel bars, whose fatigue behavior is simpler and more consistent than reinforced concrete members. However, this assumes that the mode of failure is governed by fatigue failure of the reinforcement, and not by some other mechanism. In well detailed columns designed to fail in flexure, the other possible failure mechanisms are the failure of the confined concrete initiated by the fracturing of spiral reinforcement, or by the buckling of longitudinal reinforcement.

Mander et al. [58] tested high strength (ASTM A722) and regular strength (ASTM A615 grade 40) #5 bars under cyclic loading. The experimental data was fitted for both types of steel, using different fatigue-life models and energy models. The fatigue-life models considered include a Coffin-Manson model of the form:

$$\varepsilon_p = \frac{\Delta\varepsilon_p}{2} = \varepsilon_f'(2N_f)^c \qquad (5\text{-}21)$$

where ε_p is the average plastic strain during a cycle. ε_f' and c are the constants to be determined. Mander recommends using values of 0.08 and -0.50 for ε_f' and c for all types of steel. The actual fitted parameters are shown in Table 5-6. Equation 5-21 uses the plastic strain which can be difficult to obtain because of Bauschinger effects. Instead, the model can be defined in terms of the total strain ε_t as suggested by Koh and Stephens [41]. Different parameters M and m would need to be computed for the following formula:

$$\varepsilon_t = \frac{\Delta\varepsilon}{2} = M(2N_f)^m \qquad (5\text{-}22)$$

Brown and Kunnath [9] tested #6, #7 and #8 grade 60 reinforcing bars (ASTM A615) under constant amplitude cycles and under random loading cycles similar to what would be expected during an earthquake. They noted a bar size effect on fatigue life. They also noted relatively large differences between their fatigue-life regressions and those of Mander et al. (as reported in [58], [24] and [57]). The differences were attributed to differing definitions of fatigue life, and to using a different test setup. Fatigue-life models from both studies are compared in Table 5-6.

5.6.5   Previous Evaluation and Comparison of Damage Indices

Kunnath et al. [47] investigated the effects of loading history on the capacity of circular reinforced concrete columns. The failure of 10 of the columns tested were predicted using four different damage models. The models used included the softening index, a noncumulative index based on

Table 5-6 Fatigue-life models by Mander et al. (as reported in [24] and [57]) and Brown and Kunnath [9].

Model	Mander et al.	Brown and Kunnath
Plastic Strain	$\varepsilon_p = 0.08(2N_f)^{-0.50}$ (a-1)	$\varepsilon_p = 0.102(2N_f)^{-0.473}$ (a-2)
Total Strain	$\varepsilon_t = 0.08(2N_f)^{-0.333}$ (b-1)	$\varepsilon_t = 0.112(2N_f)^{-0.433}$ (b-2)

the stiffness degradation of the column, the Kratzig index which is a cumulative energy model, the Park and Ang hybrid index, and a fatigue index which accounts for low cycle fatigue of the reinforcement. It was shown that each of the models has its shortcomings in predicting failure. The softening index was found to be extremely sensitive in the early damage stages. The energy index (Kratzig) generally overpredicted damage, while the hybrid index essentially reflected the ductility contribution due to the improper representation and calibration of the energy term. The fatigue index was proposed as the most promising, although it can only predict low-cycle fatigue failure.

Lehman et al. [50] proposed a dual-phase fatigue damage index that was calibrated using data from the column tests performed by Kunnath et al. [47], and verified using data from the five columns tested by Lehman. The proposed fatigue index consists of a concrete damage index and a steel damage index that are incremented in two stages. The steel damage index is zero until the concrete damage index reaches one, which corresponds to the spalling of concrete. The steel damage index then starts to increase until it reaches a value of one, predicting the failure of the member.

Cosenza et al. [20] analyzed a number of elastic perfectly plastic (EPP) simple inverted pendulum systems, and evaluated the results using a number of damage indices. They concluded that the Park and Ang index and the fatigue index defined by Equation 5-19 result in the same damage prediction for a wide range of periods when the two models are calibrated to experimental data.

5.6.6 Damage Prediction of Tested Columns

The ductility index, the Park and Ang index and the low-cycle fatigue index are evaluated using the observed damage of the tested specimens. The application of the ductility and Park and Ang indices is relatively straightforward. The required parameters (F_y, d_{ult} and d_y) are computed from

moment-curvature and pushover analyses (using a plastic hinge model). β is initially assumed to be 0.05. The dissipated energy is obtained by integration of the force-deformation relationships using Equation 5-8.

The Mander et al. model for low-cycle fatigue failure of reinforcing steel was also used to analyze the tested columns. The plastic strain form of the model was used (Equation 5-21), which requires knowledge of all peak strain half-cycles. Those strain peaks can be extracted from strain gage data, or calculated from curvature measurements. As shown in Section 5.5.2, the second approach is preferred because it compares well with the strain gage data, and provides reliable measurements when the strain gages fail during the test. In fiber model analyses, the strains can be read directly from the fibers and used in the damage computations. If other types of models are used, however, strains can be estimated from global displacements, using assumptions about plastic hinge length, and curvature distribution along the column height. The strain cycles can be estimated either for unidirectional loading or for general bidirectional loading. For a circular section, the strain in a bar with coordinates (b_x, b_y) measured from the center of the section can be computed as follows:

$$\varepsilon = \left(R_{col} - c - \frac{b_x dx + b_y dy}{d} \right) \phi \tag{5-23}$$

$$d = \sqrt{dx^2 + dy^2} \tag{5-24}$$

$$\phi_p = \frac{d - d_y}{\left(L - \frac{L_p}{2} \right) L_p} \tag{5-25}$$

$$\phi_e = \frac{3d}{L^2} \le \phi_y = \frac{3d_y}{L^2} \tag{5-26}$$

$$\phi_t = \phi_p + \phi_e \tag{5-27}$$

In the above:

- ε: longitudinal bar strain, ε_t and ε_p refer to total and plastic strain respectively,
- ϕ: section curvature corresponding to a total displacement of magnitude d in the x-y plane. ϕ_e, ϕ_p and ϕ_t refer to the elastic, plastic and total curvatures respectively,
- ϕ_y: yield curvature,
- dx and dy are the column top displacements in the x and y directions respectively,

- R_{col}: column radius,

- c: neutral axis depth at the ultimate state obtained from moment-curvature analysis,

- d: column top displacement in the x-y plane,

- d_y: yield displacement,

- L_p: plastic hinge length as observed from testing or obtained from a plastic hinge expression,

- L: column height.

The cycle peaks are then extracted from the strain history using the rainflow cycle counting method [37]. Although several methods exist that allow the computation of number of cycles, the rainflow method, which was developed by Endo in 1967 [94], is by far the most commonly used. One algorithm for the rainflow cycle counting method is illustrated in Figure 5-60. First, a portion of the signal is moved from the beginning to the end so the signal starts and ends at the highest peak (assuming the signal is periodic). Then, cycles are recursively identified and removed from the signal. For example, E-F forms a cycle because the following difference FG is larger than the difference EF, hence it is removed from the signal, and the next difference is considered. This process is continued until no cycles remain in the signal [23].

The corresponding damage induced by each peak is computed using Equation 5-21 with the appropriate coefficients. In this study, the total strain ε_t at each bar was computed using Equation 5-23, using the total curvature estimated from Equation 5-27. The plastic strains ε_p were then computed by subtracting ε_y from ε_t. Strain peaks smaller than ε_y were discarded. The rainflow cycle counting method was used to identify and average the peaks that form a full cycle. The averaging was performed in order to avoid having negative maxima or positive minima, and because it is consistent with the derivation of the damage models presented in Table 5-6. Note that longitudinal bars in a lightly reinforced column section will have large tensile strains and smaller compression strains, since the compression zone would be relatively shallow.

The fatigue model for plastic strain proposed by Mander et al. (Table 5-6, Equation a-1) is applied to each plastic strain peak in order to estimate the corresponding damage. Figure 5-61 shows the amount of fatigue damage imparted by each cycle for all the longitudinal bars of Specimen B1. The peaks considered span the duration of all the runs applied to Specimen B1. Figure 5-62 presents similar results for Specimen B2. Note that since Specimen B1 was loaded unidirectionally, bars 3 and 9 (along x-axis) experience the most damage, while bars 6 and 12 (along y-axis) experience almost zero damage. Additionally, bars 2 and 4 experience similar damage (due to sym-

Cycle	Range	Mean
E-F	4.0	1.0
A-B	3.0	-0.5
H-C	7.0	0.5
D-G	9.0	0.5
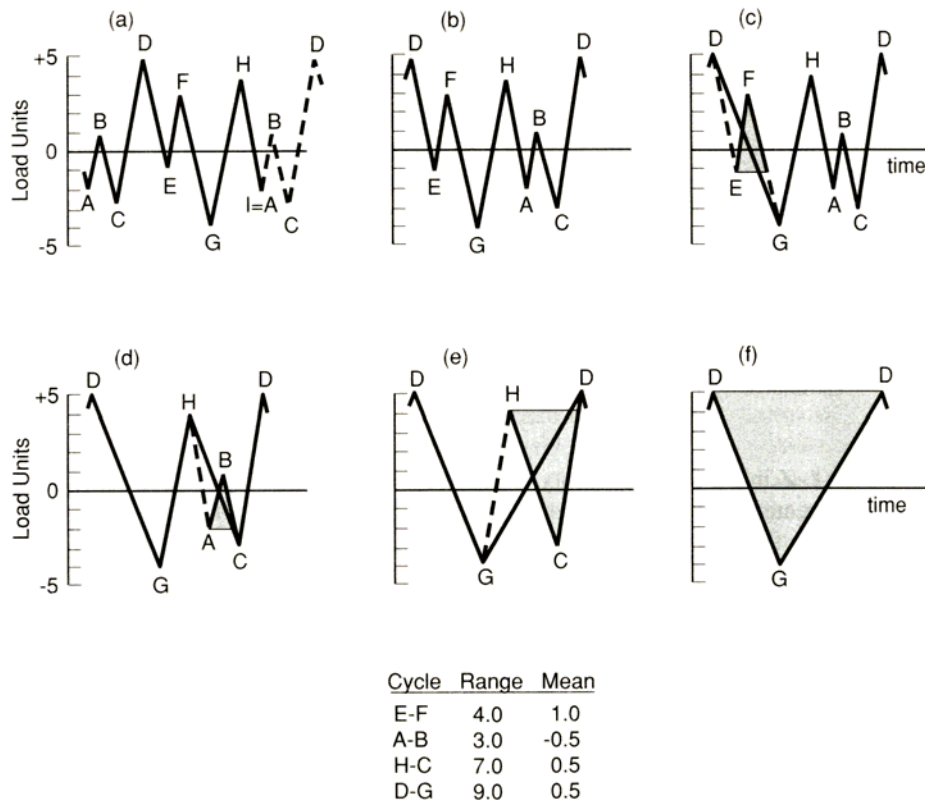
Figure 5-60. Illustration of the Rainflow cycle counting method [23].

metry). The same is observed for bars 1 and 5, bars 6 and 12, bars 7 and 11 and bars 8 and 10. In the case of Specimen B2, most of the bars experience more damage than in the unidirectional case, and the damage is not symmetric about the x-axis as it is in Specimen B1.

In Figures 5-63 through 5-66, the cumulative predicted fatigue damage for each bar is plotted against time for Specimens A1, A2, B1 and B2. Using such a plot, it is possible to predict which bars would fracture first. The damage model predicts the fracture of bar #9 in Specimens A1 and A2. The model predicts that the next bars to fracture are bars #10 and #8, then #3. In Specimen A1, #3 was the next bar to actually fracture (on the opposite side of #9). For Specimen B1, the damage model predicts failure to occur in the following order: #3, #4, #2, #9 and so on. The actual fractured bars were (in order): #3, #9 and #4. In Specimen B2, the predicted order of fracture is: #9, #10, #8, # 3 and so on, while during the test bars #3 and #9 fractured (in this order). It appears that, in general, the damage model correctly predicts the first bar to fracture, and then with less accuracy, the bars most likely to fracture next. Note that estimating the low-cycle fatigue damage index involves a significant amount of uncertainty due to several factors including:

1. Uncertainty in the fatigue-life models.

2. Difficulty in estimating curvatures and strains.

3. The estimated strain are *average strains* over a certain plastic hinge length.

4. Identification and correction of strain cycles, including the extraction of plastic strain from total strains (which can be further complicated with the presence of permanent drift).

5. Interaction of multiple failure mechanisms and the effect of prior damage. For example, the fracture of a bar might redistribute the forces in the section, and the fracture of a spiral might cause a bar to buckle and subsequently fracture.

In order to evaluate the reliability of the Park and Ang index, the ultimate monotonic displacement capacity d_{ult} and coefficient β need to be estimated. The models were evaluated for three different combinations of d_{ult} and β, as shown in Table 5-7. The procedure used to estimate these values is described below.

The failure of Specimens A1 and B1 was initiated by fracturing of the spiral reinforcement, while Specimens A2 and B2 experienced longitudinal reinforcement fracture, which is more likely associated with low-cycle fatigue.

Specimens A1 and B1 were both subjected to unidirectional loading and failed somewhat similarly (confinement failure). From Table 5-7, Specimen A1 failed at a larger displacement than B1, but dissipated less energy. If both specimens are assumed to have a Park and Ang index of 1.0 at failure, this will yield two equations in d_{ult} and β, which when solved give solutions of 10.3 in. and 0.088 for d_{ult} and β respectively. Although this estimate of the ultimate displacement capacity appears to be somewhat high, it is used in this case for comparison.

Using the plastic hinge model by Priestley et al [85], d_{ult} and L_p can be estimated as 6.17 in. (156 mm) and 13.3 in. (338 mm), respectively (see Chapter 6). This ultimate displacement was used in one of the combinations in which a typical value of 0.05 was assumed for β. The experimentally observed plastic hinge length ranged from 12 in. to 14 in. (305 mm to 356 mm), so the above estimated plastic hinge length is within the observed range. However, the observed displacement capacity was larger than the predicted capacity, which leads to unrealistically high ductility and Park and Ang indices if the predicted displacement capacity d_{ult} of 6.17 in. (156 mm) is used.

However, Specimen B1 experienced an earlier failure than Specimen A1. This was initiated by the fracture of one spiral during Run 8 (Maximum Level 2). The early spiral fracturing mainly occurred because of early buckling of the longitudinal reinforcement. This buckling occurred at a

location where the spiral reinforcement was displaced by one of the rods used to measure deformations at the face of the column, resulting in a spiral spacing that is slightly larger than the regular spacing of 1.25 in. (32 mm). Hence, Specimen B1 would be expected to fail at a smaller damage index than A1, which leads to the third case. For this last case, the test results were used to estimate d_{ult} as discussed below.

It is usually assumed that the displacement capacity under cyclic loading is less than the monotonic capacity. Thus, by observing the largest displacement experienced by the different specimens at or before failure, the displacement capacity can be estimated. The peak displacement reached before failure ranged from 3.68 in. (93 mm) for Specimen B1 to 7.45 in. (189 mm) for Specimen A2. Hence, an assumed displacement capacity between 7 in. and 8 in. appears reasonable (although the monotonic capacity may be higher). In order to evaluate this possibility, a value of d_{ult} = 7.5 in. (191 mm) was used, while a value of 0.02 was picked for β such that the Park and Ang index gave a value of about 1.0 for Specimen A1.

The results for the Park and Ang index for all three cases are shown in Table 5-7. The third case, using d_{ult} = 7.5 in. (191 mm) and β = 0.02 appears to give the best fit to the observed data.

The low-cycle fatigue model was also evaluated using three different estimates of the plastic hinge length. The values used are 12 in. (305 mm) and 14 in. (356 mm) which are the range of the observed plastic hinge length, and 13.3 in. (338 mm) obtained from the plastic hinge model [85]. The resulting damage indices at the time of failure of the different specimens are presented in Table 5-7. The fatigue damage index is very sensitive to the plastic hinge length used to estimate curvatures and strains. This sensitivity can be explained by the fact that the damage induced by one cycle is proportional to the square of the peak plastic strain in that cycle, when using the fatigue-life model for plastic strain proposed by Mander et al. (Table 5-6).

A comparison of the three indices (ductility, Park and Ang, and fatigue) is shown for each of the specimens in Figures 5-67 to 5-70. The observed time of failure of each specimen is marked by a vertical line. The highlighted rows in Table 5-7 correspond to the parameters used for the Park and Ang and low-cycle fatigue indices.

5.7   MEASURED AND COMPUTED DYNAMIC PROPERTIES

Another approach for assessing damage state of a column or bridge is by measuring changes in its dynamic properties. Thus, in this section, the free vibration properties of the specimens are esti-

Table 5-7 Various damage indices computed at the onset of failure (first fracture).

		A1	A2	B1	B2
Failure Type[a]		S	L	S	L
Failure Run		Max 3	Max 5	Max 2	Max 6
Time of Failure from Beginning of Run		2.69 s	2.10 s	17.95 s	7.76 s
Time of Failure from Beginning of 1st Run		137.01 s	215.13 s	365.80 s	619.27 s
Peak Relative Displacement (in) $\approx$ Ductility	All Runs up to Failure	6.91"	7.45"	3.68"	5.83"
	Failure Cycle	3.70"	8.12"	5.92"	2.23"
	Up to and Including Failure	6.91"	8.12"	5.92"	5.83"
	Overall[b]	7.86"	9.87"	5.92"	5.83"
Dissipated Energy E at Failure (kip.in)		683	1007	886	2108
E/E_{ult}[c] at Failure		5.76	8.50	7.47	17.79
Park and Ang Index	$d_{ult} = 10.3", \beta = 0.088$	1.00	1.30	1.00	1.63
	$d_{ult} = 6.17", \beta = 0.05$	1.50	1.89	1.40	2.00
	$d_{ult} = 7.5", \beta = 0.02$	1.02	1.26	0.90	1.09
Low-Cycle Fatigue Index	$L_p = 12"$	0.36	0.70	0.38	1.03
	$L_p = 13.3"$	0.29	0.56	0.31	0.82
	$L_p = 14"$	0.26	0.51	0.28	0.74

a. S: Spiral fracture, L: Longitudinal reinforcement fracture.

b. Includes runs following failure (as defined by the first bar fracture)

c. $E_{ult} = F_y d_{ult} = 15.8$ kips x 7.5 in = 118.5 kip.in

mated from the recorded response and reported for the different runs. The results show a clear rela-tionship between dynamic characteristics, such as the effective period of vibration and damping, and the damage state of the column.

5.7.1 Computation of Dynamic Properties

The mode shapes and natural frequencies of vibration of a multiple degree of freedom system with known dimensions and material properties can be computed by solving an eigenvalue problem. The eigenvalue problem has the form given in Equation 5-28 [14]:

$$\boldsymbol{k}\phi_n = \omega_n^2 \boldsymbol{m}\phi_n \qquad (5\text{-}28)$$
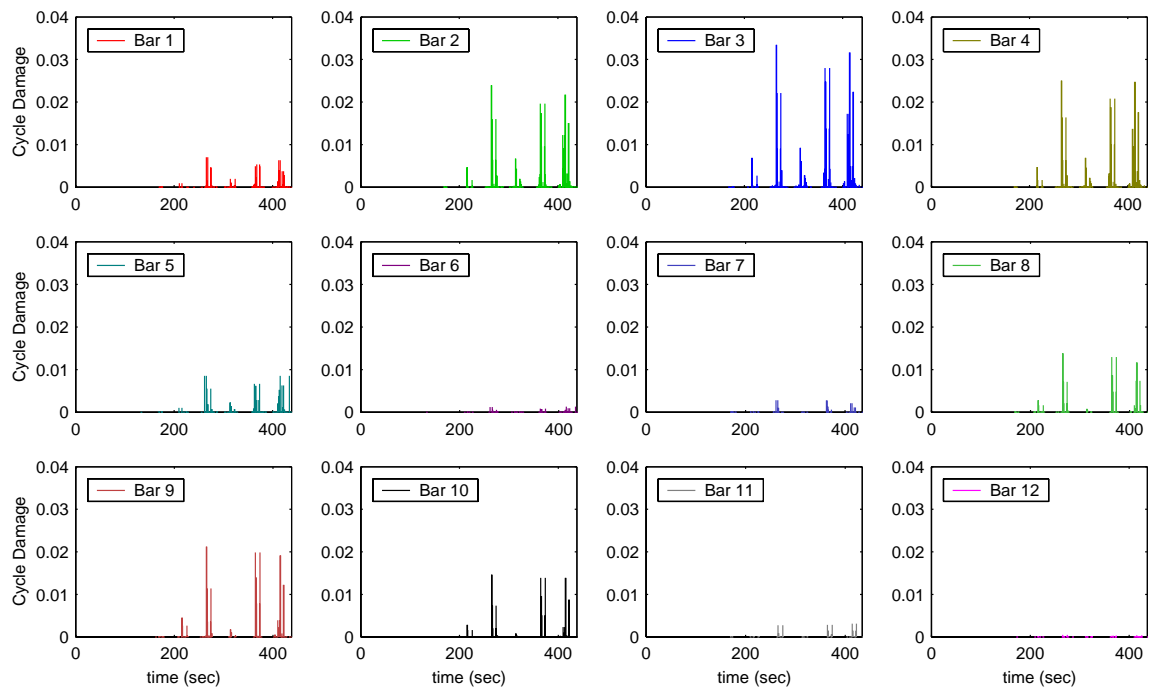
Figure 5-61. Fatigue Damage caused by individual strain peaks for all 12 bars during all the runs of Specimen B1.
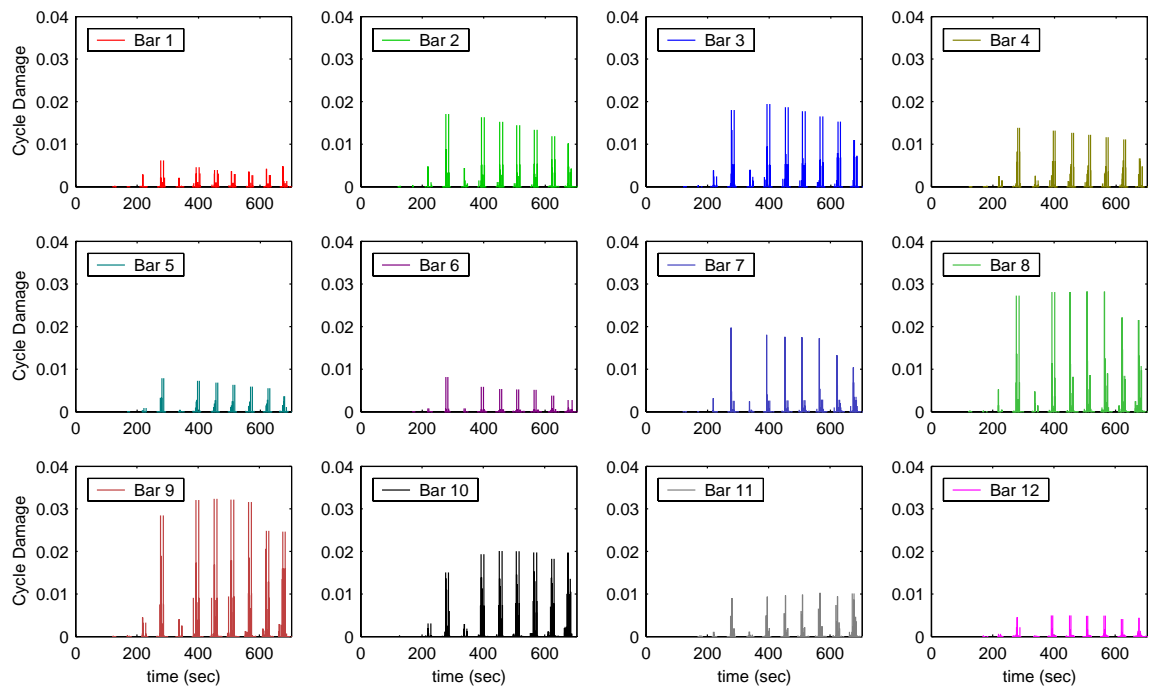
Figure 5-62. Fatigue Damage caused by individual strain peaks for all 12 bars during all the runs of Specimen B2.
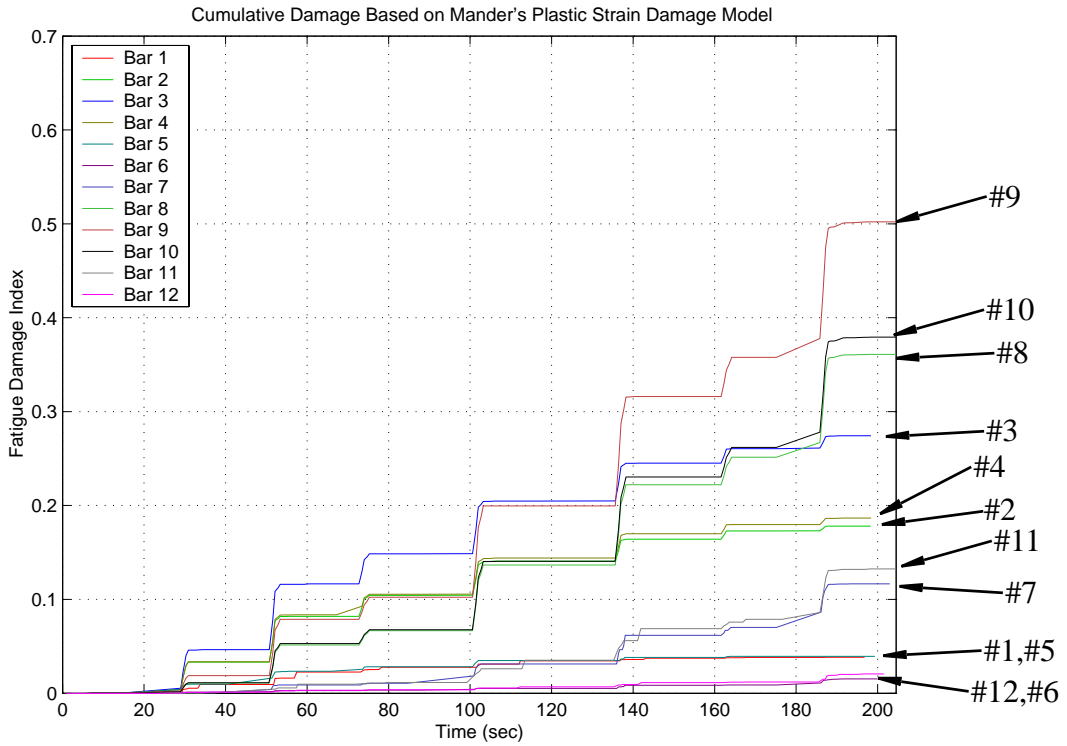
Figure 5-63. Cumulative fatigue damage experienced by individual bars during all the runs of Specimen A1.
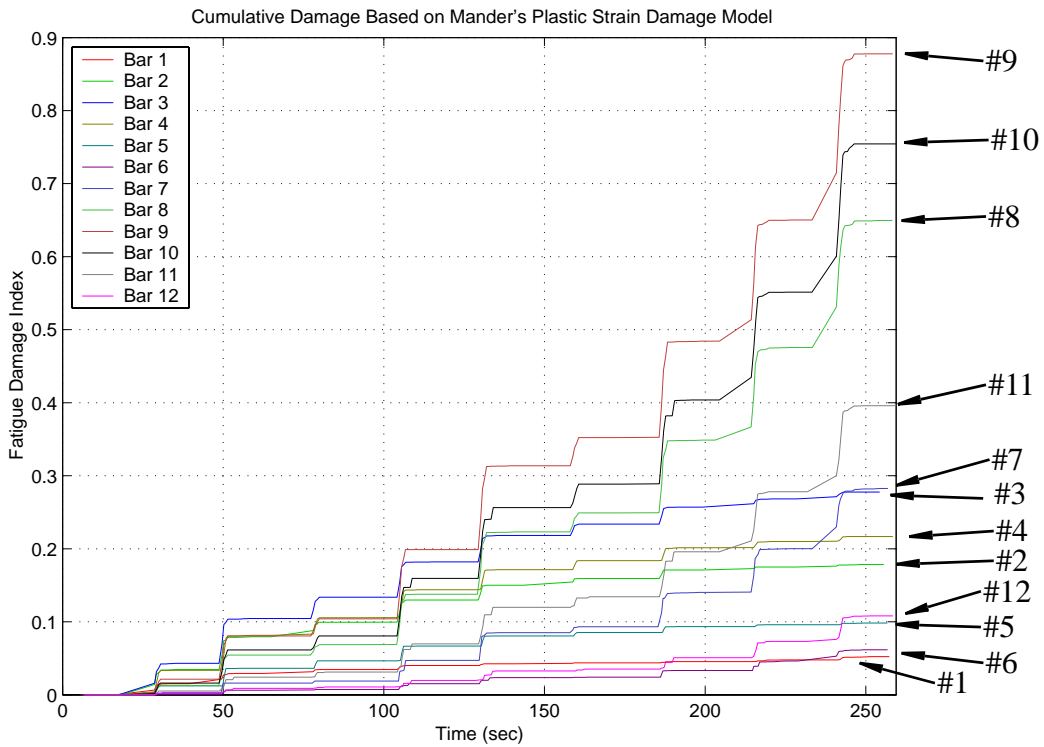
Figure 5-64. Cumulative fatigue damage experienced by individual bars during all the runs of Specimen A2.
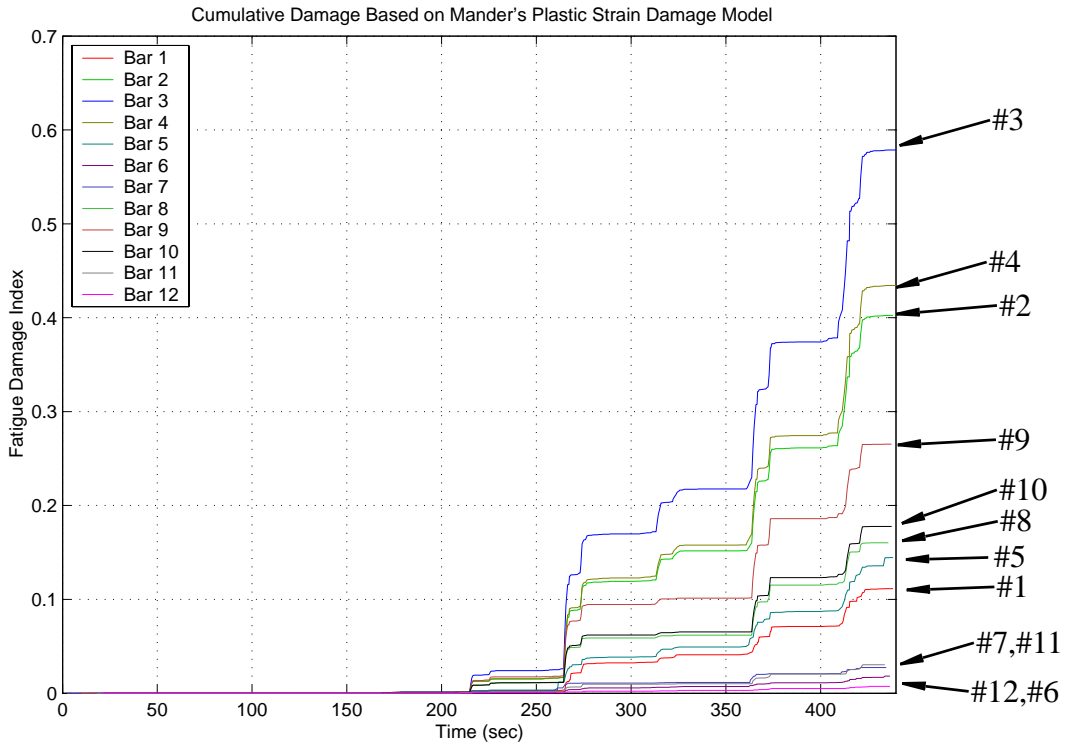
Figure 5-65. Cumulative fatigue damage experienced by individual bars during all the runs of Specimen B1.
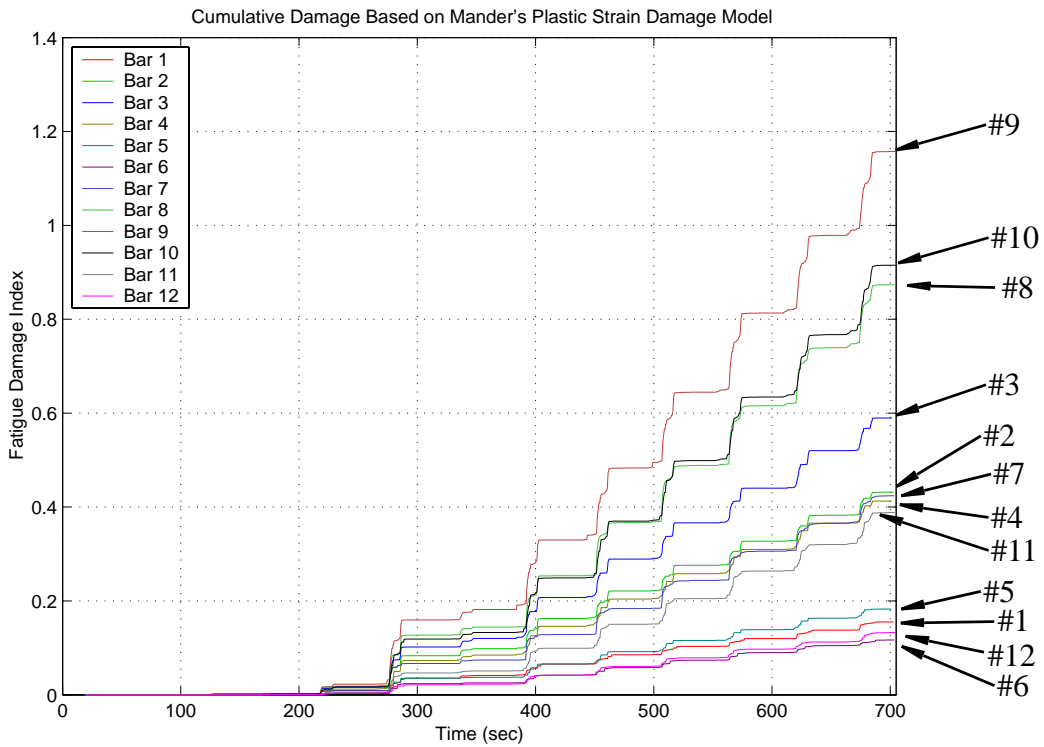
Figure 5-66. Cumulative fatigue damage experienced by individual bars during all the runs of Specimen B2.
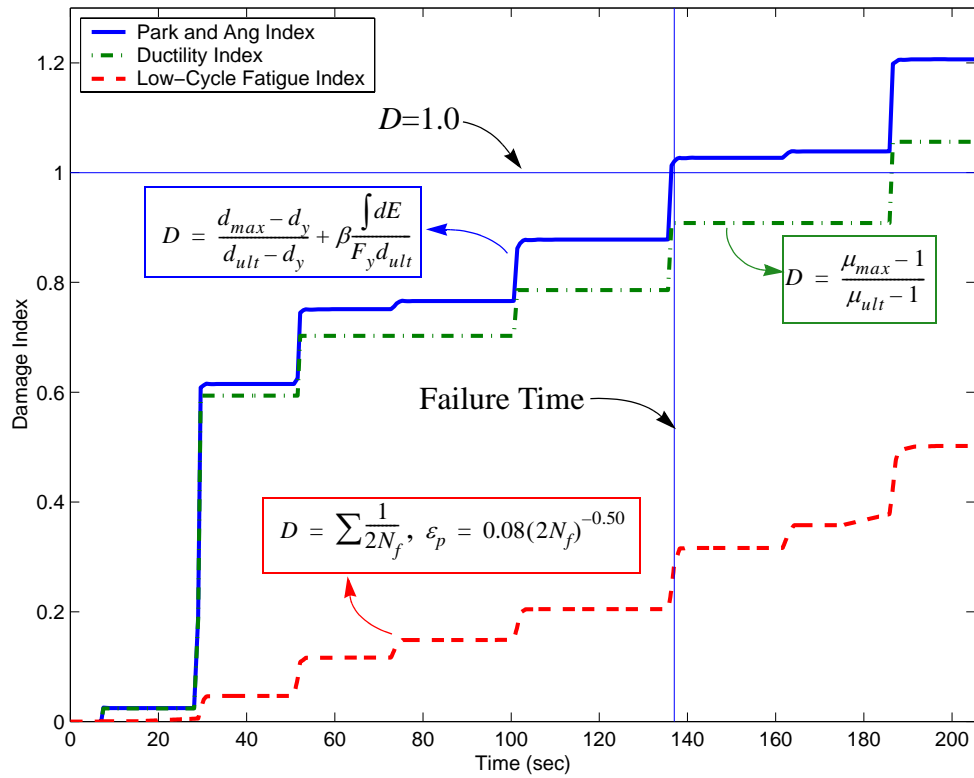
Figure 5-67. Comparison of various damage indices for Specimen A1.

The equations labeled in the figure are:

$$D = \frac{d_{max} - d_y}{d_{ult} - d_y} + \beta\frac{\int dE}{F_y d_{ult}}$$

$$D = \frac{\mu_{max} - 1}{\mu_{ult} - 1}$$

$$D = \sum\frac{1}{2N_f}, \quad \varepsilon_p = 0.08(2N_f)^{-0.50}$$
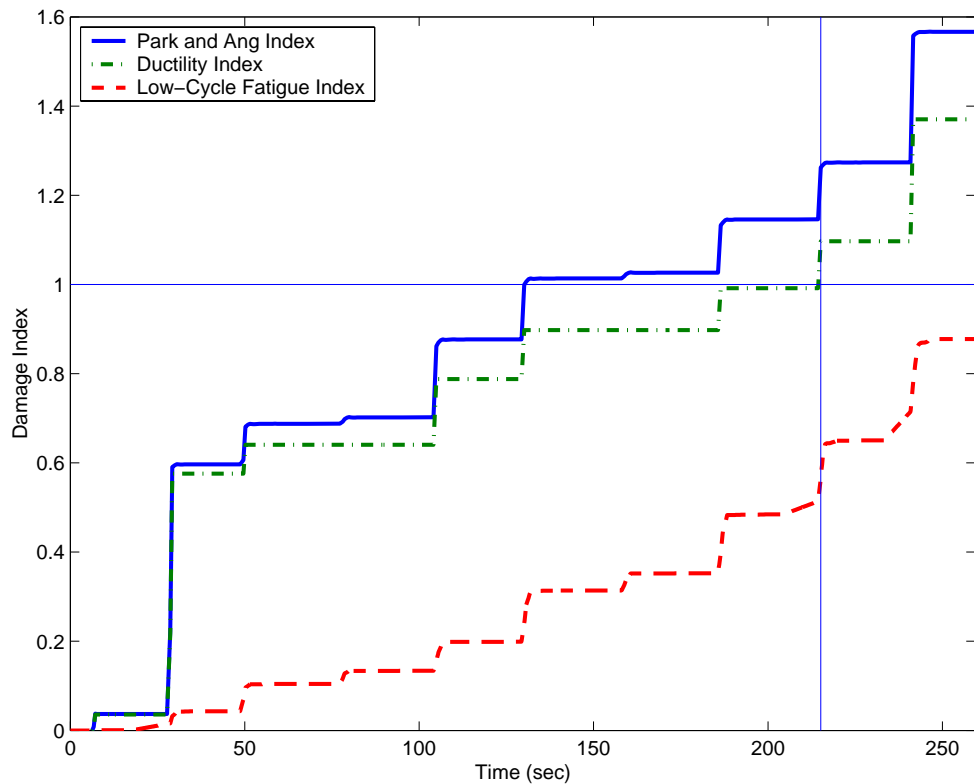
Figure 5-68. Comparison of various damage indices for Specimen A2.
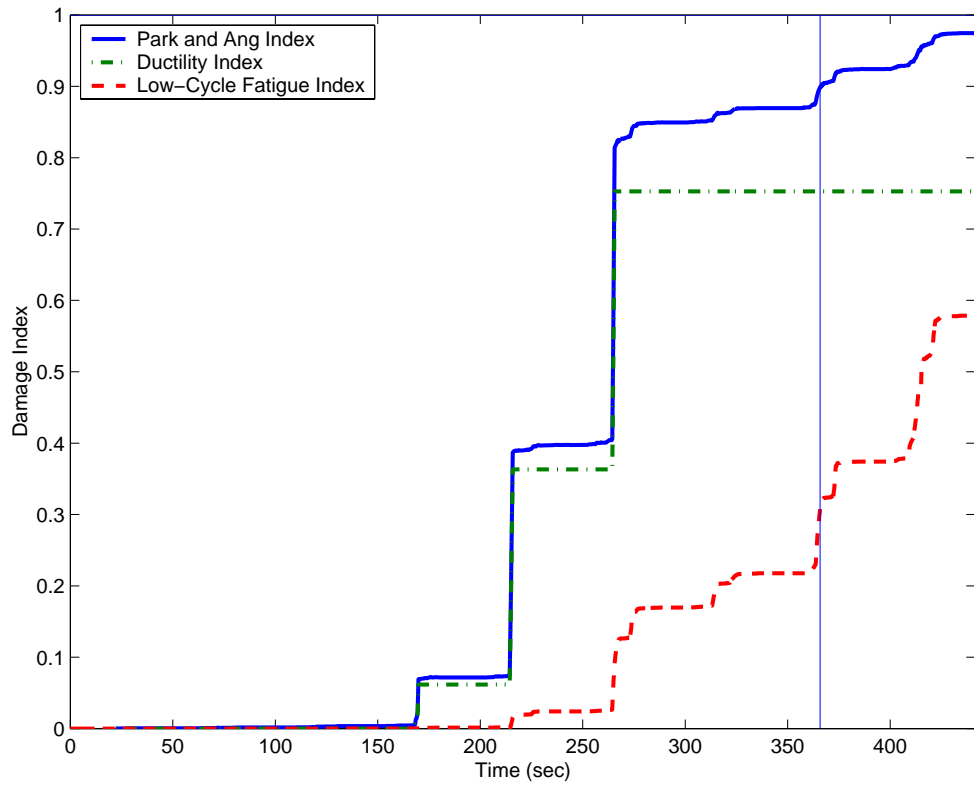
Figure 5-69. Comparison of various damage indices for Specimen B1.
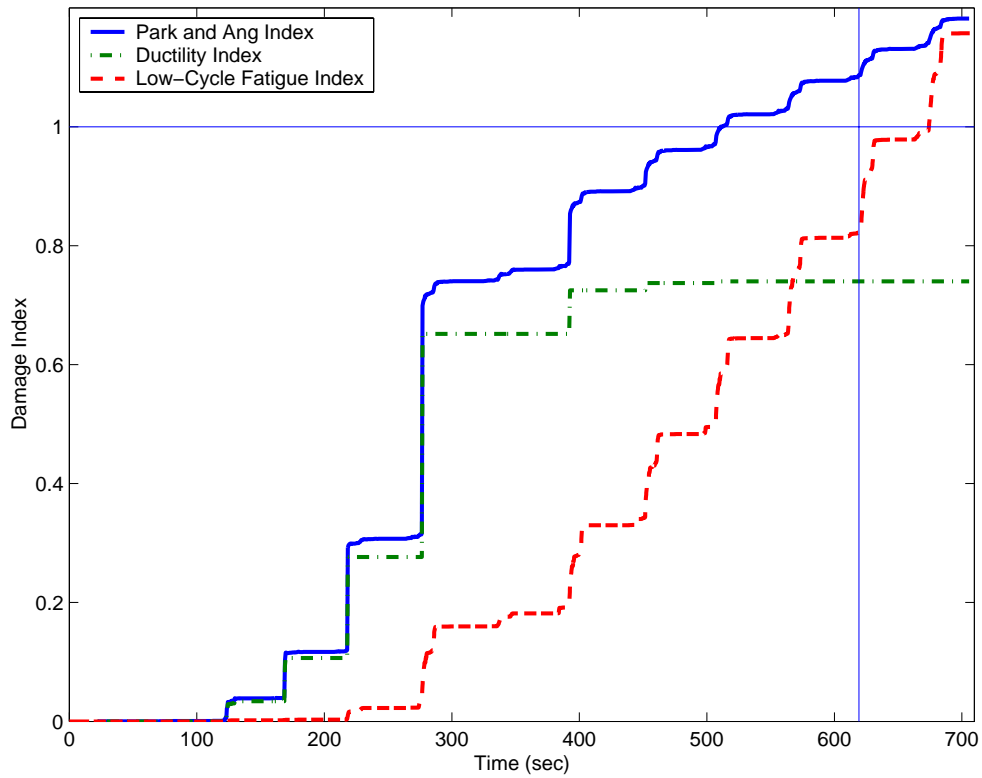
Figure 5-70. Comparison of various damage indices for Specimen B2.

153

where **k** and **m** are the stiffness and mass matrices, ω_n is the nth natural frequency of vibration and ϕ_n is the corresponding mode of vibration. A non-trivial solution is obtained by solving Equation 5-29:

$$det\left[\mathbf{k} - \omega_n^2\mathbf{m}\right] = 0 \qquad (5\text{-}29)$$

The dynamic characteristics of the specimen used in this study are estimated using three different methods to investigate the consequences of various design idealizations. The first model assumes the test specimen is an ideal single-degree-of-freedom (SDOF) system, and ignores the rotational mass of inertia and other complexities of the specimen. The second idealization assumes the specimen has two-degrees-of-freedom (2DOF) with corresponding mass and stiffness matrices. The third method is a refinement of the second method that accounts for the rigid end zone at the top of the specimen where the column is assumed to extend into the mass block. The three different idealizations are illustrated in Figure 5-71.
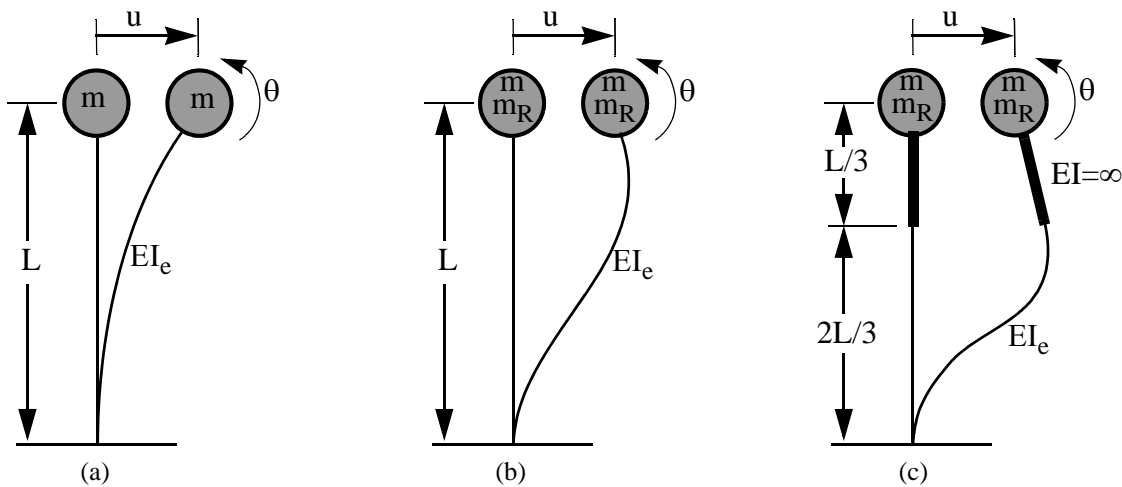
Figure 5-71. System idealizations: (a) SDOF, (b) 2DOF and (c) 2DOF with Rigid End Zone.

5.7.1.1   *Single-Degree-of-Freedom (SDOF) Model*

Assuming single-degree-of-freedom behavior provides a quick estimate of the period of vibration of the column, and is often used in design. The stiffness of the column is then computed as the force that results in unit lateral displacement (u=1) of the column. This assumption was used to design

the specimen as explained in Appendix B. The procedure is summarized in the following equations:

$$k = \frac{3EI_e}{L^3} \tag{5-30}$$

$$\omega_n = \sqrt{\frac{k}{m}} \tag{5-31}$$

where m is the mass of the block supported by the column (0.169 kip.sec²/in), EI_e is the effective stiffness of the column, assumed constant along the height (up to the center of mass), and L is the height to the center of mass (96 in). Using the convention shown in Figure 5-71. for the displacement (u) and rotation (θ) at the top of column, the resulting mode shape is:

$$\phi_1 = \begin{bmatrix} u & \theta \end{bmatrix}^T = \begin{bmatrix} 1 & \frac{-3}{2L} \end{bmatrix}^T = \begin{bmatrix} 1 & -0.015625 \end{bmatrix}^T$$

5.7.1.2   Two-Degree-of-Freedom (2DOF) Model

The SDOF method ignores the second mode of vibration due to the rotational inertia of the mass block. Equation 5-29 is used to obtain the mode shapes and natural frequencies using matrices k and m that correspond to the two degrees of freedom u and θ. The matrices k and m can be easily obtained as:

$$m = \begin{bmatrix} m & 0 \\ 0 & m_R \end{bmatrix} \tag{5-32}$$

$$k = \begin{bmatrix} \dfrac{12EI_e}{L^3} & \dfrac{6EI_e}{L^2} \\ \dfrac{6EI_e}{L^2} & \dfrac{4EI_e}{L} \end{bmatrix} \tag{5-33}$$

where m_R is the rotational mass of inertia of the supported mass (234 kip.sec².in). The solution of the above system yields the following first and second mode shapes:

$$\Phi = \begin{bmatrix} \phi_1 & \phi_2 \end{bmatrix} = \begin{bmatrix} u_1 & u_2 \\ \theta_1 & \theta_2 \end{bmatrix} = \begin{bmatrix} 1 & 1 \\ -0.0170 & 0.0425 \end{bmatrix}$$

155

5.7.1.3   Two-Degree-of-Freedom System with Rigid End Zone

By accounting for the rigid zone into the mass block, which constitutes one-third of the total column height, a more accurate analysis can be performed. The mass matrix is the same as given in Equation 5-32, but the stiffness matrix becomes:

$$k = \begin{bmatrix} \dfrac{(81/2)EI_e}{L^3} & \dfrac{27EI_e}{L^2} \\ \dfrac{27EI_e}{L^2} & \dfrac{(39/2)EI_e}{L} \end{bmatrix} \tag{5-34}$$

The solution of this above system yields the following mode shapes:

$$\Phi = \begin{bmatrix} \phi_1 & \phi_2 \end{bmatrix} = \begin{bmatrix} u_1 & u_2 \\ \theta_1 & \theta_2 \end{bmatrix} = \begin{bmatrix} 1 & 1 \\ -0.0144 & 0.0502 \end{bmatrix}$$

The first and second mode shapes are shown in Figures 5-72a and 5-72b. Figures 5-72c and 5-72d show the effect of including the rigid end zones. The first mode shape is little affected by the rigidity of the block, while the second mode shape changes significantly.

Figure 5-73 compares the periods of vibration obtained through the three different methods for modes one and two. The periods are computed for different ratios of effective stiffness to gross stiffness, ranging between zero and one. The SDOF period is consistently less than the first mode period obtained using either of the 2DOF methods. The rigid end zone model results in smaller period estimates for the models having two modes. The difference in period for the 2DOF models is very small for the first mode period (about 4%), but is much higher for the second mode period (about 47%).

5.7.2   Measured Free Vibration Properties

Prior to each of the tests, a series of pullback tests were performed in one or two of the column directions to obtain the free vibration characteristics of the specimen. The decay of the column vibrations was used to estimate the period of vibration and damping properties at low deformation amplitudes. The pullback tests were not performed between the runs however, due to time and practical constraints. Instead, a white noise signal was applied in each direction after each major runs. The white noise runs could be used to estimate the period of vibration. By obtaining the Fourier spectrum of the response to the white noise, it was possible to approximate the period of the

156
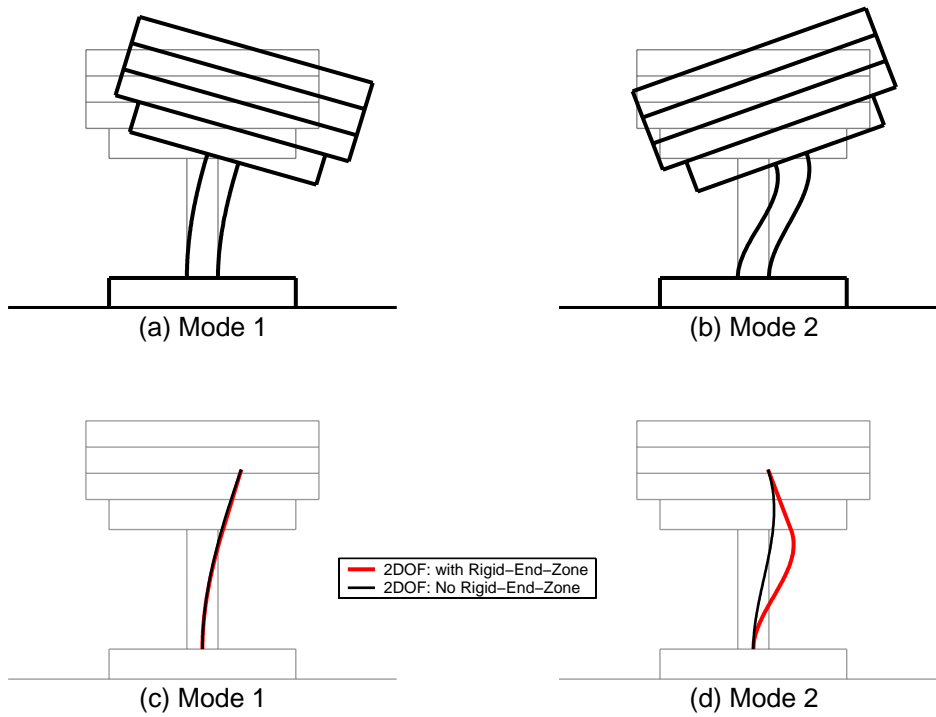
Figure 5-72. First and second mode shape comparisons.
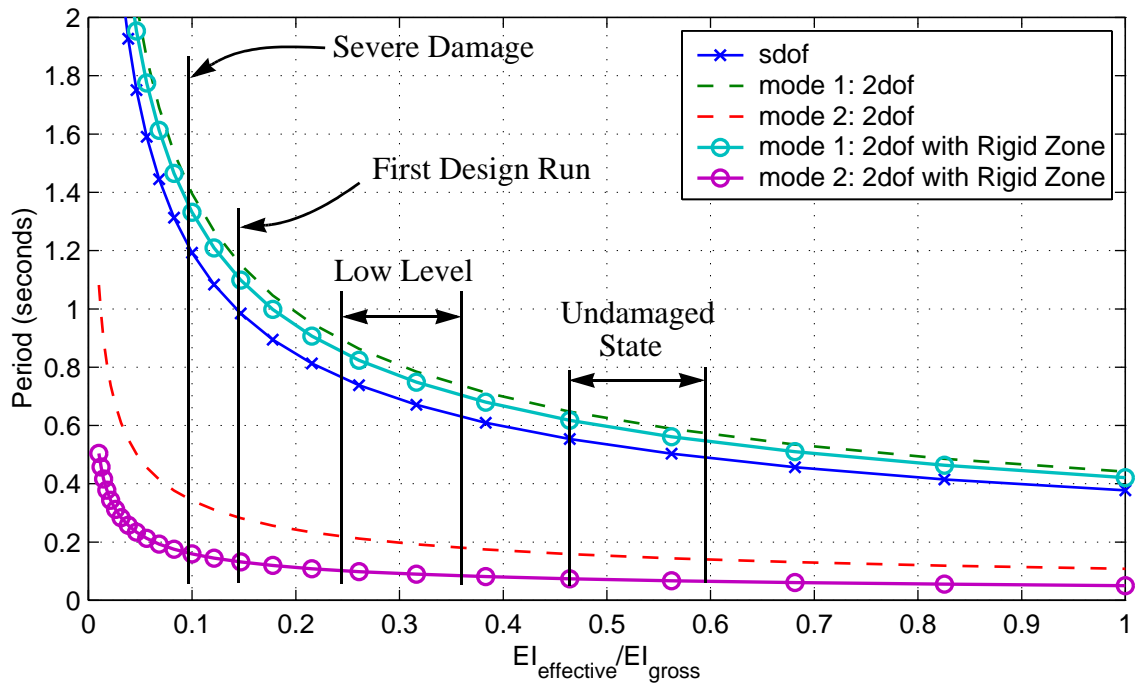
Figure 5-73. Dependence of first and second mode periods on effective stiffness.

first mode of vibration of the specimen, but the second mode period could not be determined (Figure 5-74). In order to approximate the damping, it is common to use the half-power (bandwidth) method, using a power spectral density estimate [16]. This method, however, did not yield consistent results. Thus, the free vibration portion at the end of each run (after the end of the earthquake excitation) was used to estimate damping (and first mode periods). The results obtained were fairly consistent, especially for the period of vibration. However, the results obtained were amplitude dependent and changed with the selected duration. Hence, an average damping value was selected for each run.

The vibration decay curve of a viscously damped oscillator is bounded by the envelopes defined by Equations 5-35 and 5-36:

$$u(t) = u_0 + \rho_{top} e^{-\zeta \omega_n t} \tag{5-35}$$

$$u(t) = u_0 - \rho_{bot} e^{-\zeta \omega_n t} \tag{5-36}$$

where ζ is the damping to be calculated; ω_n is the natural frequency of vibration; ρ_{top} and ρ_{bot} are the magnitudes of the top and bottom decay curves, which may be different as observed in the data; while u_0 is the displacement about which free vibration is occurring. ω_n can be assumed to be approximately equal to the measured damped natural frequency of vibration: $\omega_D = \omega_n \sqrt{1 - \zeta^2}$. For low damping, it can be approximated as: $\omega_n = 2\pi/T_n \approx 2\pi/T_D$, where the *damped period of vibration* T_D is obtained as the average measured duration between successive peaks. Equations 5-35 and 5-36 can be written as:

$$\ln(u(t) - u_0) = -\zeta \omega_n t + \ln(\rho_{top}) \tag{5-37}$$

$$\ln(u_0 - u(t)) = -\zeta \omega_n t + \ln(\rho_{bot}) \tag{5-38}$$

Each of the above equations can be solved using linear regression to obtain the best fit in terms of ζ, ρ_{top} and ρ_{bot} (for a given u_0) at the measured peaks. An iterative procedure can be used to obtain the value of u_0 which results in the computed value of ζ from equations 5-35 and 5-36 being the same [22].

The obtained vibration period and damping (at the end of each run) are plotted as they changed from one run to the other for each of the specimens in Figures 5-76 to 5-79. The values correspond to values of the period and damping measured at the end of each of the runs. Missing values in the figures indicate that a reliable estimate could not be made for the run in question because the free vibration section was too short, or was very noisy. Note that the natural period
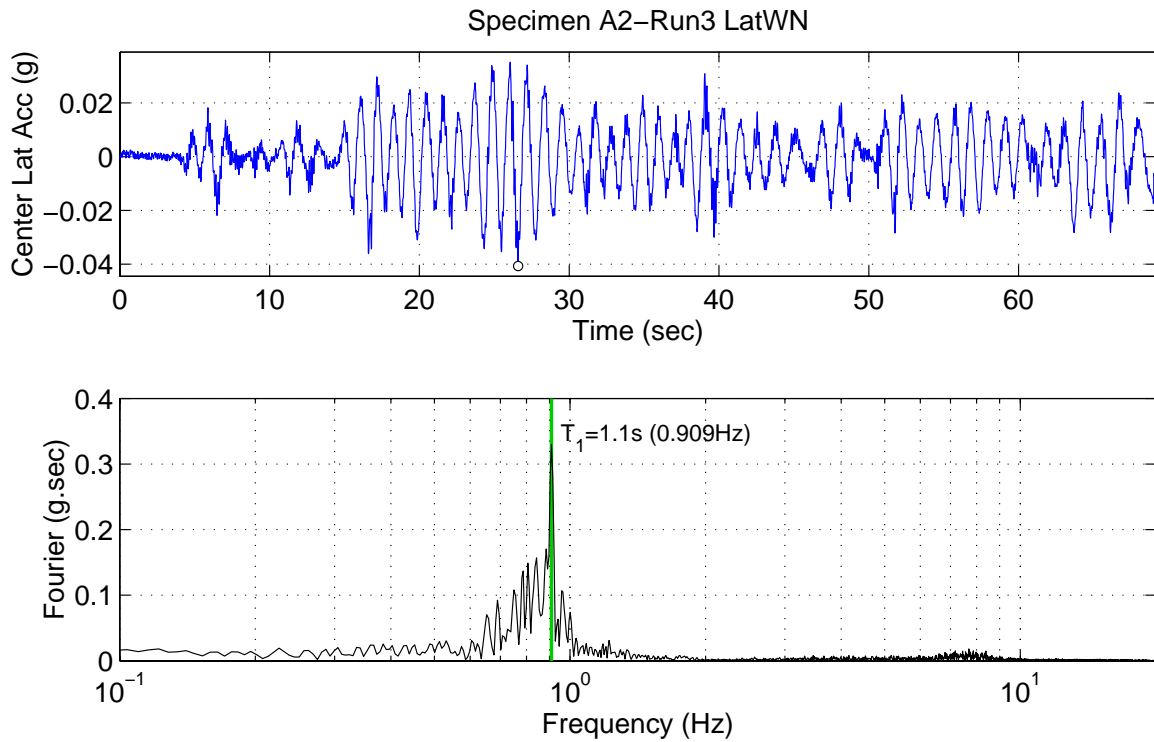
Figure 5-74. History and Fourier spectrum of the lateral acceleration due to white noise excitation of Specimen A2 (in the lateral direction) following Run 3.
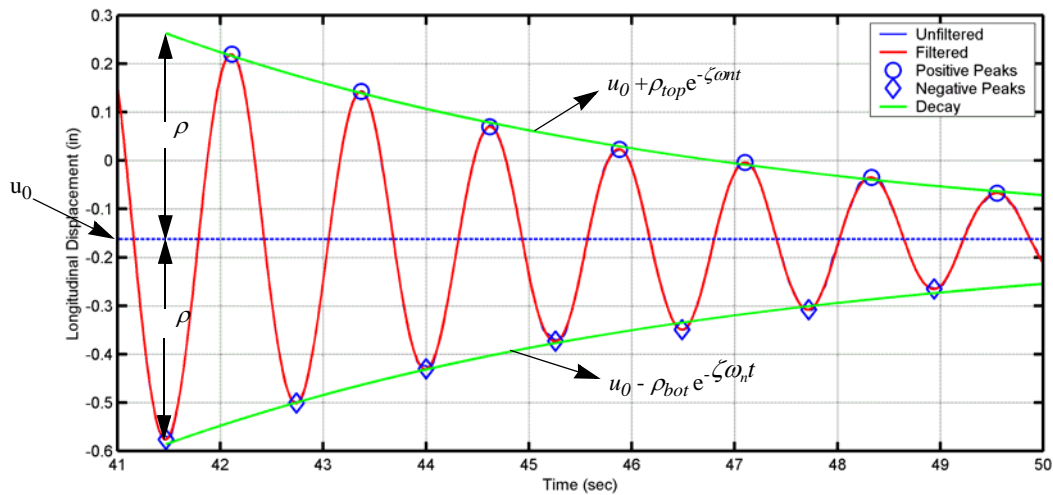
Figure 5-75. Best fit of the motion decay at the end of Run 6 (Specimen B2) in the longitudinal direction.

159

corresponds to the complete system (shaking table plus specimen), and that the specimen's period is probably slightly less than the plotted values, because of the added flexibility of the table. However, pullback tests performed with the table partially fixed yielded period values that are close to those obtained from the free vibration at the end of the runs.

From the estimated period values, the effective stiffness of the column can be calculated using one of the SDOF or 2DOF models. Figures 5-80 and 5-81 show the effective stiffnesses calculated from the estimated periods (Figures 5-76 to 5-79) using the 2DOF model with rigid end zone. Note the significant reduction in stiffness after the first design and maximum level runs. The correspondence between damage level and effective stiffness observed in Figures 5-80 and 5-81 is also indicated in Figure 5-73 for different damage level states.

In summary, after examining the period and damping at the end of each run, it was found that the column period gradually elongated from about 0.50 seconds at an undamaged state to about 1.3 seconds on average. The damping ratio followed a less obvious trend, but in general increased with repeated loading and generally ranged between 2.5% and 6%. The effective stiffness EI_e at an undamaged state was around half the gross stiffness EI_g, it decreased to about $0.3EI_g$ under low level shaking, and reached as low as $0.1EI_g$ after the design and maximum level.
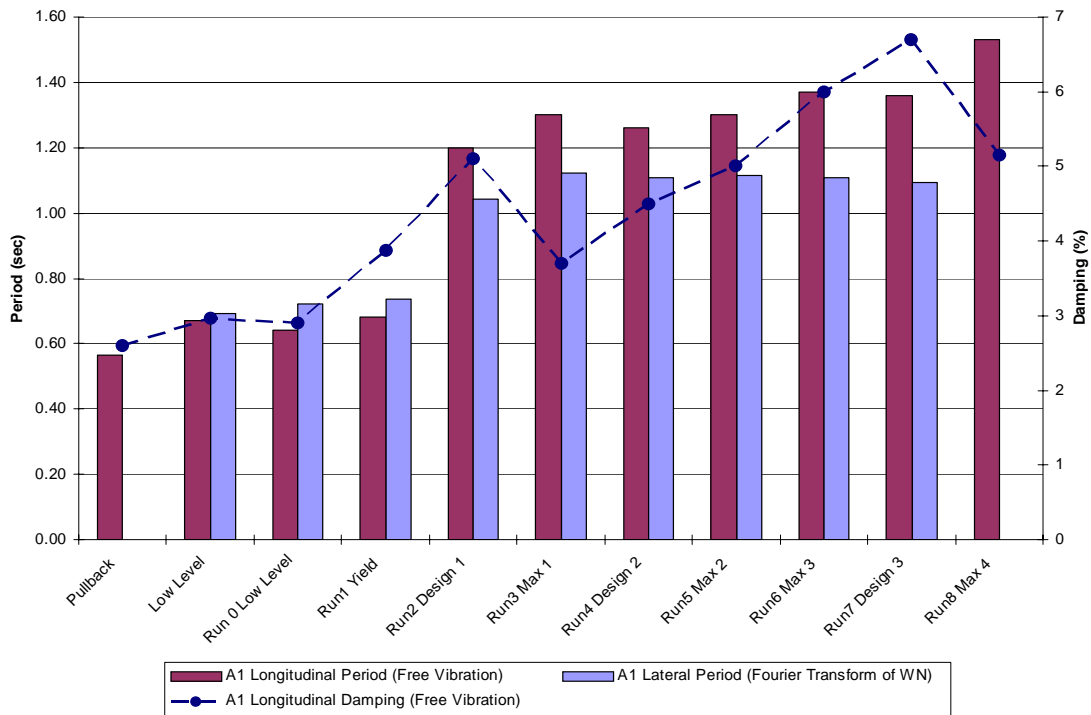
Figure 5-76. Variation of measured period and damping ratio for Specimen A1.
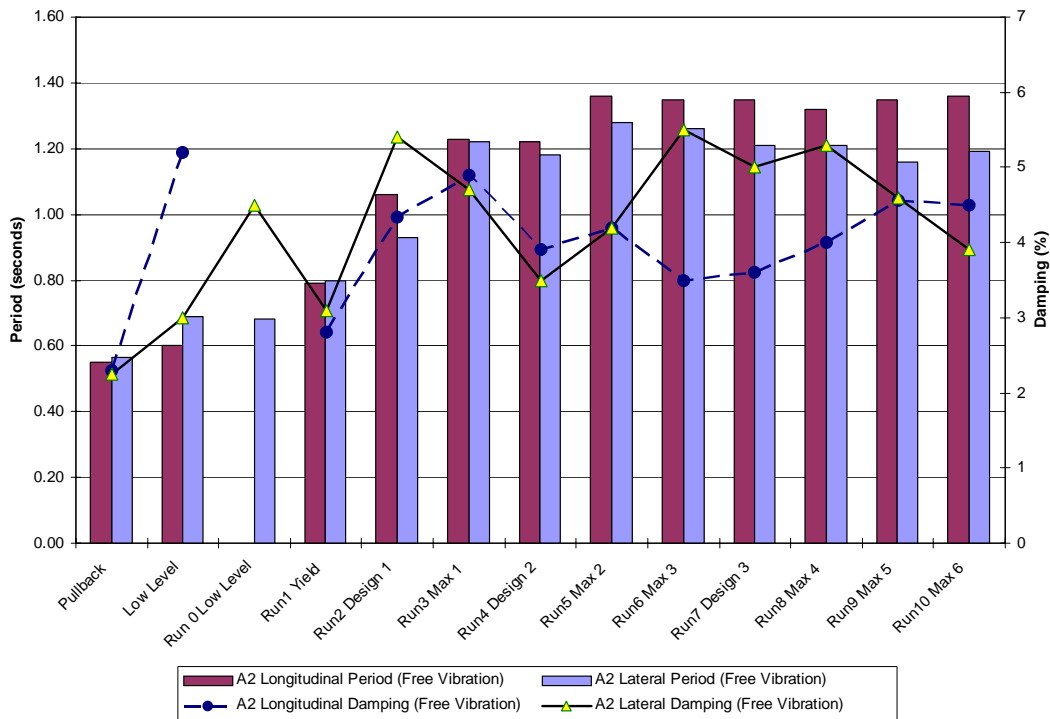
Figure 5-77. Variation of measured period and damping ratio for Specimen A2.
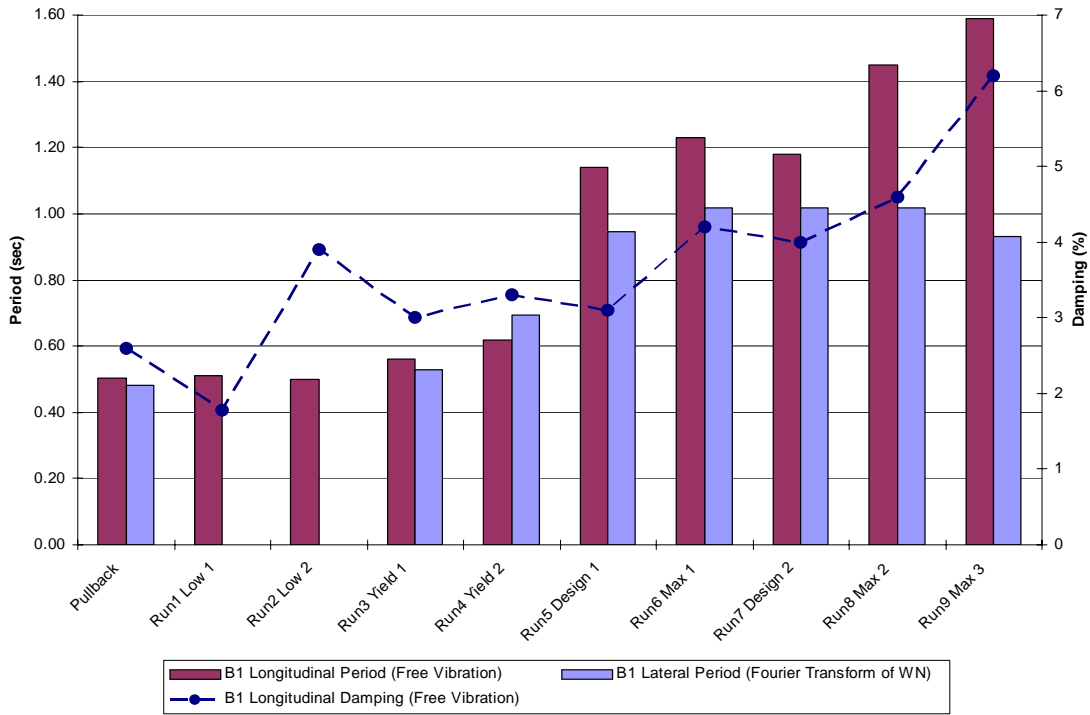
Figure 5-78. Variation of measured period and damping ratio for Specimen B1.
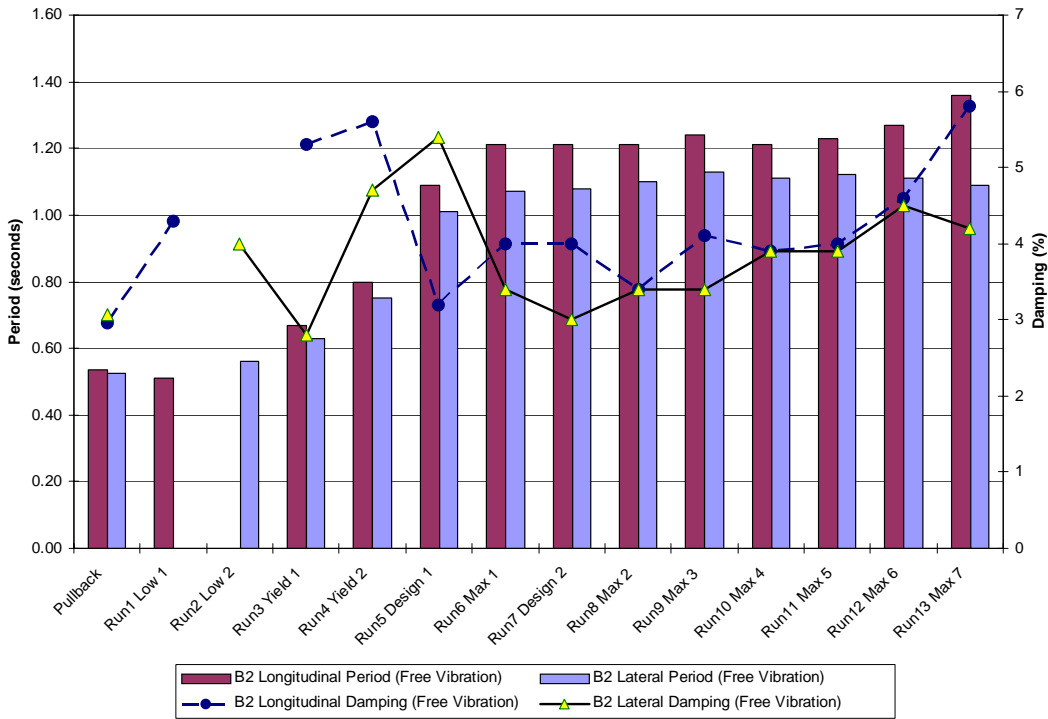
Figure 5-79. Variation of measured period and damping ratio for Specimen B2.
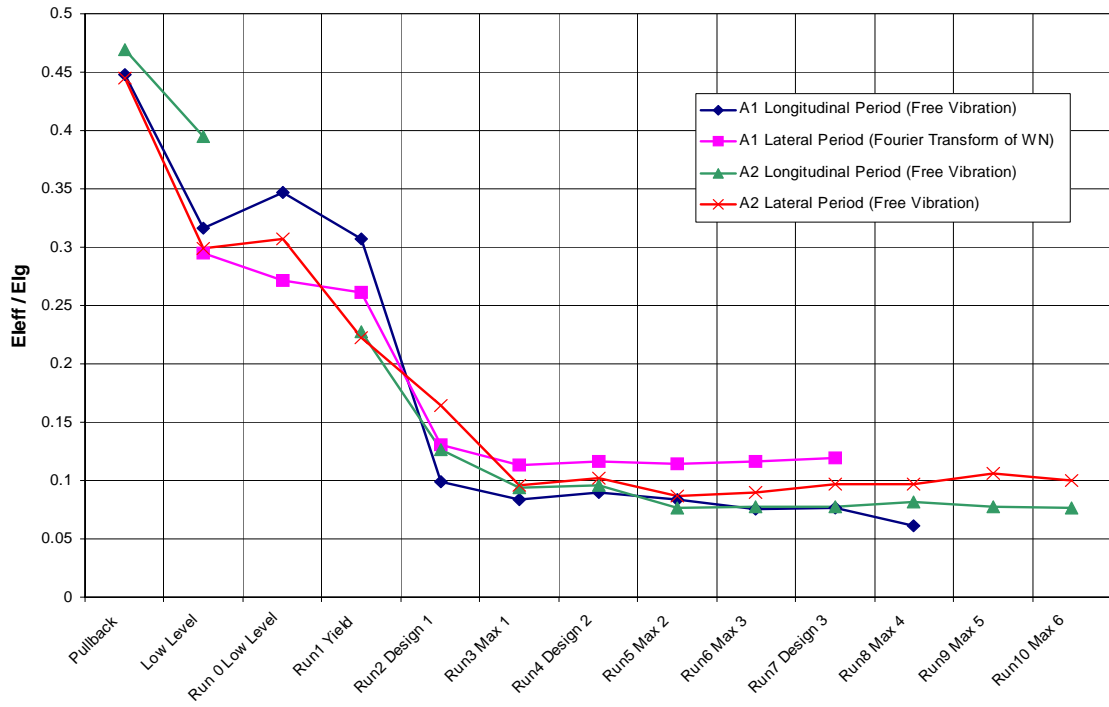
Figure 5-80. Variation of effective stiffness for various runs of Specimens A1 and A2.
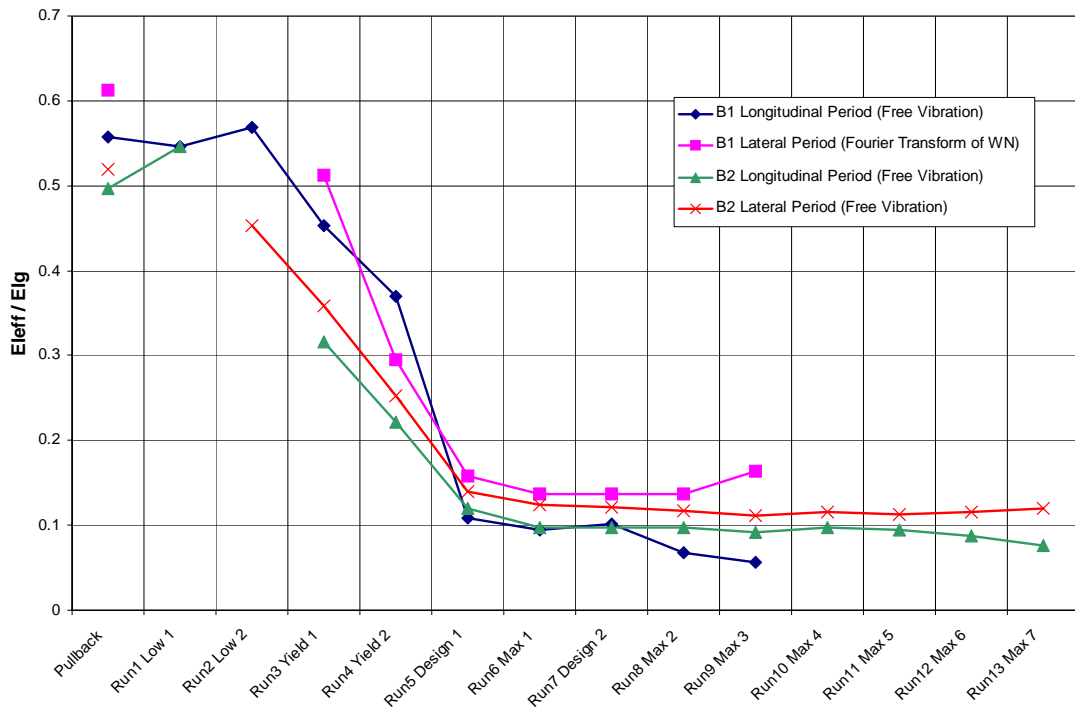
Figure 5-81. Variation of effective stiffness for various runs of Specimens B1 and B2.

163

6 Validation of Analytical Models Using Experimental Data

6.1 INTRODUCTION

One of overall objectives of this study is to evaluate procedures currently used for predicting the seismic performance of reinforced concrete bridge columns. To this end, some of the experimental results presented in Chapter 5 are compared in this chapter with the results predicted using several analysis methods and modeling approaches. Linear elastic as well as inelastic nonlinear time history analysis methods are considered. The ability of these methods to predict various global and local engineering response parameters of interest is assessed. Once calibrated to the experimental data, the best-fit analytical model is used to simulate the effect on the seismic response of the test specimens of various loading conditions not considered in the shaking table tests.

Sections 6.2 and 6.3 describe the approaches considered in this study to model reinforced concrete materials and members. In addition to elastic models that utilize effective cracked section stiffness properties, concentrated plastic hinge and fiber-based distributed plasticity models are evaluated. The results of dynamic analyses performed using these models are compared in Section 6.4 with the shaking table test results. Global response parameters such as peak displacement, base shear, overturning moment and global damage indices are considered as are local parameters such as peak moments, curvatures, strains and cumulative damage indices. Various other issues related to modeling are described in this section such as the effect of the mass moment of inertia of the mass block. Finally, Section 6.5 employs the calibrated models to investigate the likely effects on response of factors not considered in the experimental study, such as the influence of ground motion intensity, vertical excitations and gravity load eccentricity, on the response of the test specimens. A broader range of structural and ground motion parameters are considered in the analytical investigations presented in Chapter 7.

6.2   MATERIAL MODELING

Prediction of member behavior requires accurate modeling of material stress-strain response. When the hysteretic response is of interest, such as under seismic loading, adequate modeling of unloading and reloading behavior of the material may be critical. A brief description is presented below of the material models used in this study along with a discussion of a number of issues related to material characteristics.

6.2.1   Reinforcing Steel

The steel reinforcement is modeled using a Giuffre-Menegotto-Pinto model [103]. The model has a bilinear backbone curve, and hence does not account for the yield plateau of the stress strain curve (Figure 6-1c). However, the model accounts for the Bauschinger effect, which contributes to the
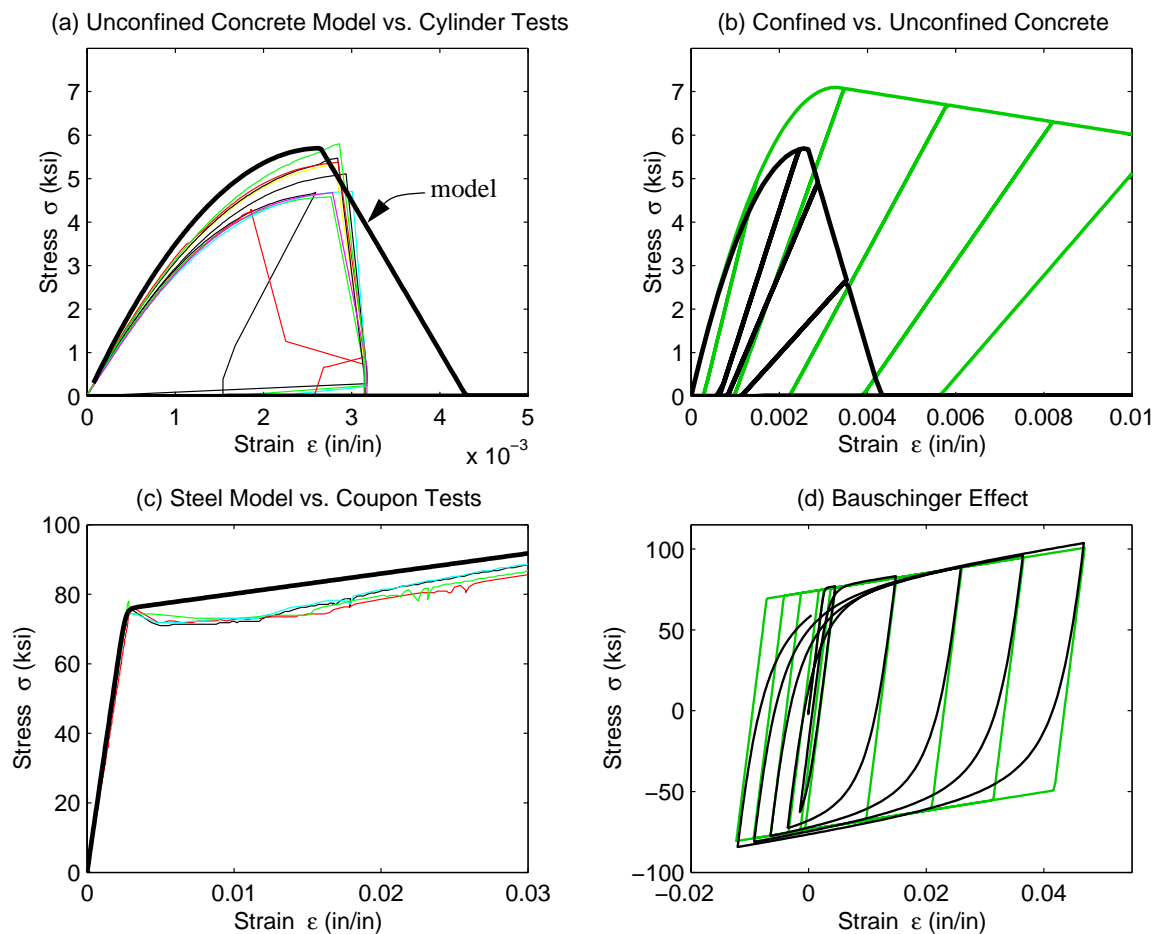
Figure 6-1. Analytical material models employed in the analysis.

gradual stiffness degradation of reinforced concrete members under cyclic response. Figure 6-1d compares the model to a bilinear model without Bauschinger effect. The yield point and hardening modulus of the model were selected to match the measured stress-strain response from coupon tests (Figure 6-1c).

6.2.2 Concrete

Concrete properties are modeled using the Kent-Scott-Park [91] uniaxial concrete model as modified by Taucer et al. [103]. The model is parabolic up to the maximum compressive strength f'_c. Beyond f'_c, the strength decreases linearly with strain. Unloading and reloading follows a linear path with a degraded stiffness. The model has zero strength in tension. This model was used for both unconfined and confined concrete as shown in Figure 6-1b. The relations by Mander [59] was used to compute enhanced strength f'_{cc} and strain capacity ε_{cu} of confined concrete (Equations 6-1 and 6-2).

$$f'_{cc} = f'_{co}\left(-1.254 + 2.254\sqrt{1 + \frac{7.94f'_l}{f'_{cc}}} - 2\frac{f'_{cc}}{f'_{co}}\right) \tag{6-1}$$

$$\varepsilon_{cu} = 0.004 + \frac{1.4\rho_{sp}f_{yh}\varepsilon_{su}}{f'_{cc}} \tag{6-2}$$

The ultimate curvature capacity ϕ_u of the column is defined as that corresponding to a maximum confined concrete strain of ε_{cu}. This ultimate concrete strain is computed through energy balance to correspond to the fracture of spiral reinforcement, and hence does not necessarily indicate complete failure or collapse. In Equation 6-2, ρ_{sp} is the spiral reinforcement volumetric ratio, f_{yh} is the spiral reinforcement yield strength and ε_{su} is the spiral ultimate strain at failure. The calculation of ε_{cu} is shown in Section B.3.1. Note that Equation 6-2 may underestimate ε_{cu} by 50% or more [85]. For the columns considered, this would underestimate the ultimate curvature capacity by more than 35%.

6.2.3 Bond Slip

The moment-curvature analysis and the fiber element model are based on a plane section assumption which implies that perfect bond exists between the concrete and the reinforcement. Hence, the model fails to predict the added flexibility due to reinforcement slip, especially at the base of the column. This leads to an overestimation of the column's stiffness. In Chapter 5, it was shown that

167

there is considerable rotation at the base of the column associated with bar slip at this location. This fixed base rotation (or flexibility) is often modelled as a rotational spring connecting the column to the underlying support [30]. Alternatively, a number of models have been proposed to represent the stress-strain response of anchored bars experiencing anchorage slip (See [4], [27], [29] and [71] for example). Lehman et al. [50] simplified a model by Eligehausen [27] for modeling the bond-slip relationship, and calibrated the model based on cyclic testing results of well-confined circular columns similar to the columns used in this study. The model proposes a bond stress of $12\sqrt{f_c'}$ as long as the stress in the reinforcing bar is below yield. The stress is reduced by half (to $6\sqrt{f_c'}$) when the bar yields. This simple model is attractive because it only requires knowledge of the stress in the reinforcement. In an analysis, this stress can easily be estimated from the moment-curvature analysis of the section at the end of the member. Based on the stress in the reinforcement and the assumed bond transfer stress, the required embedment length l_d can be computed. Equations 6-3 and 6-4 give expressions for l_{de} and l_{di}, the development lengths of the elastic and inelastic portions of the bar.

For cases where $\varepsilon_s \leq \varepsilon_y$, using a bond stress of $12\sqrt{f_c'}$ yields l_{de}:

$$l_{de} = \frac{\sigma_s A_b}{12\sqrt{f_c'}\cdot(\pi d_b)} = \frac{\sigma_s d_b}{48\sqrt{f_c'}} \tag{6-3}$$

When $\varepsilon_s > \varepsilon_y$, using the reduced bond stress of $6\sqrt{f_c'}$ yields l_{di}:

$$l_{di} = \frac{(\sigma_s - \sigma_y)A_b}{6\sqrt{f_c'}\cdot(\pi d_b)} = \frac{(\sigma_s - \sigma_y)d_b}{24\sqrt{f_c'}} \tag{6-4}$$

Assuming a linear variation of bar strain over the embedment length, the pullout deformation of the bar at the face of the joint u_s can be computed by integration of the axial strain as shown in Equations 6-5 to 6-7:

$$u_s = \int_0^{l_d} \varepsilon_s(x)dx \tag{6-5}$$

The above equation can be specialized for the elastic and inelastic cases giving u_{se} and u_{si}:

$$u_{se} = 0.5 l_{de}\varepsilon_s, \text{ when } \varepsilon_s \leq \varepsilon_y \tag{6-6}$$

$$u_{si} = 0.5 l_{di}(\varepsilon_s + \varepsilon_y) + 0.5 l_{dy}\varepsilon_y, \text{ when } \varepsilon_s > \varepsilon_y \tag{6-7}$$

In the above, ε_s and σ_s are the strain and stress in the bar at the face of the footing, ε_y and σ_y are the steel's yield strain and yield stress, and l_{dy} can be obtained by replacing σ_s by σ_y in Equation 6-3.

To illustrate this approach, the above equations were applied to stresses extracted from a moment-curvature analysis of the test column cross-section. For each longitudinal bar in the section, the development length and slip were computed at each load increment using the above equations. The obtained slippage profile of the various bars for important curvature levels are shown in Figure 6-2. The edge bars experience larger slip deformations than internal bars as expected, due to their larger strains. Figure 6-2 also shows that the edge bars experience disproportionately larger slips, because of the nonlinearity of this behavior. Clearly, this suggests that plane sections do not remain plane, especially at large curvatures. A comprehensive solution to this problem is beyond the scope of this invetigation. Thus, an approximation will be used which simply represents this complex phenomenon by a rotational spring with appropriate moment capacity, rotational stiffness and hysteretic shape. The base rotation due to slippage can be computed from bar slip using several methods. For instance, it is possible to divide the slip of the extreme bar on the tension side by the distance to the neutral axis to obtain the rotation. Alternatively, the difference of slip of the two extreme bars can be divided by the distance between them. Given the approximate nature of the whole procedure, it appears that any reasonable assumption is sufficient. In Figure 6-2, a straight line is fitted to all bars in the section using linear regression, with the slope of the line being the slip rotation angle. This approach results in about the same rotation as taking the two extreme bars, but has the advantage of being extendable to biaxial bending in a general section. In this case, a plane could be fitted to all bar slips in the section, which results in an approximate estimate of slip rotation in both directions. Figure 6-3 compares the obtained moment-rotation curve to a pinching model calibrated using the experimental slip data. This pinching model is later used as an added spring at the base of a fiber element to perform a full time history analysis.

6.3   MODELING OF REINFORCED CONCRETE MEMBERS

The increased availability of finite element models for reinforced concrete members (for example [30], [48], [70] and [96]), coupled with the availability of high-speed computing have made a wide variety of analysis options available to the design engineer. However, older methods relying on linear response spectrum and time history analysis are still typically used especially for simple
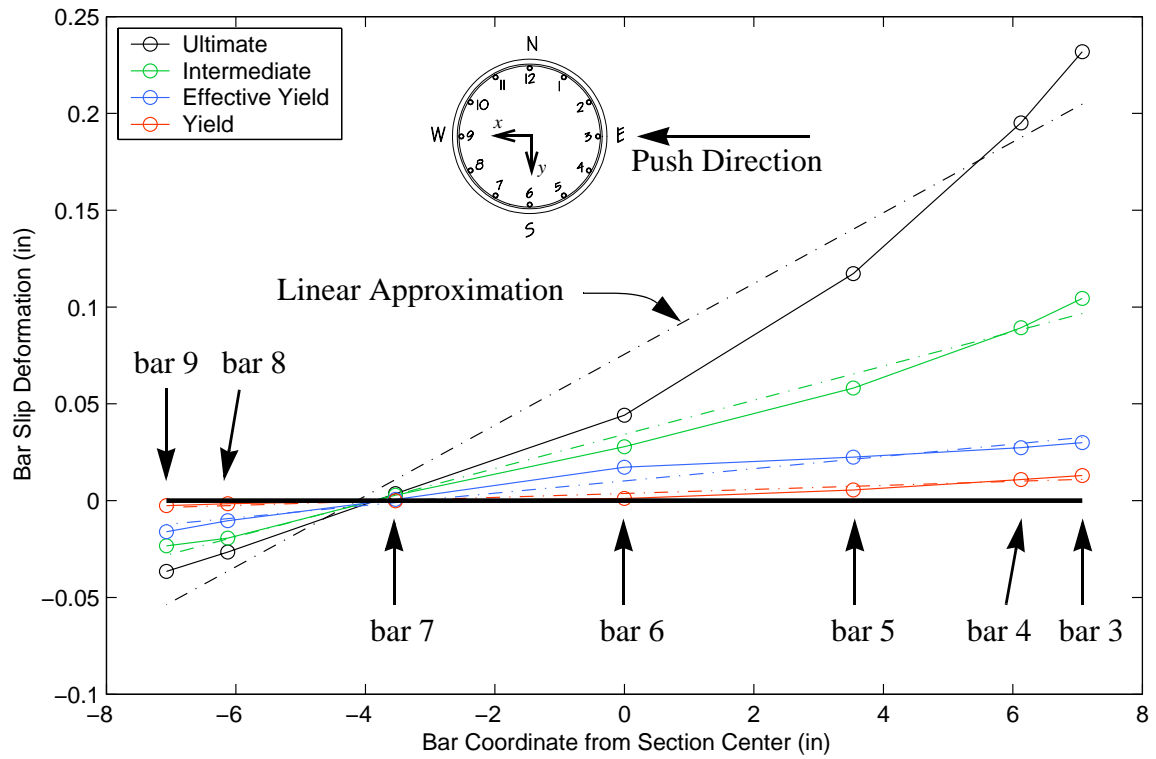
Figure 6-2. Slip profiles along section predicted at different curvature levels.
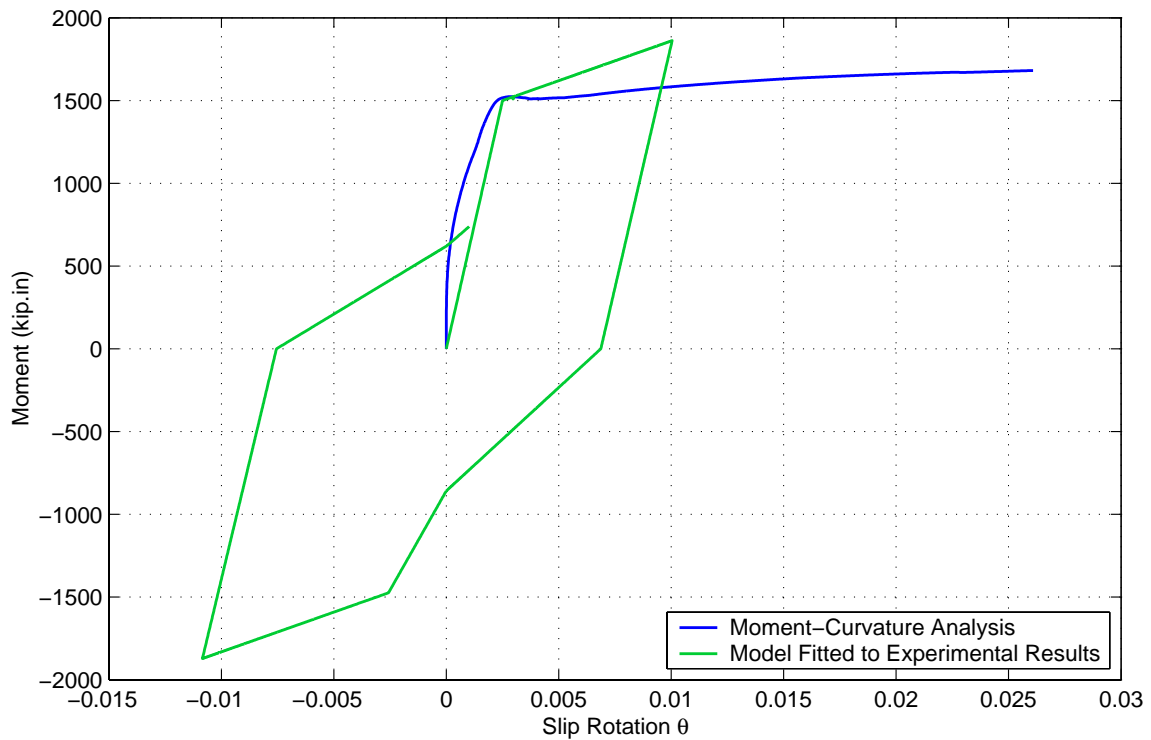
Figure 6-3. Theoretical moment vs. slip rotation using the bi-uniform model compared to an analytical model fitted to experimental results.

170

ordinary bridge structures. It is, hence, desirable to evaluate the validity of those models, and to identify the advantages to be gained from using nonlinear analysis models. Nonetheless, it must be recognized that only four well designed and detailed test specimens are considered in the assessments carried out below.

The selection of an appropriate model for use in an analytical study involves several considerations. Major considerations include correctness, complexity and accessibility. A model needs to simulate the relevant behavior modes of the element being modeled. Hence, models need to be calibrated against available experimental data. Complexity is another important factor both in implementation and element use. Typically, the simplest model capable of predicting the response parameters of interest should be used. Benchmark studies are thus needed to compare the accuracy of models of varying complexity, and illustrate their strengths and weaknesses (see for example Cofer [17]). Additionally, a large number of models developed and published in the literature are inaccessible to designers. Open source software technology promises to be a solution to this problem by allowing researchers and engineers to rapidly share new contributions. One of the attempts to realize this objective is the OpenSees (Open System for Earthquake Engineering Simulation) framework that is being developed at the Pacific Earthquake Engineering Research Center [63].

This OpenSees framework is built on the open source model, enabling researchers and engineers to easily add and share enhancements to the material and element models. the column analyses carried out in this section were performed using a flexibility based beam-column element with fiber sections [96]. This element could be used to compute the moment-curvature relationship for the sections considered, as well as to predict the overall response of the member. In addition, elastic beam-column elements and concentrated plastic hinge elements were employed.

Finite element models for reinforced concrete members can be divided into two major categories: linear elastic models, and inelastic models.

Elastic models are typically used in dynamic analysis to estimate deformation demands on structures. They are also used to determine design forces at critical locations. Elastic models usually utilize the concept of effective sectional stiffness. The effect of cracking is approximated using typical elastic element formulation with equivalent cracked stiffness under the anticipated axial load used for the entire length of the element, often approximated as $EI_{gross}/2$ or $EI_{gross}/2.5$. Forces predicted by elastic models are substantially in error since yielding is not accounted for. Peak lateral displacements predicted using these elements are often assumed to be a good approximation for those imposed during inelastic dynamic response. This may not hold in many situations

of interest, and the approach cannot predict response parameters such as residual displacement of the structure at the end of the earthquake.

Inelastic models include a wide range of different types with varying degrees of complexity. Three basic approaches can be distinguished:

1. Concentrated plastic hinge models: Because of expected flexural yielding at the ends of members, plastic hinges are represented as concentrated plastic hinge regions connected by an elastic flexural element. The plastic hinge region is often represented by a concentrated flexural spring with effective inelastic hysteretic properties or by a short length of column where the cross section is explicitly represented by fibers having effective uniaxial material properties. These models introduce varying degrees of simplification, but are able to account for local yielding, and provide response parameters that may be used to assess performance on the local level. Because yielding is accounted for, predictions of forces and displacements are generally satisfactory.

2. Distributed plasticity models: Because yielding can propagate along the length of a member, and because the flexural stiffness along the central portion of a member can change significantly if axial loads change during dynamic excitations, members which incorporate concentrated plastic hinge or fiber representation of sections along the length are also used in many cases.

3. Finite element approaches represent the full three-dimensional geometric and material properties. A wide variety of phenomena can be accounted for in such models, including bond slip between bars and concrete, interaction of behavior modes related to flexure, shear and confinement, and "true" material properties associated with three dimensional stress states and local deformation modes. This level of realism is accompanied by complexity in defining geometry and material properties, substantial computational demands, and difficulties in visualizing and interpreting response. In spite of the apparent realism of such models, difficulty is experienced in predicting behavior under cyclic force reversals into the inelastic range. Typically, such models are not used for well-detailed members whose behavior is controlled by flexure.

In this report, a series of analyses are done to assess the ability of three types of analytical models to predict observed response. These include:

1. Elastic models to predict peak displacement demands when the test column is subjected to unidirectional and bidirectional excitations.

2. Concentrated plastic hinge models where simplified hysteretic properties and effective stiffnesses in the elastic range are used.

3. Fiber-based models where different levels of refinement are used to characterize the change in properties along the length of the member.

In the following subsections, the approaches used to idealize these models for the conditions encountered in the test specimens are described.

6.3.1   Moment-Curvature Analysis

Regardless of the numerical model used, the engineer needs to predict the moment-curvature relation. This can be used to estimate the effective sectional stiffness for an elastic model, and provides the basis for computing effective properties of plastic hinges in concentrated plasticity models. By integrating the moment-curvature relationship over the length of the member, fiber models can predict the flexural behavior under complex loading conditions.

The moment-curvature relationship of any section can be calculated using well known flexural principles. Typically, the section is discretized into a number of fibers (as shown in Figure 6-4), each of which is assigned a uniaxial constitutive model corresponding to the material it represents. Consistent with Bernoulli-Navier beam theory, sections are assumed to remain plane during deformation. The moment-curvature curve is obtained by calculating the section moment corresponding to a certain imposed curvature and axial load. This is accomplished by iteratively solving for a neutral axis depth that satisfies axial load equilibrium. For reinforced concrete members, confined concrete should be modeled differently than unconfined concrete to account for enhancements in strength and strain capacities.

The moment-curvature relationship corresponding to the circular column used in the tests is presented in Figure 6-5. The analysis used a bilinear steel model and a parabolic concrete model with a linear descending branch (Section 6.2).

173

Unconfined Concrete Fiber

Total Number of Fibers: 252
Core Concrete Fibers: 200
Cover Concrete Fibers: 40
Steel Fibers: 12

Confined Concrete Fiber

Steel Fiber
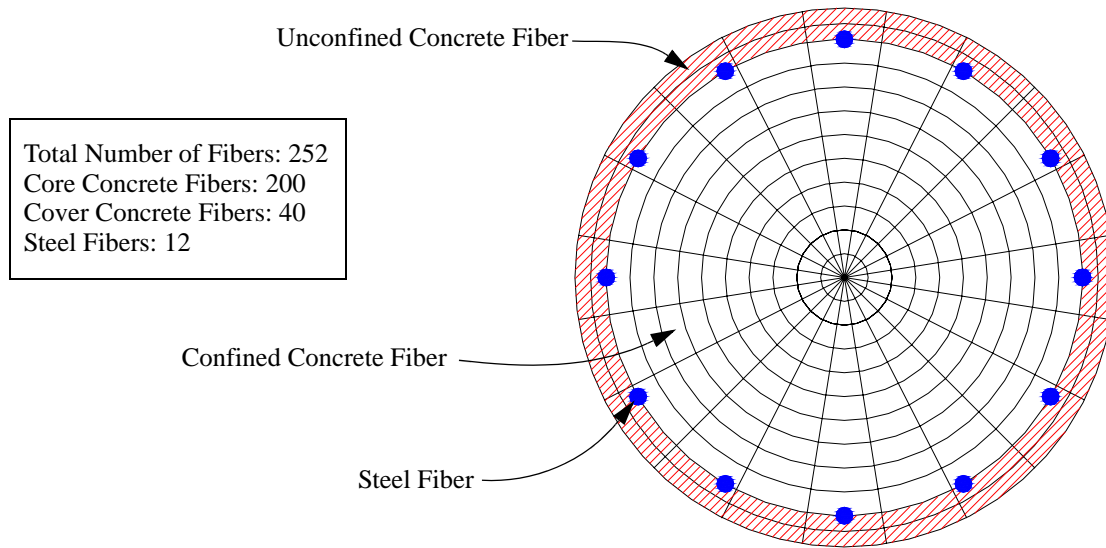
Figure 6-4. Fiber section representation of the test column.

(ϕ_u , M_u)

(ϕ_{ye} , M_n)

(ϕ_y , M_y)

EI_e

1

$f'_c = 5.7$ ksi

$f'_{cc} = 7.1$ ksi; $\varepsilon_{cu} = 0.013$

$f_y = 75$ ksi with 1% hardening

$D = 16$ in. ; cover $= 0.5$ in.

Axial Load $= 65$ Kips

$\rho_l = 1.17\%$
$\rho_{sp} = 0.54\%$

Computed Moment–Curvature
Idealized Moment–Curvature

Moment (Kip.in)

Curvature ϕ (10^{-3}/in)
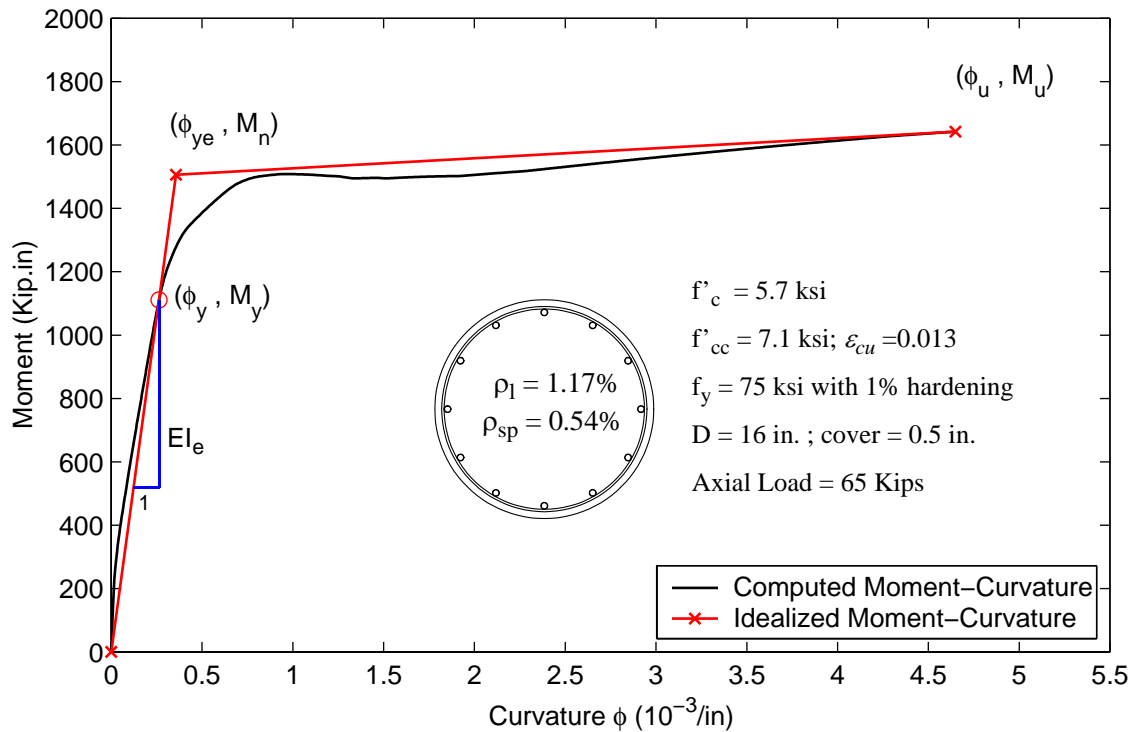
Figure 6-5. Moment-Curvature relationship of the column section.

6.3.2 Plastic Hinge Length Simplified Model

A common model for yielding elements places inelastic hinges at each end of an elastic beam-column. The plastic hinge region may be represented by a simple concentrated rotational spring, a generalized plastic hinge model based on theoretical plasticity formulation, or a fiber representation of the effective longitudinal properties of the materials used in the region. The concentrated plastic hinge model is discussed in this section and in Section 6.3.3. Fiber models with varying numbers of sections used to monitor behavior along the member are described in Section 6.3.4. Generalized plasticity models are not considered in this investigation.

To determine the properties of the concentrated plastic hinge model, it is common to develop an idealized conceptual model for the distribution of curvatures along the length of an actual member that can be used to compute member deformations. The properties of the model are then calibrated to test results. In this section, we will consider a widely used approach where the plastic hinge model is calibrated to include shear, fixed end rotations and plastic rotations within the plastic hinge region. Similar but more complex formulations have attempted to separately account for each of these sources of deformation as in Equation 6-8 ([8], [50]):

$$\Delta = \Delta_{bending} + \Delta_{slip} + \Delta_{shear} \tag{6-8}$$

For the case being considered, the moment-curvature relation for the column in question (Figure 6-5) is represented by a bilinear envelope curve. The initial "elastic" portion of the curve is drawn from the origin and extends through the point corresponding to first yielding of the steel and ends at the nominal moment capacity of the section M_n, computed assuming the material properties described in Section 6.2 and corresponding to a concrete strain of $\varepsilon_c = 0.004$ in/in. The effective uniaxial properties of the confined portions of the concrete core were determined using the model proposed by Mander [60], as described in Appendix B. The second slope of the curve extends from the nominal moment capacity point to the ultimate moment and curvature estimated for the section. The ultimate condition is based on the concrete model described in Section 6.2.2.

For the test column, this approach results in an effective stiffness EI_e of:

$$EI_e = \frac{M_n}{\phi_{ye}} = \frac{M_y}{\phi_y} \approx 0.3 EI_g \tag{6-9}$$

where I_g represents the moment of inertia of the uncracked concrete section. The effective value obtained is far less than the uncracked stiffness of the section, and even less than a typical value

175

used in design of $EI_g/2$. The actual ratio of EI_e/EI_g for a reinforced concrete section generally depends on the axial load and percentage of longitudinal reinforcement.

Figure 6-6 illustrates the application of this idealized moment-average curvature relation in the prediction of the lateral displacement of the test column. As shown in Figure 6-6, the test column is assumed to be an ideal cantilever column with zero moment at the top. For the linear moment variation over the height of the column, the average curvature distribution can be drawn. However, for simplicity, and because of the contributions due to bar pullout, shear, and other factors not considered in the moment average curvature distribution, the plastic curvatures are typically assumed to be constant over the plastic hinge length. For this distribution of curvatures and for an assumed plastic hinge length, L_p, the lateral displacement at the tip of the column is computed for the elastic range of behavior as:

$$d = (\phi/\phi_{ye})d_{ye} \quad \text{(for } \phi \le \phi_{ye}) \tag{6-10}$$

where,

$$d_{ye} = \frac{M_n L^2}{3EI_e} = \frac{\phi_{ye} L^2}{3} \tag{6-11}$$

and

$$\phi_{ye} = \frac{M_n}{M_y}\phi_y \tag{6-12}$$

For the cases where the column yields, the total lateral displacement is given by:

$$d = d_{ye} + d_p , \quad \text{(for } \phi > \phi_{ye}) \tag{6-13}$$

$$d_p = (\phi - \phi_{ye})L_p(L - L_p/2) \tag{6-14}$$

Here, d is the total lateral displacement at a stipulated curvature of ϕ, and d_p is the plastic component of the displacement. d_{ye} is the effective yield displacement corresponding to an effective yield curvature ϕ_{ye}. L_p and L are the plastic hinge length and column length, respectively.

Several investigators have calibrated this equation to test results to determine best fit values of L_p. A survey of these models is presented by Lehman et al. [50]. A widely used model proposed by Priestly et al. [85] is used as the baseline for subsequent analyses. This plastic hinge length is given by Equation 6-15:

$$L_p = 0.08L + 0.15f_y d_b, \text{ (ksi units)} \tag{6-15}$$
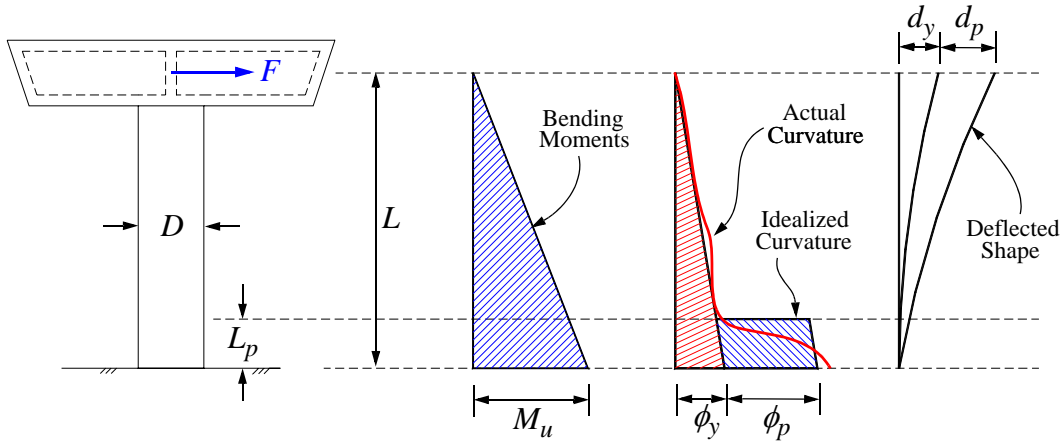
Figure 6-6. Elastic and plastic deformation components of a bridge column.

For the test column, this approach results in a plastic hinge length of 13.3 in. (338 mm), and the effective local and global properties listed in Table 6-1. For reference, the computed values correspond to lateral displacement and peak curvature ductility capacities of:

$$\mu_d = \frac{d_{ult}}{d_{ye}} = \frac{6.17}{1.11} = 5.56 \tag{6-16}$$

$$\mu_\phi = \frac{\phi_u}{\phi_{ye}} = \frac{0.00462}{0.000360} = 12.83 \tag{6-17}$$

Table 6-1 Section properties from moment-curvature analysis and plastic hinge model.

Property	Yield	Effective Yield	Ultimate
Curvature ϕ (1/in)	$\phi_y = 0.000263$	$\phi_{ye} = 0.000360$	$\phi_u = 0.00462$
Moment M (kip.in)	$M_y = 1111$	$M_n = 1521$	$M_u = 1652$
Shear V (kip)	$V_y = 11.6$	$V_n = 15.8$	$V_u = 17.2$
Shear/Mass (g)	0.18g	0.24g	0.26g
Displacement d (in)	$d_y = 0.81$	$d_{ye} = 1.11$	$d_{ult} = 6.17$
Secant Stiffness K (kip/in)	14.3	14.2	2.9
Period T (seconds)	0.68	0.69	1.52
Secant Stiffness EI (kip.in^2)	$EI_y = 4.228 \times 10^6$	$EI_{ye} = 4.228 \times 10^6$	$EI_u = 0.357 \times 10^6$
Stiffness Ratio[a] EI / EI_g	$EI_y / EI_g = 0.28$	$EI_{ye} / EI_g = 0.28$	$EI_u / EI_g = 0.024$
Neutral Axis Depth c (in)	$c_y = 4.91$	$c_{ye} = 3.94$	$c_u = 4.17$

a. $EI_g = 14.84 \times 10^6$ kip.in^2

Using values in Table 6-1, the relation between lateral force and lateral displacement for monotonically increasing lateral loads for the test specimen can be plotted as shown in Figure 6-11. In this plot, an additional correction is made to account for the effects of gravity loads on the apparent lateral capacity of the column. This P-Δ correction consists of subtracting a force equal to the product of the gravity load carried by the column times the lateral displacement of the column divided by the height of the column to the center of the mass block. While the P-Δ effects are modest in the elastic range of behavior, they become significant as the displacements increase.

6.3.3   Lateral Force-Displacement Hysteresis Model

The bilinear backbone curve derived in the previous section and plotted in Figure 6-11 can be used as the basis of simplified analysis of the test column under lateral loading. However, additional assumptions are needed to characterize its response under arbitrary cyclic loading.

Hysteretic relationships are usually defined by a backbone curve, and a number of unloading and reloading rules. A concentrated hinge is typically assigned a hysteretic relationship representing the moment rotation properties of the plastic hinge region. Although some models have rules that account for axial load and biaxial moment interactions, the majority of the models follow simple rules related to moment and rotation at the plastic hinge. Hysteretic models are selected based on the expected hysteretic behavior of the member of interest. Some hysteretic elements may include features such as strength degradation, stiffness degradation and pinching (e.g. [44], [48]), making them very useful in modeling a wide variety of structural components. Plastic theory may also be used to model axial load and biaxial interactions [54]. A number of hysteretic models were surveyed by Saatcioglu [87]. Some selected models are shown in Figures 6-7a through 6-7f.

6.3.4   Fiber Section Models

A flexibility-based fiber element was used for the refined modeling of the test columns. The element can estimate the spread of inelasticity over the its length using a number of integration points. In a flexibility formulation, a moment distribution is assumed along the element, and the curvatures are subsequently estimated. The element uses the Gauss-Lobato integration scheme to integrate displacements along its length. Both three and four integration points were used in the analysis. Since most of the yielding is expected to occur near the ends of the element, the integration points
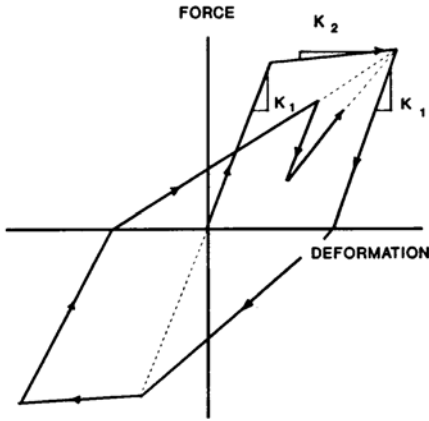
Figure 6-7a. Hysteretic model by Clough (from [87]).
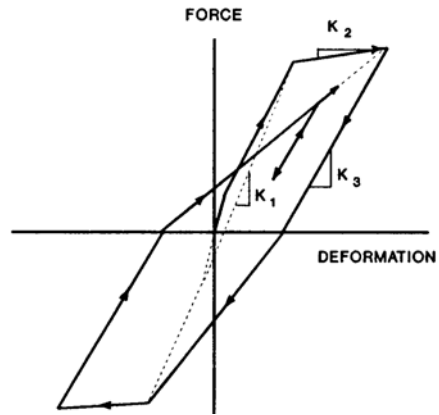
Figure 6-7b. Hysteretic model by Takeda (from [87]).
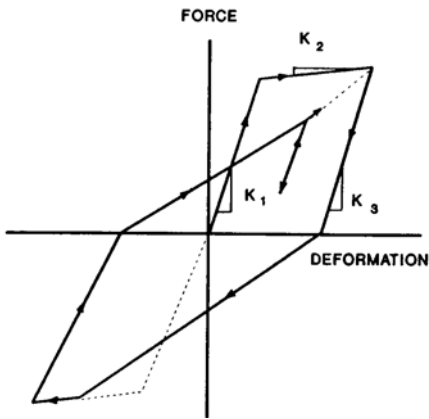
Figure 6-7c. Q-Hyst model by Saiidi and Sozen (from [87]).
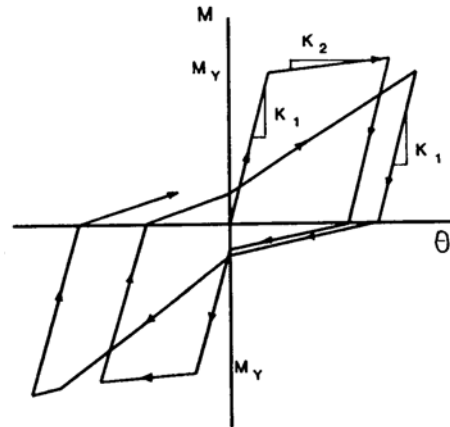
Figure 6-7d. Pinching Hysteretic model by Banon et al. (from [87]).
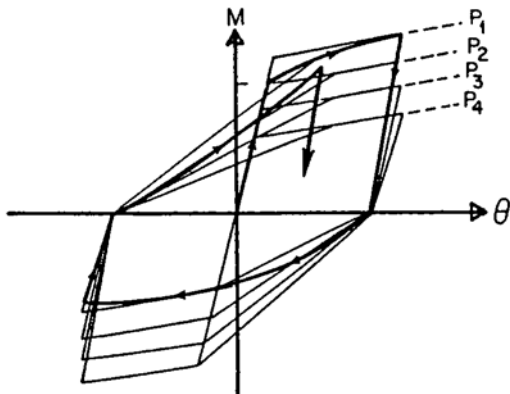
Figure 6-7e. Axial force-moment interaction model by Saatcioglu et al. (from [87]).
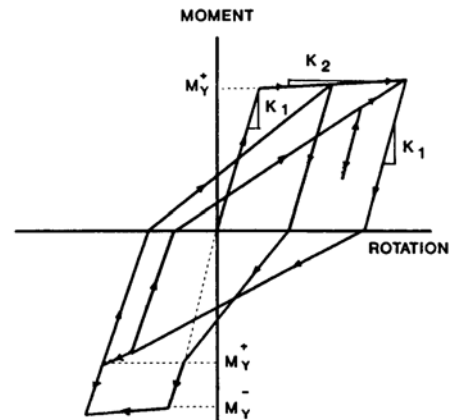
Figure 6-7f. Moment-slip rotation by Filippou and Issa (from [87]).

179

near the middle of the element are expected to experience little yielding. Hence, the integration points near the end are most critical to predicting the correct behavior.

Figure 6-8 shows an example of a fiber model with four integration points along its length. The locations and weights of the various integration points are also shown. For the column in Figure 6-8, assuming that the column is fixed at the base, the top deformation can be obtained using Equation 6-18:

$$d = \int_0^L \phi(x)(L - x)dx \tag{6-18}$$

Using the quadrature integration rule corresponding to the Gauss Lobato integration scheme (with np points), the deformation can be estimated as:

$$d \approx L \sum_{i=1}^{np} \phi_i(L - x_i)w_i \tag{6-19}$$

When a cantilever column deforms into the inelastic range, the plastic deformation component is mainly contributed by inelastic action in the bottom section. Hence, the plastic deformation can be roughly approximated as:

$$d_p \approx (\phi_{base} - \phi_y)L^2 w_1 \tag{6-20}$$

By equating the above equation to Equation 6-14, the required weight w_1 at the first integration point can be computed as follows:

$$w_1 = \frac{L_p}{L^2}(L - L_p) \approx \frac{L_p}{L} \tag{6-21}$$

Note that if the above equation is not satisfied, the fiber element will yield incorrect curvatures at a given deformation. A large weight will yield curvatures that are too small, and vice versa. Since no integration scheme may correspond to the the computed weight, the column may be divided into two or more elements, such that the edge element(s) would have section weights satisfying the following condition:

$$w_1 = \frac{L_p}{L_{end}L}(L - L_p) \approx \frac{L_p}{L_{end}} \tag{6-22}$$

where L_{end} is the length of the end element(s). This also allows the computation of the required end element length for a given integration rule. For example, if two integration points are used for the

180
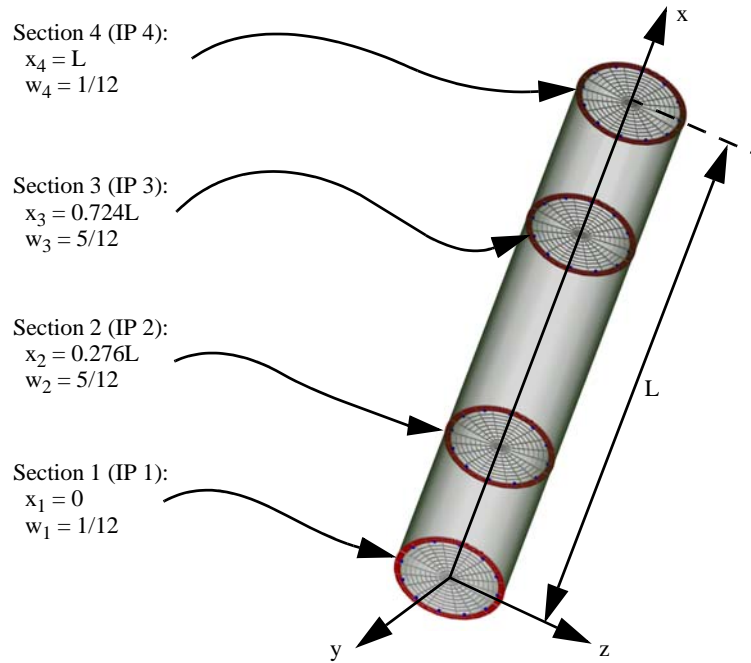
Figure 6-8. A Fiber element with four integration points used to model the column.

end element, the integration weight w_1 is 0.5 for each section, and the required end element length is:

$$L_{end} \approx \frac{L_p}{w_1} = 2L_p \tag{6-23}$$

The above observations regarding the importance of selecting the integration scheme can be illustrated using Figure 6-9 which plots the curvature-displacement relationships for different fiber models on top of those recorded from the experiments. The plastic hinge method predicts an ultimate monotonic displacement of 6.17 in. corresponding to an ultimate curvature of 0.0046/in at the base. A fiber model consisting of one element with four integration points along the height, predicts a displacement of 4.37 in. at the same base curvature, that is 28% lower than that given by the plastic hinge method. However, using a more detailed model with three elements, with the end elements having two integration points each and measuring $2L_p$, the predicted ultimate displacement is very close to the plastic hinge model. Figure 6-9 shows that using a single fiber element with four integration points yields the worst results, while the other models result in more acceptable approximations. The moments and curvatures predicted by the 3-element fiber model, are plotted along the height of the column at different displacement levels in Figure 6-10.

181
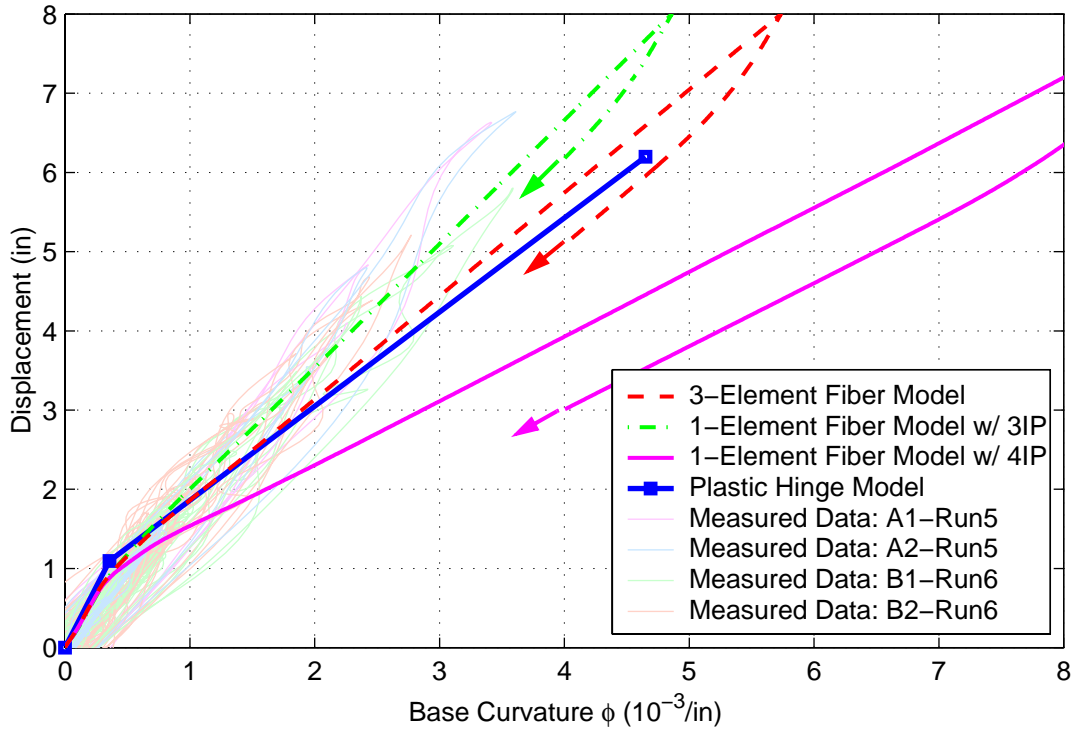
Figure 6-9. Displacement-curvature relationship for various analytical models compared to data from the maximum runs of each the four specimens.
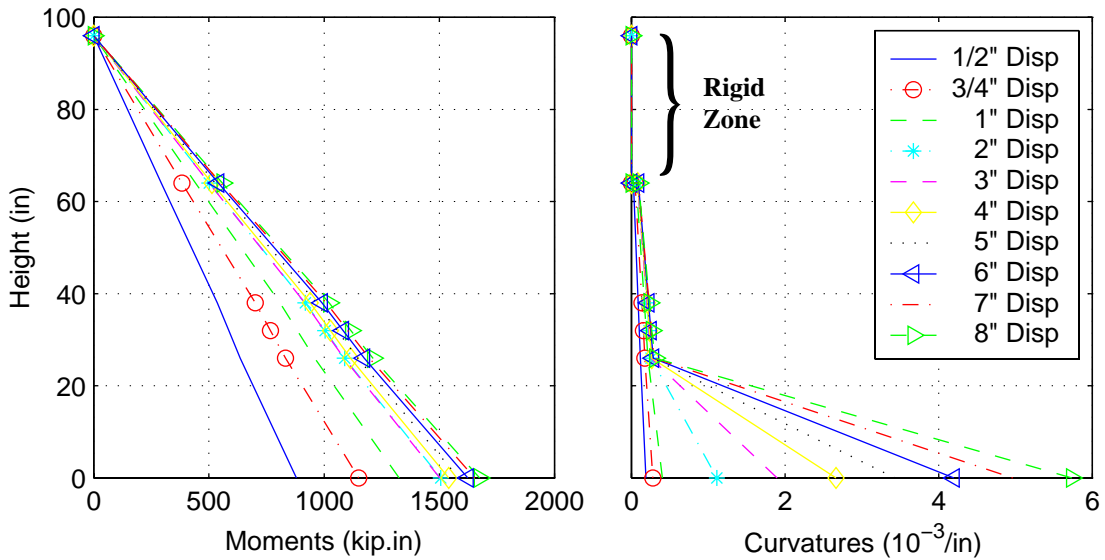
Figure 6-10. Moments and curvatures at different element sections for different displacement levels, obtained from OpenSees pushover analysis of 3-element model.

Figure 6-11 compares the monotonic force-displacement curve resulting from the plastic hinge method and the fiber element. Figure 6-12 shows the hysteretic response of the specimen with and without P-Δ effects computed using the fiber section model.
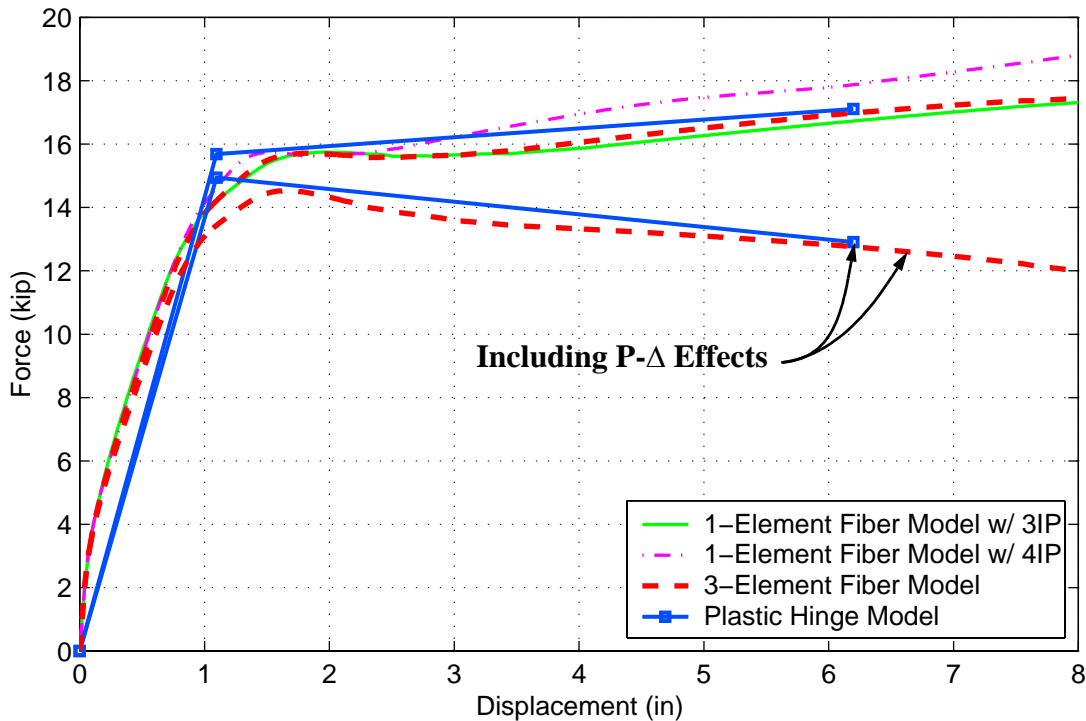
Figure 6-11. Comparison of the OpenSees fiber model to the plastic hinge model.

A limitation of the fiber model is that it does not directly account for flexibility due to shear or bond slip. Deformation due to bond slip in the footing of the column may account for a significant portion of the total column deformation. This contribution tends to increase with additional deterioration of bond capacity under cyclic loading. It is possible to account for the bond slip effect by adding a rotational spring at the end of the element to represent added flexibility. This spring can be calibrated using actual measured moment-slip rotation data from experiments as is done in this study or it can be approximated given a model for predicting the slip of individual bars ([30] and [69]).

The fiber element is usually preferred as a good intermediate solution between lumped models and full finite element models. It is more complicated than hysteretic models, but its use allows the incorporation of more realistic hysteretic material models. The fiber element also implicitly accounts for interactions between axial load and biaxial moments at the section. Hyster-
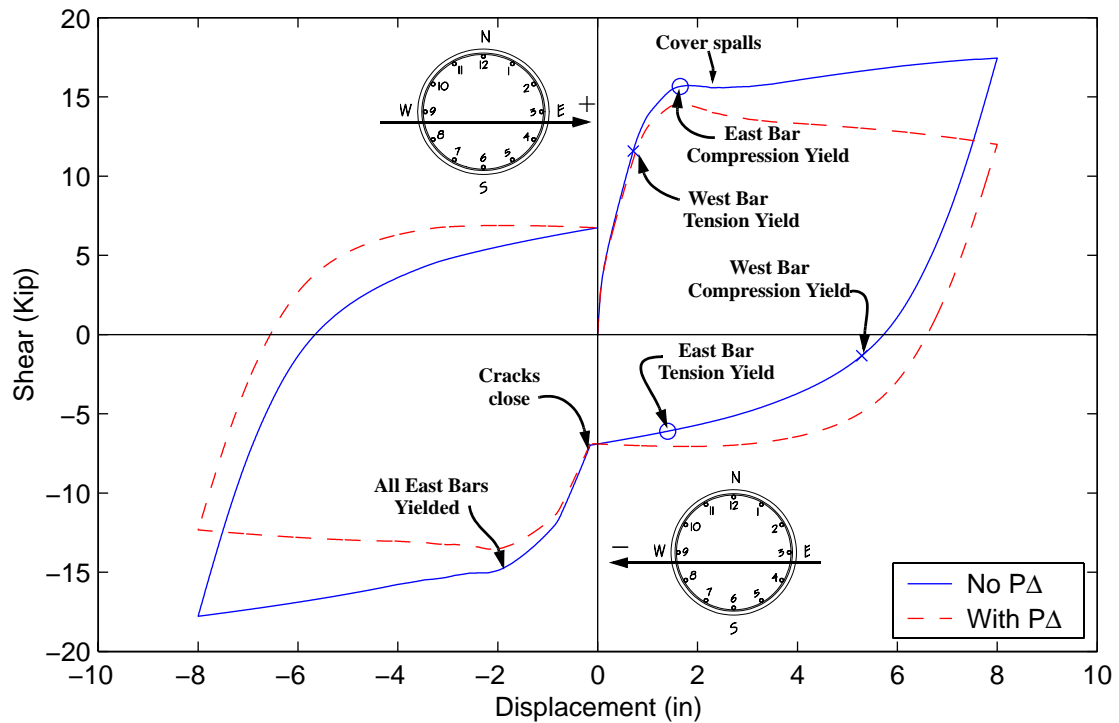
Figure 6-12. Analytical Force-Displacement curve for the test specimen.

etic models, on the other hand, are generally simpler to implement and run significantly faster in most cases. They can be calibrated to match a desired response curve or to model failure mechanisms and deformation components that cannot be easily modeled using the fiber element alone, such as shear failure and deformation due to bond slip. However, calibration of those hysteretic models is often based on experimental data which may not be available. Moreover, the parameters used are generally not intuitive and may require extensive testing and fitting, especially those required to simulate performance degradation. Ultimately, it would be desirable to have models that can predict the exact cyclic response of a member given its geometry, reinforcement details and material properties. Similar models have been proposed for monotonic loading [110], but no complete models are currently available for cyclic loading.

6.4   DYNAMIC TIME HISTORY ANALYSIS

Several analysis models will be evaluated in terms of their ability to predict the recorded specimen response. The analysis models considered range from elastic and simple hysteretic models to fiber elements with springs representing bar slip in the joint.

Using gross and effective stiffness estimates, simple linear and nonlinear analysis models can be used to analyze the column under different levels of earthquake input corresponding to those used in the shaking table tests. In the following, the effectiveness of those models is investigated and compared to more complex nonlinear models based on fiber elements.

In the different models considered, the mass block was modeled by specifying a rotational mass of inertia at the center of gravity of the block, and by using a rigid element measuring 32 in. (813 mm) to model the segment between the top of the column and the center of mass, since the column height is measured to the center of mass. P-Δ effects were also included in all analyses and a viscous damping ratio of 3.5% of critical was used. The SDC requires P-Δ effects to be considered when:

$$P \cdot d > 0.20 M_u \qquad (6\text{-}24)$$

ATC-32 has a similar requirement with a limit of $0.25 M_u$ instead. If d is assumed to be around 6 in., then $P \cdot d$ would be about $0.24 M_u$. This indicates that including P-Δ effects in the analysis is indeed required.

Analysis models are separated into linear (Section 6.4.2) and nonlinear models (Section 6.4.3). The analysis results from each model were compared to the experimental data. The quantities compared include: peak displacement, residual displacement, column shear, base and top moments, energy dissipation, and damage indices. More emphasis is placed on displacements and damage indices because of their increasingly important role in modern design and evaluation techniques, such as displacement and performance based design methodologies. Section 6.4.5 investigates the sensitivity of the analysis results to other design considerations.

6.4.1 Damping

All forms of damping that do not include hysteretic energy dissipation are usually lumped together and treated as pure viscous damping. These forms may include material damping, damping due to air resistance, friction, soil-structure interaction and non-structural components. Damping is usually expressed in terms of a damping ratio ξ, which is defined as the ratio of the damping coefficient c to the critical damping coefficient c_{cr} in the case of a single degree of freedom system (Equation 6-25).

$$\xi = \frac{c}{c_{cr}} = \frac{c}{2m\omega} \qquad (6\text{-}25)$$

185

For multiple-degree of freedom systems, Rayleigh damping is often used. Rayleigh damping allows the damping ratio to be specified at two different natural frequencies, ω_i and ω_j. The damping matrix is computed as a linear combination of the mass and stiffness matrices (Equation 6-26), whose coefficients are determined by solving a 2 by 2 system of equations (Equation 6-27).

$$c = \alpha m + \beta k_t \tag{6-26}$$

$$\frac{1}{2}\begin{bmatrix} 1/\omega_i & \omega_i \\ 1/\omega_j & \omega_j \end{bmatrix}\begin{bmatrix} \alpha \\ \beta \end{bmatrix} = \begin{bmatrix} \xi_i \\ \xi_j \end{bmatrix} \tag{6-27}$$

Damping ratio values typically used for the design of reinforced concrete structures range from 3% to 7%. The value most widely used by building codes is 5%. Hashimoto et al. [33] reviewed a large amount of data on structural damping from earthquakes and experiments involving several types of structural systems and materials. They suggest using a damping ratio of 6% for regular reinforced concrete structures. However, they note a dependence of the damping ratio on many factors including the presence of non-structural elements, structure complexity, mode of vibration and excitation magnitude. Not only does the damping ratio vary with the deformation magnitude, but damping measurements at larger magnitudes approaching or exceeding the elastic limit may include hysteretic damping contributions which complicates the process of evaluating existing damping data.

Based on the damping observed in the shaking table tests (Section 5.7.2), the Rayleigh coefficients α and β were selected such as to result with damping ratio of 3.5% at periods of 0.1 seconds and 1.0 second. Those two periods represent lower and upper bounds on the frequency content of the response. The 0.1 second period corresponds to the period of the second mode of vibration while the 1.0 second period roughly corresponds to the fundamental period of the specimen assuming a severely cracked section. The damping matrix of Equation 6-25 was formed at each analysis step using the current tangent stiffness matrix. The resulting damping ratio is shown in Figure 6-13. It can be seen that as the period of the fundamental mode increases from 0.5 seconds to more than 1.0 second due to damage softening, the damping ratio gradually increases, which is consistent with the damping observed during the tests (Figures 5-76 to 5-79).
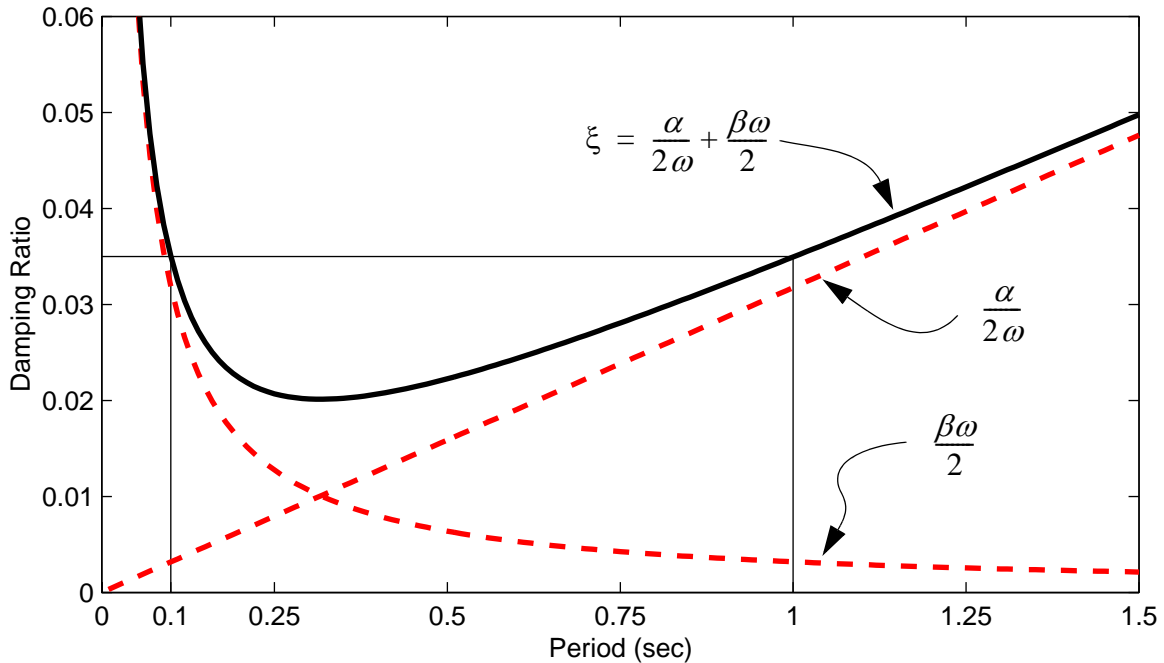
Figure 6-13. Rayleigh damping used in the dynamic analysis.

6.4.2   Comparison of Measured Response to Linear Analysis Results

Linear analysis is often used to get a preliminary estimate of displacement demand. It is also attractive since it is equivalent to using linear spectra which are easy to generate and are typically specified in design codes. The linear spectral displacement is usually very close to the nonlinear displacement if the period of the structure is in the long period range where displacements are preserved, but may differ significantly if the structure is in the short period range where energy is preserved (Figure 6-14).

6.4.2.1   *Properties of Linear Models*

The accuracy of a linear analysis depends on a good estimate of the stiffness used. To illustrate the effect of the stiffness on the response, three linear analyses are performed for each specimen as follows:

1. Linear analysis using the gross stiffness EI_g. This is performed for comparison purposes, and is most likely to result in unconservative results.

2. Linear analysis using a reduced stiffness equal to $EI_g/2$. This approach is more common in estimating nonlinear behavior, and is expected to give reasonable results, especially when displacements are preserved.
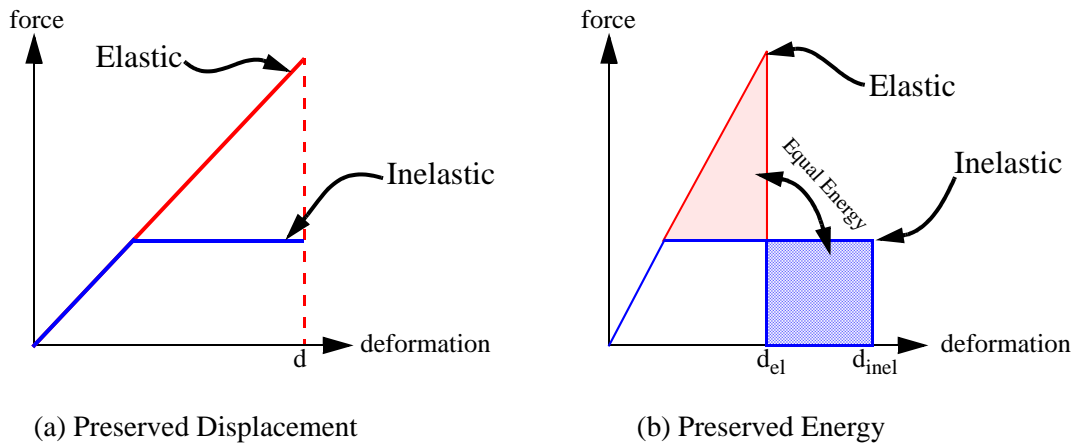
Figure 6-14. *Preserved Displacement* and *Preserved Energy* assumptions.

3. Linear analysis using the effective stiffness EI_e computed using the plastic hinge method. This stiffness was found to be equal to $0.3EI_g$ (Equation 6-9). It is expected to result in a good estimate of the effective period of the column, and should result in an improvement over the other models.

   In each case, the analytical model was subjected to a ground motion record composed of all the acceleration history recorded for each specimen. The records were spliced to each other with some time inserted in between to allow adequate damping of the response between successive runs.

6.4.2.2   Displacement Histories from Linear Analysis

   In most cases, the peak displacement demand is sufficient for proper design and detailing of a bridge column. However, one value is seldom appropriate for performance evaluation such as the estimation of residual displacements and damage indices, which requires accurate modeling of the structural response. Therefore, all of the analytical models used will be critically evaluated to determine their adequacy for estimating peak displacements, residual displacements, frequency content, and general agreement with the experimental response.

   The linear analysis displacement histories are compared to measured displacements in Figures E-1 to E-4 for Specimens A2 and B2. The response is compared for the yield, design and maximum level runs. As Figures E-1 and E-2 show, the linear analysis fails at predicting the displacement history of the columns. The results clearly show that using a stiffness of EI_g results in a response that is very different than the actual behavior both, in displacement magnitude and

188

frequency. This is true even at small levels of excitations such as in the yield level event. Using EI_g /2 as an approximation for the cracked stiffness yields slightly better agreement, but is still considered unsatisfactory. The linear model employing a stiffness of EI_e yields the best overall match with the experimental results in terms of predicting the peak displacement, but it also underestimates the natural period of vibration of the column. The bidirectional displacement trajectory obtained using EI_e slightly resembles the actual interaction, while using EI_g or EI_g/2 yields unacceptable results (Figures E-3 and E-4).

It is concluded from the above that when performing a linear analysis, the stiffness used should be no greater than the effective stiffness EI_e. However, although using a stiffness of EI_e may yield reasonable results for shaking around the yield level, even a smaller stiffness may need to be specified under higher levels of shaking, because of period elongation caused by inelastic behavior. There are many proposed methods for estimating the equivalent period of vibration and damping ratio of a yielding structure for use in linear analysis (See [14], [6]). However, those procedures can be complicated, and in general cannot overcome many of the problems of linear analysis. For example, when the input motion is amplified, the linear response is amplified by the same amount, without any changes to the shape of the response. This is rarely the case in nonlinear behavior. In fact, it can be seen by looking at the design and maximum level plots of Figure E-2 that the linear response increases by 50% between the design and maximum levels, while the peak nonlinear response only increases by 13%. This also includes the fact that the original peak (first positive peak) decreases slightly while another peak (first negative peak) becomes the largest peak. Although some equivalent linear methods use an equivalent damping that increases with the peak displacement, they seldom achieve accurate results. These are some the limitations that make nonlinear analysis a more reliable approach, even when relatively simple nonlinear models are used.

6.4.2.3 Displacement Peaks from Linear Analysis

Although it is preferable to have an accurate time history response, a good estimate of the peak displacement demand is often sufficient. The peak displacements from the linear analyses were compared to the displacements recorded from the tests for each of the performed runs. Those peak displacements are plotted for the longitudinal and lateral directions of Specimens A2 and B2 in Figures 6-15 to 6-18. The results for the longitudinal directions of Specimens A1 and B1 are very similar to those of A2 and B2 and hence are not shown.

These plots support the previous conclusions that the effective stiffness yields the best results in terms of estimating the peak displacement. This is especially true for the longitudinal dis-
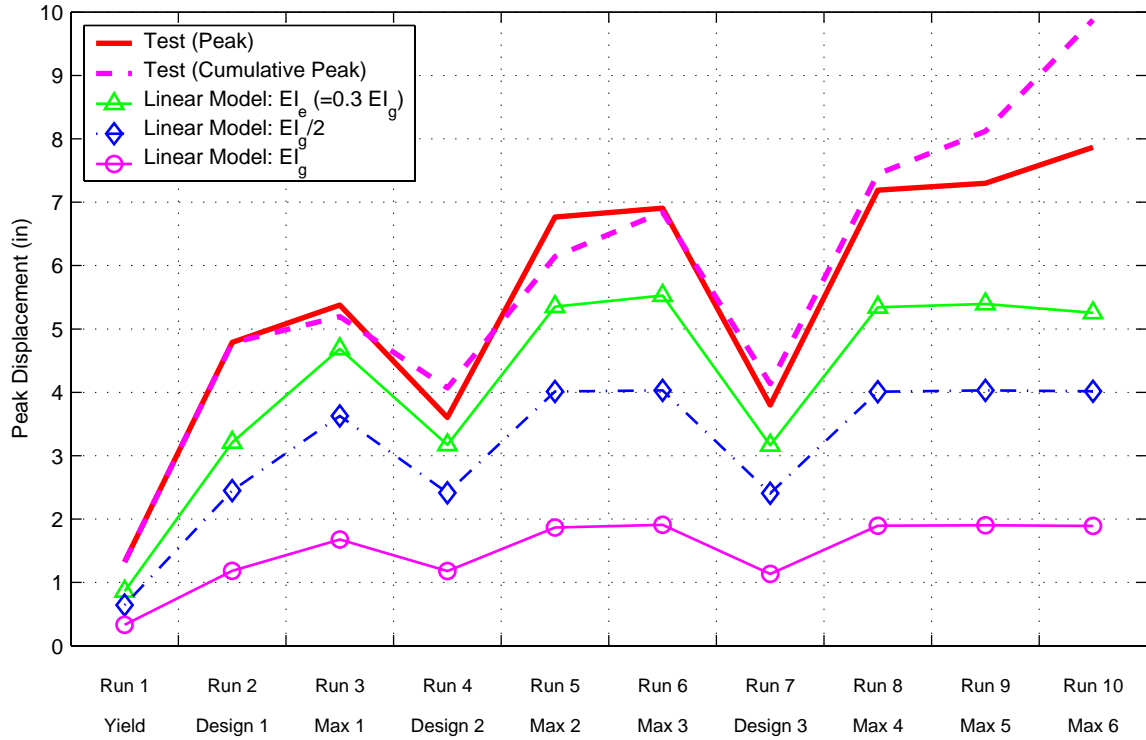
Figure 6-15. Analytical vs. experimental displacements for specimen A2 in the longitudinal direction.
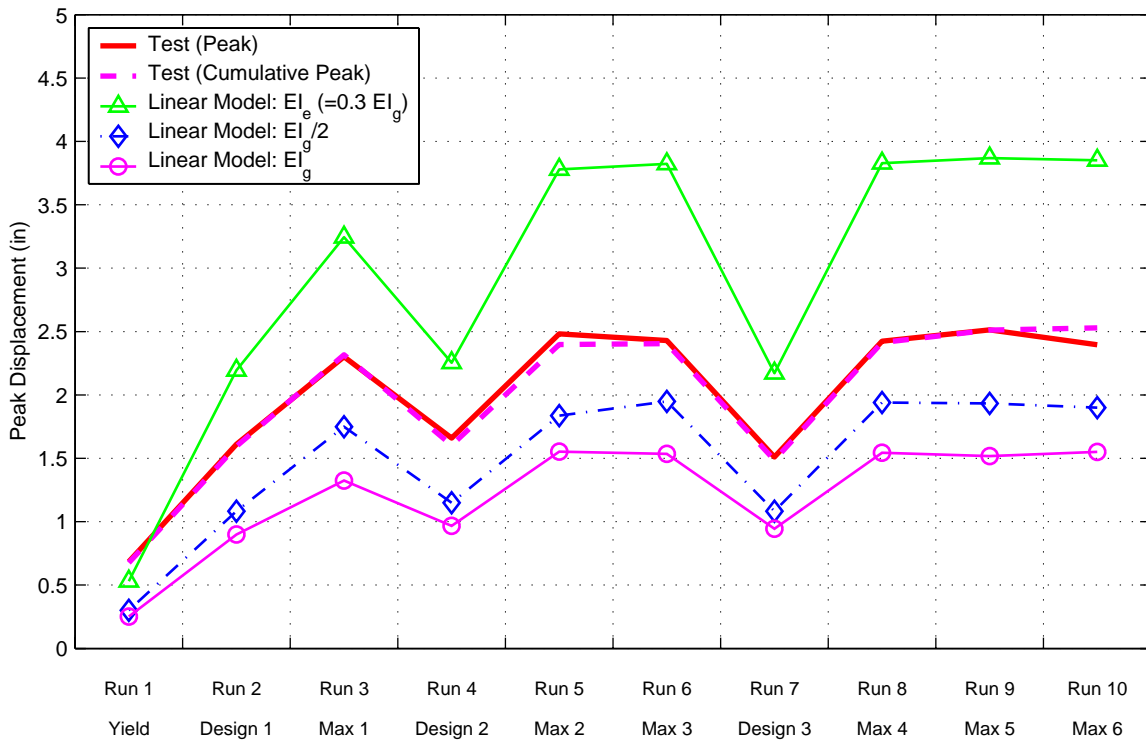
Figure 6-16. Analytical vs. experimental displacements for specimen A2 in the lateral direction.
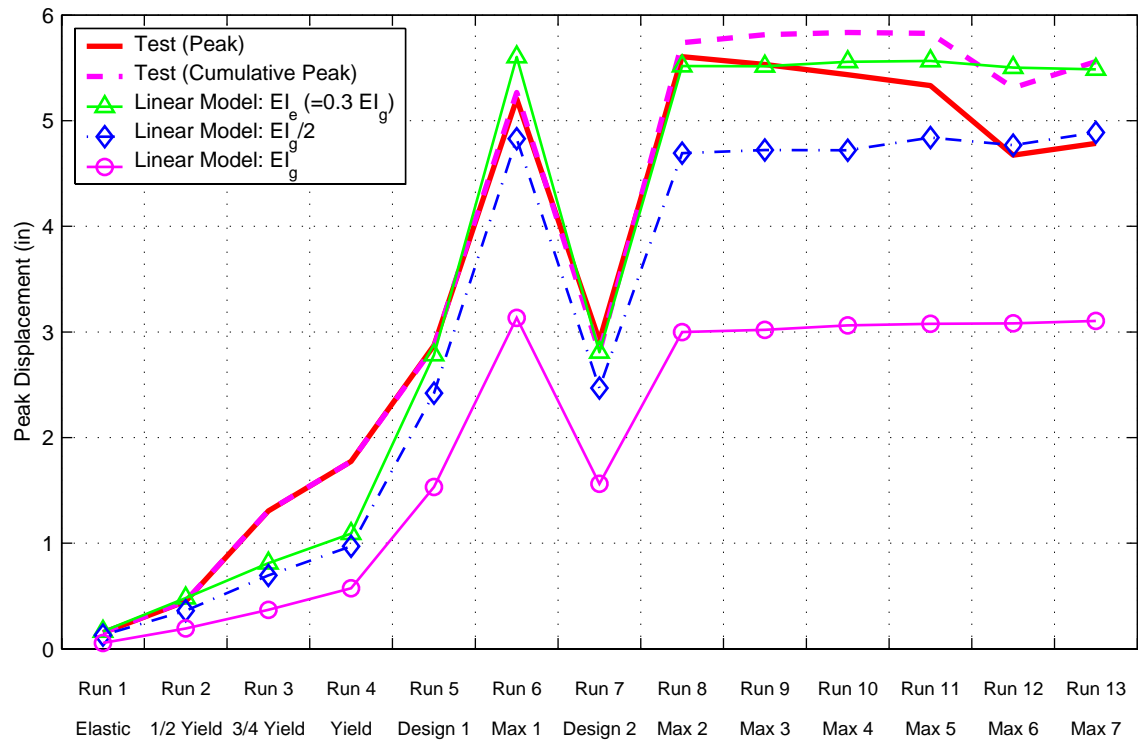
Figure 6-17. Analytical vs. experimental displacements for specimen A2 in the longitudinal direction.
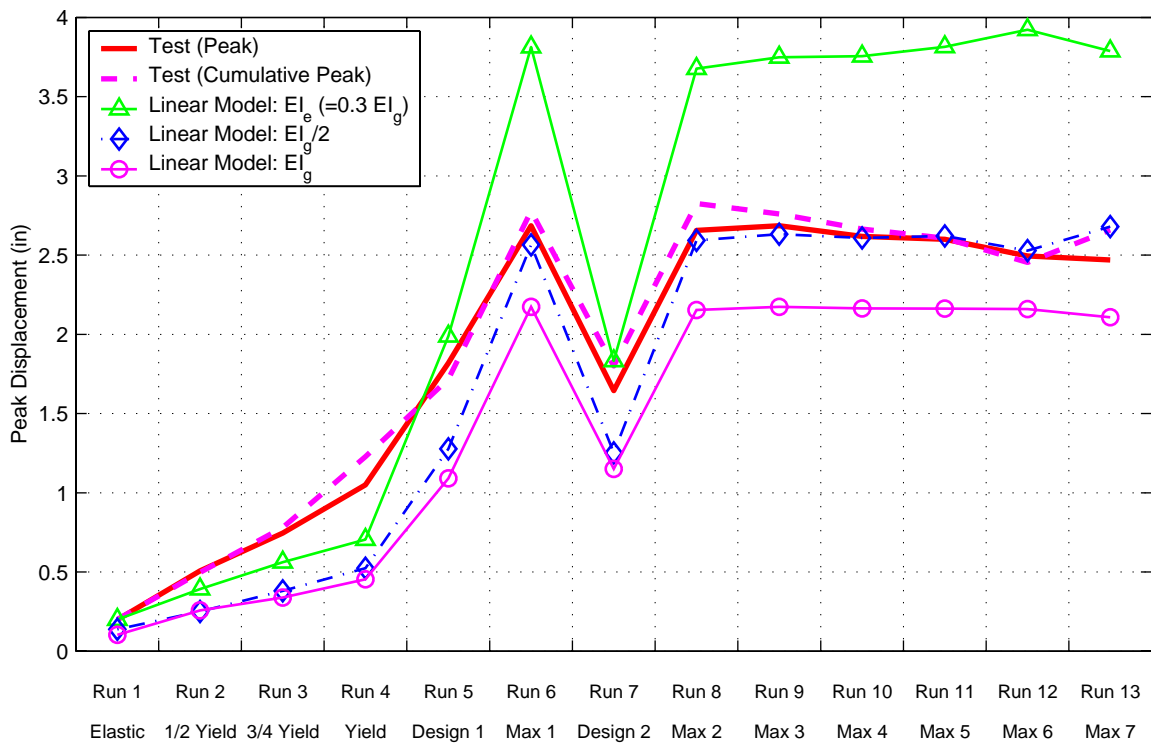
Figure 6-18. Analytical vs. experimental displacements for specimen A2 in the lateral direction.

placements. For lateral displacements however, using EI_e yields displacements that are overconservative, and $EI_g/2$ yields the right peak lateral displacements especially for Specimen B2 (Figure 6-18).

It is also noted that linear models are especially inappropriate for predicting response to repetitive loading since linear models do not have a state and hence cannot track any form of damage or deterioration.

6.4.3 Comparison of Measured Response to Nonlinear Analysis Results

A number of nonlinear models are available for modeling reinforced concrete member behavior. A number of different models are used to simulate the column tests, and are compared in terms of accuracy and complexity.

6.4.3.1 Properties of Nonlinear Models

The nonlinear models used can be divided into two categories: plastic hinge models, and fiber models. The investigated models, which are shown in Figures 6-19 and 6-20, include two plastic hinge models and three fiber models as follows:

1. Bilinear model with an effective stiffness EI_e.

2. Stiffness degrading (Clough) model with an effective stiffness EI_e.

3. Fiber element model using one element along the height of the column with both three and four integration points in order to investigate the effect of the number of integration points on the response. Results are reported for the element with three integration points.

4. Fiber element model using one element along the height of the column. A rotational spring was added at the bottom of the column to model base flexibility due to bond-slip. The base spring was modeled using a bilinear moment-rotation model with stiffness degradation whose properties were calibrated with experimental measurements. Both three and four integration points were used for the element. Results are reported for the element with four integration points.

5. A refined fiber model with three elements along the column height. The three elements along the column height have the section properties of the column. The end elements have a length of $2L_p$ (26.6 in. or 676 mm) and two integration points each, effectively resulting in a true plastic hinge length L_p. The middle element, which is expected to remain essentially elastic, has a length of 10.8 in. (374 mm) and three integration points.

192

(a) Linear Models

$$K = 3EI/L^3$$
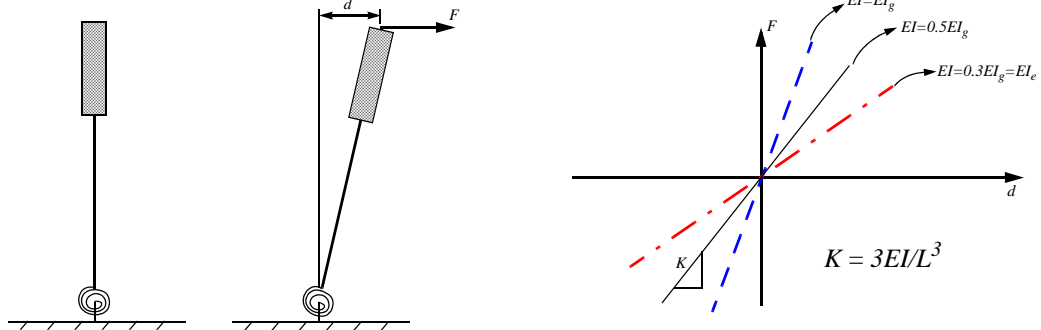
(b) Bilinear Model
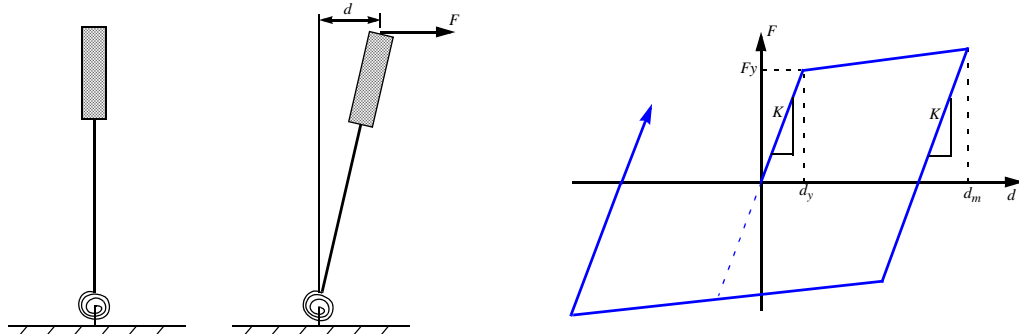
(c) Stiffness Degrading Model
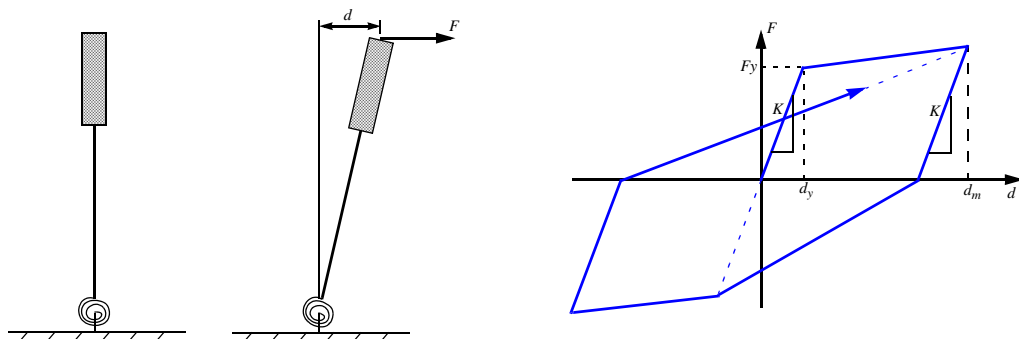
Figure 6-19. Linear and concentrated models.

193

(d) Fiber Element with Three Integration Points

Rigid End Zone

3 Integration
Points (3 IP)
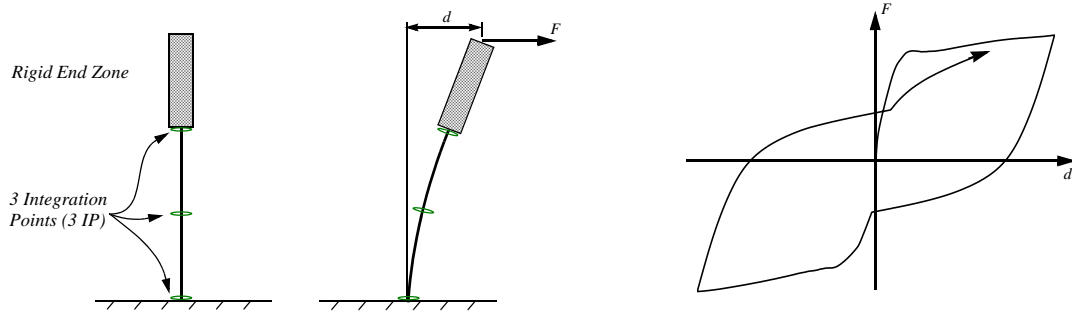
(e) Fiber Element with Four Integration Points + Base Spring

Rigid End Zone

4 Integration
Points (4 IP)

Base Spring

(f) Three Fiber Elements

Rigid End Zone

Top
Element (2 IP)

Middle
Element (3 IP)

Bottom
Element (2 IP)
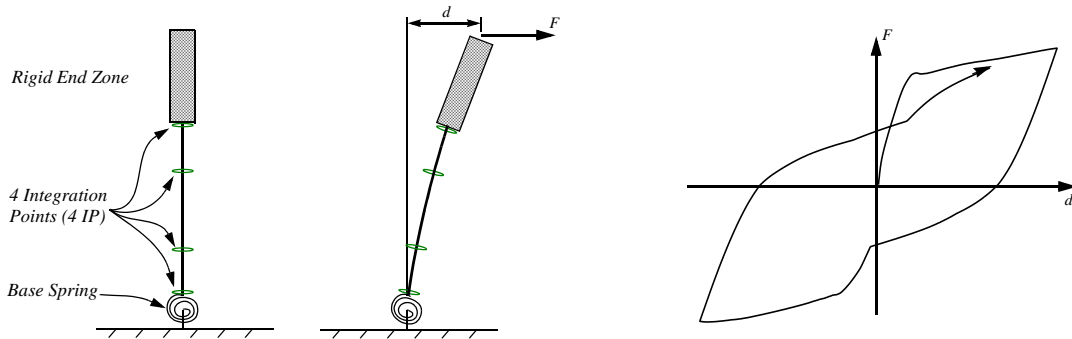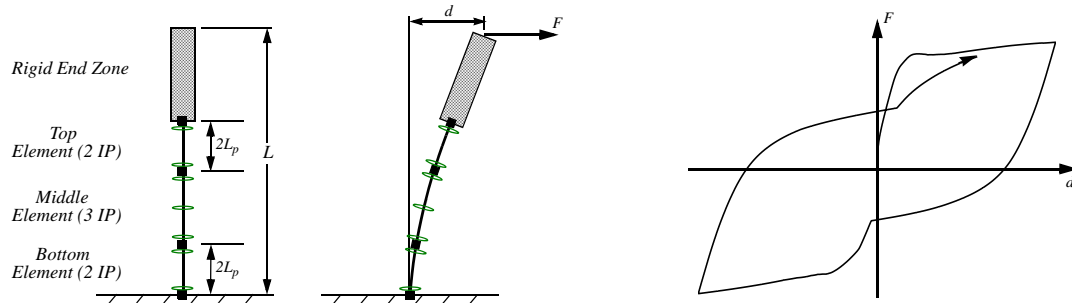
Figure 6-20. Fiber element models.

Each of the above models was used to predict the response of the specimens. The recorded shaking table accelerations were used as input ground motions, but the analyses were performed twice for each case using different methods of applying the ground motions. In the first method, the ground motions from all the runs were spliced together and analyzed in sequence as one *continuous* earthquake in order to simulate the actual starting conditions of each run including residual displacements and material loading history. In the second method, the ground motion for each run was analyzed *individually* assuming zero initial conditions at the beginning of the run. In both methods, the peak displacement and residual displacement reported in this section refer to the incremental displacement from the beginning of the run.

6.4.3.2 *Displacement Histories from Nonlinear Analysis*

Figures E-5 to E-13 compare the analytical displacement time histories to experimental results in the longitudinal and lateral directions. The accuracy of the different nonlinear models in predicting peak response and frequency content is evaluated. Only a representative portion of the results is presented, mainly concentrating on the bidirectional tests.

First, results corresponding to the analysis of Specimen A2 are inspected. Figures E-5 and E-6 compare recorded longitudinal displacements from Specimen A2 to displacements obtained from the two hysteretic models (bilinear and stiffness degrading models) and the three fiber models. It is interesting to note that the fiber models exhibit very similar responses despite some significant modeling differences. This is especially true for runs exceeding the yield level. Meanwhile, the response of the simpler bilinear and stiffness degrading models differ from the more accurate fiber model response. The bilinear model tends to be unstable especially when subjected to a continuous analysis of all the runs. The stiffness degrading model however provides a significant improvement over the bilinear model with some similarities to the response of fiber-based models. In terms of frequency content, the fiber models exhibit similar behavior and are slightly stiffer than the measured response. The hysteretic plastic hinge models exhibit an even stiffer response. The frequency difference gets larger and larger with each additional run due to period elongation of the specimen, and to the inability of the models to predict this type of behavior. All the analytical models also appear to be overdamped compared to the specimens, especially during low level excitations.

In the lateral direction, the fiber models result in a better match than the longitudinal direction (Figures E-7 and E-8). The match is best for the design and maximum levels, and is less accu-

rate at the yield level, because in the almost elastic run, stiffness and damping differences between the model and the specimen have a greater influence on the response. The fiber models perform better than the hysteretic models, with the bilinear model predicting a much larger displacement in the maximum level run.

The bidirectional displacement trajectories shown in Figures E-9 and E-10 reflect the performance of each model in both the longitudinal and lateral directions. As expected, the interaction predicted by fiber models is very satisfactory especially for larger excitations. The bilinear model fails at predicting the nature of the interaction, while the stiffness degrading model yields a fair match for the maximum level earthquake, but also fails at predicting interaction behavior at lower levels.

As for Specimen B2 (Figures E-11 to E-13), the analysis displacements are more out of phase with the test results due to the long duration of excitation. More peaks are missed, and the models that tend to be unstable diverge significantly from the actual results. This is illustrated in Figure E-11 in which the bilinear model diverges significantly from the measured response in the design level run. This carries over to the maximum level run, since the model already has a large residual deformation. Note that the analysis results are plotted such that all models appear to start at zero displacement. However, the actual residual displacements can be inferred from the previous runs.

The bidirectional response for Specimen B2 is predicted with less accuracy than in the case of Specimen A2, even with fiber models. This is attributed to the longer duration of the excitation which leads to the accumulation of error, over many cycles, due to small differences in the fundamental frequency of the column.

6.4.3.3 *Peak Displacements from Nonlinear Analysis*

A complete comparison of predicted and observed displacements is shown in Figures E-14 to E-37. Each plot compares the maximum and residual relative displacements obtained from nonlinear analysis models to the displacements measured during the test. The maximum displacements corresponding to all the runs are shown for two types of analysis: continuous analysis of the all the runs, or individual analysis of each individual run. For continuous analysis results, the reported peak displacement and residual displacement are modified by subtracting the residual displacement at the beginning of the run.

Looking at longitudinal displacement predictions for *individually analyzed* runs (Figures E-14, E-18, E-26 and E-30), it is generally observed that displacements at lower shaking levels

196

(around yield) are underestimated by up to 50%. On average, longitudinal displacement estimates for Specimens A1 and A2 (Figures E-14 and E-18) are better than those corresponding to Specimens B1 and B2 (Figures E-26 and E-30), which tend to be unconservative (low). It is also observed that the analytical models predict similar results for runs with equal magnitude, which is expected since the analyses were carried individually with zero initial conditions at the beginning of each analysis, including the assumption of zero residual displacement. For example, in Specimens A1/A2, the last run experienced a peak displacement that was larger than the peak seen in other runs with similar magnitude, while the opposite occurred with Specimens B1/B2. In all four cases, the analytical models predicted approximately the same deformations for all runs with similar magnitude.

The hysteretic models (bilinear and stiffness degrading) generally yielded smaller displacements for Specimens A1/A2, and larger displacements for Specimens B1/B2 than the other fiber models. In general, while all the models resulted in acceptable predictions, none was significantly superior to the others.

In the case of *continuously analyzed* runs, the predicted longitudinal displacements (Figures E-15, E-19, E-27 and E-31) are somewhat lower than those corresponding to individually analyzed runs, resulting in unconservative estimates for most runs. The bilinear model is very unstable in this type of analysis because of its tendency to overestimate residual displacements. Those residual displacements are carried over to following runs, which eventually leads to collapse due to P-Δ effects.

The fiber models yielded similar results in most cases, and the stiffness degrading model was satisfactory, and in some cases, superior to the fiber models (in terms of displacement prediction).

Since Specimens A2 and B2 were subjected to bidirectional excitations, the lateral displacement predictions were also compared to the experimental displacements. In general, the bilinear model significantly overestimated deformations for individually analyzed runs, and it became unstable during continuous analysis. The lateral displacements estimated by the other models were reasonable in general. They were slightly higher than measured in the case of Specimen A2, and slightly lower in the case of Specimen B2.

Residual displacements at the end of each run were poorly predicted by all nonlinear models. In general, the fiber models predicted the small residual displacement at the first design level, but failed to predict any further residuals, and were generally incapable of predicting large residu-

197

als. In most cases, the residual displacement predicted by the fiber model were smaller than measured. The hysteretic models were incapable of predicting any of the residual deformations, and the bilinear model was especially erroneous. The residuals predicted during continuous analysis by fiber models, were generally better than those predicted during individual analyses. In summary, the concentrated models exaggerated the residual displacements, often in the wrong direction, while the fiber models underestimated the residual displacements.

6.4.3.4   *Peak Curvatures from Nonlinear Analysis*

In addition to the estimation of global displacements, a good approximation of local behavior is essential for performance based design and evaluation. The quantity of immediate interest is the curvature in the plastic hinge region. It was shown in Section 5.5.2 that when the neutral axis depth is known, section strains can be obtained from the curvature using plane section assumptions. It was also shown that the curvatures themselves may be approximated from the tip displacement using Equations 5-25 through 5-27. This allows the curvatures to be indirectly computed for the hysteretic models for a cantilever column. Fiber models, on the other hand, are capable of reporting both curvatures and strains, which is expected to be reasonably accurate, provided that the weights of the integration points of the elements are appropriately selected.

The curvatures obtained from the analytical results were compared to the measured curvatures in Figures E-38 and E-39. In general, the fiber models whose number of integration points were carefully selected (fiber element with 3 integration points, and fiber model consisting of 3 elements), were the best in predicting curvatures. The hysteretic models (especially the stiffness degrading model) produced good estimates when their displacement estimates were reasonable, since for those models, curvatures are directly calculated from displacements.

Regardless of the model used, a priori knowledge of the plastic hinge length is essential for proper prediction of local response.

6.4.3.5   *Peak Forces and Moments from Nonlinear Analysis*

Good estimates of the peak shear forces and moments are needed to ensure that the strength capacity of an element is not exceeded at critical locations, and for critical modes of failure. In the analysis of specimens A1 and A2, the fiber models overestimated longitudinal shears by up to 100% when runs were analyzed individually (Figure E-40), but showed a great improvement with continuous analysis (Figure E-42). Lateral shears were underestimated for all models.

For Specimens B1 and B2, all models tended to underestimate the longitudinal shear force. The 3-element fiber model yielded the best results under both continuous and individual run anal-

ysis. The lateral shear forces were predicted with adequate accuracy. Overall, the 3-element model outperformed the other models in predicting the shear variations across runs, but only under continuous analysis, and with some magnitude discrepancies.

Considering base moment predictions obtained by continuous analysis of all the runs (Figures E-46 to E-49), the most obvious observation for all the models is an underestimation of the base moment in the longitudinal direction by around 20% to 25%.

Results for moments in the lateral directions were mixed. For Specimen A2, the lateral base moment was overestimated by about 15% with fiber models to more than 50% with hysteretic models. For Specimen B2 however, fiber model estimates for the lateral base moment were generally in line with observations, while hysteretic models overestimated the moments. It is noted that the base moments observed in the lateral direction were significantly smaller than those recorded in the longitudinal direction, and that analyzing each run individually appears to have little or no effect on the base moments.

Top moments for Specimens A1 and A2 are well estimated in the longitudinal direction (Figure E-50), but are underestimated by around 50% in the lateral direction (Figure E-51). For Specimens B1 and B2, both longitudinal and lateral moments are underestimated by about 30% during the design and maximum level runs (Figures E-52 and E-53). In all cases, top moments are overestimated for small excitation levels by up to 150%. Individual analysis of each run does not affect fiber model moments, but results in a significant decrease in top moments obtained from the bilinear and stiffness degrading models.

6.4.3.6   Energy Dissipation from Nonlinear Analysis

The nonlinear response of a structure to a ground motion depends on the amount of energy dissipated due to inelastic cyclic loading. The amount of dissipated energy is often used in computing damage indices and in the state determination of some types of elements. It is therefore important to evaluate the different analytical models and compare their predicted energy dissipation to the experimental data. Figures E-54 to E-65 show the energy dissipated at each run during the actual test and each of the analysis simulations. Results are shown both for continuous and individual analysis cases.

In the longitudinal direction, the energy dissipation is relatively well predicted by all analysis models, except in the case of the bilinear model which becomes unstable under continuous analysis. The stiffness degrading model also has a tendency to overestimate energy dissipation. A greater discrepancy between fiber and hysteretic models appears in the lateral direction, in which

199

the hysteretic models significantly overestimate energy dissipation, while the fiber models some-what underestimate it. Overall, the fiber models gave the overall agreement with the actual energy dissipation observed.

6.4.3.7   *Damage Indices from Nonlinear Analysis*

Damage indices are compared for all considered models in Figures E-66 to E-73. Results for both the Park and Ang and the low-cycle fatigue damage indices are shown for continuous anal-ysis. Each figure shows both the cumulative damage after each run and the incremental damage induced by that run. A significant difference between the Park and Ang index and the fatigue damage index is that the Park and Ang index becomes almost saturated after the first or second large excitation (due to the displacement contribution d_{max}/d_{ult}), while the fatigue index keeps increasing at a somewhat steady rate. This is particularly the case for well confined columns for which energy dissipation generally has a small contribution to the Park and Ang index. Overall, all analysis models underestimate both damage indices. This is largely attributed to the fact that all of the models considered generally underestimated the peak displacement, which is the most impor-tant factor in both the Park and Ang and fatigue damage indices.

6.4.4   Summary of Analysis Observations

In order to facilitate the evaluation of the different analytical models used in this section, a subset of the results reported in Appendix E are plotted in Figures 6-21 to 6-27. Results shown include measured and computed quantities mainly during the first design and first maximum level excita-tions of each specimen. In Figures 6-21 to 6-24, the peak displacement, curvature, energy, shear force, base moment and top moment were compared by plotting the ratio of the analytical to the measured response. Each quantity is reported for each of the analytical models, in both the longi-tudinal and lateral directions. A ratio of one would indicate that the specified model is in full agree-ment with the experimental results. The relative error for each model is computed for each case as the ratio of analytical to experimental results minus one, and each of the five models is ranked from 1 to 5 based on the absolute value of the error. The relative error and rank are listed on top of the corresponding vertical bar in Figures 6-21 to 6-24.

Figures 6-25 and 6-26 show the amounts of incremental and cumulative damage experi-enced during the design and maximum levels, as predicted by three different damage indices. Figure 6-27 shows the cumulative indices at the time of failure, defined at the first fracture of either the spiral or longitudinal reinforcement. Note the great similarity between the ductility and Park

and Ang indices, which is attributed to the small energy contribution in the Park and Ang model, since β is taken as 0.02.

Instead of selecting the best model visually or by inspection, a process governed by subjective judgement, a procedure is followed to rank the overall suitability of any given model for predicting a given response quantity, or for the general ability of one model to predict most response quantities with acceptable accuracy. A number of evaluation methods are considered:

1. The first method considered involves ranking each model (from 1 to 5) in terms of estimating a given quantity for either the design or maximum run of a specimen. The ranks are summed for each model over different quantities and/or multiple runs and specimens. The model with the lowest rank is the best model overall.

2. The second method sums the relative error amounts (in absolute value) for each model over different quantities and/or multiple runs and specimens. The model with the lowest total error is the best overall model.

3. The third method is similar to the second, however, the sum of the squares of the errors is used instead of a simple absolute sum.

The first method is dismissed because it tends to give very different scores to results that are very close to each other, such as the results for base moment in Figure 6-21. The second method is picked as the most balanced, while the third method is abandoned since it overly penalizes a model for yielding a large error for one quantity. The results of this evaluation are shown in Tables 6-2 and 6-3 for the longitudinal and lateral directions, respectively. The quantities evaluated are those shown in Figures 6-21 to 6-24. The table results clearly show that the fiber model with three elements along the length yields the best overall average for both the longitudinal and lateral directions, and is followed by the fiber model with one element and three integration points. The bilinear model yields the worst overall accuracy for each of the specimens, in both the longitudinal and lateral directions.

6.4.5   Sensitivity to Other Modeling Considerations

6.4.5.1   Rotational Moment of Inertia

The rotational moment of inertia causes a second mode contribution to the column's response, especially to the shear force in the column. Figure 6-28 shows the effect of varying the amount of
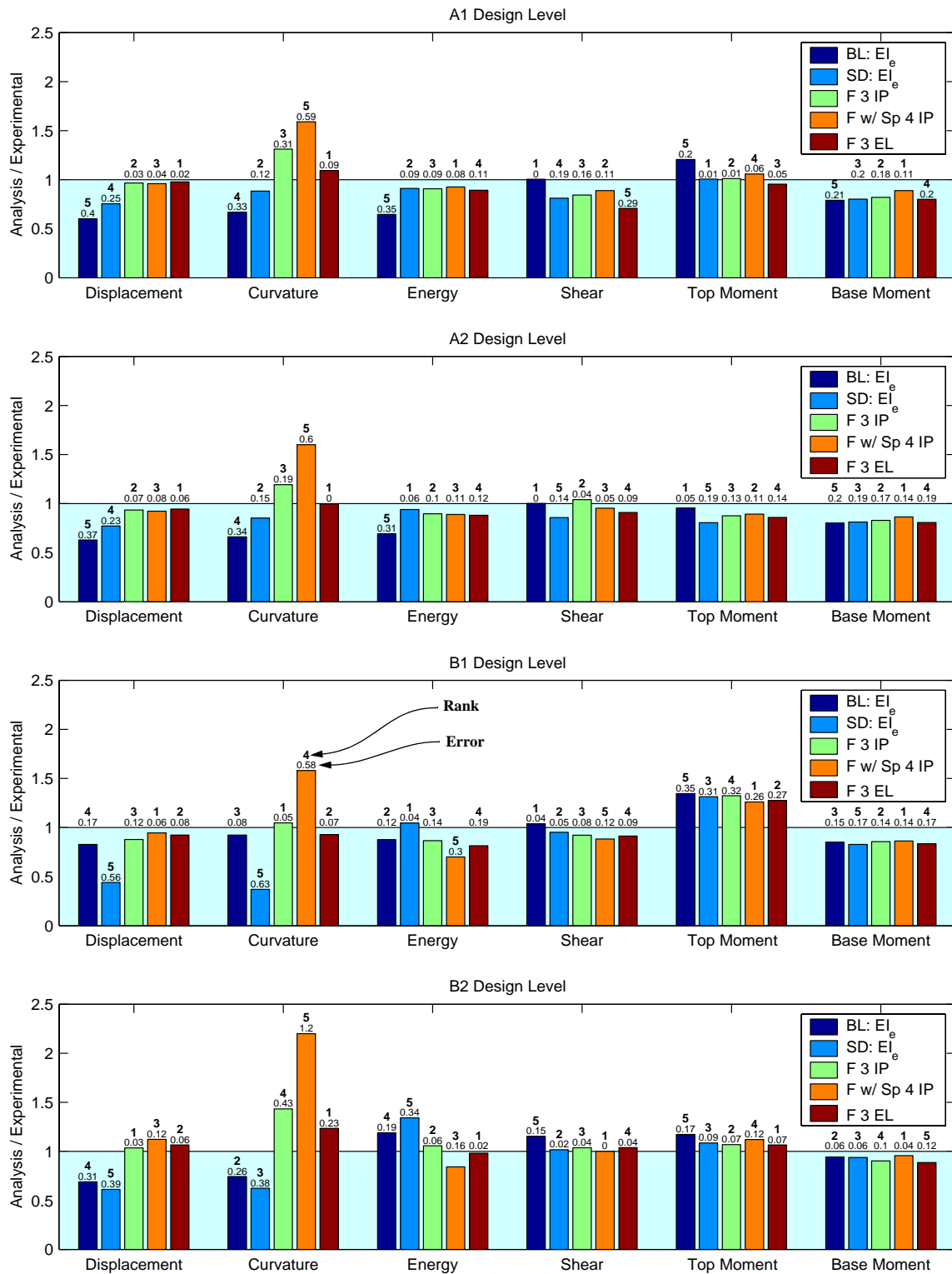
Figure 6-21. Ratio of analytical to experimental results for various response quantities in the longitudinal direction at the first design level.

202
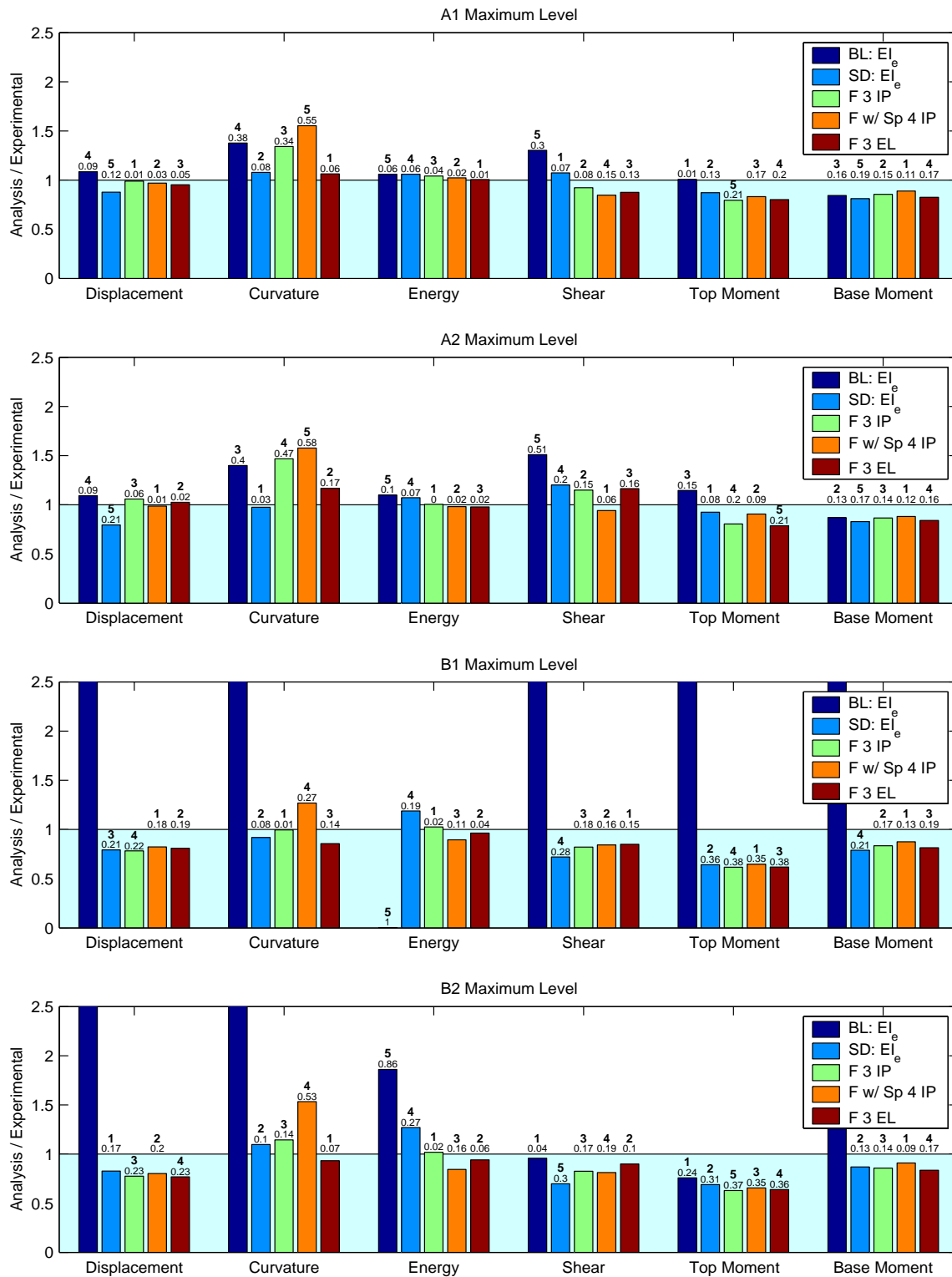
Figure 6-22. Ratio of analytical to experimental results for various response quantities in the longitudinal direction at the first maximum level.
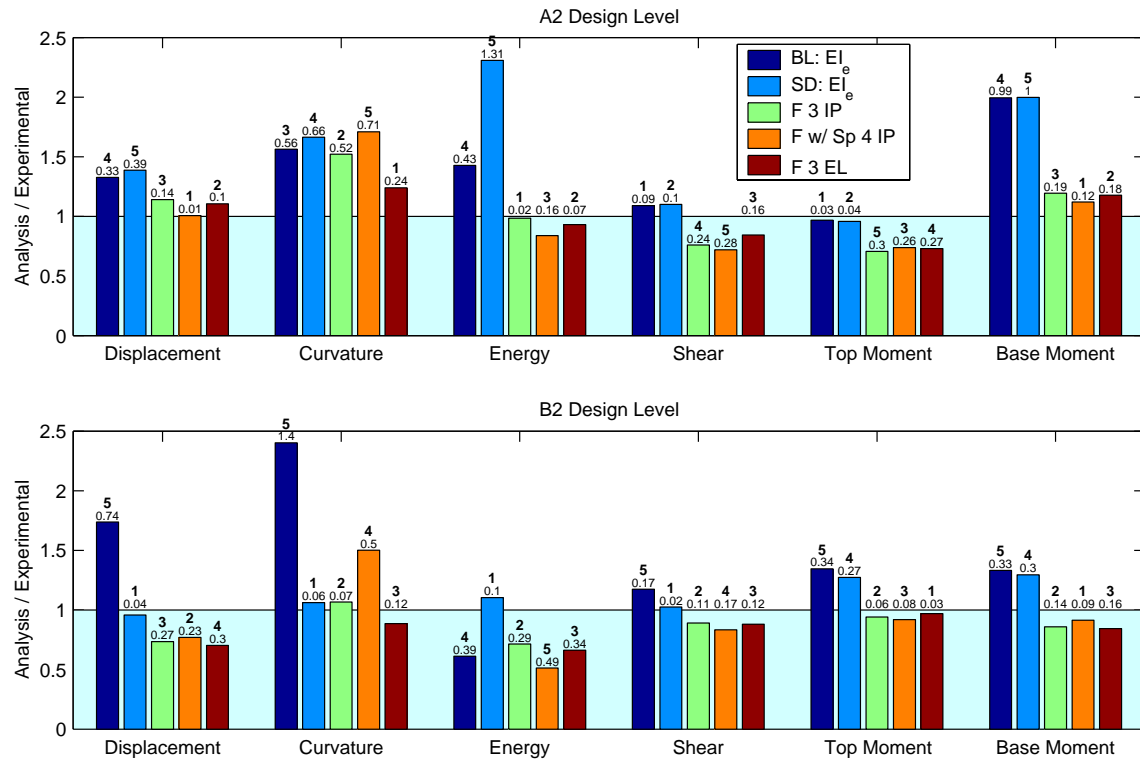
Figure 6-23. Ratio of analytical to experimental results for various response quantities in the lateral direction at the first design level.
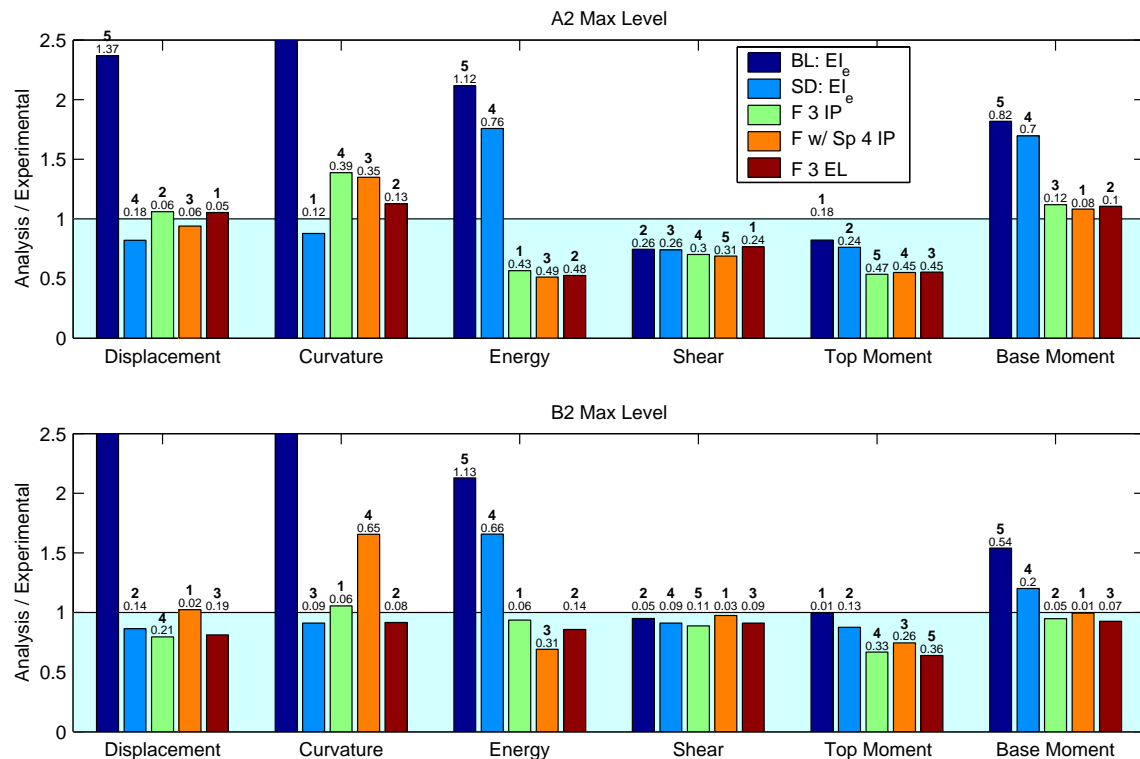
Figure 6-24. Ratio of analytical to experimental results for various response quantities in the lateral direction at the first maximum level.
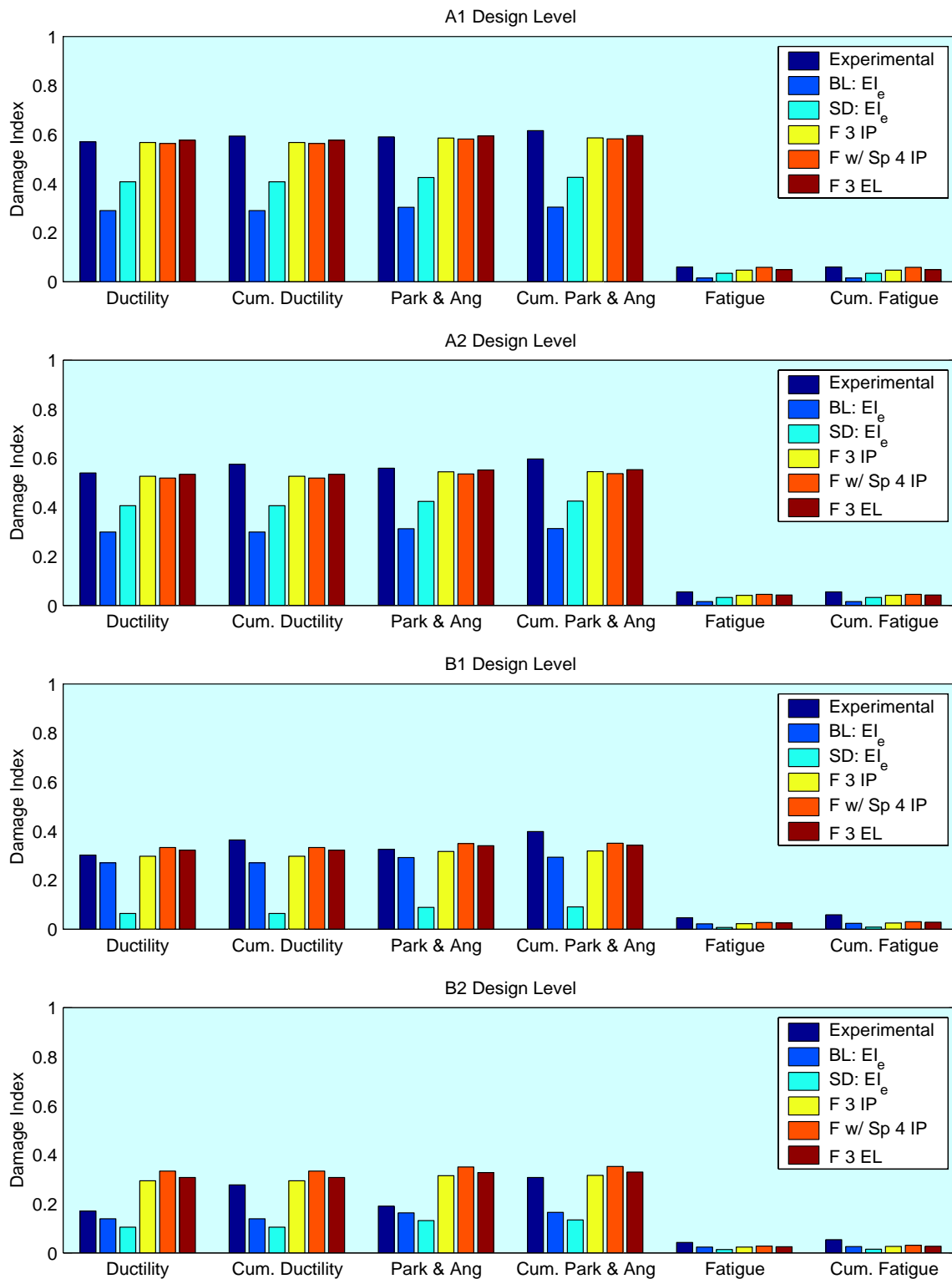
Figure 6-25. Analytical and experimental results for various damage indices at the first design level.
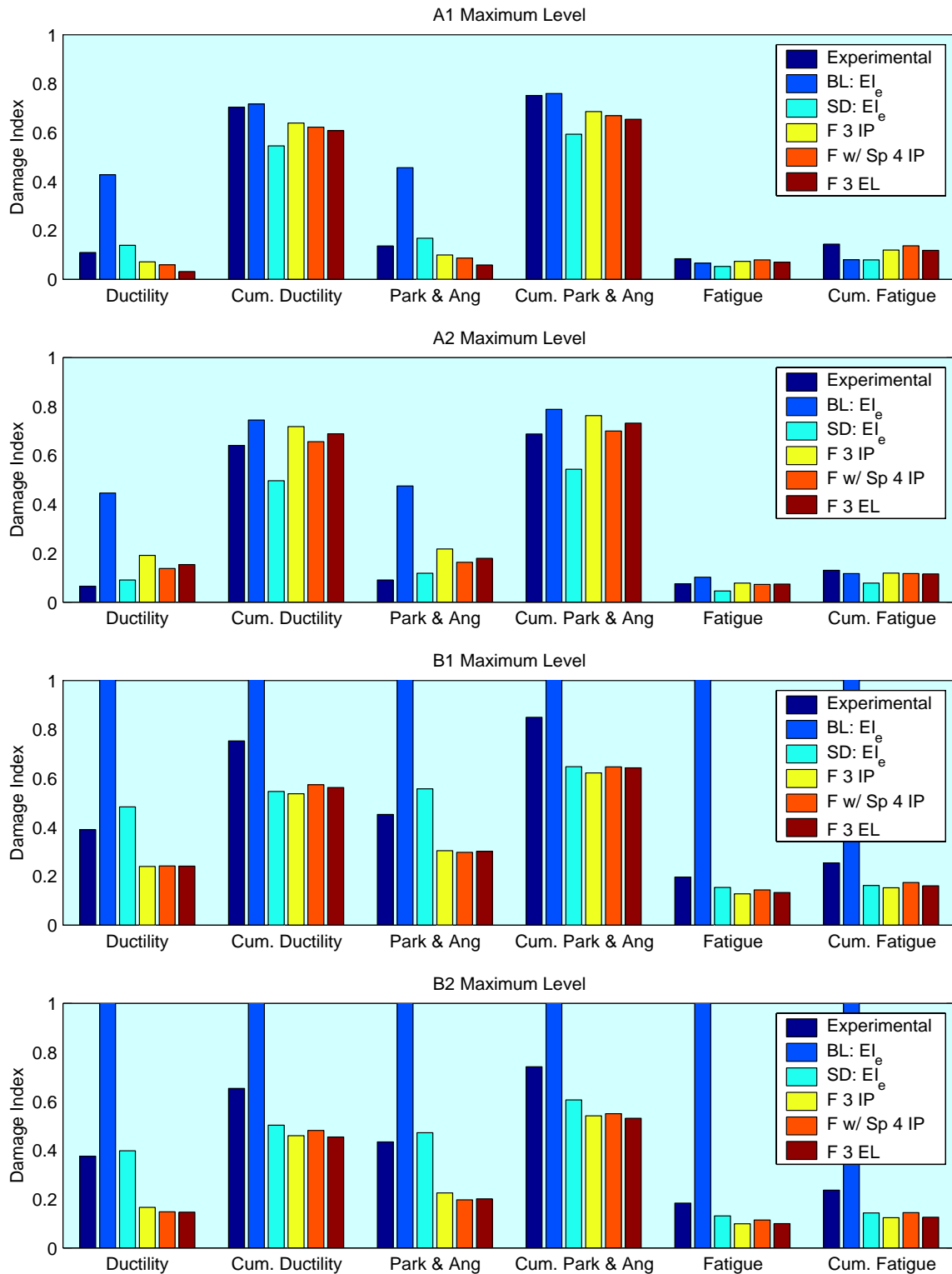
Figure 6-26. Analytical and experimental results for various damage indices at the first maximum level.
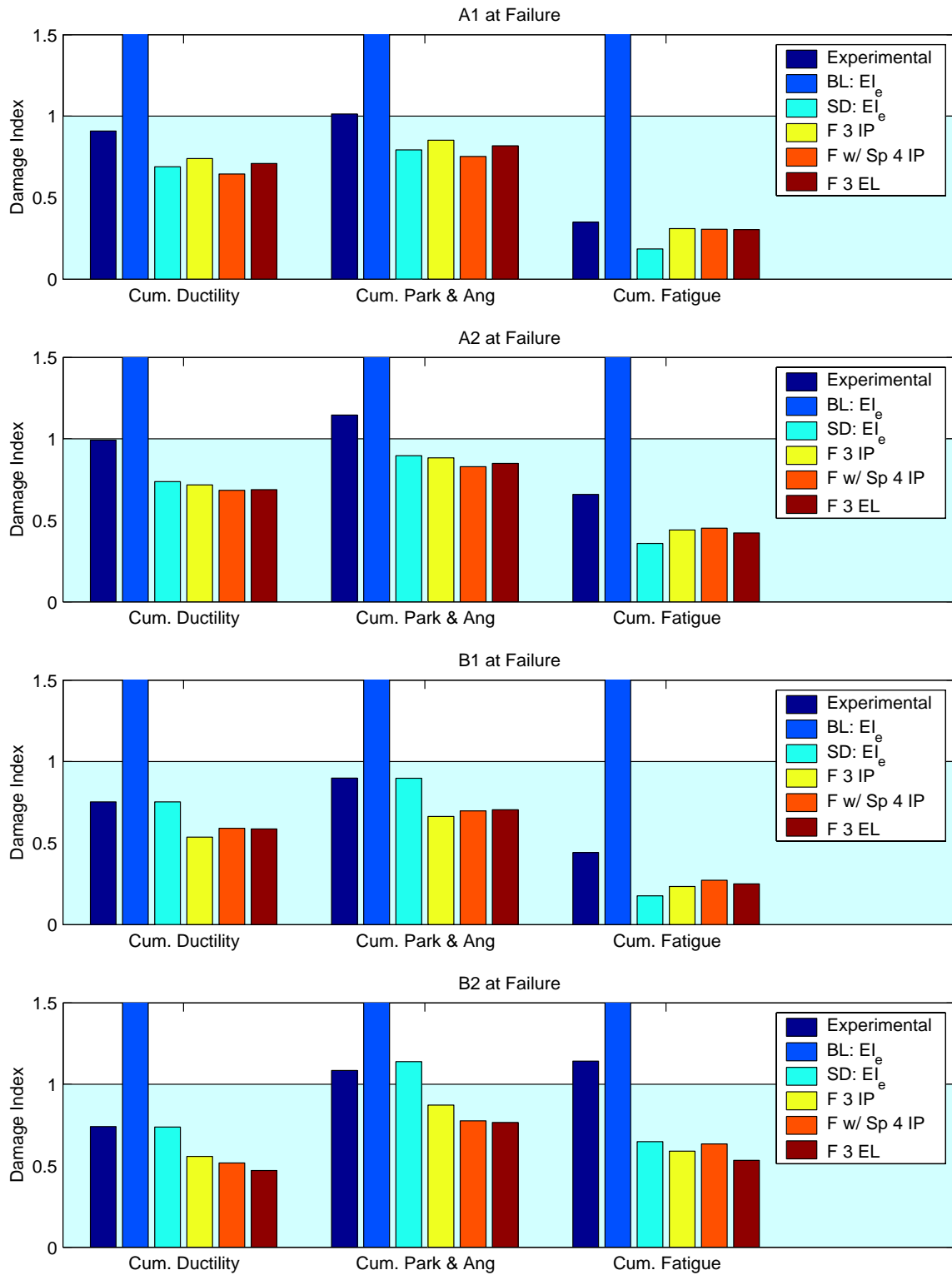
Figure 6-27. Analytical and experimental results for various damage indices at failure.

Table 6-2 Error evaluation and accuracy ranking of the different analytical models for predicting displacements, forces and energy dissipation in the longitudinal direction.

	Bilinear Model		Stiffness Degrading Model		Fiber Model with 3 IP		Fiber Model with Spring and 4 IP		Fiber Model with 3 Elements	
	Error Sum	Rank	Error Sum	Rank	Error Sum	Rank	Error Sum	Rank	Error Sum	Rank
A1 Design	1.505	5	0.844	3	0.789	2	0.986	4	0.763	1
A1 Max	0.988	4	0.653	2	0.823	3	1.041	5	0.615	1
A1 Avg	1.247	5	0.749	2	0.806	3	1.014	4	0.689	1
A2 Design	1.267	5	0.966	3	0.702	2	1.082	4	0.606	1
A2 Max	1.375	5	0.75	1	1.01	4	0.885	3	0.752	2
A2 Avg	1.321	5	0.858	3	0.856	2	0.983	4	0.679	1
B1 Design	0.908	3	1.773	5	0.852	1	1.453	4	0.867	2
B1 Max	8165	5	1.334	4	0.981	1	1.192	3	1.097	2
B1 Avg	4083	5	1.554	4	0.916	1	1.323	3	0.982	2
B2 Design	1.141	3	1.27	4	0.727	2	1.646	5	0.537	1
B2 Max	14.32	5	1.284	3	1.077	2	1.513	4	0.989	1
B2 Avg	7.731	5	1.277	3	0.902	2	1.58	4	0.763	1
ALL Design	1.205	3	1.213	4	0.767	2	1.292	5	0.693	1
ALL Max	2045	5	1.005	3	0.972	2	1.158	4	0.863	1
ALL Avg	**1023**	**5**	**1.109**	**3**	**0.87**	**2**	**1.225**	**4**	**0.778**	**1**

Table 6-3 Error evaluation and accuracy ranking of the different analytical models for predicting displacements, forces and energy dissipation in the lateral direction.

	Bilinear Model		Stiffness Degrading Model		Fiber Model with 3 IP		Fiber Model with Spring and 4 IP		Fiber Model with 3 Elements	
	Error Sum	Rank	Error Sum	Rank	Error Sum	Rank	Error Sum	Rank	Error Sum	Rank
A2 Design	2.433	4	3.498	5	1.407	2	1.54	3	1.018	1
A2 Max	6.074	5	2.258	4	1.765	3	1.744	2	1.445	1
A2 Avg	4.254	5	2.878	4	1.586	2	1.642	3	1.231	1
B2 Design	3.377	5	0.802	1	0.931	2	1.553	4	1.06	3
B2 Max	13.25	5	1.302	4	0.824	1	1.274	3	0.943	2
B2 Avg	8.315	5	1.052	3	0.878	1	1.414	4	1.001	2
ALL Design	2.905	5	2.15	4	1.169	2	1.547	3	1.039	1
ALL Max	9.664	5	1.78	4	1.295	2	1.509	3	1.194	1
ALL Avg	**6.285**	**5**	**1.965**	**4**	**1.232**	**2**	**1.528**	**3**	**1.116**	**1**

rotational inertia, relative to the specimen, on the displacement, shear, base moment and top moment in the column. Increasing the rotational inertia generally decreases displacement demands while increasing the shear and top moment in the column.
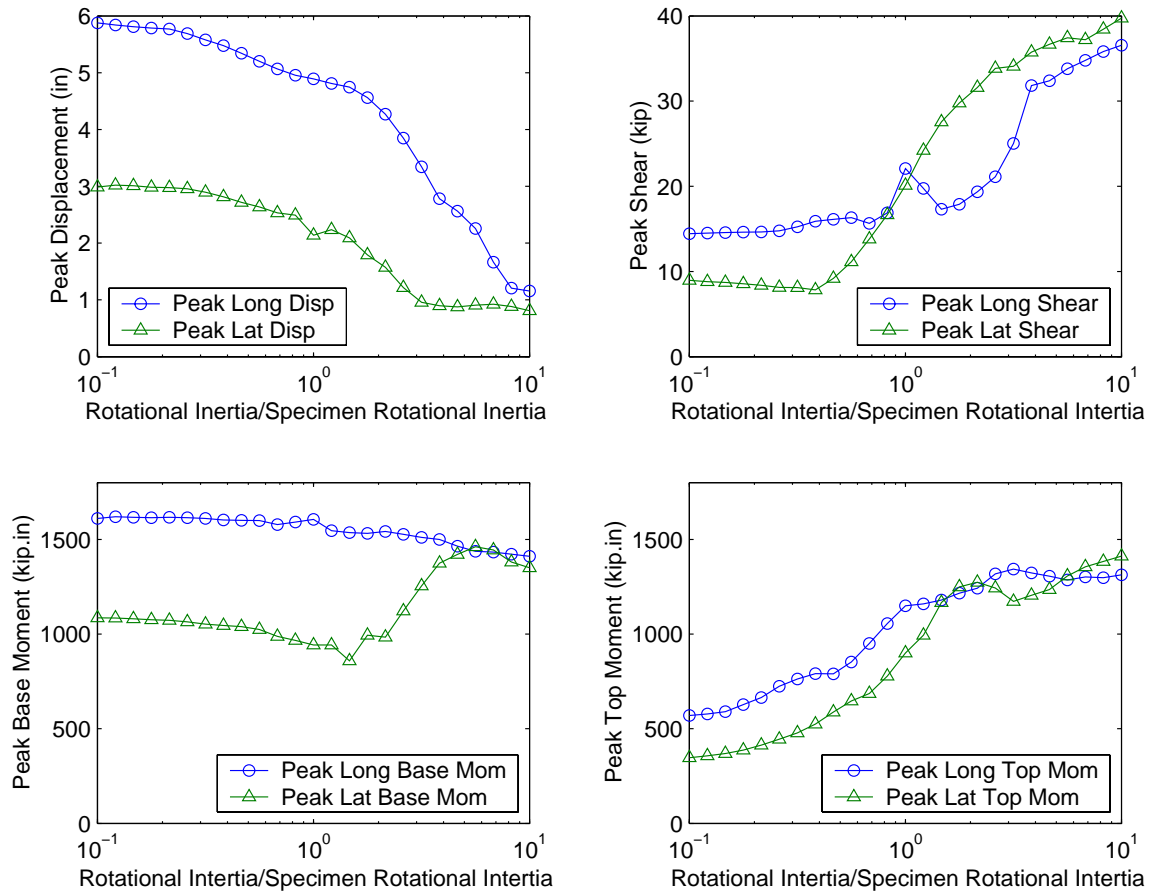
Figure 6-28. Effect of rotational moment of inertia on response quantities.

6.4.6   Recommendations for Modeling Reinforced Concrete Columns

Based on the above observations, the following conclusions are made regarding the dynamic analysis of circular reinforced concrete columns:

1. Bilinear models should be avoided when possible, because of their inability to model the stiffness degrading behavior characteristic of reinforced concrete members.

2. Stiffness degrading models offer significant advantages over bilinear models. However, their partial inability to predict residual displacements and bidirectional interaction must be recognized. They may be used in certain circumstances when computational expense is important.

3. Fiber models are preferred to concentrated models, because of their inherent ability to represent bidirectional and axial load interaction and because of their numerical stability.

4. Refinements of fiber models may not yield significant improvements in prediction of global response quantities such as peak and residual displacements. In particular, using concentrated hinges to model the effect of bar slip at the base of the column may introduce convergence problems especially if the properties of the spring are not well-tuned to the section properties. It is hence recommended that the bond-slip formulation be included in the section determination of the plastic region in order to ensure compatibility. When such a model is not available, the added flexibility due to bond slip could be compensated for by adding a linear spring, or by using a larger equivalent plastic hinge length.

5. For columns subjected to multiple earthquakes, continuous analysis of the structure is preferred since this preserves information on prior damage and strain states. However, a significant gain in accuracy from this approach is only expected for models that are accurate and capable of predicting all the aspects of the response in the first place.

6.5   PARAMETRIC ANALYSES BASED ON THE TEST SPECIMENS

In the test program, only a few loading conditions could be investigated. As such, the 3-element fiber model identified in the previous section is now used to assess the effect of other variables related to ground motions intensity and loading conditions. The different analyses aimed at evaluating the effect of ground motion intensity on:

1. Bidirectional column response as compared to unidirectional response.

2. The effect of vertical ground acceleration on column response.

3. The relationship between inelastic and elastic response.

4. The effect of axial load eccentricity on stability and displacement demand.

All of the analyses included P-Δ effects and used the 3-element fiber model identified in the previous section. The mass supported by the column was included in the model in the x, y and z directions. For simplicity and consistency in the comparisons, the rotational mass of inertia of the mass block was not considered.

The ground motions used were based on the same ground motions used in the experimental study: the Northridge Olive View and the Llolleo records. However, these parametric analyses used the original unfiltered records with their durations scaled by an appropriate time scale factor similar to that used for the shaking table tests. The time scale factors used for the Olive View and Llolleo records were $\sqrt{4.5}$ and $\sqrt{2}$, respectively. The additional filtering done in the experiments to account for the characteristics of the shaking table were not applied. The time histories and spectral ordinates of the records are shown in Figures 6-29 through 6-32 for an intensity factor of one.

Using the column's nominal yield strength and supported mass, it is estimated that the column would yield at a spectral acceleration of about 0.24g. Assuming an effective period of vibration of about 0.5 seconds at low amplitudes, the spectral demands due to the Olive View and Llolleo records at the effective period of vibration are computed as 0.92g and 0.90g, respectively. Hence, the column is expected to remain almost elastic for ground motion intensity factors less than 0.26 and 0.27, respectively, under the Olive View and Llolleo records.

6.5.1   Effect of Bidirectional Excitation

The experiments showed that the peak displacement in the longitudinal direction did not change significantly when a second horizontal component was applied concurrently. This behavior is analytically investigated for different levels of ground motion shaking by subjecting the analytical model to unidirectional and bidirectional excitations, scaled by different amplification factors.

Time Histories of the model displacement under one-dimensional (1D) and two-dimensional (2D) horizontal excitations are compared in Figure 6-33 for analyses performed using the Northridge record. The analysis results show that going from 1D to 2D excitation causes a small decrease in the peak longitudinal displacement (dx). However, going from 1D to 2D excitation in the lateral direction causes a larger difference in the lateral displacement (dy) history. This reaffirms previous observations that bidirectional interaction effects are more pronounced in the direction subjected to the weaker component of the earthquake.

The dependence of this behavior on the ground motion intensity is shown in Figures 6-34 and 6-35. The top plot of each figure shows the peak displacements for a given intensity of the input ground motion. dx, dy and d (Equation 6-28) represent the peak longitudinal, lateral and radial displacements, respectively. The results show that while the peak longitudinal displacement is virtually unchanged between the 1D and 2D loading cases, as illustrated by the ratio dx_{2D}/dx_{1D}, the peak lateral displacement shows larger variations over some intensity ranges (ratio dy_{2D}/dy_{1D}),
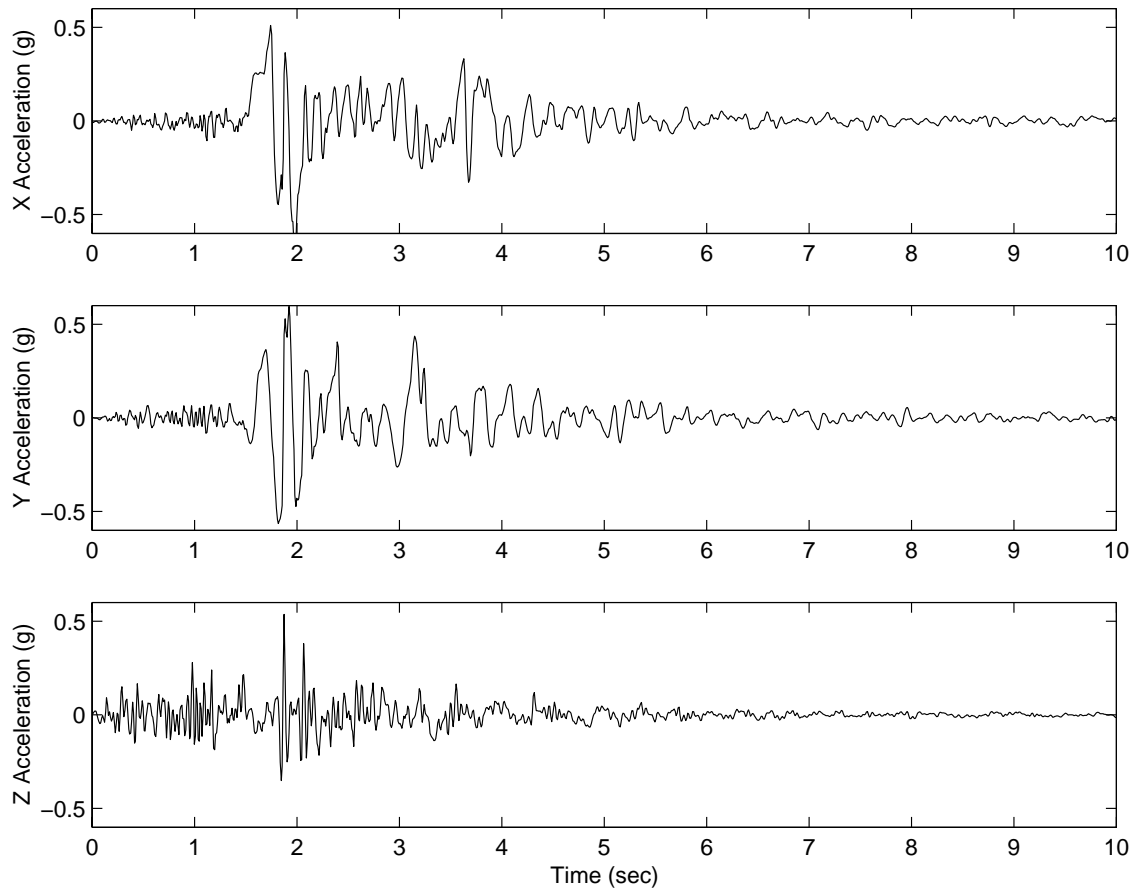
Figure 6-29. Acceleration components of the 1994 Northridge Olive View record. The duration of the record was scaled by $1/\sqrt{4.5}$.
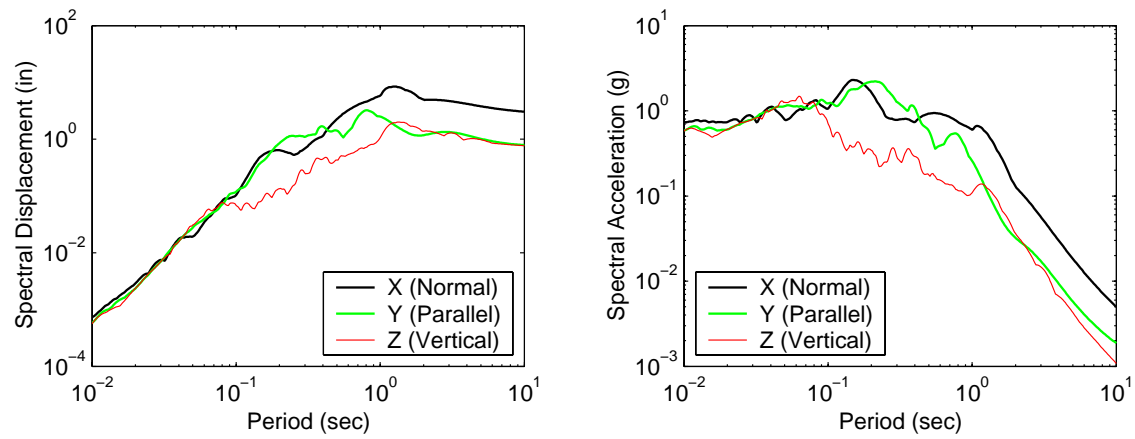
Figure 6-30. Displacement and acceleration spectra for the three components of the Northridge Olive View record. The duration of the record was scaled by $1/\sqrt{4.5}$.
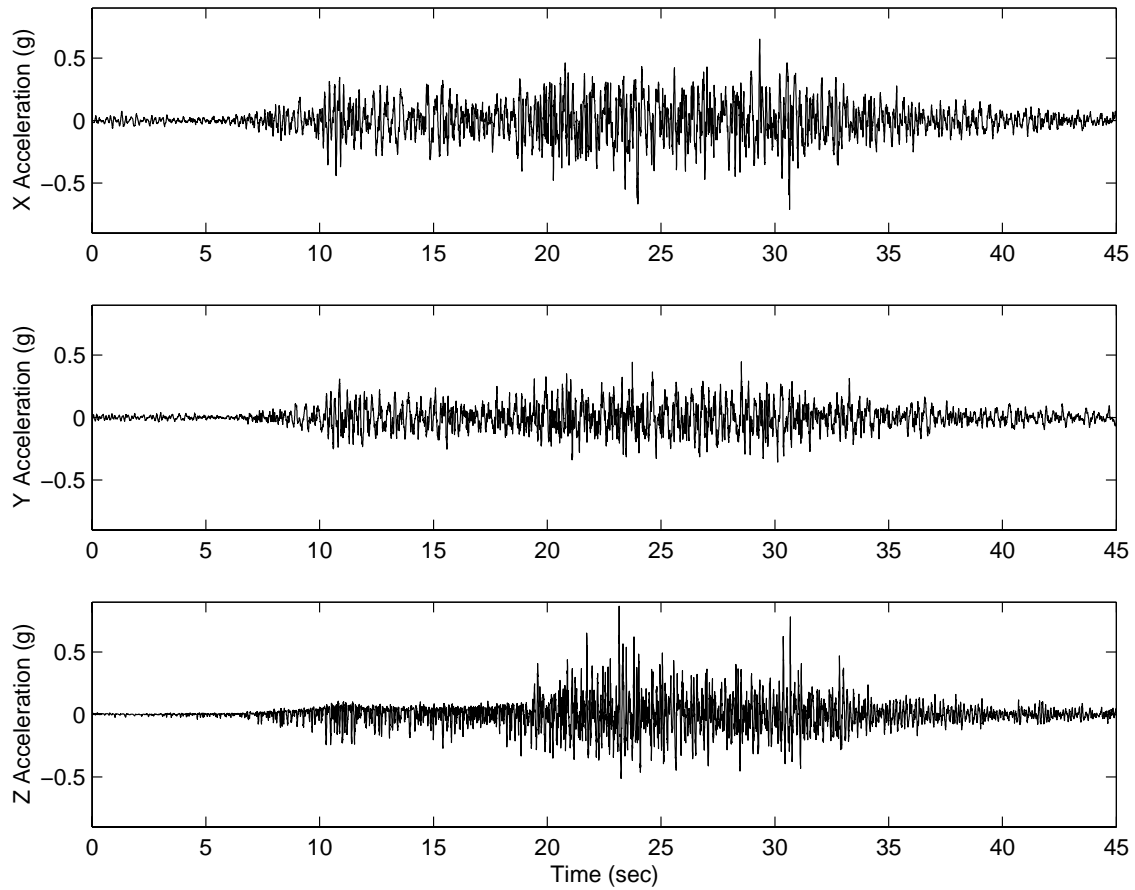
Figure 6-31. Acceleration components of the Llolleo record from the 1985 Chile earthquake. The duration of the record was scaled by $1/\sqrt{2}$.
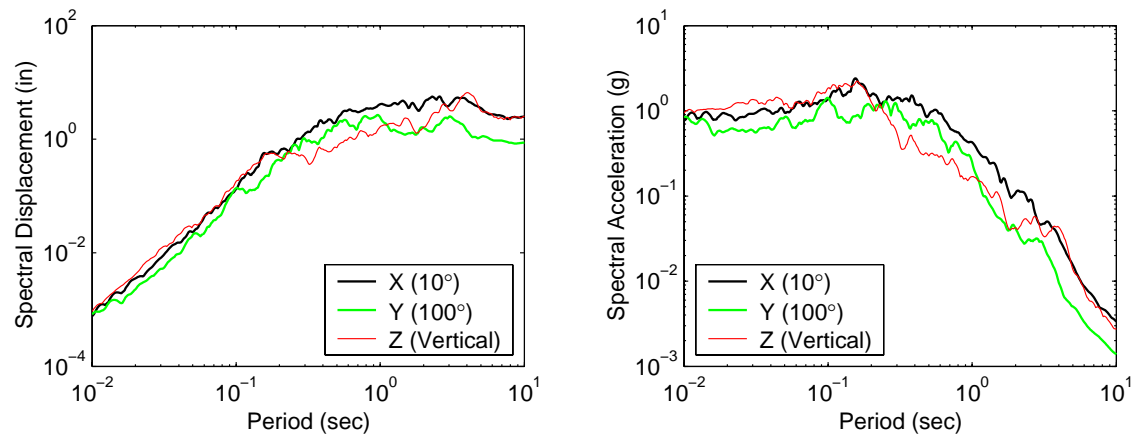
Figure 6-32. Displacement and acceleration spectra for the three components of the Llolleo record. The duration of the record was scaled by $1/\sqrt{2}$.

213
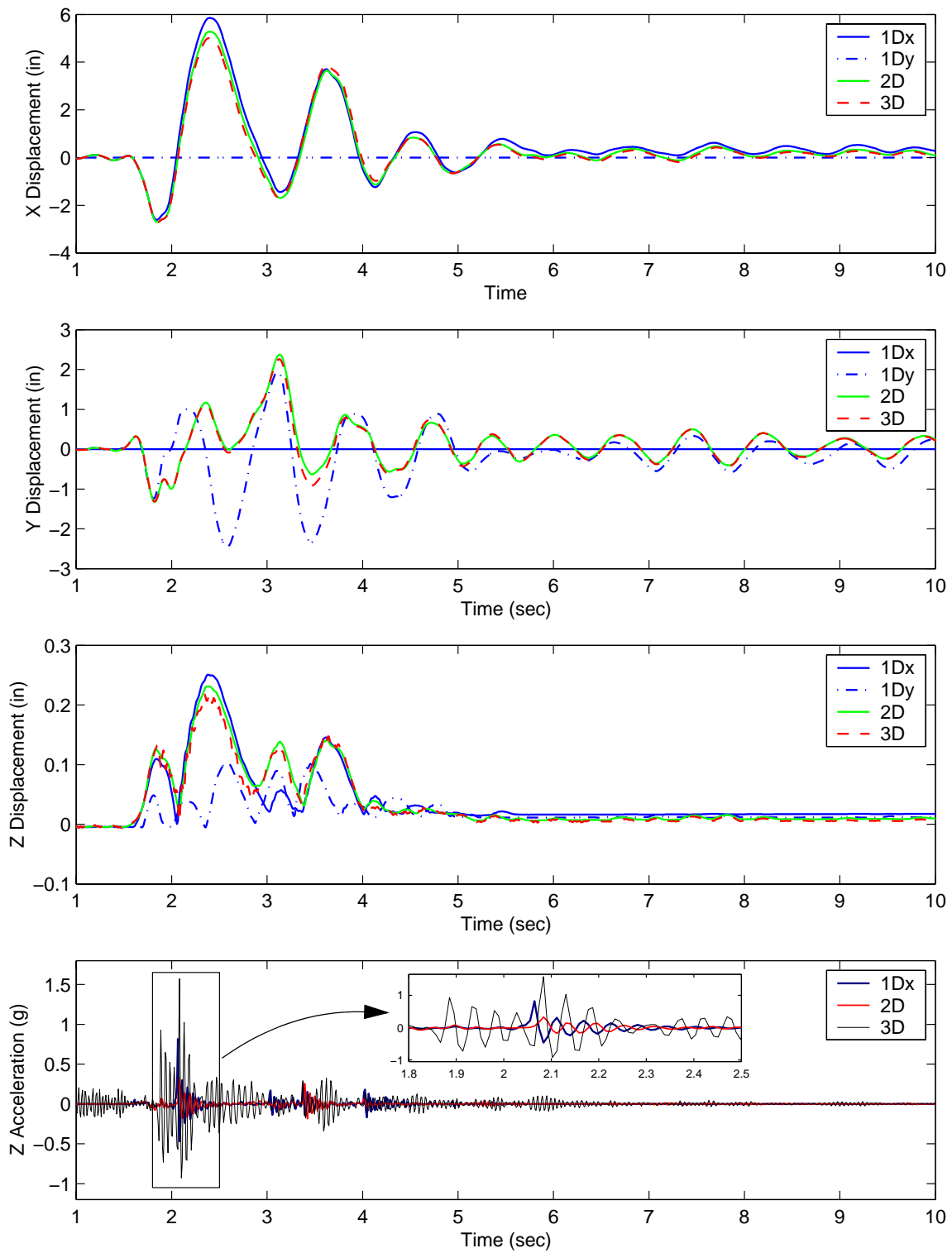
Figure 6-33. Analytical *x*, *y* and *z* displacements and *z* acceleration at the center of mass under 1D, 2D and 3D excitations of the specimen by the Northridge Olive View record shown in Figure 6-29 with an intensity factor of 1.

214

especially at ground motion intensities less than one. Bidirectional loading generally causes a small decrease in the displacement in each direction as compared to unidirectional loading in that direction. These figures also show that the peak radial displacement d (Equation 6-28) is nearly identical to the peak displacement in the longitudinal direction, d_x.

$$d = \sqrt{d_x^2 + d_y^2} \qquad (6\text{-}28)$$

The other ratios shown in Figures 6-34 and 6-35 are: the ratio of maximum bidirectional plane displacement to the maximum unidirectional longitudinal displacement (dx_{2D}/dx_{1D}), and the ratio of the plane displacement estimated from the unidirectional analyses (d_{SRSS}/d_{2D}) to the bidirectional plane displacement. The estimated displacement d_{SRSS} is computed using the SRSS rule as shown in Equation 6-29.

$$d_{SRSS} = \sqrt{dx_{1D}^2 + dy_{1D}^2} \qquad (6\text{-}29)$$

The ratio d_{2D}/dx_{1D} is close to one for most intensities with some fluctuations at low intensities (intensity factor < 0.25). This shows that for the model and ground motions used, the peak response can be predicted with fair accuracy from the longitudinal component, and that the smaller lateral component can be ignored.

Under the Northridge record, the ratio d_{SRSS}/d_{2D} takes values between 1 and 1.2. Hence, the bidirectional displacement is slightly overestimated using the SRSS rule and the unidirectional results. Under the Llolleo record, the SRSS prediction is even more conservative, with d_{SRSS}/d_{2D} reaching about 1.5 at high intensity factors, and exceeding 2 at intensity factors less than 0.25.

6.5.2   Effect of Vertical Ground Motion

In general, the effect of vertical ground motion records on the response of bridges has often been ignored. However, research by Saadeghvaziri and Foutch [86], Button et al. [10] and others suggests that vertical acceleration should be considered, especially for sites close to active faults, and when large peak ground accelerations are expected. Saadeghvaziri and Foutch modeled the non-linear behavior of actual bridges, and found that the fluctuating axial forces in the columns caused by the vertical motion can cause instability of the hysteretic loops and possibly increase the ductility demand. The variation of axial forces was also found to cause fluctuations in the shear and moment capacities of the section. In addition, large forces may be generated in the foundations and abutments. Button et al. used attenuation relationships by Sadigh et al. [89] and Abrahamson and
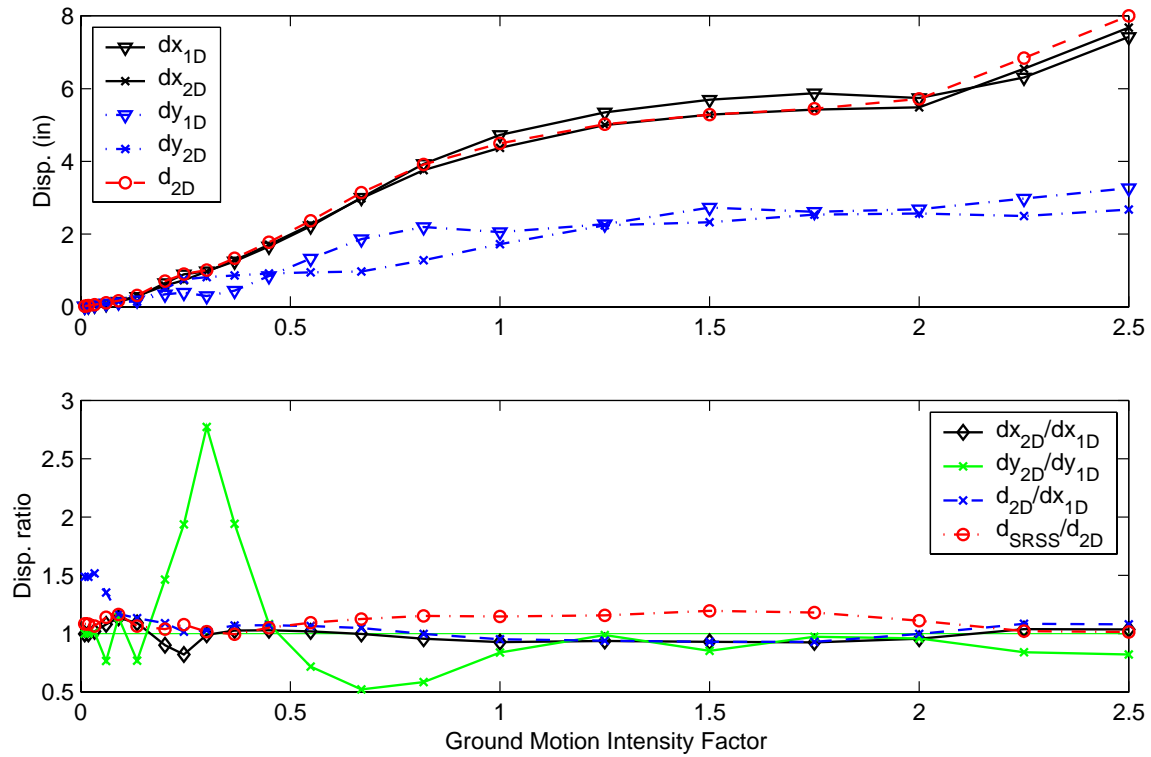
Figure 6-34. Effects of bidirectional excitation and intensity on the peak analytical response under the Northridge Olive View record.
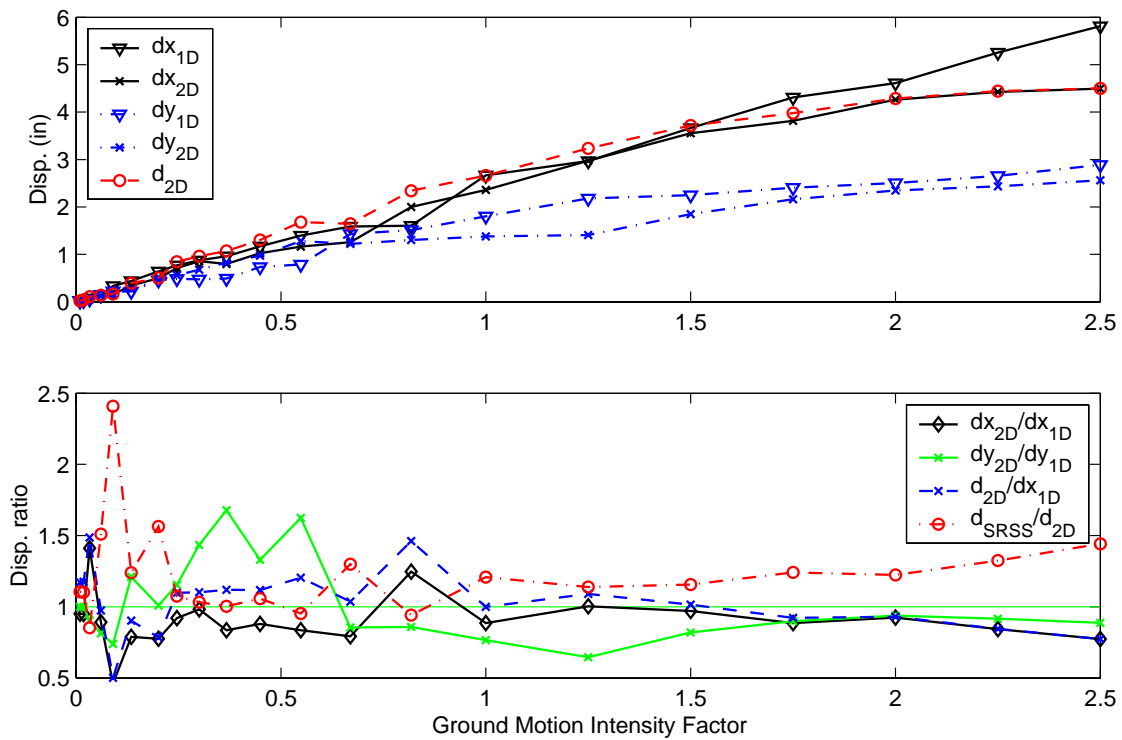
Figure 6-35. Effects of bidirectional excitation and intensity on the peak analytical response under the Llolleo record.

Silva [1] to compute the ratio of vertical to horizontal spectral accelerations for different earthquake magnitudes, and for a range of distances and site conditions (rock and soil). Several bridges were analyzed under linear response spectrum and linear time history analysis, and one bridge was analyzed under nonlinear time history analysis. The analysis results suggest that the vertical motions had more impact on the vertical response (deck deformation and moments), while the horizontal response was not significantly affected. Overall, it appears that the effect of the vertical ground motion on the horizontal displacement response of bridge piers is not significant.

To assess these issues for the case of the test specimens, the response of the specimens was examined under three components of excitation corresponding to the Northridge and Llolleo records. Time histories for the Olive View records are shown in Figure 6-33 when one, two and three components of excitation are applied. Very little difference is noted in the horizontal displacement when vertical excitations are included, while somewhat larger differences are noted in the vertical direction of displacement. The intensity of the ground motion was again varied from a scale of 0 to 2.5. Displacements and displacement ratios plotted in Figure 6-36 show that the effect of the vertical acceleration on the horizontal response remains minimal over the entire intensity range. The response due to the 3D excitation is essentially similar to the response due to the 2D excitation for the Northridge record. The same observations hold for the Llolleo record except for a moderate increase at ground motion intensity factors of less than 0.5, and some decrease at scales larger than 2.

6.5.3   Vertical Vibration under Horizontal Excitations

The bottom plot in Figure 6-33 shows the vertical acceleration computed at the top of the column. It is interesting to note that both the 1D and 2D cases show significant vertical acceleration at the top, even though no vertical input is applied. For the 1D horizontal loading case, vertical accelerations of up to 0.8g are noted. As the column is cycled laterally between positive and negative peaks, the top of the column experiences varying amounts of axial elongation due to the variation of the neutral axis position. This results in a measurable vertical deformation of up to 0.25 in. (6 mm), and causes vertical vibration of the column. This behavior was also pointed out by Ranzo et al. [84], who suggest that this vertical vibration could cause significant fluctuations in axial loads, and might have an impact on ductility demand and capacity that would exceed that of vertical ground acceleration. It is worth noting that the analytically predicted vertical acceleration is significantly smaller under bidirectional loading than unidirectional loading. This high peak acceleration
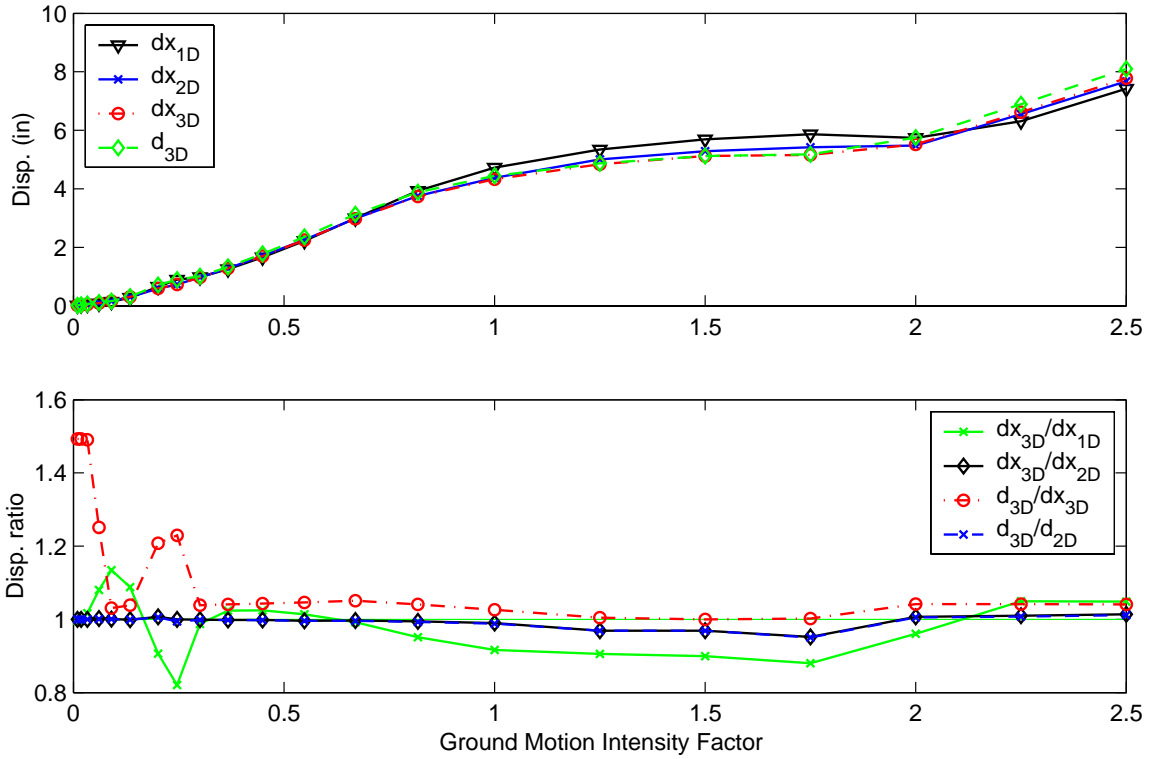
Figure 6-36. Effects of vertical excitation on the peak analytical response under different intensities of the Northridge Olive View record.
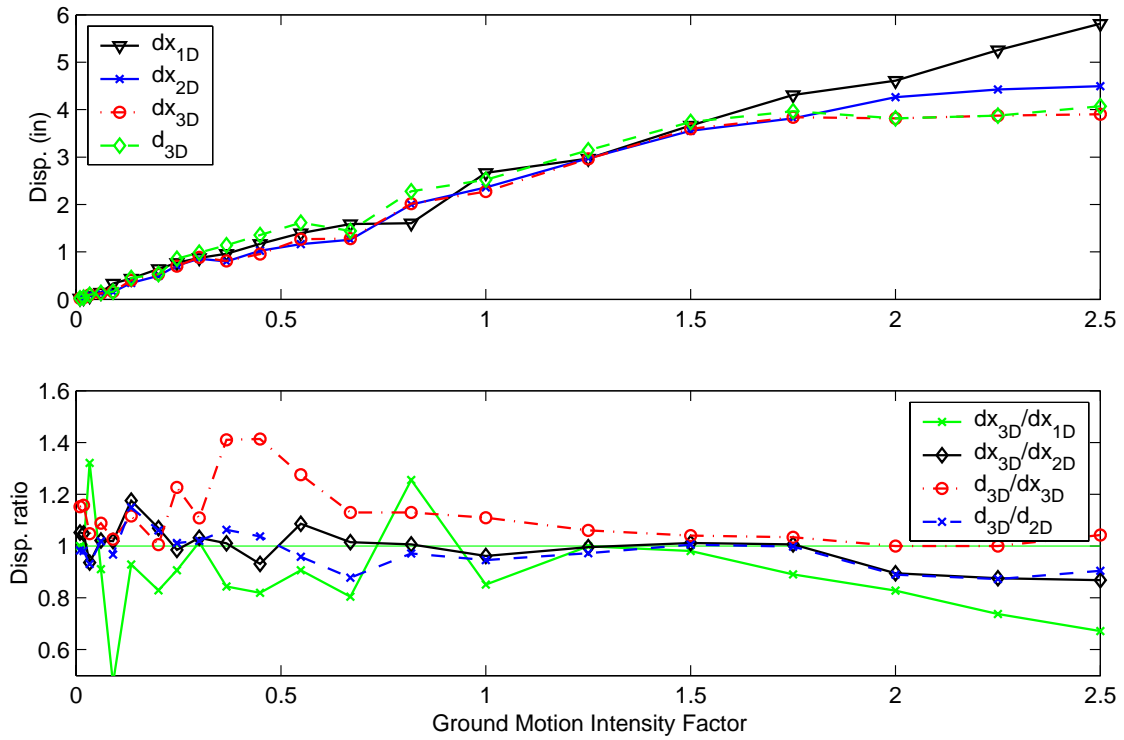
Figure 6-37. Effects of vertical excitation on the peak analytical response under different intensities of the Llolleo record.

218

and the difference in peak vertical acceleration from 1D to 2D excitations is not consistent with observed results, however. The experimental results show a peak vertical acceleration of around 0.1g-0.2g for all four specimens. It is also observed that the vertical vibrations observed in the analysis and from experimental results have a dominant frequency that is much higher than the horizontal frequency. While the vertical accelerations do not appear to have in these cases a significant impact on horizontal or vertical response, additional study is warranted to understand differences.

6.5.4   Nonlinear vs. Linear Response

Peak nonlinear displacement demands are often assumed to be the same as the those predicted from elastic analysis results, especially for structures that fall in the long period range. It has been observed that the ratio of inelastic to elastic displacement is usually much larger than one for yielding structures with short periods of vibration and approaches unity for longer periods ([66], [73]). For such comparisons, the initial stiffnesses of the elastic and inelastic systems are the same. In this case, the fiber model predicts continuous inelastic response once cracking occurs. Thus, for the elastic model, an effective stiffness is assumed. Using an effective elastic flexural stiffness of αEI_g, an elastic version of the column model is subjected to varying intensities of the Northridge Olive View record as illustrated in the previous sections. The ratios of nonlinear displacements to linear displacements are shown in Figure 6-38. The top plot shows the ratios of d_x, d_y and d, for flexural stiffnesses of $0.3EI_g$ which is the effective flexural stiffness that matches the moment-curvature relation at the applied axial load (Section 6.3.1), and $0.5EI_g$ which is a value often used in simplified analyses. The peak elastic displacements decrease for the stiffer elastic system as expected. This gives larger inelastic to elastic displacement ratios. The bottom plot in Figure 6-38 confirms this trend for the radial displacement d, using five different elastic stiffnesses. It is also noted that the ratios for d_x, d_y and d are different from each other, and vary significantly with variations of the ground motion intensity. Nonetheless, it is clear for this structure, that when the appropriate effective stiffness is assumed, that elastic analyses do indeed predict peak inelastic lateral displacements.

6.5.5   Eccentric Column Bents

In single column bridge bents, care is usually exercised to locate the column directly below the center of gravity of the bridge. However, even when the load is concentrically applied, some eccen-
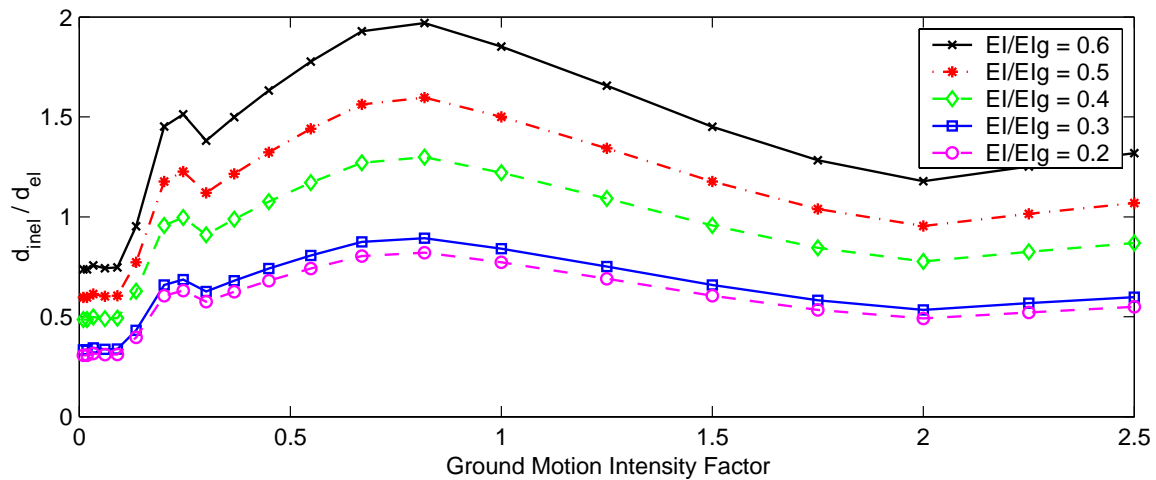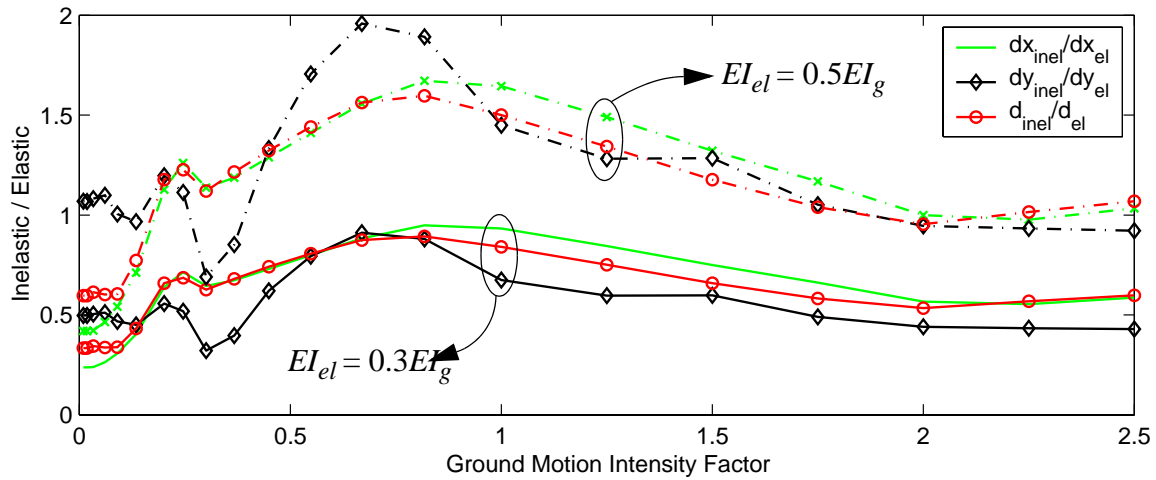
Figure 6-38. Ratio of inelastic to elastic displacements.

tricity is usually introduced due to construction offsets, curvature effects, and the uneven distribution of gravity loads. In other instances, the geometry of the bridge and the road alignment might dictate one or more columns to have some eccentricity. If the column has a symmetrical distribution of reinforcement, an eccentrically applied axial load will induce permanent moments that will make the column effectively weaker against lateral loading in one direction than the other.

All of the previous analyses have assumed a perfectly centered axial load. To quantify the effect of eccentricity, the numerical nonlinear fiber model was subjected to varying intensities of the Northridge and Llolleo ground motions, for different values of eccentricity e_x in the x direction. The effect of eccentricity values of up to 10 in. (≈ 250 mm or about 63% of the column's diameter) were considered in each direction. The time history response of the 16 in. (≈ 400 mm) diameter column for various eccentricities is shown in Figures 6-39 and 6-41. In both earthquake records

considered, the columns with higher eccentricity tend to have substantially larger residual displacement, proportional to and in the same direction of the eccentricity. The eccentricity has a more significant effect on the response of the near-fault record (Olive View) as compared to the far-field record (Llolleo). The peak displacements of specimens with eccentricity e_x and subjected to excitations with intensity factors varying from 0.1 to 3 are shown in Figures 6-40 and 6-42. Both the actual peak displacement and a normalized displacement ratio are shown in the plots. The normalized displacement is defined as follows:

$$Normalized\ Displacement_{e,s} = \frac{Peak\ Displacement\ (eccentricity = e\ ,\ scale = s)}{Peak\ Displacement\ (eccentricity = 0\ ,\ scale = s)}$$

The bottom axis in Figures 6-40 and 6-42 plots the eccentricity in inches, while the top axis plots the ratio of the eccentricity induced dead load moment to the total plastic moment capacity ($P = 65$ kips). The peak displacement generally increases with both eccentricity and ground motion intensity. In some cases, a small eccentricity might cause a small decrease in peak displacement. This appears to be associated with ground motion directivity as the displacement is generally increased in such cases when the sign of the ground motion is reversed. For intensity factors in the range of 1-1.5 times the original record (which brackets the design level of the column), eccentricities larger than 6 in. (150 mm) cause large magnifications of the peak displacement. This corresponds to a moment ratio ($P\ e_x\ /\ M_p$) of about 0.25.

This analysis illustrates the effect of two different types of earthquakes on the column under consideration when subjected to different axial load eccentricities. More analysis is needed on a larger sample of columns, involving more ground motions, in order to make general conclusions.

221
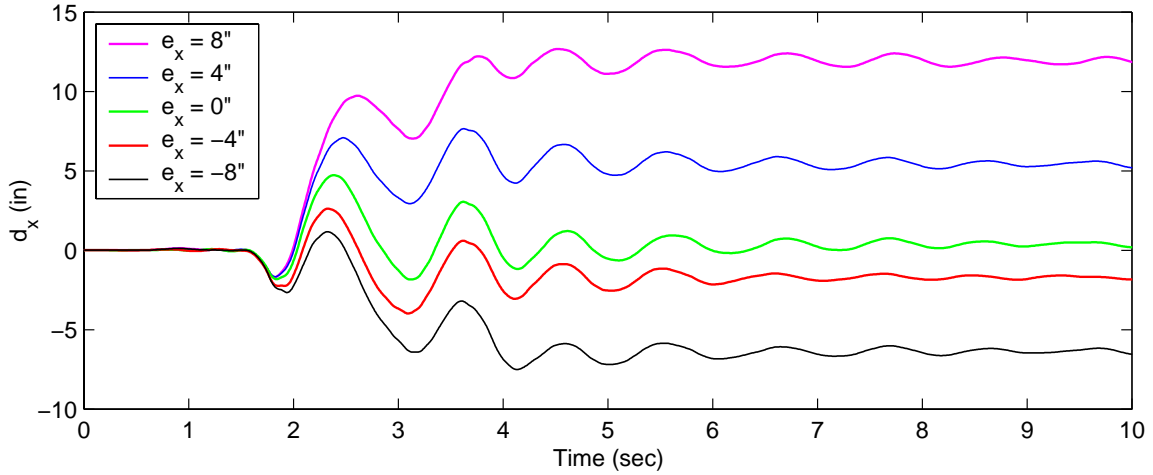
Figure 6-39. Effect of eccentricity on the response under the Northridge record.
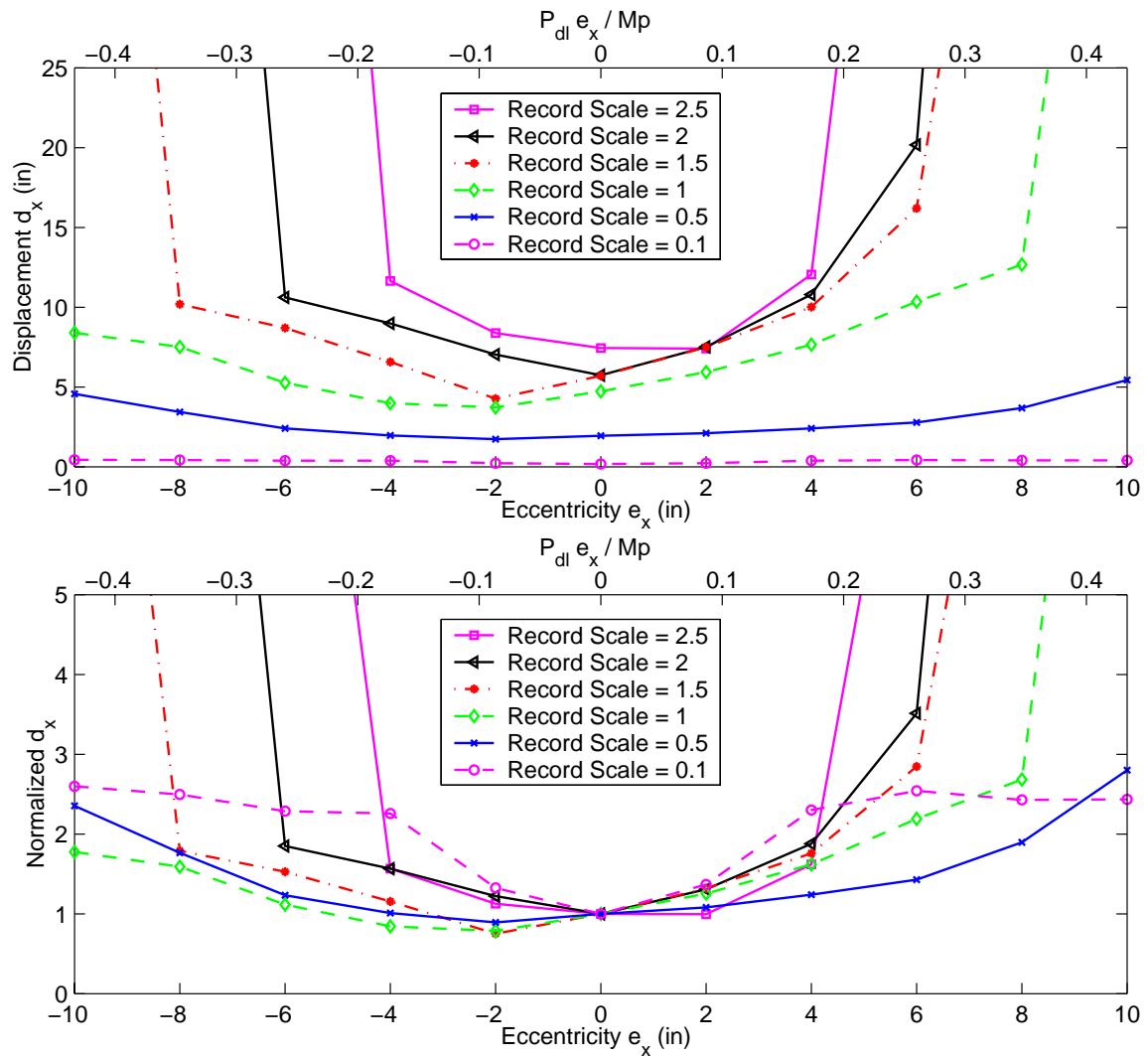
Figure 6-40. Effect of eccentricity and ground motion scale on the peak displacement response under the Northridge record.
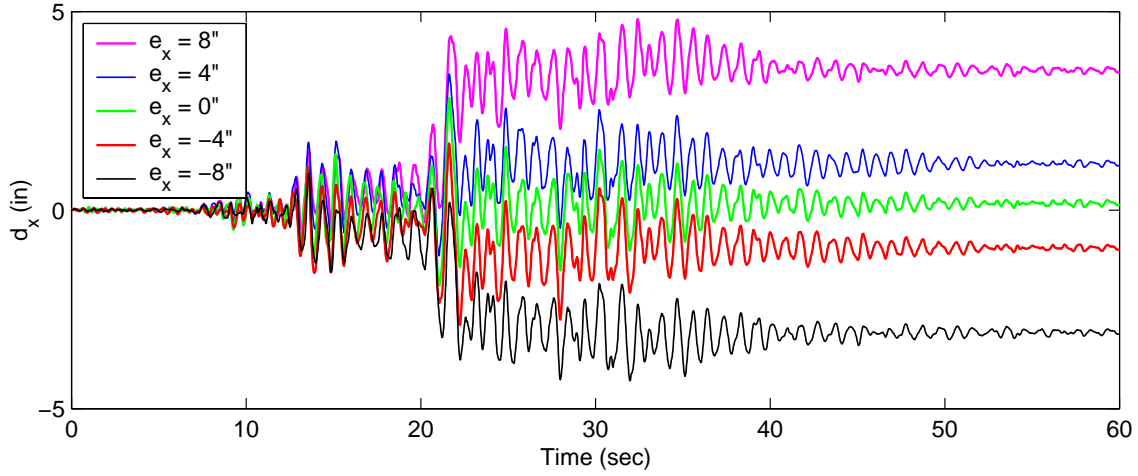
Figure 6-41. Effect of eccentricity on the response under the Llolleo record.
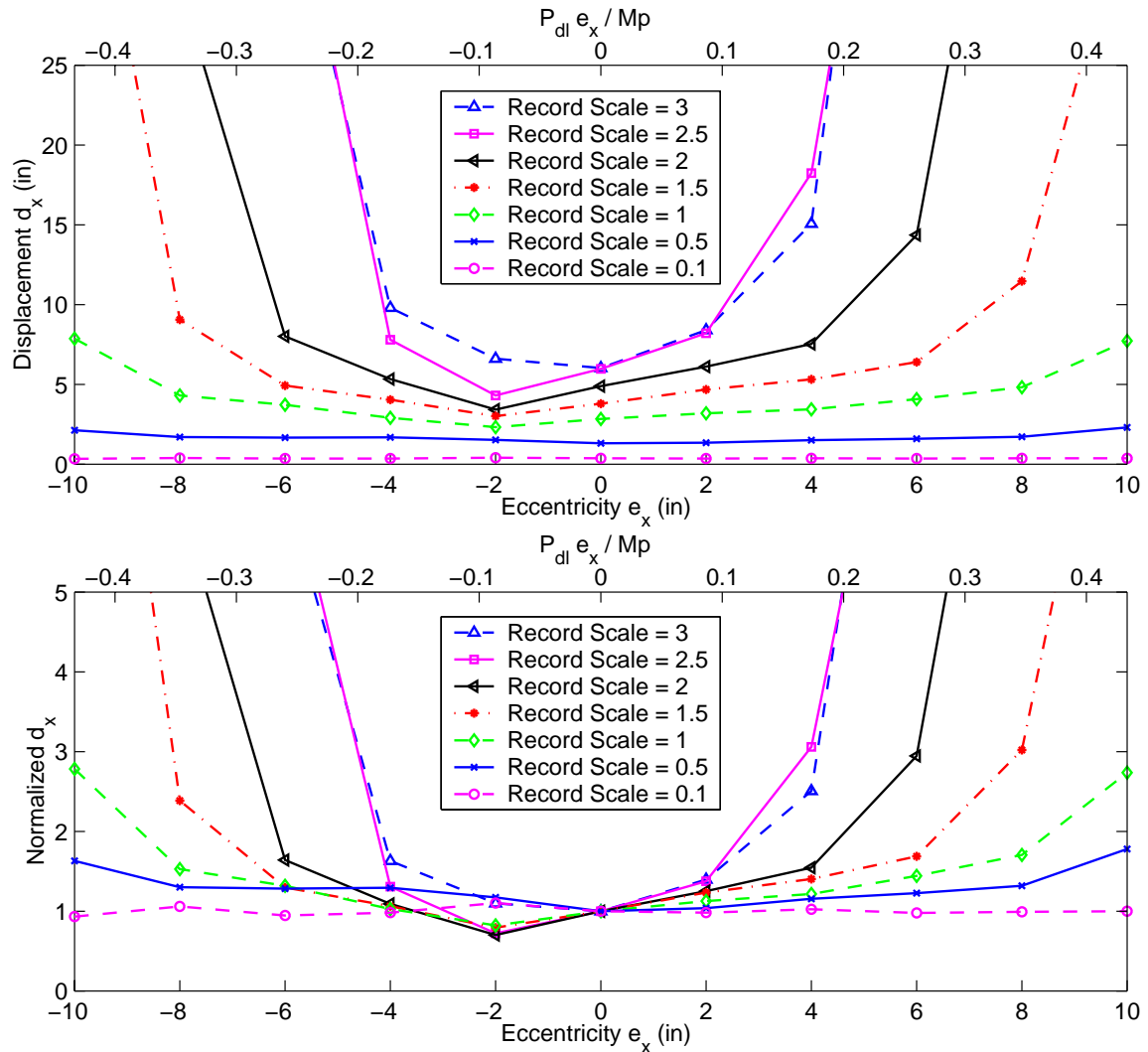
Figure 6-42. Effect of eccentricity and ground motion scale on the peak displacement response under the Llolleo record.

223

7   Analytical Investigation of the Performance of Bridge Columns

7.1   INTRODUCTION

While the experiments and analyses presented in the previous chapters provide substantial insight into the seismic behavior of reinforced concrete bridge columns and the ability of current analytical methods to predict performance, the investigations were based on a single column design and a limited number of ground motions. Consequently, the analytical models validated in Chapter 6 are now used to study the seismic behavior of a wide range of well-detailed, ductile circular reinforced concrete columns subjected to a large number of excitations. Two series of dynamic analyses are conducted, one focusing on response under unidirectional excitation, and the other focusing on the effects of bidirectional excitation.

The first series of analyses examines systematically the inelastic behavior of more than 2000 columns having different diameters, height to diameter (aspect) ratios and axial load intensities designed according to three different bridge design criteria. Each column was subjected to twenty ground motions scaled to match in an average sense the ARS response spectrum used in the design of the columns. Because of the large number of analyses undertaken, simplified hysteretic models are used. However, the parameterization of the problem allows the results to be presented in a familiar response spectrum format. This series of analyses is described in Section 7.5.

In the second set of analyses, detailed fiber models are constructed for 27 of the columns considered in the first set of analyses, and each was subjected to the same ground motion records. However, in this case, bidirectional as well as unidirectional excitation was considered to allow for the effect of multiple components of excitation and various elastic and inelastic simplified analysis approaches to predict seismic performance. This set of analyses is described in Section 7.6.

7.2   SUMMARY OF OBJECTIVES OF THE ANALYTICAL INVESTIGATIONS

A common approach used to assess seismic response is to compute an inelastic response spectrum for a given earthquake ground motion considering a range of structures characterized by an initial structural period, yield strength, viscous damping ratio and a representative hysteretic model. While this approach is convenient and provides valuable insight into the basic parameters that influence seismic behavior, the results obtained are not directly related to specific aspects of the design and detailing used. For instance, a wide variety of structures with vastly different weights, diameters, heights, and longitudinal reinforcement ratios may all have a period of 1 second and a lateral strength corresponding to 0.3W. In this situation, it is difficult to interpret the results presented in a conventional inelastic response spectrum relative to the capacity of the structure to develop the predicted demands. Moreover, some combinations of parameters considered in the generation of a response spectrum may not correspond to actual structures. For instance, assumed strengths may correspond to reinforcement ratios well above or below values permitted in design.

Thus, it would be desirable to retain the convenience and conceptual simplicity of response spectrum but incorporate features that allow more definitive assessment of performance. This would distinguish between a short heavily loaded column and one that is taller, but more lightly loaded. It should also be able to assess the impact of detailing that would reduce or increase the deformation or energy dissipation capacity of a structure. In this way, it would be possible to systematically assess the effect on performance of various design approaches and detailing criteria.

In this and the following sections, a methodology is developed to develop such response spectra. The columns considered are parameterized according to their diameter, aspect ratio, axial load intensity, and material properties. An automated process was used to design more than 2000 columns corresponding to three sets of design criteria (SDC, BDS, ATC-32). Each of these columns was subjected to twenty ground motions scaled to match the ARS response spectrum used in the design of the columns. Results are plotted in terms of the diameter or period of the column, and include information on peak relative displacement, displacement demand to capacity ratios, and damage indices based on the Park and Ang model as well as the a low-cycle fatigue bar facture model. Section 7.3 describes the design of the columns considered. Section 7.4 describes the performance parameters used to assess the column response. The analytical modeling, ground motions and results used to assess the effect of design criteria is on performance are presented in Section 7.5.

Section 7.6 presents a second set of analyses that uses fiber elements to model the behavior of the column. This was done to get a more refined set of results, and to model behavior aspects not captured by simpler hysteretic models such as bidirectional interaction. The second set included both unidirectional and bidirectional dynamic analyses, but only a subset of the columns used in first set were analyzed due to the greater computational demands of the fiber element.

7.3   DESIGN OF COLUMNS CONSIDERED IN PARAMETRIC INVESTIGATIONS

Three different approaches to the design of bridge columns are considered. These include the criteria in the 1990 Bridge Design Specifications (BDS), recommendations in ATC-32, and the criteria contained in he 1999 SDC. The SDC requirements introduced fairly significant changes to the seismic design of reinforced concrete bridge columns [98]. As stated in the introduction of the document, "the SDC is a compilation of new seismic design criteria and existing seismic design criteria previously documented in various locations."

7.3.1   Summary of SDC Design Requirements

The SDC introduces several changes to the BDS design requirements. As far as seismic demand, the SDC contains new ARS curves for California, and defines separate curves for different soil types and earthquake magnitudes. The SDC also has a provision for near fault ground motions, which requires the ARS demand to be increased by 20% for structures closer than 10 miles (15 km) to a fault, that have a period of vibration longer than 1 second (1.5 seconds for deep soil sites). For smaller periods, the increases diminishes linearly to zero for periods less or equal to 0.5 seconds.

Regarding column design, the strength requirement for concrete columns is partially removed, and it is instead replaced by a displacement-based requirement. The equal displacement assumption is usually used to predict the nonlinear displacement demand. Hence, the response modification factor Z is no longer applicable. Instead, the displacement capacity of the column has to be checked against the expected demand displacement obtained from the ARS spectra at a period corresponding to the effective (cracked) stiffness of the structure. However, the *Seismic Design Methodology* (Memo to Designers 20-1 [99]), warns that the equal displacement assumption is mostly valid for intermediate periods between 0.7 seconds and 3 seconds. It states that the assumption becomes overconservative for longer periods, and that it significantly underestimates displace-

227

ments for periods less than 0.7 seconds. The document recommends either designing the column to behave elastically or to use a displacement amplification factor.

Additionally, columns are required to resist a minimum lateral force equal to 10% of the column tributary dead load. The SDC also limits the maximum longitudinal reinforcement ratio to 4% of the gross area, with a minimum of 1%. The SDC states that P-Δ effects may be ignored if the moment due to P-Δ does not exceed 20% of the flexural moment capacity.

The SDC defines new equations for the shear capacity that depend on the expected ductility demand of the column. As far as target ductility capacity and demand, the SDC recommends limiting ductility demands to 4 and 5, respectively, for single and multi-column bents. Some of the differences between the SDC, and BDS and ATC-32 methodologies are described in subsequent sections.

7.3.2 Design of Columns for Parametric Analysis

The design criteria summarized above were followed in the design of each of the columns analyzed. This was automated by the use of a computer script. This script was developed to closely simulate the iterations undergone by a design engineer to satisfy design requirements.

7.3.2.1 Automated Design

The design process is accomplished by iterating to satisfy, for given column dimensions, properties, and axial load, the minimum strength and deformability requirements for each column. Each iteration specifies an amount of longitudinal and spiral reinforcement to satisfy those limits. In each iteration, a moment-curvature analysis is performed, which when used in conjunction with the plastic hinge method assumptions, yields the effective stiffness (and period), strength, and displacement capacity of the column. The iteration is repeated until all relevant requirements are satisfied.

SDC requirements do not specify a force reduction factor, but rather require the satisfaction of minimum strength and deformation capacities. This is in contrast with the original BDS requirements, which specify a constant reduction factor of 4 for ordinary bridges. On the other hand, ATC-32 suggests that the reduction factor be linearly reduced from 4 to 1 between periods of 1 and 0 seconds, as illustrated in Figure 2-2.

The three design procedures were automated based on these requirements. Apart from the differing strength requirements, all three procedures essentially conformed to the SDC requirements. The three design procedures are illustrated using the flowcharts in Figures 7-1 and 7-2.
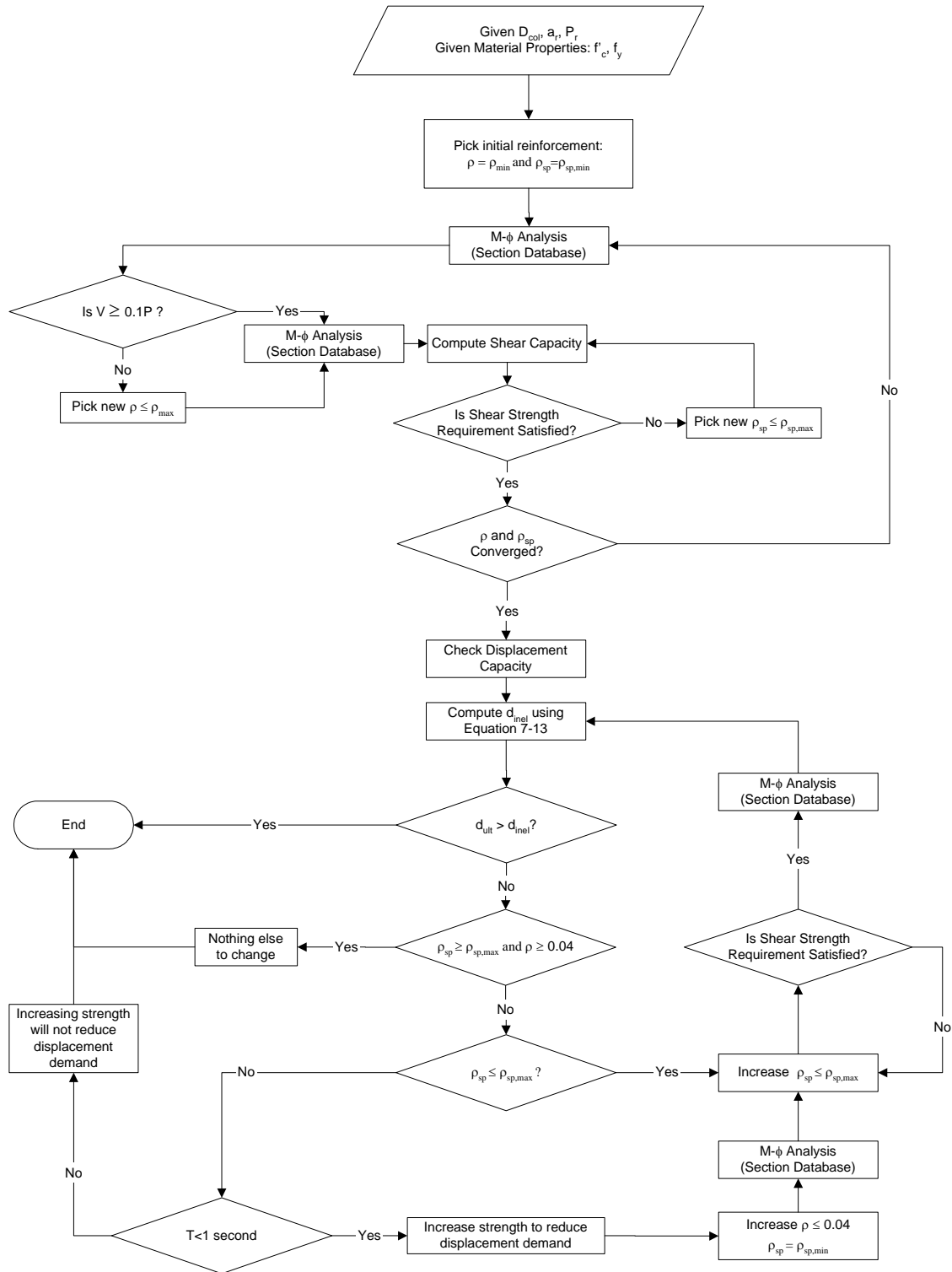
Figure 7-1. Simple representation of the design process (SDC method).
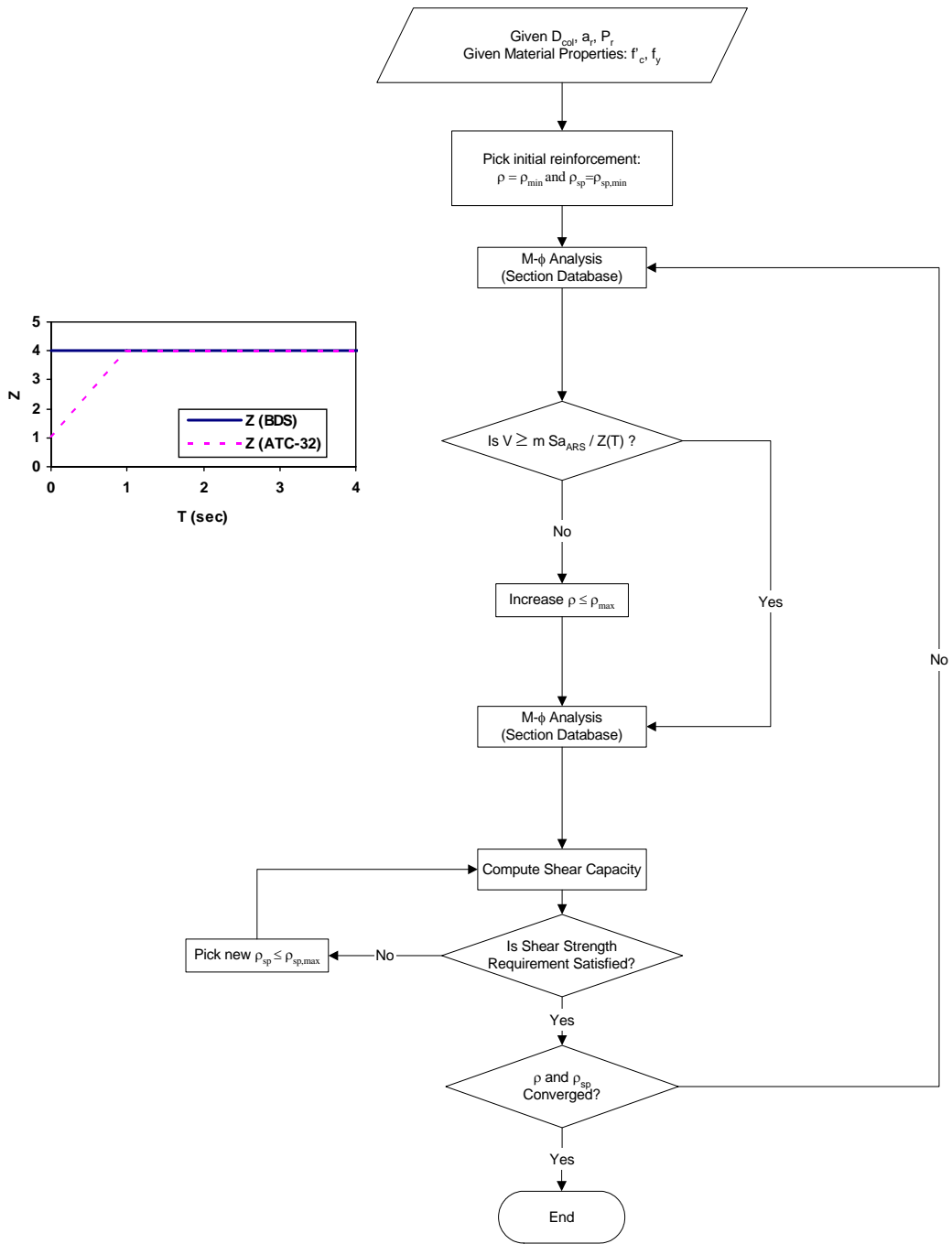
Figure 7-2. Simple representation of the design process (BDS and ATC-32 methods).

7.3.2.2　　Shear Strength Requirement

SDC shear equations and reinforcement limits were used for all three methods. The itera-tion over the spiral reinforcement was performed to ensure that the column is not shear critical, as required by Equation 7-1 where the factor 1.2 represents an overstrength factor (SDC Section 4.3.1).

$$\phi V_n \geq V_o = \frac{M_o}{L} = \frac{1.2 M_u}{L} \tag{7-1}$$

The shear capacity V_n is computed using Equations 7-2 to 7-8 (SDC Section 3.6), which use psi units.

$$V_n = V_c + V_s \tag{7-2}$$

Where the concrete shear resistance, V_c, can be obtained from Equations 7-3 through 7-6:

$$V_c = v_c A_e = v_c (0.8 A_g) \tag{7-3}$$

$$v_c = \alpha \beta \sqrt{f_c'} \leq 4\sqrt{f_c'} \tag{7-4}$$

$$0.3 \leq \alpha = \frac{\rho_{sp} f_{yh}}{150} + 3.67 - \mu_d < 3 \tag{7-5}$$

$$\beta = 1 + \frac{P}{2000 A_g} < 1.5 \tag{7-6}$$

The shear resistance due to spiral reinforcement, V_s, is given by Equations 7-7 and 7-8.

$$V_s = \frac{\pi}{2} \frac{A_v f_{yh} D'}{s} \leq 8\sqrt{f_c'} A_e \tag{7-7}$$

$$A_v \geq 25 \frac{D'}{f_{yh}} \tag{7-8}$$

Equation 7-8 can be rewritten give an lower limit for the shear reinforcement ratio ρ_{sp}. Sim-ilarly, Equation 7-7 gives the maximum effective amount of shear reinforcement. Those two limits are expressed in Equation 7-9.

$$\frac{100}{f_{yh}} \leq \rho_{sp} \leq \frac{64\sqrt{f_c'}}{\pi f_{yh}} \frac{A_e}{D'^2} \tag{7-9}$$

7.3.2.3　　Confinement Requirement

The lower bound in Equation 7-9 almost never controls in columns, since the confinement requirements given by Equations 7-10 to 7-12 are substantially higher.

$$\rho_{sp} = 0.45\left(\frac{A_g}{A_c} - 1\right)\frac{f_c{}'}{f_{yh}} \tag{7-10}$$

$$\rho_{sp} = 0.45\left(\frac{A_g}{A_c} - 1\right)\frac{f_c{}'}{f_{yh}}\left(0.5 + \frac{1.25P}{f_c{}'A_g}\right), (D \leq 3 \text{ ft}) \tag{7-11}$$

$$\rho_{sp} = 0.12\frac{f_c{}'}{f_{yh}}\left(0.5 + \frac{1.25P}{f_c{}'A_g}\right), (D > 3 \text{ ft}) \tag{7-12}$$

Hence, for given section dimensions, materials properties and axial load, the minimum allowed spiral reinforcement will be controlled by confinement requirements.

7.3.2.4   Displacement Capacity Requirement

The displacement capacity requirement ($d_{ult} \geq d_{inel}$) was only applied in the SDC method. It was assumed that displacements are preserved for periods above 1 second. For periods smaller than 1 second, the displacement demand was amplified by the factor suggested by Nassar and Krawinkler [67]:

$$d_{inel} = \frac{1}{R}\left(1 + \frac{(R^c - 1)}{c}\right)S_d \tag{7-13}$$

$$c = \frac{T^a}{1 + T^a} + \frac{b}{T} \tag{7-14}$$

$$R = \frac{S_a(T) \cdot m}{F_y} \tag{7-15}$$

a and *b* are constants that depend on the second slope of the hysteretic curve and the damping. For systems without hardening, a and b assume values of 1 and 0.42 respectively. Those values were used for all cases regardless of their hardening.

The hysteretic properties of the column were obtained from the cross-section moment-curvature analysis using the assumptions of the plastic hinge method introduced in Section 6.3.2. The equations are restated here in a slightly different form. ϕ_u is the ultimate section curvature corresponding to the maximum compressive strain capacity of the confined concrete (Equation 7-18).

$$d_{ult} = \frac{M_u}{M_y}d_y + (\phi_u - \phi_{ye})L_p(L - L_p/2) \tag{7-16}$$

$$L_p = 0.08L + 0.15f_yd_b, \text{ (ksi units)} \tag{7-17}$$

$$\varepsilon_{cu} = 0.004 + 1.4\frac{\rho_{sp}f_{yh}\varepsilon_{su}}{f_{cc}{}'} \tag{7-18}$$

$$f_{cc}' = f_{co}' \left(-1.254 + 2.254 \sqrt{1 + \frac{7.94 f_l'}{f_{co}'}} - 2\frac{f_l'}{f_{co}'} \right)$$

(7-19)

7.3.2.5 Bar Spacing

Since the plastic hinge length equation depends on the bar diameter, an equivalent bar diameter is needed for each section being designed. While the reinforcement ratio has to satisfy design requirements, any bar size can be selected as long as it satisfies detailing spacing requirements. It is obvious that a unique bar diameter cannot be determined analytically, and in some cases, it may not be possible nor critical to satisfy all spacing requirements in the automated design process. However, an approximate estimate of an equivalent bar size is computed that satisfies, as closely as possible, the bar spacing requirements of the SDC and BDS.

The BDS requires the clear spacing between bars to be more than $1.5 d_b$ or 1.5 in. (BDS Section 8.21.1). It was found that first condition is more critical since most of the considered sections will have bars larger than #8. This is reflected in the following equation, where the diameter of the concrete core D' and D are assumed equal for simplicity:

$$\pi D \geq 2.5 d_b \cdot n$$

(7-20)

where n is the number of bars in the section. Using Equation 7-20 with Equation 7-21 which follows from the definition of ρ, leads to Equation 7-22.

$$\rho \cdot D^2 = n \cdot d_b^2$$

(7-21)

$$d_b \geq \frac{2.5 \rho D}{\pi}$$

(7-22)

Equation 7-21 can be used again to obtain an expression for n, in which Equation 7-22 is used for d_b:

$$n = \frac{\rho \cdot D^2}{d_b^2} \leq \frac{(\pi / 2.5)^2}{\rho} = \frac{1.579}{\rho}$$

(7-23)

Additionally, the maximum bar spacing should be less than 8 in. per BDS requirement 8.21.1.2. This is expressed in Equation 7-24.

$$n \geq \frac{\pi D}{8} = 0.39 D$$

(7-24)

However, since 8 in. is somewhat extreme, the target number of bars was set as $0.75D$. Hence, the number of bars will be taken as $0.75D$ except when Equation 7-23 needs to be satisfied which leads to the following rule:

$$n = minimum\left(0.75D, \frac{1.579}{\rho}\right) \tag{7-25}$$

Consequently, d_b can be obtained from Equation 7-26 where it is checked that the bar is larger than #5.

$$d_b = \sqrt{\frac{\rho D^2}{n}} \geq \frac{5''}{8} \tag{7-26}$$

The above procedure was performed in the automated design of each of the columns. The above rules were tested for ranges of column diameter D and reinforcement ratio ρ. This is illustrated in Figures 7-3 and 7-4. Figure 7-3 plots the number of required bars for each combination of D and ρ. Note that the vertical portion of the contour lines represents the first condition in Equation 7-25, while the horizontal portion corresponds to the second condition. Figure 7-4 shows contour lines for the bar diameter d_b. The resulting d_b's are not discrete but rather continuous due to the nature of Equation 7-26. Contour lines representing actual bar sizes are shown. For d_b's larger than available bar sizes, it was assumed that more than one bar are bundled together. Only reinforcement ratios up to 4% are of interest, since this is the upper limit specified by SDC. Although this assures a certain degree of consistency in designing all columns, it is acknowledged that this is not a perfect representation of columns in actual bridges, where special requirements may dictate the design, and decisions on column size and reinforcement are governed by general project requirements in addition to the code equations.

7.3.3 Development of a Section Properties Database

The iterative design procedure illustrated in Figures 7-1 to 7-2 requires multiple moment-curvature analyses for the design of each column. The section diameter, axial load and material properties are the same for each iteration, while the longitudinal and spiral reinforcement ratios, and confined properties of the core concrete are different. Instead of performing those numerous section analyses for each column, a task that is time consuming and redundant, it was decided to compile a database with results of pre-computed cross-section analyses, and to use that database to obtain the properties of any desired section, by interpolation.
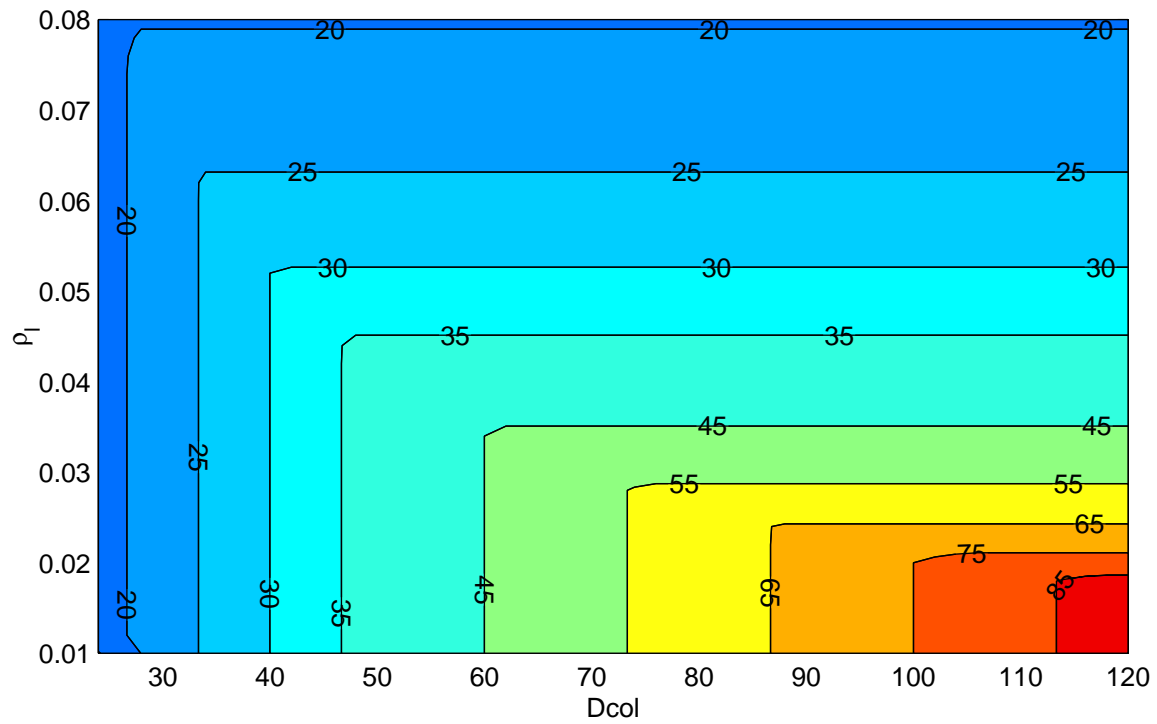
Figure 7-3. Number of bars used in sections with various diameters and longitudinal reinforcement ratios.
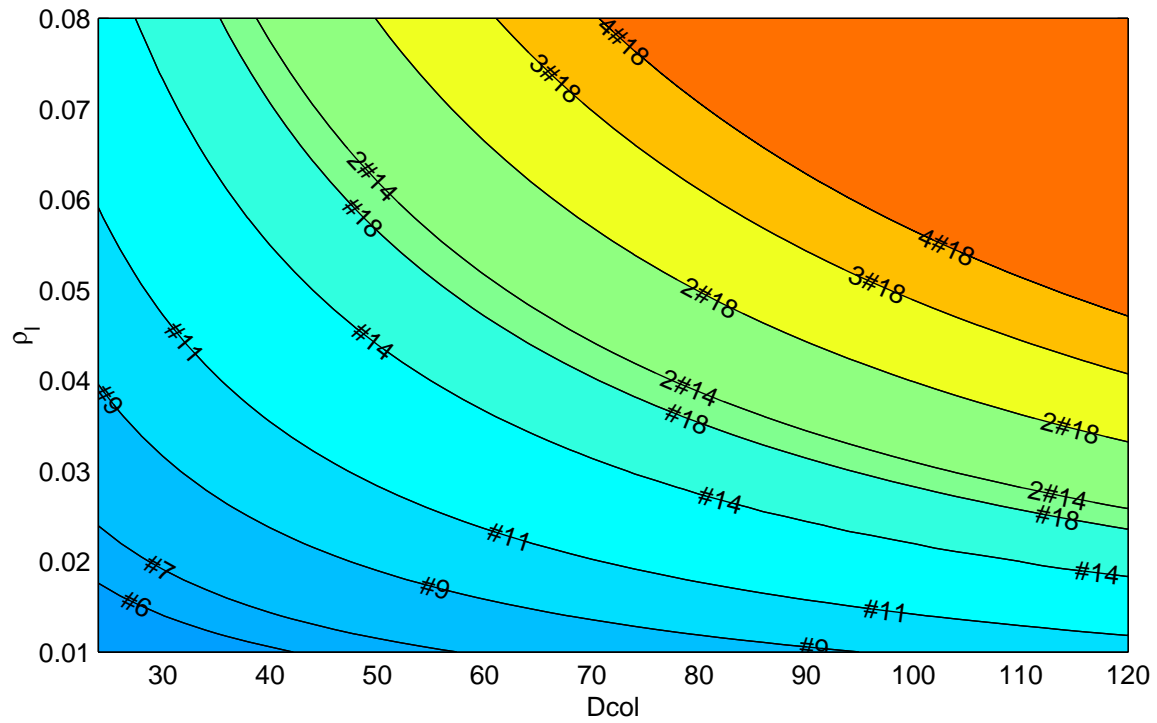
Figure 7-4. Bar size used in sections with various diameters and longitudinal reinforcement ratios.

7.3.3.1   Section Design Procedure

A total of 23,328 section moment-curvature analyses were performed with the following variables: column diameter D_{col}, axial load ratio $P_r = P/(f_c'A_g)$, longitudinal reinforcement ratio ρ, spiral reinforcement ratio ρ_{sp}, concrete strength f_c', and steel yield strength f_y. For each analysis, the moment-curvature relation was computed and a number of parameters were extracted and stored. Three different values for the spiral reinforcement ratio were considered for each section. The first value $\rho_{sp,min}$, the minimum amount required for confinement, is determined based on the minimum BDS confinement requirements (Equations 7-10 to 7-12). The second value $\rho_{sp,max}$, corresponds to the amount of spiral reinforcement that would result in the maximum allowed shear resistance of the column (Equation 7-9). The third value was taken as the average of the confinement and shear ratios. This was accomplished by using a normalized spiral reinforcement ratio $\rho_{sp,norm}$, with values of 0.0, 0.5 and 1.0:

$$\rho_{sp,norm} = \frac{\rho_{sp} - \rho_{sp,min}}{\rho_{sp,max} - \rho_{sp,min}} \qquad (7\text{-}27)$$

The spiral reinforcement ratio was used to estimate the enhanced stress and strain capacities of confined concrete, f_{cc}' and ε_{cu} (Equations 7-18 and 7-19).

The moment-curvature curve was idealized as a bilinear curve with the initial stiffness going through the first yield point. It was assumed that the section fails when the concrete strain ε_c exceeds ε_{cu} or the steel strain ε_s exceeds the ultimate strain capacity ε_{su} (taken as 0.12). The failure point and type (steel or concrete failure) are stored in the database (Table 7-1). Other quantities of interest include the neutral axis depth for the estimation of strains along the section.

The first seven fields in Table 7-1 are the main parameters used to construct the database. The remaining fields are the results from the moment-curvature analyses for each parameter combination. The values used for each of the main parameters are illustrated in Table 7-2. The database was used to simulate a moment-curvature analysis by simultaneous linear interpolation along the dimensions listed in Table 7-2. The database entries were normalized to linearize their variation as much as possible. For example, curvatures were normalized by $1/D_{col}$ while moments were normalized by D_{col}^3.

The process of obtaining the moment-curvature properties of a column section is illustrated in Figure 7-3.

Table 7-1 Section properties database.

Field Name	Description
Dcol	Column Diameter (in)
rho	Column Longitudinal Reinforcement ratio
Pr	Axial load ratio
rho_sp_norm	Normalized Spiral Reinforcement Ratio (0 to 1)
cover	Clear Cover (in)
fy	Steel Yield Strength (ksi)
fc	Unconfined Concrete Compressive Strength (ksi)
FAILURE	Failure Type (1 CONCRETE, 2 STEEL)
fcc	Confined Concrete Compressive Strength (ksi)
ecu	Ultimate Confined Concrete Strain
rho_sp	Spiral Reinforcement ratio
PHIy	Yield curvature (1/in)
PHIn	Nominal curvature (1/in)
PHIu	Ultimate curvature (1/in)
My	Yield moment (kip.in)
Mn	Nominal moment (kip.in)
Mu	Ultimate moment (kip.in)
Cy	Neutral axis depth at yield moment (in)
Cn	Neutral axis depth at nominal moment (in)
Cu	Neutral axis depth at ultimate moment (in)
EI	Effective Stiffness (kip.in/in)

Table 7-2 Parameter values used to construct the section properties database.

Field Name	Values
Dcol	24" 30" 36" 48" 60" 72" 96" 120"
rho	0.5% 1.0% 1.5% 2.0% 3.0% 4.0% 6.0% 8.0% 10.0%
Pr	0% 5% 10% 15% 20% 25% 30% 40% 50%
rho_sp_norm	0.0 0.5 1.0
cover	2"
fy	60 70 80 (ksi)
fc	3 4 5 6 (ksi)
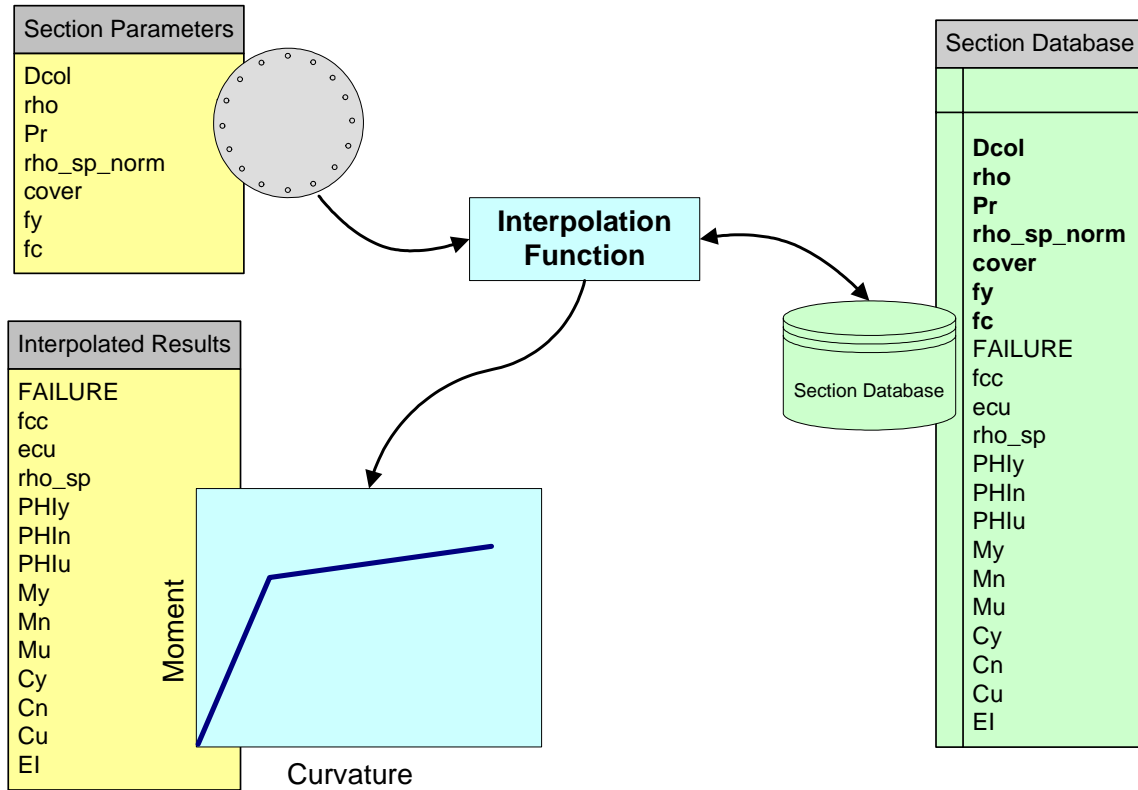
Figure 7-5. Using the section database to obtain moment-curvature properties for a section by interpolation.

7.3.3.2 *Section Properties*

To illustrate the use of the section database, various section properties are shown in Figures 7-6 to 7-9 for different combinations of D_{col}, P_r and ρ. The results shown correspond to $\rho_{sp}=\rho_{sp,min}$, which corresponds to the BDS confinement requirements. ρ_{sp} is dependent on D_{col} and P_r but not on ρ. The variation of ρ_{sp} alone (See Figure 7-6 for example) contributes significantly to the irregularities in the various section properties. Changing ρ_{sp} affects the confined concrete properties f'_{cc} and ε_{cu} (which follow a similar pattern), hence affecting the moment capacity Mu and ultimate curvature capacity ϕ_u. Another source of variation is the disproportionate effect of the section cover, assumed constant for all sections, on sections with varying diameters. In small diameter sections, the unconfined concrete constitutes a more significant portion of the section's concrete than in larger sections. This results in the fact that the ratio M_u/D_{col}^3 actually increases with D_{col} (Figure 7-6).

The ultimate curvature capacity generally decreases with increasing D_{col} and P_r and ρ, while M_u tends to increase. The neutral axis depth c generally increases with ρ and P_r.

238
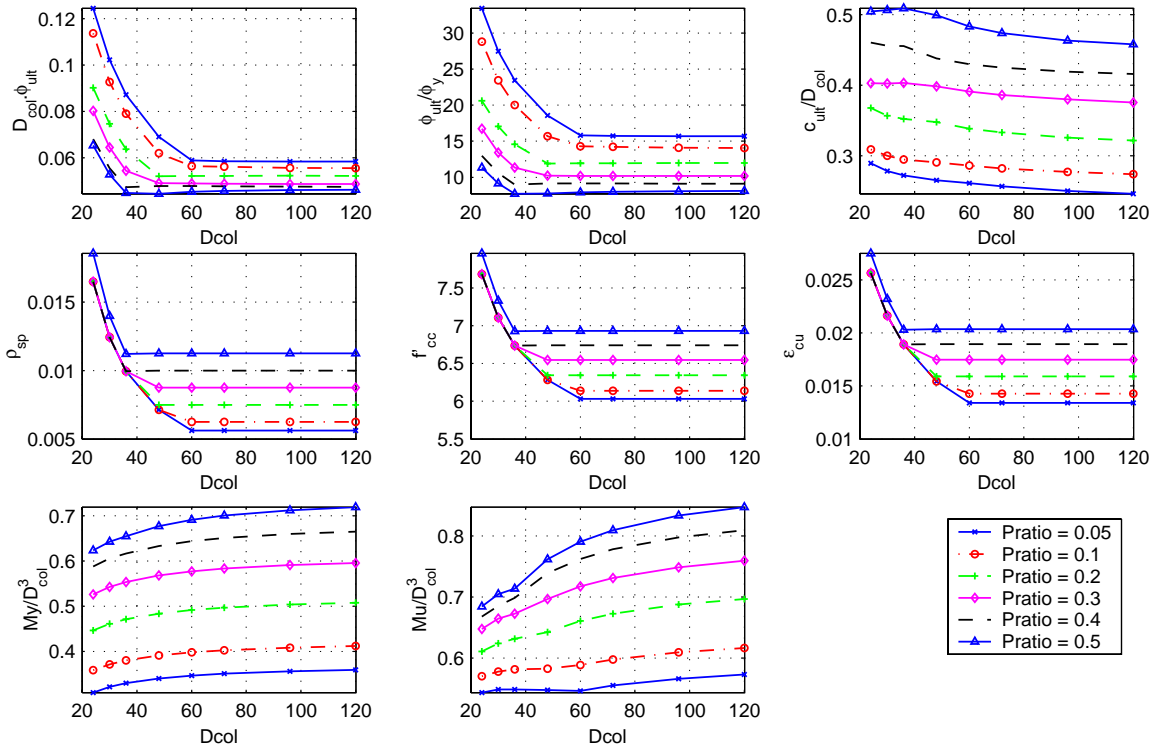
Figure 7-6. Properties of circular section with ρ =2% and varying D_{col} and P_r.
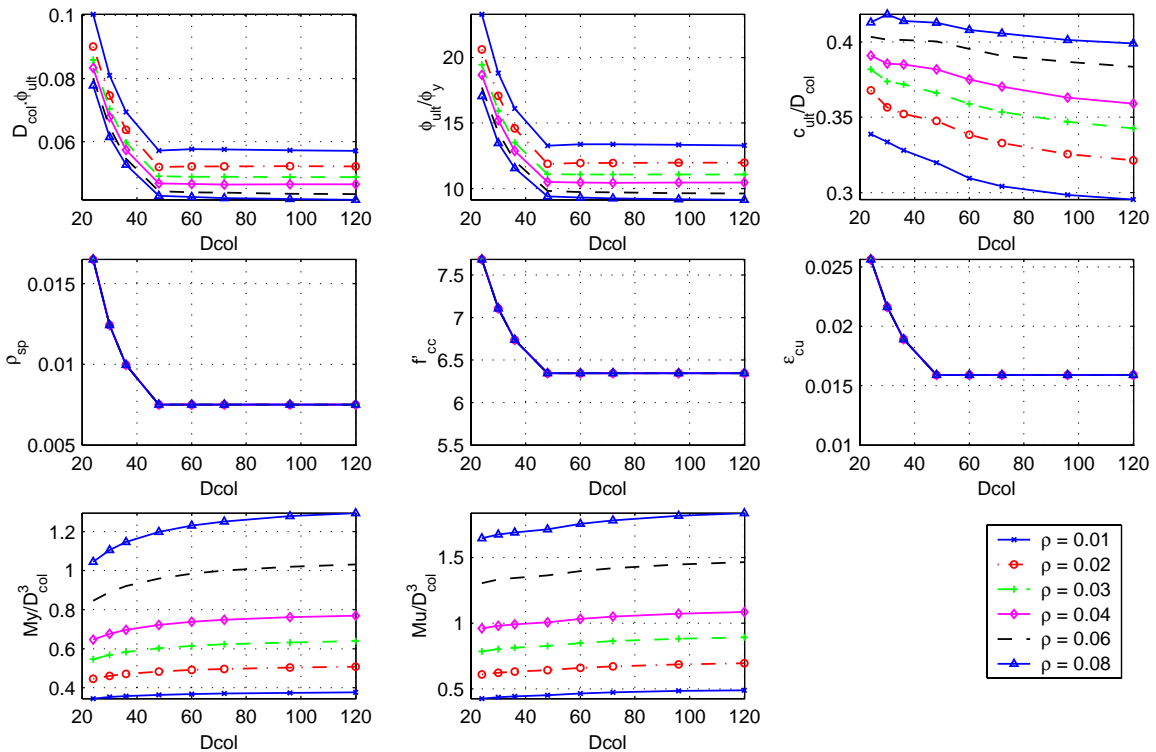
Figure 7-7. Properties of circular section with P_r=0.2 and varying D_{col} and ρ.
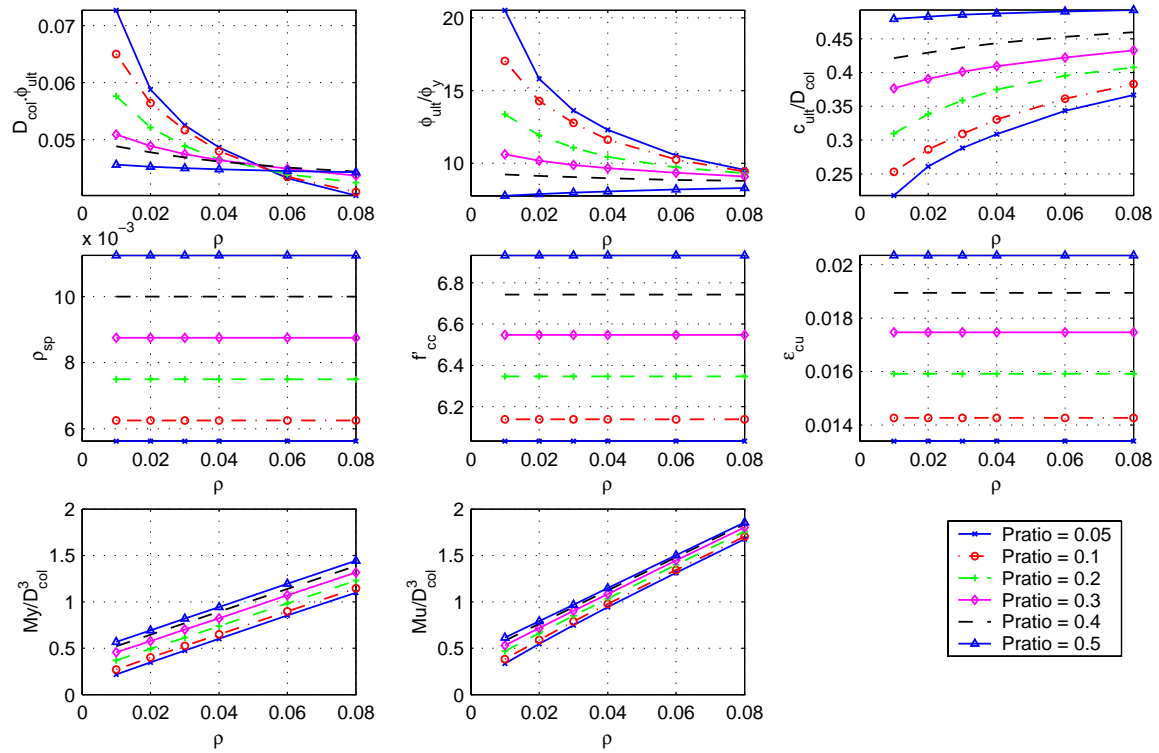
Figure 7-8. Properties of circular section with D_{col}=60 in. and varying ρ and P_r.
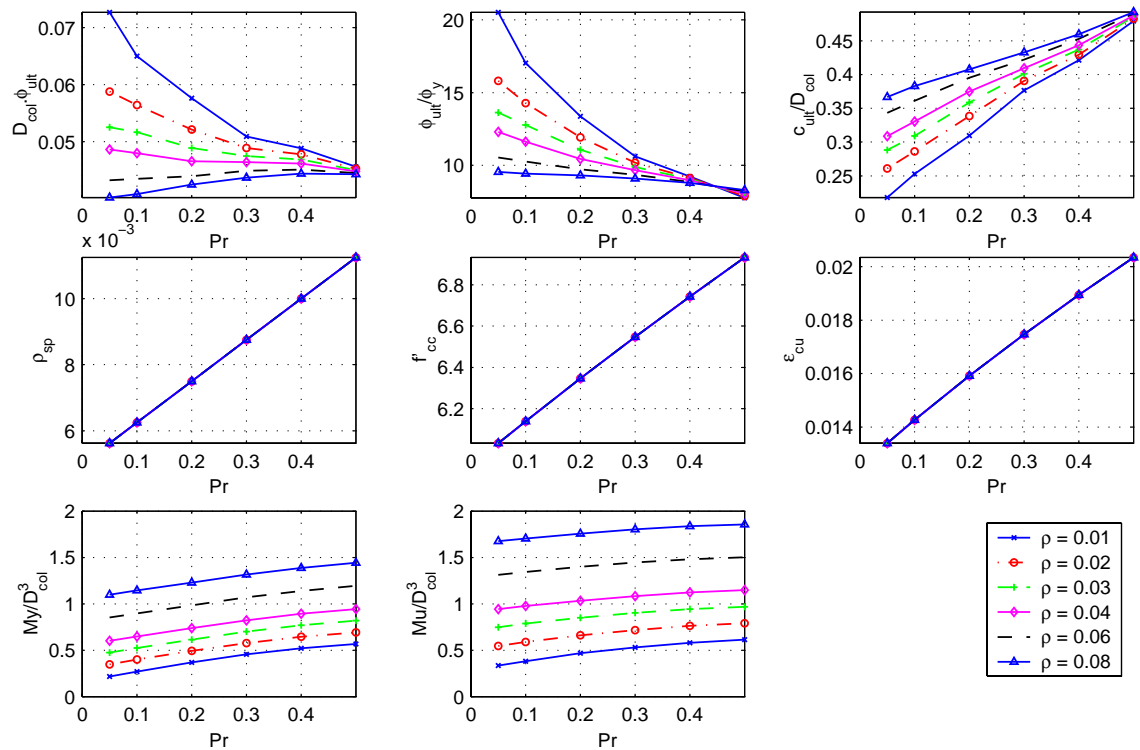
Figure 7-9. Properties of circular section with D_{col}=60 in. and varying ρ and P_r.

7.4   PERFORMANCE EVALUATION

Maximum displacement and ductility capacities of members are commonly used to evaluate column demand, but capacities vary significantly depending on member size, reinforcement and axial load. As such, damage indices are also used herein.

7.4.1   Damage Indices

This analytical study will use some of the damage indices that were introduced in Section 5.6. The indices of interest are the fatigue index, and the Park and Ang index (Equation 7-28) which for well confined columns (small β), closely reflects the ductility index (Equation 7-29). A β value of 0.05 was consistently used in this study.

$$D = \frac{d_{max}}{d_{ult}} + \beta \frac{\int dE}{F_y d_{ult}}, \; \beta = 0.05 \tag{7-28}$$

$$D = \frac{d_{max}}{d_{ult}} = \frac{\mu_{max}}{\mu_{ult}} \tag{7-29}$$

Failure is assumed to occur when the damage index D reaches 1.0, while a value of 0 represents an undamaged state. The ductility index reaches 1.0 when the maximum displacement reaches d_{ult}, the displacement capacity of the column. For most sections, d_{ult} is the displacement at which the maximum compressive strain in the confined concrete region exceeds ε_{cu}. This may be delayed by supplying a larger amount of spiral reinforcement. Other forms of failure may not be preventable however, such as low cycle fatigue failure of the longitudinal reinforcement. The fatigue life model by Mander et al. [58] for steel reinforcing bars was used to estimate the fatigue index of each column. The total strain form of the model was used as shown below:

$$D = \sum \frac{1}{2N_f} \tag{7-30}$$

$$\varepsilon_t = 0.08(2N_f)^{-0.33} \tag{7-31}$$

In the above, $2N_f$ is the number of half-cycles to failure at a specific strain level ε_t. The model is applied to bar strain cycles that are estimated from the displacement history for a circular section under general bidirectional loading. For any bar within the section, the total strain history to be used in the total strain version of the model can be computed from equations 5-23 to 5-27.

The cycle peaks are then extracted from the strain time history using the rainflow cycle counting method, and are plugged into Equations 7-30 and 7-31 to compute the fatigue index of the bar.

The damage index of the column was assumed equal to the damage index of the most critical bar. When the model used in the dynamic analysis is a hysteretic model which does not include discrete reinforcement bars, a search algorithm is used to locate the direction along which the reinforcement will experience the largest possible fatigue demand (assuming an infinite number of bars). The search algorithm can be summarized as follows:

1. Compute the damage index at assumed bars located at equally spaced angles. The strain histories at those points are estimated from the global displacement histories, using an assumed plastic hinge length. The fatigue damage index can then be calculated from the cycles extracted using the rainflow method. It was found that 8 locations (spaced at 45° angles) were necessary to locate the angle with the peak damage index.

2. Locate the angle that has the maximum damage index, and its two neighboring angles.

3. Solve for the quadratic polynomial that fits the three points. Solve for the new angle that maximizes the value of the damage function. Pick the two neighboring angles.

4. Repeat Step 3 until convergence is achieved or 5 iterations are performed.

7.5   EFFECTS OF DESIGN METHODOLOGY ON SEISMIC PERFORMANCE

Bridges designed to resist seismic demands are generally expected to respond in the inelastic range. A response modification factor (Z) has generally been used to reduce seismic forces relative to those expected in a bridge if it remained elastic. Different approaches were proposed over time for designing bridge columns, including using a constant Z factor of 4 (BDS method), using a linearly varying Z factor for short periods (ATC-32 method), or using a displacement based design methodology (SDC method). A large collection of columns with varying diameter, aspect ratio and axial load ratio were designed according to the three different methods, and their mean response to a suite of 20 ground motions was evaluated.

7.5.1   Properties of Designed Columns

A total of 2023 of columns were designed according to the three methods mentioned above. All columns had a circular cross-section, and each was designed as cantilevered column with a tributary mass equal the applied dead load. The parameters considered were the diameter, aspect ratio

and axial load ratio as shown in Table 7-3. Note that the same material properties and cover dimension were assumed for all columns.

Table 7-3 Parameter values used to design columns.

Parameter	Values	Number of Values
P_r - Axial Load Ratio	0.05, 0.10, 0.15, 0.20, 0.30, 0.40, 0.50	7
D_{col} - Column Diameter (ft)	2',2.5',3', ... , 9', 9.5', 10'	17
a_r - Column Aspect Ratio	2, 2.5, 3, ... , 9, 9.5, 10	17
cover - Section Cover (in)	2"	1
f'_c - Unconfined Concrete Strength	5 ksi	1
f_y - Longitudinal Reinforcement Yield	70 ksi	1

Figures 7-10 to 7-15 show some of the properties for columns with axial load ratios of 0.05 and 0.20, that are designed using the three methods. The *Overstrength* ratio is defined as the ratio of the actual flexural strength of the column to that required by each of the design methods. For example, the strengths required by BDS and ATC-32 are similar for periods greater than 1 second; and the strength required by SDC is 0.10W for all periods.

Considering the properties of columns with low axial load ($P_r = 0.05$), we observe that the BDS and SDC methods result in minimum longitudinal (ρ) and spiral (ρ_{sp}) reinforcement for almost all cases. The ATC-32 method requires more longitudinal reinforcement for short period columns (short columns with smaller diameters). A larger amount of spiral reinforcement may also be needed in some columns in order to ensure that they are controlled by flexural yielding. All three methods satisfy the respective strength requirements as evident in the large overstrength ratios. The ultimate displacement ductility (d_{ult}/d_y) is very similar for all methods. It is also apparent that the minimum spiral reinforcement requirements were sufficient to satisfy the SDC displacement capacity requirement, since the ultimate displacement capacity d_{ult} of all the columns is significantly larger than the inelastic displacement demand d_{inel} estimated from the elastic response spectrum. d_{inel} depends on the strength of the column and on the elastic spectral demand from the ARS spectrum. It is computed using the Nassar and Krawinkler equation as shown in Section 7.3.2.4.

The differences between the three design methods are somewhat more evident in the higher axial load case ($P_r = 0.2$). The longitudinal reinforcement (ρ) and flexural strength ($F_y/Mass$) of the SDC designed columns now exhibit a significant variation from the two other methods. Being weaker than the BSD and ATC-32 designed columns, the inelastic displacement demand on the

243

SDC columns is higher, and a higher amount of confinement is required in order to increase the displacement capacity to meet demand. Hence, the SDC method results in more ductile but weaker columns than the other two methods, while the ATC-32 method results in the most heavily reinforced columns. Other factors also affect the design, further complicating the results. For example, in the ATC-32 method, very short columns are required to be very strong (Z close to 1.0). Hence a larger spiral reinforcement ratio is needed to prevent shear failure, which also results in a large ductility capacity because of the increased confinement effect. The constructability of such heavily reinforced columns may be questionable although this issue is not considered the current study.

Figures 7-16 and 7-17 show contours of the period and spiral reinforcement percentage ratio plotted on a grid of column diameters and aspect ratios. As expected, the period increases smoothly with the column diameter and aspect ratio. The spiral reinforcement ratio ρ_{sp} decreases with increasing column diameter due to the nature of the confinement equations (Equations 7-10 to 7-12). ρ_{sp} also increases with smaller aspect ratios because of shear requirements, and in the case of the SDC method, because of the deformability requirement.

Figure 7-18 shows contours of the ductility capacity vs. diameter and aspect ratio. The ductility capacity increases for short columns, due to higher confinement ratios and relatively longer plastic hinge lengths.

A significant difference in the longitudinal reinforcement ratio is observed between SDC designed columns and columns designed using a Z factor. Using the SDC method, the reinforcement ratio is near minimum at short periods, and increases with period, which is opposite to the columns designed using the two other methods (Figure 7-19). This results in a more ductile design (for SDC designed columns), and significantly reduced P-Δ demands on longer period columns with large axial loads (Figure 7-20).

Figure 7-21 shows the strength of the designed columns, normalized by the mass. The plots resemble the shape of the ARS spectra, especially for the BDS method (constant Z). The corresponding actual Z ratios are shown in Figure 7-22. Note that the SDC ratios can be significantly higher than those resulting from the other two methods, while the ATC-32 ratios tend to be the smallest at short periods (Z close to 1). In some instances, Z ratios may be higher than the target because the section design is controlled by maximum reinforcement criteria.
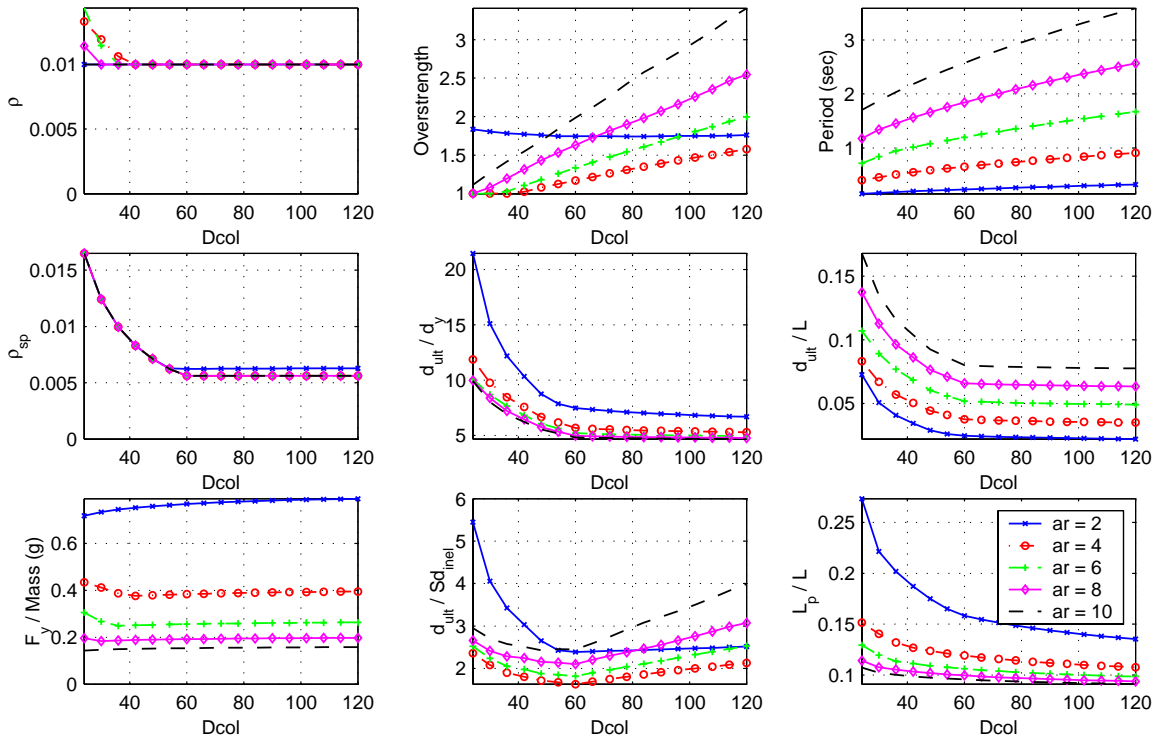
Figure 7-10. Properties of columns designed using the BDS method with P_r=0.05.
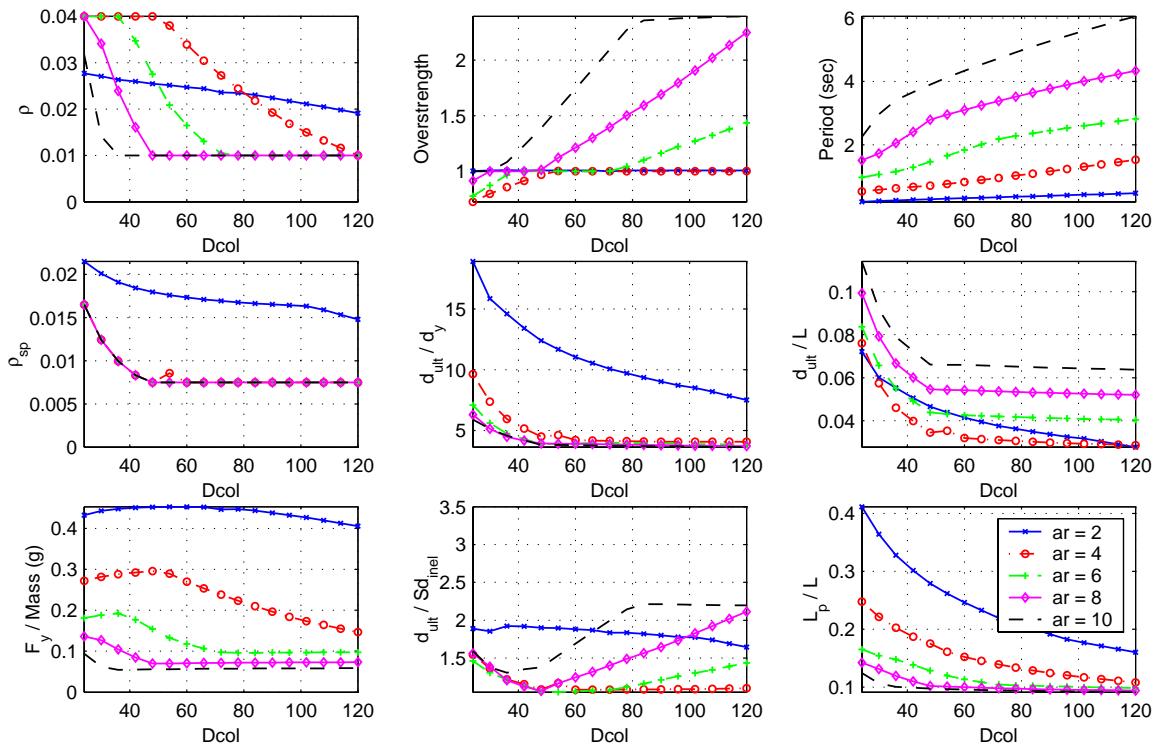
Figure 7-11. Properties of columns designed using the BDS method with P_r=0.2.

245
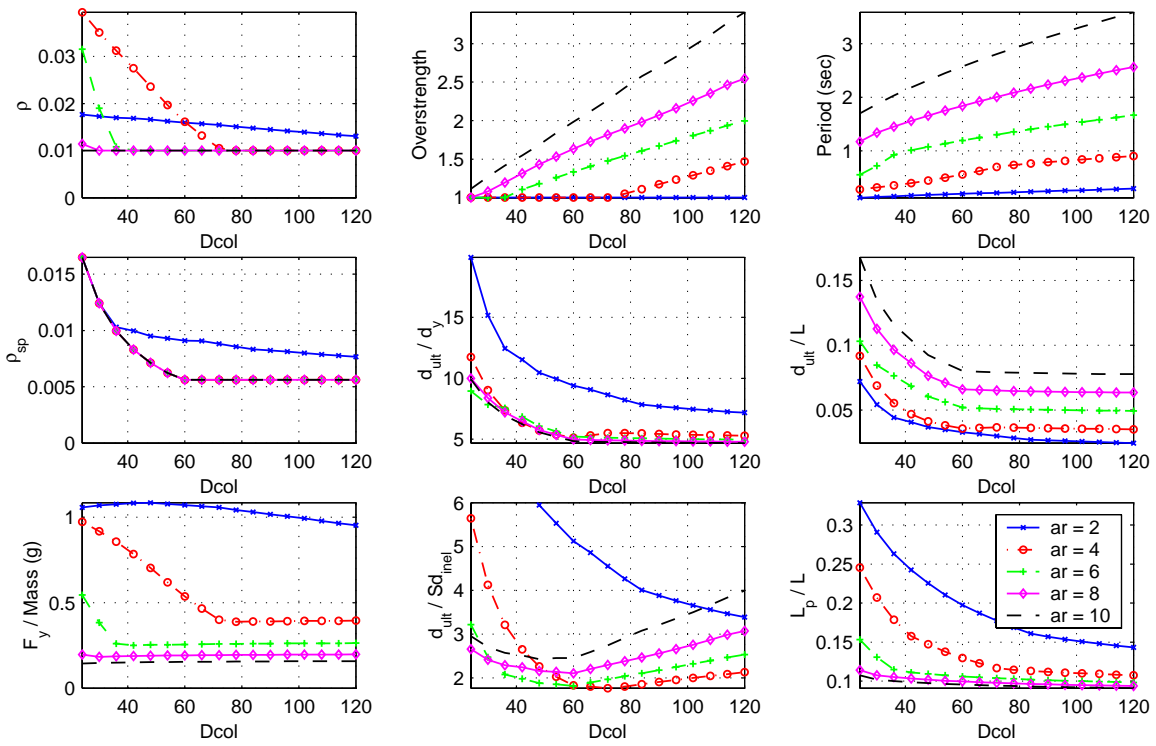
Figure 7-12. Properties of columns designed using the ATC-32 method with P_r=0.05.
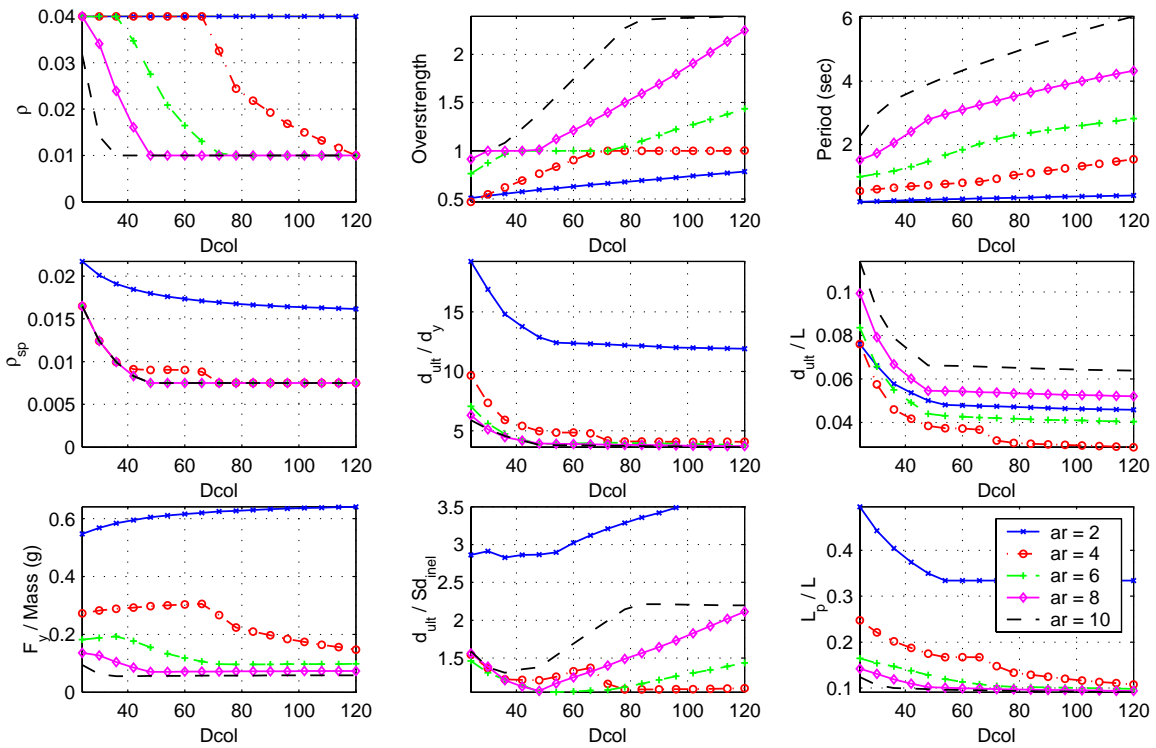
Figure 7-13. Properties of columns designed using the ATC-32 method with P_r=0.2.

246
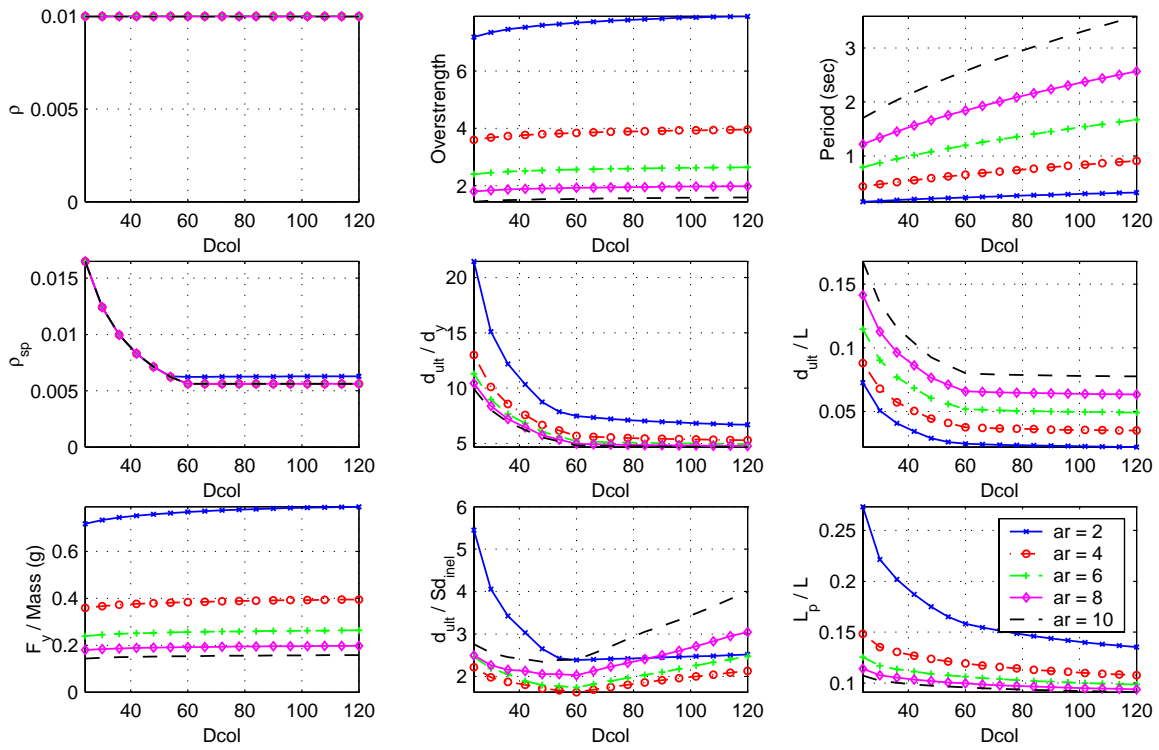
Figure 7-14. Properties of columns designed using the SDC method with P_r=0.05
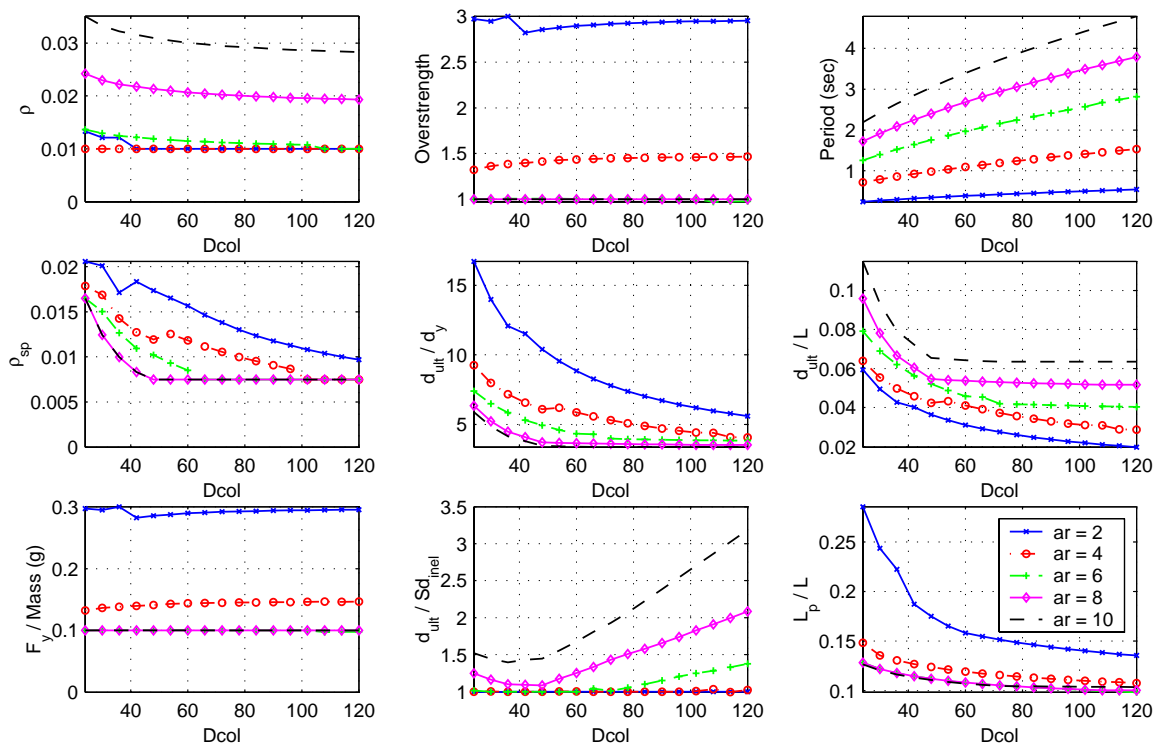
Figure 7-15. Properties of columns designed using the SDC method with P_r=0.2.
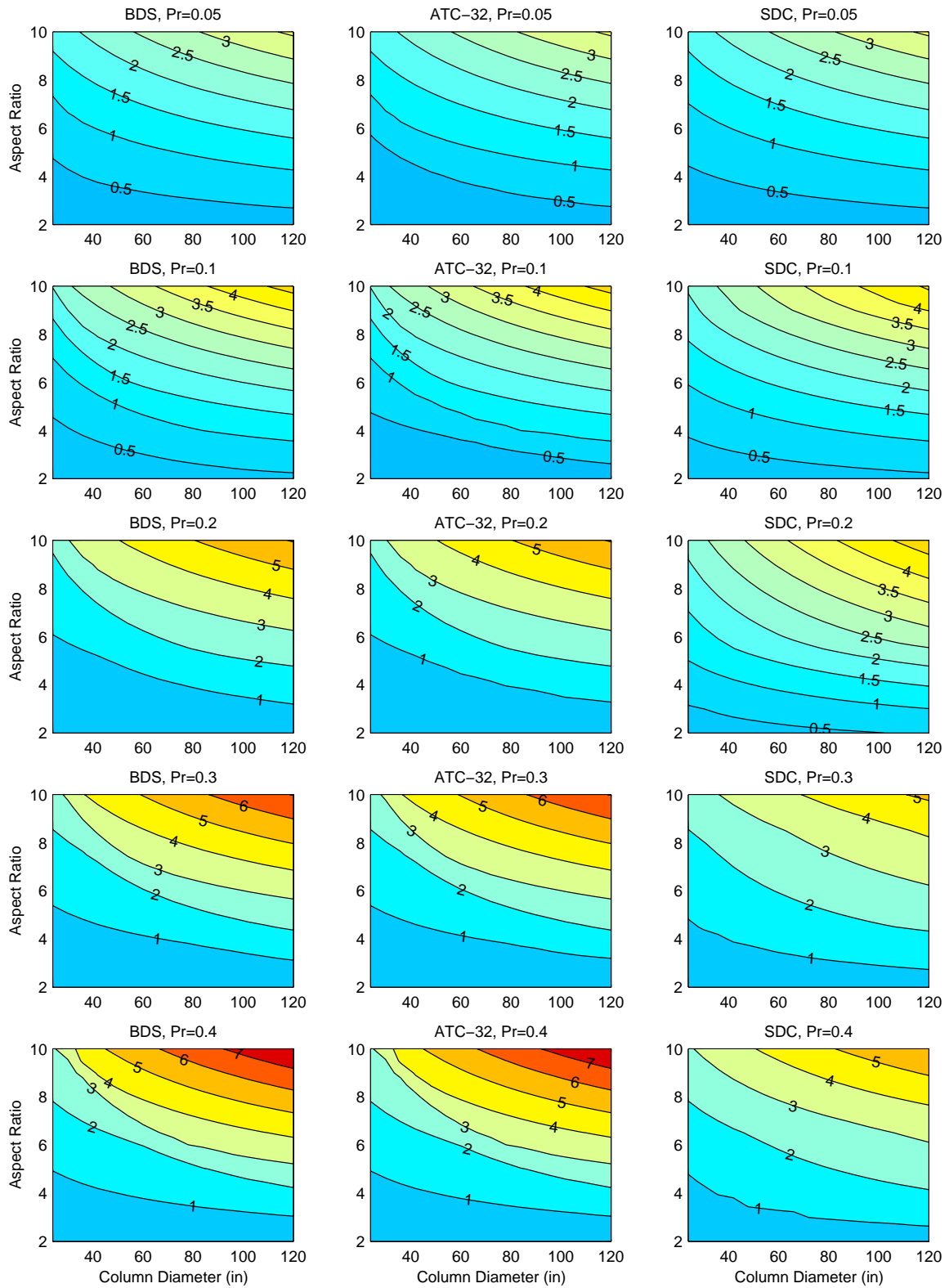
Figure 7-16. Period contours for series of columns designed by the BDS, ATC-32 and SDC methods.

248
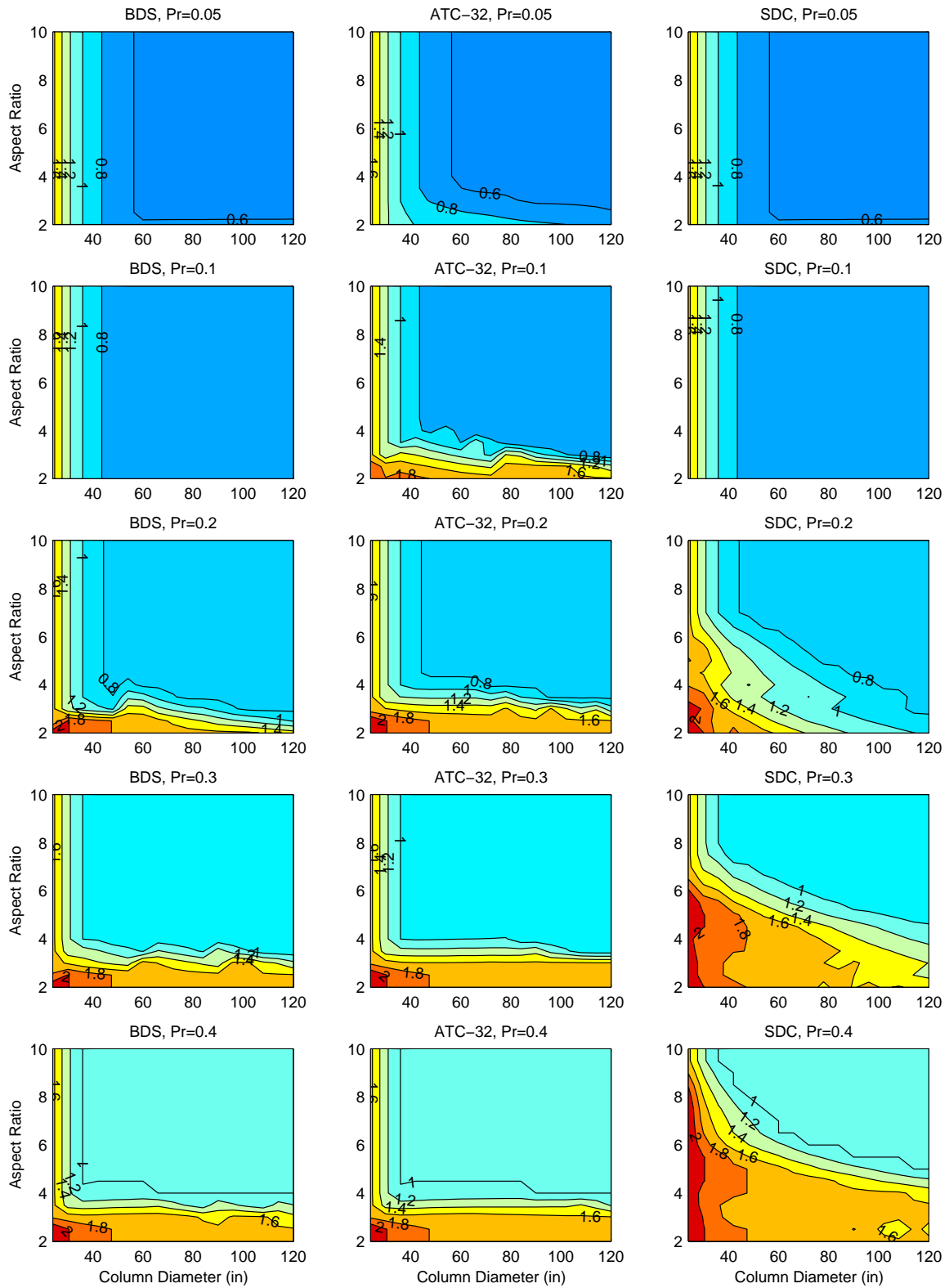
Figure 7-17. Spiral reinforcement percentage ratio ρ_{sp} contours for series of columns designed by the BDS, ATC-32 and SDC methods.
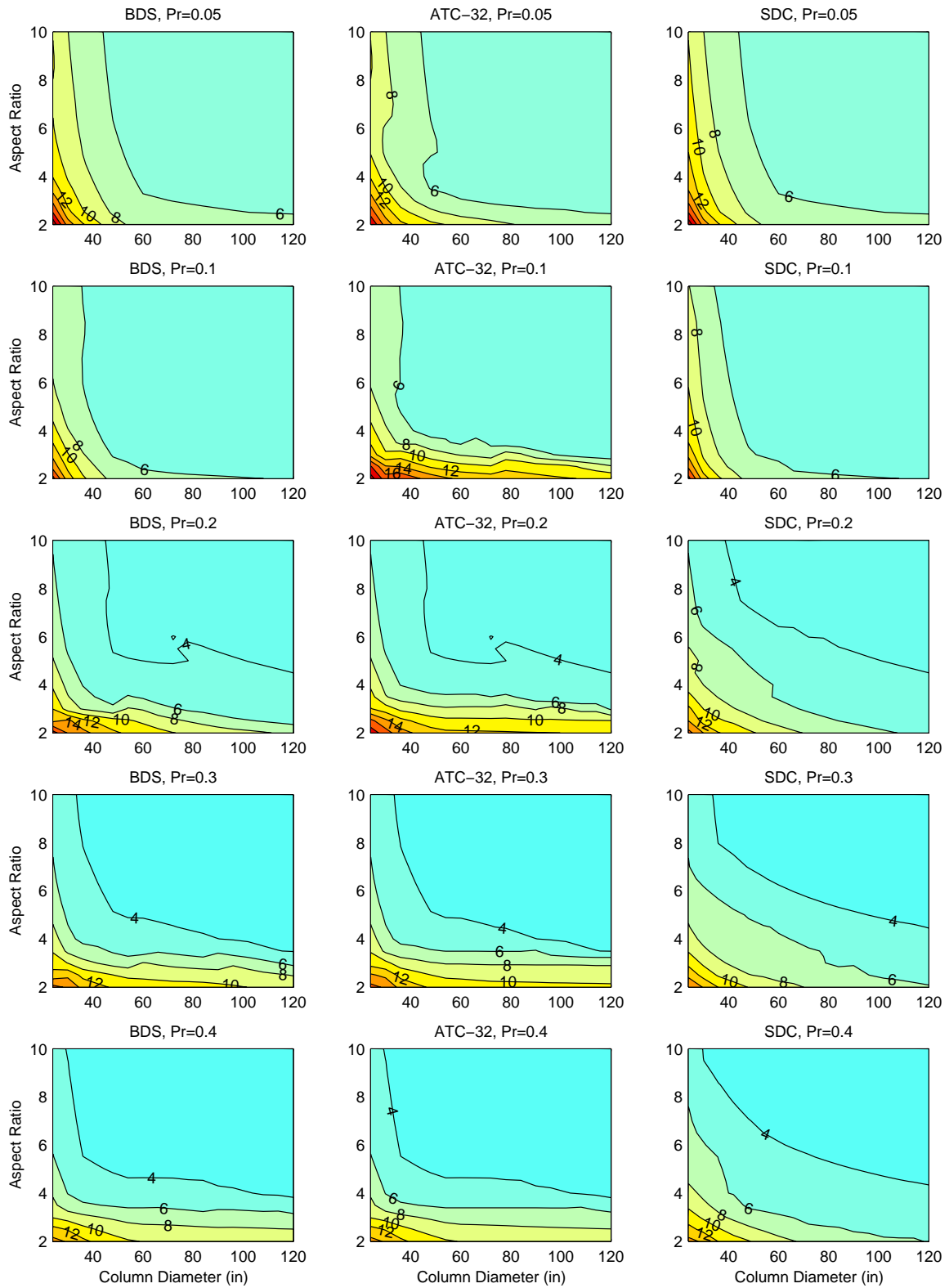
Figure 7-18. Ductility capacity ratio d_{ult}/d_y contours for series of columns designed by the BDS, ATC-32 and SDC methods.
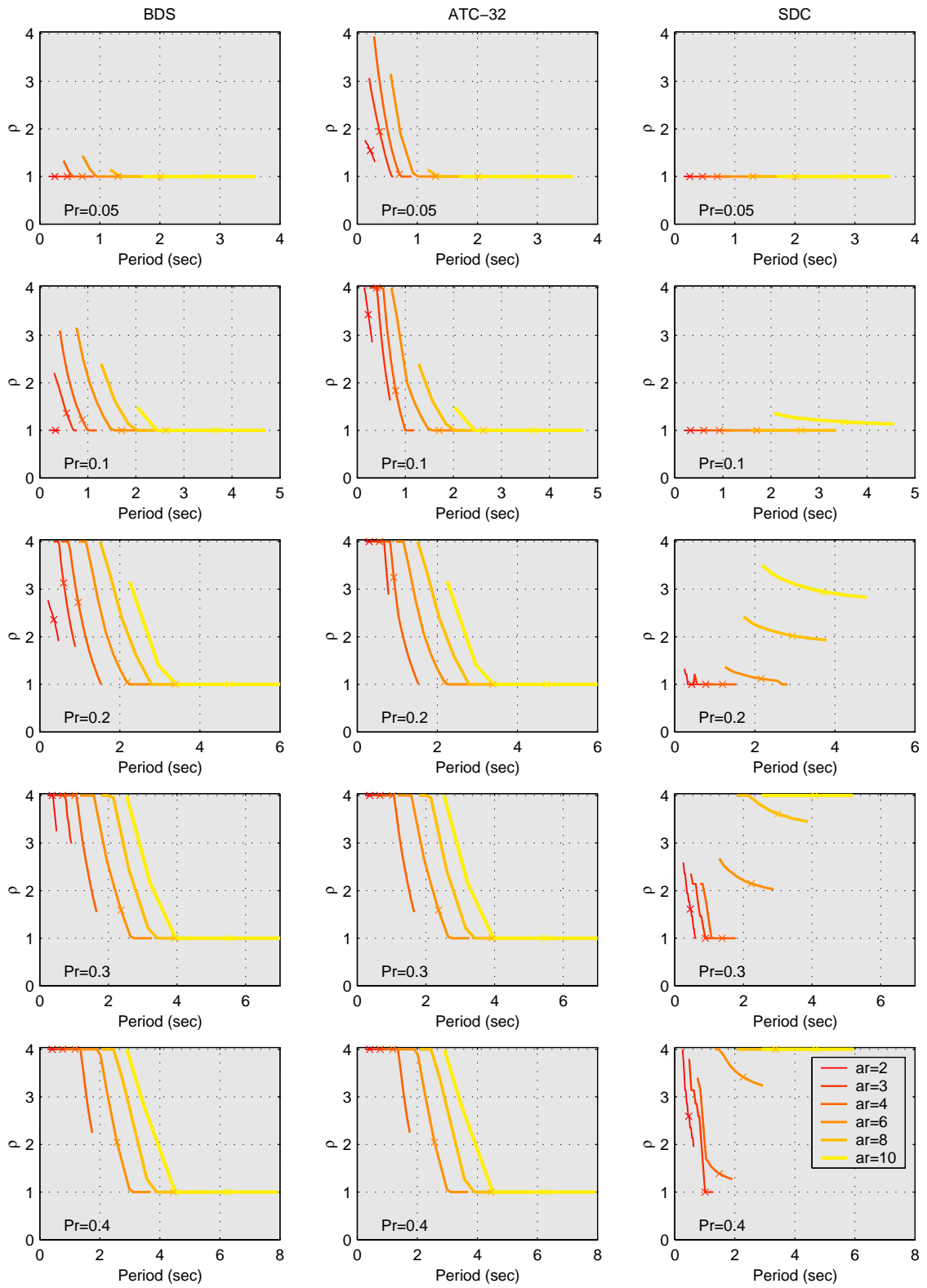
Figure 7-19. Longitudinal reinforcement percentage ratio ρ vs. period for series of columns designed by the BDS, ATC-32 and SDC methods.
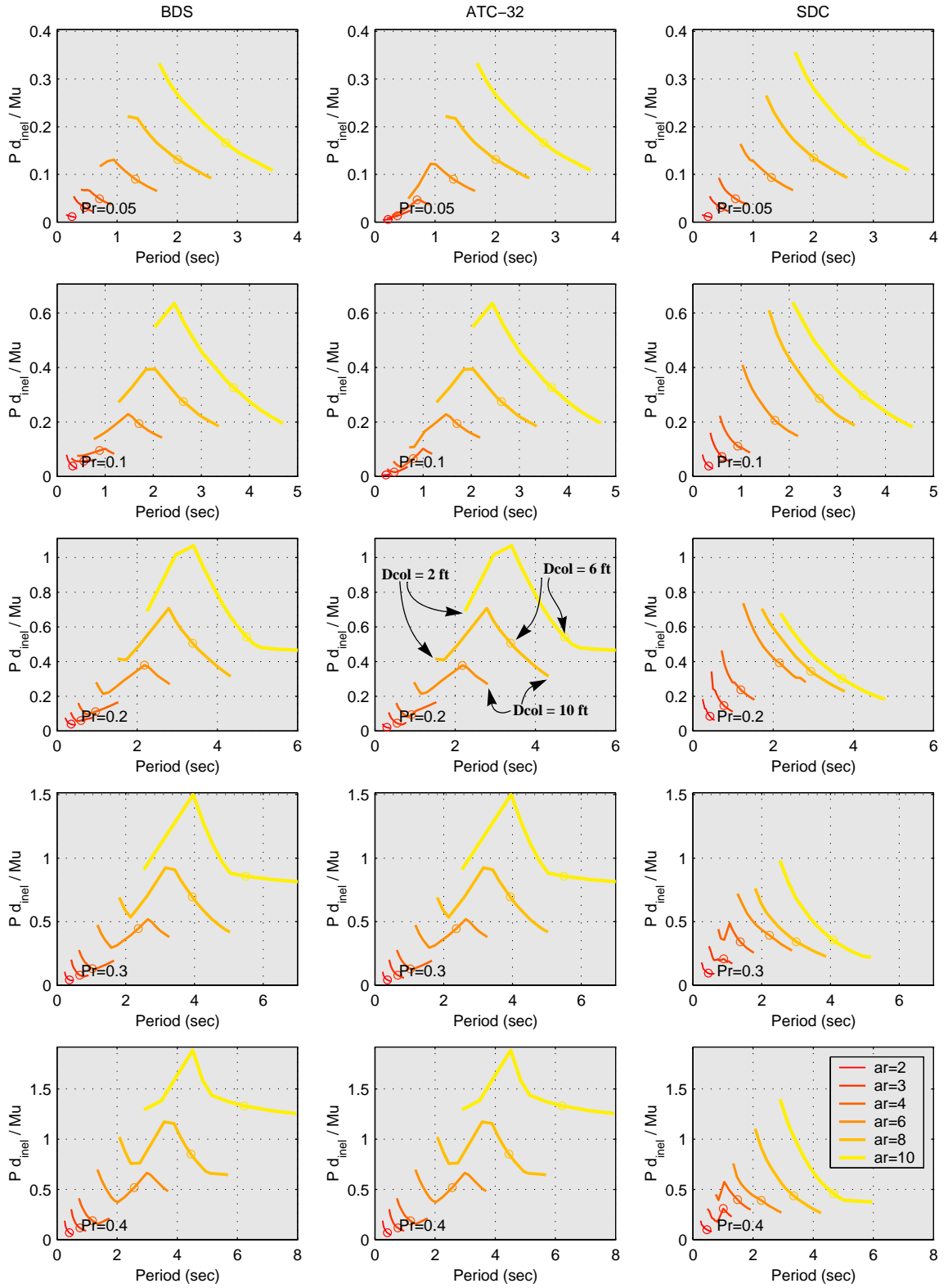
Figure 7-20. P-Δ effect vs. period for series of columns designed by the BDS, ATC-32 and SDC methods.
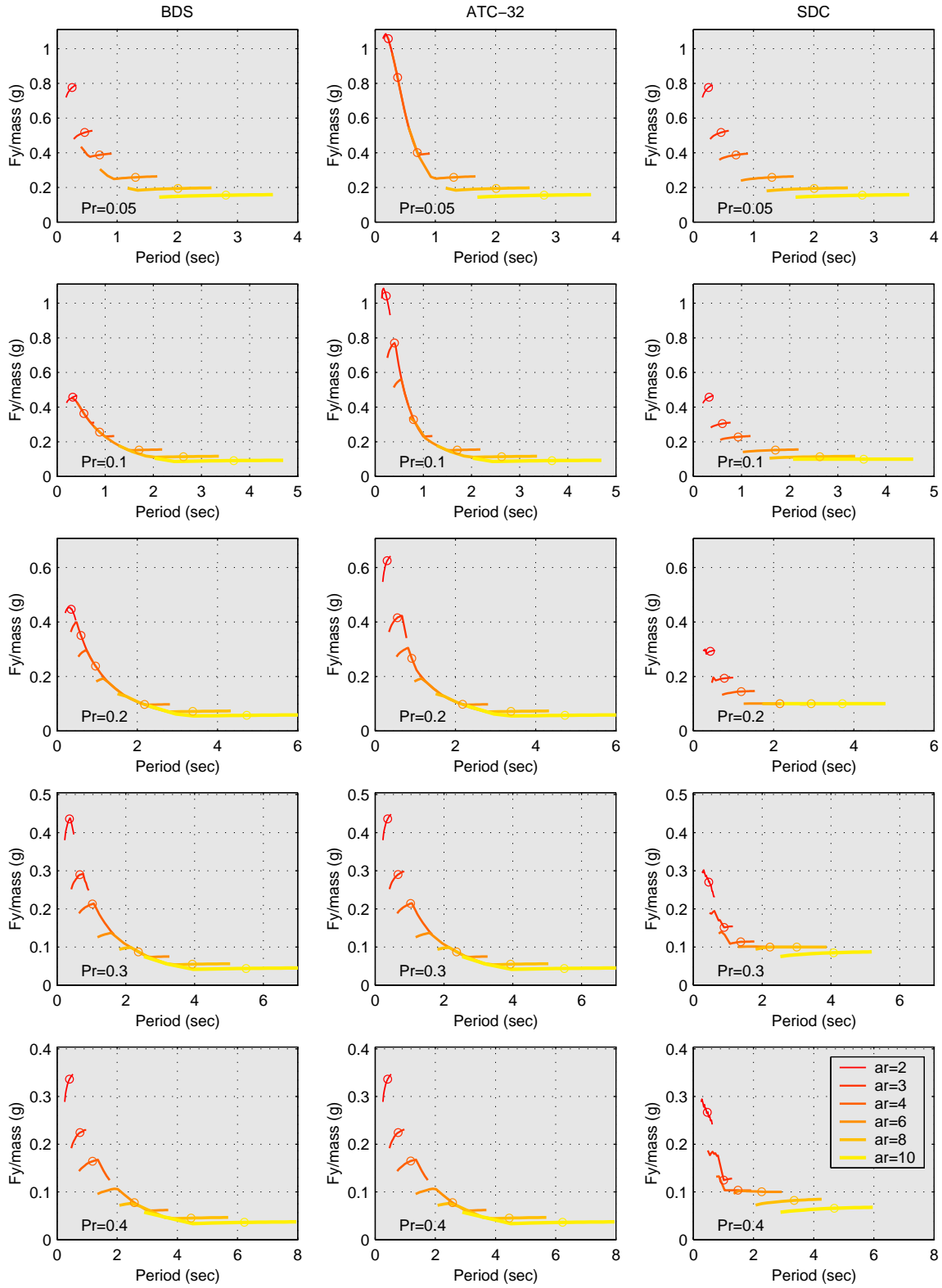
Figure 7-21. Normalized strength ratio vs. period for series of columns designed by the BDS, ATC-32 and SDC methods.
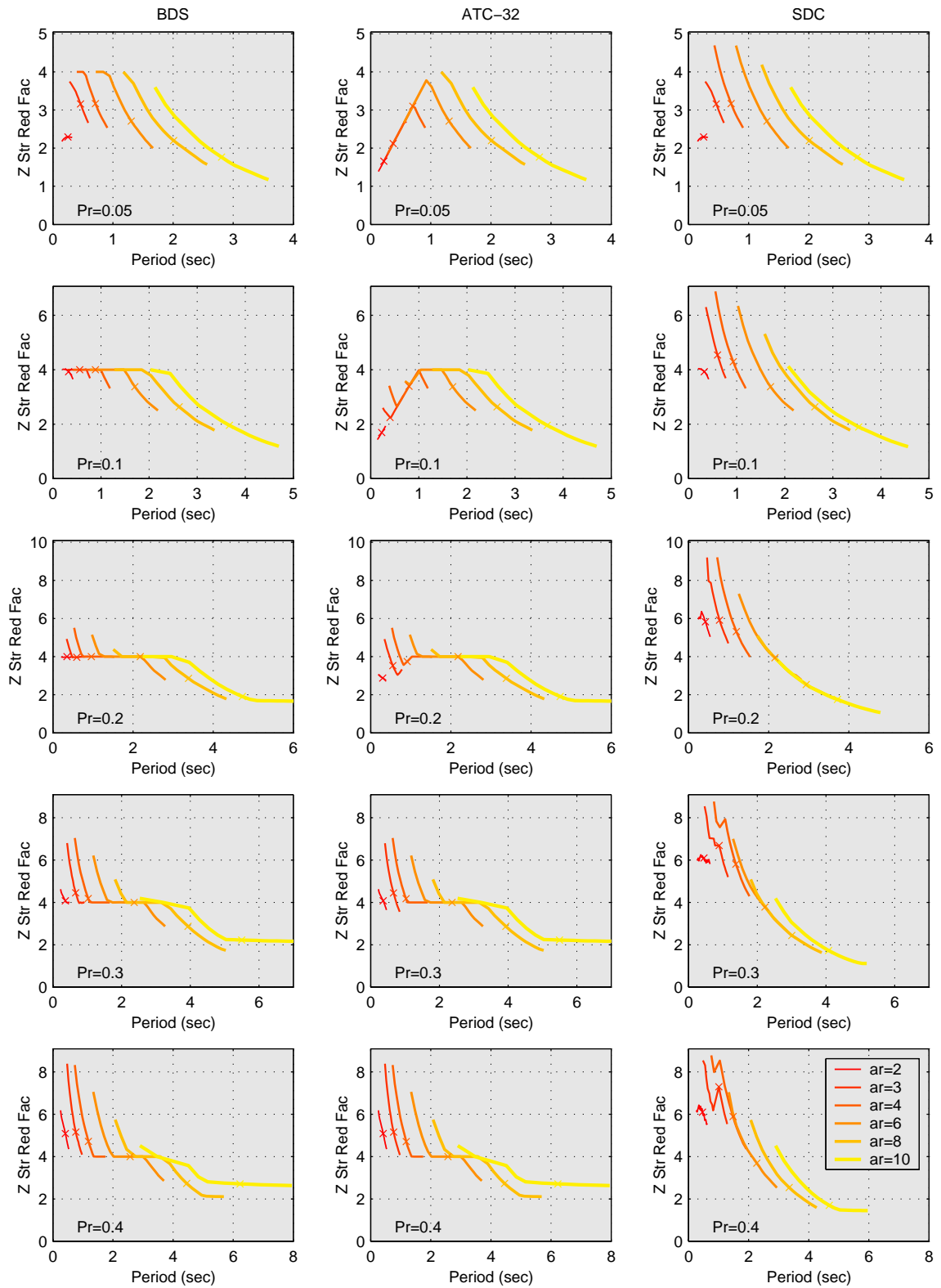
Figure 7-22. Effective reduction factor *Z* vs. period for series of columns designed by the BDS, ATC-32 and SDC methods.

7.5.2 Ground Motion Suite

A suite of 20 ground motion records was used to analyze the designed columns. The suite of records was selected to represent large events occurring at relatively small distances (< 30 km). As shown in (Figure 7-23), the suite of ground motions was scaled such that its mean matches the ARS spectrum (Magnitude 7.0, soil type B, 0.70g PGA). A list of the ground motion records used is provided in Table 7-4.

7.5.3 Element Modeling

Using the column properties obtained from the design procedure, a backbone curve can be constructed for each of the columns. A stiffness degrading model with varying unloading stiffness (Takeda model) is used to defined the hysteretic behavior of each column. The parameters of the model's backbone curve were computed from the interpolated moment-curvature results. Figure 7-24 presents an example curve for one of the designed columns.

7.5.4 Seismic Response of Designed Columns

The designed columns were analyzed under all 20 ground motions using the computer program Bispec [32]. Each column was modeled using a single degree-of-freedom system with a mass corresponding to the axial load ratio and 5% viscous damping. For each analysis, a number of spectral values and damage measures were computed, and statistical values (mean, standard deviation, coefficient of variation, etc.) relating to the different quantities were calculated.

Figures 7-25 to 7-29 show the average results of the dynamic response of the columns to the suite of ground motions. The quantities plotted are the ductility index, the Park and Ang index and the fatigue index.

The ductility index and the Park and Ang index show great similarities due to the small contribution of the energy term in the Park and Ang index (Figures 7-25 and 7-26).

The performance of the ATC-32 designed columns as reflected by the Park and Ang index is better than the performance of columns designed using the other two methods (BDS and SDC). The performance of the SDC columns is similar to the BDS columns at low axial loads, but becomes worse for shorter columns with higher axial loads ($P_r > 0.10$). This appears to be especially the case for columns with periods shorter than 1 second. Figure 7-27 shows contours of the
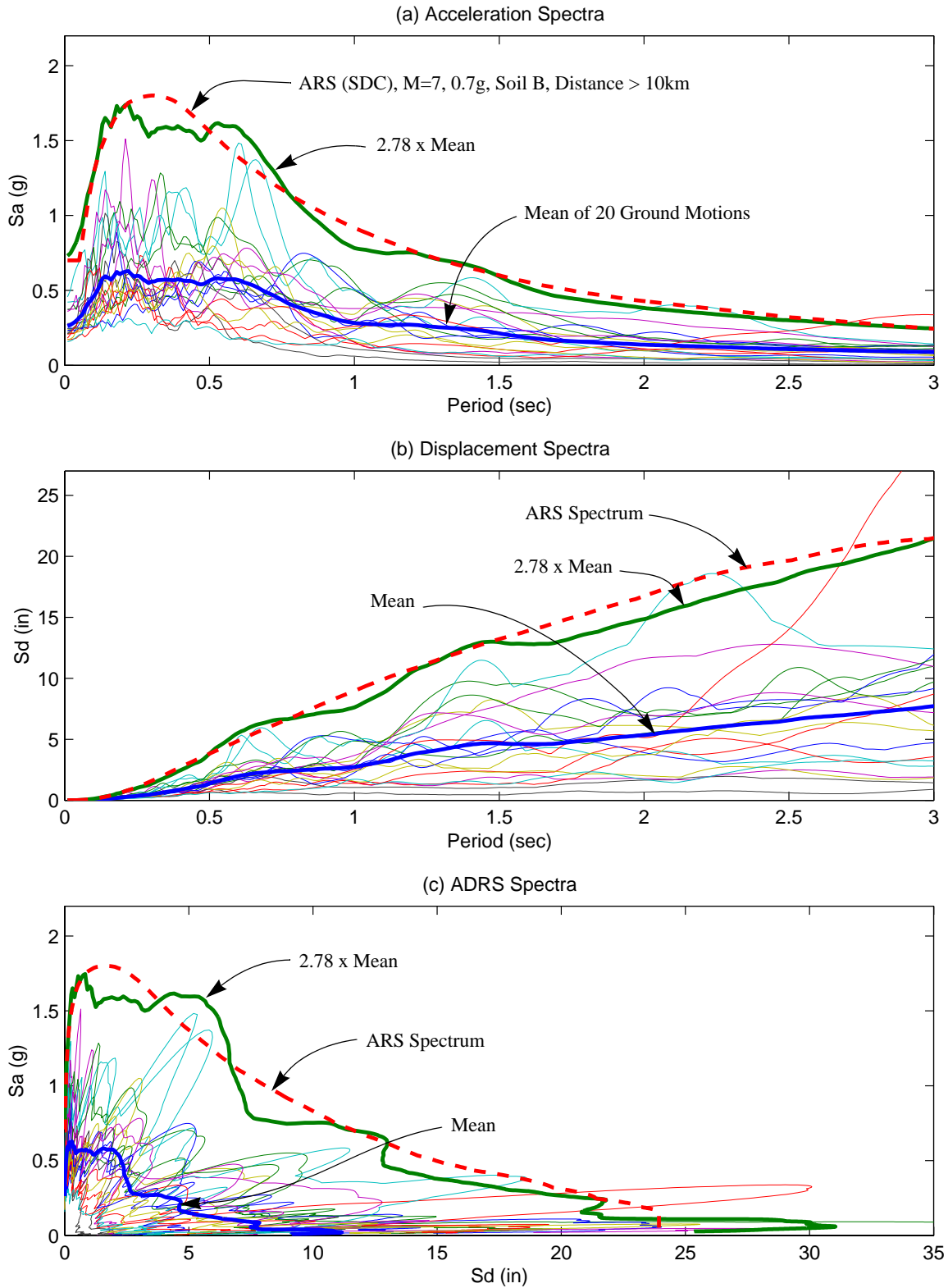
Figure 7-23. Spectral accelerations and displacements for the 20 ground motions used in the parametric analysis.

Table 7-4 Suite of 20 unidirectional ground motion records used to analyze the designed columns.

Record	comp	Event	Year	Magnitude	Station	R (km)
I-ELC	270	Imperial Valley	1940	7.0	El Centro Array #9	12.0
YER	270	Landers	1992	7.3	Yermo Fire Station #	24.9
AGW	000	Loma Prieta	1989	6.9	Agnews State Hospital	28.2
CAP	090	Loma Prieta	1989	6.9	Capitola	14.5
G03	090	Loma Prieta	1989	6.9	Gilroy Array #3	14.4
G04	090	Loma Prieta	1989	6.9	Gilroy Array #4	16.1
GMR	000	Loma Prieta	1989	6.9	Gilroy Array #7	24.2
HCH	090	Loma Prieta	1989	6.9	Hollister City Hall	28.2
HDA	255	Loma Prieta	1989	6.9	Hollister Differential Array	25.8
SVL	270	Loma Prieta	1989	6.9	Sunnyvale - Colton Ave.	28.8
CNP	196	Northridge	1994	6.7	Canoga Park - Topanga Can	15.8
FAR	000	Northridge	1994	6.7	LA - N Faring Rd	23.9
FLE	234	Northridge	1994	6.7	LA - Fletcher Dr	29.5
GLP	267	Northridge	1994	6.7	Glendale - Las Palmas	25.4
HOL	090	Northridge	1994	6.7	LA - Holywood Stor FF #	25.5
STC	090	Northridge	1994	6.7	Northridge - 17645 Saticoy St	13.3
PEL	180	San Fernando	1971	6.6	LA - Hollywood Stor Lot	21.2
B-BRA	225	Superstition Hills	1987	6.7	Brawley	18.2
B-ICC	000	Superstition Hills	1987	6.7	El Centro Imp. Co. Cent	13.9
B-WSM	090	Superstition Hills	1987	6.7	Westmorland Fire Station	13.3

Park and Ang index, and allows the determination of the undesirable combinations of diameter, aspect ratio and axial load.

The fatigue index of the various columns is shown in Figures 7-28 and 7-29. It is immediately apparent that the SDC designed columns are more susceptible to fatigue failure. The worst case scenario appears to be columns with small diameter and aspect ratio and axial load ratio of around 0.20. This is attributed to the lower reinforcement ratios of short period SDC columns. The lower reinforcement ratio increases the maximum tensile strain demand on the reinforcement. This is coupled with large displacement demands due to low strength, and with a larger number of cycles because of the short period.

In summary, it appears that the SDC design methodology produces ductile columns that have a large factor of safety for shear failure, but that are somewhat lacking in strength in the short
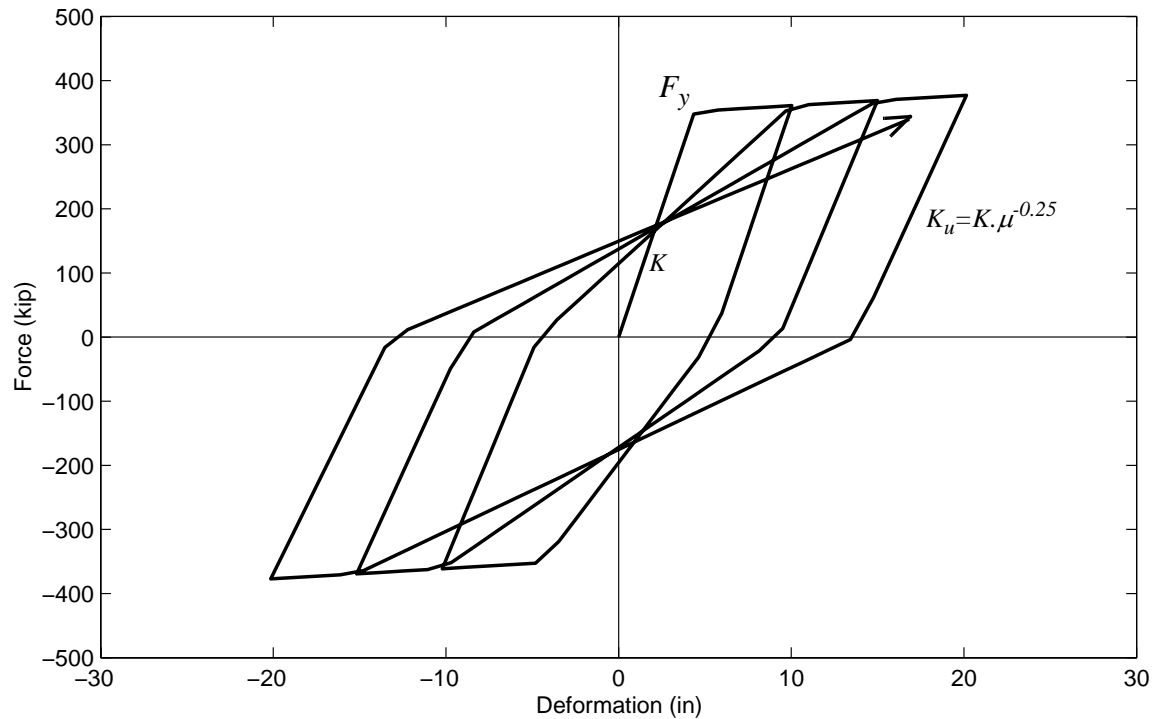
Figure 7-24. Stiffness degrading model for a designed column with $D_{col} = 72$ in., $P_r = 0.15$ and $a_r = 6$.

period range. Because of the lower reinforcement ratio, SDC designed columns may be more sus-ceptible to fatigue failure especially for short period columns. However, the SDC design method results in larger amounts of the reinforcement in the long period range which reduces P-Δ demands. The ATC-32 designed columns exhibit a better behavior, but columns designed according to this method may end up with a significant amount of longitudinal and spiral reinforcement.

7.6   EFFECTS OF BIDIRECTIONAL LOADING ON PERFORMANCE

The second analytical investigation involved studying the dynamic response of 27 columns designed according to the SDC design requirements. The columns were analyzed under both uni-directional and bidirectional ground motion excitations. In order for the analysis to capture the bidirectional interaction effects, a refined 2-element fiber model was used. The properties of the 27 columns were obtained by varying three parameters: diameter D_{col}, aspect ratio a_r, and axial load ratio P_r. For each parameter, three values were selected, which were meant to represent low and high extremes, in addition to an average or typical value. This ensures that the 27 combinations
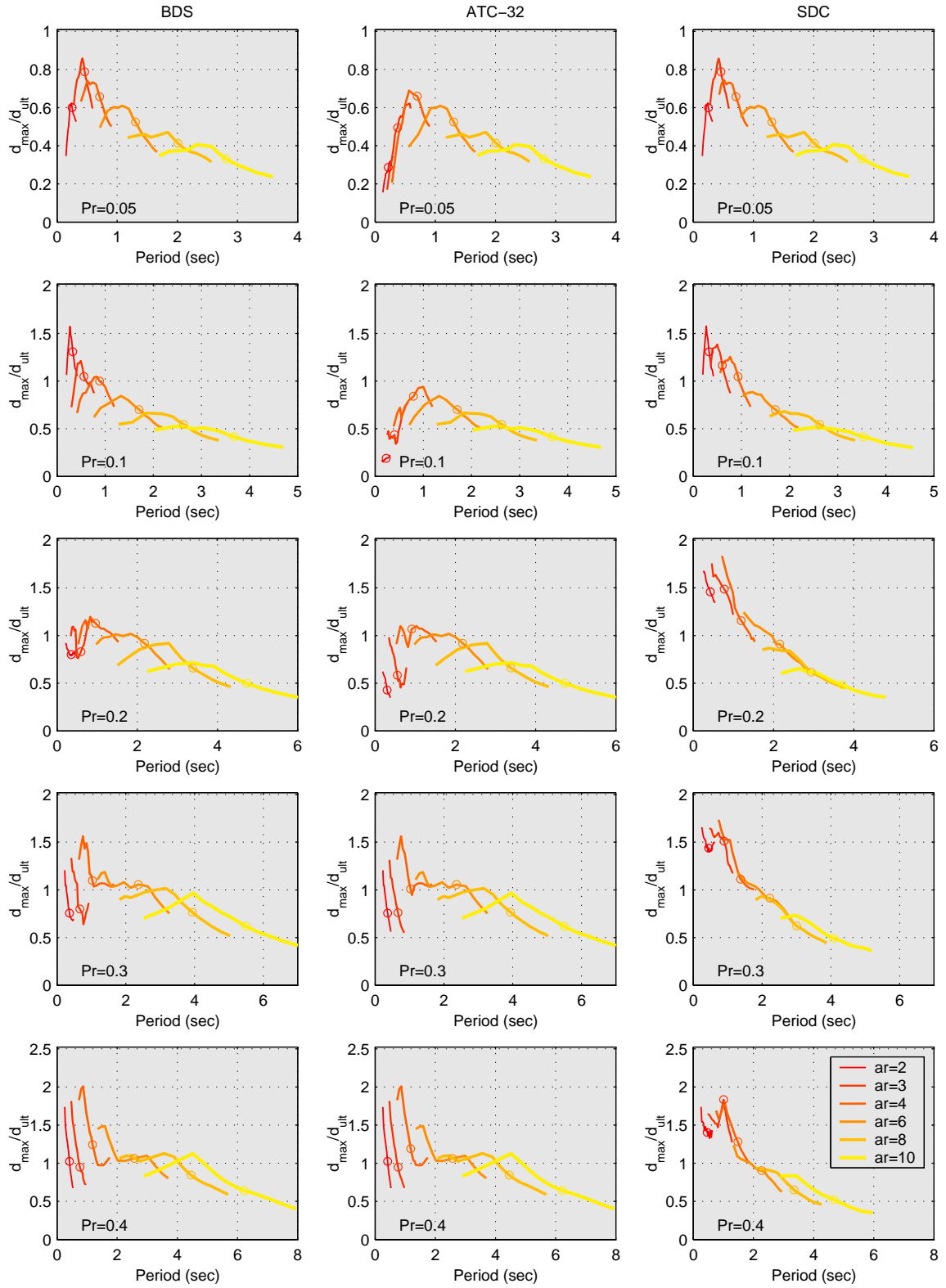
Figure 7-25. Mean of d_{max}/d_{ult} vs. period for series of columns designed by the BDS, ATC-32 and SDC methods, and analyzed under 20 ground motions.
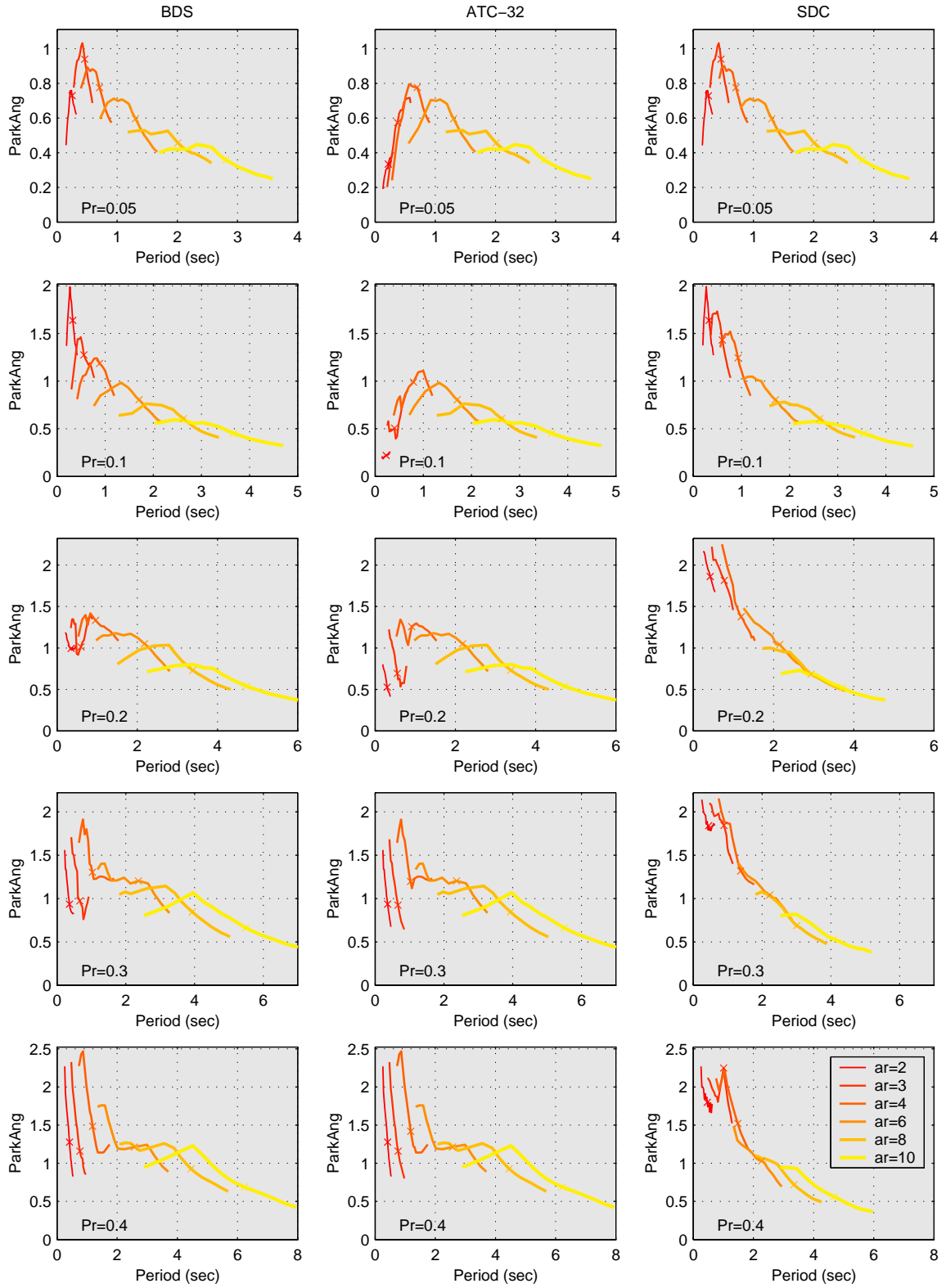
Figure 7-26. Mean of Park and Ang index vs. period for series of columns designed by the BDS, ATC-32 and SDC methods, and analyzed under 20 ground motions.
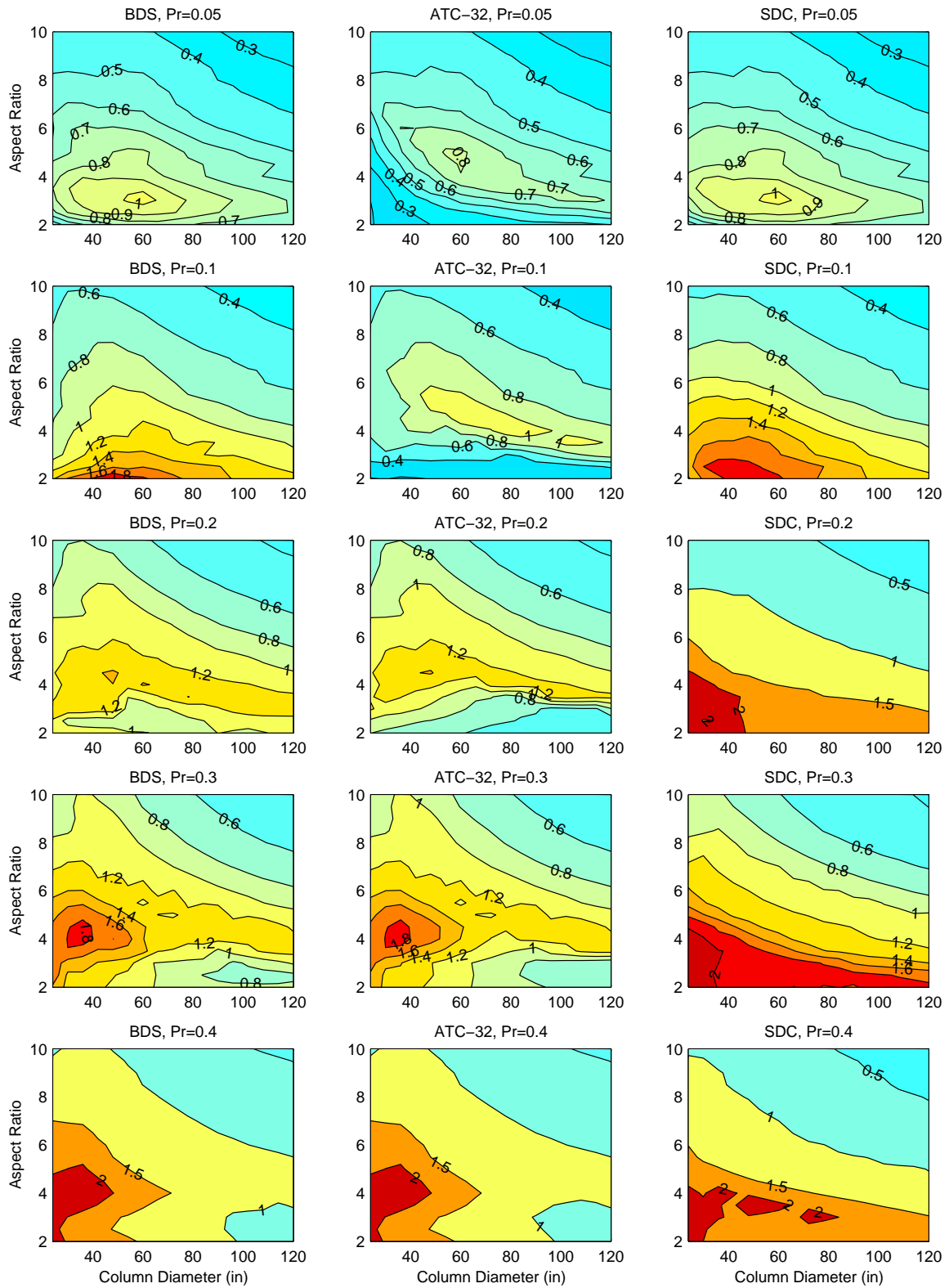
Figure 7-27. Contour of mean Park and Ang index vs. period for series of columns designed by the BDS, ATC-32 and SDC methods, and analyzed under 20 ground motions.

261
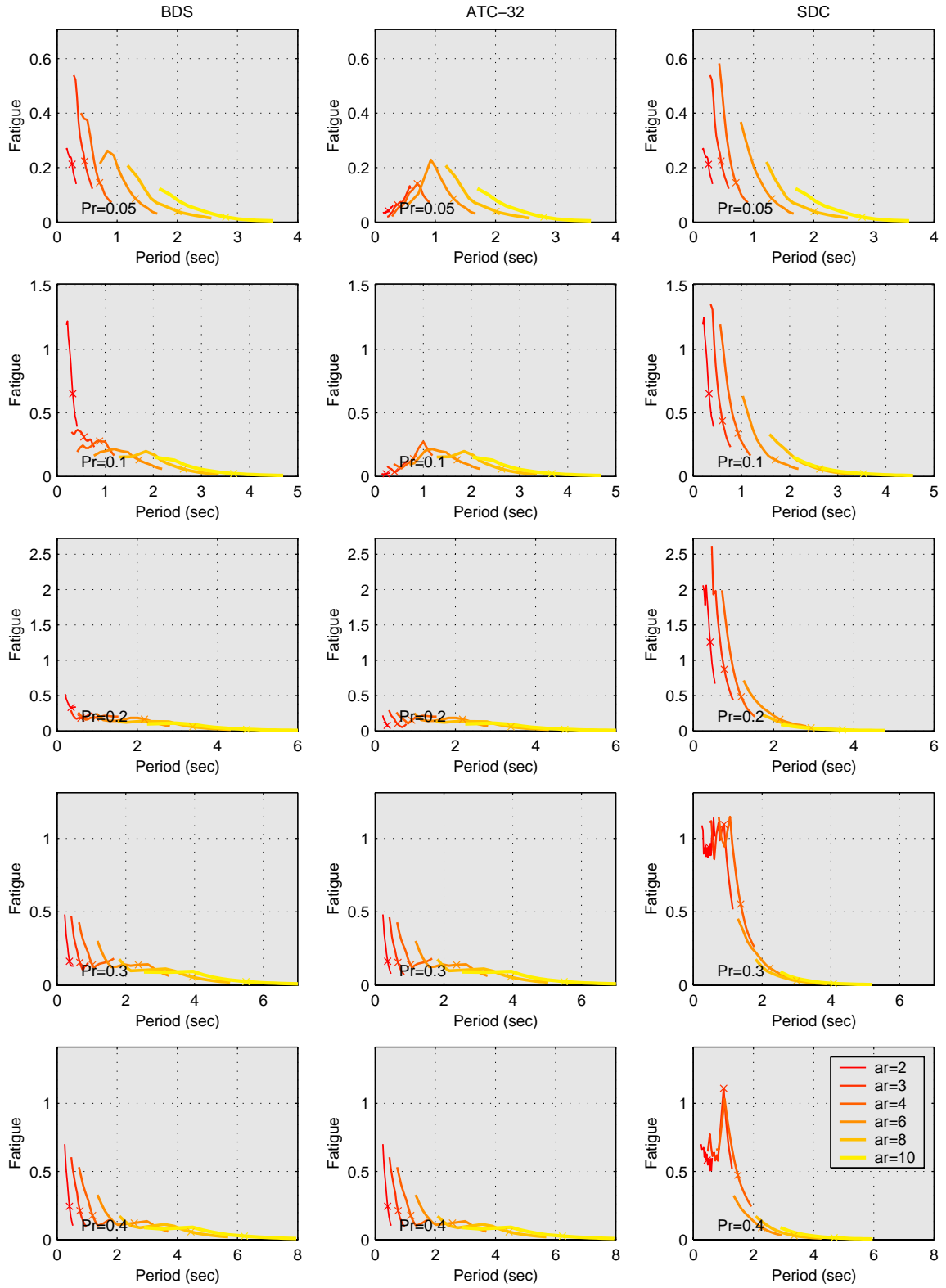
Figure 7-28. Mean of bar fatigue index vs. period for series of columns designed by the BDS, ATC-32 and SDC methods, and analyzed under 20 ground motions.
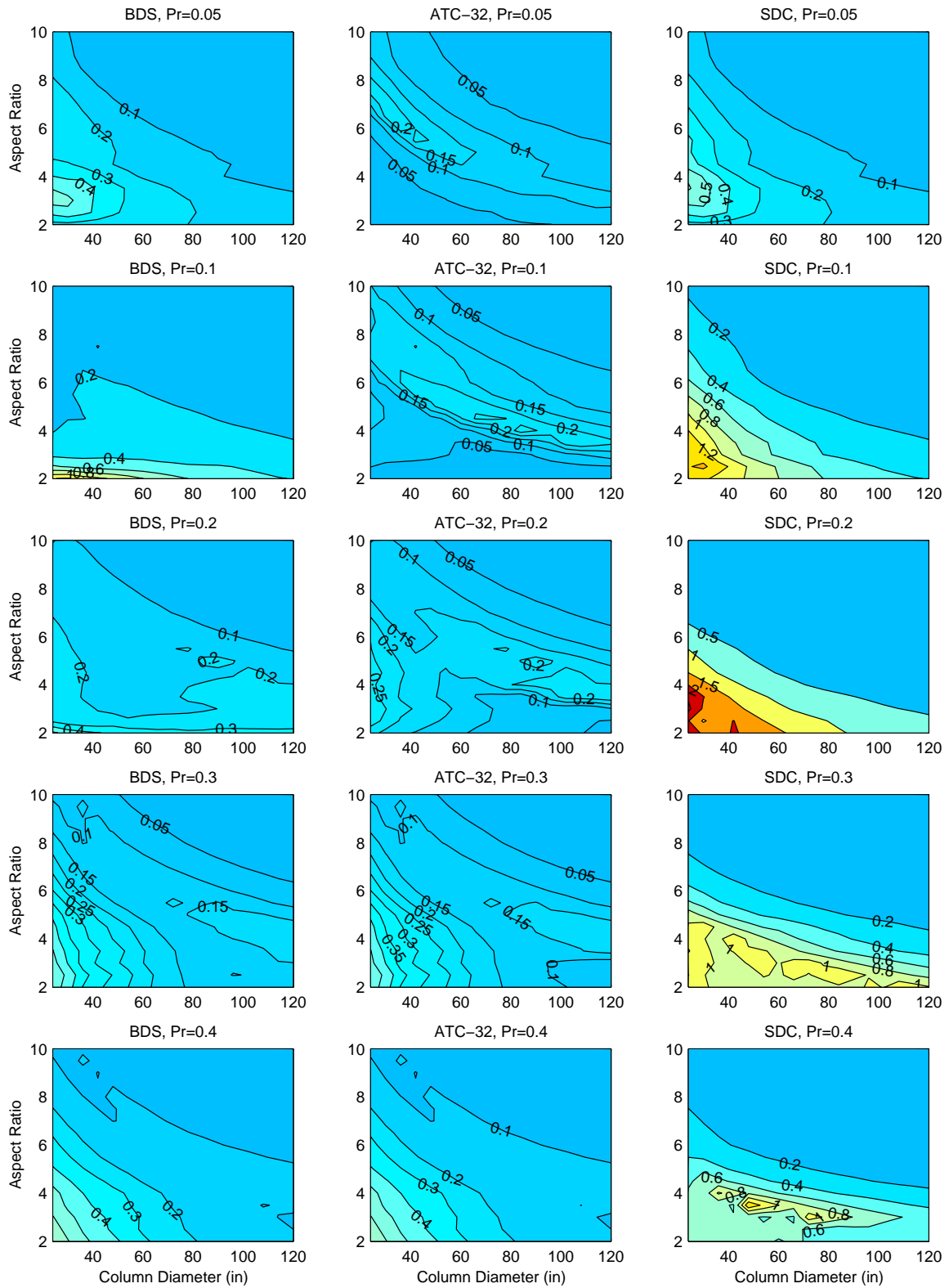
Figure 7-29. Contour of mean bar fatigue index vs. period for series of columns designed by the BDS, ATC-32 and SDC methods, and analyzed under 20 ground motions

263

of those three parameters would yield data points that encompass almost every possible column configuration which satisfies the assumed boundary conditions (cantilevered column).

Since the main objective of using the fiber element is modeling the bidirectional interaction of column sections, the focus of this section will be mainly devoted to the effects of bidirectional interaction on displacement demands and damage indices, and to comparing unidirectional and bidirectional results.

7.6.1   Load-Deformation Characteristics of the 27 Columns

Using three different values for each of D_{col}, a_r, and P_r resulted in 27 combinations. The parameters used are summarized in Table 7-5 for the columns which were numbered 1 through 27. Each column was designed according to the SDC requirements satisfying flexural strength, shear strength, displacement capacity and detailing requirements as discussed in Section 7.3. The section properties database was used in the design of each column according to the design chart in Figure 7-1. As a verification of the design procedure, the fiber model representing each column was first subjected to a pushover analysis. The pushover curve was then compared to the backbone curve predicted using the section database. Figure 7-33 shows this comparison for Column 5. Also plotted is the backbone curve that is directly estimated from the fiber model pushover. The agreement between the two backbone curves is satisfactory. Similar comparisons are performed for each of the columns, which all show similar agreement (Figures 7-34 through 7-36). Figures 7-37 and 7-38 show another comparison between columns that have the same diameter and height but different axial loads. This illustrates the effect of axial load on the ductility and load-displacement of columns designed according to seismic requirements (SDC). Higher axial loads generally increase the strength of the column while reducing the ultimate displacement capacity. When nonlinear geometry effects are considered, higher axial loads also cause a significant degradation of post-yield stiffness, especially for slender columns (Figure 7-38).

Since the 27 columns considered are a subset of the columns studied in the previous section, they share their properties which were described in Section 7.5.1.

7.6.2   Ground Motion Suite

The same suite of 20 ground motions used in the previous section was used in the current analysis, except that both components of each record were used. Some of the components were switched

Table 7-5 Properties of the 27 designed columns.

#	P_r	a_r	D_{col}	L	L_p	L_p/L	ρ	ρ_{sp}	K	Kh/K	P	T	F_y	ovrstr	d_{ult}	μ_{ult}	$P\Delta$	FS	Sa_{ARS}	Sd_{ARS}	d_{inel}	d_{ult}/d_{inel}
			in	in	in	%	%	Kip/in	%	Kip	sec	Kip		in				g	in	in	
1			36	108	15.9	0.15	1.00%	1.00%	233	1.78%	254	0.33	126	4.97	5.1	9.4	0.01	2.03	1.80	2.0	2.7	1.91
2		3	72	216	27.6	0.13	1.00%	0.56%	490	2.31%	1018	0.46	526	5.17	6.4	6.0	0.01	1.49	1.63	3.4	3.8	1.69
3			120	360	42.1	0.12	1.00%	0.56%	832	2.83%	2827	0.59	1490	5.27	10.1	5.6	0.01	1.66	1.40	4.8	4.9	2.05
4			36	216	24.6	0.11	1.00%	1.00%	29	2.26%	254	0.94	63	2.48	16.6	7.7	0.04	4.23	0.97	8.4	8.1	2.05
5	0.05	6	72	432	44.8	0.10	1.00%	0.56%	61	2.79%	1018	1.30	263	2.58	22.0	5.1	0.04	3.36	0.70	11.7	11.7	1.89
6			120	720	70.9	0.10	1.00%	0.56%	104	3.31%	2827	1.67	745	2.64	35.5	5.0	0.04	3.32	0.53	14.4	14.4	2.47
7			36	360	36.1	0.10	1.00%	1.00%	6	2.54%	254	2.03	38	1.49	41.7	6.9	0.11	7.05	0.42	17.0	17.0	2.45
8		10	72	720	67.9	0.09	1.00%	0.56%	13	3.05%	1018	2.81	158	1.55	56.9	4.8	0.11	5.60	0.27	21.1	21.1	2.70
9			120	1200	109.3	0.09	1.00%	0.56%	22	3.55%	2827	3.59	447	1.58	93.1	4.7	0.10	5.53	0.19	23.4	23.4	3.99
10			36	108	15.9	0.15	1.00%	1.30%	307	1.17%	763	0.50	169	2.22	4.7	8.5	0.02	1.33	1.55	3.9	4.7	1.00
11		3	72	216	27.6	0.13	1.00%	0.81%	638	1.70%	3054	0.70	706	2.31	6.0	5.4	0.02	1.26	1.24	5.9	6.0	1.00
12			120	360	42.1	0.12	1.00%	0.69%	1080	2.09%	8482	0.90	1997	2.35	8.5	4.6	0.02	1.38	1.01	8.0	7.6	1.11
13			36	216	24.6	0.11	1.00%	1.00%	38	1.19%	763	1.43	84	1.11	12.8	5.8	0.09	3.10	0.64	12.7	12.7	1.01
14	0.15	6	72	432	44.8	0.10	1.00%	0.69%	80	1.92%	3054	1.98	352	1.15	18.8	4.2	0.09	3.02	0.43	16.6	16.6	1.13
15			120	720	70.9	0.10	1.00%	0.69%	135	2.44%	8482	2.54	998	1.18	30.1	4.1	0.09	3.13	0.32	19.8	19.8	1.52
16			36	360	39.5	0.11	2.18%	1.00%	12	2.36%	763	2.60	76	1.00	30.9	4.7	0.18	4.02	0.31	20.2	20.2	1.53
17		10	72	720	72.2	0.10	2.01%	0.69%	23	3.20%	3054	3.65	305	1.00	47.8	3.7	0.18	3.57	0.18	23.5	23.5	2.03
18			120	1200	115.3	0.10	1.93%	0.69%	39	3.62%	8482	4.70	848	1.00	77.4	3.6	0.18	3.62	0.11	23.9	23.9	3.23
19			36	108	21.3	0.20	2.14%	1.87%	480	1.56%	1527	0.57	293	1.92	5.2	8.5	0.03	1.47	1.44	4.6	5.1	1.01
20		3	72	216	27.6	0.13	1.00%	1.68%	780	1.83%	6107	0.89	927	1.52	7.5	6.3	0.04	1.92	1.01	7.9	7.5	1.00
21			120	360	42.1	0.12	1.00%	1.40%	1316	2.19%	16965	1.15	2621	1.54	10.3	5.2	0.04	1.73	0.80	10.3	10.3	1.00
22			36	216	28.6	0.13	2.43%	1.61%	63	2.25%	1527	1.57	155	1.02	13.7	5.6	0.11	2.56	0.57	13.7	13.7	1.00
23	0.3	6	72	432	49.6	0.11	2.15%	0.97%	126	2.93%	6107	2.23	613	1.00	18.4	3.8	0.11	2.12	0.38	18.4	18.4	1.00
24			120	720	78.0	0.11	2.03%	0.88%	209	3.40%	16965	2.88	1696	1.00	27.8	3.4	0.11	2.06	0.26	21.3	21.3	1.31
25			36	360	43.3	0.12	4.00%	1.00%	17	3.11%	1527	2.99	122	0.80	26.3	3.8	0.24	2.52	0.25	21.5	21.5	1.23
26		10	72	720	81.7	0.11	4.00%	0.88%	38	4.15%	6107	4.08	521	0.85	46.3	3.3	0.23	2.32	0.15	23.9	23.9	1.93
27			120	1200	136.1	0.11	4.00%	0.88%	64	4.47%	16965	5.19	1488	0.88	76.9	3.3	0.22	2.30	0.10	25.8	25.8	2.98

with the objective of making the first component (x) larger than the second component (y), as measured by the record's peak ground acceleration. The resulting records and their respective components are summarized in Table 7-6, and plotted in Figures 7-30 to 7-32. All records were scaled by 2.50 such that the mean of the 20 larger components had the best fit to the ARS acceleration spectra (Magnitude 7, 0.70g PGA, Soil B, d > 10 km).

7.6.3   Unidirectional and Bidirectional Analyses Performed

A series of unidirectional and bidirectional analyses were performed using OpenSees. The model consisted of two fiber section elements. The element at the base of the column had a length equal to twice the plastic hinge length as estimated from Equation 7-17. Each column was analyzed under the suite of 20 records. Three nonlinear dynamic analyses were performed for each earthquake-column combination: two unidirectional analyses using each of the two components of the record individually, and one bidirectional analysis with both components applied simultaneously. All of the analyses considered the effects of nonlinear geometry (P-Δ effects).

The Newmark integration scheme ($\gamma = 0.5$, $\beta = 0.25$) was used in the analysis with a time step of 0.02 seconds. In the case the analysis did not converge, it was repeated with a time steps of 0.005 seconds. Failure to converge with the smaller time step was considered an indication of instability, as it was generally accompanied by divergence in deformations and forces. The non-converged analyses were not considered when computing statistical information such as means and medians. In fact, for each ground motion analysis of each column, if the analysis failed during either one of the unidirectional analyses (x or y) or during the bidirectional analysis, all three analyses were discarded. This is essential in cases where the bidirectional and unidirectional analyses are compared. Figures 7-39 through 7-42 show the percentage of converged analysis for each direction. Note that some earthquakes tend to have lower convergence ratios than other (Figure 7-39). Similarly, some columns tend to have lower convergence ratios (Figure 7-40). Columns with higher axial loads tend have the lowest convergence rates because of P-Δ effects (Figure 7-42).

Using Rayleigh damping, the damping matrix was computed from the mass matrix and tangent stiffness matrix as:

$$c \ = \ \alpha m + \beta k_t \tag{7-32}$$

266

Table 7-6 Suite of 20 bidirectional ground motion records used to analyze the designed columns.

Record	comp1	comp2	Event	Year	Magnitude	Station	R (km)
I-ELC	180	270	Imperial Valley	1940	7.0	El Centro Array #9	12.0
YER	270	360	Landers	1992	7.3	Yermo Fire Station #	24.9
AGW	000	090	Loma Prieta	1989	6.9	Agnews State Hospital	28.2
CAP	000	090	Loma Prieta	1989	6.9	Capitola	14.5
G03	000	090	Loma Prieta	1989	6.9	Gilroy Array #3	14.4
G04	000	090	Loma Prieta	1989	6.9	Gilroy Array #4	16.1
GMR	090	000	Loma Prieta	1989	6.9	Gilroy Array #7	24.2
HCH	090	180	Loma Prieta	1989	6.9	Hollister City Hall	28.2
HDA	255	165	Loma Prieta	1989	6.9	Hollister Differential Array	25.8
SVL	360	270	Loma Prieta	1989	6.9	Sunnyvale - Colton Ave.	28.8
CNP	196	106	Northridge	1994	6.7	Canoga Park - Topanga Can	15.8
FAR	000	090	Northridge	1994	6.7	LA - N Faring Rd	23.9
FLE	234	144	Northridge	1994	6.7	LA - Fletcher Dr	29.5
GLP	177	267	Northridge	1994	6.7	Glendale - Las Palmas	25.4
HOL	360	090	Northridge	1994	6.7	LA - Holywood Stor FF #	25.5
STC	180	090	Northridge	1994	6.7	Northridge - 17645 Saticoy St	13.3
PEL	090	180	San Fernando	1971	6.6	LA - Hollywood Stor Lot	21.2
B-BRA	225	315	Superstition Hills	1987	6.7	Brawley	18.2
B-ICC	000	090	Superstition Hills	1987	6.7	El Centro Imp. Co. Cent	13.9
B-WSM	180	090	Superstition Hills	1987	6.7	Westmorland Fire Station	13.3

α and β were selected to give a damping of 5% at periods of $T_{eff}/2$ and $2T_{eff}$, which resulted in a damping of 4% at the effective period T_{eff}. This results in little variation of the damping ratio as the column softens due to yielding.

Peak values of displacements and damage indices were computed for each analysis. In the bidirectional case, both unidirectional and bidirectional peaks were computed. For instance, the peak displacement in each direction dx and dy are compared, in addition to the resultant radial displacement d. Often in this section, unidirectional and bidirectional results are differentiated using the symbols 1D and 2D.

Since it is common to estimate the bidirectional response using two unidirectional analyses, a fourth set of results was constructed from the two unidirectional analyses. This set is referred to

as bidirectional uncoupled, and consists of combining the x and y histories from the x and y unidi-rectional analyses. Hence, one can compute $d_{2D\ uncoupled}$ from dx_{1D} and dy_{1D}, and compare its value to d_{2D} to evaluate whether bidirectional deformations can be approximated using two sets of unidirectional analyses.

7.6.4 Interpretation of Analysis Results

The significance of the analysis results is examined from several perspectives. The main focus is on the effect of bidirectional interaction on column demand. Additional observations include the correlation of nonlinear analytical displacements d_{nl} to elastic spectral displacements Sd_{el} and to inelastic spectral displacement estimates d_{inel}, obtained by modifying spectral displacements based on period and strength [73].

7.6.4.1   Adequacy of Elastic and Inelastic Displacement Estimates

For each analysis, the earthquake spectral displacement at the period of the column can be easily obtained for each direction. A bidirectional spectral estimated can also be obtained by gen-erating a bidirectional spectrum which is obtained by running a series of bidirectional linear anal-yses and recording the peak radial displacement [32]. This spectral ordinate would then be used as an estimate of the nonlinear bidirectional displacement. For each column, the average ratio of the nonlinear displacement to the spectral displacement is computed over all records. This average ratio is useful for estimating nonlinear displacement demand from spectral demand for this column configuration. Different ratios can be computed for each of the unidirectional and bidirectional cases. Figures 7-43 through 7-54 show the relationship between nonlinear and spectral displace-ments for 9 of the 27 columns. The straight lines represent the best fit to each data set, and have a slope equal to the average ratio of nonlinear to spectral displacement. The top left corner of each plot also lists the correlation coefficient between the two quantities. A similar fit is also performed using inelastic spectral displacement estimate d_{inel}, for columns with a period less than 1.0 second. This is unnecessary for more flexible columns since $d_{inel} = Sd_{el}$ for long periods.

It is observed that the scatter of the data about the straight line fit increases with displace-ment. This is due to the nonlinear response at larger deformations. The scatter is more significant for short period columns (for example Column 1 and Column 10) than for longer period columns (Columns 18 and 27) which have correlation coefficients of nearly 1.0. Figures 7-55 through 7-62 present a summary of the individual fits and correlations for each of the columns. The data used in

the plots is presented in Tables 7-7. Table 7-8 presents the same results ordered by column period in order to facilitate comparison with figures.

Figure 7-55 plots the median ratio of nonlinear displacement to elastic spectral displacement. Those values are averaged over the two unidirectional analyses performed for each column. The average ratio is roughly equal to 1.0 for periods larger than 1.0 second where displacements are preserved, but reaches a value of more than 1.6 for shorter periods. Figure 7-56 shows the correlation between d_{nl} and Sd_{el}, averaged over unidirectional results in the x and y directions. The correlation coefficient is significantly better for columns with longer period, while it is as low as 0.5 for shorter period columns. Using Sd_{el} as an estimate of the nonlinear displacement is clearly inappropriate in the short period range. Using available expressions for amplifying the linear displacement can yield a better estimate d_{inel} (Equation 7-13). Figures 7-57 and 7-58 show the median ratio and correlation of d_{nl} and d_{inel}. The ratio shows an improvement over using Sd_{el} in the short period range, as the maximum ratio goes down to 1.31. The correlation coefficient does not improve however, implying no significant reduction in scatter.

Similar trends are observed in Figures 7-59 to 7-62 which show the median ratio and correlation of d_{nl} to Sd_{el} and d_{inel} for bidirectional displacements. Larger displacement ratios of up to 2.07 are observed when using elastic spectral estimates, with correlation coefficient as low as 0.20 in one case. Using the inelastic displacement estimate results in some improvement in the short period range, but again the correlation coefficients are about the same.

7.6.4.2   Comparison of Bidirectional and Unidirectional Displacements

Figure 7-56 shows the ratio of bidirectional displacement to the maximum unidirectional displacement for each column and earthquake combination. The mean for each column is also shown as a circle. The mean results are plotted in Figures 7-64 to 7-66 in which the different symbols in each figure correspond to a_r, D_{col} and P_r, respectively. The mean values tend to vary between 0.95 to 1.3. In general, the displacement ratio seems mostly dependent on the period and tends to be higher at short periods. It also tends to be higher for smaller aspect ratios and axial load ratios.

Figures 7-67 and 7-68 show the ratio of the bidirectional displacement to the uncoupled bidirectional displacement obtained from two unidirectional nonlinear analyses. In Figure 7-67, the mean and standard deviation of the ratio for each ground motion record are shown. Both the mean and the standard deviation show dependence on the ground motion. The mean and standard deviation are also computed for each column as shown in Figure 7-68 where they are plotted

269

against the column period. The average ratios for all columns typically range between 0.96 to 1.20, and tend to decrease with increasing period. However, a significant scatter is observed for some columns.

7.6.4.3 Damage Measures

Several damage measures were used to evaluate the performance of the columns in this study. The first measure is the ratio of maximum nonlinear displacement to the ultimate displacement capacity, which is assumed to be constant along any loading direction. The other two measures are the Park and Ang damage index and the low-cycle fatigue index. A fourth indicator of damage is the amount of residual displacement at the end of the earthquake. A significant residual displacement may render the repair of a bridge expensive or even impossible. It is therefore important to assess the potential for such a problem.

Figures 7-69 to 7-71 show the ratio of peak displacement to ultimate displacement capacity for peak displacements under unidirectional analyses, and for the peak radial displacement under a bidirectional analysis. Both results follow similar trends. The average ratio is smaller than about 0.55 for all period larger than 1.15 seconds. Some of the shorter period columns have ratios that are in the neighborhood of 1.5 to 1.6, which means that on average, the ultimate displacement capacity may be exceeded by 50-60%. Ratios for individual records may be significantly larger. The average ratio from bidirectional analysis is plotted in Figure 7-72. The ratio is higher for shorter periods and smaller column aspect ratios.

The Park and Ang damage index computed using a β value of 0.05 is shown in Figures 7-73 and 7-74 for unidirectional and bidirectional analyses, respectively. The index is slightly larger under bidirectional loading, but both the unidirectional and bidirectional results follow the same trend. In fact, they are both very similar to the ratio of d/d_{ult} since the ductility component contributes a significant portion of the Park and Ang index, especially when using a low value for β. This is illustrated in Figure 7-76 which shows the contribution of the energy term to the Park and Ang index. The contribution is around 15-20% at small periods where the index is high. The energy contribution at longer periods depends on the equation used for the Park and Ang index, specifically the ductility part of the equation. The two forms of the ductility index (Equations 5-10 and 5-11) give close results when the displacement is close to the ultimate displacement capacity, but can be significantly different when the displacement is small. This causes the large divergence in contribution seen in Figure 7-76. The maximum difference is expected to occur when the displacement ductility is close to 1.0 (say between 0 and 2.0), which is the case for longer period columns as can

be seen in Figure 7-78. The energy index (Equation 5-12) is plotted in Figure 7-77 for the average of the two unidirectional directions. Similar to displacement and ductility demands, the energy dissipation demand decreases with period, but at a faster rate. Since dissipated energy is proportional to displacement, it is obvious that the energy index would be higher for higher displacement demands. Another factor that further increases the energy dissipation for shorter periods is the greater number of cycles that the column undergoes during a given record, because of its shorter period of vibration.

Figures 7-79 to 7-85 show the low-cycle fatigue index for columns analyzed under bidirectional excitations, and compare it to values from unidirectional analyses. Figures 7-79 and 7-81 show the mean and median values for each column, while Figure 7-80 shows the coefficient of variation. The mean values are typically twice or more larger than the median, indicating a nonuniform distribution. This is confirmed by the coefficient of variation which is somewhat high. However, both the median and mean follow similar trends. It is also noted that the two columns with the largest fatigue index have an axial load ratio of 0.15, an aspect ratio of 3 and diameter of 36 in. and 72 in. (Columns 10 and 11). This is consistent with the observation made in Section 7.5.4 where it was observed that shorter columns with small diameters and axial load ratios of around 0.20 have the largest low-cycle fatigue demands (see Figures 7-28 and 7-29). Figure 7-82 shows the fatigue index data for each column-ground motion combination that was used to compute the statistical averages, on a logarithmic scale. It is interesting to note that the data points span several orders of magnitude. It is also observed that low-cycle fatigue demands decrease significantly for periods longer than about 1.20 seconds.

Figure 7-83 compares fatigue demands for the unidirectional and bidirectional analyses, while Figure 7-84 shows the average ratio of the bidirectional fatigue index to the maximum value from the two unidirectional analyses in the x and y directions. Both the unidirectional and bidirectional cases show similar variation, with the bidirectional case being larger as expected. The ratio of bidirectional to unidirectional results is generally high, up to a value of about 2.0. It also exhibits a large variance as can be seen in Figure 7-85 which shows that the mean plus standard variation can be up to 2.5 larger than the mean itself. Hence, it appears that unidirectional analysis cannot be used to reliably predict bar fatigue in columns subjected to bidirectional shaking.

Figure 7-86 highlights an interesting observation regarding the amplification of unidirectional deformations due to bidirectional shaking. The figure shows the ratio of the peak displacement in each direction under bidirectional analysis to the peak displacement in the same direction

under unidirectional analysis. Instead of categorizing directions as x and y, the axes of each analysis were categorized into strong and weak, referring to the strength of the shaking in either direction. The strong axis is the axis that undergoes the larger unidirectional displacement while the weak experiences the smaller displacement. The figure clearly shows that on average, the weak direction experiences more amplification than the strong direction. This is an interesting observation since it shows that the effect of bidirectional shaking is more pronounced in the direction that experiences *less* demand under unidirectional shaking.

The final damage measure that is considered is the residual displacement. Figures 7-87 and 7-88 show the mean and standard deviation of the ratio of the residual bidirectional displacement to the peak bidirectional displacement. The statistical values of Figure 7-87, which are computed for each individual earthquake record, show that the mean and variance change from one earthquake to another, which suggests that susceptibility to residual deformation is not just a function of the column hysteretic properties, but that it greatly depends on the ground motion characteristics. Figure 7-88 shows the mean and standard deviation of the same ratio calculated over the runs of each column. The plot shows a clear correlation between residual displacements and the axial load ratio. Columns with higher axial loads have more significant P–Δ effects, which typically result in larger residual displacements. Figure 7-89 shows the median ratio of bidirectional residual displacement to the bidirectional uncoupled residual displacement. The ratio varies from about 1.0 to about 6.0, which indicates a significant increase in residual displacements due to bidirectional shaking. Figure 7-90 shows the ratio of the median ratio of bidirectional uncoupled residual displacement to the maximum unidirectional residual displacement among the two directions. All average ratios are less than 1.15, which indicates that the bidirectional uncoupled residual displacement can be reasonably estimated from the unidirectional residuals displacements. It also indicates that a plot of the ratio of the bidirectional residuals to the unidirectional residuals would look very similar to Figure 7-89.

Table 7-7 Median ratios and correlations between nonlinear displacement and elastic and inelastic spectral estimates for 27 columns ordered by column number.

					X Direction				Y Direction				Average (X,Y)				2D			
					d_{nl} vs Sd		d_{nl} vs d_{inel}		d_{nl} vs Sd		d_{nl} vs d_{inel}		d_{nl} vs Sd		d_{nl} vs d_{inel}		d_{nl} vs Sd		d_{nl} vs d_{inel}	
#	P_r	a_r	D_{col}	T	ratio	corr	ratio	corr	ratio	corr	ratio	corr	ratio	corr	ratio	corr	ratio	corr	ratio	corr
1	0.05	3	36	0.334	1.67	0.72	1.14	0.70	1.65	0.63	1.20	0.59	1.66	0.67	1.17	0.65	2.07	0.67	1.40	0.65
2	0.05	3	72	0.461	1.22	0.72	1.14	0.72	1.24	0.66	1.07	0.64	1.23	0.69	1.11	0.68	1.40	0.67	1.18	0.66
3	0.05	3	120	0.590	0.94	0.78	0.92	0.77	0.99	0.76	0.97	0.76	0.97	0.77	0.94	0.77	1.07	0.70	1.04	0.69
4	0.05	6	36	0.944	1.07	0.81	1.11	0.81	1.21	0.66	1.25	0.66	1.14	0.73	1.18	0.73	1.38	0.73	1.47	0.73
5	0.05	6	72	1.304	0.92	0.87	0.92	0.87	1.00	0.78	1.00	0.78	0.96	0.82	0.96	0.82	0.88	0.69	0.88	0.69
6	0.05	6	120	1.668	1.00	0.88	1.00	0.88	1.05	0.81	1.05	0.81	1.02	0.85	1.02	0.85	1.10	0.72	1.10	0.72
7	0.05	10	36	2.032	1.03	0.93	1.03	0.93	0.85	0.92	0.85	0.92	0.94	0.93	0.94	0.93	0.94	0.87	0.94	0.87
8	0.05	10	72	2.807	0.95	0.93	0.95	0.93	1.02	0.81	1.02	0.81	0.98	0.87	0.98	0.87	0.98	0.80	0.98	0.80
9	0.05	10	120	3.589	1.00	0.86	1.00	0.86	1.06	0.91	1.06	0.91	1.03	0.89	1.03	0.89	0.99	0.88	0.99	0.88
10	0.15	3	36	0.504	1.58	0.52	1.34	0.52	1.35	0.62	1.11	0.60	1.46	0.57	1.22	0.56	2.01	0.49	1.65	0.49
11	0.15	3	72	0.699	1.29	0.69	1.28	0.69	1.20	0.36	1.19	0.35	1.25	0.52	1.23	0.52	1.78	0.49	1.77	0.49
12	0.15	3	120	0.896	0.95	0.77	0.95	0.77	1.22	0.56	1.26	0.56	1.09	0.66	1.10	0.66	1.28	0.66	1.36	0.66
13	0.15	6	36	1.427	0.87	0.77	0.87	0.77	0.89	0.95	0.89	0.95	0.88	0.86	0.88	0.86	0.76	0.72	0.76	0.72
14	0.15	6	72	1.980	1.02	0.85	1.02	0.85	0.84	0.93	0.84	0.93	0.93	0.89	0.93	0.89	0.91	0.77	0.91	0.77
15	0.15	6	120	2.535	0.93	0.88	0.93	0.88	0.92	0.77	0.92	0.77	0.92	0.83	0.92	0.83	0.83	0.76	0.83	0.76
16	0.15	10	36	2.598	1.04	0.77	1.04	0.77	0.98	0.85	0.98	0.85	1.01	0.81	1.01	0.81	0.83	0.82	0.83	0.82
17	0.15	10	72	3.649	1.00	0.93	1.00	0.93	1.05	0.82	1.05	0.82	1.03	0.87	1.03	0.87	1.01	0.84	1.01	0.84
18	0.15	10	120	4.704	1.03	0.93	1.03	0.93	1.02	0.96	1.02	0.96	1.03	0.94	1.03	0.94	1.00	0.91	1.00	0.91
19	0.3	3	36	0.570	1.27	0.15	1.11	0.15	1.05	0.86	0.97	0.86	1.16	0.51	1.04	0.50	1.01	0.20	0.87	0.20
20	0.3	3	72	0.895	1.05	0.73	1.09	0.73	1.46	0.37	1.53	0.36	1.25	0.55	1.31	0.54	1.34	0.69	1.41	0.69
21	0.3	3	120	1.148	1.03	0.66	1.03	0.66	1.11	0.75	1.11	0.75	1.07	0.71	1.07	0.71	1.41	0.61	1.41	0.61
22	0.3	6	36	1.573	0.94	0.55	0.94	0.55	0.83	0.98	0.83	0.98	0.89	0.77	0.89	0.77	0.93	0.91	0.93	0.91
23	0.3	6	72	2.228	0.99	0.81	0.99	0.81	0.90	0.94	0.90	0.94	0.95	0.88	0.95	0.88	0.91	0.66	0.91	0.66
24	0.3	6	120	2.881	0.94	0.77	0.94	0.77	0.98	0.79	0.98	0.79	0.96	0.78	0.96	0.78	0.91	0.70	0.91	0.70
25	0.3	10	36	2.991	1.05	0.97	1.05	0.97	1.00	0.91	1.00	0.91	1.02	0.94	1.02	0.94	0.98	0.99	0.98	0.99
26	0.3	10	72	4.078	1.00	0.94	1.00	0.94	0.97	0.95	0.97	0.95	0.99	0.94	0.99	0.94	0.95	0.91	0.95	0.91
27	0.3	10	120	5.188	0.93	0.94	0.93	0.94	1.02	0.93	1.02	0.93	0.98	0.94	0.98	0.94	0.98	0.95	0.98	0.95
Avg	0.167	6.3	76	2.010	1.06	0.78	1.03	0.78	1.07	0.79	1.04	0.78	1.07	0.78	1.03	0.78	1.13	0.73	1.09	0.73
Min	0.05	3	36	0.334	0.87	0.15	0.87	0.15	0.83	0.36	0.83	0.35	0.88	0.51	0.88	0.50	0.76	0.20	0.76	0.20
Max	0.3	10	120	5.188	1.67	0.97	1.34	0.97	1.65	0.98	1.53	0.98	1.66	0.94	1.31	0.94	2.07	0.99	1.77	0.99

Table 7-8 Median ratios and correlations between nonlinear displacement and elastic and inelastic spectral estimates for 27 columns ordered by column period.
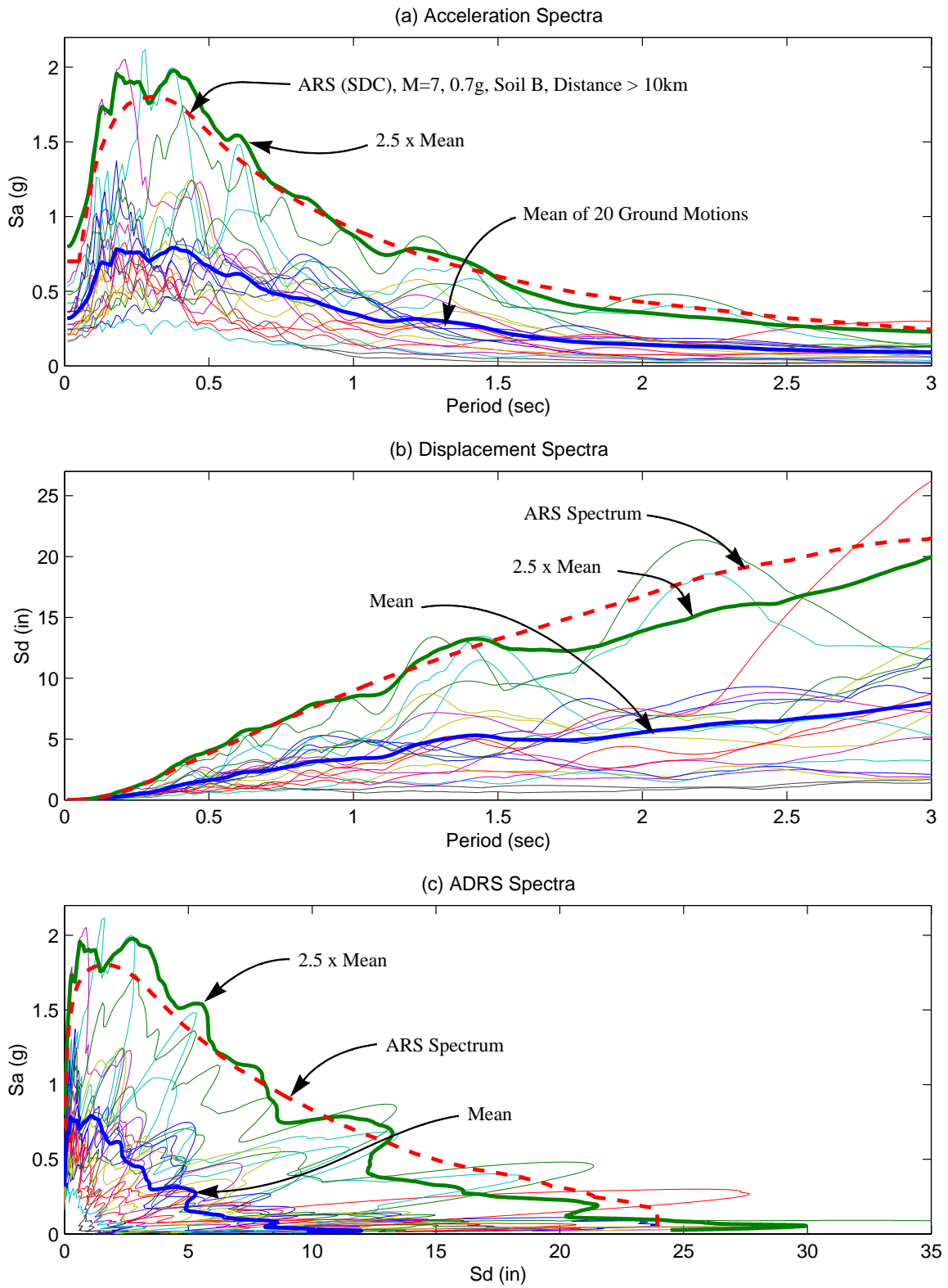
#	P_r	a_r	D_{col}	T	X Direction d_{nl} vs Sd ratio	corr	X Direction d_{nl} vs d_{inel} ratio	corr	Y Direction d_{nl} vs Sd ratio	corr	Y Direction d_{nl} vs d_{inel} ratio	corr	Average (X,Y) d_{nl} vs Sd ratio	corr	Average (X,Y) d_{nl} vs d_{inel} ratio	corr	2D d_{nl} vs Sd ratio	corr	2D d_{nl} vs d_{inel} ratio	corr
1	0.05	3	36	0.334	1.67	0.72	1.14	0.70	1.65	0.63	1.20	0.59	1.66	0.67	1.17	0.65	2.07	0.67	1.40	0.65
2	0.05	3	72	0.461	1.22	0.72	1.14	0.72	1.24	0.66	1.07	0.64	1.23	0.69	1.11	0.68	1.40	0.67	1.18	0.66
10	0.15	3	36	0.504	1.58	0.52	1.34	0.52	1.35	0.62	1.11	0.60	1.46	0.57	1.22	0.56	2.01	0.49	1.65	0.49
19	0.3	3	36	0.570	1.27	0.15	1.11	0.15	1.05	0.86	0.97	0.86	1.16	0.51	1.04	0.50	1.01	0.20	0.87	0.20
3	0.05	3	120	0.590	0.94	0.78	0.92	0.77	0.99	0.76	0.97	0.76	0.97	0.77	0.94	0.77	1.07	0.70	1.04	0.69
11	0.15	3	72	0.699	1.29	0.69	1.28	0.69	1.20	0.36	1.19	0.35	1.25	0.52	1.23	0.52	1.78	0.49	1.77	0.49
20	0.3	3	72	0.895	1.05	0.73	1.09	0.73	1.46	0.37	1.53	0.36	1.25	0.55	1.31	0.54	1.34	0.69	1.41	0.69
12	0.15	3	120	0.896	0.95	0.77	0.95	0.77	1.22	0.56	1.26	0.56	1.09	0.66	1.10	0.66	1.28	0.66	1.36	0.66
4	0.05	6	36	0.944	1.07	0.81	1.11	0.81	1.21	0.66	1.25	0.66	1.14	0.73	1.18	0.73	1.38	0.73	1.47	0.73
21	0.3	3	120	1.148	1.03	0.66	1.03	0.66	1.11	0.75	1.11	0.75	1.07	0.71	1.07	0.71	1.41	0.61	1.41	0.61
5	0.05	6	72	1.304	0.92	0.87	0.92	0.87	1.00	0.78	1.00	0.78	0.96	0.82	0.96	0.82	0.88	0.69	0.88	0.69
13	0.15	6	36	1.427	0.87	0.77	0.87	0.77	0.89	0.95	0.89	0.95	0.88	0.86	0.88	0.86	0.76	0.72	0.76	0.72
22	0.3	6	36	1.573	0.94	0.55	0.94	0.55	0.83	0.98	0.83	0.98	0.89	0.77	0.89	0.77	0.93	0.91	0.93	0.91
6	0.05	6	120	1.668	1.00	0.88	1.00	0.88	1.05	0.81	1.05	0.81	1.02	0.85	1.02	0.85	1.10	0.72	1.10	0.72
14	0.15	6	72	1.980	1.02	0.85	1.02	0.85	0.84	0.93	0.84	0.93	0.93	0.89	0.93	0.89	0.91	0.77	0.91	0.77
7	0.05	10	36	2.032	1.03	0.93	1.03	0.93	0.85	0.92	0.85	0.92	0.94	0.93	0.94	0.93	0.94	0.87	0.94	0.87
23	0.3	6	72	2.228	0.99	0.81	0.99	0.81	0.90	0.94	0.90	0.94	0.95	0.88	0.95	0.88	0.91	0.66	0.91	0.66
15	0.15	6	120	2.535	0.93	0.88	0.93	0.88	0.92	0.77	0.92	0.77	0.92	0.83	0.92	0.83	0.83	0.76	0.83	0.76
16	0.15	10	36	2.598	1.04	0.77	1.04	0.77	0.98	0.85	0.98	0.85	1.01	0.81	1.01	0.81	0.83	0.82	0.83	0.82
8	0.05	10	72	2.807	0.95	0.93	0.95	0.93	1.02	0.81	1.02	0.81	0.98	0.87	0.98	0.87	0.98	0.80	0.98	0.80
24	0.3	6	120	2.881	0.94	0.77	0.94	0.77	0.98	0.79	0.98	0.79	0.96	0.78	0.96	0.78	0.91	0.70	0.91	0.70
25	0.3	10	36	2.991	1.05	0.97	1.05	0.97	1.00	0.91	1.00	0.91	1.02	0.94	1.02	0.94	0.98	0.99	0.98	0.99
9	0.05	10	120	3.589	1.00	0.86	1.00	0.86	1.06	0.91	1.06	0.91	1.03	0.89	1.03	0.89	0.99	0.88	0.99	0.88
17	0.15	10	72	3.649	1.00	0.93	1.00	0.93	1.05	0.82	1.05	0.82	1.03	0.87	1.03	0.87	1.01	0.84	1.01	0.84
26	0.3	10	72	4.078	1.00	0.94	1.00	0.94	0.97	0.95	0.97	0.95	0.99	0.94	0.99	0.94	0.95	0.91	0.95	0.91
18	0.15	10	120	4.704	1.03	0.93	1.03	0.93	1.02	0.96	1.02	0.96	1.03	0.94	1.03	0.94	1.00	0.91	1.00	0.91
27	0.3	10	120	5.188	0.93	0.94	0.93	0.94	1.02	0.93	1.02	0.93	0.98	0.94	0.98	0.94	0.98	0.95	0.98	0.95
Avg	0.167	6.3	76	2.010	1.06	0.78	1.03	0.78	1.07	0.79	1.04	0.78	1.07	0.78	1.03	0.78	1.13	0.73	1.09	0.73
Min	0.05	3	36	0.334	0.87	0.15	0.87	0.15	0.83	0.36	0.83	0.35	0.88	0.51	0.88	0.50	0.76	0.20	0.76	0.20
Max	0.3	10	120	5.188	1.67	0.97	1.34	0.97	1.65	0.98	1.53	0.98	1.66	0.94	1.31	0.94	2.07	0.99	1.77	0.99

274

# Table 7-9 Statistical averages of various damage measures for 27 columns ordered by column number.

#	P_r	a_r	D_{col}	T	% Conv.	dx Mean	dy Mean	d Mean	$FI_{x,1D}$ Mean	$FI_{y,1D}$ Mean	FI_{2D} Mean	FI_{2D} Cov	FI_{2D} Med	FI_{2D}/FI_{1D} Mean	$EI_{x,1D}$ Mean	$EI_{y,1D}$ Mean	$PA_{x,1D}$ Mean	$PA_{y,1D}$ Mean	$\beta EI/PA$ Mean %
1	0.05	3	36	0.334	100	0.79	0.53	0.74	0.29	0.07	0.46	1.69	0.14	2.01	3.45	2.21	0.94	0.59	22.35
2	0.05	3	72	0.461	100	0.77	0.57	0.69	0.09	0.03	0.13	1.72	0.05	1.88	2.79	1.78	0.86	0.58	18.89
3	0.05	3	120	0.590	100	0.58	0.45	0.49	0.03	0.01	0.05	1.77	0.02	1.28	1.81	1.11	0.58	0.40	24.56
4	0.05	6	36	0.944	100	0.59	0.55	0.61	0.10	0.07	0.20	1.20	0.10	1.73	1.77	1.52	0.62	0.57	21.39
5	0.05	6	72	1.304	100	0.48	0.46	0.50	0.02	0.01	0.04	1.41	0.02	2.02	1.15	1.02	0.43	0.39	32.36
6	0.05	6	120	1.668	100	0.34	0.34	0.36	0.01	0.00	0.01	1.62	0.00	2.00	0.58	0.56	0.23	0.23	41.39
7	0.05	10	36	2.032	75	0.24	0.26	0.28	0.00	0.00	0.01	1.51	0.00	1.98	0.40	0.43	0.15	0.18	39.94
8	0.05	10	72	2.807	100	0.30	0.29	0.31	0.00	0.00	0.01	1.43	0.00	1.45	0.41	0.37	0.19	0.16	44.73
9	0.05	10	120	3.589	100	0.22	0.20	0.21	0.00	0.00	0.00	1.66	0.00	1.55	0.22	0.16	0.08	0.05	56.81
10	0.15	3	36	0.504	65	1.30	1.04	1.12	0.77	0.44	1.19	1.43	0.28	1.20	4.89	3.93	1.59	1.24	17.00
11	0.15	3	72	0.699	100	1.50	1.36	1.56	0.65	0.33	1.23	1.41	0.62	1.90	5.14	4.16	1.86	1.64	15.55
12	0.15	3	120	0.896	100	1.11	1.07	1.16	0.20	0.13	0.45	1.54	0.20	2.02	3.47	2.99	1.31	1.25	20.02
13	0.15	6	36	1.427	45	0.49	0.47	0.44	0.03	0.02	0.04	1.29	0.01	1.32	1.27	1.07	0.44	0.42	29.94
14	0.15	6	72	1.980	75	0.57	0.58	0.64	0.02	0.02	0.05	1.69	0.03	1.52	1.20	1.13	0.52	0.53	27.88
15	0.15	6	120	2.535	100	0.58	0.52	0.55	0.02	0.01	0.03	1.53	0.01	1.85	1.04	0.95	0.53	0.44	33.16
16	0.15	10	36	2.598	55	0.32	0.35	0.33	0.00	0.00	0.00	1.16	0.00	1.85	0.45	0.44	0.20	0.22	37.76
17	0.15	10	72	3.649	90	0.38	0.36	0.35	0.00	0.00	0.00	1.19	0.00	1.07	0.46	0.43	0.25	0.20	45.93
18	0.15	10	120	4.704	100	0.31	0.26	0.28	0.00	0.00	0.00	2.74	0.00	1.39	0.27	0.24	0.17	0.08	59.61
19	0.3	3	36	0.570	45	0.82	0.63	0.65	0.10	0.04	0.10	1.48	0.04	0.91	3.34	2.44	0.96	0.70	18.25
20	0.3	3	72	0.895	60	1.02	0.93	0.94	0.26	0.28	0.40	1.36	0.17	1.00	2.90	2.88	1.16	1.07	14.52
21	0.3	3	120	1.148	100	1.19	1.22	1.44	0.41	0.38	0.86	1.49	0.24	1.18	3.30	3.34	1.40	1.44	19.22
22	0.3	6	36	1.573	30	0.29	0.33	0.31	0.00	0.00	0.00	1.33	0.00	1.11	0.46	0.63	0.17	0.23	31.12
23	0.3	6	72	2.228	60	0.49	0.51	0.57	0.01	0.01	0.01	1.76	0.00	1.64	0.96	1.02	0.39	0.42	36.71
24	0.3	6	120	2.881	95	0.63	0.56	0.57	0.01	0.01	0.01	1.60	0.00	1.56	1.11	0.94	0.58	0.45	37.80
25	0.3	10	36	2.991	40	0.25	0.34	0.34	0.00	0.00	0.00	1.56	0.00	1.36	0.20	0.36	0.07	0.17	56.94
26	0.3	10	72	4.078	75	0.32	0.33	0.32	0.00	0.00	0.00	2.02	0.00	1.08	0.36	0.34	0.17	0.15	52.16
27	0.3	10	120	5.188	100	0.28	0.29	0.26	0.00	0.00	0.00	1.77	0.00	1.32	0.24	0.26	0.11	0.11	62.19
Avg	0.17	6.33	76	2.010	81.9	0.60	0.55	0.59	0.11	0.07	0.20	1.57	0.07	1.53	1.62	1.36	0.59	0.52	34.01
Min	0.05	3	36	0.334	30.0	0.22	0.20	0.21	0.00	0.00	0.00	1.16	0.00	0.91	0.20	0.16	0.07	0.05	14.52
Max	0.3	10	120	5.188	100.0	1.50	1.36	1.56	0.77	0.44	1.23	2.74	0.62	2.02	5.14	4.16	1.86	1.64	62.19

# Table 7-10 Statistical averages of various damage measures for 27 columns ordered by column period.

#	P_r	a_r	D_{col}	T	% Conv.	d/d_{ult} dx Mean	dy Mean	d Mean	Fatigue Index $FI_{x,1D}$ Mean	$FI_{y,1D}$ Mean	FI_{2D} Mean	FI_{2D} Cov	FI_{2D} Med	FI_{2D}/FI_{1D} Mean	Energy Index $EI_{x,1D}$ Mean	$EI_{y,1D}$ Mean	Park & Ang Index $PA_{x,1D}$ Mean	$PA_{y,1D}$ Mean	$\beta EI/PA$ Mean %
1	0.05	3	36	0.334	100	0.79	0.53	0.74	0.29	0.07	0.46	1.69	0.14	2.01	3.45	2.21	0.94	0.59	22.35
2	0.05	3	72	0.461	100	0.77	0.57	0.69	0.09	0.03	0.13	1.72	0.05	1.88	2.79	1.78	0.86	0.58	18.89
10	0.15	3	36	0.504	65	1.30	1.04	1.12	0.77	0.44	1.19	1.43	0.28	1.20	4.89	3.93	1.59	1.24	17.00
19	0.3	3	36	0.570	45	0.82	0.63	0.65	0.10	0.04	0.10	1.48	0.04	0.91	3.34	2.44	0.96	0.70	18.25
3	0.05	3	120	0.590	100	0.58	0.45	0.49	0.03	0.01	0.05	1.77	0.02	1.28	1.81	1.11	0.58	0.40	24.56
11	0.15	3	72	0.699	100	1.50	1.36	1.56	0.65	0.33	1.23	1.41	0.62	1.90	5.14	4.16	1.86	1.64	15.55
20	0.3	3	72	0.895	60	1.02	0.93	0.94	0.26	0.28	0.40	1.36	0.17	1.00	2.90	2.88	1.16	1.07	14.52
12	0.15	3	120	0.896	100	1.11	1.07	1.16	0.20	0.13	0.45	1.54	0.20	2.02	3.47	2.99	1.31	1.25	20.02
4	0.05	6	36	0.944	100	0.59	0.55	0.61	0.10	0.07	0.20	1.20	0.10	1.73	1.77	1.52	0.62	0.57	21.39
21	0.3	3	120	1.148	100	1.19	1.22	1.44	0.41	0.38	0.86	1.49	0.24	1.18	3.30	3.34	1.40	1.44	19.22
5	0.05	6	72	1.304	100	0.48	0.46	0.50	0.02	0.01	0.04	1.41	0.02	2.02	1.15	1.02	0.43	0.39	32.36
13	0.15	6	36	1.427	45	0.49	0.47	0.44	0.03	0.02	0.04	1.29	0.01	1.32	1.27	1.07	0.44	0.42	29.94
22	0.3	6	36	1.573	30	0.29	0.33	0.31	0.00	0.00	0.00	1.33	0.00	1.11	0.46	0.63	0.17	0.23	31.12
6	0.05	6	120	1.668	100	0.34	0.34	0.36	0.01	0.00	0.01	1.62	0.00	2.00	0.58	0.56	0.23	0.23	41.39
14	0.15	6	72	1.980	75	0.57	0.58	0.64	0.02	0.02	0.05	1.69	0.03	1.52	1.20	1.13	0.52	0.53	27.88
7	0.05	10	36	2.032	75	0.24	0.26	0.28	0.00	0.00	0.01	1.51	0.00	1.98	0.40	0.43	0.15	0.18	39.94
23	0.3	6	72	2.228	60	0.49	0.51	0.57	0.01	0.01	0.01	1.76	0.00	1.64	0.96	1.02	0.39	0.42	36.71
15	0.15	6	120	2.535	100	0.58	0.52	0.55	0.02	0.01	0.03	1.53	0.01	1.85	1.04	0.95	0.53	0.44	33.16
16	0.15	10	36	2.598	55	0.32	0.35	0.33	0.00	0.00	0.00	1.16	0.00	1.85	0.45	0.44	0.20	0.22	37.76
8	0.05	10	72	2.807	100	0.30	0.29	0.31	0.00	0.00	0.01	1.43	0.00	1.45	0.41	0.37	0.19	0.16	44.73
24	0.3	6	120	2.881	95	0.63	0.56	0.57	0.01	0.01	0.01	1.60	0.00	1.56	1.11	0.94	0.58	0.45	37.80
25	0.3	10	36	2.991	40	0.25	0.34	0.34	0.00	0.00	0.00	1.56	0.00	1.36	0.20	0.36	0.07	0.17	56.94
9	0.05	10	120	3.589	100	0.22	0.20	0.21	0.00	0.00	0.00	1.66	0.00	1.55	0.22	0.16	0.08	0.05	56.81
17	0.15	10	72	3.649	90	0.38	0.36	0.35	0.00	0.00	0.00	1.19	0.00	1.07	0.46	0.43	0.25	0.20	45.93
26	0.3	10	72	4.078	75	0.32	0.33	0.32	0.00	0.00	0.00	2.02	0.00	1.08	0.36	0.34	0.17	0.15	52.16
18	0.15	10	120	4.704	100	0.31	0.26	0.28	0.00	0.00	0.00	2.74	0.00	1.39	0.27	0.24	0.17	0.08	59.61
27	0.3	10	120	5.188	100	0.28	0.29	0.26	0.00	0.00	0.00	1.77	0.00	1.32	0.24	0.26	0.11	0.11	62.19
Avg	0.17	6.33	76	2.010	81.9	0.60	0.55	0.59	0.11	0.07	0.20	1.57	0.07	1.53	1.62	1.36	0.59	0.52	34.01
Min	0.05	3	36	0.334	30.0	0.22	0.20	0.21	0.00	0.00	0.00	1.16	0.00	0.91	0.20	0.16	0.07	0.05	14.52
Max	0.3	10	120	5.188	100.0	1.50	1.36	1.56	0.77	0.44	1.23	2.74	0.62	2.02	5.14	4.16	1.86	1.64	62.19

Figure 7-30. Spectral accelerations and displacements in the first direction (x) of the 20 ground motions.

(a) Acceleration Spectra

(b) Displacement Spectra

(c) ADRS Spectra
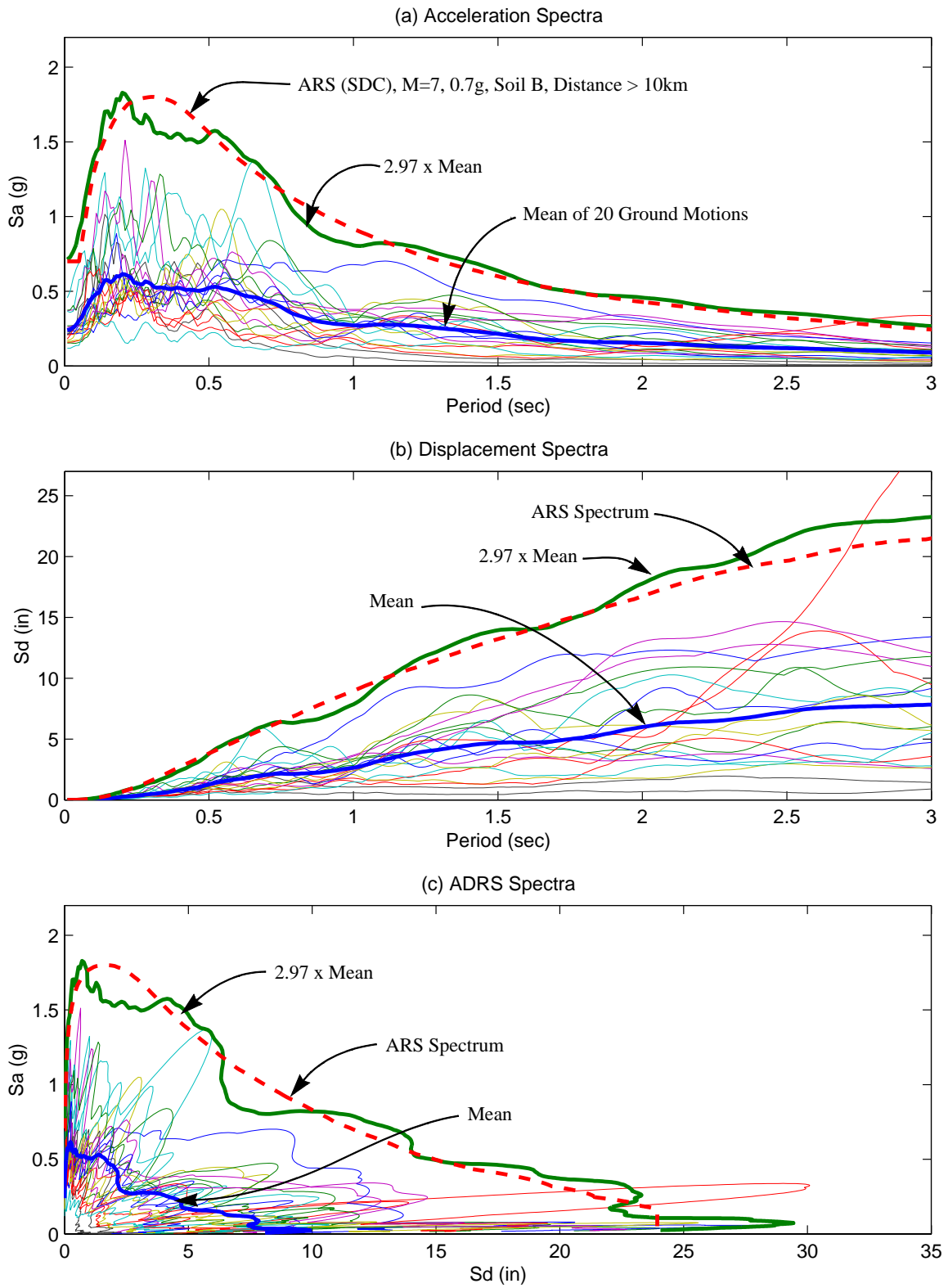
Figure 7-31. Spectral accelerations and displacements in the second direction (y) of the 20 ground motions.
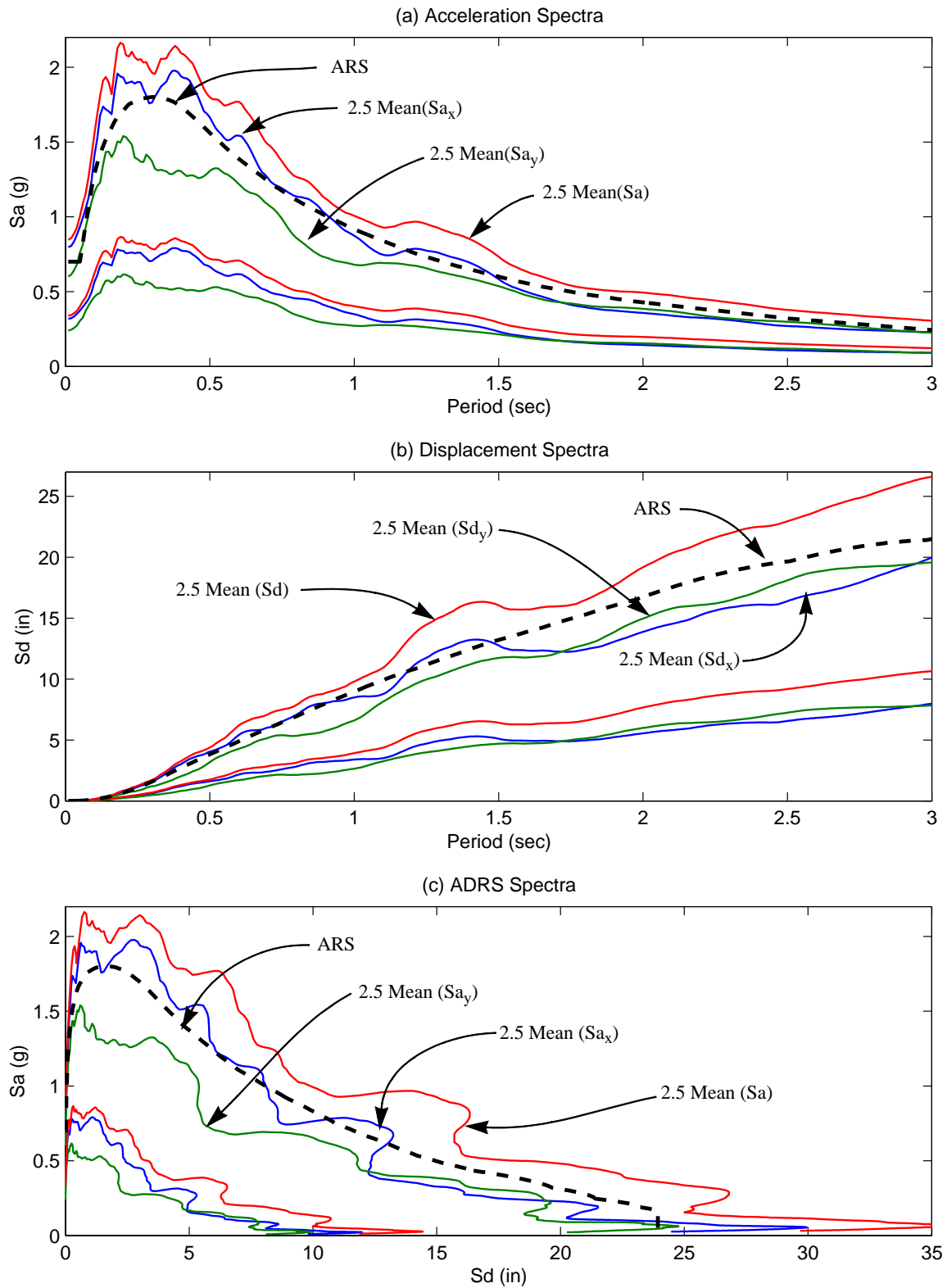
Figure 7-32. Mean and amplified spectral accelerations and displacements of the 20 ground motions.
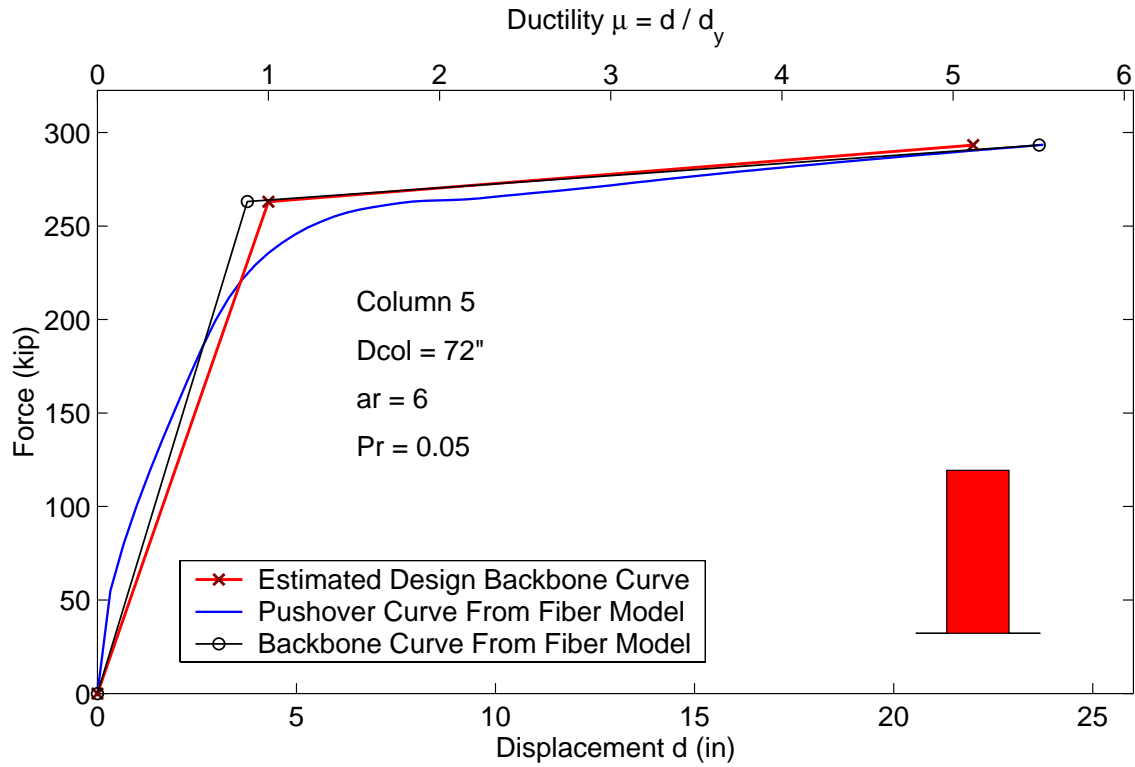
Figure 7-33. Comparison of estimated backbone curve to pushover curve obtained from a fiber model pushover analysis of Column 5.
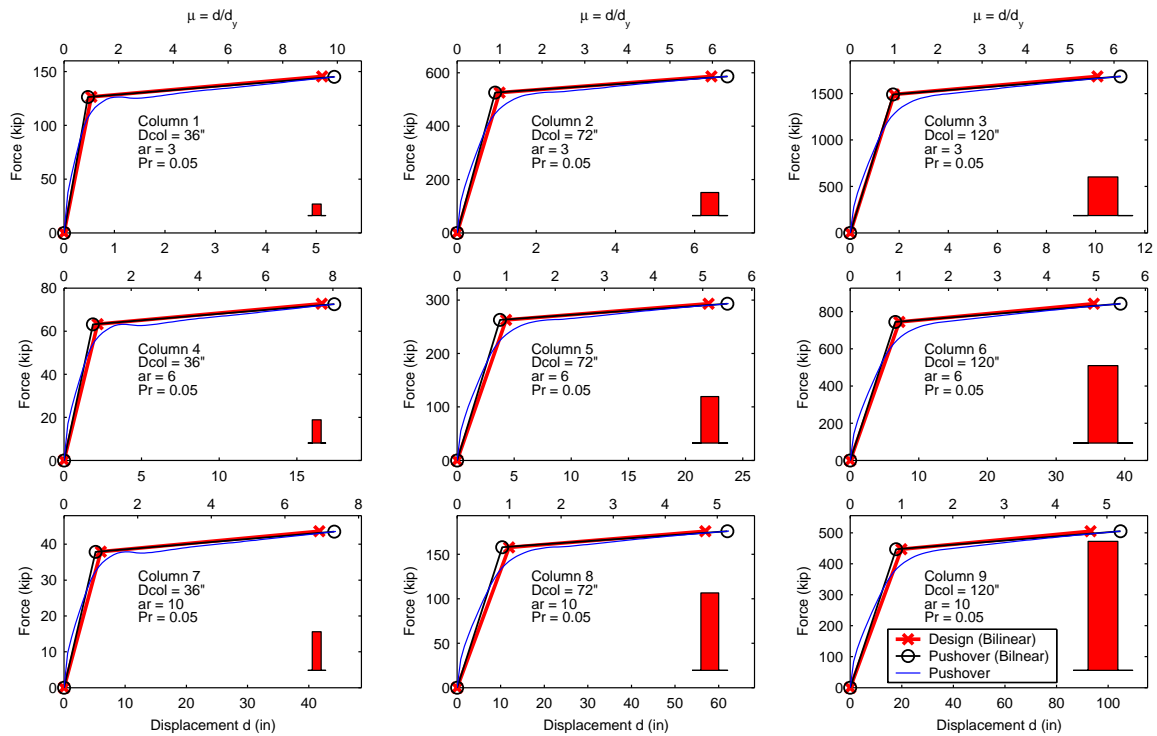
Figure 7-34. Comparison of estimated backbone curves to analytical pushover curves for Columns 1 to 9 ($P_r = 0.05$).
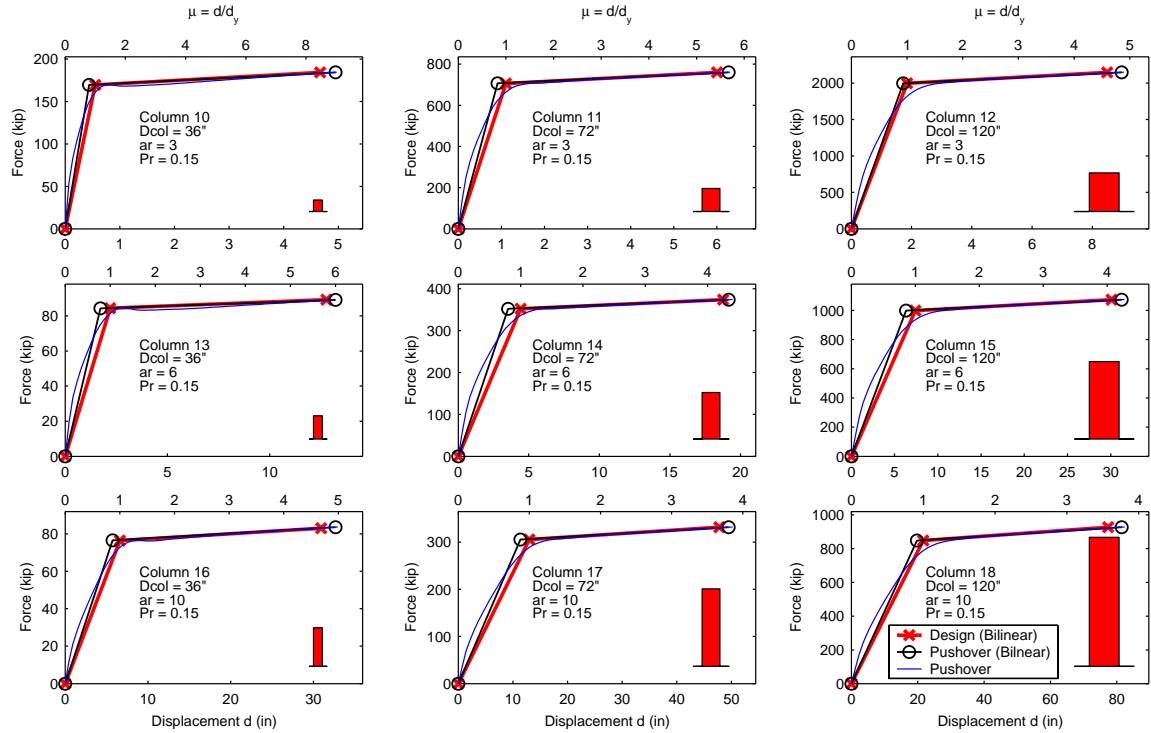
Figure 7-35. Comparison of estimated backbone curves to analytical pushover curves for Columns 10 to 18 ($P_r = 0.15$).
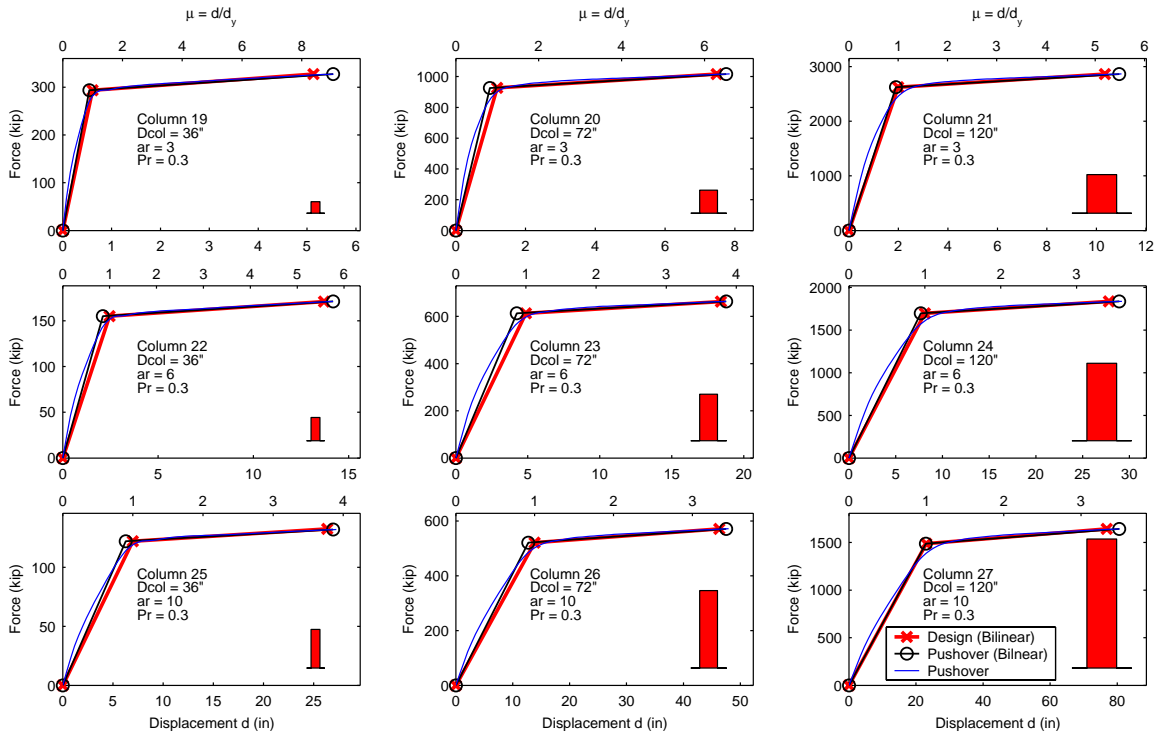
Figure 7-36. Comparison of estimated backbone curves to analytical pushover curves for Columns 19 to 27 ($P_r = 0.30$).
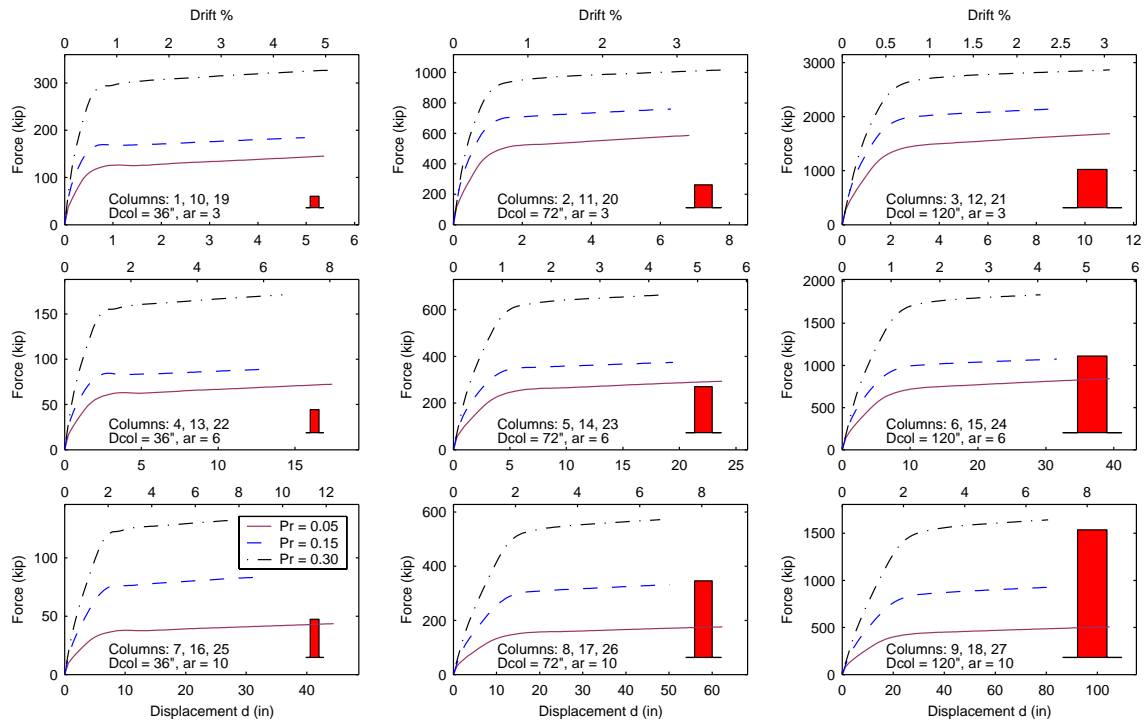
Figure 7-37. Comparison of pushover curves for columns with similar dimensions and different axial loads.
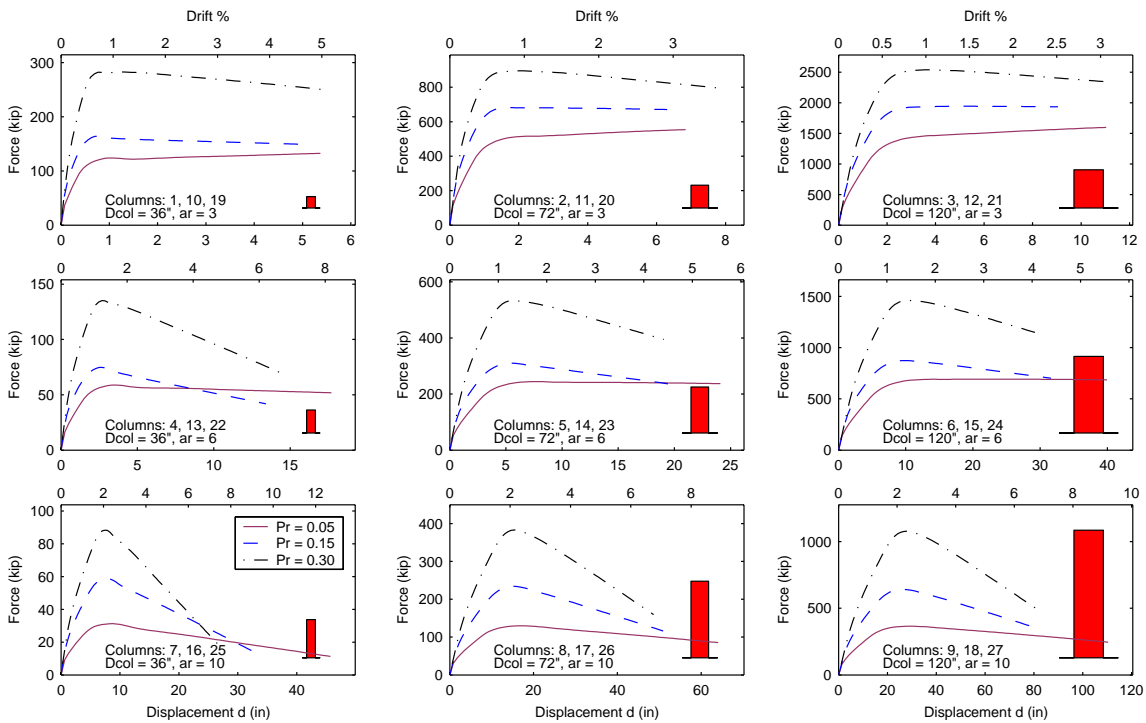
Figure 7-38. Comparison of pushover curves for columns with similar dimensions and different axial loads (including P-Δ effects).

282
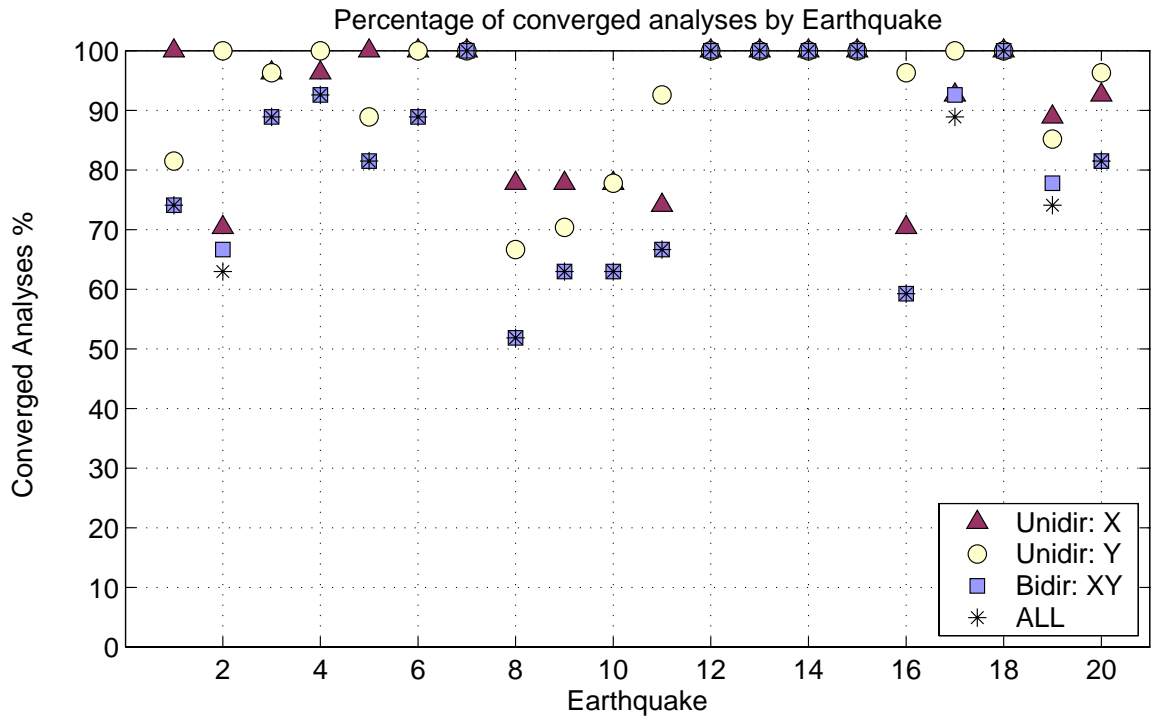
Figure 7-39. Percentage of converged analyses for each earthquake.
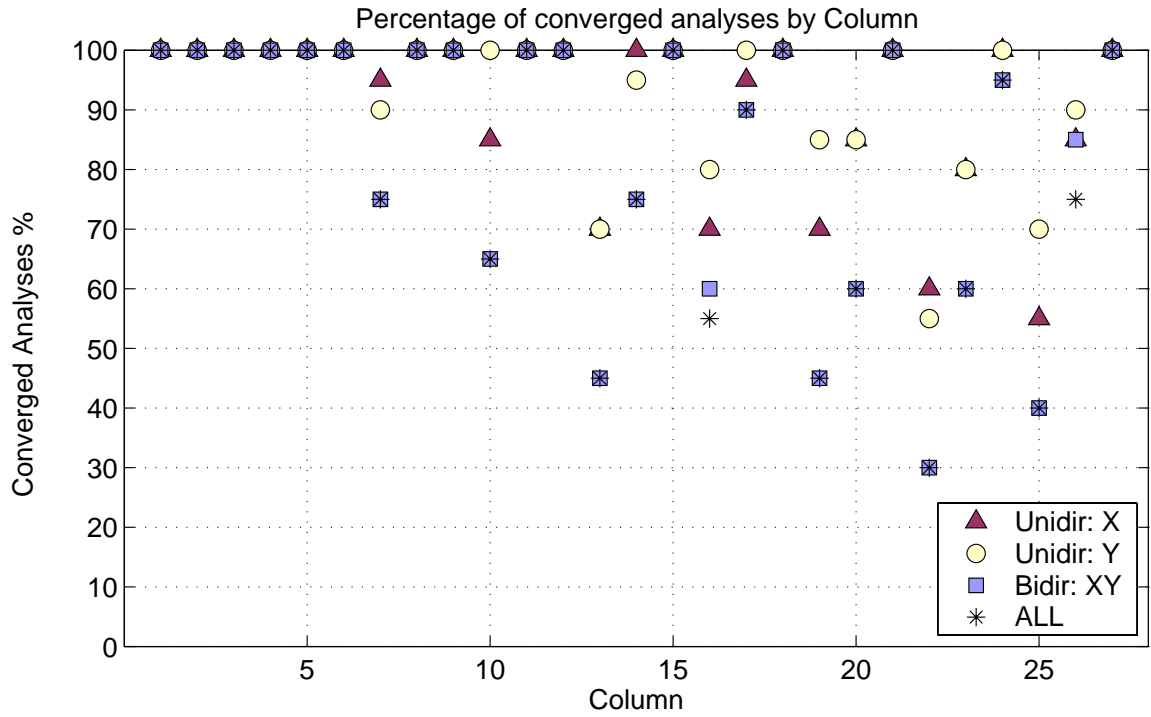
Figure 7-40. Percentage of converged analyses for each column.
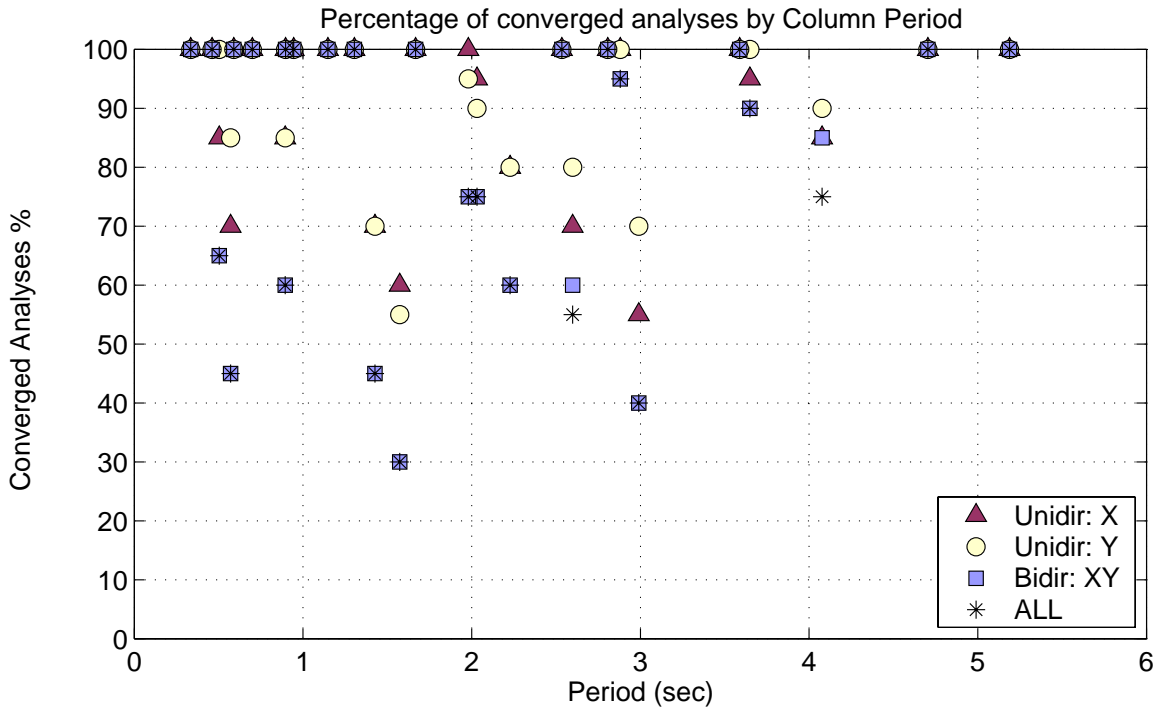
Figure 7-41. Percentage of converged analyses for each column.
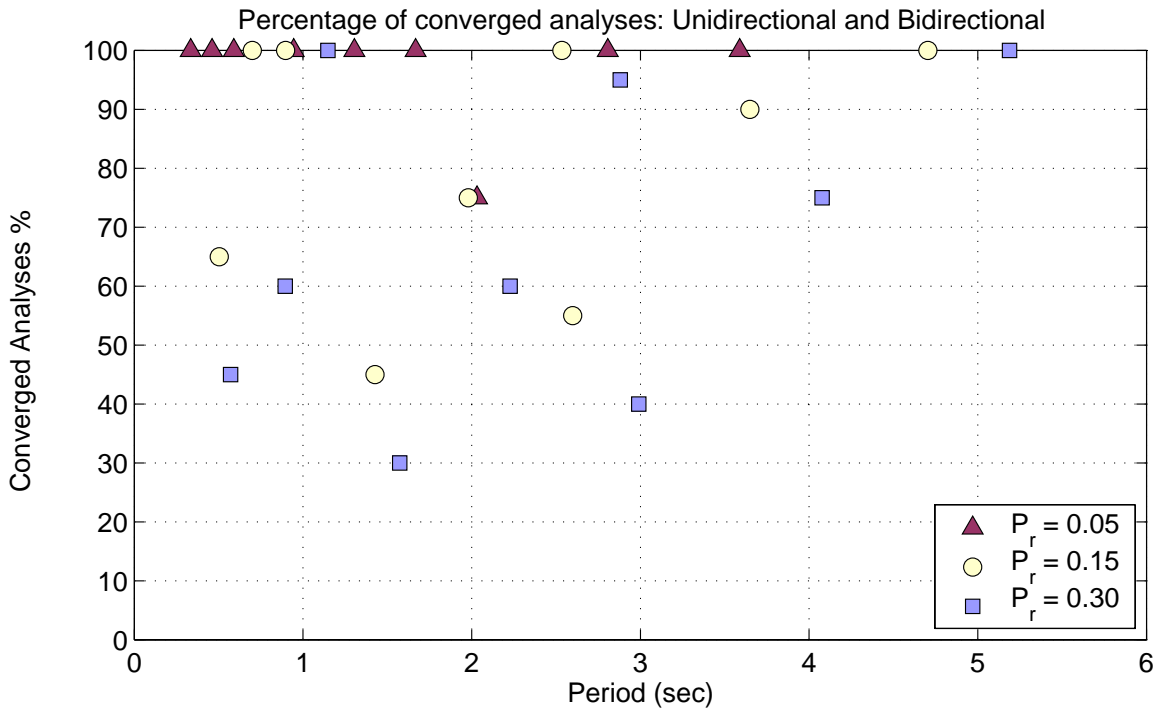
Figure 7-42. Percentage of analyses that converged in both unidirectional and bidirectional analyses.

284
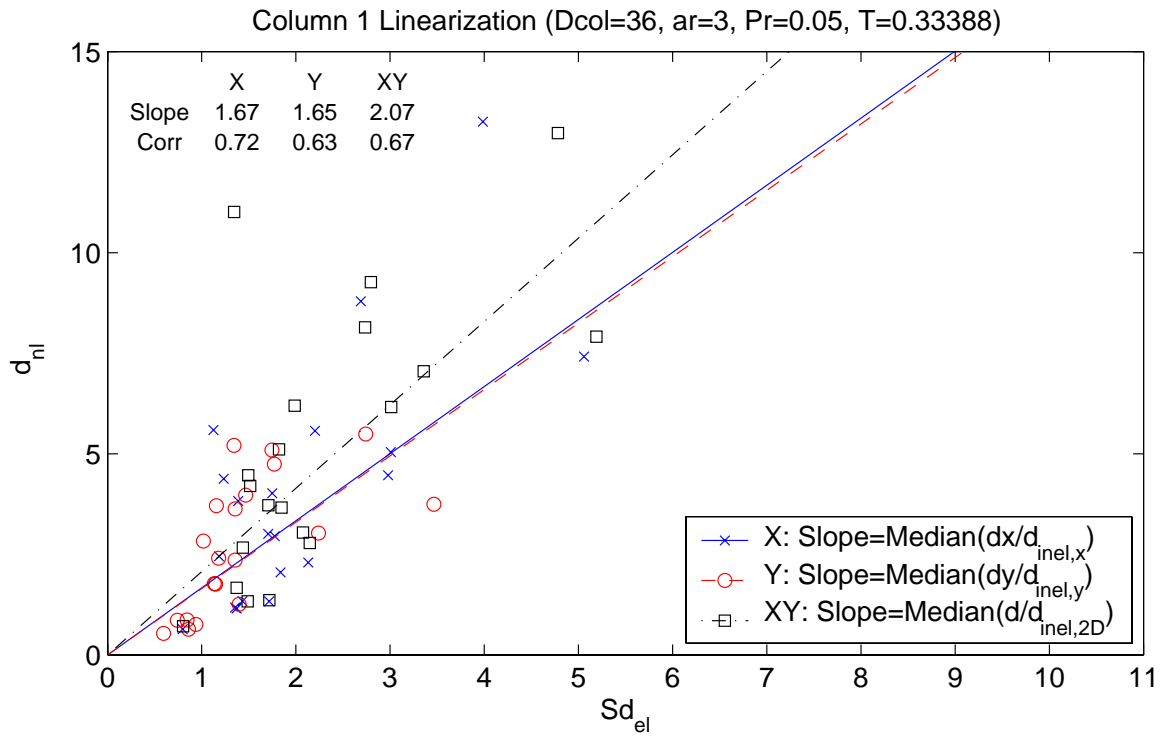
Figure 7-43. Linear regression of Sd and d_{nl} for Column 1.
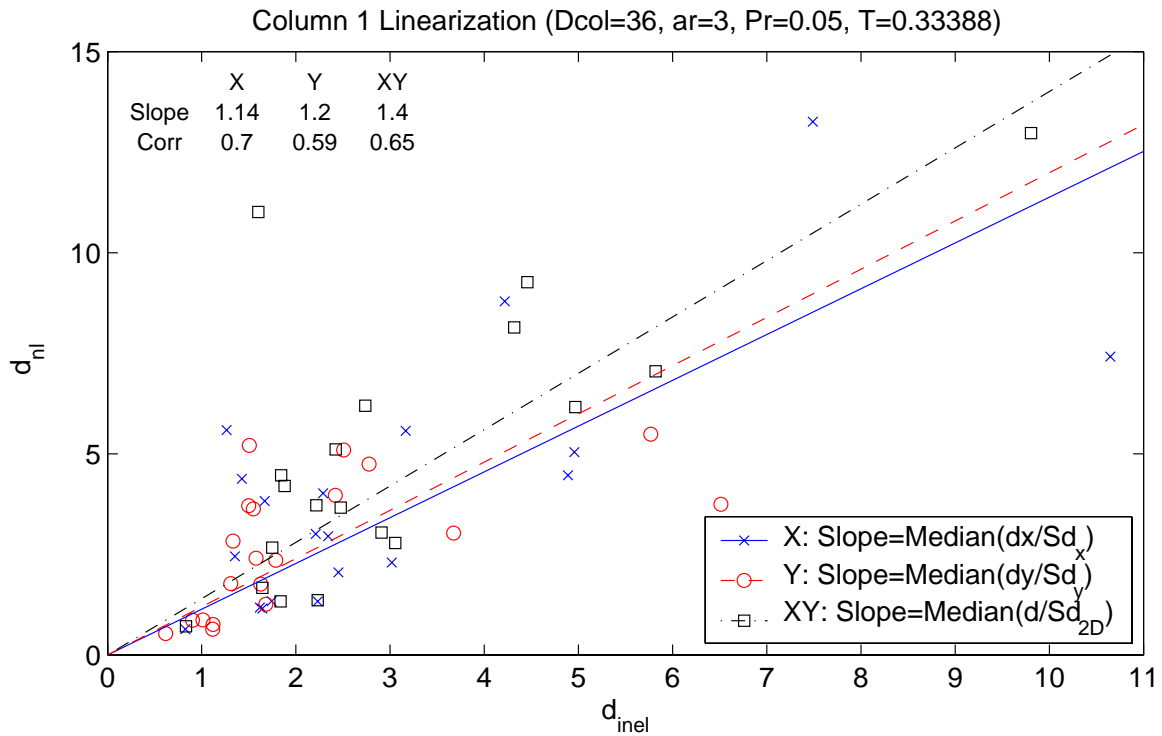
Figure 7-44. Linear regression of d_{inel} and d_{nl} for Column 1.
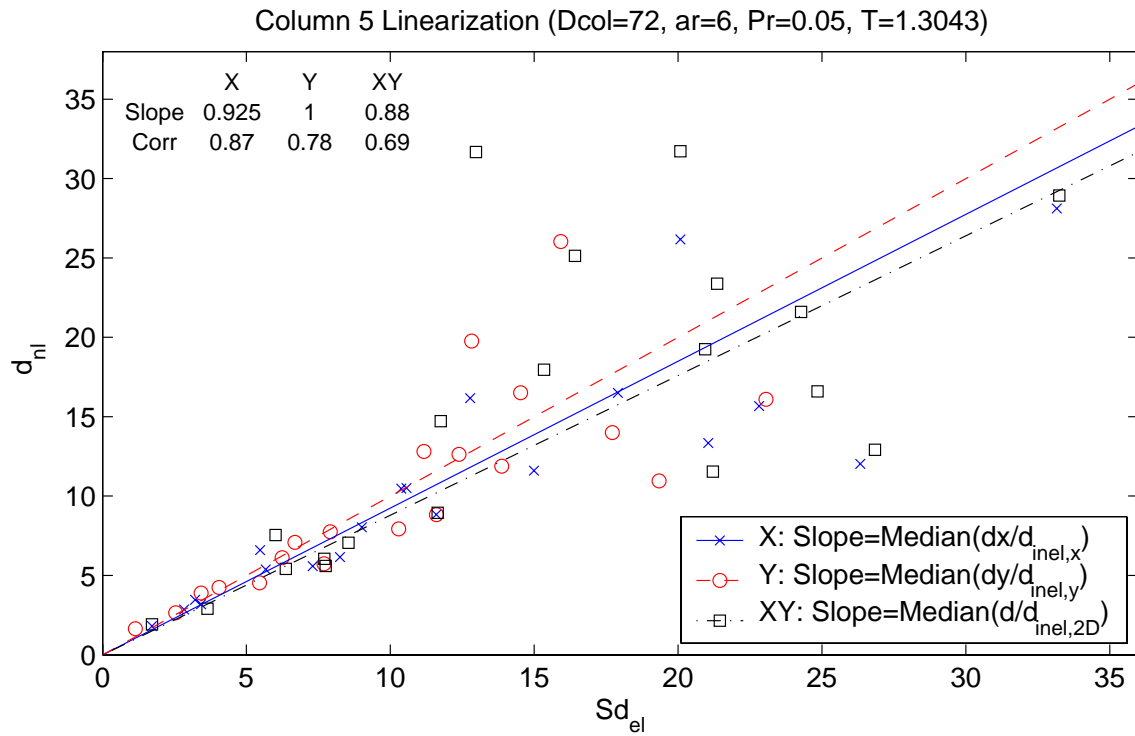
Figure 7-45. Linear regression of Sd and d_{nl} for Column 5.
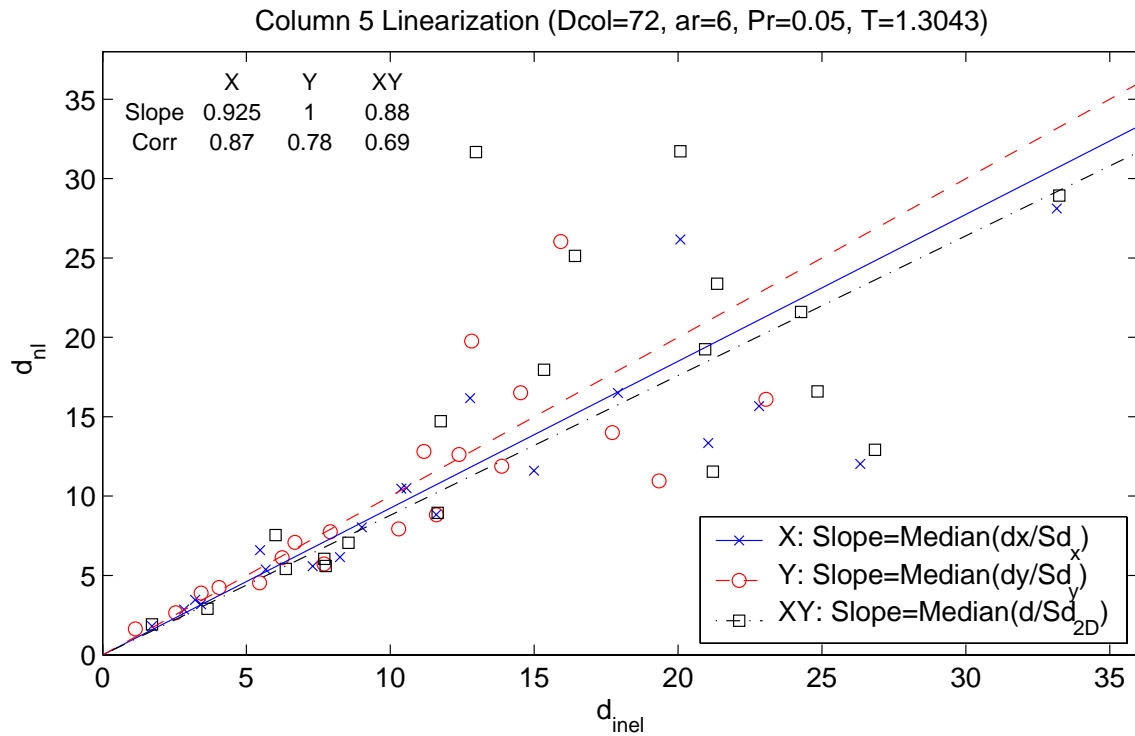
Figure 7-46. Linear regression of d_{inel} and d_{nl} for Column 9.
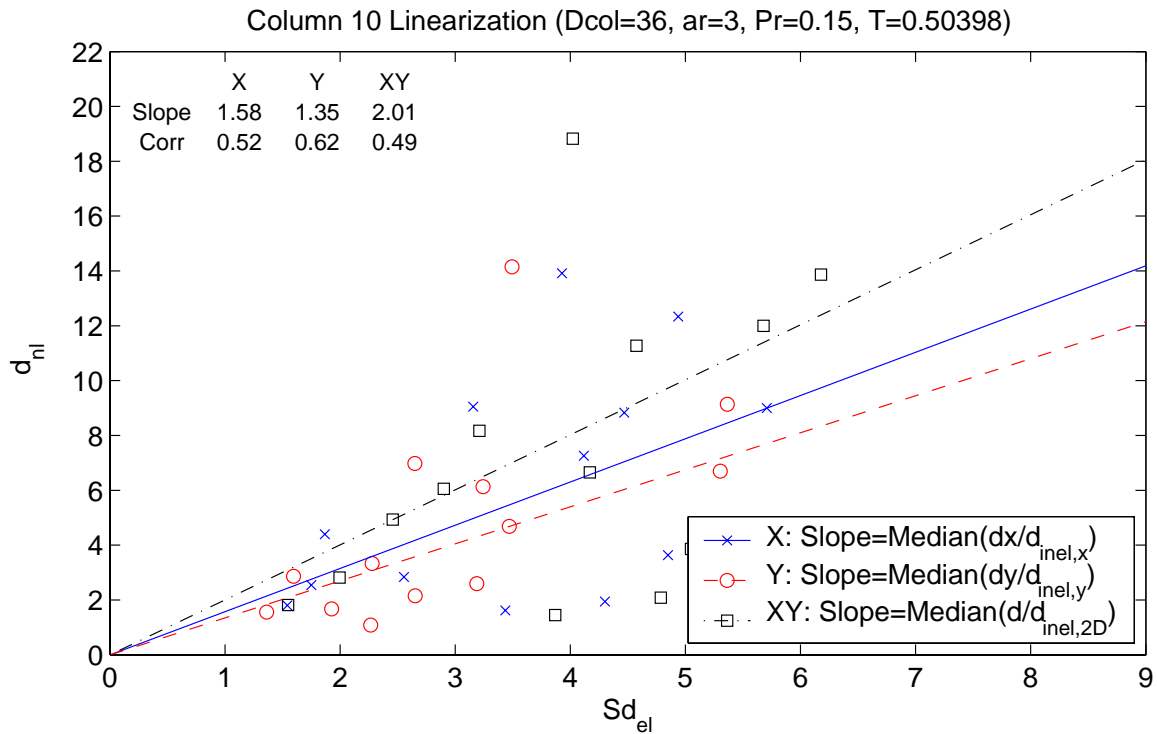
Figure 7-47. Linear regression of Sd and d_{nl} for Column 10.
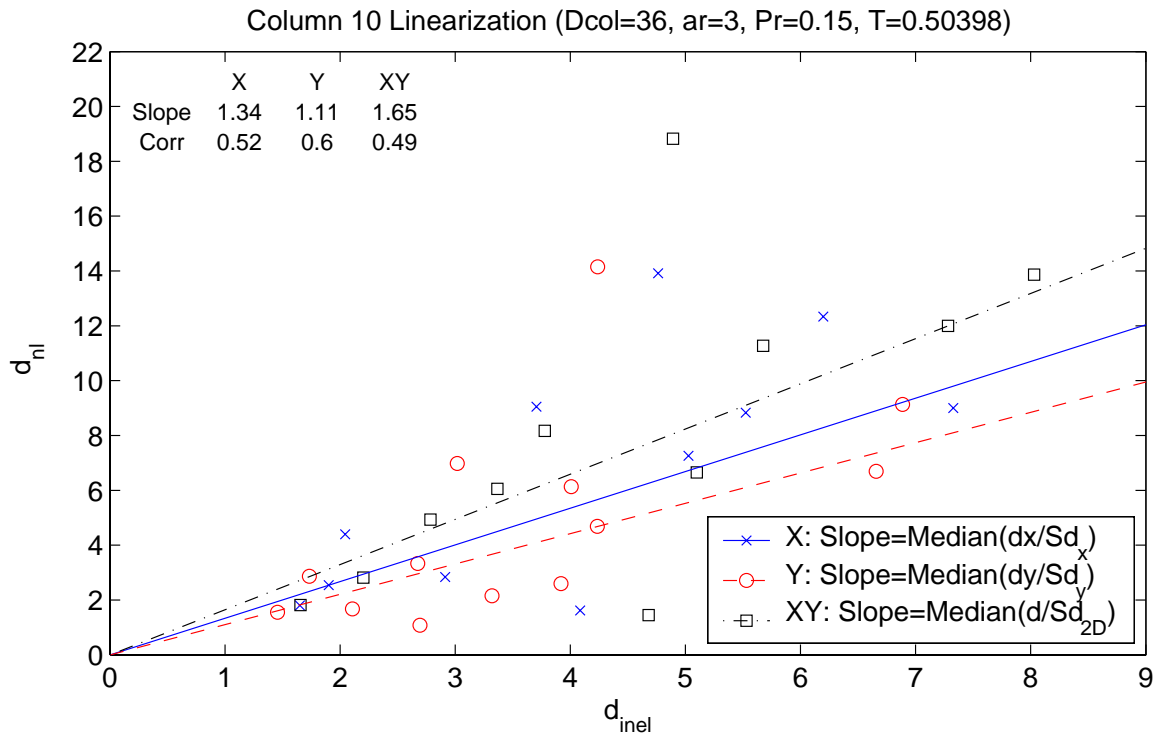
Figure 7-48. Linear regression of d_{inel} and d_{nl} for Column 10.
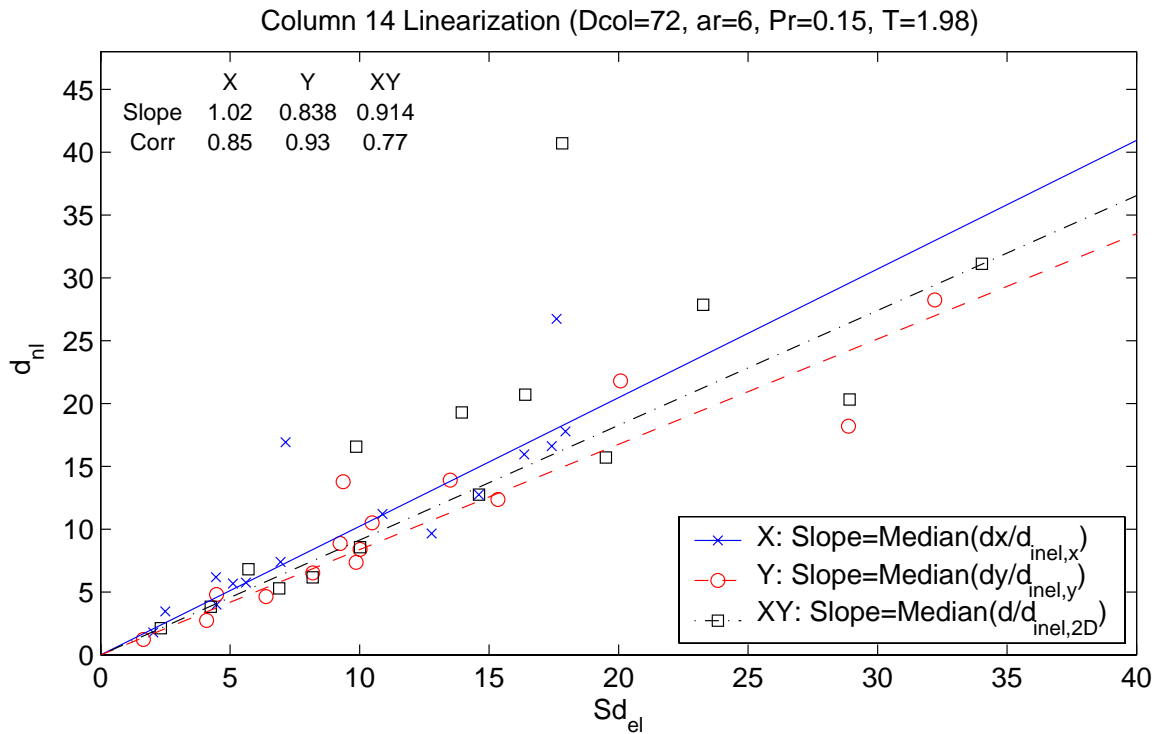
Figure 7-49. Linear regression of *Sd* and d_{nl} for Column 14.
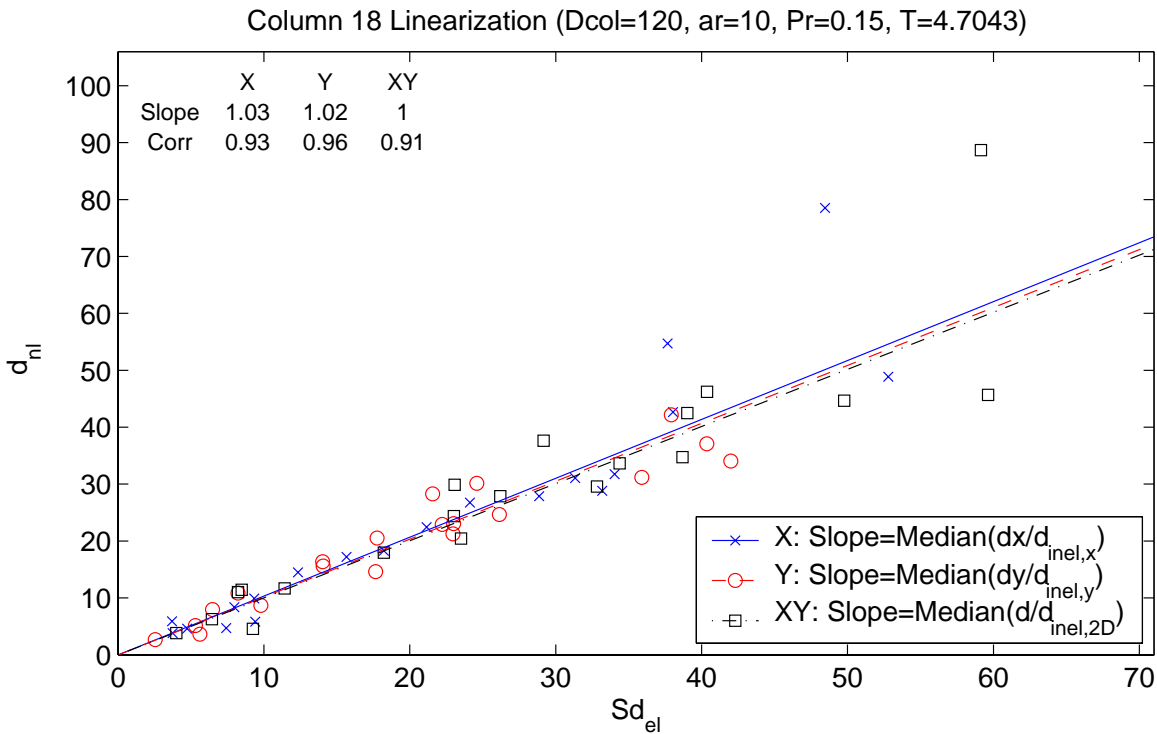
Figure 7-50. Linear regression of *Sd* and d_{nl} for Column 18.
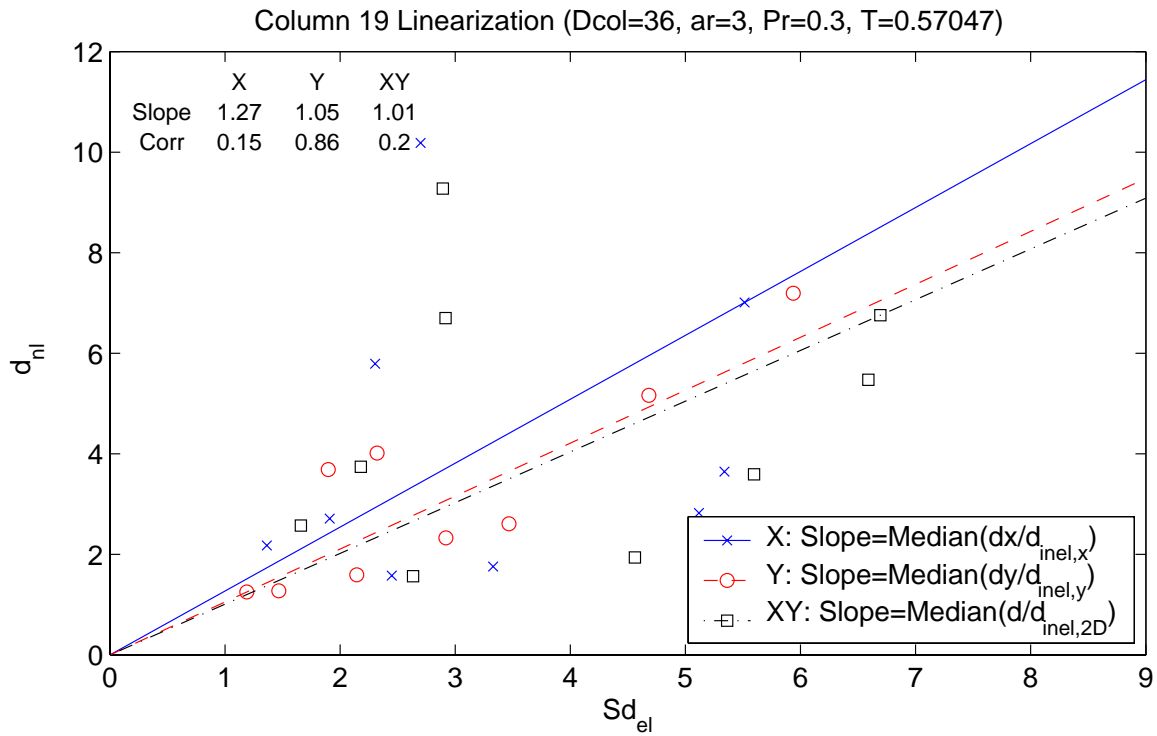
Figure 7-51. Linear regression of Sd and d_{nl} for Column 19.
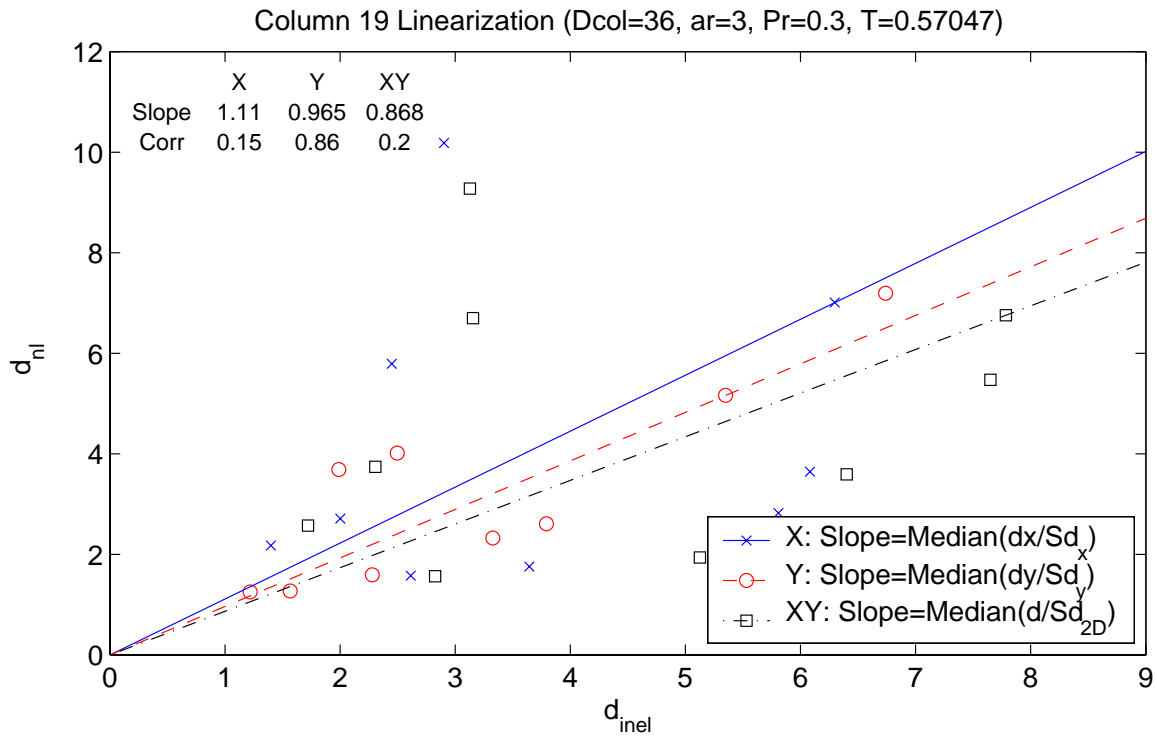
Figure 7-52. Linear regression of d_{inel} and d_{nl} for Column 19.
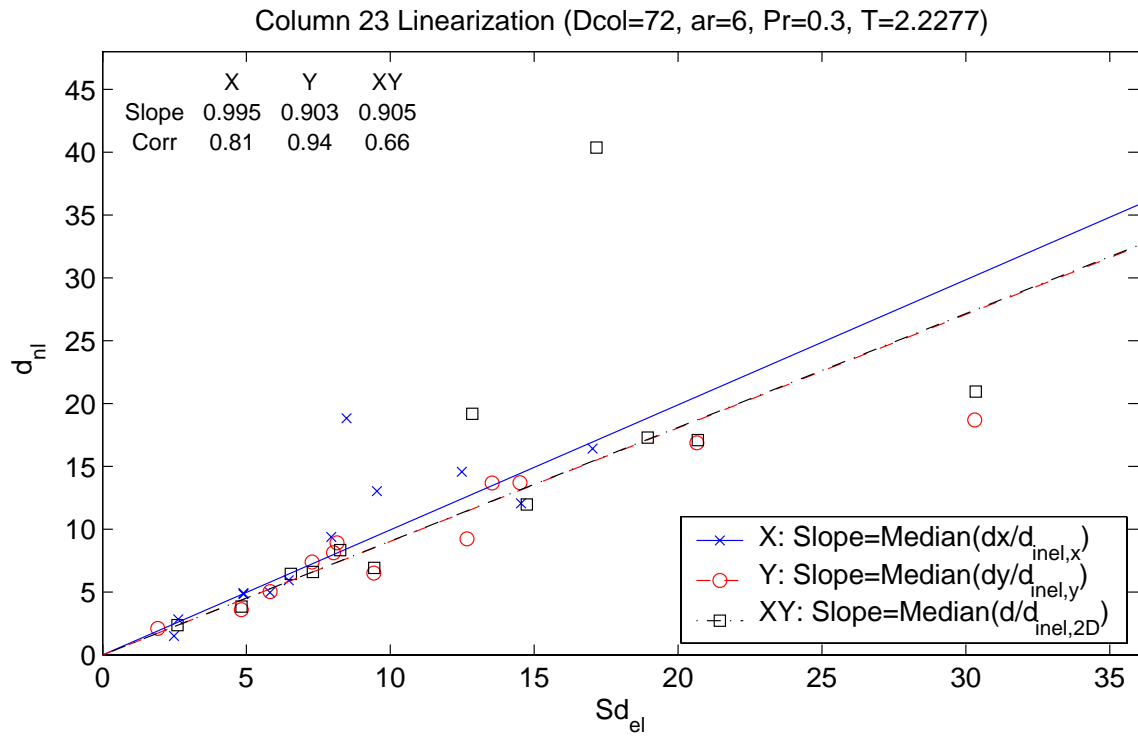
Figure 7-53. Linear regression of *Sd* and d_{nl} for Column 23.
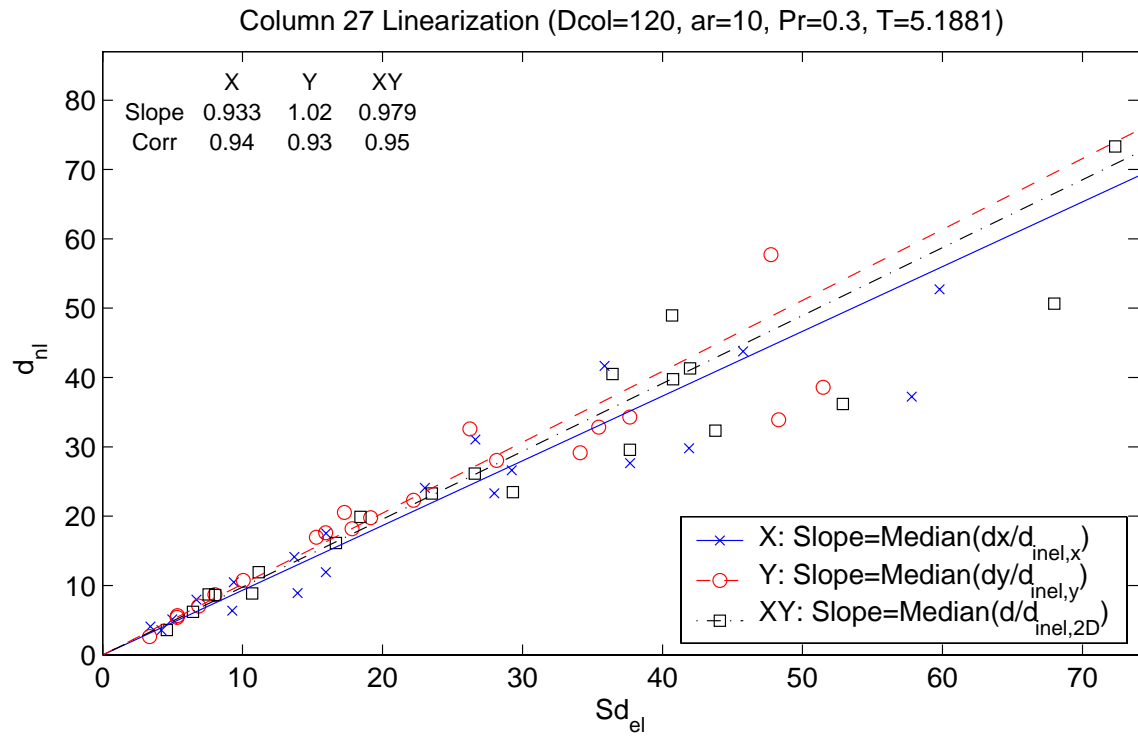
Figure 7-54. Linear regression of *Sd* and d_{nl} for Column 27.
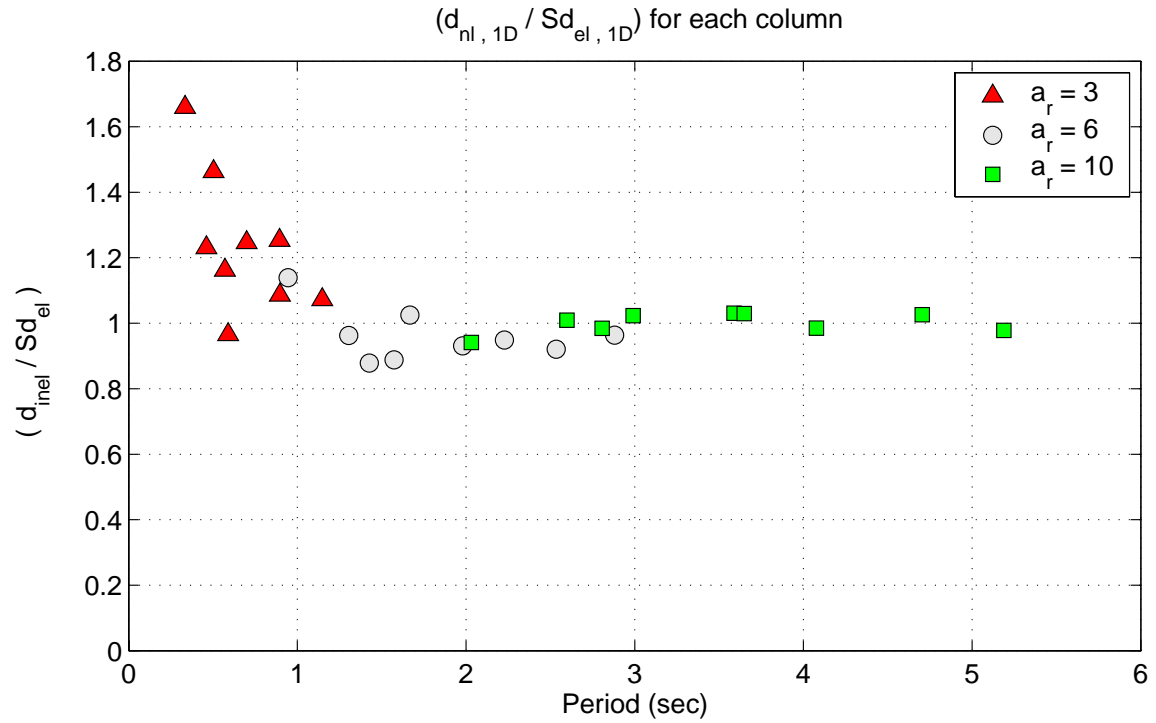
Figure 7-55. Average ratio of unidirectional nonlinear displacement to linear spectral displacement.
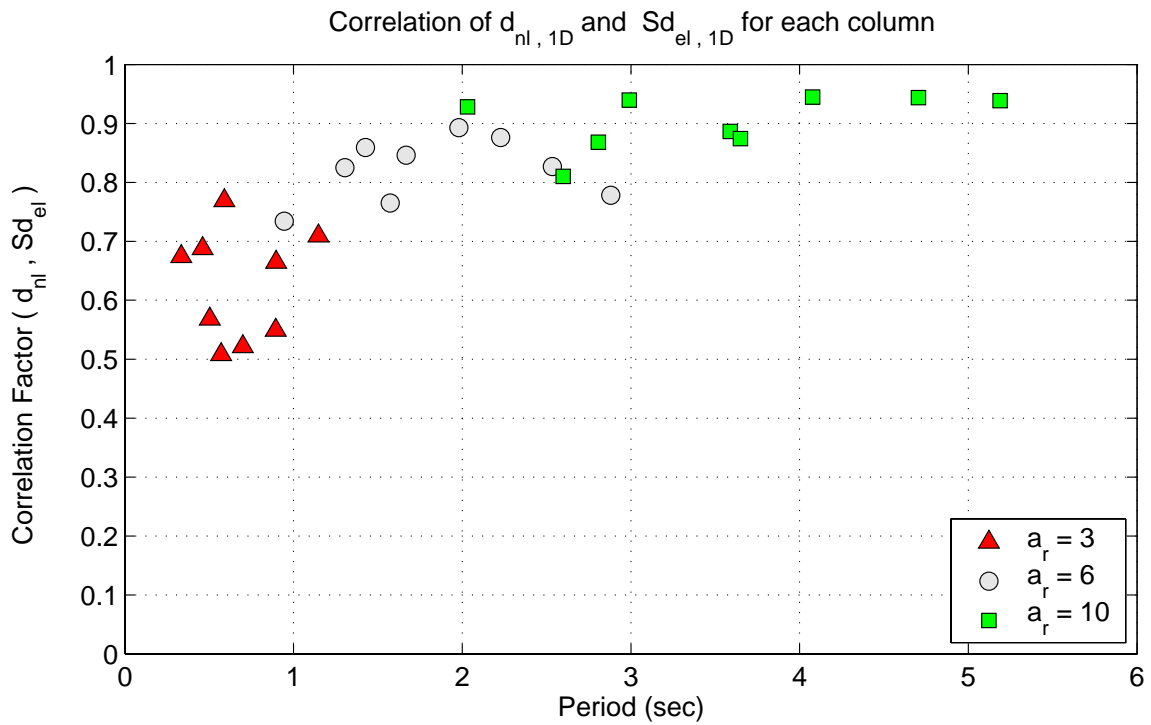
Figure 7-56. Correlation of unidirectional nonlinear displacement and linear spectral displacement.

291
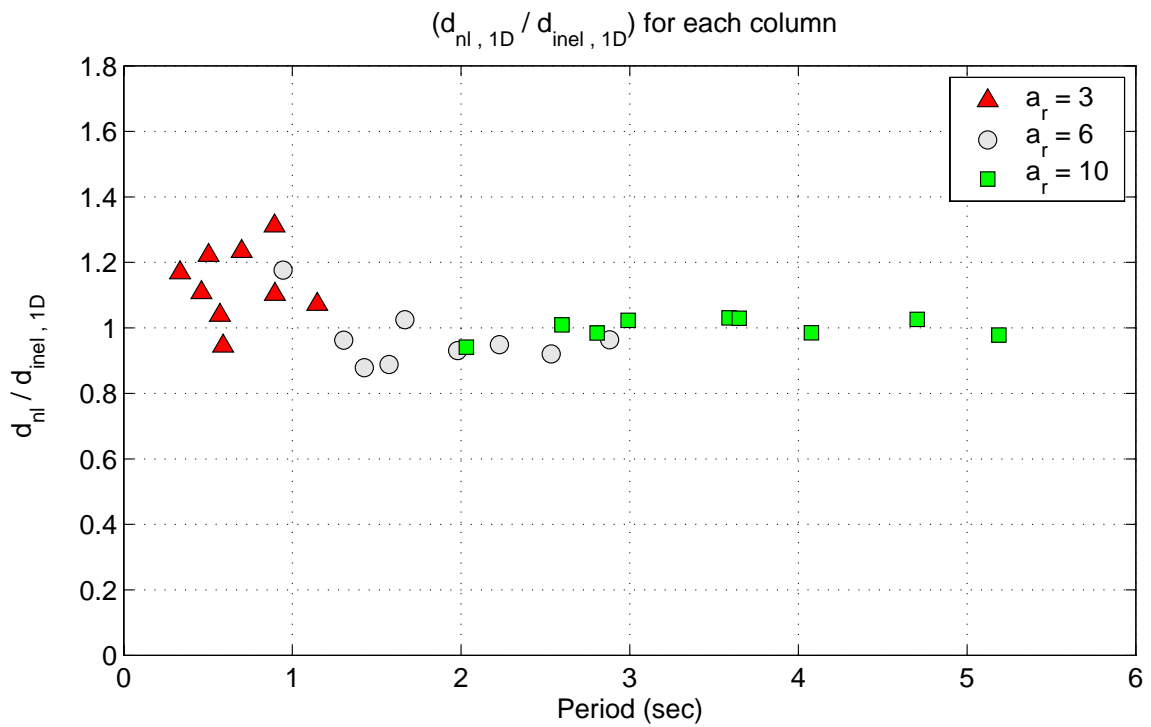
Figure 7-57. Average ratio of unidirectional nonlinear displacement to inelastic displacement demand estimate.
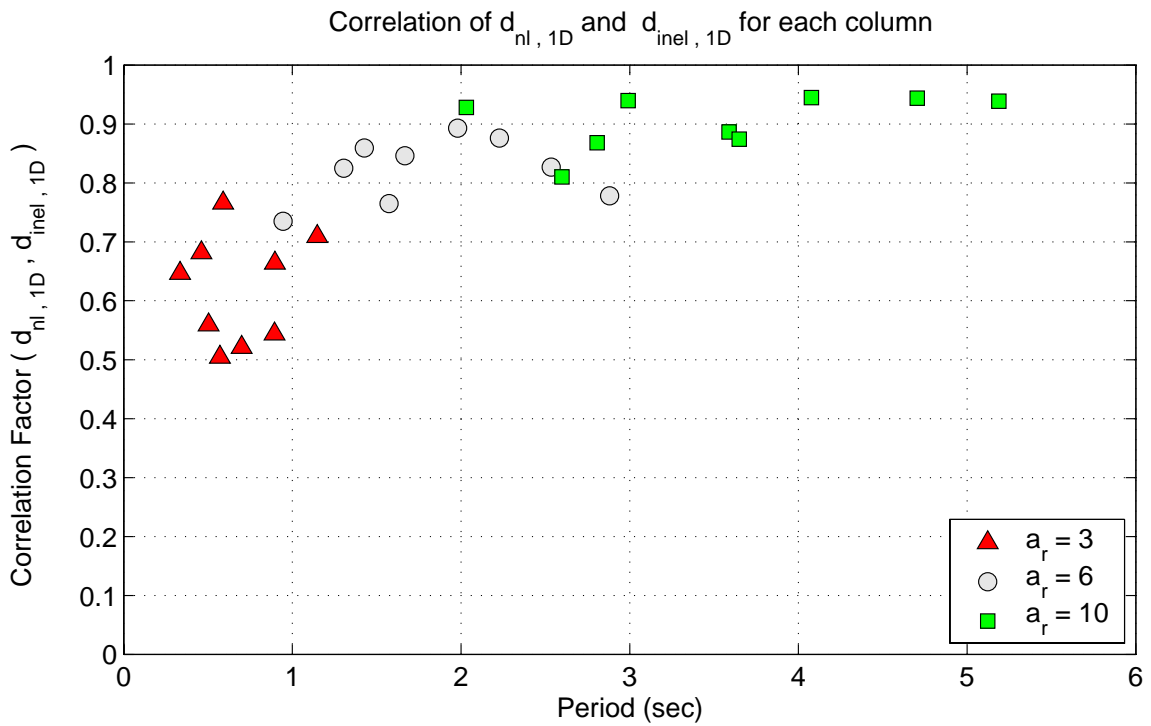
Figure 7-58. Correlation of unidirectional nonlinear displacement and inelastic displacement demand estimate.
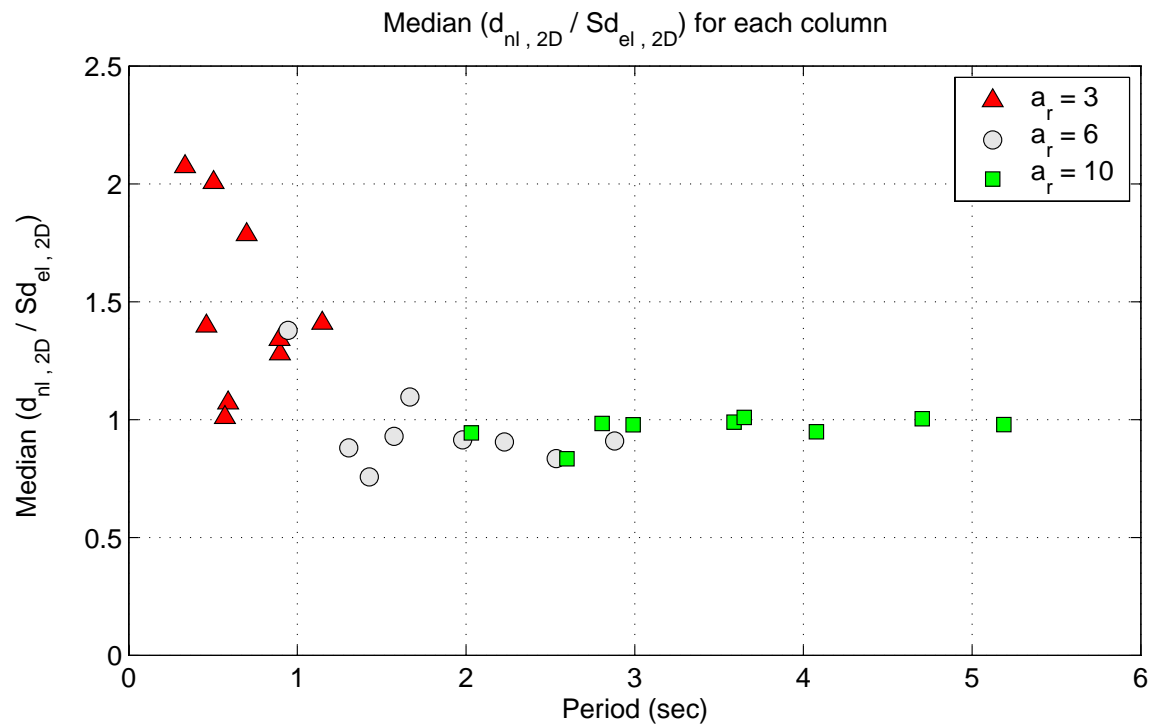
Figure 7-59. Average ratio of bidirectional nonlinear displacement to bidirectional linear spectral displacement.
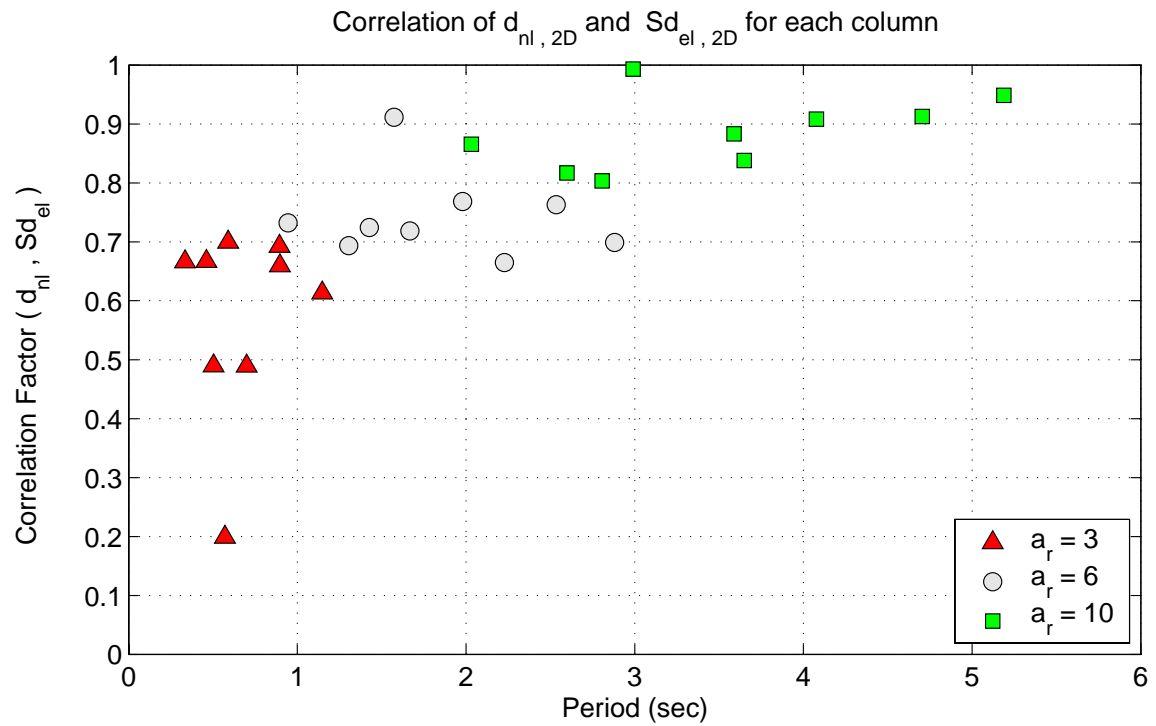
Figure 7-60. Correlation of bidirectional nonlinear displacement to bidirectional linear spectral displacement.
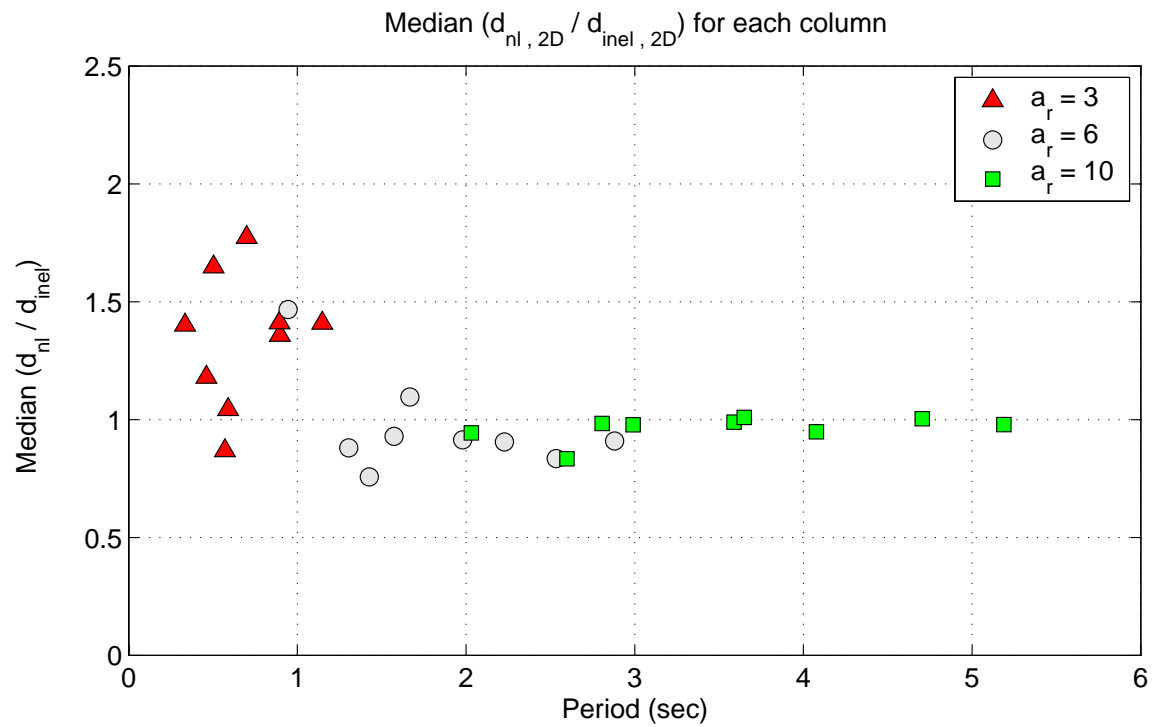
Figure 7-61. Average ratio of bidirectional nonlinear displacement to bidirectional inelastic displacement demand estimate.
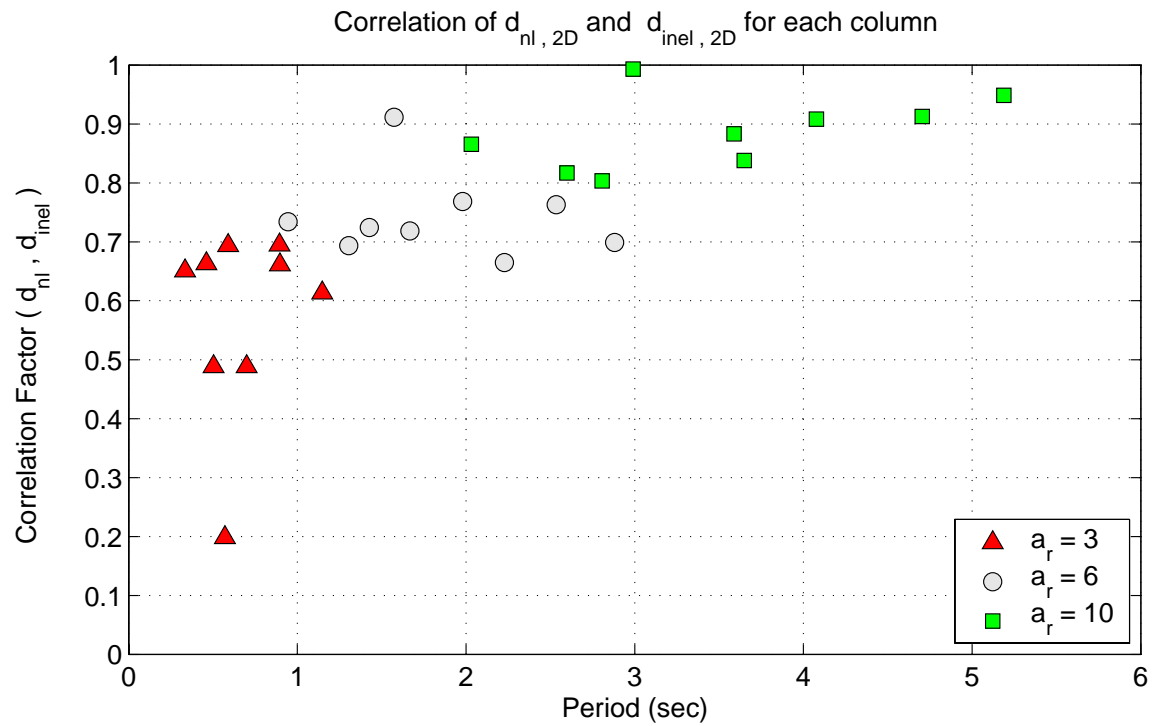
Figure 7-62. Correlation of bidirectional nonlinear displacement and bidirectional inelastic displacement demand estimate.
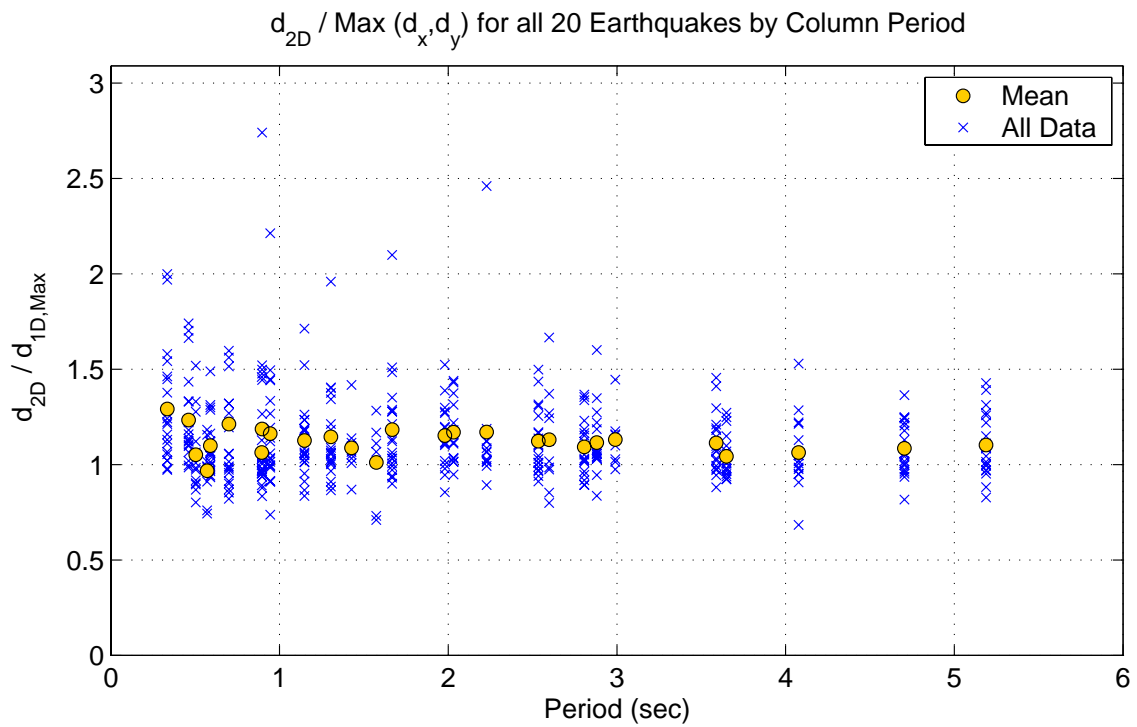
Figure 7-63. Ratio of bidirectional to unidirectional peak displacement demand.
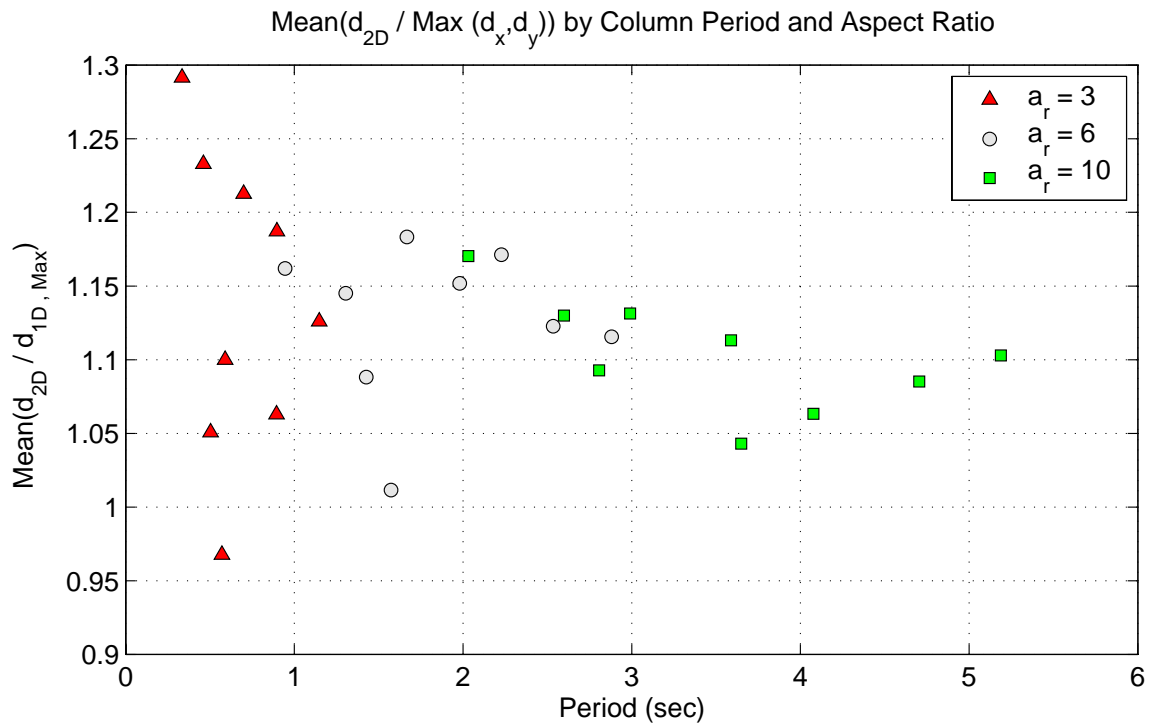
Figure 7-64. Average ratio of bidirectional to unidirectional peak displacement demand.
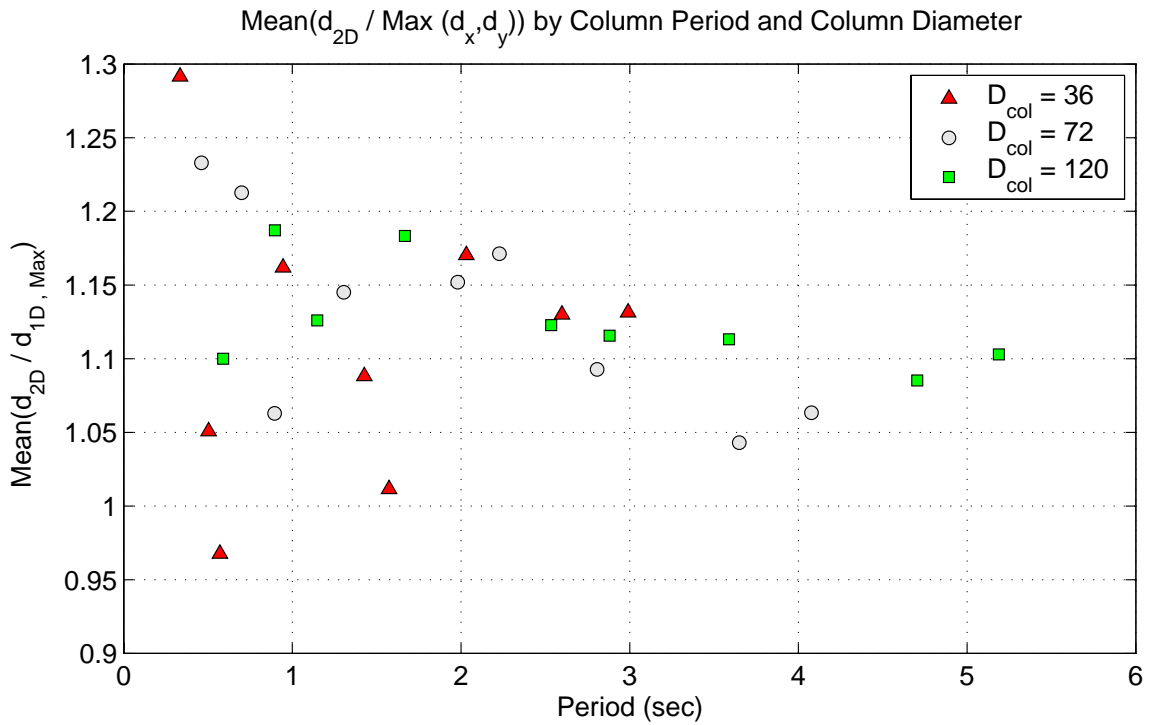
Figure 7-65. Average ratio of bidirectional to unidirectional peak displacement demand.
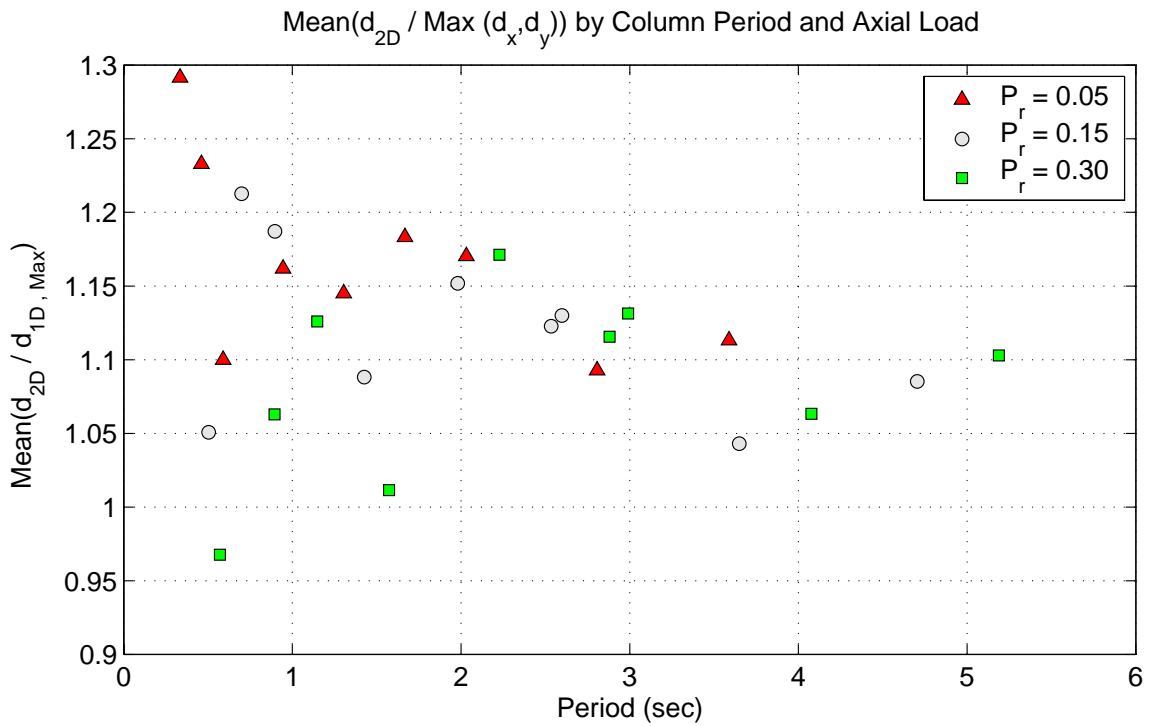
Figure 7-66. Average ratio of bidirectional to unidirectional peak displacement demand.
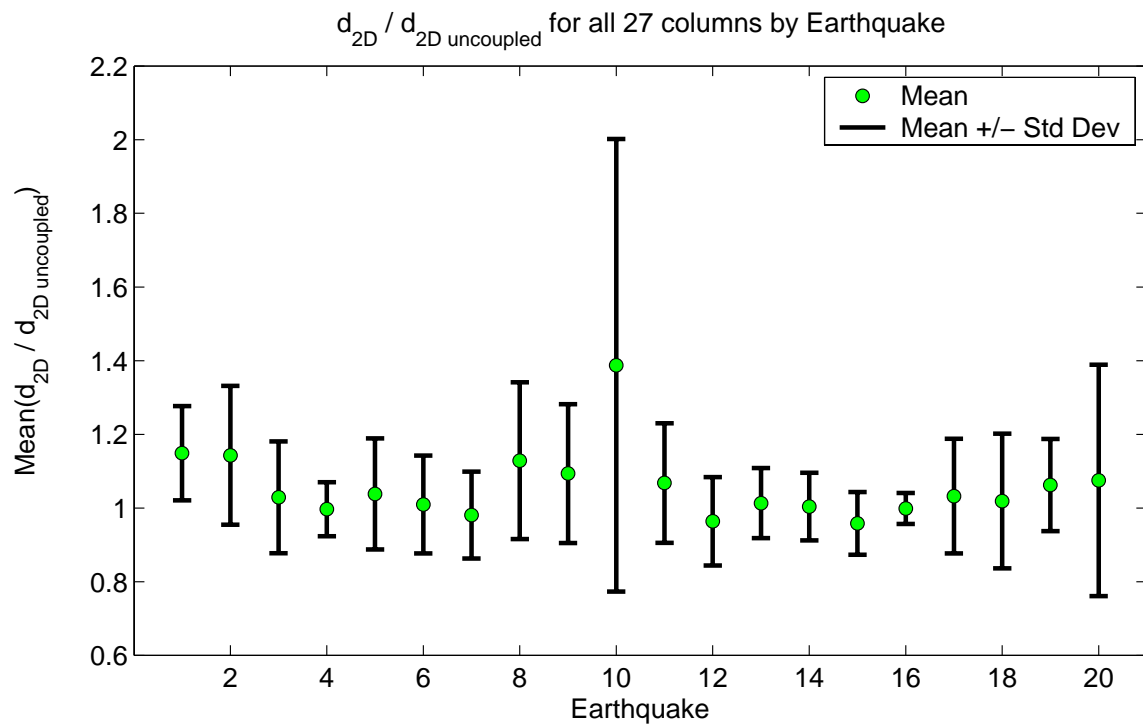
Figure 7-67. Effect of coupling ground motion components on the peak bidirectional displacement estimate.
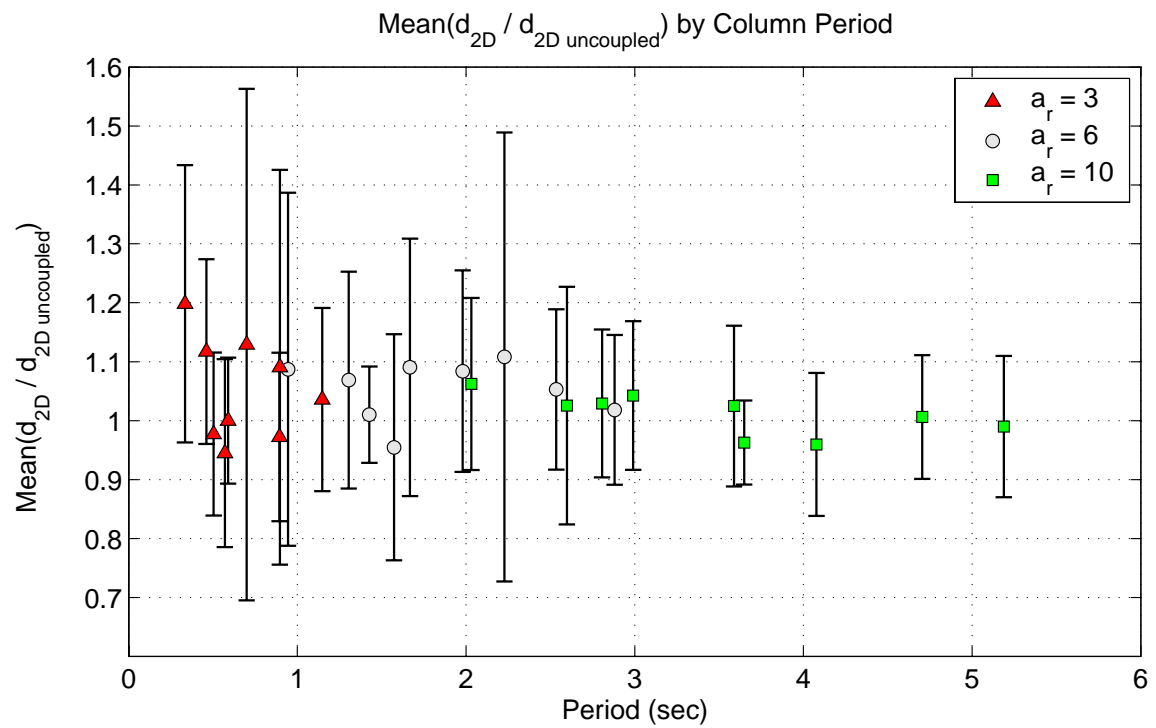
Figure 7-68. Ratio of bidirectional displacement demands estimated using coupled and uncoupled analyses.
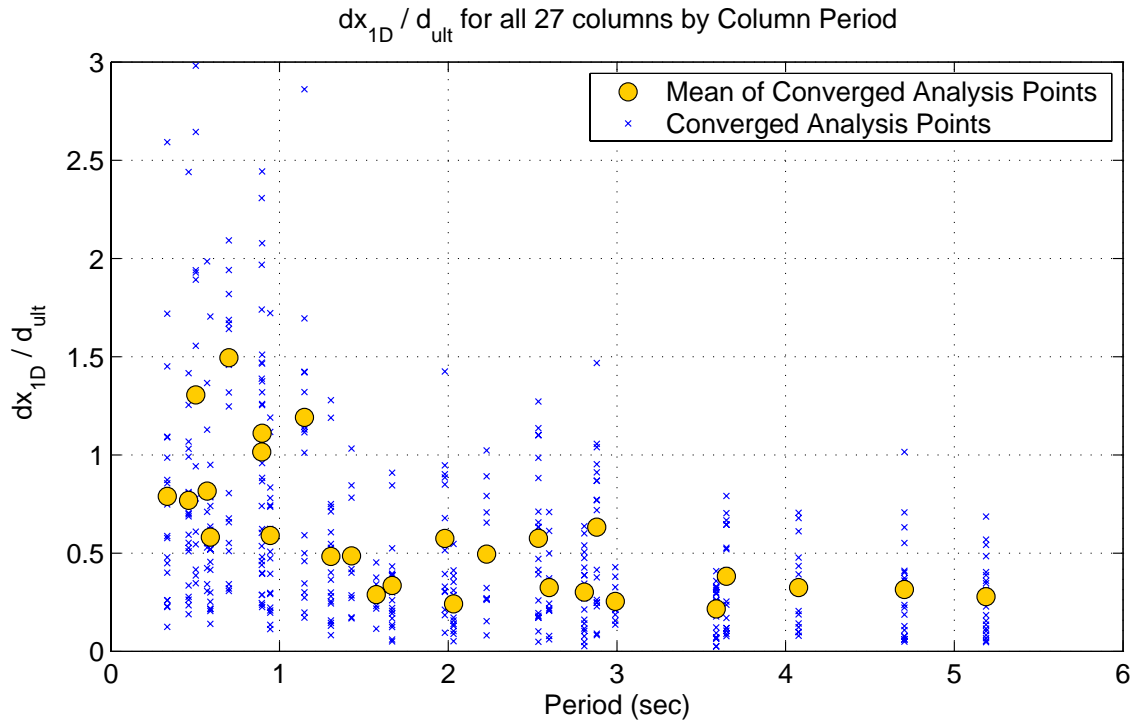
Figure 7-69. Ratio of peak unidirectional displacement demand to column deformation capacity (x-direction).
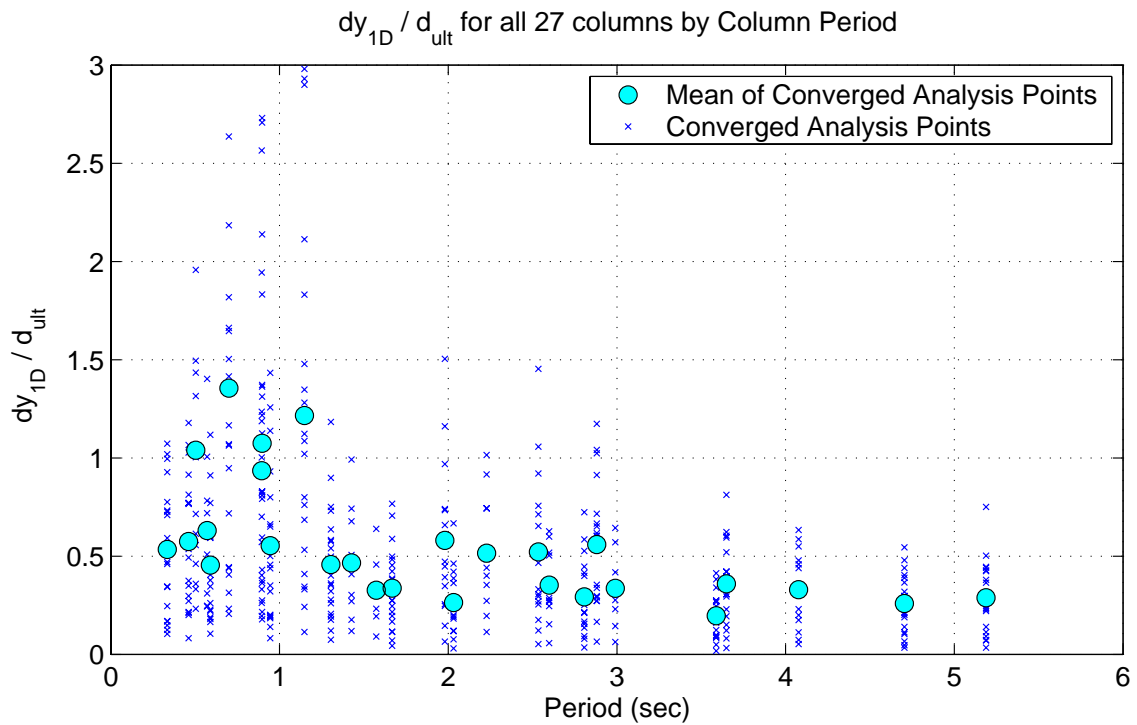
**Figure 7-70.** Ratio of peak unidirectional displacement demand to column deformation capacity (y-direction).
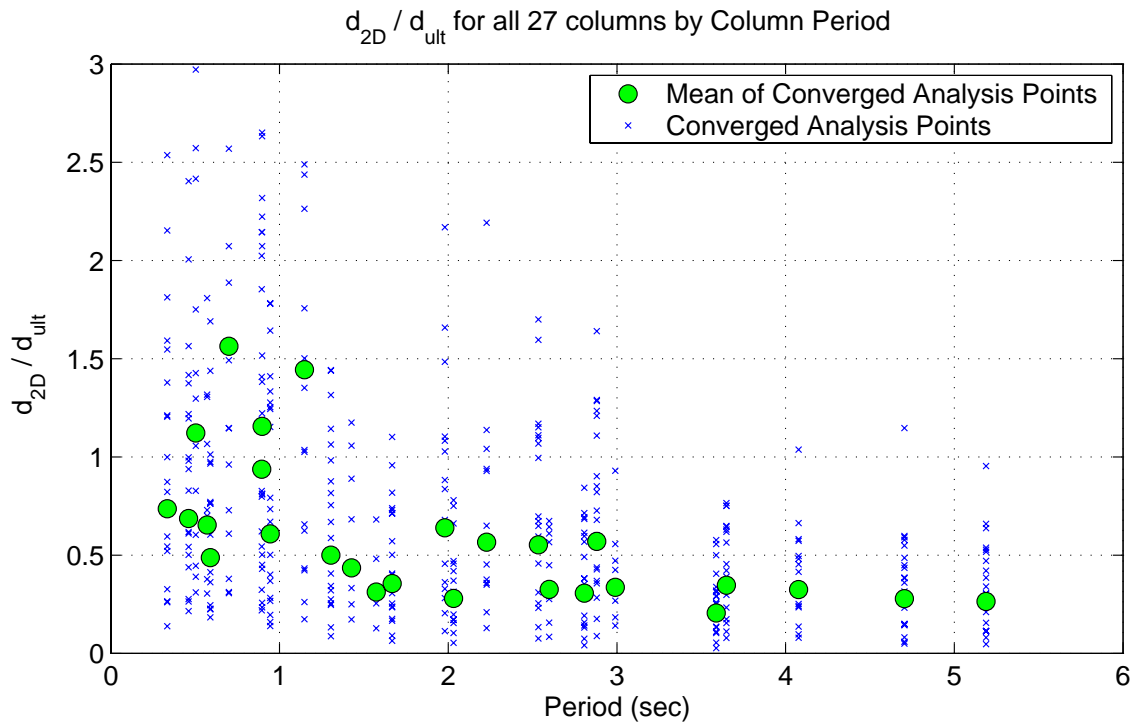
Figure 7-71. Ratio of peak bidirectional displacement demand to column deformation capacity.
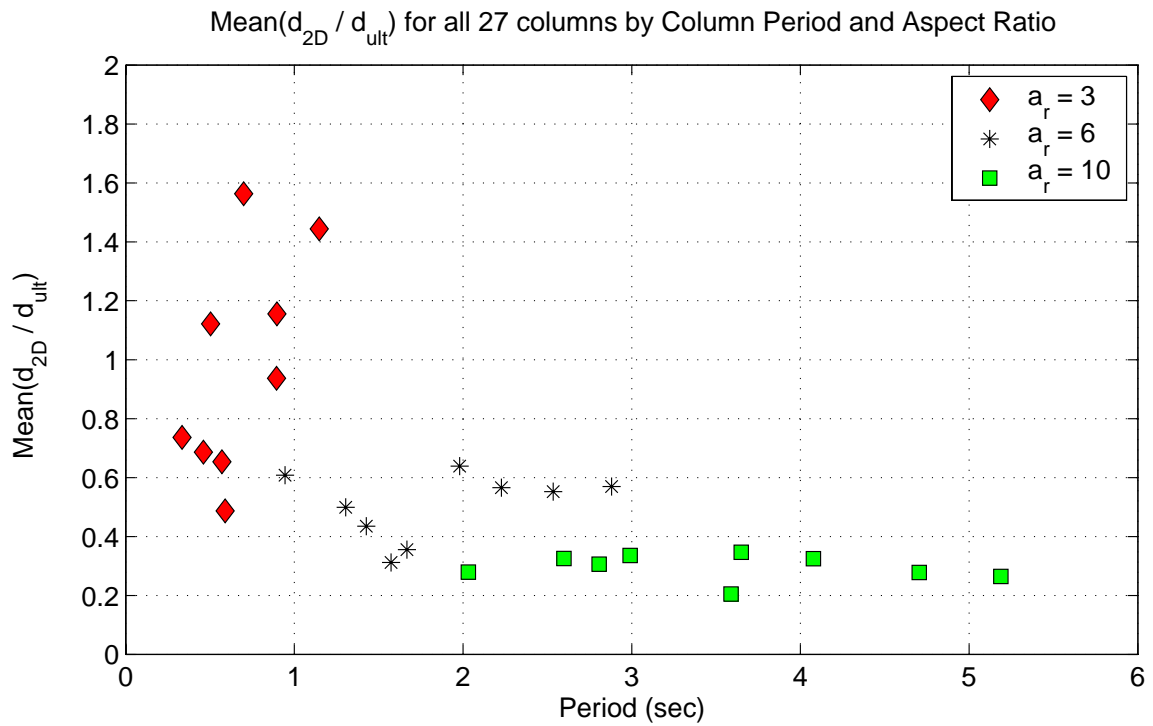
Figure 7-72. Average ratio of peak bidirectional displacement demand to column deformation capacity.
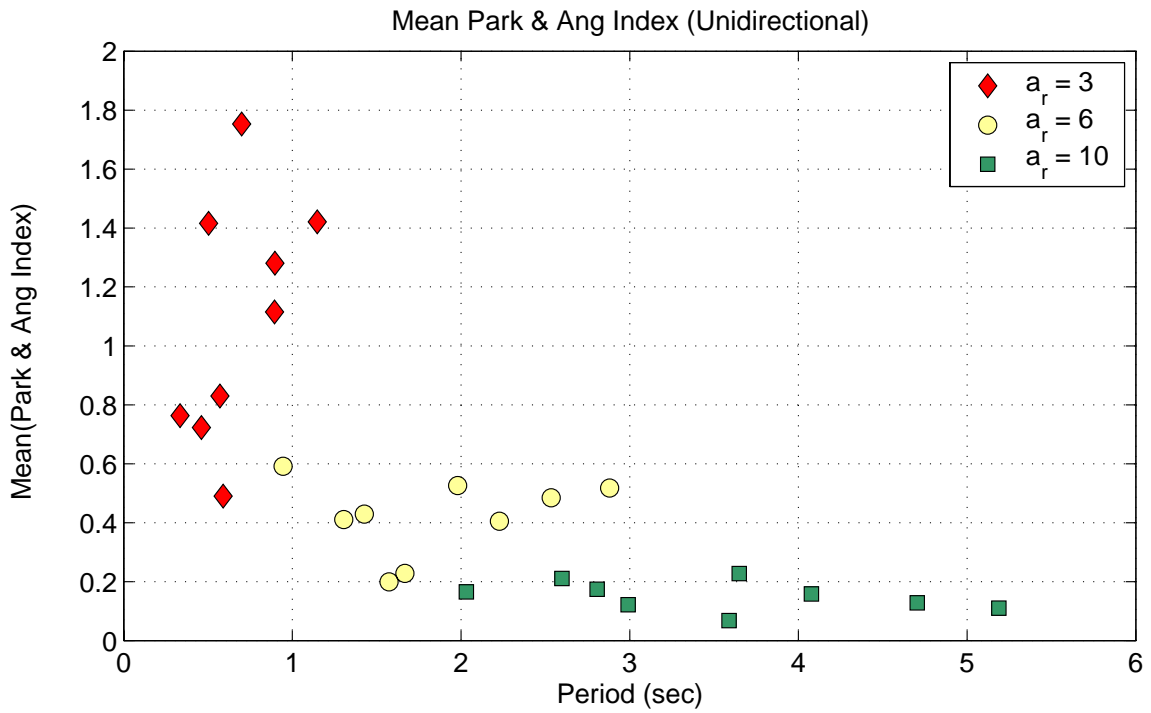
Figure 7-73. Park and Ang Damage Index (average of x and y unidirectional analysis).
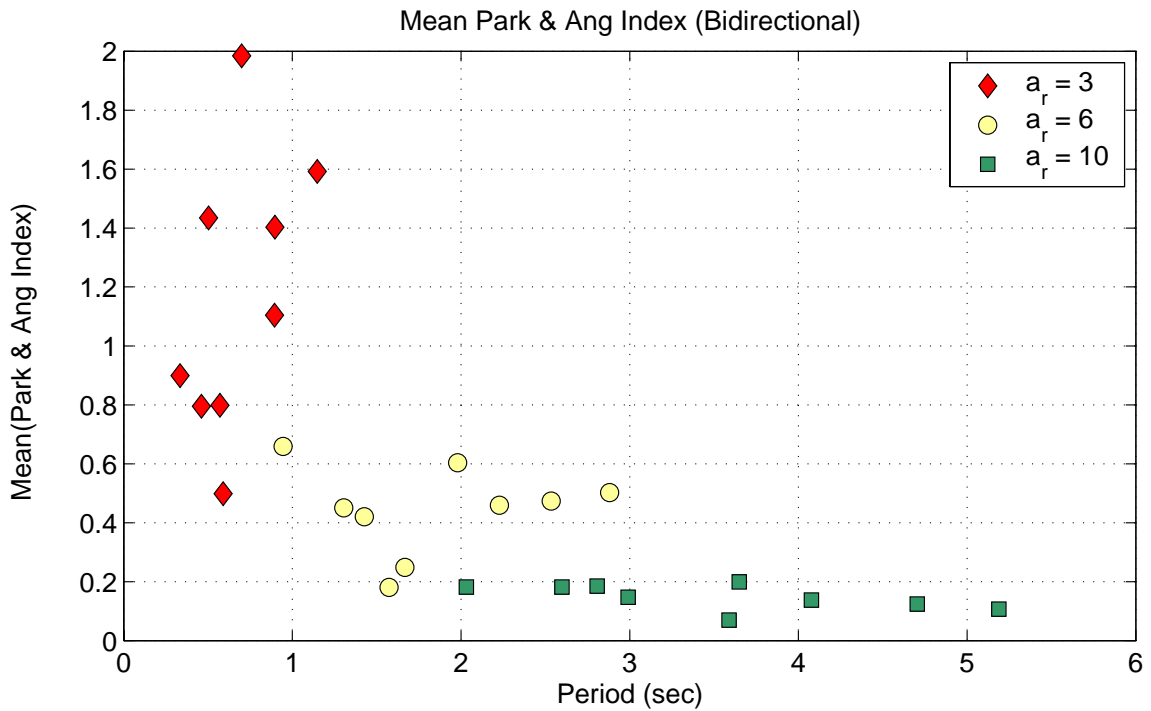
**Figure 7-74.** Park and Ang Damage Index (average of x and y directions from bidirectional analysis results).
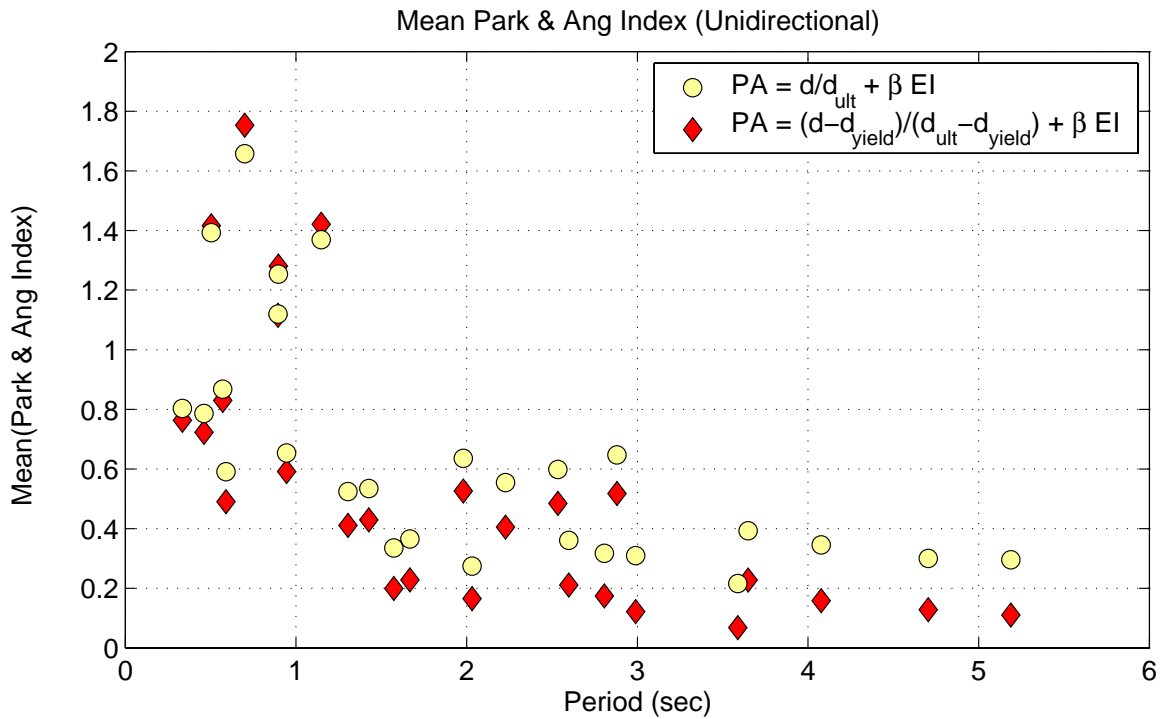
Figure 7-75. Average Park and Ang index for the two unidirectional analyses computed using two different methods.
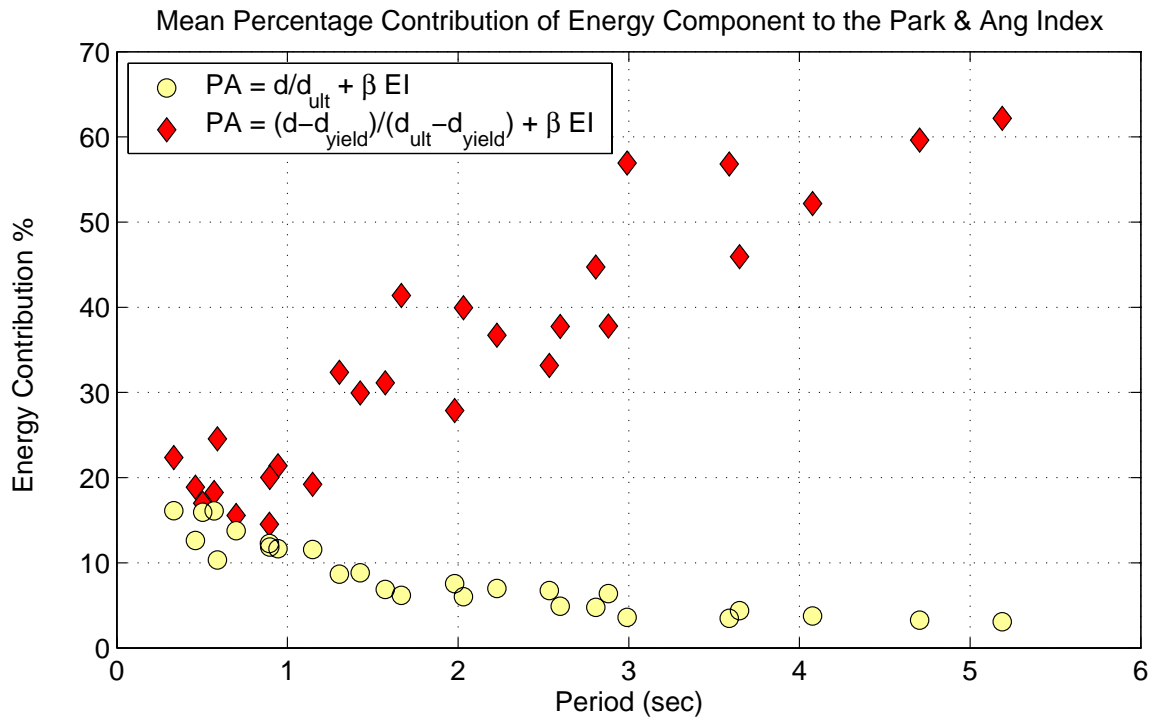
Figure 7-76. Contribution of the energy component to the Park and Ang damage index (average of x and y unidirectional analyses).
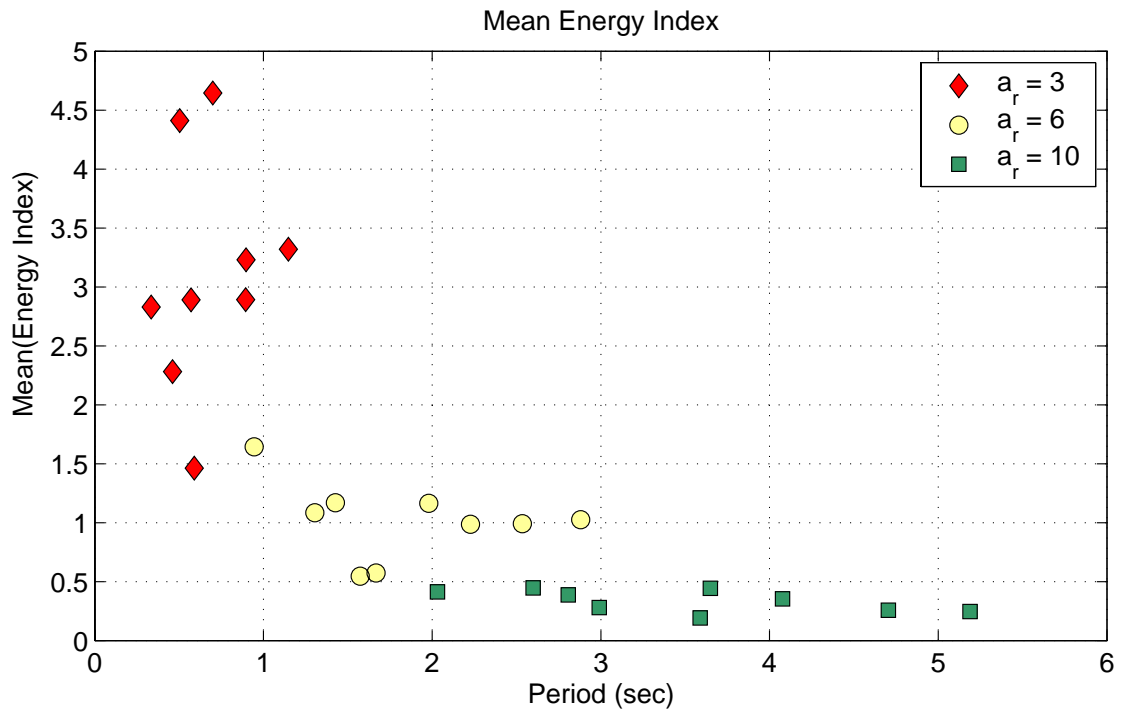
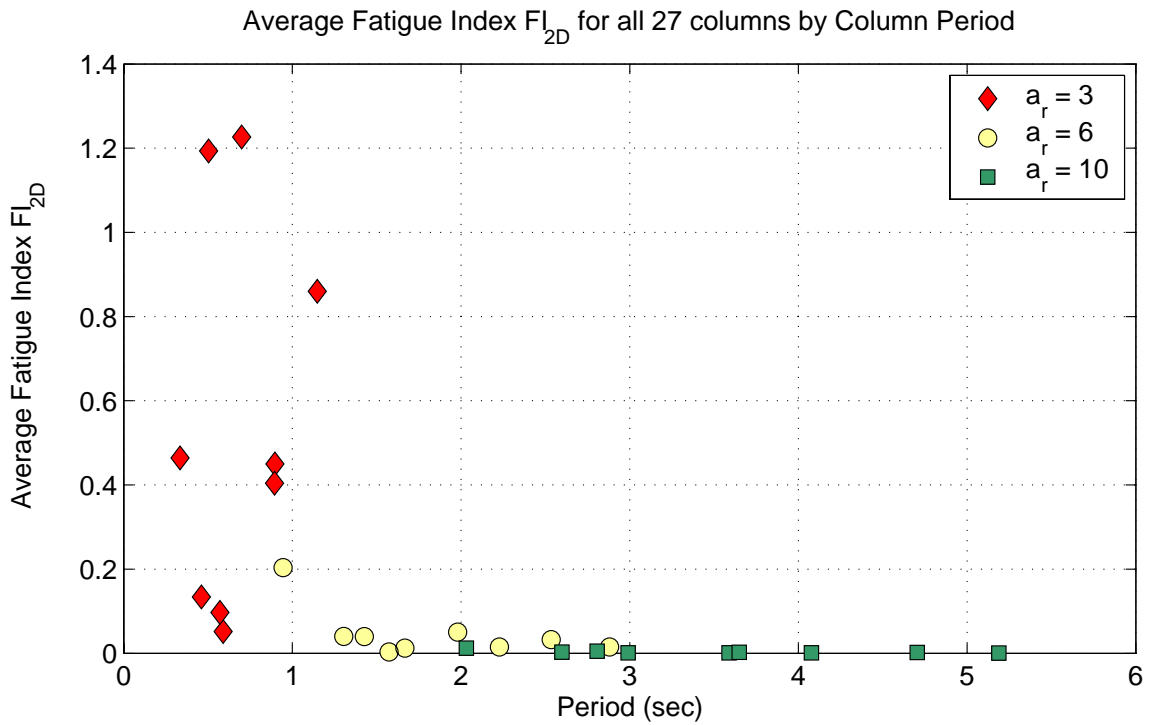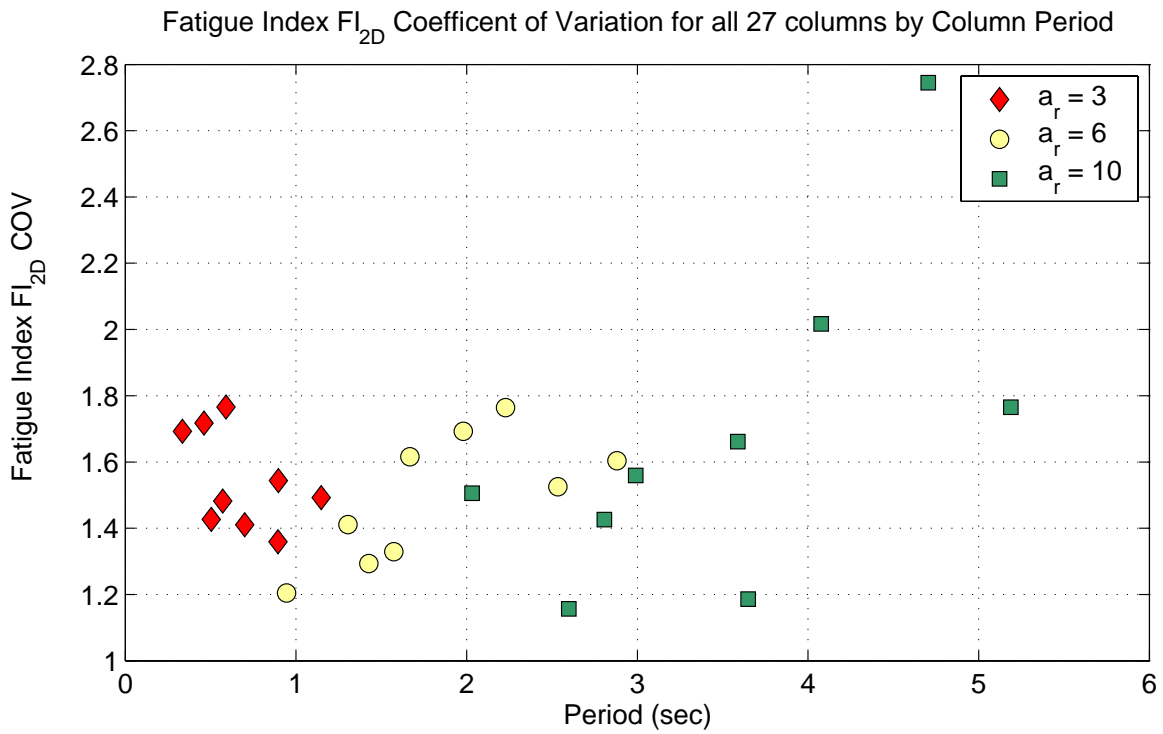**Figure 7-77.** Average Energy Index (average of x and y unidirectional analyses).
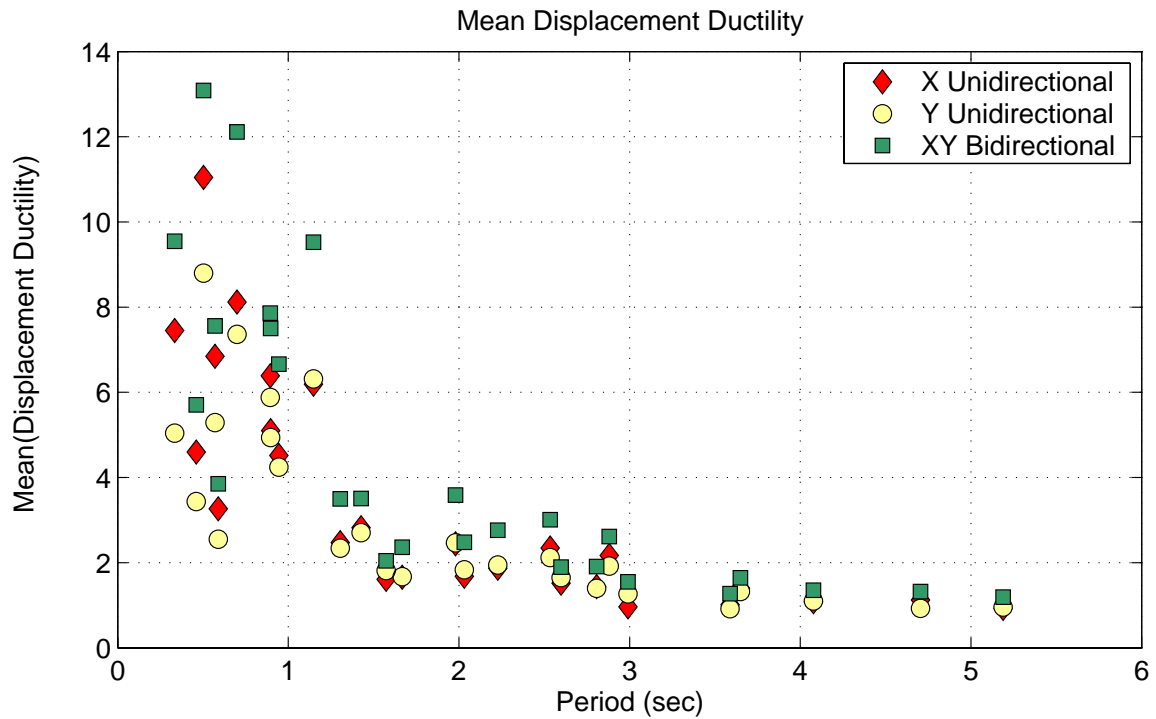
Figure 7-78. Average ductility demand for each under unidirectional and bidirectional input.

302

Figure 7-79. Average low cycle fatigue index for columns subjected to bidirectional loading

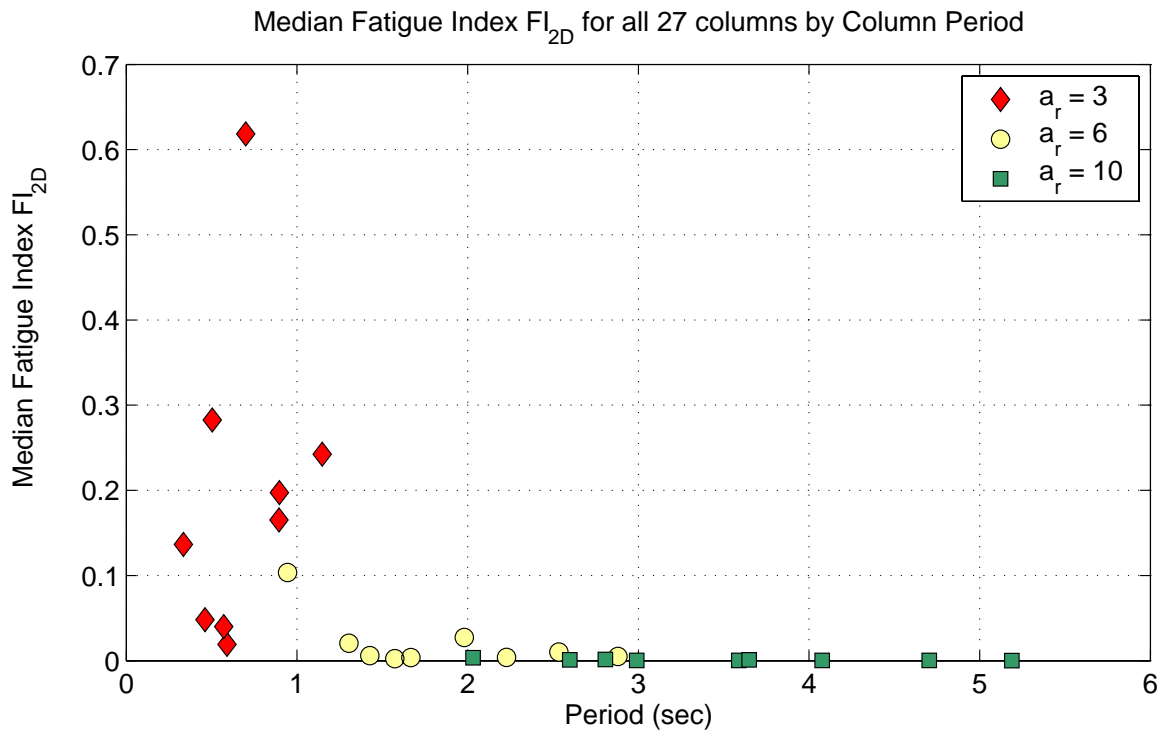**Figure 7-80.** Coefficient of variation of the bidirectional analysis fatigue index.

Figure 7-81. Median low cycle fatigue index for columns subjected to bidirectional loading.
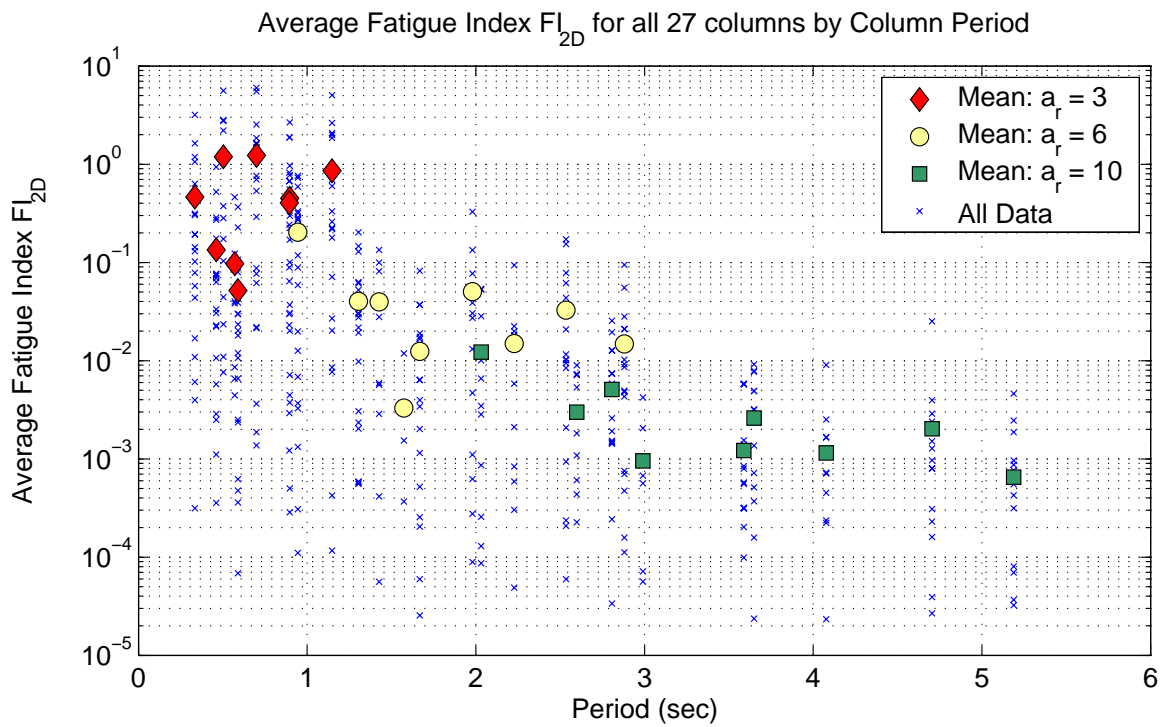

Figure 7-82. Average low cycle fatigue index for columns subjected to bidirectional loading.
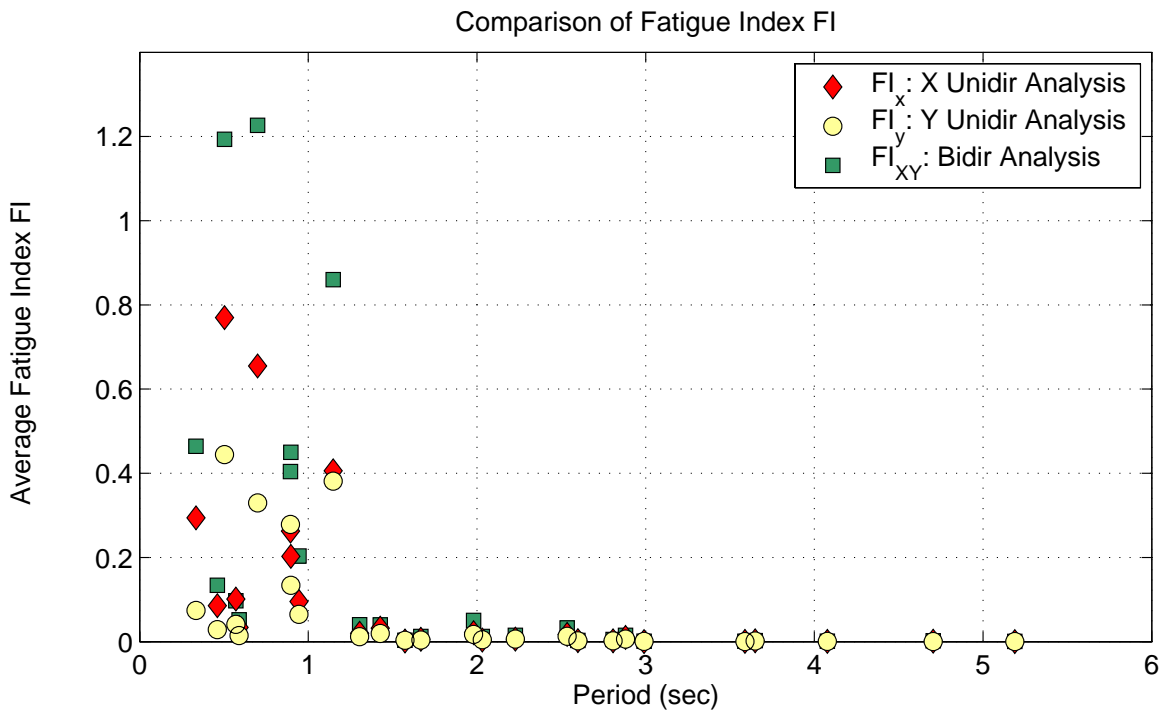
Figure 7-83. Fatigue index comparison of unidirectional and bidirectional loading.
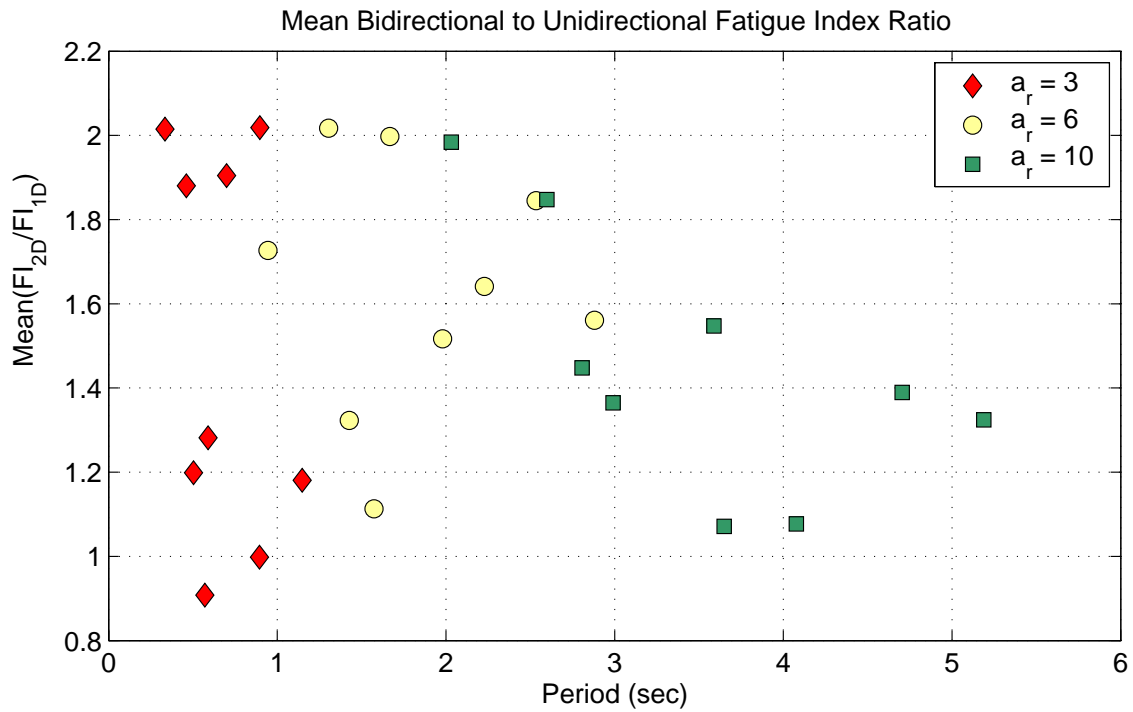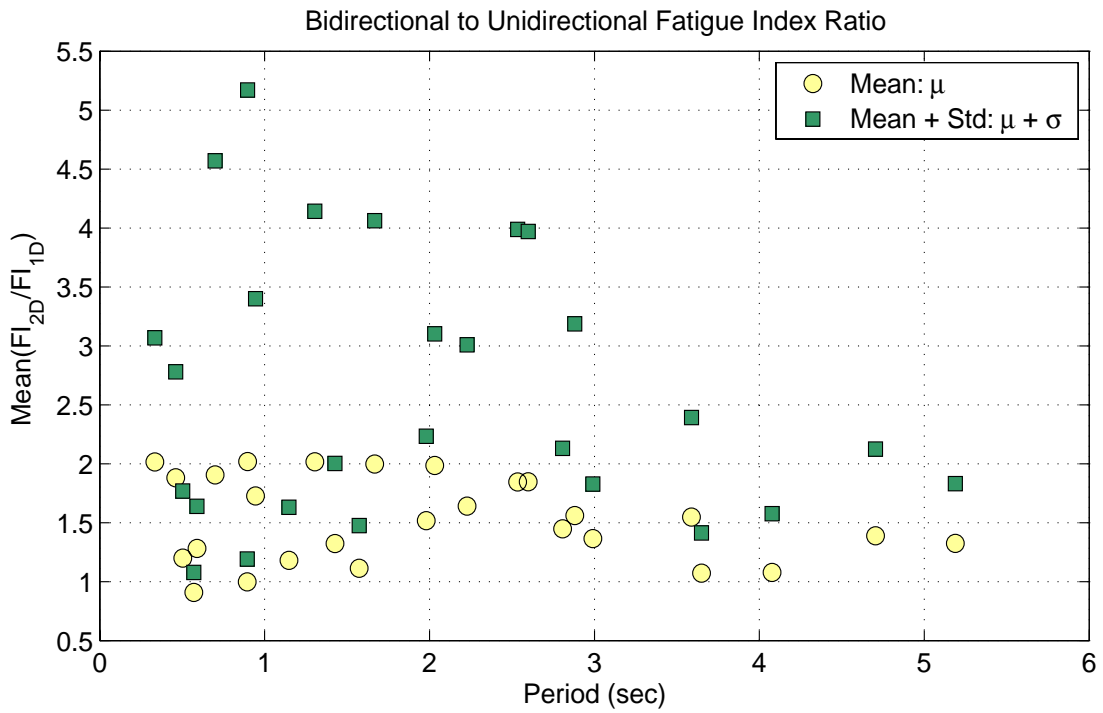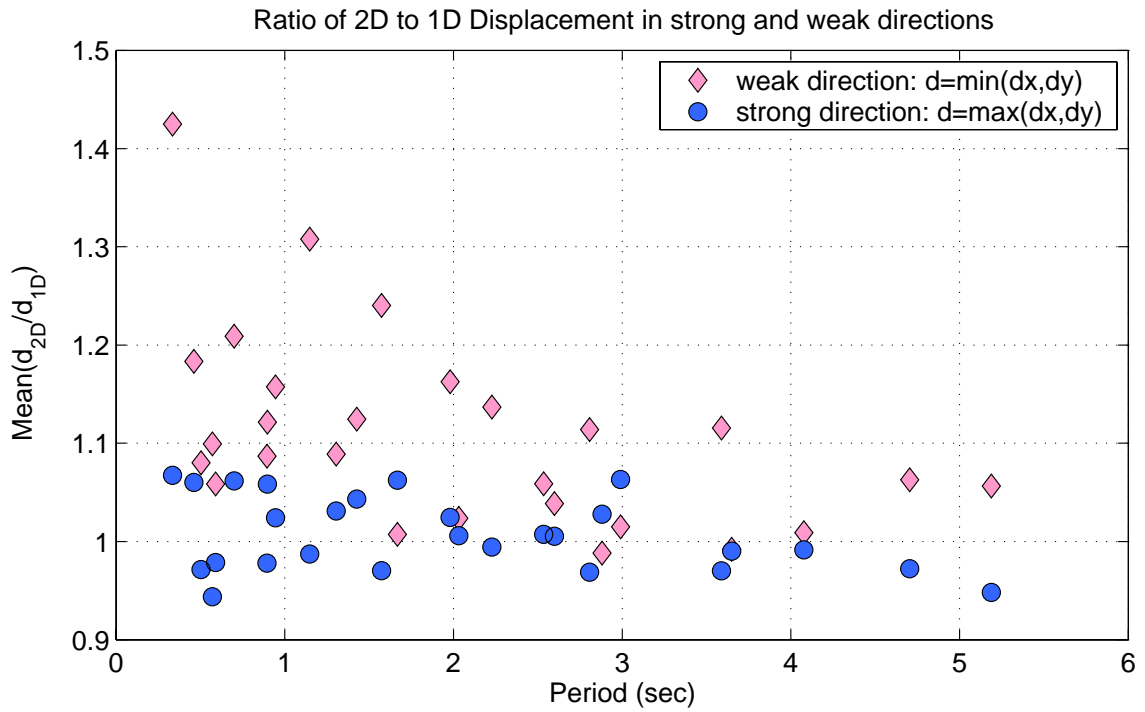

Figure 7-84. Average fatigue index ratio of bidirectional and unidirectional analyses: Comparing by aspect ratio.

Figure 7-85. Fatigue index ratio of bidirectional and unidirectional analyses: Mean and variation.

Figure 7-86. Increase in minimum and maximum unidirectional displacement due to bidirectional loading.
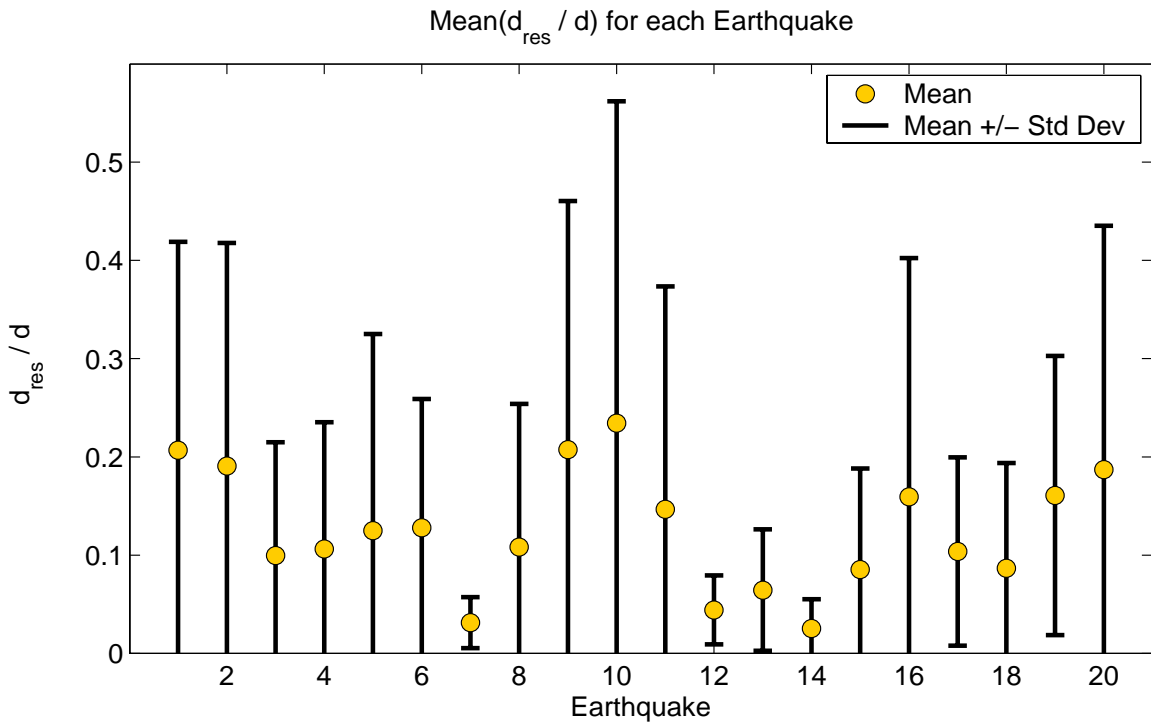
Figure 7-87. Ratio of bidirectional residual to peak displacement.
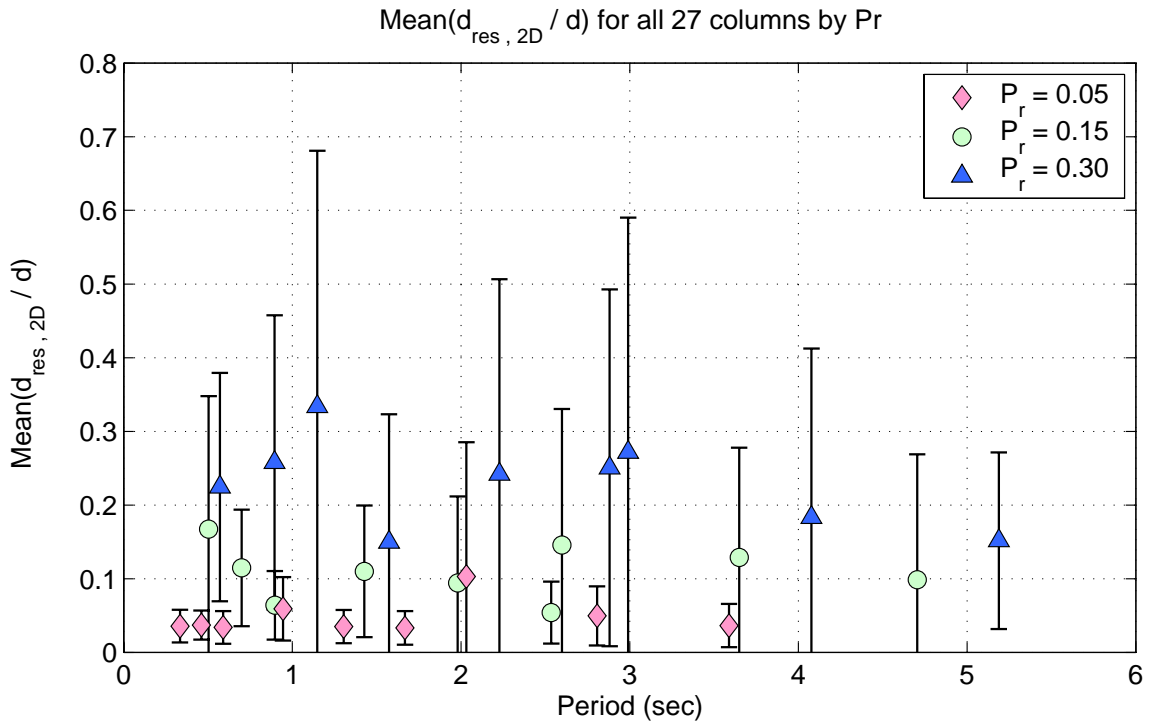
Figure 7-88. Ratio of bidirectional residual to peak displacement.
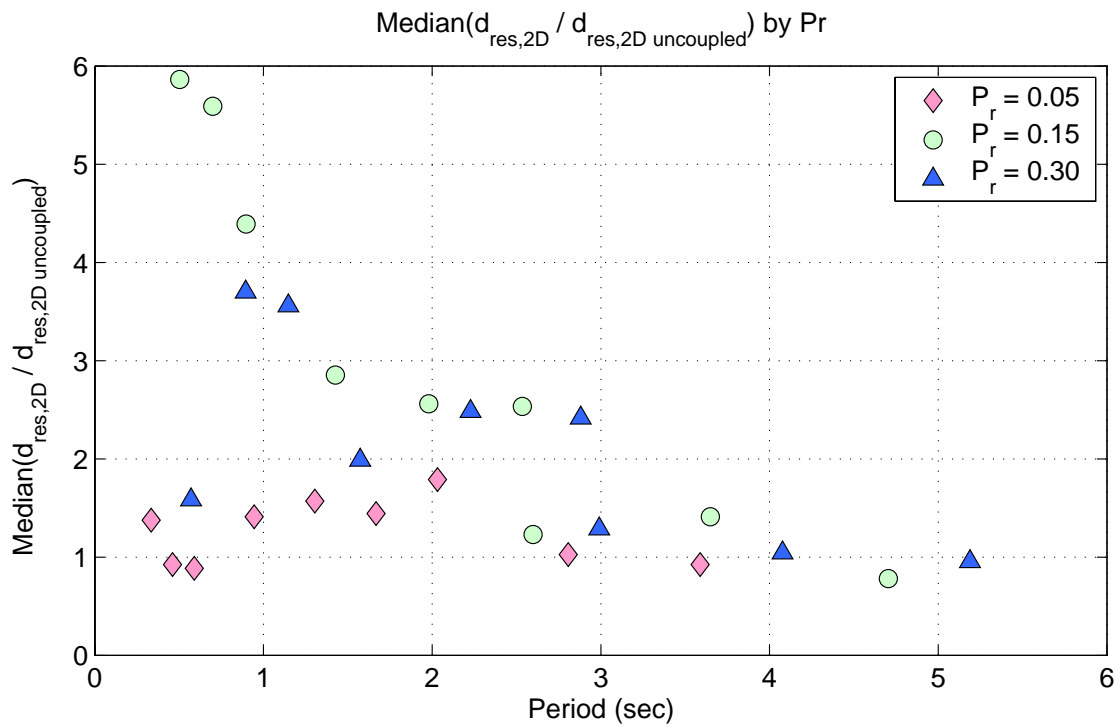
Figure 7-89. Comparison of coupled and uncoupled residual displacements from unidirectional and bidirectional analyses.

Figure 7-90. Ratio of uncoupled bidirectional residual displacement to the maximum unidirectional residual displacement.

8   Summary, Conclusions and Future Research

8.1   SUMMARY

A research program was undertaken to evaluate the performance of ductile circular reinforced concrete columns designed according to modern design specifications. The research objectives were to investigate the effect of bidirectional shaking as com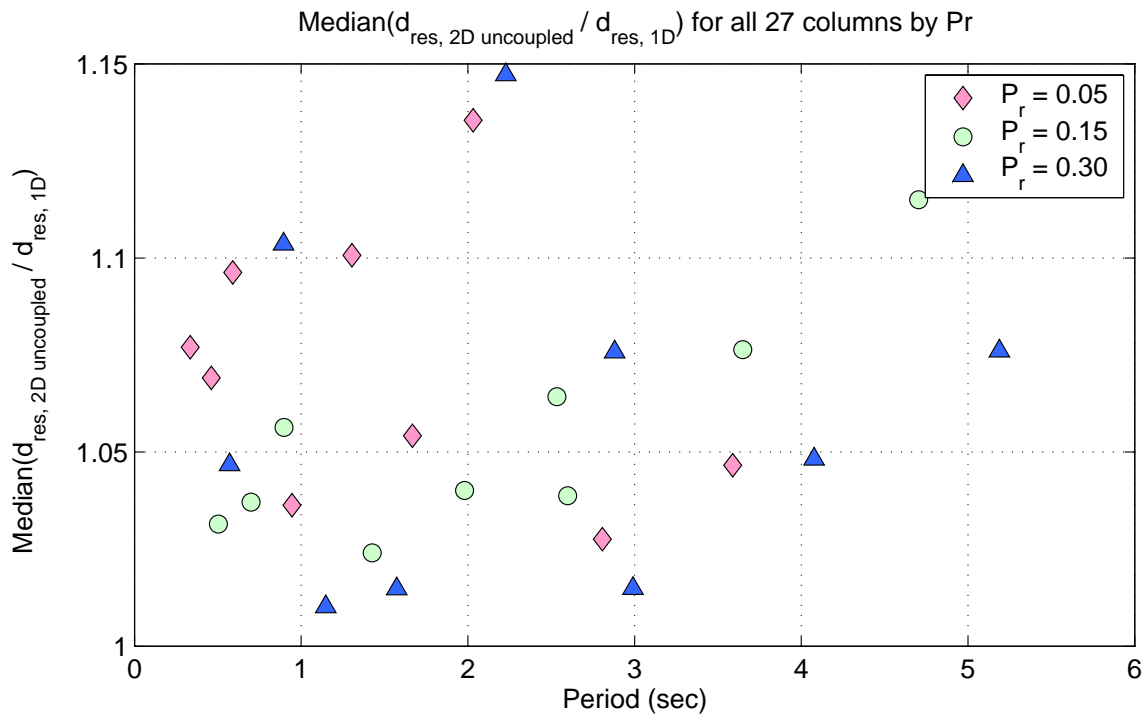pared to unidirectional shaking, to compare the damaging effects of near-fault ground motions to damage resulting from large magnitude long-duration ground motions, and to assess the ability of current available computer models to predict seismic performance.

The research program consisted of an experimental investigation which involved testing of four 1/4.5 scale columns on the shaking table under unidirectional and bidirectional shaking using two different ground motions, and an analytical investigation. The ground motions used were the Olive View record of the Northridge earthquake, and the Llolleo record of the 1985 Chile earthquake. The analytical phase of the investigation consisted of two studies:

1. The evaluation and verification of available models for modeling reinforced concrete elements by comparing the measured experimental results to those obtained from analysis.

2. The parametric evaluation of reinforced concrete columns with a wide range of sizes and proportions and supported weights, when subjected to a suite of ground motion records. The performance of each column was examined using a number of measures and damage indices.

8.1.1   Experimental Investigation

The experimental investigation involved testing four identical reinforced concrete circular columns with ductile detailing conforming to the Bridge Design Specifications (BDS) of the California Department of Transportation (Caltrans). Each column supported a mass block representing the tributary weight and inertia of the column. The columns were 16 in. (406.4 mm) in diameter, with

a longitudinal reinforcement ratio of 1.2% and spiral reinforcement ratio of 0.54%. The clear height of each column was 64 in. (1.63 m), while the distance from the base to the center of gravity of the supported mass was 96 in. (2.44 m), hence giving an effective aspect ratio of 6. A scale factor of 4.5 was assumed for the model columns, which would make them representative of a prototype column that is 6 ft (1.83 m) in diameter and 36 ft high (11.0 m). The columns were proportioned to resist lateral forces obtained using the ARS spectra, assuming a force reduction factor Z of 4.

The column was tested on the shaking table with its base prestressed to the simulator platform, while the top was unrestrained. The four specimens were divided into two pairs. Each pair was tested using one of two records: a near-fault record (Olive View, Northridge 1994), and a long duration record (Llolleo, Chile 1985). Within each pair, one specimen was subjected to the larger of the two components of the record, while the other specimen was subjected to both components simultaneously. Testing of each specimen progressed starting with low level excitations, followed by a design level excitation corresponding to the same spectral acceleration as the design ARS spectra. The design level excitation was followed by a maximum level excitation equal to more than 1.5 times the design level, which might represent a maximum credible earthquake. Since performance was judged excellent up to that point, a series of design and maximum level excitations were repeated until failure of the column, in order to characterize the column's energy dissipation capacity, and the final failure mode.

The instrumentation setup included various transducers to monitor accelerations and displacements at various points along the height of the specimen. Strain gages were attached to longitudinal and spiral reinforcement in the expected plastic hinge region, and extending into the footing. Other displacement transducers were used to measure curvatures and axial elongation at critical locations of the column. Cracks were marked following the end of each excitation, and video recording was used to document the damage progression in the plastic hinge region during each dynamic test.

8.1.2   Interpretation of Experimental Results

The data measured from each specimen were evaluated and compared. Measured accelerations were used to compute inertial forces, which were in turn used to estimate the shear and bending moment distribution along the column. Global response quantities such as peak forces and displacements, and local quantities such as curvatures and strains were tracked and compared. Local curvatures and strains were subsequently used to test the validity and usability of plastic hinge and

other analysis models to predict local damage. The response due to different repetitions of the same record were compared for the same specimen and for specimens in the same pair. In addition to displacements and forces, damage index measures were used to quantify the progression of damage with repeated loading. The damage indices used include the Park and Ang index and a low-cycle fatigue model which was applied to each bar in the section. Finally, the effect of repetitive loading on the column's stiffness, period and damping was investigated.

8.1.3   Verification of Analytical Models with Experimental Results

Shaking table tests have the advantage of representing, as closely as possible in the laboratory, the actual shaking experienced by structures during earthquakes. Hence, experimental data obtained from shaking table tests present a unique opportunity to calibrate and verify the accuracy of element and material models, and dynamic analysis techniques, and to identify shortcomings and areas that need improvement. Based on this premise, a series of analytical models were used to analyze the specimens under the same sequence of shaking that was applied experimentally. The results were used to rate the different models based on their ability to predict different aspects of the response, relative to their complexity. The element models included linear and nonlinear models. Nonlinear models were classified into simple hysteretic models, and more complicated models based on fiber discretization of the cross-section. One of the fiber models considered included an added spring to model the slip rotation flexibility.

A sensitivity study was also performed to investigate the effects of several variables on the response, using a model of the specimen and the same ground motions used in the tests. The variables considered included the intensity of the ground motion, bidirectional vs. unidirectional loading, linear vs. nonlinear analysis results, the effect of vertical ground motion, and the result of accidental or intended eccentricity of vertical loads on the seismic behavior of the column.

8.1.4   Parametric Performance Evaluation Reinforced Concrete Columns

Using the experimental and analytical results and conclusions from studying the response of the tested columns, a parametric analysis was performed to expand the investigation to a large number of columns spanning a wide range of bridge columns. The columns were obtained by varying three main parameters: column diameter, aspect ratio, and axial load ratio. Each column was then designed according to seismic criteria, using an automated design process.

In the first part of the study, 2023 columns were designed and analyzed under unidirectional shaking using a suite of twenty ground motions. The Caltrans Seismic Design Criteria (SDC) were used to design the columns in conjunction with the BDS. However, three lateral strength requirements were investigated, consisting of: (1) the SDC requirement that displacement capacity should exceed the demand and the lateral resistance of the column should be more than 10% of the axial load, (2) the BDS original recommendation of using a Z factor of 4, and (3) the ATC-32 recommendations which require varying Z from 1 to 4 for periods ranging between 0 and 1 second. The effects of the different design assumptions on the column properties, and average seismic demands and damage indices, were investigated. Due to the large number of analyses undertaken, a simplified stiffness degrading hysteretic model was used to model the column behavior. The properties of each section were obtained from a database populated with pre-computed moment-curvature analysis results of a large number of sections with varying diameter, reinforcement, axial load, and material properties. P-Δ effects were disregarded for these analyses.

The second part of the study considered 27 columns that were analyzed under bidirectional shaking using the same suite of twenty ground motions. A fiber model was used to model each of the columns, in order to capture the effect of bidirectional interaction. P-Δ effects were included in these analyses. The results of the parametric study were used to evaluate the adequacy of the elastic and inelastic displacement estimates, and the effect of bidirectional shaking on demands and damage measures.

8.2 CONCLUSIONS

The main conclusions drawn from the research summarized above are presented in the following text.

8.2.1 Experimental Investigation

The following is a compilation of observations regarding the shaking table tests, and conclusions resulting from the analysis of collected data:

1. The four columns exhibited stable ductile behavior under both the design level and maximum level excitations. Damage visible after these tests consisted of minor to moderate spalling of the unconfined cover at the column base and evidence of cracks that had formed during the excitations but had subsequently closed. In fact, it took several repetitions of the maximum

level earthquake to finally cause failure, as defined herein by the fracture of longitudinal or spiral reinforcement. Even after one or more bars had fractured, some of the specimens were still able to resist one or more repetitions of the design or maximum level earthquake.

2. The maximum displacements of each specimen were generally the same in each repetition of the same amplitude excitation except in the final run when one or more bars had fractured. In cases where the peak displacement did increase, that seemed to be more caused by accumulating residual displacements, than by the deterioration of the column's displacement and moment capacities.

3. The peak base moment tended to stay the same with repetitions of shaking, until bar fracture occurred, which caused a reduction in moment capacity. The base moments recorded during the design level runs were smaller than those recorded during maximum level runs. This is attributed to strain hardening due to larger displacements.

4. The rotational inertia of the supported mass introduced second mode effects into the response. In particular, the induced base shear was higher than what would be predicted by dividing the base moment by the height to the center of the mass block. The degree to which the second mode contributed to the response depended on the frequency content of the excitation and on the damage condition of the column. The second mode contributions decreased with increasing damage. For instance, it was noted that the lateral response of specimen A2 experienced particularly large contribution from the rotational inertia of the mass block because of its relatively undamaged state and the high frequency content of the excitation imposed in that direction.

5. The mass block also results in a shorter clear height of the column. For the test specimen, this further increased in some cases shear demands to 3 times what would have been expected using a cantilever assumption. This shear demand is consistent with plastic hinging at the top and bottom of the column considering the actual clear column height and double curvature. As the rotational inertia of the mass block is within the range that might occur in actual single column viaducts, the implications of this increased shear demand should be carefully considered in design.

6. Unlike the base moment, the base shear tended to decrease with repeated shaking. This was mainly due to a reduction in second mode contribution with the softening of the column.

7. Bidirectional shaking of the test specimens did not cause deterioration in their response. In fact, the bidirectionally loaded columns behaved similarly to the unidirectionally loaded columns in the initial design and maximum level runs, and were able to sustain more runs before bar fracture occurred. The second (lateral) component introduced in the bidirectional tests had smaller spectral demands than the first (longitudinal) component. As such, the peak displacement in the longitudinal direction and the maximum radial displacement were very close to the peak longitudinal displacement observed in the unidirectional test. It appears that bidirectional loading does not adversely impact performance. This observation is examined in greater detail in the analytical portions of this investigation.

8. Bidirectional interaction had a more prominent effect in the weaker (lateral) direction, as evidenced by a reduced maximum base moment in that direction. Conversely, the response in the longitudinal direction (stronger earthquake component) seemed little affected by the lateral component.

9. The progression of damage during repetition of the design and maximum level events was generally similar in all specimens with some minor differences. The various damage levels consisted of cover spalling, followed in later runs by longitudinal bar buckling, spiral fracturing and longitudinal bar fracture. The order of the last three varied slightly between the specimens. The unidirectional tests tended to have more buckling initially followed by spiral fracture, while in the bidirectional tests, the longitudinal reinforcement tended to fracture first, with less buckling overall. This was especially the case for Specimen B2 (Llolleo record, bidirectional loading), which showed high resistance to repeated loading, and finally experienced bar fracture that appeared to be more caused by low-cycle fatigue than from buckling and loss of confinement. The as-built spiral reinforcement spacing in Specimen B2 was slightly smaller than the other specimens, which might partially explain its increased toughness.

10. The integration of measured curvatures along the height of the column resulted in excellent agreement with externally measured displacements at various levels along the height of the column, indicating that for the test specimens shear deformation was not significant.

11. Deformations due to pullout of the longitudinal reinforcement from the foundation contributed up to 30% of the peak displacement for all specimens.

12. The strain history of the longitudinal reinforcement at the base of the column could be reasonably estimated from the average curvature measurements in the plastic hinge zone.

13. The peak strains recorded in the longitudinal reinforcement were about 30-40 milli-strain. The peak strains recorded in the spiral reinforcement were in the range of 4-6 milli-strain.

14. Comparing the energy dissipation due to the Olive View and Llolleo records, it is observed that in the Olive View record (near-fault) most of the energy dissipation occurs during one cycle which lasts about 1 second, while in the case of the Llolleo record, the energy is dissipated in a more uniform manner over a significantly longer duration. Mainly due to its longer duration, the Llolleo records imposes about 2.5 the energy dissipation demand as the Olive View record, despite the fact that they both caused similar displacement demands.

15. A low-cycle fatigue model was applied to the strain history of each longitudinal bar. The fatigue index for a section was taken as that of the bar with the maximum damage index. By tracking the damage index of each bar, it was possible to predict which bars would fracture first, and the order of fracture. The fatigue index, however, is very sensitive to the assumed plastic hinge length, and to the way curvatures and strains are estimated from the displacement history. In addition, the fatigue life models themselves involve significant uncertainty. Hence, care and judgement should be exercised when interpreting fatigue index results

16. Examination of the various types of damage indices yielded several observations. The Park and Ang index with a β coefficient of 0.02 gave reasonable damage level predictions for all four specimens at failure. However, it is apparent that it fails to provide prediction of when failure actually occurs, since it experiences relatively little change over several repetitions of the record before and after the actual failure. The low-cycle fatigue index at failure was about 0.30 to 0.6, except Specimen B2, which had a fatigue index of about 0.8, indicating that fatigue was a likely important contributor to failure. This confirms the previous observations regarding Specimen B2.

17. Examining the period and damping at the end of each run, it was found that the column period gradually elongated from about 0.50 seconds in its undamaged state to about 1.3 seconds on average. The damping ratio followed a less obvious trend, but in general increased with repeated loading and generally increased from about 2.5 to 6% at the end of the tests. The effective stiffness EI_e in the undamaged state was around half the gross stiffness EI_g, it decreased to about $0.3EI_g$ under low level shaking, and reached as low as $0.1EI_g$ after the design and maximum level.

8.2.2 Analytical Modeling of Reinforced Concrete Columns

Experimental results were compared to various elastic and inelastic elements for reinforced concrete columns. These focused on the modeling employed with each element, and the accuracy of the response predictions made by each type of element. Some of the conclusions related to modeling using plastic hinge and fiber models are:

1. The plastic hinge method results in a good estimate of the plastic hinge length (13.3 in. or 338mm), but the ultimate displacement capacity estimate of 6.17 in. (157mm) is lower than observed. Some of the test specimens saw maximum displacements of up to 7.5 in. (191mm) without significant damage.

2. When using fiber models, the number of integration points used along the length of the element may be critical, if the accuracy of the curvatures and strains is important. In general, the number of integration points should be selected such that the weight of the integration point at the base is close to the ratio L_p/L. The fiber element with four integration points, for example, tended to overestimate the curvatures in the plastic hinge region at a given displacement, while the same fiber element with three integration points gave much better results. Typically, it is difficult for any one choice of integration scheme to yield the correct integration point weight at the base of the column, but this can be overcome by subdividing the column into two or more elements, which gives greater control over how the curvatures at each section are weighted. This may be critical when evaluating the local performance of the section, such as when trying to determine the failure point based on the maximum strain in the concrete, or when using strains in the reinforcement to compute a fatigue damage index. For the Gauss-Lobato integration method, the use of end elements with a length of $2L_p$ and two integration points each is recommended for modeling the plastic hinge regions of the member.

Based on the comparison of several finite element models, the following conclusions reached regarding the modeling of reinforced concrete columns are restated:

1. Elastic models are generally capable of estimating peak displacements, when their effective stiffness is properly selected. However, they are generally less reliable than nonlinear methods, and they are inappropriate for predicting response to repetitive loading since linear models do not track any form of damage or deterioration. When performing an elastic analysis, the stiffness used should be no greater than the effective stiffness EI_e. However, although using a

stiffness of EI_e may yield reasonable results for shaking around the yield level, even a smaller stiffness may need to be specified under higher levels of shaking, because of period elongation caused by inelastic behavior.

2. Simple bilinear hysteretic models for the member of plastic hinge region should be avoided when possible, because of their inability to model the stiffness degrading behavior of reinforced concrete members.

3. Stiffness degrading hysteretic models offer significant advantages over bilinear models. They may be used in nonlinear analysis when the computational expense is important or when only information on global displacement is required. However, their partial inability to predict residual displacements and to account for axial and bidirectional interaction must be recognized.

4. Fiber models are preferred to concentrated plastic hinge models, because of the inherent ability to account for bidirectional and axial load interaction and because of their numerical stability. They provide when properly implemented superior information on local demands, as noted above. However, refinements of fiber models alone may not yield significant improvements in global response quantities, such as peak and residual displacements.

5. Using concentrated hinges at the base of the column to model the slip contribution may introduce convergence problems, especially if the properties of the spring are not well tuned to the section properties. It is hence recommended that the bond-slip formulation be included in the section determination of the plastic region in order to ensure compatibility. When such a model is not available, the added flexibility due to bond slip could be compensated for by adding a linear spring, or by using a larger plastic hinge length.

6. For repetitive loading, continuous analysis of the structure is preferred to running each excitations independently. This preserves historical response information. However, a significant gain in accuracy is only expected for models that are accurate and capable of predicting all the aspects of the response in the first place.

8.2.3 Sensitivity of Test Specimen to Loading Conditions

A sensitivity study investigated the effects of additional variables such as varying the intensity of the ground motion, the effects of vertical ground motions, and the effects of vertical load eccentricity. The conclusions of the study are summarized below:

317

1. For the two ground motions considered, bidirectional interaction effects are more pronounced in the direction subjected to the weaker component of the earthquake. In the case of two components with one dominant component, the peak bidirectional displacement is almost equal to the peak unidirectional displacement in the dominant direction.

2. The effect of the vertical acceleration on the horizontal response is minimal over a wide range of ground motion intensity.

3. Unlike the linear-elastic analysis displacement results which vary linearly with the ground motion intensity, the dependence of the nonlinear displacement response on the intensity is irregular. The required effective section stiffness that would result in linear displacements similar to nonlinear displacements is hence different at different intensities.

4. For the column considered, vertical load eccentricities of $0.38D$ to $0.5D$ caused a large amplification of the total displacement demand and/or collapse under an earthquake intensity corresponding to the design level of the concentrically loaded column. This corresponds to a ratio of the eccentricity moment to the moment capacity of the column of about 0.3.

8.2.4 Parametric Performance Evaluation of Reinforced Concrete Columns

The first part of the parametric study investigated the effect of design methodology on seismic demands, and the general demands on columns subjected to unidirectional shaking. The main conclusions of this study are:

1. The performance of columns designed with a Z factor that approaches unity as the period tends to zero (ATC-32) as reflected by the Park and Ang damage index is better than that obtained with columns designed using the other two methods considered (BDS and SDC). The performance of the SDC columns is similar to the BDS columns at low axial loads, but becomes worse for shorter columns with higher axial loads ($P_r > 0.10$). This appears to be especially the case for columns with periods shorter than 1 second.

2. SDC designed columns are more susceptible to fatigue failure than those designed using the other two methods. The worst case is for columns with small diameter and aspect ratio and with an axial load ratio around 0.20. This is attributed to the lower reinforcement ratios provided in short period SDC columns. The lower reinforcement ratio increases the maximum tensile strain demand on the reinforcement. This is coupled with large displacement demands

due to lower strength, and with a larger number of cycles because of the short period. As noted by many other researchers, displacements experienced by yielding systems with short periods are greater than those predicted by elastic analysis and are sensitive to strength.

3. In summary, it appears that the SDC design methodology produces ductile columns that have a large factor of safety against shear failure, but result in larger than expected displacements in the short period range. Even though a displacement amplification factor was considered for short period columns, they were still weaker than necessary to produce performance consistent with long period columns. Because of the lower reinforcement ratio, SDC designed columns may also be more susceptible to fatigue failure. Hence, vulnerability to fatigue failure should be investigated especially for short period columns. However, the SDC design method results in larger amounts of the reinforcement in the long period range which reduces P-Δ demands. The ATC-32 designed columns exhibit a better behavior, but columns designed according to this method may end up with a significant amount of longitudinal and spiral reinforcement.

The second part of the parametric investigation examined the effect of bidirectional shaking on seismic demands using a fiber element to model the moment interaction along the principal axes of the column's cross-section, and compared elastic and inelastic estimates of the nonlinear displacements. The columns were designed according to the SDC approach. The following conclusions are based on statistical results (generally mean or median) for a suite of 20 ground motions:

1. On average, the peak nonlinear displacement can be estimated by the elastic spectral analysis for periods longer than one second. For smaller periods, the nonlinear displacements can be significantly larger, up to 1.6 times for unidirectionally loaded columns, and up to more than 2 times for bidirectionally loaded column. Using an inelastic estimate of displacements (by modification of the elastic response spectrum according to period and strength) reduced the above maximum ratios to about 1.3 and 1.75, respectively.

2. The mean ratio of bidirectional to unidirectional nonlinear displacements generally falls in the range 1.05-1.15 for long period columns (T > 1 sec.). For shorter periods, the ratio is generally between 1.05 and 1.3.

3. The mean ratio of nonlinear bidirectional displacement to bidirectional displacements esti-mated from two uncoupled unidirectional nonlinear analyses is generally around 1.0 for longer periods (T > 2 sec.), and varies between 0.95 and 1.2 for shorter periods.

4. The mean Park and Ang index decreases with period from a maximum of 2 at short periods, to less than 0.1 at longer periods. At short periods, the contribution of the energy term to the Park and Ang index is around 15-20% of the total ($\beta = 0.05$).

5. The mean energy index decreases with period from around 4.5 at short periods to less than 0.2 at longer periods.

6. The fatigue index shows significant scatter, and is very small for periods longer than 1 second. For shorter periods, the mean is as high as 1.2 with a high coefficient of variation. The fatigue index may double (on average) due to bidirectional loading.

7. The effect of bidirectional loading on displacements in the two directions is generally not the same. The direction with the smaller displacement under unidirectional loading generally experiences a larger amplification under bidirectional loading (between 1.0 and 1.4). The direction with the larger displacement only sees an amplification of 0.95 to 1.05.

8. The residual displacement is strongly dependent on the axial load ratio. Larger axial load ratios result in larger residual displacements, in large part because of P-Δ effects.

9. Residual displacements under bidirectional loading, can be several times larger than those predicted using unidirectional analysis.

8.3   FUTURE RESEARCH

There are only a limited number of bidirectional shaking table tests performed on bridge columns and bridge sub-assemblages. The current research attempted to answer many questions regarding the behavior of bridge columns. A number of issues are worth further investigation, including:

1. The effect of bidirectional shaking on columns with non-circular cross-sections, such as columns with interlocking spirals.

2. The effect of different types of ground motions on the bidirectional response. Of main interest are ground motions that have similar intensities in both directions. Instrumentation to enable the distinction of structural restoring forces from viscous effects would be especially desir-able.

3. The performance of systems consisting of more than one column. A limitation of the current study is the fact that the top of the column was free to rotate in both directions. While this may be partially justified in some cases, most bridge columns in California are fixed at the top along the longitudinal direction of the bridge, and may be fixed transversely in the case of bents with two or more columns. A test setup in which columns are free to deform in single curvature in one direction, but are forced to deform in double curvature in the other, might reveal an interesting behavior. Similarly, a simple bridge model having elements with different properties would be useful to assess the ability of anlytical models to track the redistribution of internal forces and the more complex system behavior that might result.

4. More experimental research is needed to characterize the behavior of biaxially loaded columns. The effects of biaxial loading on the displacement and energy dissipating capacities of the column, and on the type and progression of damage, including the size of the plastic hinge zone need to be investigated.

5. The low-cycle fatigue index is very useful, since it can be directly extended to bidirectional loading. However, fatigue life models need to be improved and better calibrated. The effect of the interaction of the spiral and longitudinal reinforcement, including the buckling of reinforcement prior to fracture need to be incorporated in fatigue indices.

From an analytical point of view, several aspects of modeling and analysis deserve further research:

1. Models for reinforced concrete members that account for bar slip are needed to model this critical aspect of the behavior.

2. The prediction of residual displacements is generally difficult, and results are very sensitive to the model parameters. The dependence of residual displacement on model properties, such as bar slip and the hysteretic material rules, and other factors such as damping, deserves further investigation.

3. Strain rate effects should be investigated to determine whether they should be included in the material models. If so, adequate hysteretic models need to be implemented.

References

[1] Abrahamson, N. A.; Silva, W. J. "Empirical response spectral attenuation relations for shallow crustal earthquakes." Seismological Research Letters, 68, 1, Jan.-Feb. 1997, pages 94-127.

[2] ACI Committee 318, "Building Code Requirements for Reinforced Concrete (ACI 318-95)," American Concrete Institute, Detroit, 1995.

[3] Aktan, A.E; Pecknold, D.A. and Sozen, M.A. "R/C Column Earthquake Response in Two Dimensions." Journal of the Structural Division, ASCE, 100, ST10, Oct. 1974, pages 1999-2015.

[4] Alsiwat, J. M., and Saatcioglu, M. "Reinforcement anchorage slip under monotonic loading." Journal of Structural Engineering, ASCE, Vol. 118, No. 9, Sept. 1992, pp. 2421-2438.

[5] Applied Technology Council. ATC-32: Improved Seismic Design Criteria for California Bridges: Provisional Recommendations. 1996

[6] Applied Technology Council. ATC-40: Seismic Evaluation and Retrofit of Concrete Buildings. 1996.

[7] Ammann, W., Nussabaumer H. 1995. Behavior of Concrete and Steel under Dynamic Actions, *Vibration Problems in Structures*, pp. 177-183.

[8] Aschheim, M.A, Moehle, J.P and Mahin, S.A. "Design and Evaluation of Reinforced Concrete Bridges for Seismic Resistance." Report No. UCB/EERC-97/04, Earthquake Engineering Research Center, University of California at Berkeley, March 1997.

[9] Brown, Jeff; Kunnath, Sashi K. "Low cycle fatigue behavior of longitudinal reinforcement in reinforced concrete bridge columns." Report No. MCEER-00-0007, Multidisciplinary Center for Earthquake Engineering Research, Buffalo, N.Y., 2000.

[10] Button, Martin R.; Cronin, Colman J.; Mayes, Ronald L. "Effect of vertical ground motions on the structural response of highway bridges." MCEER-99-0007, Multidisciplinary Center for Earthquake Engineering Research, Buffalo, N.Y., 1999, 166 pages.

[11] Chai, Y. H.; Priestley, M. J. N.; Seible, F. "Analytical model for steel-jacketed RC circular bridge columns." Journal of Structural Engineering, 120, 8, Aug. 1994, pages 2358-2376.

[12] Chai, Y. H.; Romstad, K. M.; Bird, S. M. "Energy-based linear damage model for high-intensity seismic loading." Journal of Structural Engineering, 121, 5, May 1995, pages 857-864.

[13] Chen, Wai-Fah; Duan, Lian. *Bridge engineering handbook*. CRC Press, Boca Raton, Fla., 2000.

[14] Chopra, Anil K. *Dynamics of structures: Theory and applications to earthquake engineering*. Englewood Cliffs, N.J. : Prentice Hall, 1995.

[15] Chung, Y. S.; Meyer, C.; Shinozuka, M. "Seismic damage assessment of reinforced concrete members." NCEER-87-0022, National Center for Earthquake Engineering Research, Buffalo, N.Y., Oct. 1987.

[16] Clough, R. W.; Penzien, J. Dynamics of structures, 2nd ed. New York : McGraw-Hill, 1993.

[17] Cofer, W.F. "Documentation of Strengths and Weaknesses of Current Computer Analysis Methods for Seismic Performance of Reinforced Concrete Members." PEER-1999/07, Berkeley: Pacific Earthquake Engineering Research Center, University of California, Nov. 1999.

[18] Coffin, L. F. Jr. "A study on the effects of cyclic thermal stresses on a ductile metal." Transactions of the American Society of Mechanical Engineers, New York, N.Y., 76, 1954, pages 931-950.

[19] Comité Euro-International du Béton (CEB). "Concrete Structures Under Impact and Impulsive Loading." Bulletin d'Information No. 187, 1988.

[20] Cosenza, E.; Manfredi, G.; Ramasco, R. "The use of damage functionals in earthquake engineering: a comparison between different methods." Earthquake Engineering & Structural Dynamics, 22, 10, Oct. 1993, pages 855-868.

[21] Cuadra, C.; Inoue, N.; Ogawa, J. "Pseudodynamic test to study the behavior of reinforced concrete columns subjected to two dimensional input motions." Proceedings of the Eleventh European Conference on Earthquake Engineering, A. A. Balkema, Rotterdam, 1998.

[22] Dodd, L. L. and Cooke, N. "The Dynamic Behaviour of Reinforced-Concrete Bridge Piers Subjected to New Zealand Seismicity." Research Report 92-04, Department of Civil Engineering, University of Canterbury, Christchurch, New Zealand, June 1992.

[23] Dowling, Norman E. *Mechanical behavior of materials: Engineering methods for deformation, fracture, and fatigue*. Prentice Hall, Upper Saddle River, NJ, 1999, 830 pages, 2nd ed.

[24] Dutta, Anindya; Mander, John B.; Kokorina, Tatiana. "Retrofit for control and repairability of damage." Earthquake Spectra, 15, 4, Nov. 1999, pages 657-679.

[25] Dutta, Anindya; Mander, John B. "Capacity design and fatigue analysis of confined concrete columns." MCEER-98-0007, Multidisciplinary Center for Earthquake Engineering Research, Buffalo, N.Y., 1998, 243, 19 pages.

[26] Eibl, J.; Schmidt-Hurtienne, B. "Strain-rate-sensitive constitutive law for concrete." Journal of Engineering Mechanics, 125, 12, Dec. 1999, pages 1411-1420.

[27] Eligehausen, R.; Popov, E. P.; Bertero, V. V. "Local bond stress-slip relationships of deformed bars under generalized excitations." UCB/EERC-83/23, Berkeley: Earthquake Engineering Research Center, University of California, Oct. 1983, 169 pages.

[28] Falk, Wayne M. "An Elastic Explanation for the Observed Buckling Mode of Reinforcing Bars in Concrete." UCB/SEMM-1999/08, Department of Civil and Environmental Engineering, University of California, Berkeley, California, Aug. 1999, 55 pages.

[29] Filippou, F. C. "A simple model for reinforcing bar anchorages under cyclic excitations." Journal of Structural Engineering, 112, 7, July 1986, pages 1639-1659.

[30] Filippou, Filip C.; D'Ambrisi, Angelo; Issa, Ahmad. "Effects of reinforcement slip on hysteretic behavior of reinforced concrete frame members." ACI Structural Journal, 96, 3, May-June 1999.

[31] Gutierrez, E.; et al. "Real time and pseudodynamic tests on a SDOF reinforced concrete structure." Proceedings of the Tenth World Conference on Earthquake Engineering, A. A. Balkema, Rotterdam, Vol. 6, 1992, pages 3353-3358.

[32] Hachem, Mahmoud M. "Bispec: Interactive Computer Program for Computation of Bidirectional Nonlinear Spectra." NISEE Software Library, 1999.
<http://nisee.berkeley.edu/software>

[33] Hashimoto, P. S.; et al. "Review of structure damping values for elastic seismic analysis of nuclear power plants." NUREG/CR-6011, Div. of Engineering, Office of Nuclear Regulatory Research, U.S. Nuclear Regulatory Commission, Washington, D.C., Mar. 1993.

[34] Henry, L.; "Study of buckling of longitudinal bars in reinforced concrete bridge columns." Master's Thesis, University of California, Berkeley 1998.

[35] Inoue, Norio; et al. "Shaking table tests of reinforced concrete columns subjected to simulated input motions with different time durations." Proceedings of the 12th World Conference on Earthquake Engineering, New Zealand, 2000, Paper No. 1734.

[36] Jeong, G. D.; Iwan, W. D. "The effect of earthquake duration on the damage of structures." Earthquake Engineering & Structural Dynamics, 16, 8, Nov. 1988, pages 1201-121.

[37] Johannesson, P., "Matlab Toolbox: Rainflow Cycles for Switching Processes." Department of Mathematical Statistics, Lund Institue of Technology, Lund University, Lund 1997.

[38] Kappos A.J; Xenos A. "A reassessment of ductility and energy-based seismic damage indices of reinforced concrete structures." Proceedings Eurodyn'96 (3rd European Conference on Structural Dynamics), Florence, Italy, June 1996, Vol. 2. Rotterdam, Balkema. 1996: 965-970.

[39] Kitajima, K.; et al. "Response characteristics of reinforced concrete columns under bi-directional earthquake motions." Proceedings of the Tenth World Conference on Earthquake Engineering, A. A. Balkema, Rotterdam, Vol. 5, 1992, pages 3019-3024.

[40] Kitajima, K.; Adachi, H.; Nakanishi, M. "Response characteristics of reinforced concrete structures under bi-directional earthquake motions." Eleventh World Conference on Earthquake Engineering [Proceedings], Pergamon, Elsevier Science Ltd., [Oxford, England], 1996, Disc 1, Paper No. 566.

[41] Koh, S. K., Stephens, R. I. "Mean stress effects on low cycle fatigue for a high strength steel." Fatigue Fractures of Engineering Materials and Structures, 14(4), pages 413-428.

[42] Kogoma, I.; Hayashida, T.; Minowa, C. "Experimental studies on the collapse of RC columns during strong earthquake motions." Proceedings of the Tenth World Conference on Earthquake Engineering, A. A. Balkema, Rotterdam, Vol. 5, 1992, pages 3013-3017.

[43] Kowalsky, M. J.; Priestley, M. J. N.; Seible, F, "Dynamic shake table testing of lightweight concrete bridges." Proceedings of the National Seismic Conference on Bridges and Highways: "Progress in Research and Practice", Sacramento, California, July, 1997.

[44] Krawinkler, Helmut; et al. "Seismic demands for performance-based design." PEER-1999/ 10, U.S.-Japan Workshop on Performance-Based Earthquake Engineering Methodology for Reinforced Concrete Building Structures, September 1999, Maui, Hawaii, Berkeley: Pacific Earthquake Engineering Research Center, University of California, Dec. 1999.

[45] Krawinkler, H.; Moncarz, P. D. "Similitude requirements for dynamic models." Dynamic Modeling of Concrete Structures SP 73-1, American Concrete Inst., Detroit, Michigan, 1982, pages 1-22.

[46] Krawinkler, H.; Zohrei, M. "Cummulative damage in steel structures subjected to earthquake ground motions." Computers & Structures, 16, 1-4, 1983, pages 531-541.

[47] Kunnath, S. K. et al. "Cumulative Seismic Damage of Reinforced Concrete Bridge Piers." Report No. 6075, National Institute of Standards and Technology (NIST), October 1997.

[48] Kunnath, S. K.; Reinhorn, A. M.; Lobo, R. F. "IDARC version 3.0: a program for the inelastic damage analysis of reinforced concrete structures." NCEER-92-0022, National Center for Earthquake Engineering Research, Buffalo, N.Y., Aug. 1992.

[49] Kunnath, S. K.; Reinhorn, A. M.; Park, Y. J. "Analytical modeling of inelastic seismic response of R/C structures." Journal of Structural Engineering, 116, 4, Apr. 1990, pages 996-1017.

[50] Lehman, D.E.; Moehle, J.P. "Seismic Performance of Well-Confined Concrete Bridge Columns." PEER-1998/01, Berkeley: Pacific Earthquake Engineering Research Center, University of California, 1998.

[51] Lehman, D. E.; Calderone, A. J.; Moehle, J. P. "Behavior and design of slender columns subjected to lateral loading." Proceedings of the Fifth Caltrans Seismic Research Workshop, CALTRANS, Sacramento, 1998.

[52] Lehman, D.; Moehle, J. P.; Mahin, S. A. "Design of an experimental study on the influence of aspect ratio and longitudinal reinforcement ratio on column response." Proceedings of the Fourth Caltrans Seismic Research Workshop, CALTRANS, Sacramento, 1996.

[53] Macrae, G.A.; Hodges C.; Priestley, M.J.N. and Frieder, S. "Shake Table Tests of As-Built and Retrofitted Bridge Bents." Report No. SSRP-94/18, Structural Systems Research, Univ. of California, San Diego, La Jolla, Nov. 1994, 246 pages.

[54] Mahin, S.A., "State-of-the-art report: inelastic behavior and modeling of reinforced concrete columns under multidirectional seismic excitations." Proceedings of the Ninth World Conference on Earthquake Engineering, Tokyo, Vol. VIII, 1989.

[55] Mahin, S. A.; Bertero, V. V. "An evaluation of inelastic seismic design spectra." Journal of the Structural Division, ASCE, 107, ST9, Sept. 1981.

[56] Mahin, S. A.; Bertero, V. V. "Rate of loading effects on uncracked and repaired reinforced concrete members." Report No. UCB/EERC-72/09, Earthquake Engineering Research Center, University of California at Berkeley, Dec. 1972, 148 pages.

[57] Mander, J. B.; Cheng, C.-T. "Replaceable hinge detailing for bridge columns." SP-187-9, Seismic Response of Concrete Bridges, ACI International, Farmington Hills, Michigan, 1999, pages 185-204.

[58] Mander J.B., Panthaki, F.D., and Kasalanti, A. "Low Cycle Fatigue Behavior of Reinforcing Steel." Journal of Materials in Civil Engineering, ASCE, Vol. 6, No.4, 1985.

[59] Mander, J.B.; Priestley, M. J. N.; Park, R. "Seismic design of bridge piers." Research Report 84-02, Department of Civil Engineering, University of Canterbury, Christchurch, New Zealand, 1983.

[60] Mander, J.B, Priestly M.J.N, and Park. "Theoretical Stress-Strain Model for Confined Concrete." Journal of Structural Engineering, Vol. 114, No. 8, ASCE, Aug 1988.

[61] Manson, S. S. "Behavior of materials under conditions of thermal stress." Heat Transfer Symposium, University of Michigan Engineering Research Institue, Ann Arbor, Michigan, 1953, pages 9-75.

[62] Miner, M. A. "Cumulative damage in fatigue." Journal of Applied Mechanics, Vol. 12, 1945, pages A-159

[63] McKenna, Frank. "Object-Oriented Finite Element Programming: Frameworks for Analysis, Algorithms and Parallel Computing." Ph.D Thesis, University of California, Berkeley 1997.

[64] Minowa, C.; Obgawa, N. "Shaking Table Collapse Tests of of RC Columns." NIST SP 843, Wind and Seismic Effects, Proceedings of the 24th Joint Meeting of the U.S.-Japan Cooperative Program in Natural Resources Panel on Wind and Seismic Effects, National Inst. of Standards and Technology, Gaithersburg, Maryland, Sept. 1992.

[65] Minowams, Chikahiro; et al, "Shaking table failure tests of actual size RC structures." NIST SP 871, Wind and Seismic Effects, Proceedings of the 26th Joint Meeting of the U.S.-Japan Cooperative Program in Natural Resources Panel on Wind and Seismic Effects, National Inst. of Standards and Technology, Gaithersburg, Maryland, Sept. 1994.

[66] Miranda, E. and Bertero, V.V. "Evaluation of Strength Reduction Factors for Earthquake-Resistant Design." Earthquake Spectra, Vol. 10, No. 2, 1994.

[67] Miranda, E. "Estimation of inelastic deformation demands of SDOF systems." Journal of Structural Engineering, 127, 9, 2001.

[68] Moehle, J.P. "Displacement Based Design of RC Structures." Proceedings, Tenth WCEE, Rotterdam, Balkema, 1992.

[69] Monti, G.; Filippou, F. C.; Spacone, E. "Finite element for anchored bars under cyclic load reversals." Journal of Structural Engineering, 123, 5, 1997.

[70] Monti, Giorgio; Spacone, Enrico. "Reinforced concrete fiber beam element with bond-slip." Journal of Structural Engineering, 126, 6, 2000.

[71] Murayama, Y.; et al. "Stress-slip model of the longitudinal reinforcing bars in a reinforced concrete column joint." Eleventh World Conference on Earthquake Engineering, Pergamon, Elsevier Science Ltd., Oxford, England, 1996

[72] Nakayama, T.; et al. "Shaking table tests of reinforced concrete structures under bidirectional earthquake motions." Eleventh World Conference on Earthquake Engineering, Oxford, England, 1996, Paper No. 1001.

[73] Nassar, A. A.; Krawinkler, H. "Seismic demands for SDOF and MDOF systems." Report No. 95, John A. Blume Earthquake Engineering Center, Stanford, California, June 1991.

[74] Nigam, N. C. "Inelastic interactions in the dynamic response of structures." California Institute of Technology, Earthquake Engineering Research Lab., Pasadena, 1967, 195 pages.

[75] Ogawa, J.; et al. "Damage behavior of reinforced concrete columns under uniaxial and biaxial lateral loading." Journal of Structural and Construction Engineering, 419, 1991, pages 87-98.

[76] Ogawa, J.; et al. "Earthquake damage evaluation of reinforced concrete columns." Proceedings of the Tenth World Conference on Earthquake Engineering, A. A. Balkema, Rotterdam, Vol. 5, 1992, pages 3053-3058.

[77] Ogawa, J.; et al. "Flexural behavior of precast and reinforced concrete columns under biaxial loadings." Proceedings, 10th European Conference on Earthquake Engineering, A. A. Balkema, Rotterdam, 1995, pages 2383-2388, Vol. 3.

[78] Otani, S.; Cheung, V. W.-T.; Lai, S. S. "Behaviour and analytical models of reinforced concrete columns under biaxial earthquake loads." Third Canadian Conference on Earthquake Engineering, Canadian National Committee for Earthquake Engineering et al., Montreal, 1979, pages 1141-1167, Vol. 2.

[79] Park, Y.-J.; Ang, A.H.-S. "Mechanistic seismic damage model for reinforced concrete." Journal of Structural Engineering, 111, 4, 1985.

[80] Park, Y. J.; Ang, A. H.-S.; Wen, Y. K. "Damage-limiting aseismic design of buildings." Earthquake Spectra, 3, 1, Feb. 1987, pages 1-26.

[81] Park, Y.J.; Ang, Alfred H-S.; Wen, Y.K. "Seismic damage analysis and damage-limiting design of R.C. buildings." Structural research series no. 516, Dept. of Civil Engineering, University of Illinois at Urbana-Champaign, Urbana, Ill., 1984, 163 pages.

[82] Park, Y. J.; Reinhorn, A. M.; Kunnath, S. K. "IDARC: inelastic damage analysis of reinforced concrete frame-shear-wall structures." NCEER-87-0008, National Center for Earthquake Engineering Research, Buffalo, N.Y., July 20, 1987.

[83] Pecknold, D. A. "Inelastic structural response to 2D ground motion." Journal of the Engineering Mechanics Division, ASCE, 100, EM5, Oct. 1974, pages 949-963.

[84] Ranzo, Giulio; Petrangeli, Marco; Pinto, Paolo E. "Vertical oscillations due to axial-bending coupling during seismic response of RC bridge piers." Earthquake Engineering & Structural Dynamics, 28, 12, Dec. 1999, pages 1685-1704.

[85] Priestley, N., Seible, F., and Calvi, G. 1996. *Seismic Design and Retrofit of Bridges*. New York: John Wiley and Sons.

[86] Saadeghvaziri, M. A.; Foutch, D. A. "Dynamic behaviour of R/C highway bridges under the combined effect of vertical and horizontal earthquake motions." Earthquake Engineering & Structural Dynamics, 20, 6, June 1991, pages 535-549.

[87] Saatcioglu, M. "Modeling Hysteretic Force-Deformation Relationships for Reinforced Concrete Elements." ACI Special Publication SP-127,1991.

[88] Saatcioglu, M.; Ozcebe, G. "of reinforced concrete columns to simulated seismic loading." ACI Structural Journal, 86, 1, Jan.-Feb. 1989, pages 3-12.

[89] Sadigh, K.; et al. "Attenuation relationships for shallow crustal earthquakes based on California strong motion data." Seismological Research Letters, 68, 1, Jan.-Feb. 1997, pages 180-189.

[90] Sanders, David H.; et al, "Concrete Columns Tested Under Shaking Table Loading." Proceedings of the 5th Caltrans Seismic Research Workshop: California Dept. of Transportation, Sacramento, 1998.

[91] Scott, B. D.; Park, R.; Priestley, M. J. N. "Stress-strain behavior of concrete confined by overlapping hoops at low and high strain rates." Journal of the American Concrete Institute, 79, 1, Jan.-Feb. 1982.

[92] Shimazaki, Kazushi; Wada, Akira. "Dynamic analysis of a reinforced concrete shear wall with strain rate effect." ACI Structural Journal, 95, 5, Sept.-Oct. 1998, pages 488-497.

[93] Shing, P.-S. B.; Mahin, S. A. "Rate-of-loading effects on pseudodynamic tests." Journal of Structural Engineering, 114, 11, Nov. 1988, pages 2403-2420.

[94] Socie, Darrell. "Rainflow Counting Method: A historical Perspective." The rainflow method in fatigue : the Tatsuo Endo memorial volume. Papers presented at the International Symposium on Fatigue Damage Measurement and Evaluation Under Complex Loadings in memory of Prof. Tatsuo Endo, Fukuoka, Japan, July 1991.

[95] Somerville, P. et al, "Development of Ground Motion Time Histories for Phase 2, Background Document." SAC/BD-97/04, FEMA/SAC Steel Project, Richmond, CA, 1997.

[96] Spacone, E.; Filippou, F.C.; Taucer, F. F. "Fibre beam-column model for non-linear analysis of R/C frames: part I. formulation." Earthquake Engineering & Structural Dynamics, 25, 7, July 1996.

[97] State of California Department of Transportation (1991) Bridge Design Specifications Manual, 1991.

[98] State of California Department of Transportation (1999) Seismic Design Criteria, version 1.1, July 1999.

[99] State of California Department of Transportation (1999) Seismic Design Methodology, Memo to Designers 20-1, January 1999.

[100] Stone, William C.; Taylor, Andrew W. "System identification of spirally reinforced circular bridge columns subjected to cyclic lateral loading." NIST SP 820, Wind and Seismic Effects, Proceedings of the 23rd Joint Meeting of the U.S.-Japan Cooperative Program in Natural Resources Panel on Wind and Seismic Effects, National Inst. of Standards and Technology, Gaithersburg, Maryland, Sept. 1991, pages 269-293.

[101] Stone, W. C.; Taylor, A. W. "A predictive model for hysteretic failure parameters." Proceedings of the Tenth World Conference on Earthquake Engineering, A. A. Balkema, Rotterdam, Vol. 5, 1992, pages 2575-2580.

[102] Tanaka, H. "Effect of lateral confining reinforcement on the ductile behaviour of reinforced concrete columns." 90-2, Dept. of Civil Engineering, Univ. of Canterbury, Christchurch, New Zealand, June 1990, 458 pages, Ph.D. thesis.

[103] Taucer, F.; Spacone, E.; Filippou, F. C. "A fiber beam-column element for seismic response analysis of reinforced concrete structures." UCB/EERC-91/17, Berkeley: Earthquake Engineering Research Center, University of California, Dec. 1991, 142 pages.

[104] Taylor, A. W.; Stone, W. C. "Evaluating the seismic performance of lightly-reinforced circular concrete bridge columns." Proceedings, 1993 National Earthquake Conference, Central United States Earthquake Consortium, Memphis, 1993, pages 543-552, Vol. II.

[105] The Mathworks. *MATLAB User's and reference manual*. Version 5.3, Natick, MA, 1999.

[106] Wakabayashi, M.; et al. "Effect of strain rate on stress-strain relationships of concrete and steel." Proceedings of the Fifth Japan Earthquake Engineering Symposium, Architectural Inst. of Japan et al., Tokyo, Nov. 1978, pages 1313-1320, Paper No. 165.

[107] Williams, M. S.; Sexsmith, R. G. "Seismic damage indices for concrete structures: a state-of-the-art review." Earthquake Spectra, 11, 2, May 1995.

[108] Wu, S.; Liu, Z, "A study on the sudden-crack-change of R/C column under dynamic vibration-strength and deformation." Proceedings of the Fourth U.S. National Conference on Earthquake Engineering, Earthquake Engineering Research Inst., El Cerrito, California, 1990.

[109] Yashinsky, M. "New developments in CALTRANS seismic analysis and design procedures for bridges." SP-187-6, Seismic Response of Concrete Bridges, ACI International, Farmington Hills, Michigan, 1999, pages 89-130.

[110] Yalcin, C.; Saatcioglu, M. "Inelastic analysis of reinforced concrete columns." Computers & Structures, 77, 5, July 21, 2000.

[111] Yen, W. P.; et al, "Comparison of U.S. and Japanese highway bridge column seismic design and shake-table test of scaled models." Proceedings of the National Seismic Conference on Bridges and Highways: "Progress in Research and Practice", Sacramento, California, July, 1997.

Appendix A Data Channels and Test Runs

In each of the four shaking table tests, the response of specimen was monitored through 144 channels of instrumentation. Those channels recorded the displacements, accelerations and strains at various locations in the specimen. Table A-1 outlines the different channels, and their locations on the specimen. Table A-2 summarizes all test runs performed on each specimen.

Table A-1. Instrumentation for specimens A1, A2, B1 and B2.

Channel No[a]	Transducer[b]	Variable Name[c]	Orien-tation[d]	Transducer Location[e]	Coordinates[f] (in.)		
					x	y	z
-	-	date	-	-	-	-	-
-	-	time	-	-	-	-	-
1	LVDT	table.h1od	+x	Horizontal actuators below simulator platform	?	48.0	-41.0
2	LVDT	table.h2od	+y		-53.0	?	-41.0
3	LVDT	table.h3od	+x		?	-48.0	-41.0
4	LVDT	table.h4od	+y		53.0	?	-41.0
5	LVDT	table.v1od	+z	Vertical actuators below simulator platform	102.0	102.0	?
6	LVDT	table.v2od	+z		-102.0	102.0	?
7	LVDT	table.v3od	+z		-102.0	-102.0	?
8	LVDT	table.v4od	+z		102.0	-102.0	?
9	ACC	table.h12a	-x	Simulator platform	-8.0	96.0	-29.5
10	ACC	table.h34a	-x		-8.0	-96.0	-29.5
11	ACC	table.h41a	-y		96.0	-8.0	-29.5
12	ACC	table.h23a	-y		96.0	-8.0	-29.5
13	ACC	table.v1a	+z	Simulator platform	94.4	94.4	-28.5
14	ACC	table.v2a	+z		-94.4	94.4	-28.5
15	ACC	table.v3a	+z		-94.4	-94.4	-28.5
16	ACC	table.v4a	+z		94.4	-94.4	-28.5
17	SG	gages.NL1	z	Longitudinal reinforce-ment strain gages on the North side	0	-7.32	-10
18	SG	gages.NL2	z		0	-7.32	-5
19	SG	gages.NL3	z		0	-7.32	0
20	SG	gages.NL4	z		0	-7.32	6
21	SG	gages.NL5	z		0	-7.32	12
22	SG	gages.NL6	z		0	-7.32	24
23	SG	gages.NL7	z		0	-7.32	48
24	SG	gages.WL1	z	Longitudinal reinforce-ment strain gages on the West side	7.32	0	-10
25	SG	gages.WL2	z		7.32	0	-5
26	SG	gages.WL3	z		7.32	0	0
27	SG	gages.WL4	z		7.32	0	6
28	SG	gages.WL5	z		7.32	0	12
29	SG	gages.WL6	z		7.32	0	24
30	SG	gages.WL7	z		7.32	0	48

Table A-1. Instrumentation for specimens A1, A2, B1 and B2.

Channel No[a]	Transducer[b]	Variable Name[c]	Orientation[d]	Transducer Location[e]	Coordinates[f] (in.)		
					x	y	z
31	SG	gages.SL1	z	Longitudinal reinforcement strain gages on the South side	0	7.32	-10
32	SG	gages.SL2	z		0	7.32	-5
33	SG	gages.SL3	z		0	7.32	0
34	SG	gages.SL4	z		0	7.32	6
35	SG	gages.SL5	z		0	7.32	12
36	SG	gages.SL6	z		0	7.32	24
37	SG	gages.SL7	z		0	7.32	48
38	SG	gages.EL1	z	Longitudinal reinforcement strain gages on the East side	-7.32	0	-10
39	SG	gages.EL2	z		-7.32	0	-5
40	SG	gages.EL3	z		-7.32	0	0
41	SG	gages.EL4	z		-7.32	0	6
42	SG	gages.EL5	z		-7.32	0	12
43	SG	gages.EL6	z		-7.32	0	24
44	SG	gages.EL7	z		-7.32	0	48
45	SG	gages.NS1	x	Spiral reinforcement strain gages on the North side	0	-7.32	2.5
46	SG	gages.NS2	x		0	-7.32	5.0
47	SG	gages.NS3	x		0	-7.32	7.5
48	SG	gages.NS4	x		0	-7.32	10.0
49	SG	gages.NS5	x		0	-7.32	12.5
50	SG	gages.WS1	y	Spiral reinforcement strain gages on the West side	7.32	0	2.5
51	SG	gages.WS2	y		7.32	0	5.0
52	SG	gages.WS3	y		7.32	0	7.5
53	SG	gages.WS4	y		7.32	0	10.0
54	SG	gages.WS5	y		7.32	0	12.5
55	SG	gages.SS1	x	Spiral reinforcement strain gages on the South side	0	7.32	2.5
56	SG	gages.SS2	x		0	7.32	5.0
57	SG	gages.SS3	x		0	7.32	7.5
58	SG	gages.SS4	x		0	7.32	10.0
59	SG	gages.SS5	x		0	7.32	12.5

Table A-1. Instrumentation for specimens A1, A2, B1 and B2.

Channel No[a]	Transducer[b]	Variable Name[c]	Orien- tation[d]	Transducer Location[e]	Coordinates[f] (in.)		
					x	y	z
60	SG	gages.ES1	y	Spiral reinforcement strain gages on the East side	-7.32	0	2.5
61	SG	gages.ES2	y		-7.32	0	5.0
62	SG	gages.ES3	y		-7.32	0	7.5
63	SG	gages.ES4	y		-7.32	0	10.0
64	SG	gages.ES5	y		-7.32	0	12.5
65	DCDT	DCDT.N1	z	DCDT instruments on the North face of the column	-0.75	-11.38	0.75→4[g]
66	DCDT	DCDT.N2	z		0	-11.38	0→4
67	DCDT	DCDT.N3	z		0	-11.38	4→8
68	DCDT	DCDT.N4	z		0	-11.38	8→12
69	DCDT	DCDT.N5	z		0	-11.38	12→20
70	DCDT	DCDT.N6	z		0	-11.38	20→28
71	DCDT	DCDT.N7	z		0	-11.38	28→44
72	DCDT	DCDT.N8	z		0	-11.38	44→64
73	DCDT	DCDT.W1	z	DCDT instruments on the West face of the column	11.38	-0.75	1.5→4.75
74	DCDT	DCDT.W2	z		11.38	0	0→4.75
75	DCDT	DCDT.W3	z		11.38	0	4.75→8.75
76	DCDT	DCDT.W4	z		11.38	0	8.75→12.75
77	DCDT	DCDT.W5	z		11.38	0	12.75→20.75
78	DCDT	DCDT.W6	z		11.38	0	20.75→28.75
79	DCDT	DCDT.W8	z		11.38	0	28.75→44.75
80	DCDT	DCDT.W7	z		11.38	0	44.75→64
81	DCDT	DCDT.S1	z	DCDT instruments on the South face of the column	-0.75	11.38	0.75→4
82	DCDT	DCDT.S2	z		0	11.38	0→4
83	DCDT	DCDT.S3	z		0	11.38	4→8
84	DCDT	DCDT.S4	z		0	11.38	8→12
85	DCDT	DCDT.S5	z		0	11.38	12→20
86	DCDT	DCDT.S6	z		0	11.38	20→28
87	DCDT	DCDT.S8	z		0	11.38	28→44
88	DCDT	DCDT.S7	z		0	11.38	44→64

Table A-1. Instrumentation for specimens A1, A2, B1 and B2.

Channel No[a]	Transducer[b]	Variable Name[c]	Orien-tation[d]	Transducer Location[e]	Coordinates[f] (in.)		
					x	y	z
89	DCDT	DCDT.E1	z	DCDT instruments on the East face of the column	-11.38	-0.75	1.5→4.75
90	DCDT	DCDT.E2	z		-11.38	0	0→4.75
91	DCDT	DCDT.E3	z		-11.38	0	4.75→8.75
92	DCDT	DCDT.E4	z		-11.38	0	8.75→12.75
93	DCDT	DCDT.E5	z		-11.38	0	12.75→20.75
94	DCDT	DCDT.E6	z		-11.38	0	20.75→28.75
95	DCDT	DCDT.E8	z		-11.38	0	28.75→44.75
96	DCDT	DCDT.E7	z		-11.38	0	44.75→64
97	ACC	acc.BWx	+x	Bottom West Side	49.0	0	-8.0
98	ACC	acc.BWy	+y		49.0	0	-8.0
99	ACC	acc.BYz	+z		49.0	0	-8.0
100	ACC	acc.BNx	+x	Bottom North Side	0	-49.0	-8.0
101	ACC	acc.BNy	+y		0	-49.0	-8.0
102	ACC	acc.BNz	+z		0	-49.0	-8.0
103	ACC	acc.TWx	+x	Top West Side	61.0	0	96.6
104	ACC	acc.TWy	+y		61.0	0	96.6
105	ACC	acc.TWz	+z		61.0	0	96.6
106	ACC	acc.TNx	+x	Top North Side	0	-61.0	96.6
107	ACC	acc.TNy	-y		0	-61.0	96.6
108	ACC	acc.TNz	+z		0	-61.0	96.6
109	ACC	acc.TMx	+x	Top Middle	0	0	124.0
110	ACC	acc.TMy	+y		0	0	124.0
111	ACC	acc.TMz	+z		0	0	124.0
112	ACC	acc.CFN	-y	North Face	0	-16.0	32.0
113	ACC	acc.CFW	+x	West Face	16.0	0	32.0
114	ACC	acc.CFS	+y	South Face	0	16.0	32.0
115	ACC	acc.CFE	-x	East Face	-16.0	0	32.0

Table A-1. Instrumentation for specimens A1, A2, B1 and B2.

Channel No[a]	Transducer[b]	Variable Name[c]	Orientation[d]	Transducer Location[e]	Coordinates[f] (in.)		
					x	y	z
116	LP	disp.NW2	$+y$	North Face	36.0	-61.0	72.0
117	LP	disp.NW3	$+y$		36.0	-61.0	122.0
118	LP	disp.NE2	$+y$		-36.0	-61.0	72.0
119	LP	disp.NM1	$+y$		0	-49.0	-8.0
120	LP	disp.NM2	$+y$		0	-12.0	4.0
121	LP	disp.NM3	$+y$		0	-12.0	8.0
122	LP	disp.NM4	$+y$		0	-12.0	12.0
123	LP	disp.NM6	$+y$		0	-12.0	28.0
124	LP	disp.NM7	$+y$		0	-12.0	44.0
125	LP	disp.NE3	$+y$		-36.0	-61.0	122.0
126	LP	disp.WN2	$-x$	West Face	61.0	-36.0	72.0
127	LP	disp.NM8	$+y$	North Face	0	-61.0	96.6
128	LP	disp.NM5	$+y$		0	-12.0	20.0
129	LP	disp.WM2	$-x$	West Face	12.0	0	4.75
130	LP	disp.WM3	$-x$		12.0	0	8.75
131	LP	disp.WM4	$-x$		12.0	0	12.75
132	LP	disp.WM5	$-x$		12.0	0	20.75
133	LP	disp.WM6	$-x$		12.0	0	28.75
134	LP	disp.WM7	$-x$		12.0	0	44.75
135	LP	disp.WM8	$-x$		12.0	0	96.6
136	LP	disp.WS1	$-x$		48.0	36.0	-8.0
137	LP	disp.WS3	$-x$		61.0	36.0	122.0
138	LP	disp.WS2	$-x$		61.0	36.0	72.0
139	LP	disp.WN3	$-x$		61.0	-36.0	122.0
140	LP	disp.CNW	$+z$	Top of Footing	28.0	-28.0	0→64
141	LP	disp.WN1	$-x$	West Face	48.0	-36.0	-8.0
142	LP	disp.CSE	$+z$	Top of Footing	-28.0	28.0	0→64
143	LP	disp.CSW	$+z$	Top of Footing	28.0	28.0	0→64
144	LP	disp.CNE	$+z$	Top of Footing	-28.0	-28.0	0→64

a. The channel number corresponds to the column number in the data file. The first two columns are for date and time, but are not counted.

b. ACC = Accelerometer; DCDT = Direct Current Displacement Transducer; LVDT = Displacement Transducer; LP = Linear Potentiometer; SG = Strain Gage.

c. The variable name used in the Data Reduction Routine (DRR), and in Figures 4-4, 4-7, 4-8, 4-9 and 4-10 to show the instrument locations.

d. The (+/-) sign indicates whether the measured quantity is along the positive or negative global direction (when applicable). Displacements and accelerations are later corrected to have a positive orientation consistent with the global coordinate system. For the global (x y z) coordinate system, see Figure 4-9.

e. Location of the instrument on the specimen.

f. Coordinates of the point for which a global measurement is being recorded (location of ACC, SG or LP target) or coordinates of the two points between which relative deformation is being measured (all DCDT and some LP instruments).

g. $a \rightarrow b$: indicates that the measurement is occuring between two points located at coordinates a and b, respectively. This convention is used for DCDT and some LP instruments.

Table A-2. Summary of all shaking table runs.

#	Name	Data File Name	Description	Span 1	Span 2
1	A1-Static Zero	981110200040.txt	Static Zero	0	0
2	A1-Pullback 1	981110200333.txt	East-West	0	0
3	A1-Pullback 2	981110203555.txt	East-West	0	0
4	A1-Pullback 3	981111140548.txt	East-West	0	0
5	A1-PB3 LongWN	981111174454.txt	Longitudinal 10 Hz White Noise	10	0
6	A1-PB3 LatWN	981111174932.txt	Lateral 10 Hz White Noise	0	10
7	A1-Low Lev	981111190836.txt	Elastic	123	0
8	A1-LL LongWN	981111192328.txt	Longitudinal 10 Hz White Noise	10	0
9	A1-LL LatWN	981111192517.txt	Lateral 10 Hz White Noise	0	10
10	A1-Run0	981111195107.txt	Yield Level 0	164	0
11	A1-Run0 LongWN1	981111195541.txt	Longitudinal 10 Hz White Noise	10	0
12	A1-Run0 LatWN1	981111195707.txt	Lateral 10 Hz White Noise	0	10
13	A1-Run0 LongWN2	981112183413.txt	Longitudinal 10 Hz White Noise	10	0
14	A1-Run0 LatWN2	981112183552.txt	Lateral 10 Hz White Noise	0	10
15	A1-Run0 LongWN3	981113135950.txt	Longitudinal 10 Hz White Noise	10	0
16	A1-Run0 LatWN3	981113140212.txt	Lateral 10 Hz White Noise	0	10
17	A1-Run1	981113141816.txt	Yield Level 1	164	0
18	A1-Run1 LongWN	981113142612.txt	Longitudinal 10 Hz White Noise	10	0
19	A1-Run1 LatWN	981113142740.txt	Lateral 10 Hz White Noise	0	10
20	A1-Run2	981113143724.txt	Design Level 1	600	0
21	A1-Run2 LongWN	981113150921.txt	Longitudinal 10 Hz White Noise	10	0
22	A1-Run2 LatWN	981113151145.txt	Lateral 10 Hz White Noise	0	10
23	A1-Run3	981113152212.txt	Max Level 1	900	0
24	A1-Run3 LongWN	981113164320.txt	Longitudinal 10 Hz White Noise	10	0
25	A1-Run3 LatWN	981113164435.txt	Lateral 10 Hz White Noise	0	10
26	A1-Run4	981113165205.txt	Design Level 2	600	0
27	A1-Run4 LongWN	981113165426.txt	Longitudinal 10 Hz White Noise	10	0
28	A1-Run4 LatWN	981113165545.txt	Lateral 10 Hz White Noise	0	10
29	A1-Run5	981113173643.txt	Max Level 2	1000	0
30	A1-Run5 LongWN	981113175505.txt	Longitudinal 10 Hz White Noise	10	0
31	A1-Run5 LatWN	981113175619.txt	Lateral 10 Hz White Noise	0	10

Table A-2. Summary of all shaking table runs.

#	Name	Data File Name	Description	Span 1	Span 2
32	A1-Run6	981113180412.txt	Max Level 3	1000	0
33	A1-Run6 LongWN	981113181720.txt	Longitudinal 10 Hz White Noise	10	0
34	A1-Run6 LatWN	981113181838.txt	Lateral 10 Hz White Noise	0	10
35	A1-Run7	981113182615.txt	Design Level 2	600	0
36	A1-Run7 LongWN	981113183101.txt	Longitudinal 10 Hz White Noise	10	0
37	A1-Run7 LatWN	981113183224.txt	Lateral 10 Hz White Noise	0	10
38	A1-Run8	981113184846.txt	Max Level 4	1000	0
39	A2-Static Zero	981120180651.txt	Static Zero	0	0
40	A2-Pullback 1	981120181401.txt	North-South	0	0
41	A2-Pullback 2	981120184918.txt	North-South	0	0
42	A2-Pullback 3	981123121832.txt	East_West	0	0
43	A2-Pullback 4	981123123556.txt	East_West	0	0
44	A2-PB4 LongWN	981123140842.txt	Longitudinal 10 Hz White Noise	10	0
45	A2-PB4 LatWN	981123141044.txt	Lateral 10 Hz White Noise	0	10
46	A2-Low Lev	981123151030.txt	Elastic	123	38
47	A2-LL LongWN	981123151553.txt	Longitudinal 10 Hz White Noise	10	0
48	A2-LL LatWN	981123151718.txt	Lateral 10 Hz White Noise	0	10
49	A2-Run0	981123161241.txt	Yield Level 0	164	50
50	A2-Run0 LongWN1	981123161903.txt	Longitudinal 10 Hz White Noise	10	0
51	A2-Run0 LatWN1	981123162021.txt	Lateral 10 Hz White Noise	0	10
52	A2-Run1	981123163725.txt	Yield Level 1	164	50
53	A2-Run1 LongWN	981123164253.txt	Longitudinal 10 Hz White Noise	10	0
54	A2-Run1 LatWN	981123164602.txt	Lateral 10 Hz White Noise	0	10
55	A2-Run2	981123165216.txt	Design Level 1	600	e184

Table A-2. Summary of all shaking table runs.

#	Name	Data File Name	Description	Span 1	Span 2
56	A2-Run2 LongWN	981123172256.txt	Longitudinal 10 Hz White Noise	10	0
57	A2-Run2 LatWN	981123172604.txt	Lateral 10 Hz White Noise	0	10
58	A2-Run3	981123174112.txt	Max Level 1	900	277
59	A2-Run3 LongWN	981123180855.txt	Longitudinal 10 Hz White Noise	10	0
60	A2-Run3 LatWN	981123181321.txt	Lateral 10 Hz White Noise	0	10
61	A2-Run4	981123192041.txt	Design Level 2	600	184
62	A2-Run4 LongWN	981123194018.txt	Longitudinal 10 Hz White Noise	10	0
63	A2-Run4 LatWN	981123194324.txt	Lateral 10 Hz White Noise	0	10
64	A2-Run5	981123195232.txt	Max Level 2	1000	307
65	A2-Run5 LongWN	981123200849.txt	Longitudinal 10 Hz White Noise	10	0
66	A2-Run5 LatWN	981123201135.txt	Lateral 10 Hz White Noise	0	10
67	A2-Run6	981123201817.txt	Max Level 3	1000	307
68	A2-Run6 LongWN	981123203221.txt	Longitudinal 10 Hz White Noise	10	0
69	A2-Run6 LatWN	981123203524.txt	Lateral 10 Hz White Noise	0	10
70	A2-Run7	981123204300.txt	Design Level 3	600	184
71	A2-Run7 LongWN	981123204736.txt	Longitudinal 10 Hz White Noise	10	0
72	A2-Run7 LatWN	981123205055.txt	Lateral 10 Hz White Noise	0	10
73	A2-Run8	981123205747.txt	Max Level 4	1000	307
74	A2-Run8 LongWN	981123212041.txt	Longitudinal 10 Hz White Noise	10	0
75	A2-Run8 LatWN	981123212405.txt	Lateral 10 Hz White Noise	0	10
76	A2-Run9	981123213028.txt	Max Level 5	1000	307
77	A2-Run9 LongWN	981123214157.txt	Longitudinal 10 Hz White Noise	10	0
78	A2-Run9 LatWN	981123214446.txt	Lateral 10 Hz White Noise	0	10
79	A2-Run10	981123214931.txt	Max Level 6	1000	307
80	A2-Run10 LongWN	981123220112.txt	Longitudinal 10 Hz White Noise	10	0
81	A2-Run10 LatWN	981123220450.txt	Lateral 10 Hz White Noise	0	10
82	B1-Static Zero	981204195016.txt	Static Zero	0	0
83	B1-Pullback 1	981204195546.txt	North-South	0	0
84	B1-Pullback 2	981207132309.txt	North-South	0	0
85	B1-Pullback 3	981207140221.txt	East-West	0	0
86	B1-Pullback 4	981207141856.txt	East-West	0	0

Table A-2. Summary of all shaking table runs.

#	Name	Data File Name	Description	Span 1	Span 2
87	B1-PB4 LongWN	981207190111.txt	Longitudinal 10 Hz White Noise	10	0
88	B1-PB4 LatWN	981207190258.txt	Lateral 10 Hz White Noise	0	10
89	B1-Run1	981207191936.txt	Elastic	50	0
90	B1-Run2	981207192951.txt	1/2 Yield	100	0
91	B1-Run3	981207193854.txt	3/4 Yield	150	0
92	B1-LL3 LongWN	981207195555.txt	Longitudinal 10 Hz White Noise	10	0
93	B1-LL3 LatWN	981207195726.txt	Lateral 10 Hz White Noise	0	10
94	B1-Run4	981207201354.txt	Yield	200	0
95	B1-YL1 LongWN1	981207202456.txt	Longitudinal 10 Hz White Noise	10	0
96	B1-YL1 LatWN1	981207202628.txt	Lateral 10 Hz White Noise	0	10
97	B1-YL1 LongWN2	981208124846.txt	Longitudinal 10 Hz White Noise	10	0
98	B1-YL1 LatWN2	981208125128.txt	Lateral 10 Hz White Noise	0	10
99	B1-Run5	981208131302.txt	Design 1	500	0
100	B1-DL1 LongWN	981208140319.txt	Longitudinal 10 Hz White Noise	10	0
101	B1-DL1 LatWN	981208140442.txt	Lateral 10 Hz White Noise	0	10
102	B1-Run6	981208142302.txt	Max 1	1000	0
103	B1-ML1 LongWN	981208154241.txt	Longitudinal 10 Hz White Noise	10	0
104	B1-ML1 LatWN	981208154408.txt	Lateral 10 Hz White Noise	0	10
105	B1-Run7	981208155554.txt	Design 2	500	0
106	B1-DL2 LongWN	981208162020.txt	Longitudinal 10 Hz White Noise	10	0
107	B1-DL2 LatWN	981208162148.txt	Lateral 10 Hz White Noise	0	10
108	B1-Run8	981208162806.txt	Max 2	1000	0
109	B1-ML2 LongWN	981208165320.txt	Longitudinal 10 Hz White Noise	10	0
110	B1-ML2 LatWN	981208165442.txt	Lateral 10 Hz White Noise	0	10
111	B1-Run9	981208170709.txt	Max 3	1000	0
112	B1-ML3 LongWN	981208172008.txt	Longitudinal 10 Hz White Noise	10	0
113	B1-ML3 LatWN	981208172135.txt	Lateral 10 Hz White Noise	0	10
114	B2-Pullback 1	981216190231.txt	North-South	0	0
115	B2-Pullback 2	981216190951.txt	North-South	0	0
116	B2-Pullback 3	981216192046.txt	East-West	0	0
117	B2-Pullback 4	981217135142.txt	East-West	0	0

Table A-2. Summary of all shaking table runs.

#	Name	Data File Name	Description	Span 1	Span 2
118	B2-Pullback 5	981217143105.txt	North-South	0	0
119	B2-PB5 LongWN	981217160432.txt	Longitudinal 10 Hz White Noise	10	0
120	B2-PB5 LatWN	981217160557.txt	Lateral 10 Hz White Noise	0	10
121	B2-Run1	981217162627.txt	Elastic	50	20
122	B2-Run2	981217163144.txt	1/2 Yield	100	40
123	B2-Run3	981217164217.txt	3/4 Yield	150	60
124	B2-LL3 LongWN	981217170334.txt	Longitudinal 10 Hz White Noise	10	0
125	B2-LL3 LatWN	981217170459.txt	Lateral 10 Hz White Noise	0	10
126	B2-Run4	981217171517.txt	Yield	200	80
127	B2-YL1 LongWN	981217175143.txt	Longitudinal 10 Hz White Noise	10	0
128	B2-YL1 LatWN	981217175309.txt	Lateral 10 Hz White Noise	0	10
129	B2-Run5	981217180454.txt	Design 1	500	200
130	B2-DL1 LongWN	981217183334.txt	Longitudinal 10 Hz White Noise	10	0
131	B2-DL1 LatWN	981217183457.txt	Lateral 10 Hz White Noise	0	10
132	B2-Run6	981217185137.txt	Max 1	1000	400
133	B2-ML1 LongWN	981217194326.txt	Longitudinal 10 Hz White Noise	10	0
134	B2-ML1 LatWN	981217194454.txt	Lateral 10 Hz White Noise	0	10
135	B2-Run7	981217195224.txt	Design 1	500	200
136	B2-DL2 LongWN1	981217200944.txt	Longitudinal 10 Hz White Noise	10	0
137	B2-DL2 LatWN1	981217201107.txt	Lateral 10 Hz White Noise	0	10
138	B2-DL2 LongWN2	981218115827.txt	Longitudinal 10 Hz White Noise	10	0
139	B2-DL2 LatWN2	981218120004.txt	Lateral 10 Hz White Noise	0	10
140	B2-Run8	981218121641.txt	Max 2	1000	400
141	B2-ML2 LongWN	981218123548.txt	Longitudinal 10 Hz White Noise	10	0
142	B2-ML2 LatWN	981218123716.txt	Lateral 10 Hz White Noise	0	10
143	B2-Run9	981218124252.txt	Max 3	1000	400
144	B2-ML3 LongWN	981218130457.txt	Longitudinal 10 Hz White Noise	10	0
145	B2-ML3 LatWN	981218130615.txt	Lateral 10 Hz White Noise	0	10
146	B2-Run10	981218131322.txt	Max 4	1000	400
147	B2-ML4 LongWN	981218132937.txt	Longitudinal 10 Hz White Noise	10	0
148	B2-ML4 LatWN	981218133103.txt	Lateral 10 Hz White Noise	0	10

Table A-2. Summary of all shaking table runs.

#	Name	Data File Name	Description	Span 1	Span 2
149	B2-Run11	981218133807.txt	Max 5	1000	400
150	B2-Run12	981218134814.txt	Max 6	1000	400
151	B2-ML6 LongWN	981218140550.txt	Longitudinal 10 Hz White Noise	10	0
152	B2-ML6 LatWN	981218140717.txt	Lateral 10 Hz White Noise	0	10
153	B2-Run13	981218141448.txt	Max 7	1000	400
154	B2-ML7 LongWN	981218143041.txt	Longitudinal 10 Hz White Noise	10	0
155	B2-ML7 LatWN	981218143200.txt	Lateral 10 Hz White Noise	0	10

Appendix B Section Properties and Capacity Estimation

B.1   OVERVIEW

The main computations used in the design process to estimate the dimensions and properties of the specimens are presented in this appendix.

B.2   COMPUTATION OF SPECIMEN PROPERTIES

The following is a description of the main dimensions of the specimen and the supported mass system.

B.2.1   Column Dimensions and Properties

B.2.1.1   Column Dimensions

$D = 16$ in $= 406.4$ mm $=$ Outside diameter of the column section

$A_g = \pi D^2/4 = 201.06$ in$^2 = 129.7$x10^3 mm$^2 =$ Gross area

$I_g = \pi D^4/64 = 3217$ in$^4 = 0.155$ ft$^4 = 1.339$x10^9 mm$^4 =$ Gross second moment of inertia

$D_c = D - 2c - d_{sp} = 14.82$ in $= 376.4$ mm $=$ Core diameter measured to the center of the spiral

$L = 8$ ft $= 96$ in $= 2438.4$ mm $=$ Height of the column measured from the top of the footing to the center of the mass consisting of the top slab and the three mass blocks

$L_{clear} = 64$ in $= 1625.6$ mm $=$ Clear height of the column measured from the top of the footing to the bottom of the top slab

$a_r = L/D = 6 =$ Aspect ratio of the column

$A_c = \pi D_c^2/4 = 172.5$ in$^2 = 112.3$x10^3 mm$^2 =$ Core area

$c = 0.5$ in $= 12.7$ mm $=$ Clear cover to spiral

$V_{column} = A_g L_{clear} = 201.06$ in^2 x 64 in $= 7.45$ ft$^3 = 0.211$ m$^3 =$ Volume of column

$W_{column} = V_{column}\, \rho_{concrete} = (7.45 \text{ ft}^3) \text{ x } (0.15 \text{ kip/ft}^3) = 1.12 \text{ kips} = 4.97 \text{ kN}$

$P = 65.3 \text{ kips} = 290.5 \text{ kN} = $ Axial load on the column neglecting the column own weight (see below for computation)

$P_r = P/(A_g f'_c) = 65.3 \text{ kips} / (201.06 \text{ in}^2 \text{ x } 5.70 \text{ ksi}) = 5.7\% = $ Axial load ratio

B.2.1.2   Spiral Reinforcement Dimensions

$d_{sp} = 0.178 \text{ in} = 4.52 \text{ mm} = $ Spiral reinforcement diameter (W2.5 plain bar)

$A_{sp} = 0.025 \text{ in}^2 = 16.1 \text{ mm}^2 = $ Spiral reinforcement area

$\rho_{sp} = 4A_{sp} / (s.D_c) = 0.54\%$

$s = 1.25 \text{ in} = 31.75 \text{ mm} = $ Pitch of spiral reinforcement
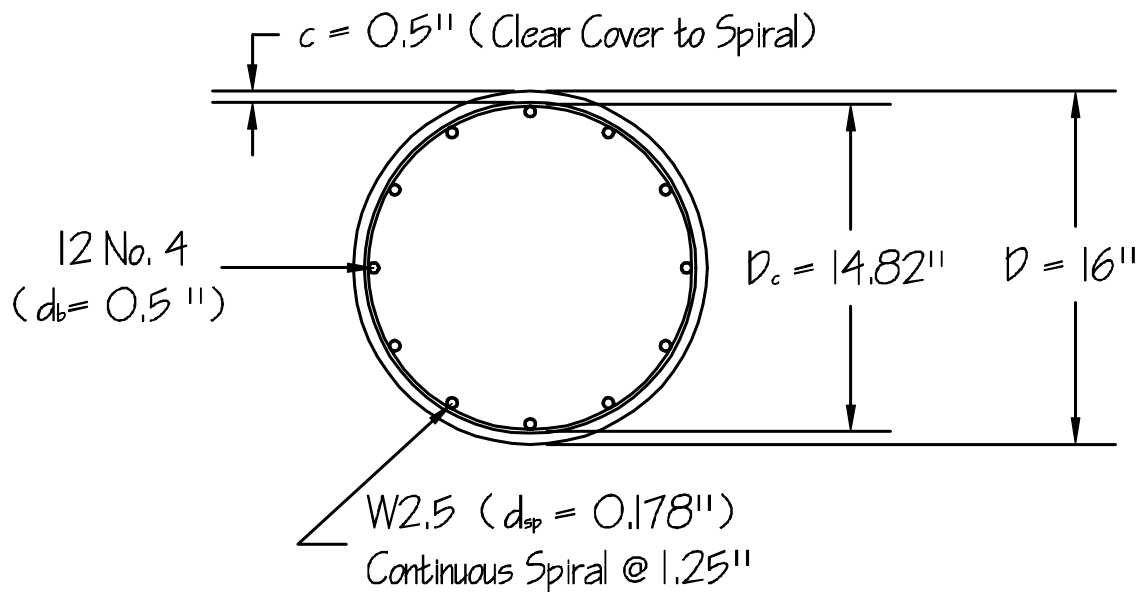
Figure B-1. Cross-section details (1 in. = 25.4 mm).

B.2.1.3   Longitudinal Reinforcement Dimensions

$d_b = 0.50 \text{ in} = 12.7 \text{ mm} = $ Longitudinal bar diameter (#4)

$A_b = 0.196 \text{ in}^2 = 126.5 \text{ mm}^2 = $ Longitudinal bar area

$A_l = 12\, A_b = 2.35 \text{ in}^2 = 1516 \text{ mm}^2 = $ Total longitudinal steel area

$\rho_l = A_l / A_g = 2.35/201.06 = 1.17\%$

B.2.2 Footing and Top Slab Dimensions

Dimensions and weight of the footing and top slab (8 ft x 8 ft x 16 in):

$b_{Top\ Slab} = b_{footing}$ = 8 ft = 96 in = 2438.4 mm = Footing width

$d_{Top\ Slab} = d_{footing}$ = 16 in = 406.4 mm = footing depth

$V_{Top\ Slab} = V_{footing} = d_{footing}$ x $b_{footing}^2$ = 85.33 ft^3 = 2.42 m^3 = Footing volume

$W_{Top\ Slab} = W_{footing} = V_{footing}$ x $\rho_{concrete}$ = (85.33 ft^3) x (0.15 kip/ft^3) = 12.8 kips = 56.94 kN

B.2.3 Supported Mass Dimensions and Properties

Dimensions and weight of an individual weight block (10 ft x 10 ft x 14 in):

b_{block} = 10 ft = 120 in = 3048 mm = Width of an individual "weight block"

d_{block} = 14 in = 355.6 mm = Depth of block

$V_{block} = d_{block}\ b_{block}^2$ = 116.67 ft^3 = 3.30 m^3 = Volume of block

$W_{block} = V_{block}\ \rho_{concrete}$ = (116.67 ft^3) x (0.15 kip/ft^3) = 17.5 kips = 77.85 kN

Total weight (and mass) of the mass block (3 weight blocks + top slab):

$W_{total\ mass}$ = 3 W_{block} + $W_{Top\ Slab}$ = 3 x 17.5 + 12.8 = 65.3 kips = 290.5 kN

$M_{total\ mass}$ = $W_{total\ mass}$ / g = (65.3 kips) / (386 in/sec^2) = 0.169 kip.sec^2/in = 29,596 kg

z_{cen} = $z_{bot} + L_{clear}$, where z_{bot} is the centroid location from bottom of top slab

$\quad$ = [$W_{Top\ Slab}$ x 0.5$d_{Top\ Slab}$ + 3W_{block} x ($d_{Top\ Slab}$ + 1.5d_{block})]/$W_{total\ mass}$ + L_{clear}

$\quad$ = [12.8 kips x 8 in + 3 x 17.5 kips x (16 in + 1.5 x 14 in)]/(65.3 kips) + 64 in

$\quad$ = 31.32 in + 64 in

$\quad$ = 95.32 in = 2421 mm ≈ 96 in (8 ft) = 2438 mm = L

$\quad$ = Center of mass location measured from the column base

I_r = Rotational moment of inertia

$$= \frac{1}{g} \sum_{i=1}^{4} W_i \left(\frac{b_i^2 + h_i^2}{12} \right) + W_i(z_{cen} - z_i)^2 \quad, g = 386 \text{ in/sec}^2$$

$$= 233.94 \text{ kip.in.sec}^2$$

$$= 26,432 \text{ kg.m}^2$$

In the above, i corresponds to the four individual weight components (top slab + 3 weight blocks), z_i is the centroid of each component, while z_{cen} is the centroid location of the total mass. From the rotational moment of inertia, the radius of gyration can be computed as follows:

Radius of gyration = r_g = $\sqrt{\dfrac{I_r}{M}}$ = $\sqrt{\dfrac{233.94}{0.169}}$ = 37.2 in = 945 mm.

B.3   CONCRETE PROPERTIES

B.3.1   Estimation of Confined Concrete Strength

At the time of testing, the concrete unconfined strength f'_{co} was about 5700 psi (39.3 MPa). Using Mander's model for confined concrete [60] (see Figure B-2), the confined compressive strength can be computed as:

$$f'_{cc} = f'_{co}\left(-1.254 + 2.254\sqrt{1 + \frac{7.94f'_l}{f'_{cc}}} - 2\frac{f'_{cc}}{f'_{co}}\right) \tag{B-1}$$

where f'_{co} = unconfined concrete compressive strength; and f'_l is the effective confining stress given by:

$$f'_l = K_e f_l \tag{B-2}$$

where K_e can be taken as 0.95 for circular sections, and f_l is given by:

$$f_l = \frac{1}{2}\rho_{sp}f_{yh} \tag{B-3}$$

Using (B-3) and assuming a yield strength of f_{yh} = 85 ksi for the spiral reinforcement:

$$f_l = 0.0054 \text{ x } 85 \text{ ksi } / 2 = 0.23 \text{ ksi}$$

which can be used to compute: $f'_l = K_e f_l = 0.95$ x 0.23 ksi = 0.22 ksi, from (B-2). Inserting this value in (B-1) gives:

$$f'_{cc} = 5.7\left(-1.254 + 2.254\sqrt{1 + \frac{7.94 \cdot 0.22}{5.7}} - 2\frac{0.22}{5.7}\right) = 5.7(1.245) = 7.1 \text{ ksi} = 49 \text{ MPa}$$

The ultimate compression strain can be estimated by the following equation:

$$\varepsilon_{cu} = 0.004 + \frac{1.4\rho_{sp}f_{yh}\varepsilon_{su}}{f'_{cc}} = 0.004 + \frac{1.4 \cdot 0.0054 \cdot 85 \cdot 0.10}{7.1} = 0.013$$

Using the ultimate concrete compressive strain, it is possible to estimate the displacement capacity of the column. This requires making assumptions on the plastic hinge length and the curvature distribution over the column height. Resutls will later be compared to a more rigorous analysis using a fiber model computer element.
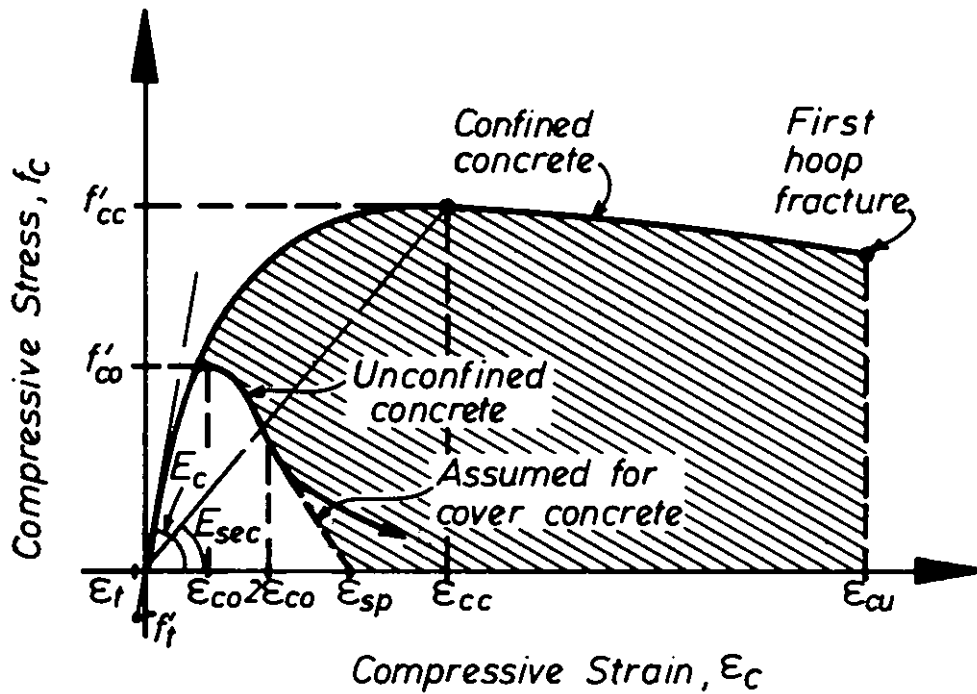
Figure B-2. Mander stress-strain model for confined and unconfined concrete [60].

B.4   DESIGN PROCESS

B.4.1   Estimation of Effective Period of Vibration

An expression for the effective period of vibration is derived as a function of the variables involved. The effective period of a single degree of freedom system is obtained through Equation B-4.

$$T_{eff} = 2\pi \sqrt{\frac{m}{k_{eff}}} \tag{B-4}$$

The effective stiffness (k_{eff}) is usually assumed to be one-half of the gross stiffness (kg), and is used as a quick estimate of the reduced stiffness of a concrete column due to cracking:

$$k_{eff} = 3\frac{(EI)_e}{L^3} \cong \frac{k_g}{2} = \frac{3}{2}\frac{(EI)_g}{L^3} \tag{B-5}$$

Using equation (B-5), the gross and effective model stiffness can be approximated as:

$$k_g = 3 \cdot \frac{(57 \cdot \sqrt{5700} \cdot ksi)(3217 \cdot in^4)}{(96 \cdot in)^3} = 46.9 \ \text{kip/in}$$

351

while the effective stiffness can be obtained as:

$$k_{eff} = k_g/2.0 = 46.9/2 = 23.5 \text{ kip/in}$$

Based on equation (B-4), the period based on both the gross and effective stiffness of the specimen can be computed as:

$$T_{gross,model} = 2\pi\sqrt{\frac{0.169 \cdot kip \cdot s^2/in}{46.9 \cdot kip/in}} = 0.38 \text{ sec}$$

$$T_{effective,model} = 2\pi\sqrt{\frac{0.169 \cdot kip \cdot s^2/in}{23.5 \cdot kip/in}} = 0.53 \text{ sec}$$

which is the effective period of the model. This can be related to the effective period of the proto-type, assuming a scale factor S_d of 4.5, by multiplying by S_t (Table 3-1). Hence, the period of the prototype is:

$$T_{effective,prototype} = T_{eff,model} \cdot S_t = T_{eff,model} \cdot \sqrt{S_d} = 1.13 \cdot seconds$$

B.4.2 Design Forces

Using the effective period, the design acceleration can now be obtained from the appropriate ARS spectra (Figure 2-1). Designing for the maximum acceleration of 0.70g, at a period of 1.13 seconds, the required pseudo-acceleration can be obtained as 1.0g. This assumes elastic behavior, and needs to be reduced by the appropriate reduction factor Z. A value of 4 was selected for Z, which results in a design acceleration of:

$$a_{design} = \frac{a_{elastic}}{Z} = \frac{1.0g}{4} = 0.25g$$

The model design acceleration will be similar since the acceleration scale factor $S_a = 1.0$ (Table 3-1). Hence, the model design force (and moment) can be obtained as:

$$F_{design} = mass \cdot a_{design} = 65.3 \cdot 0.25 = 16.3 \text{ kips} = 72.5 \text{ kN}$$

$$M_{design} = F_{design} \cdot L = 16.3 \cdot 96 = 1567 \text{ kip.in} = 177 \text{ kN.m}$$

B.5   DISPLACEMENT CAPACITY

Displacement can be related to local quantities such as strain and curvature. Although this is a complicated procedure that is affected by many variables, it can be simplified to a certain degree in the case of a single column response. Such relationships will be derived next.

Assuming a bilinear behavior of column (ignoring initial elastic behavior until cracking), the yield displacement can be obtained by the following:

$$d_y = \frac{1}{3}\phi_y L^2 \tag{B-6}$$

where d_y and ϕ_y are the yield displacement and yield curvature, respectively.

If we assume that additional loading results in an increase in inelastic curvature in the plastic hinge zone, then displacements larger than d_y can be expressed as:

$$d = d_y + (\phi - \phi_y)L_p\left(L - \frac{L_p}{2}\right) \tag{B-7}$$

where L_p, the plastic hinge length can be assumed to be equal to αD, D being the diameter of the column section [68]. α will be taken to be 0.75 in this case, since the plastic hinge was observed to be about $0.75D$ during the tests. At ultimate, the displacement can be further simplified, and expressed as a function of ϕ_u, L and L_p, neglecting elastic curvatures outside the plastic hinge zone, and assuming that the inelastic action is centered at the bottom of the column.

$$d_{ult} \approx \phi_u \cdot L_p \cdot L \tag{B-8}$$

The above simplifications of the displacement can be used to relate the peak displacement to the maximum tensile (ε_t) or compressive (ε_c) strain experienced at the section. With the assumption that plane sections remain plane:

$$\phi = \frac{\varepsilon_c}{c} = \frac{\varepsilon_c}{\beta D} \tag{B-9}$$

where c is the distance from the compression face to the section to the neutral axis, and is taken as a fraction β of the column diameter. Equations (B-8) and (B-9) lead to:

$$d_{ult} = \varepsilon_{cu}\frac{L_p L}{\beta D} = \varepsilon_{cu}\frac{\alpha}{\beta}L \tag{B-10}$$

Equation (B-10) give the allowed displacements such that certain strain conditions are not exceeded in the section. This is a useful result that can be used to predict capacity, but can also be used in design to control performance.

Using (B-10), and assuming that β is between 0.10 and 0.15, the ultimate capacity displacement d_{ult} can be estimated to be between 6.2 in. and 9.4 in. (between 160 mm and 240 mm). A more refined section analysis reveals that β is closer to 0.15, hence the 6.2 in. estimate is closer to the actual displacement capacity.

B.6   ROTATIONAL MOMENT OF INERTIA

Since the method of supporting the mass on top of the specimen results in a rotational moment of inertia in addition to the translational inertia equal to the mass of the deck, second mode effects can be expected in the specimen's response. In order to certify the validity of such effects, the rotational mass is compared to what would be expected in an actual bridge. Naturally, the geometry of the deck may vary significantly, and a range of rotational inertias can be expected even for the same translational mass. As a quick check, a deck section was selected from the *Bridge Engineering Handbook* [13] as shown in Figure B-3.
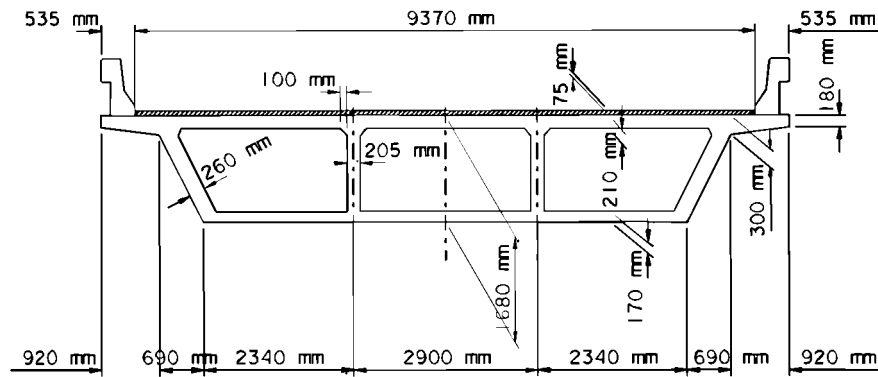
Figure B-3. Example of a cross-section of a bridge deck [13].

Assuming that this deck would be supported by the prototype column ($D = 6$ ft $= 1829$ mm), and that the deck section is uniform, we can compute the radius of gyration of the section as shown in Equations B-11 to B-13, where the section is divided into N rectangular sections with dimensions b and h, and whose centroid is located at a distance d from the centroid of the whole section.

$$r = \sqrt{\frac{I_r}{A}} \tag{B-11}$$

$$A = \sum_{i=1}^{N} A_i = \sum_{i=1}^{N} b_i h_i \tag{B-12}$$

$$I_r = \sum_{i=1}^{N} A_i \left(\frac{b_i^2 + h_i^2}{12} \right) + A_i d_i^2 \tag{B-13}$$

The prototype dead load that needs to be carried by the column is about 1322 kips (5881 kN). The required length of the above deck section that would have this weight is about 136 ft (41.5 m). A quick check shows that the section is slightly smaller than required for such a span,

354

since it is recommended that $H \geq 0.055L$ [13]. This requires increasing the section depth H by 30%, which changes the span to about 128 ft (39 m). Assuming that the modified section satisfies design criteria, the resulting radius of gyration is computed as 128.6 in (3.27 m), which corresponds to 28.6 in (726 mm) at specimen scale, using the scale factor of 4.5. The radius of gyration for the specimen's mass was previously computed as 37.2 in (945 mm), which is about 30% larger. This means that the rotational moment of inertia of the specimen is about 69% larger than computed using the above example section. Although the difference is significant, the rotational mass is not considered unrealistic since the example section considered is not an extreme case, and it is also possible that the column in question could support a wider section (with a higher radius of gyration). This comparison is not intended to show an exact match, but rather that the rotational moment of inertia of the specimen is within the normal range for typical bridges.

Appendix C Documentation of Damage Progression

The progression of damage during various runs, and from one run to another was tracked using photographs, video recording and by documenting the column cracking and spalling following each of the runs. In Figures C-2 to C-24, the crack pattern after each of the runs on all four faces of the column are shown. For example, Figure C-2 shows the cracking pattern of specimen A1 right after Run 2 (first design level). The figure shows the flattened surface of the column circumference. Different sides are marked as W, S, E and N standing for West, South, East and North faces respectively (See Figure C-1). Grid dimensions are presented in Section 5.1.

Photos showing the state of damage of each specimen after each major run are shown in Figures C-25 to C-54. This extensive documentation is intended to give a clear picture of the progression of damage for the different specimens, and of the mode failure at the final runs.
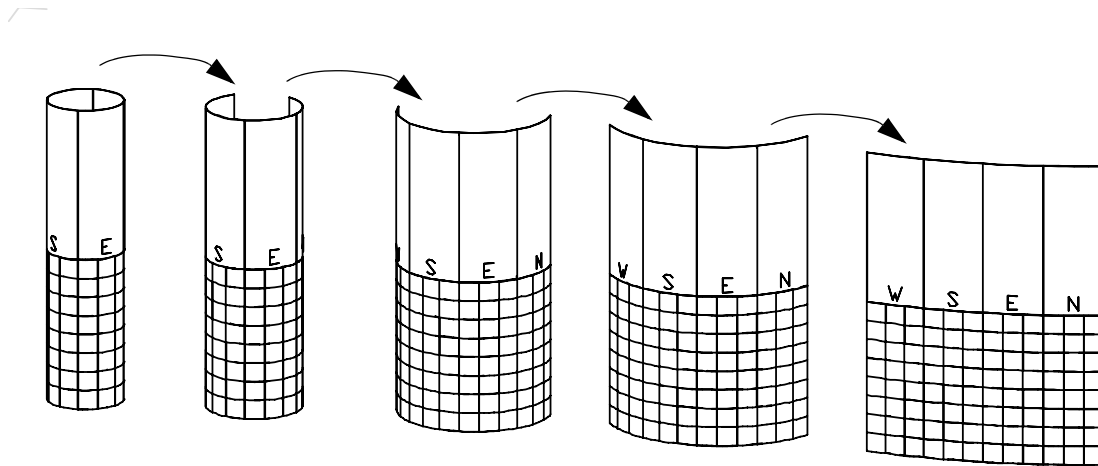
Figure C-1. Illustration of convention used in Figures C-2 to C-24.
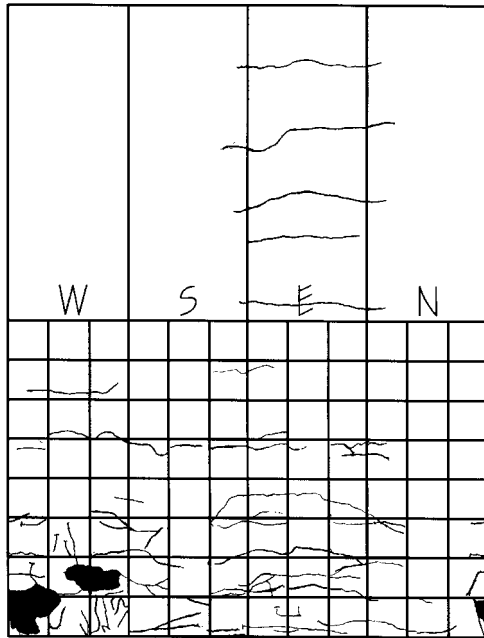
Figure C-2. A1-Run 2 (Design 1).
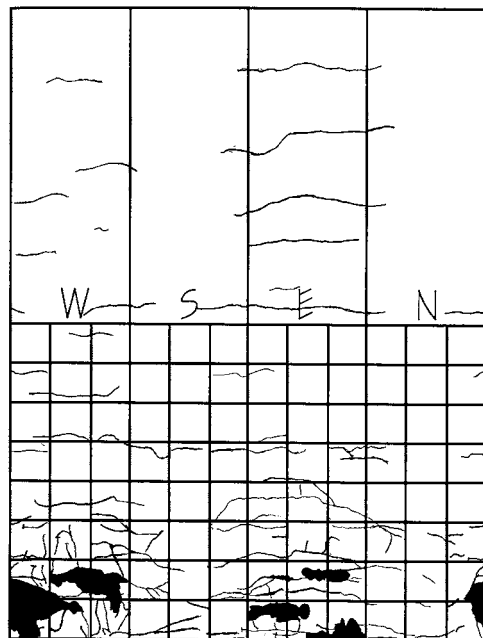
Figure C-3. A1-Run 3 (Max 1).
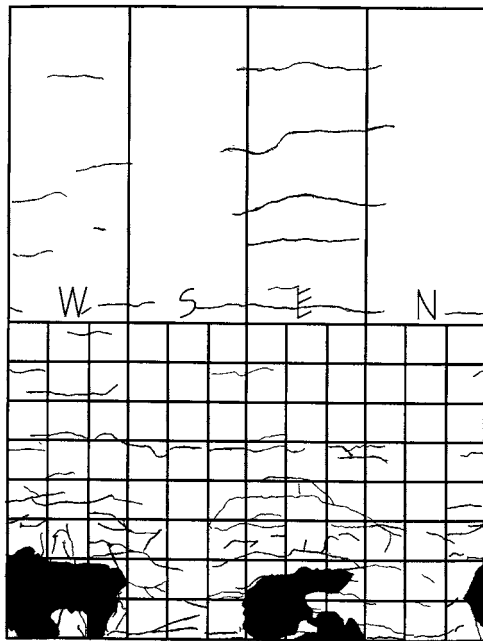
Figure C-4. A1-Run 5 (Max 2).
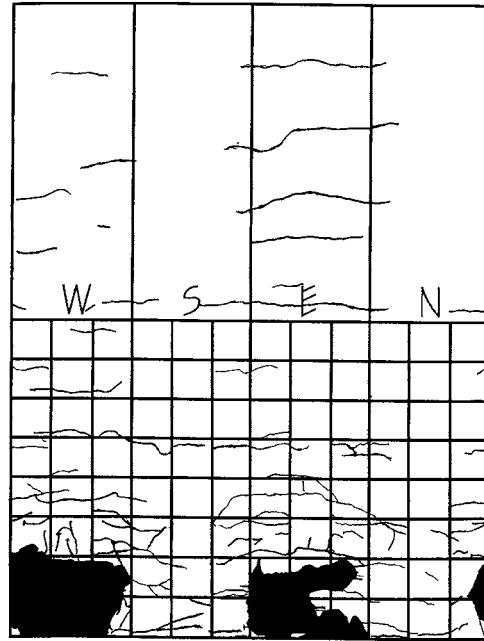
Figure C-5. A1-Run 6 (Max 3).
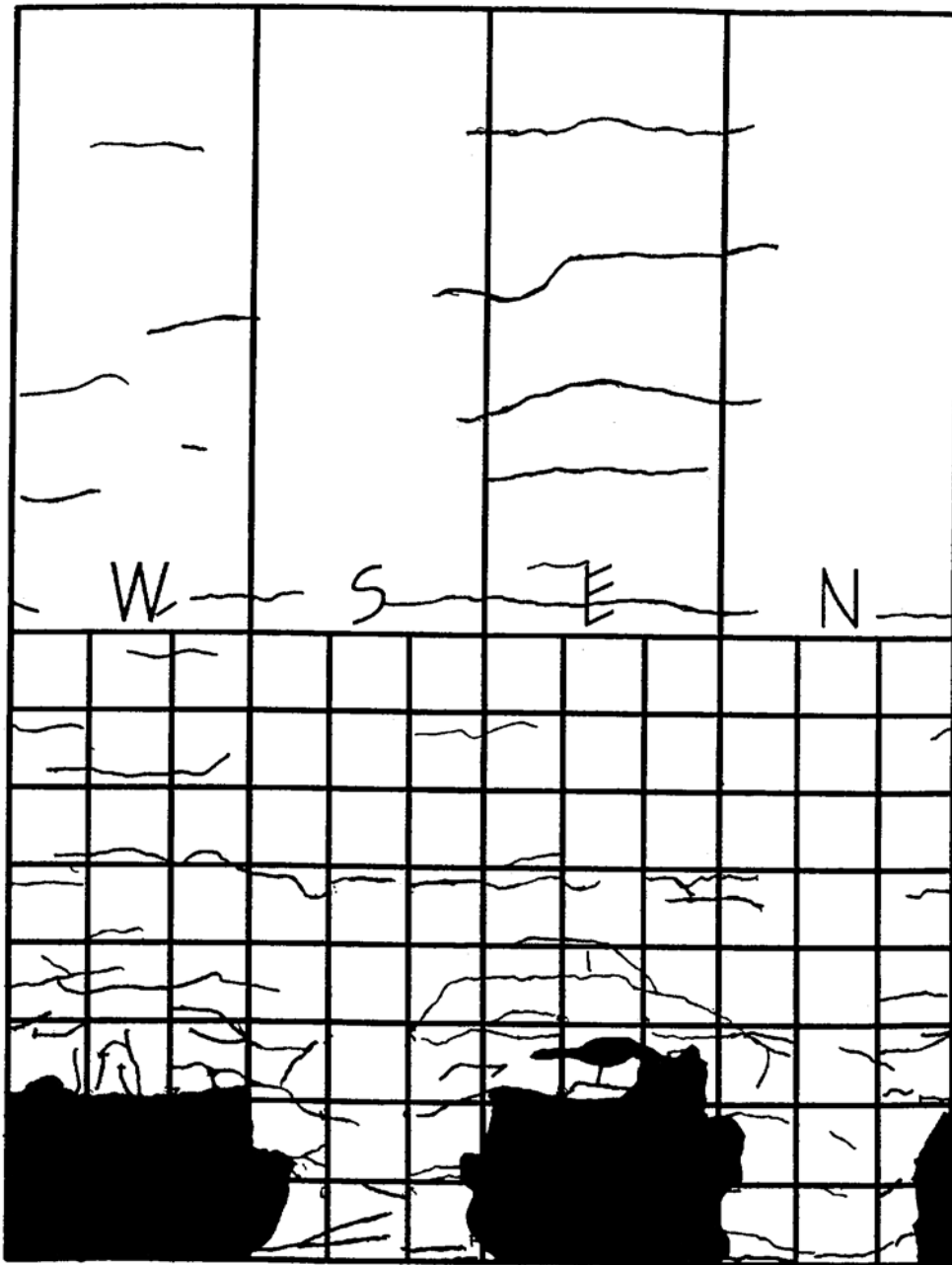
Figure C-6. A1-Run 8 (Max 4).
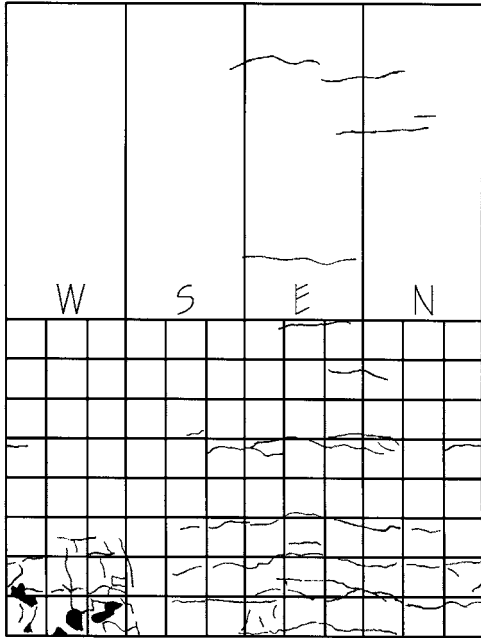
Figure C-7. A2-Run 2 (Design 1).
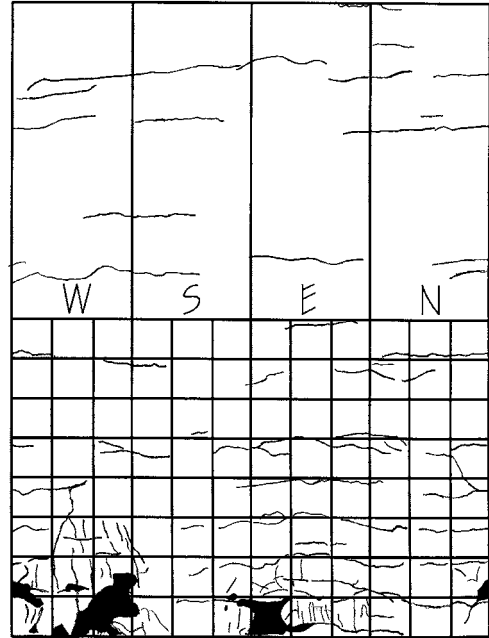
Figure C-8. A2-Run 3 (Max 1).
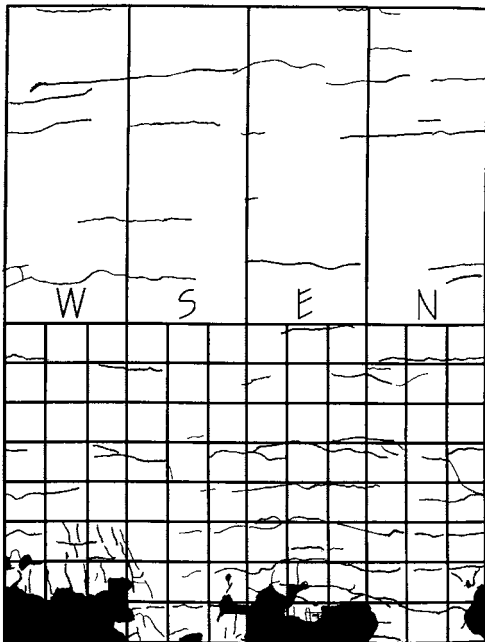
Figure C-9. A2-Run 5 (Max 2).
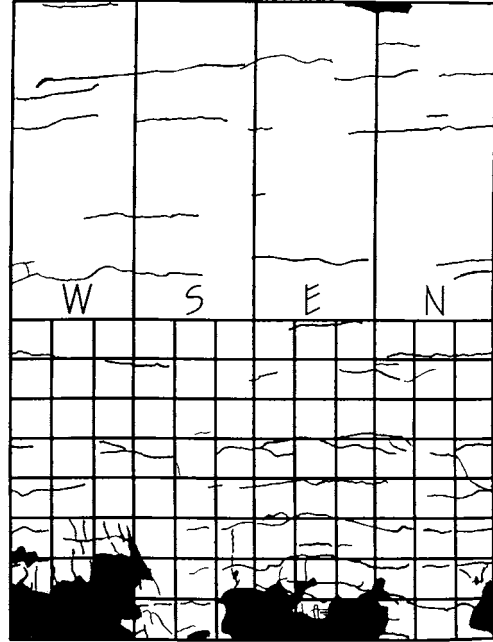
Figure C-10. A2-Run 6 (Max 3).
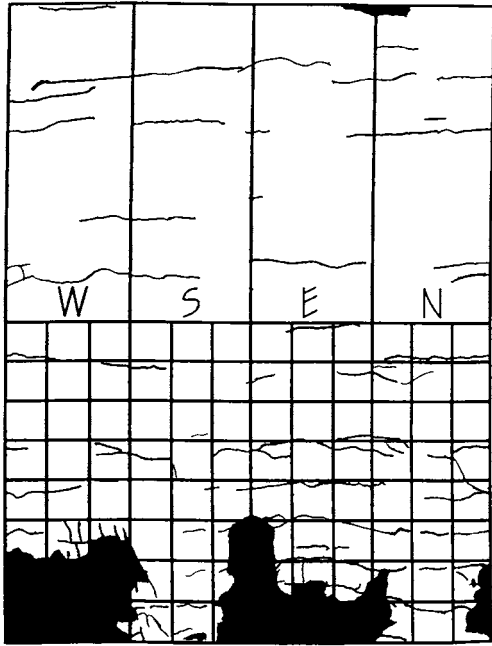
Figure C-11. A2-Run 8 (Max 4).
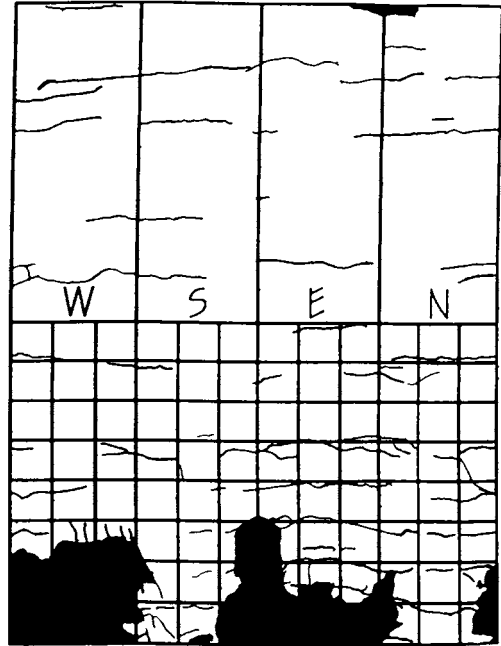
Figure C-12. A2-Run 9 (Max 5).
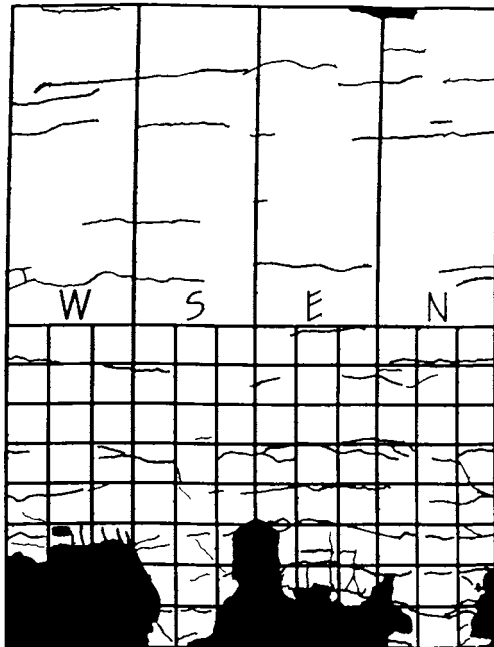
Figure C-13. A2-Run 10 (Max 6).
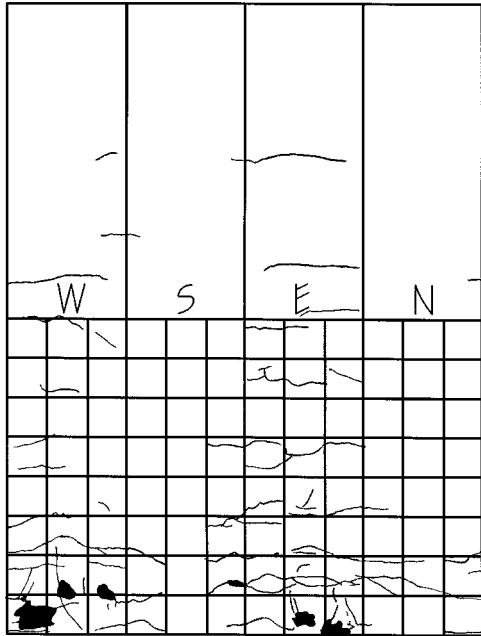
Figure C-14. B1-Run 5 (Design 1).
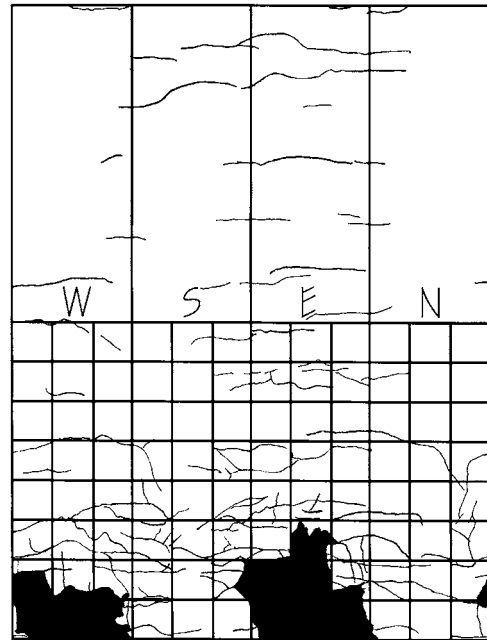
Figure C-15. B1-Run 6 (Max 1).
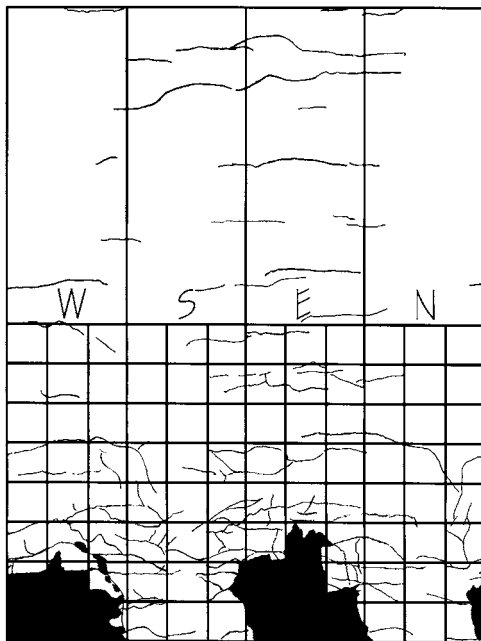
Figure C-16. B1-Run 8 (Max 2).
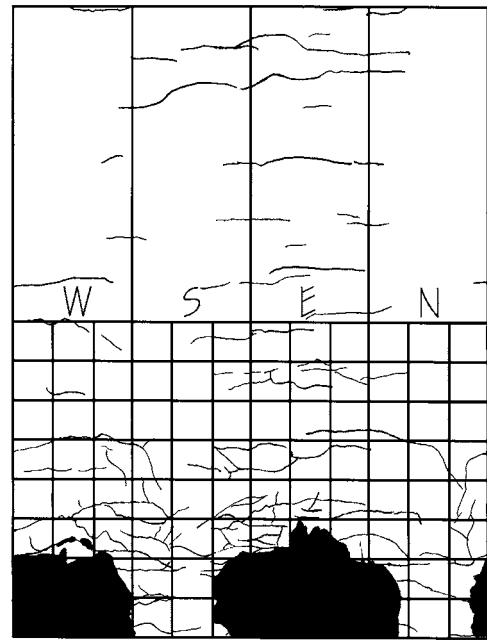
Figure C-17. B1-Run 9 (Max 3).
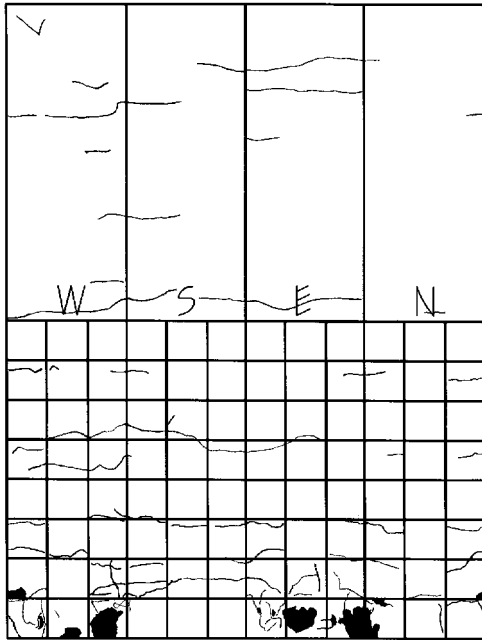
Figure C-18. B2-Run 5 (Design 1).
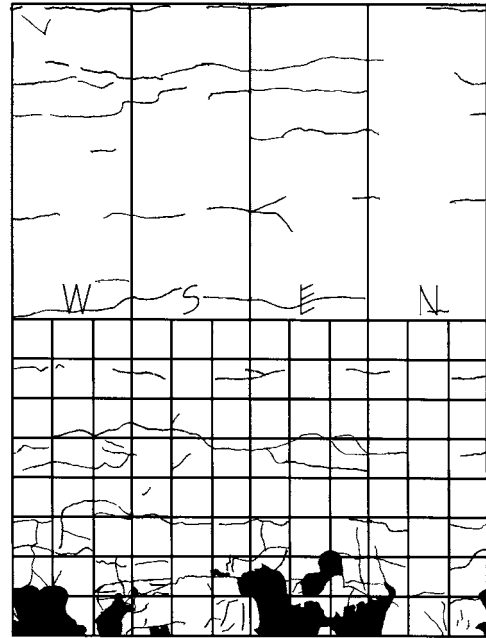
Figure C-19. B2-Run 6 (Max 1).
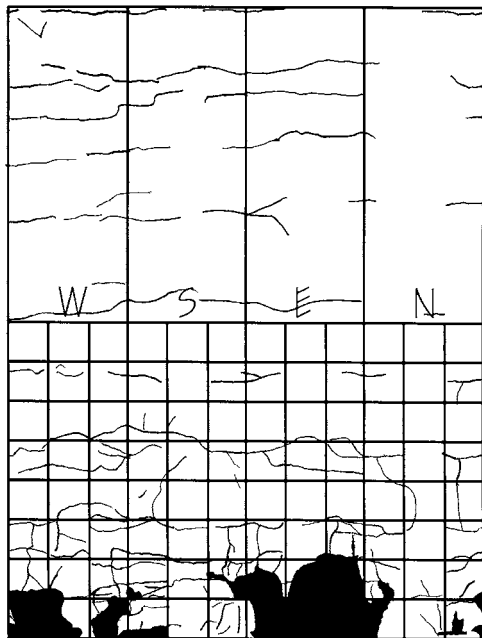
Figure C-20. B2-Run 8 (Max 2).
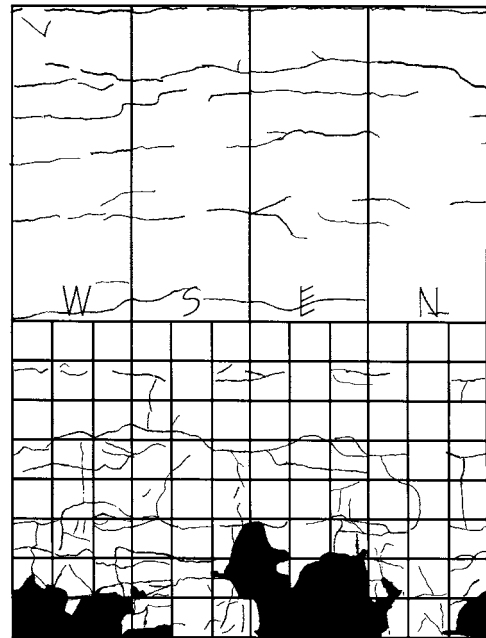
Figure C-21. B2-Run 9 (Max 3).
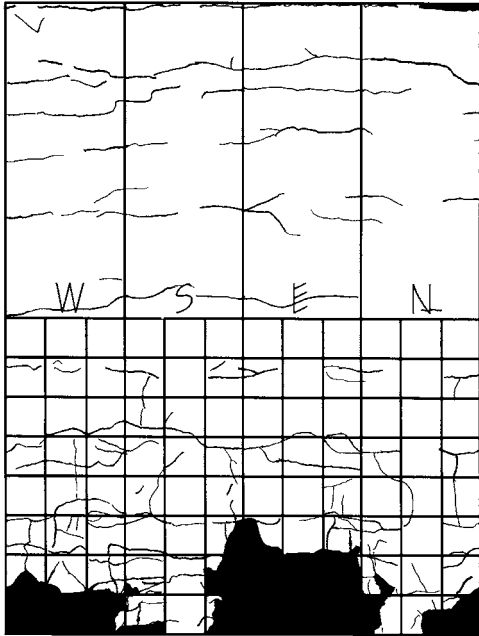
Figure C-22. B2-Run 10 (Max 4).
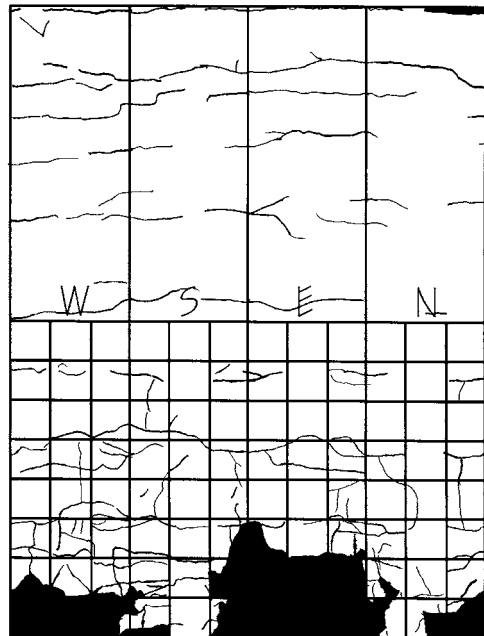
Figure C-23. B2-Run 11 (Max 5).
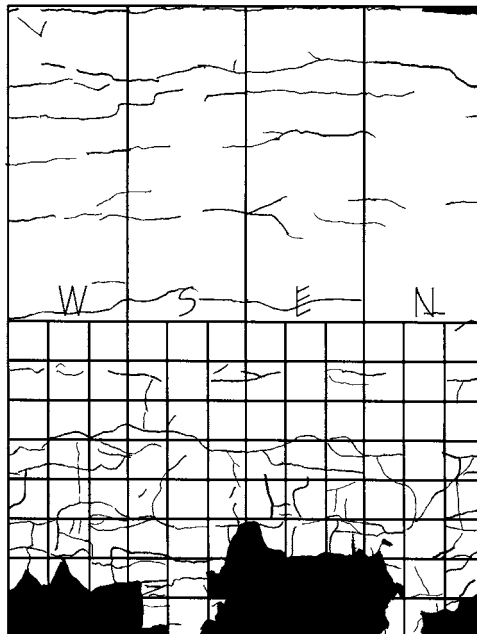
Figure C-24. B2-Run 13 (Max 7).
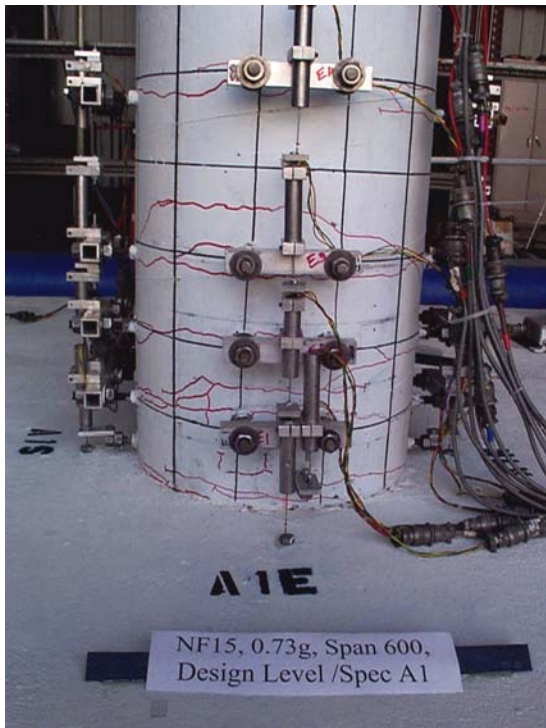
Figure C-25. Specimen A1 after Run 2 (east face).
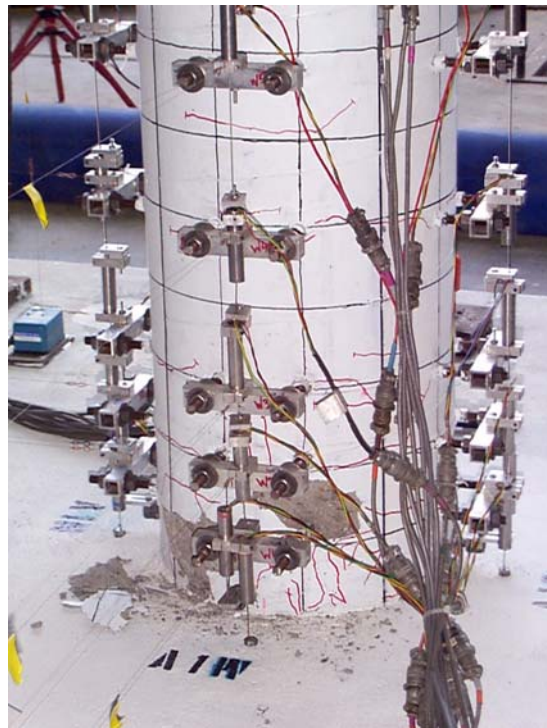
Figure C-26. Specimen A1 after Run 2 (west face).
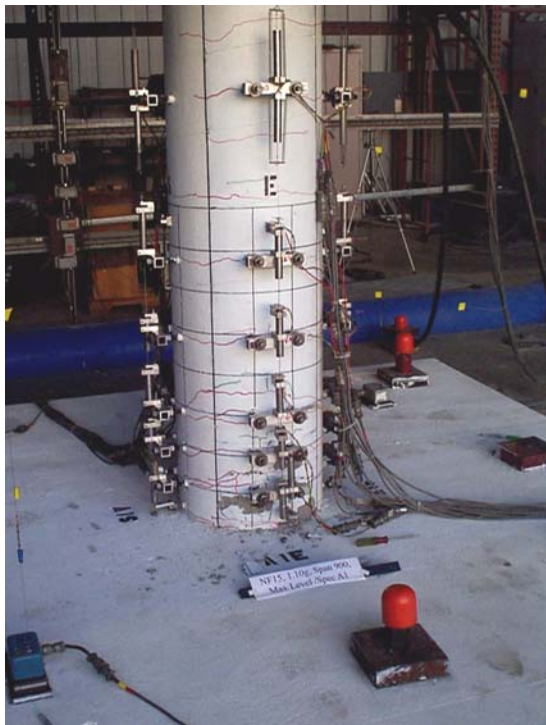
Figure C-27. Specimen A1 after Run 3 (east face).
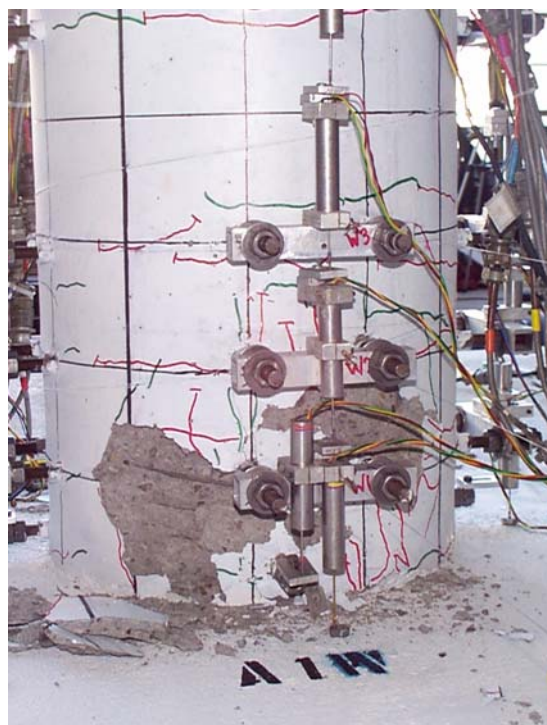
Figure C-28. Specimen A1 after Run 3 (west face).
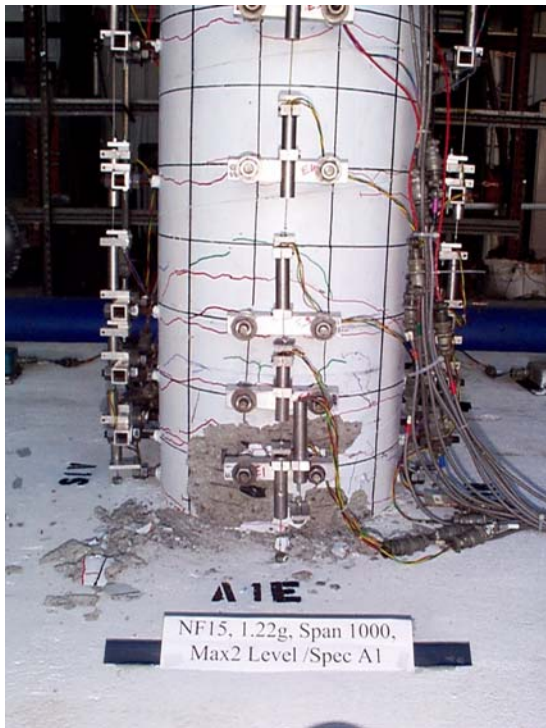
Figure C-29. Specimen A1 after Run 5 (east face).
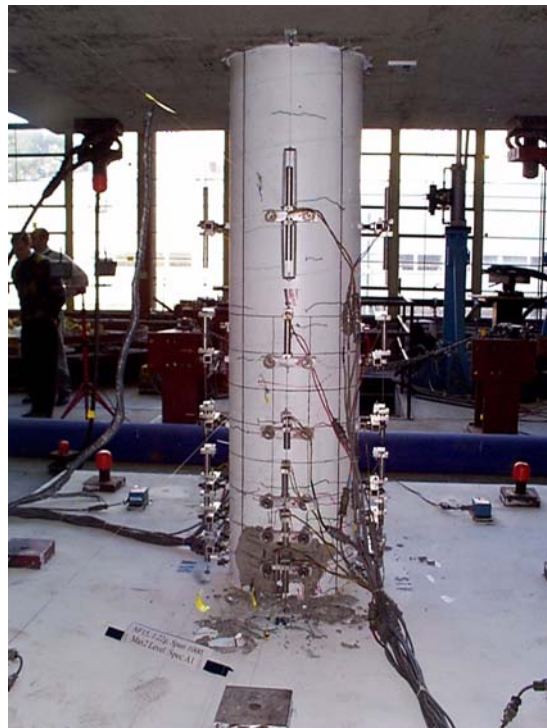
Figure C-30. Specimen A1 after Run 5 (west face).

Figure C-31. Specimen A1 after Run 8 (east face).
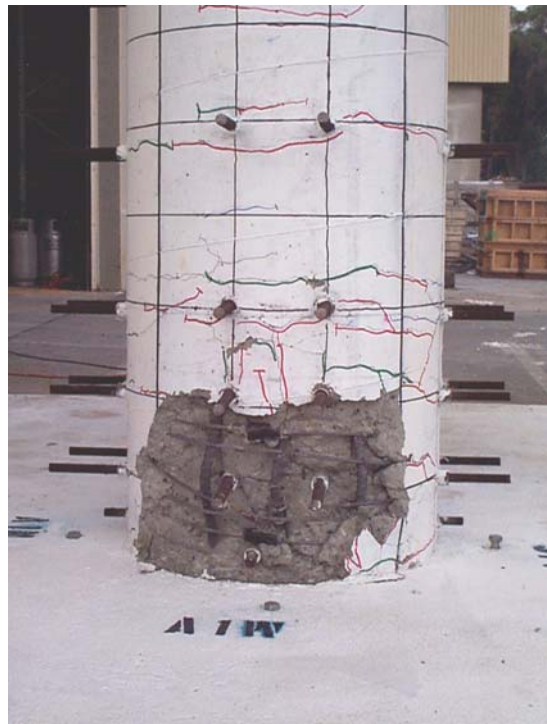
Figure C-32. Specimen A1 after Run 8 (west face).

Figure C-33. Specimen A1 after Run 8. Fractured bar #3 on the east face is shown.

Figure C-34. West face of specimen A1 after Run 8. One fractured bar (#9), a buckled bar (#10), and a fractured spiral are shown.
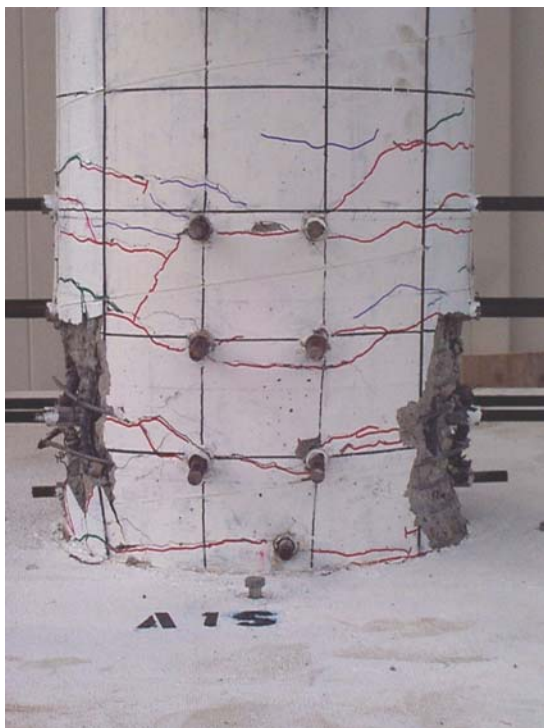
Figure C-35. Specimen A1 after Run 8 (south face).

Figure C-36. Specimen A1 after Run 8. Another view of the west face with the fracture bar (#9).

367

Figure C-37. Specimen A2 after Run 2 (east face).
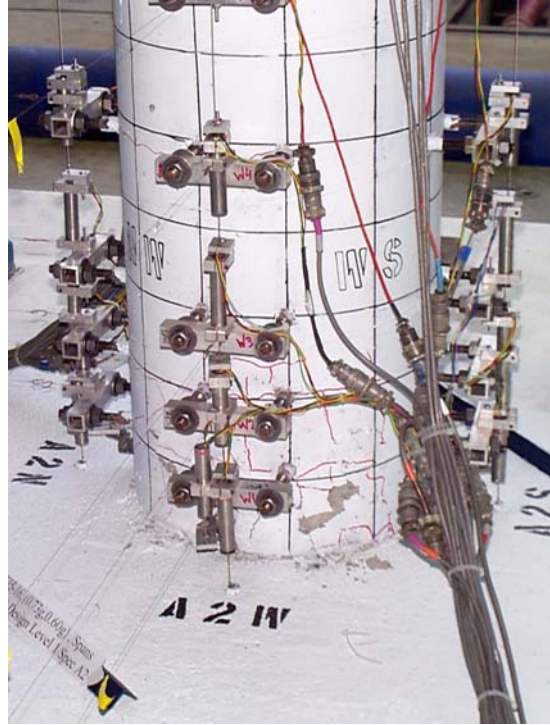
Figure C-38. Specimen A2 after Run 2 (west face).
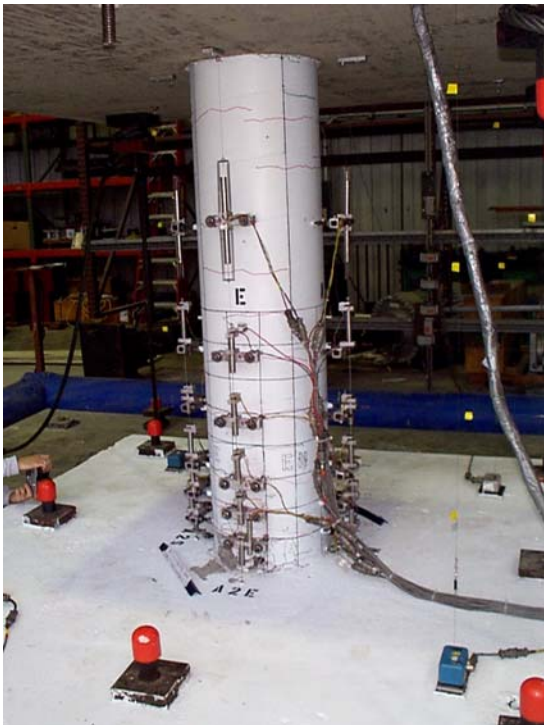
Figure C-39. Specimen A2 after Run 3 (east face).
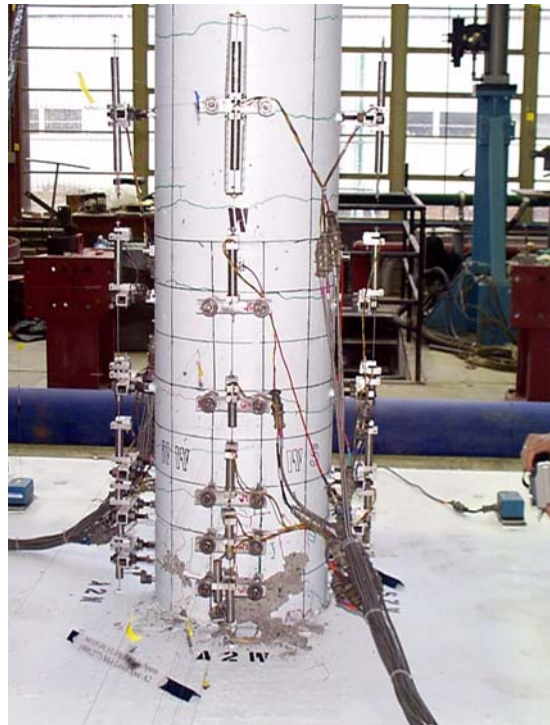
Figure C-40. Specimen A2 after Run 3 (west face).
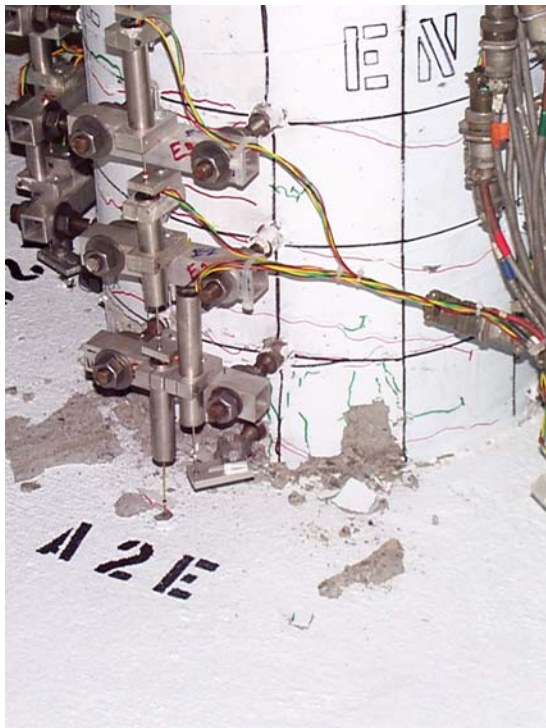
Figure C-41. Specimen A2 after Run 4 (east face).

Figure C-42. Specimen A2 after Run 4 (west face).
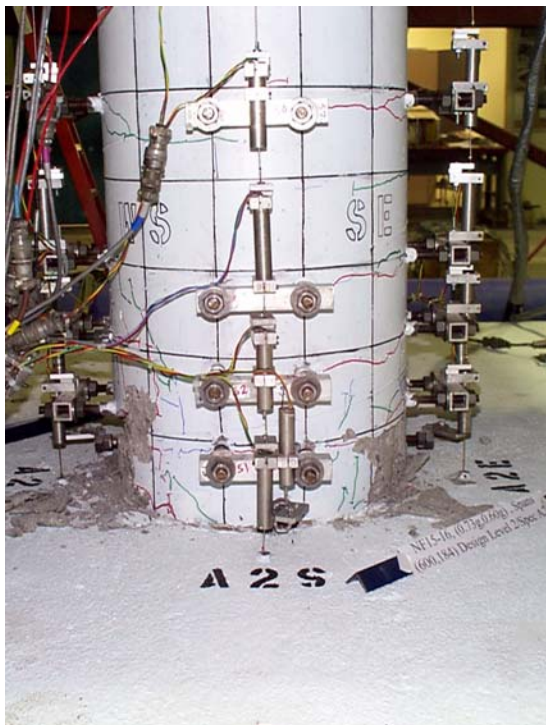
Figure C-43. Specimen A2 after Run 4 (south face).
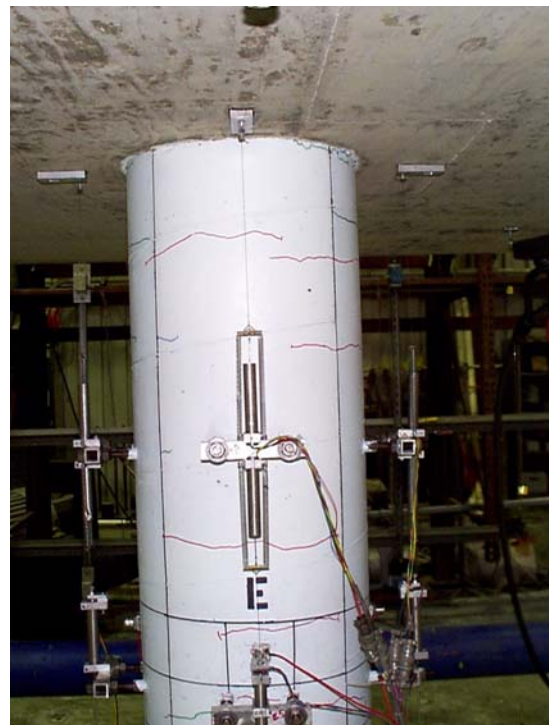
Figure C-44. Specimen A2 after Run 4 (east face). Cracks extended throughout the height of the column.
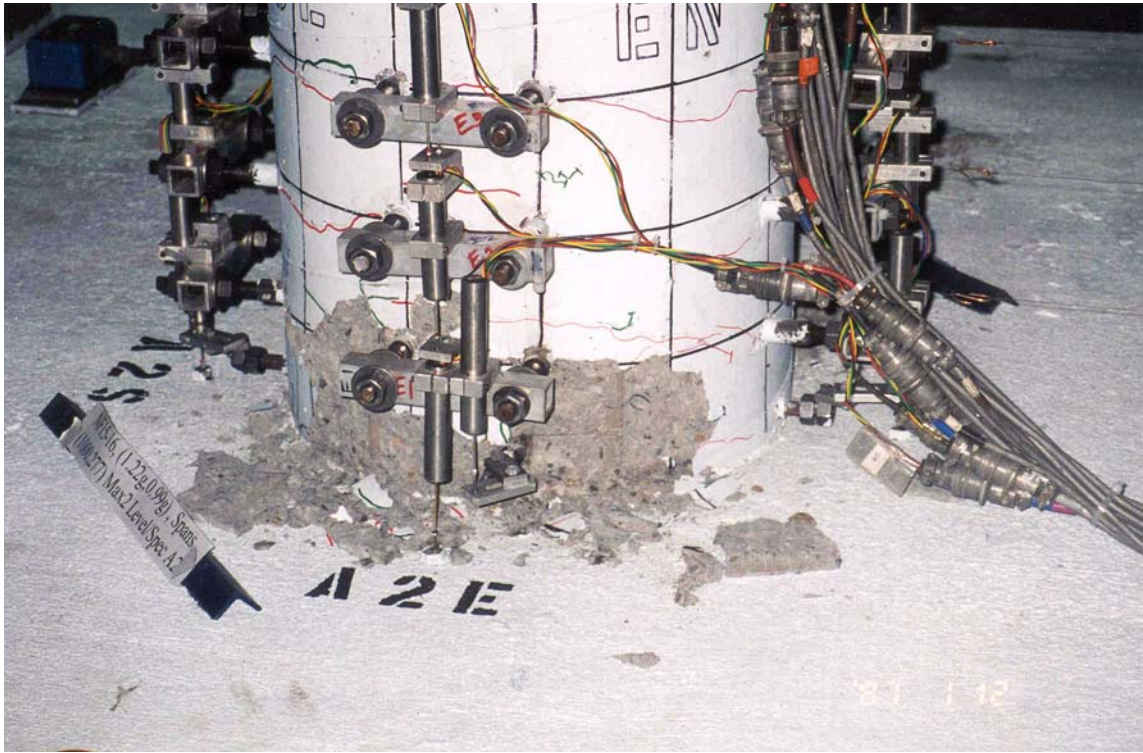
Figure C-45. Specimen A2 after Run 5 (east face).
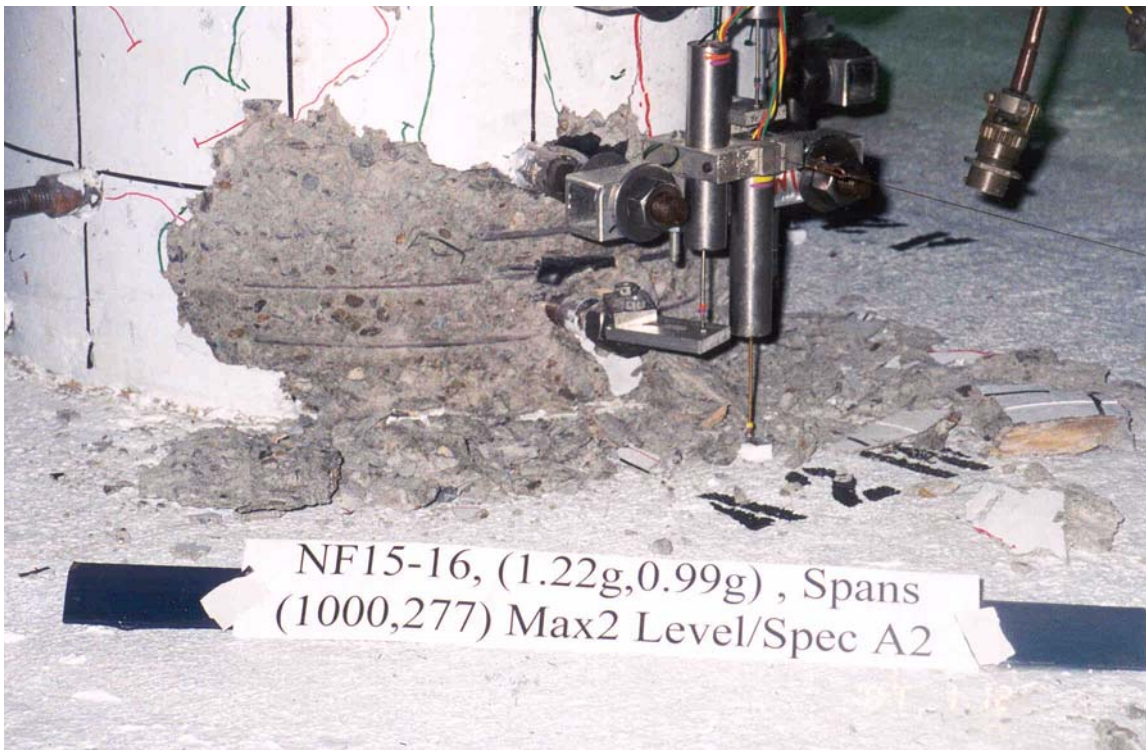
Figure C-46. Specimen A2 after Run 5 (west face).
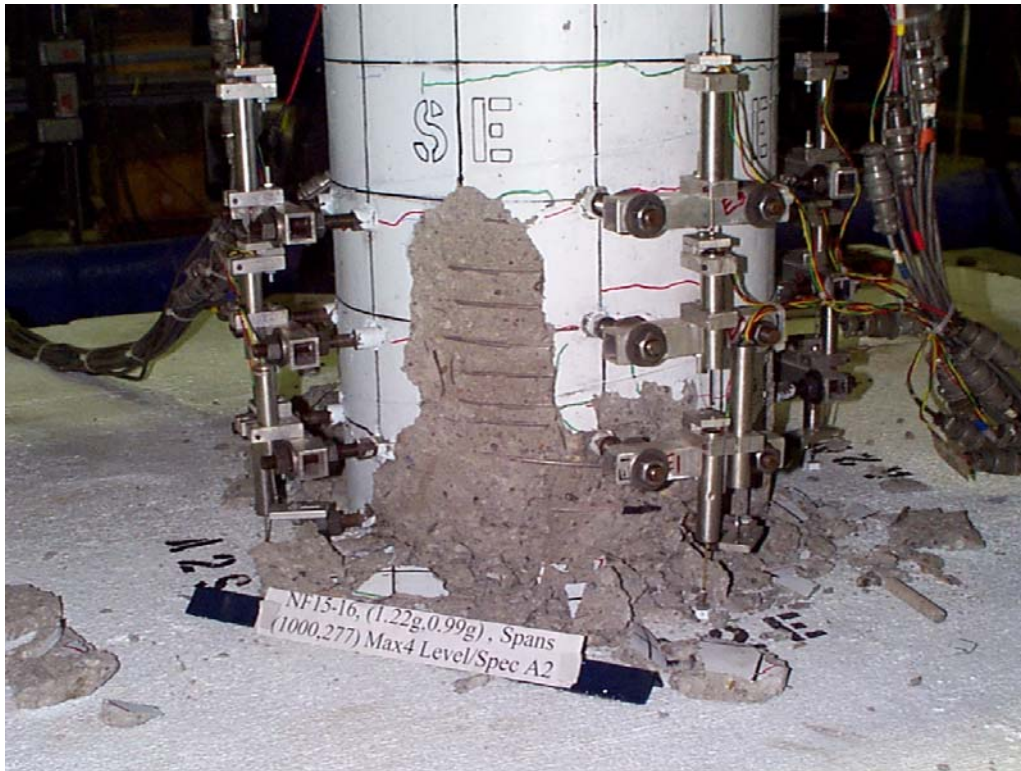
Figure C-47. Specimen A2 after Run 8 (east face).
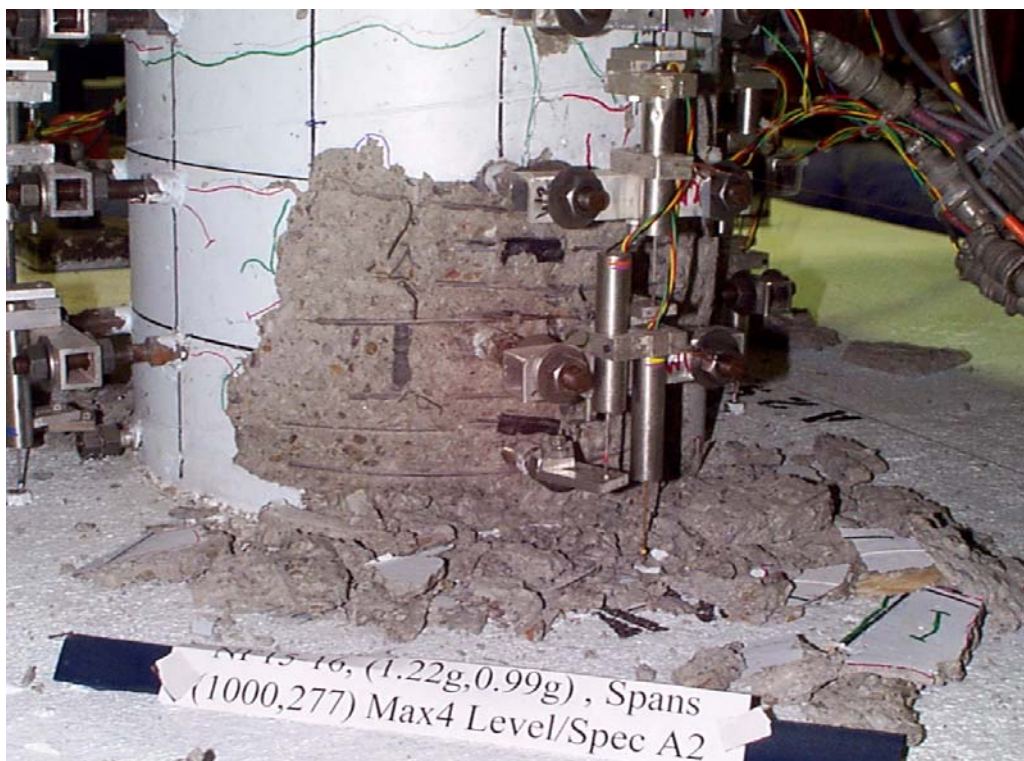
Figure C-48. Specimen A2 after Run 8 (west face).
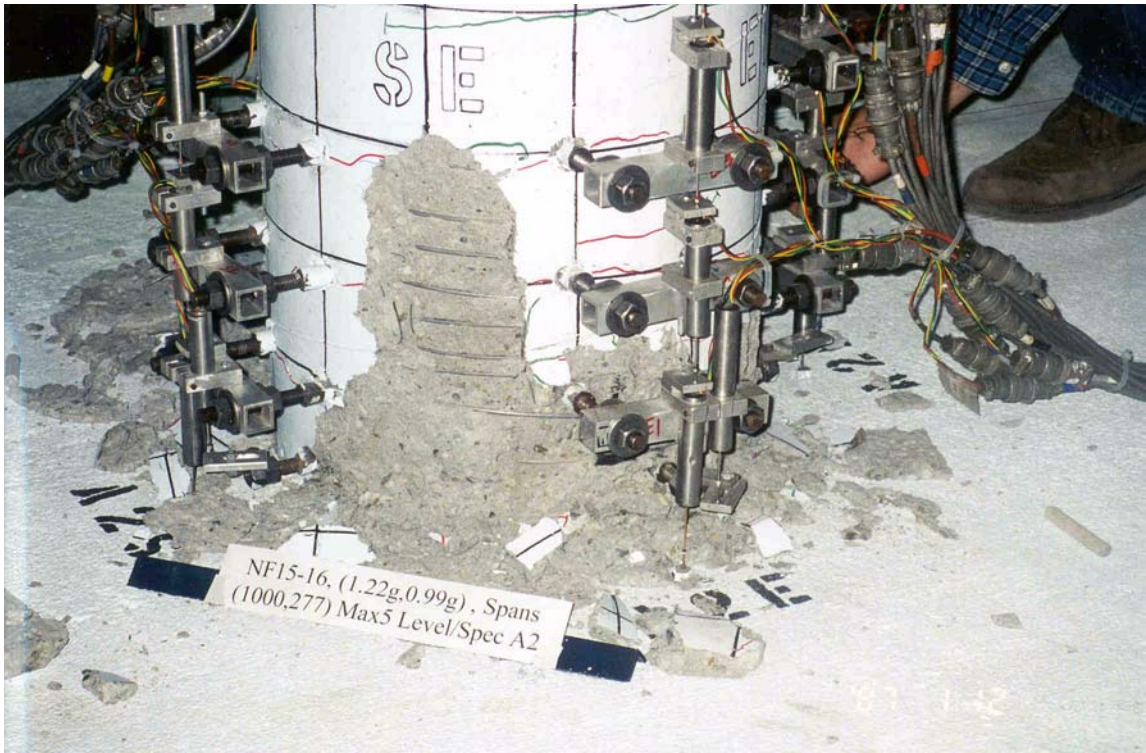
Figure C-49. Specimen A2 after Run 9 (east face).

Figure C-50. Specimen A2 after Run 9 (west face).

Figure C-51. Specimen A2 after Run 10 (east face).

Figure C-52. Specimen A2 after Run 10 (west face).

Figure C-53. Specimen A2 at the end of the last run (Run 10). The column had a residual displacement of about 6 inches (at the mass center).

Figure C-54. Close-up on bar #9 on the west side which fractured in Run 9. The distance between the ends of the bar is caused by the residual displacement at the end of the test.

373
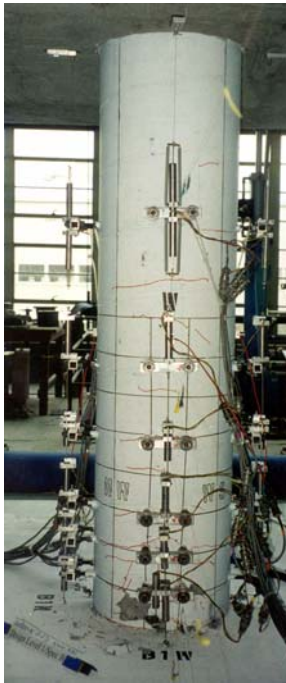
Figure C-55.
Specimen B1 after
Run 5 (west face).

Figure C-56.
Specimen B1 after
Run 5 (south face).
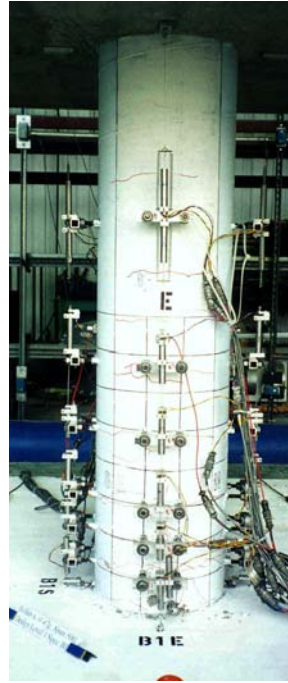
Figure C-57.
Specimen B1 after
Run 5 (east face).
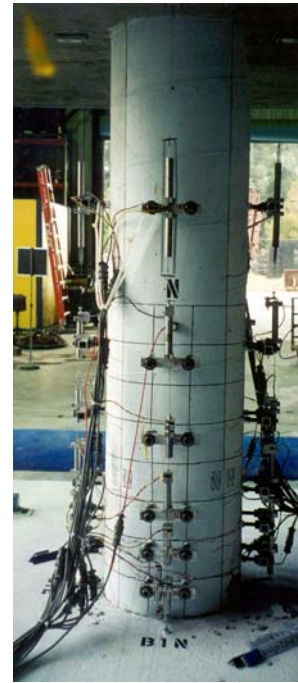
Figure C-58.
Specimen B1 after
Run 5 (north face).
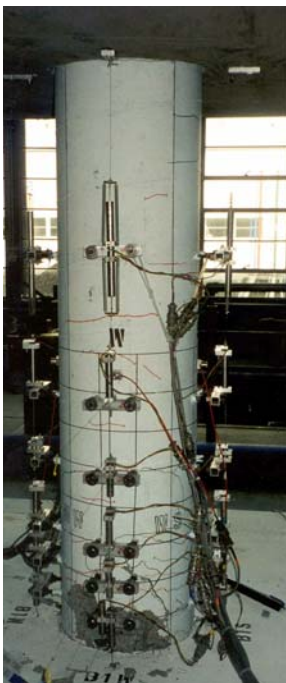
Figure C-59.
Specimen B1 after
Run 6 (west face).
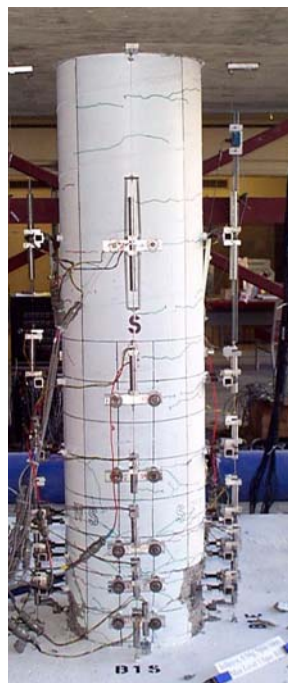
Figure C-60.
Specimen B1 after
Run 6 (south face).
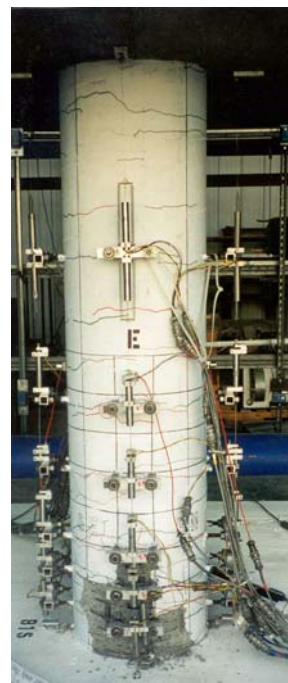
Figure C-61.
Specimen B1 after
Run 6 (east face).
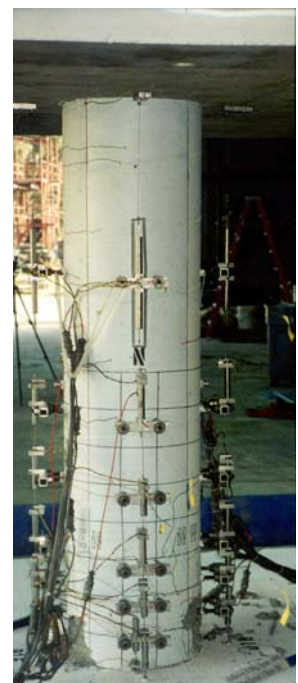
Figure C-62.
Specimen B1 after
Run 5 (north face).

374
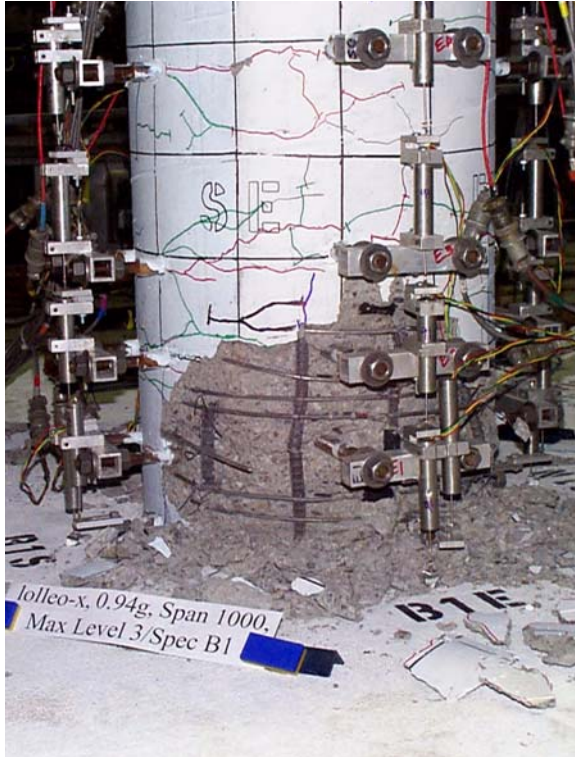
Figure C-63. Specimen B1 after Run 9 (east face).
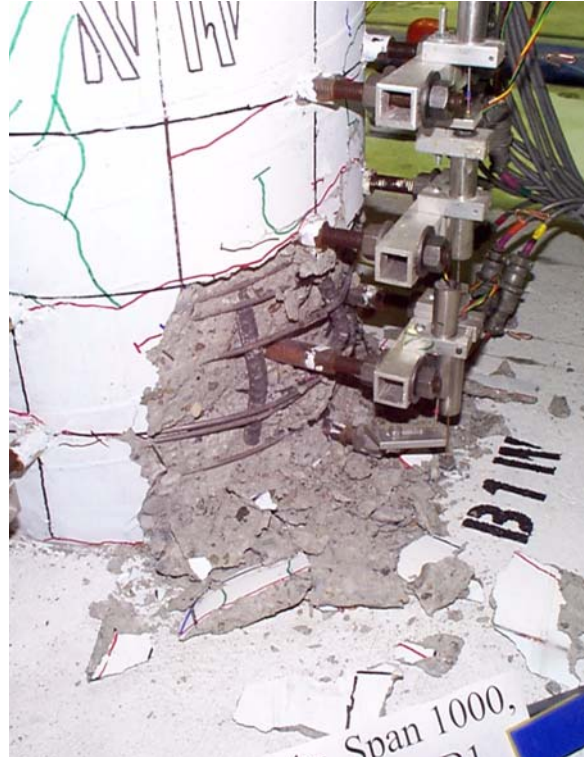
Figure C-64. Specimen B1 after Run 9 (west face).
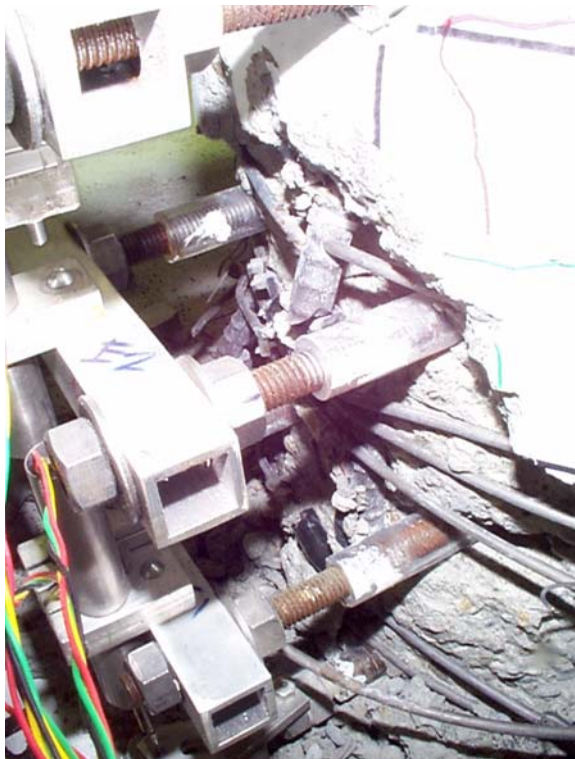
Figure C-65. Close-up on bar #3 on the east side which fractured in Run 8.
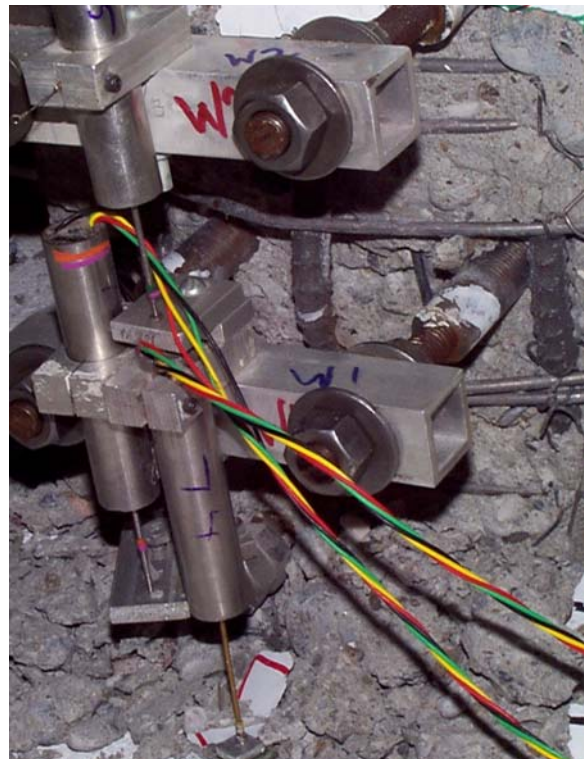
Figure C-66. Close-up on bar #9 on the west side which fractured in Run 8.

Figure C-67.
Specimen B2 after
Run 8 (west face).

Figure C-68.
Specimen B2 after
Run 8 (south face).
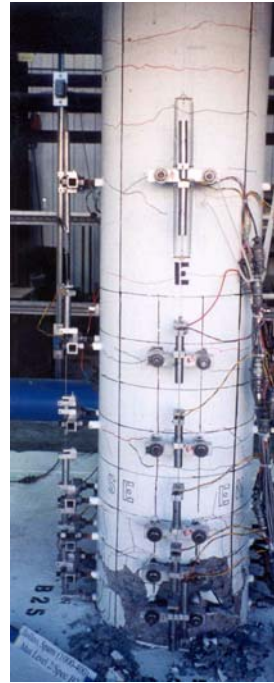
Figure C-69.
Specimen B2 after
Run 8 (east face).

Figure C-70.
Specimen B2 after
Run 8 (north face).
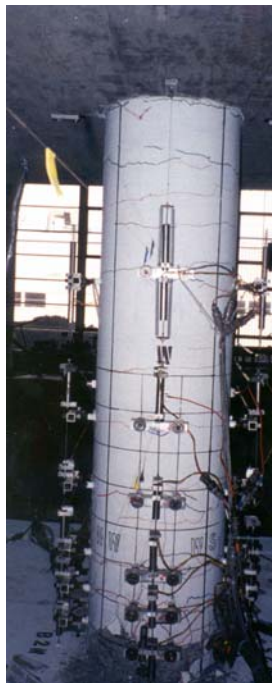
Figure C-71.
Specimen B2 after
Run 9 (west face).

Figure C-72.
Specimen B2 after
Run 9 (south face).

Figure C-73.
Specimen B2 after
Run 9 (east face).

Figure C-74.
Specimen B2 after
Run 9 (north face).

376

Figure C-75. Specimen B1 after Run 11 (east face).
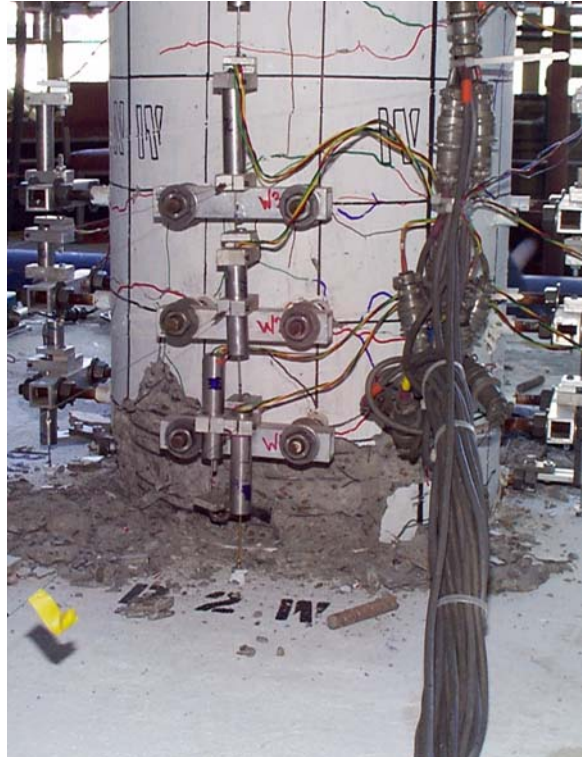
Figure C-76. Specimen B1 after Run 11 (west face).
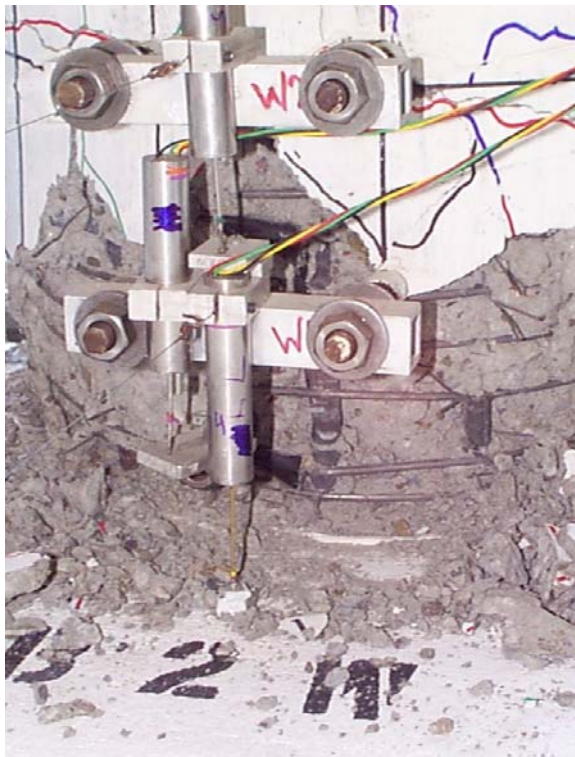
Figure C-77. Specimen B1 after Run 12 (east face).
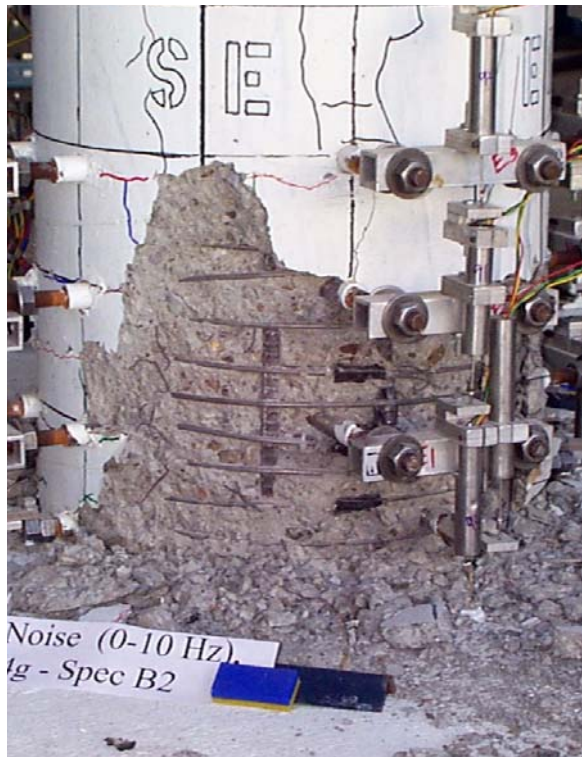
Figure C-78. Specimen B1 after Run 12 (west face).

Figure C-79. Specimen B1 after Run 13 (east face).

Figure C-80. Specimen B1 after Run 13 (west face).

Figure C-81. Close-up on bar #3 on the east side which fractured in Run 12.

Figure C-82. Close-up on bar #9 on the west side which fractured in Run 12.

Appendix D History Plots of Experimental Data

This appendix summarizes the main displacement and force response quantities for every direction of some selected runs. They are organized as follows:

1. Specimen A1: Figures D-1 to D-4.

2. Specimen A2: Figures D-5 to D-14.

3. Specimen B1: Figures D-15 to D-18.

4. Specimen B2: Figures D-19 to D-28.

379
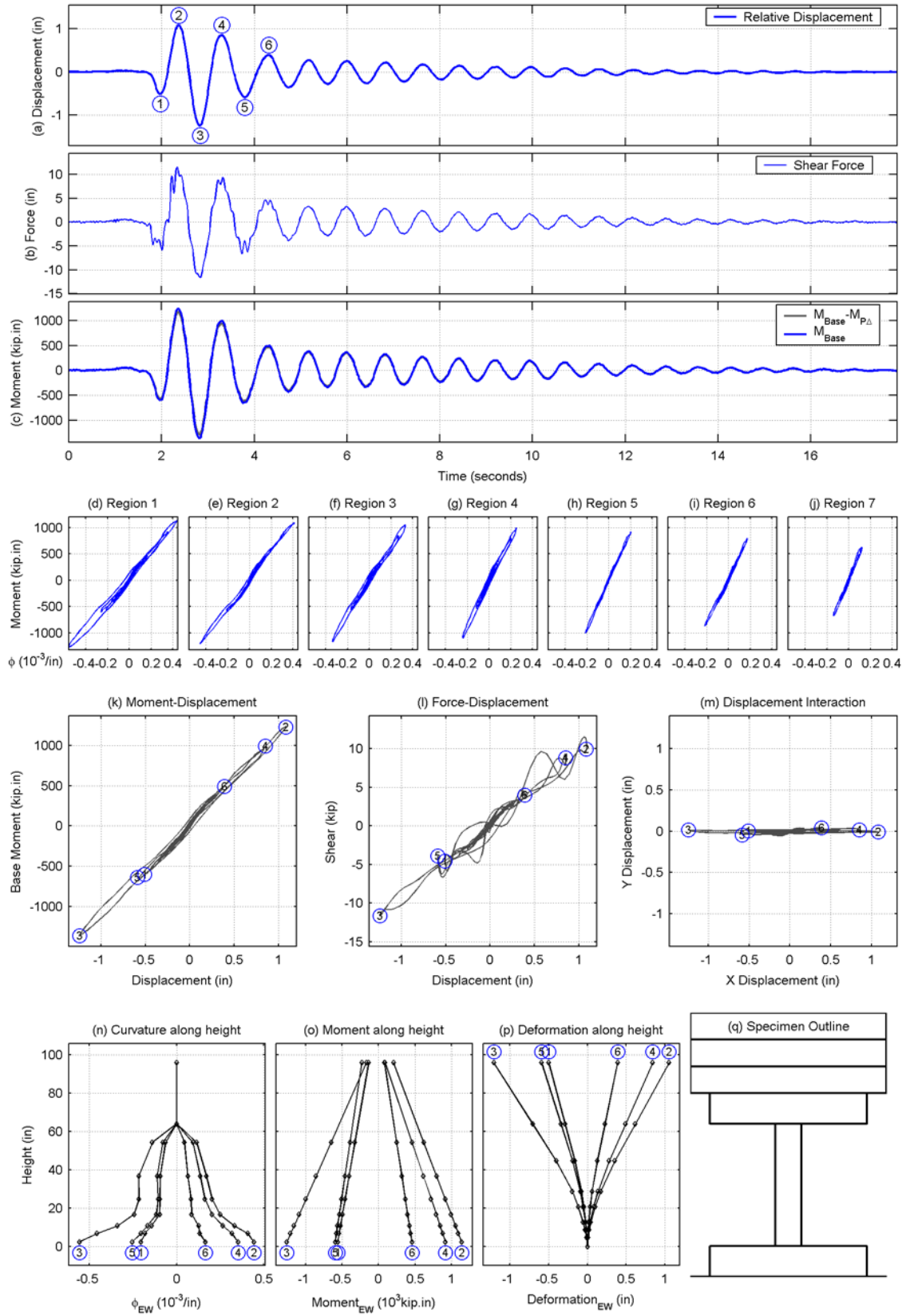
Figure D-1. Time histories and hysteresis in the longitudinal direction of Run 1 in test A1.
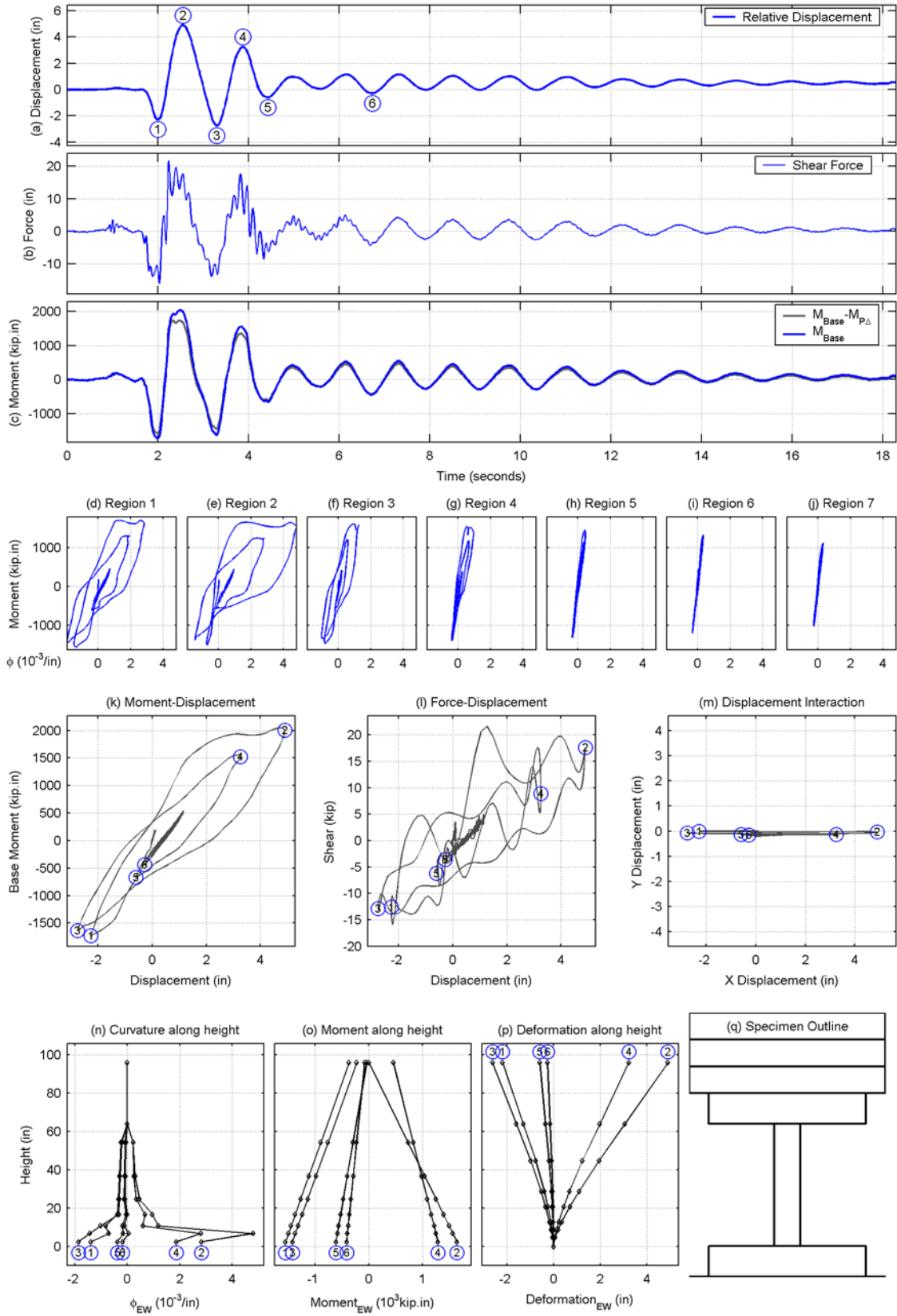
Figure D-2. Time histories and hysteresis in the longitudinal direction of Run 2 in test A1.
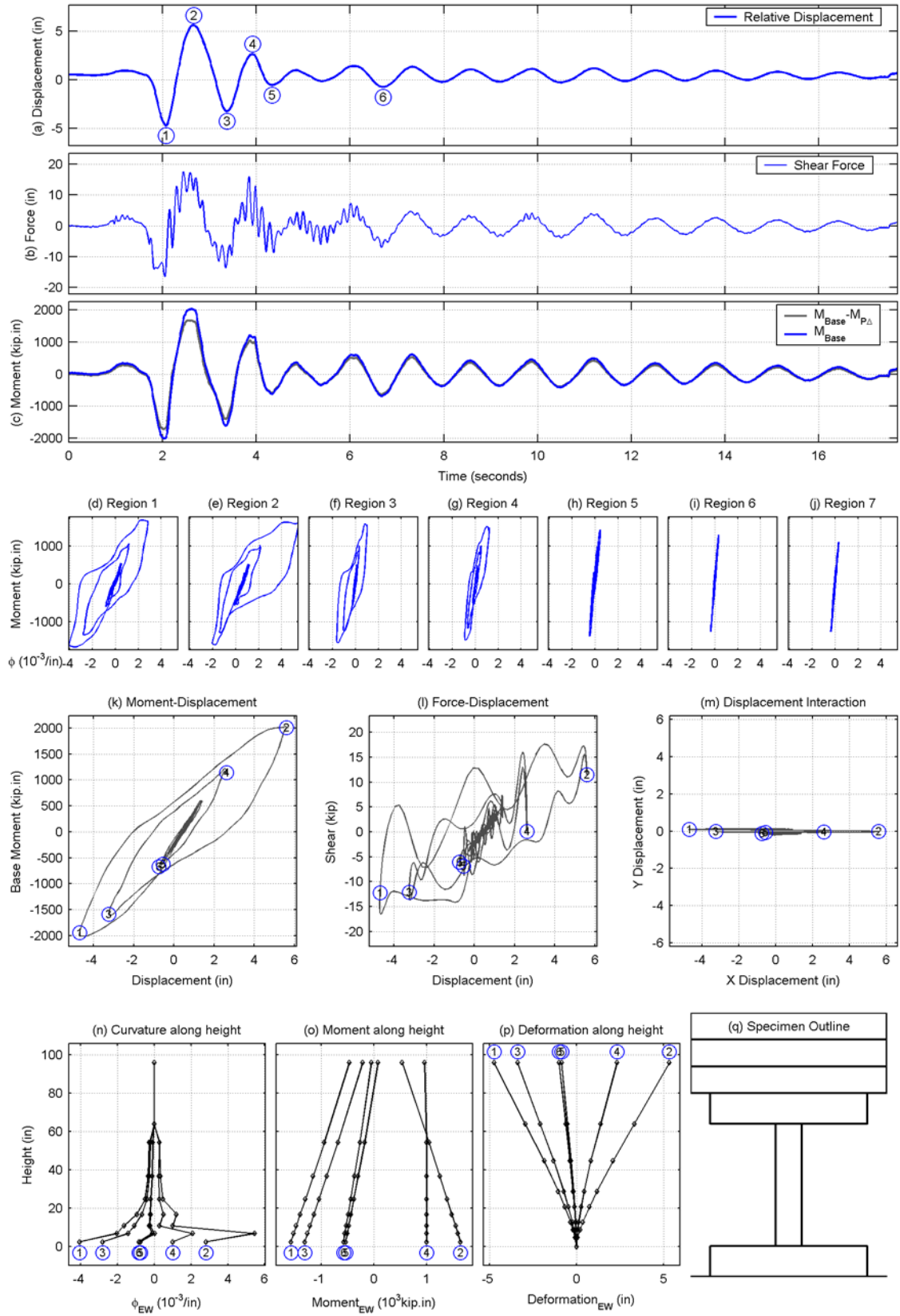
Figure D-3. Time histories and hysteresis in the longitudinal direction of Run 3 in test A1.

382
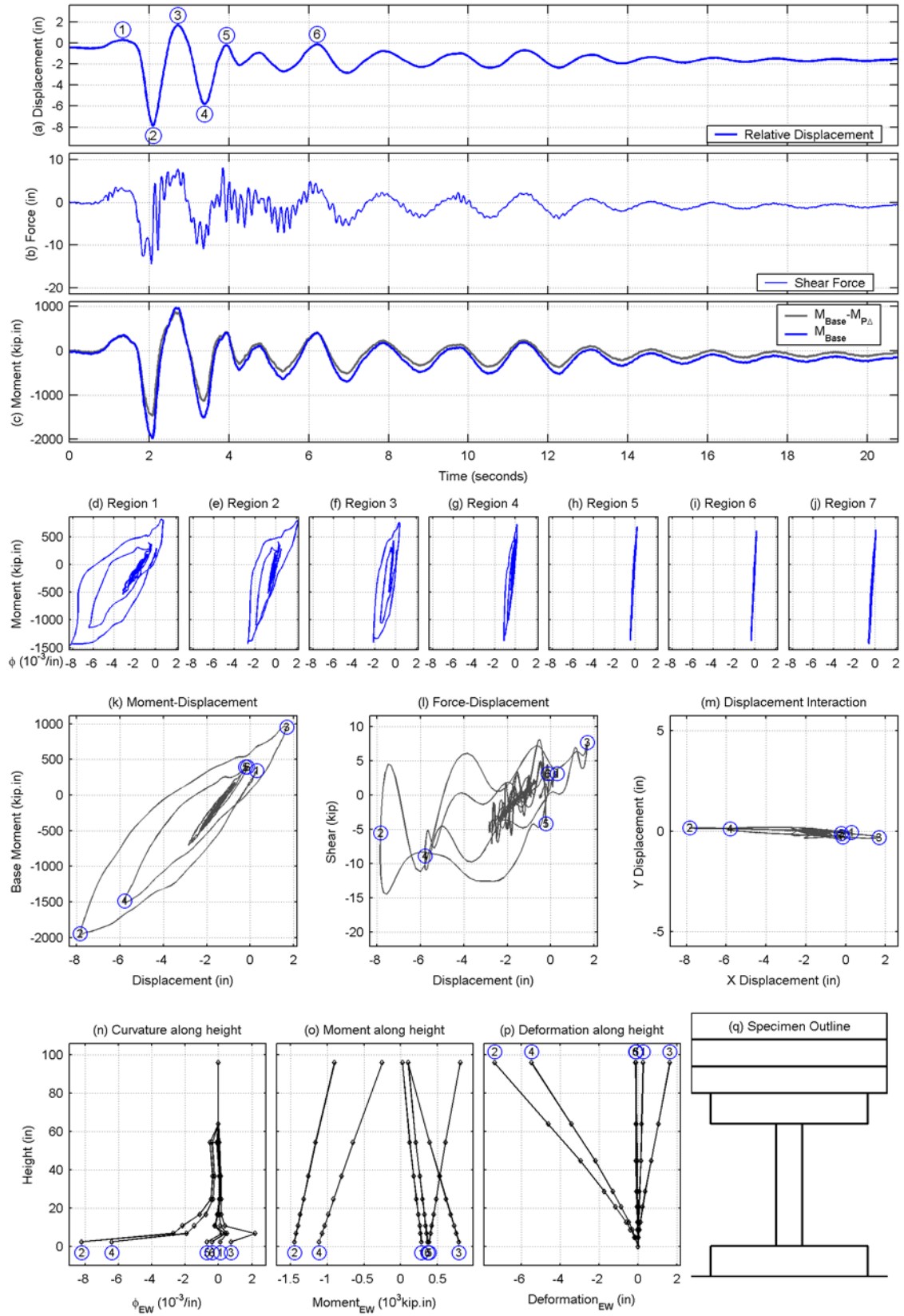
Figure D-4. Time histories and hysteresis in the longitudinal direction of Run 8 in test A1.
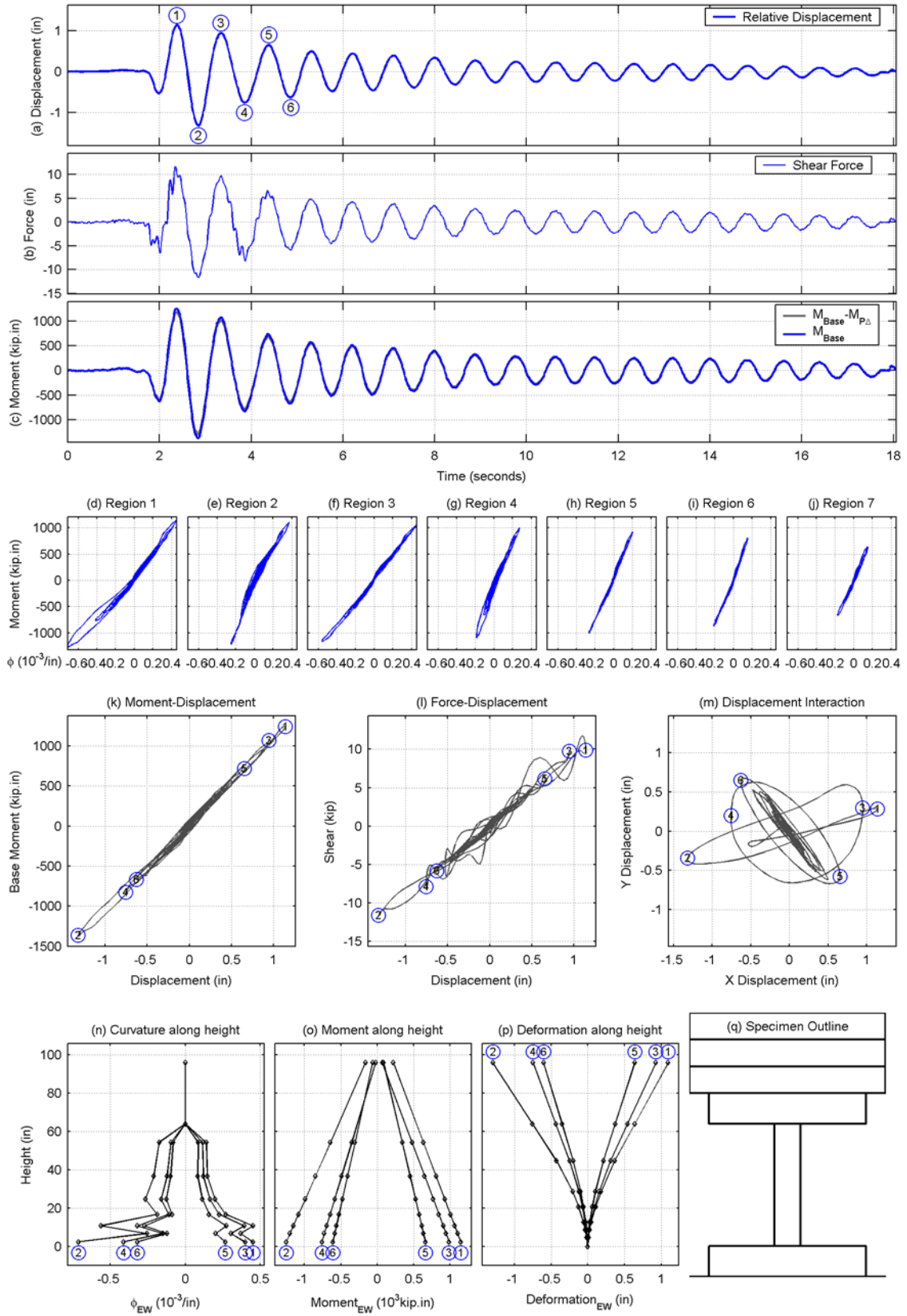
Figure D-5. Time histories and hysteresis in the longitudinal direction of Run 1 in test A2.

384
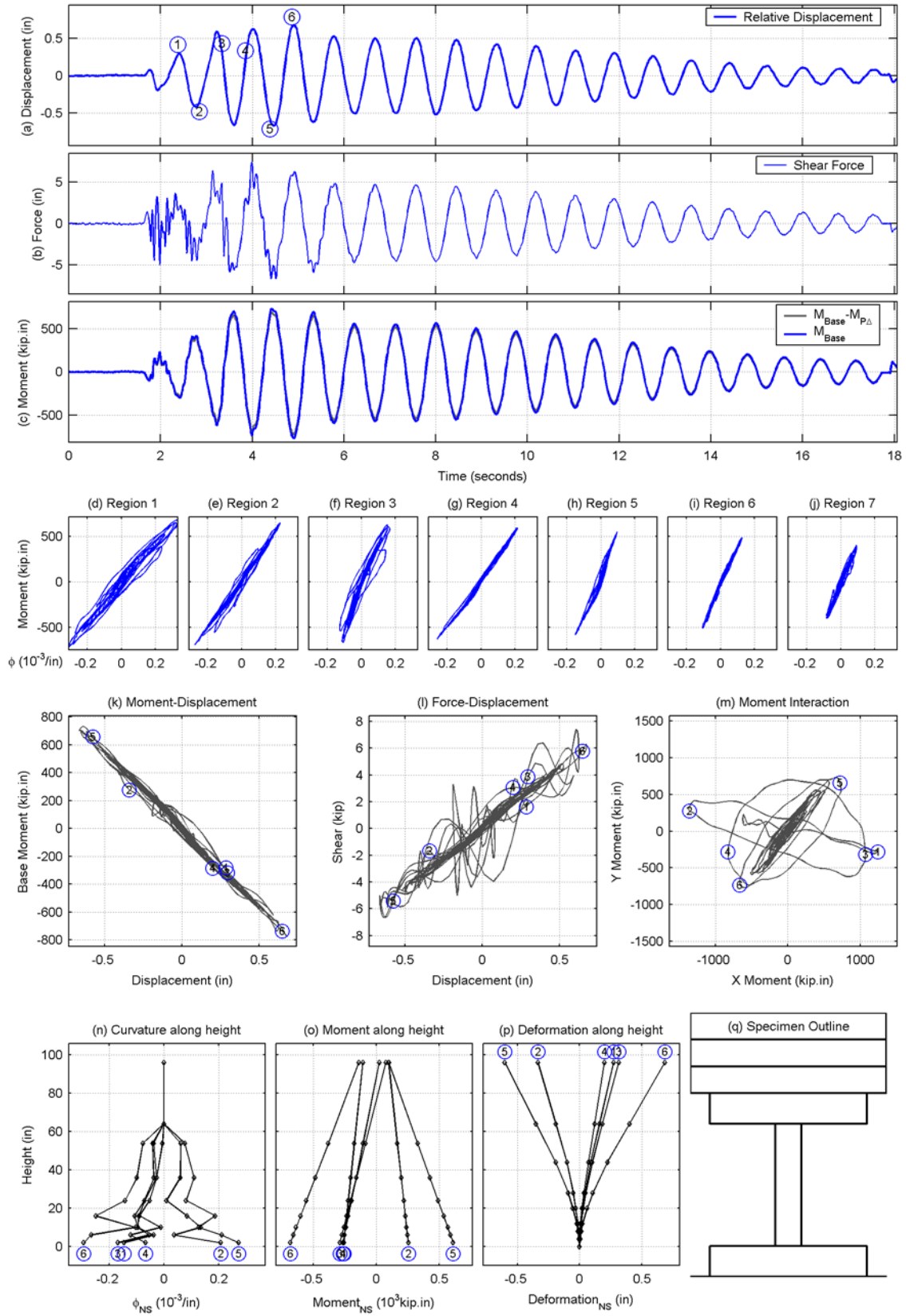
Figure D-6. Time histories and hysteresis in the lateral direction of Run 1 in test A2.
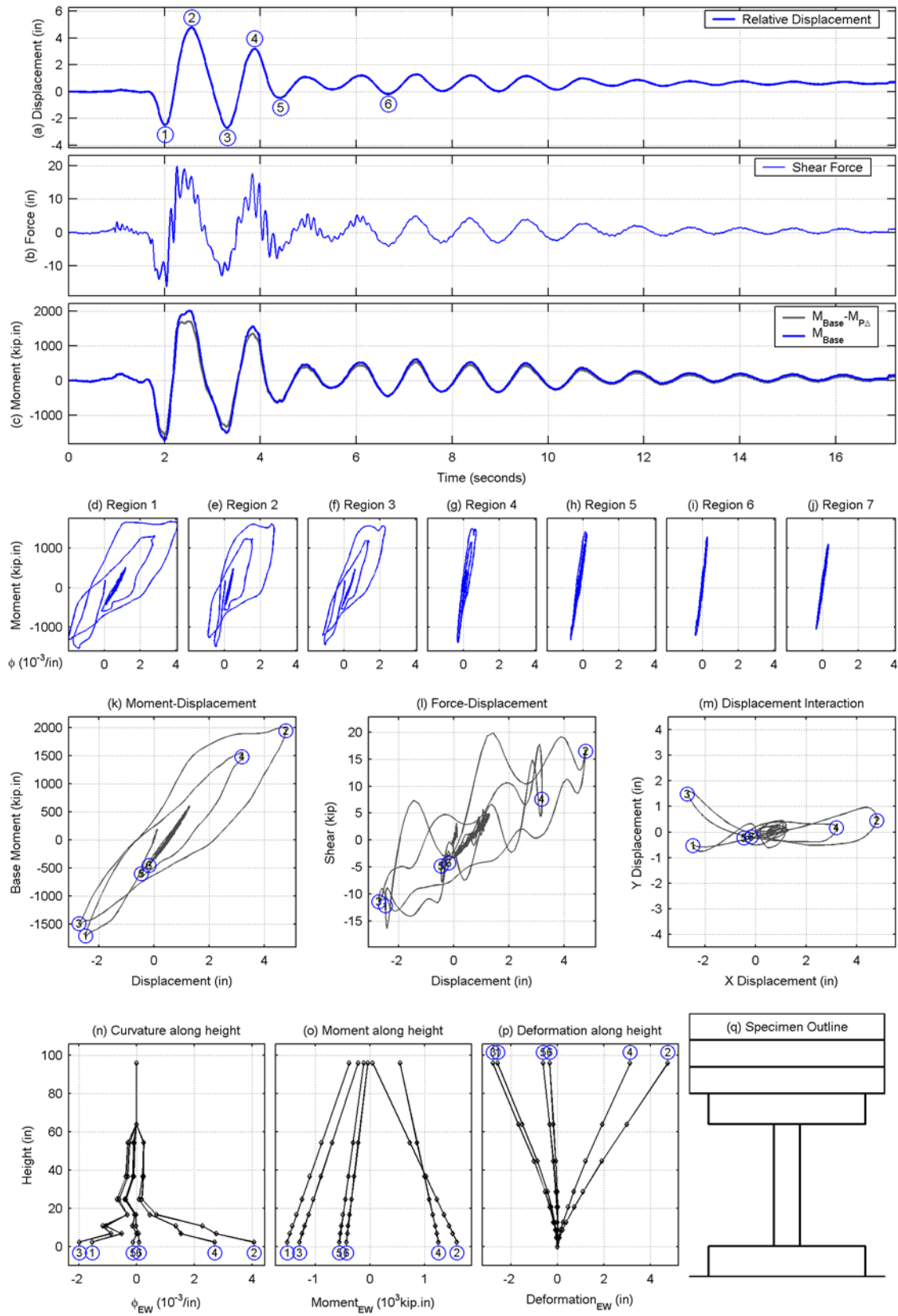
Figure D-7. Time histories and hysteresis in the longitudinal direction of Run 2 in test A2.
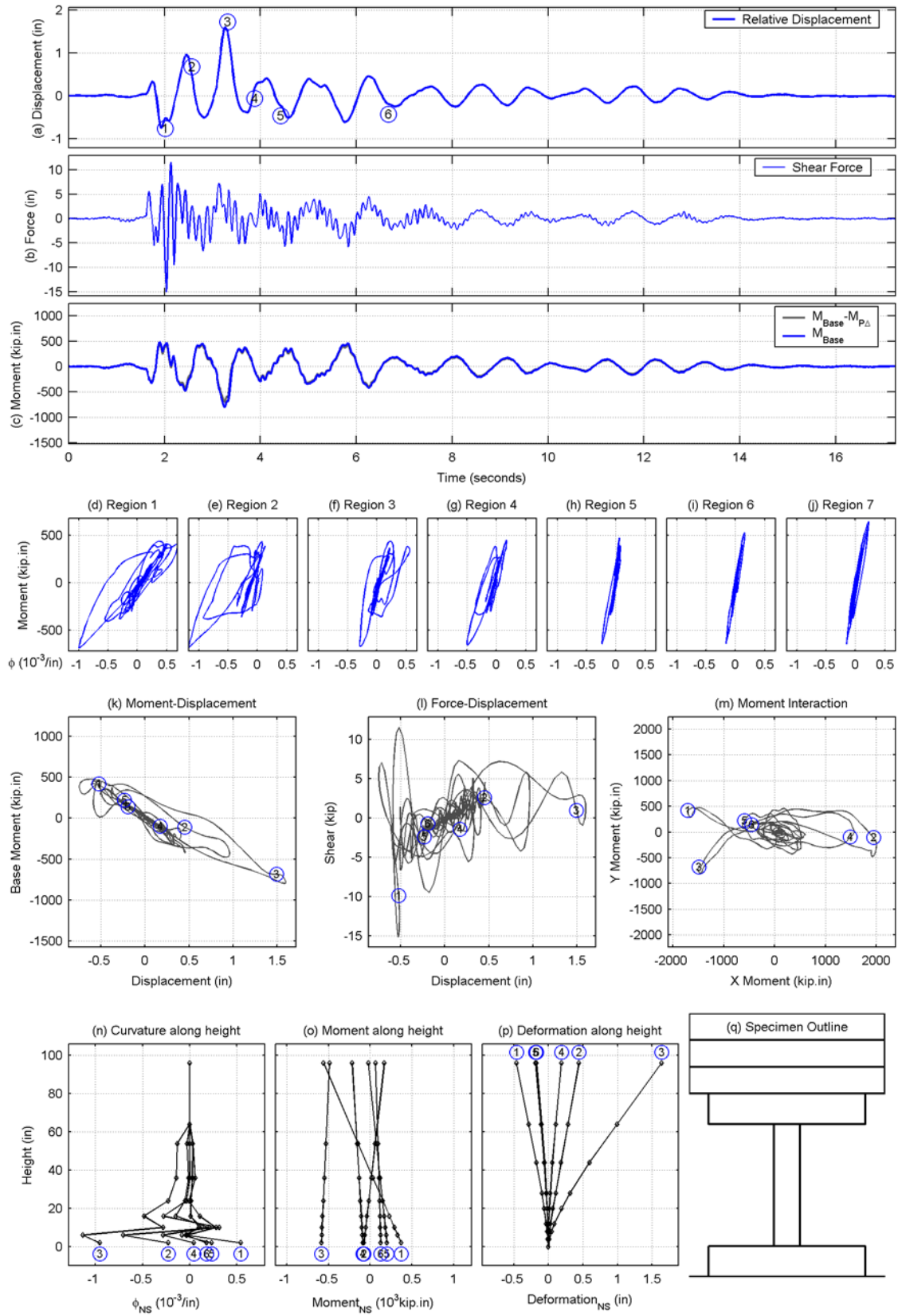
Figure D-8. Time histories and hysteresis in the lateral direction of Run 2 in test A2.
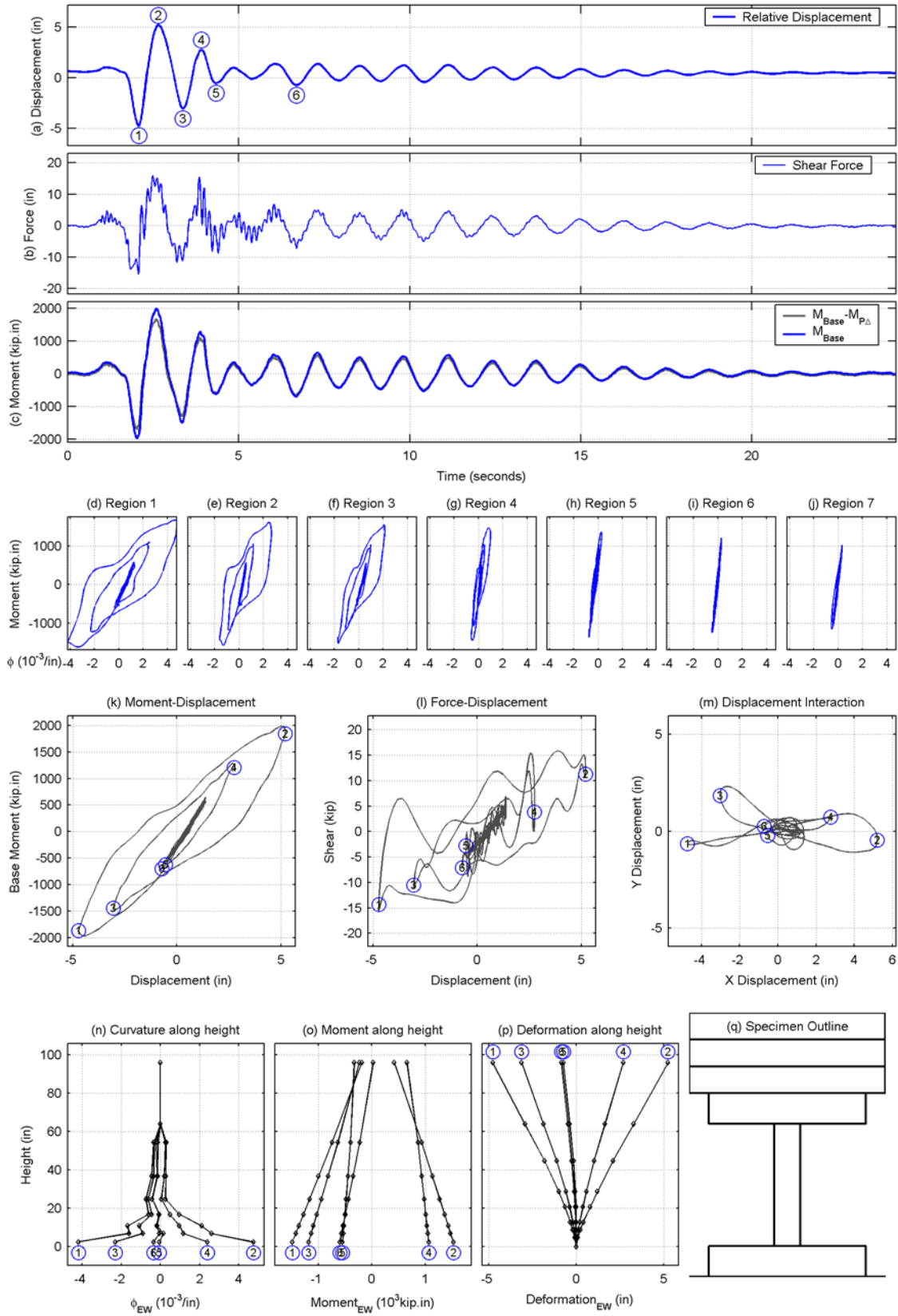
Figure D-9. Time histories and hysteresis in the longitudinal direction of Run 3 in test A2.

388
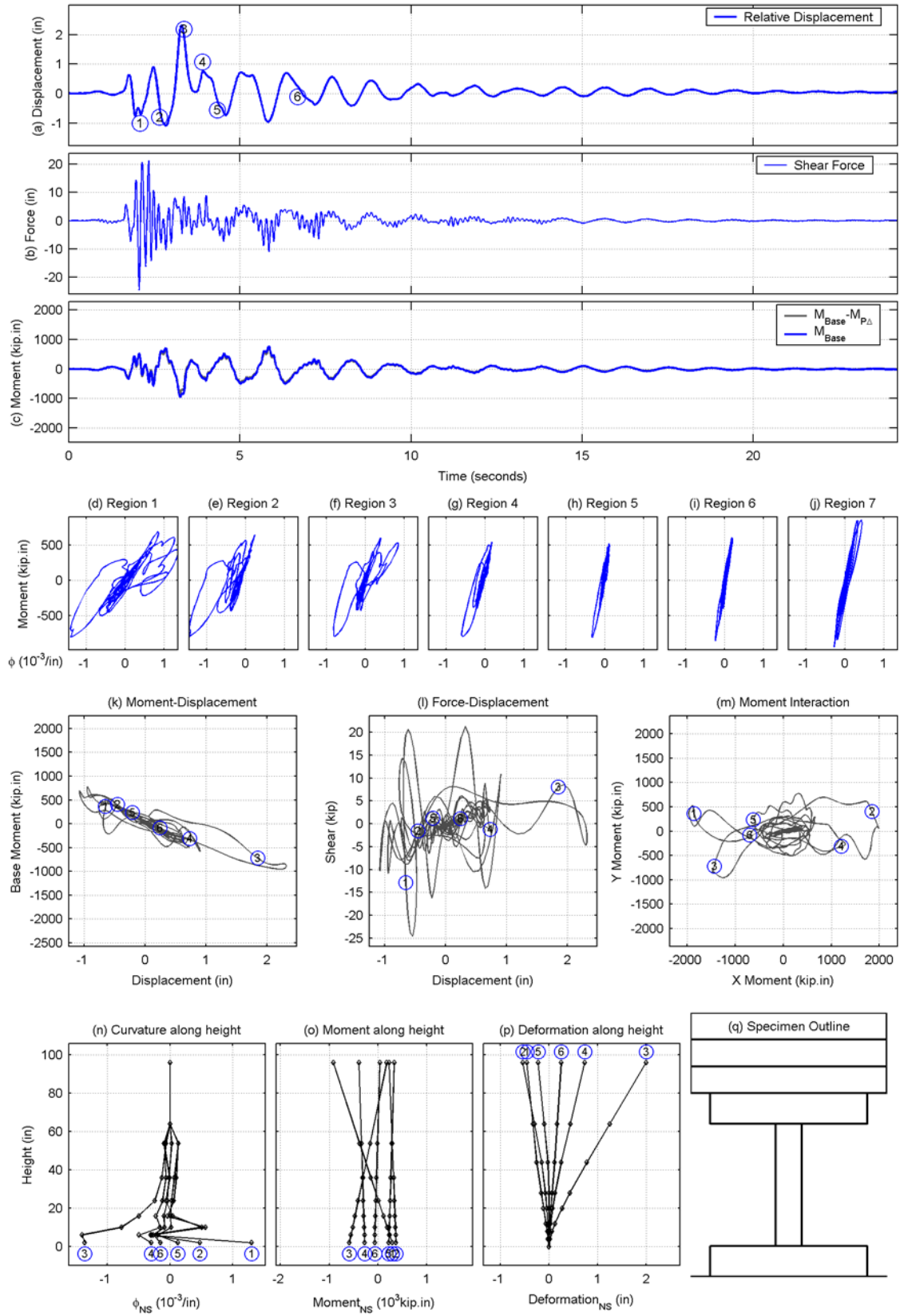
Figure D-10. Time histories and hysteresis in the lateral direction of Run 3 in test A2.

389
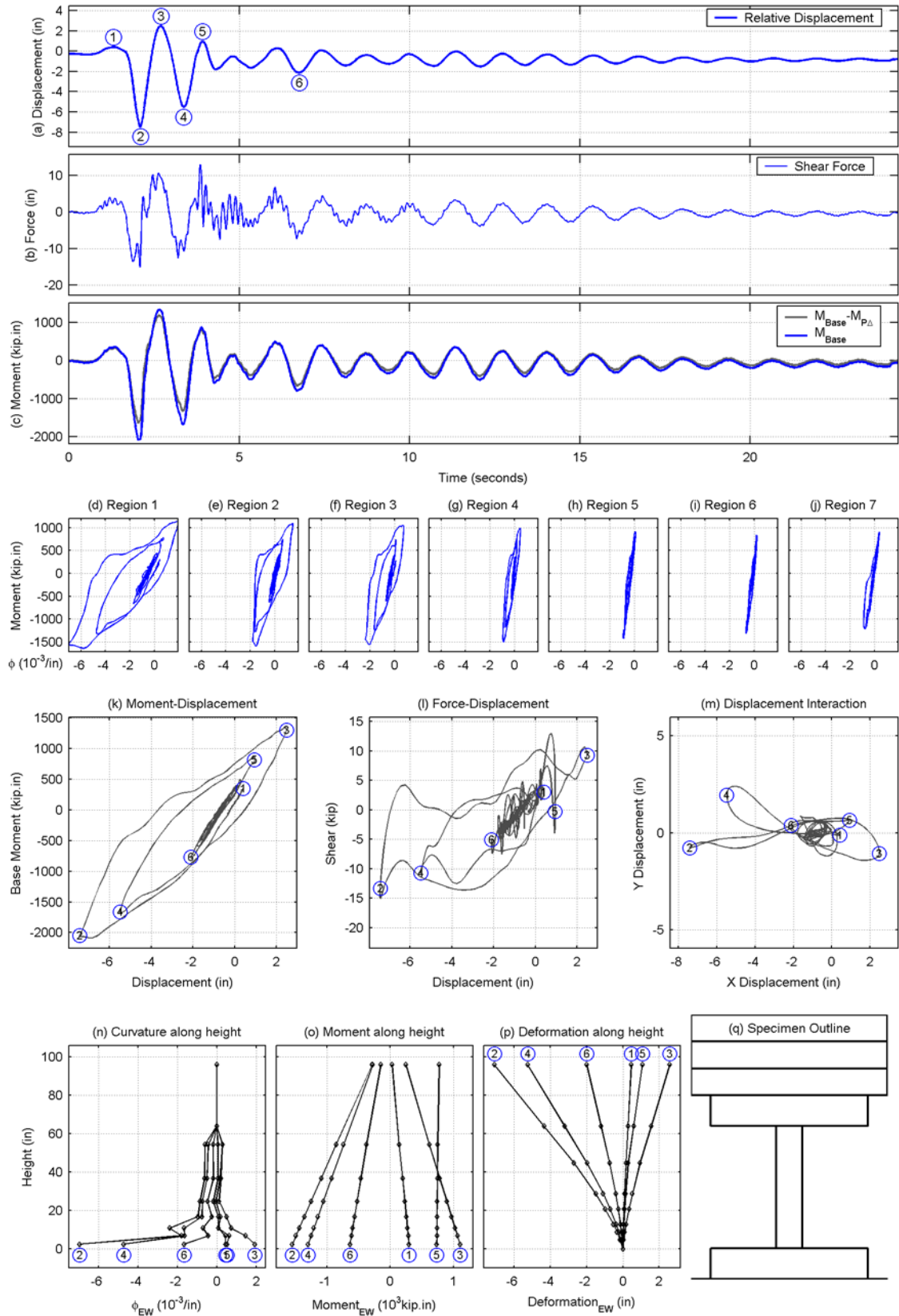
Figure D-11. Time histories and hysteresis in the longitudinal direction of Run 8 in test A2.
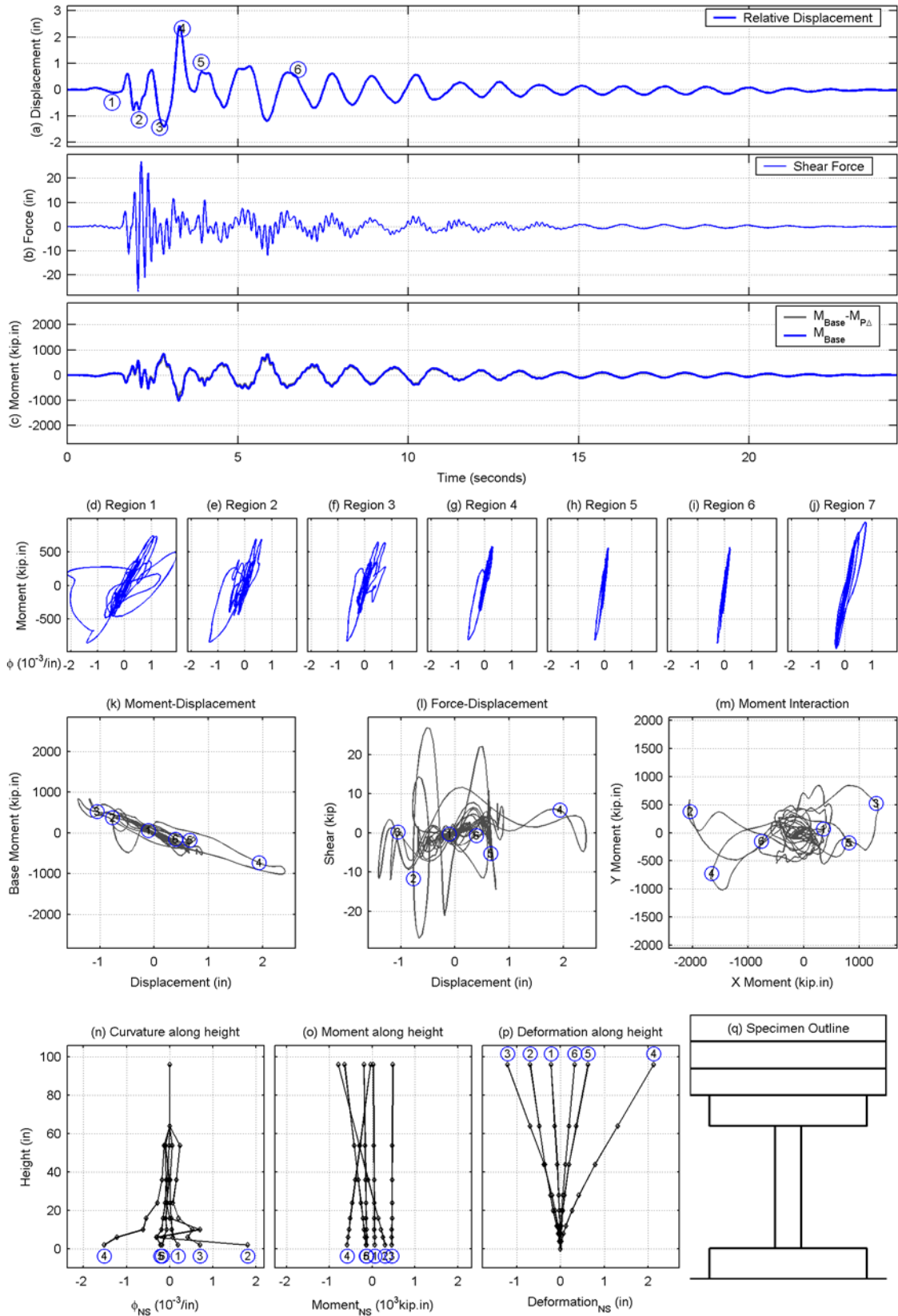
Figure D-12. Time histories and hysteresis in the lateral direction of Run 8 in test A2.
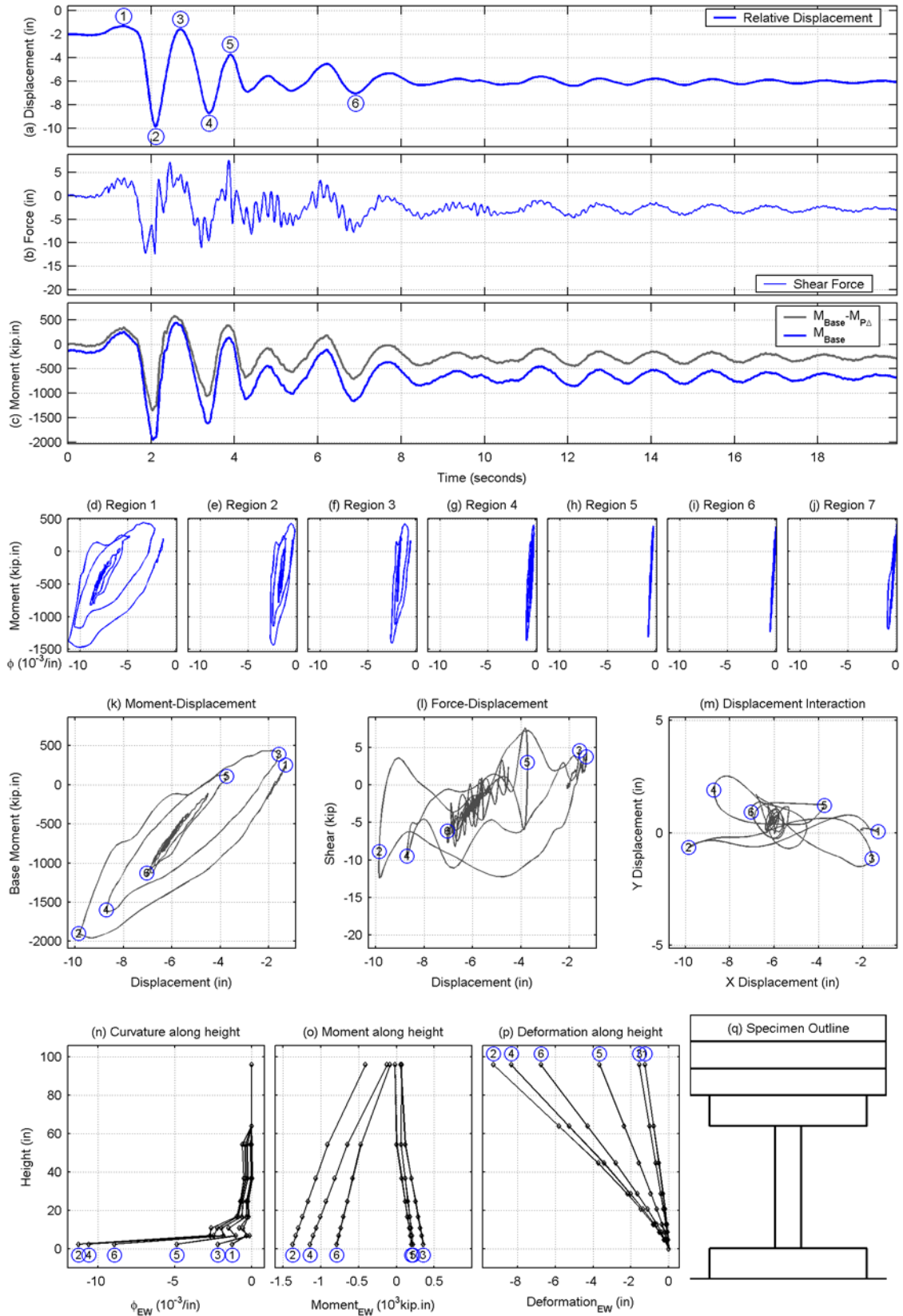
Figure D-13. Time histories and hysteresis in the longitudinal direction of Run 10 in test A2.
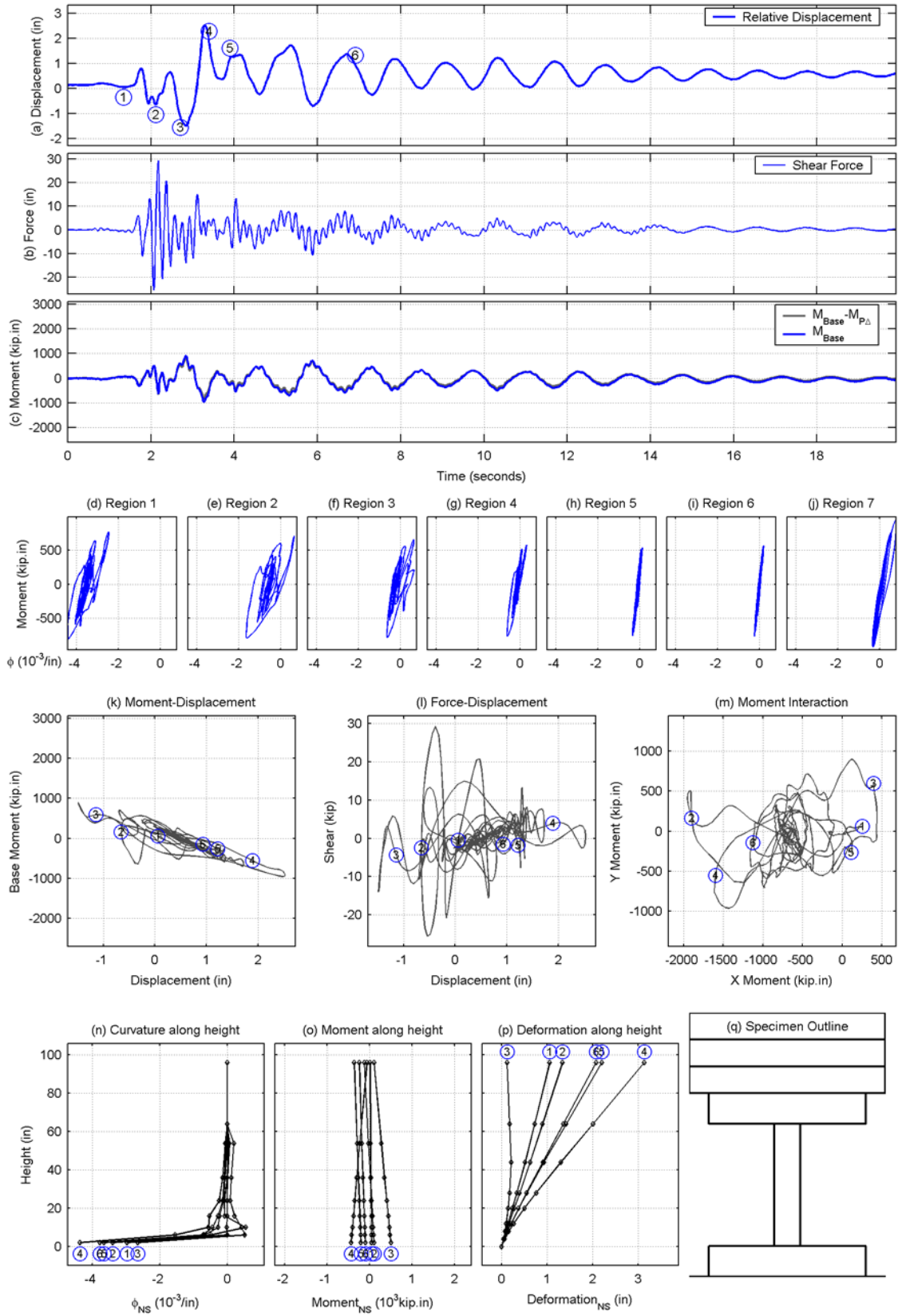
Figure D-14. Time histories and hysteresis in the lateral direction of Run 10 in test A2.
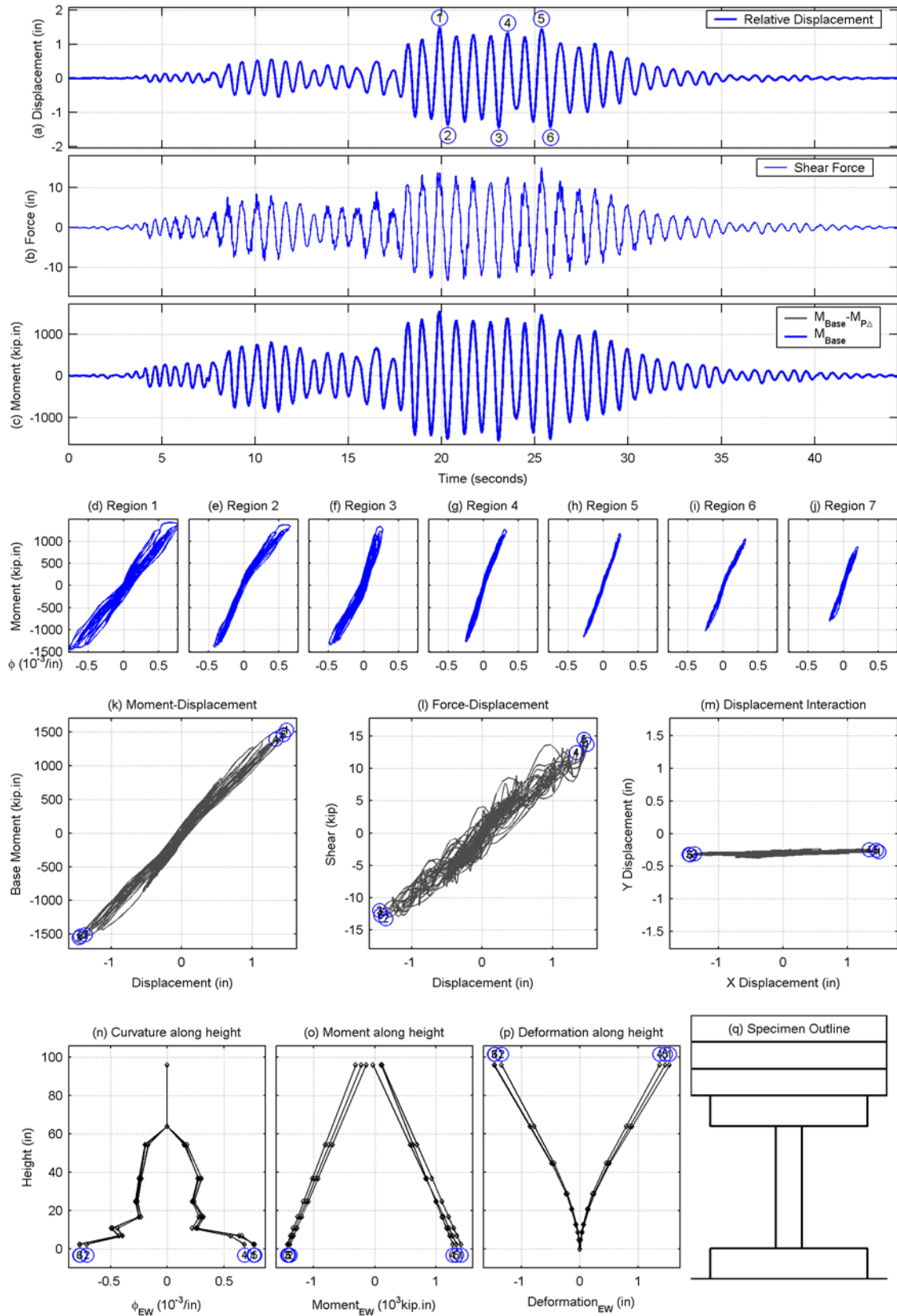
Figure D-15. Time histories and hysteresis in the longitudinal direction of Run 4 in test B1.
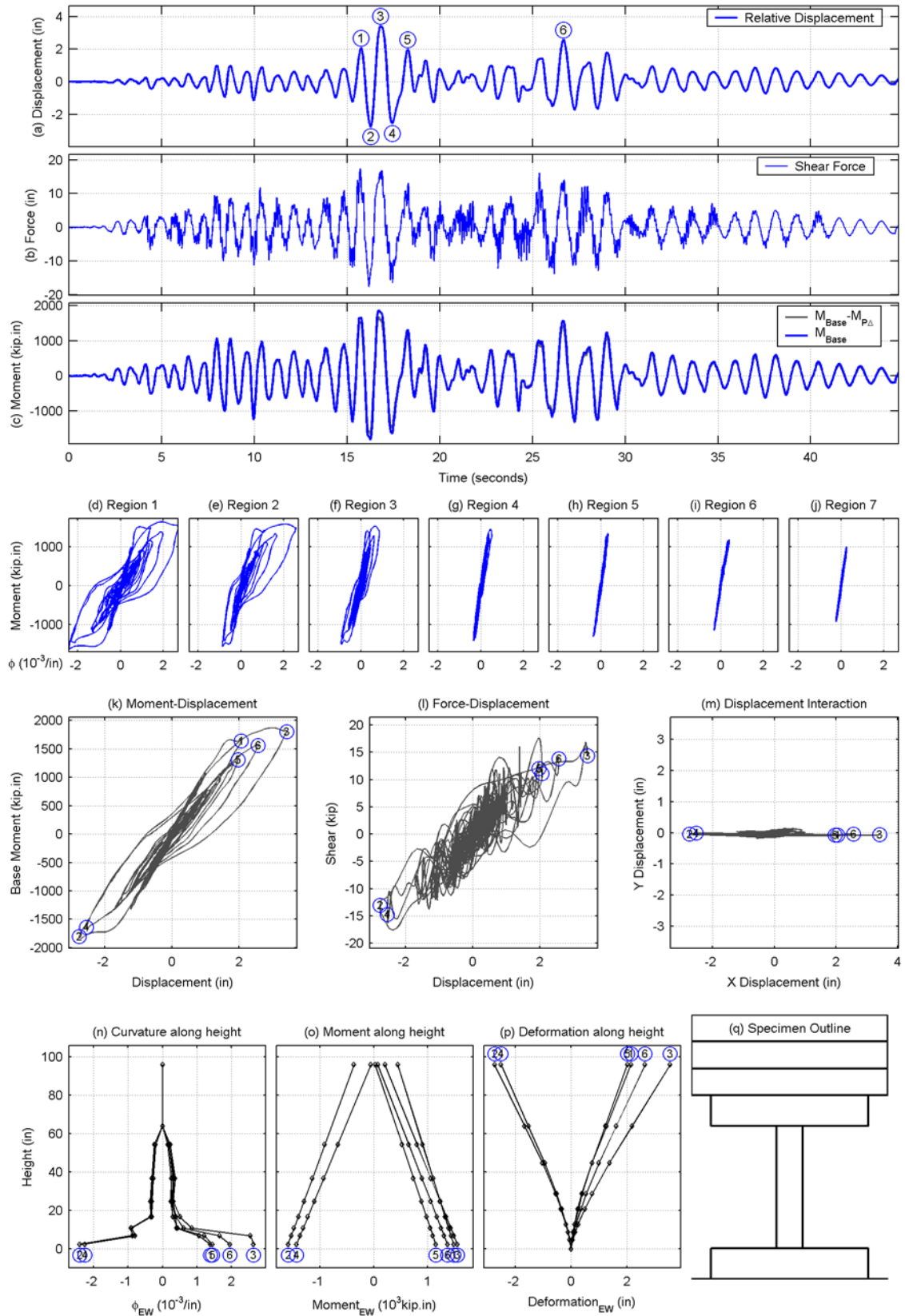
Figure D-16. Time histories and hysteresis in the longitudinal direction of Run 5 in test B1.
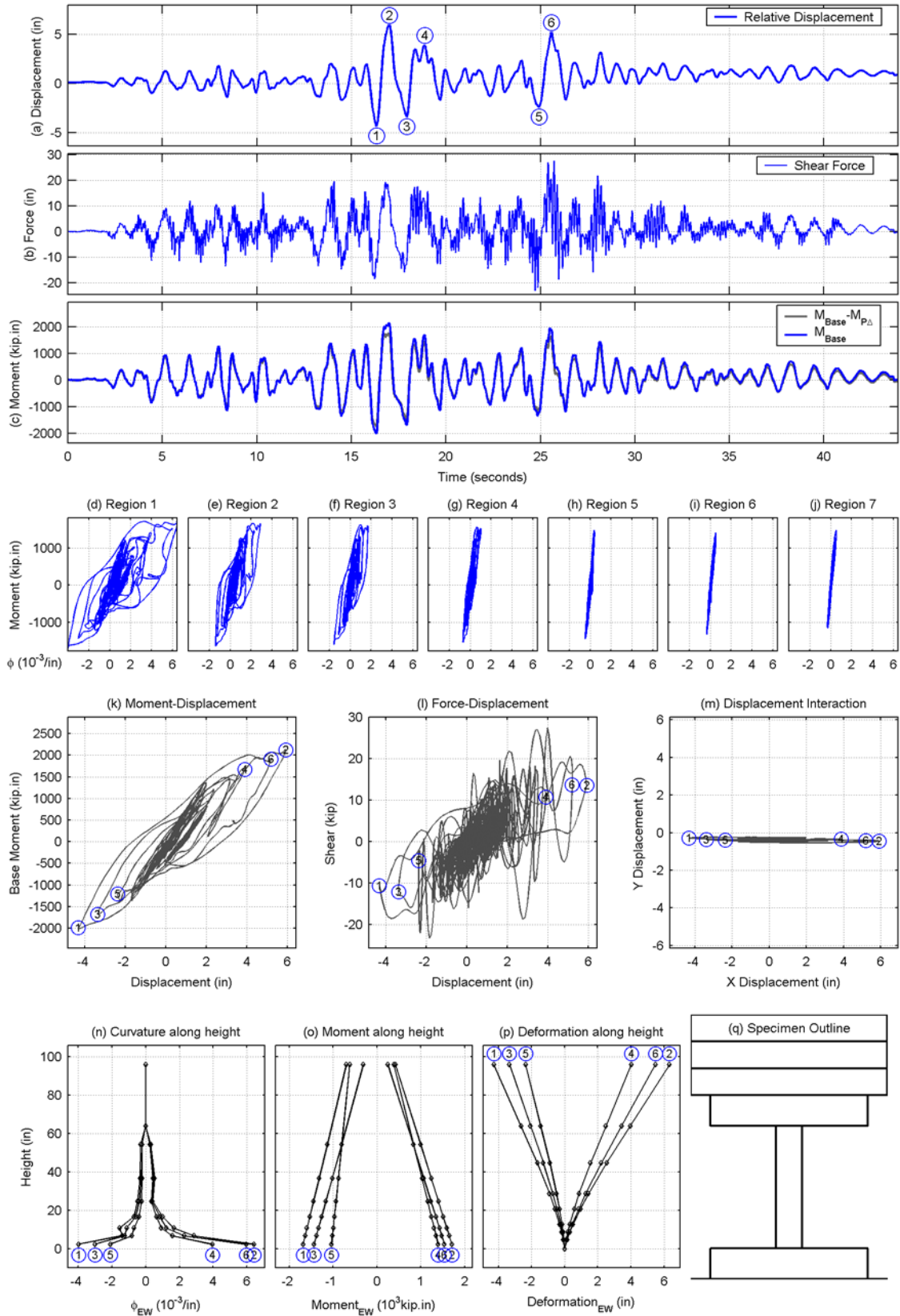
Figure D-17. Time histories and hysteresis in the longitudinal direction of Run 6 in test B1.
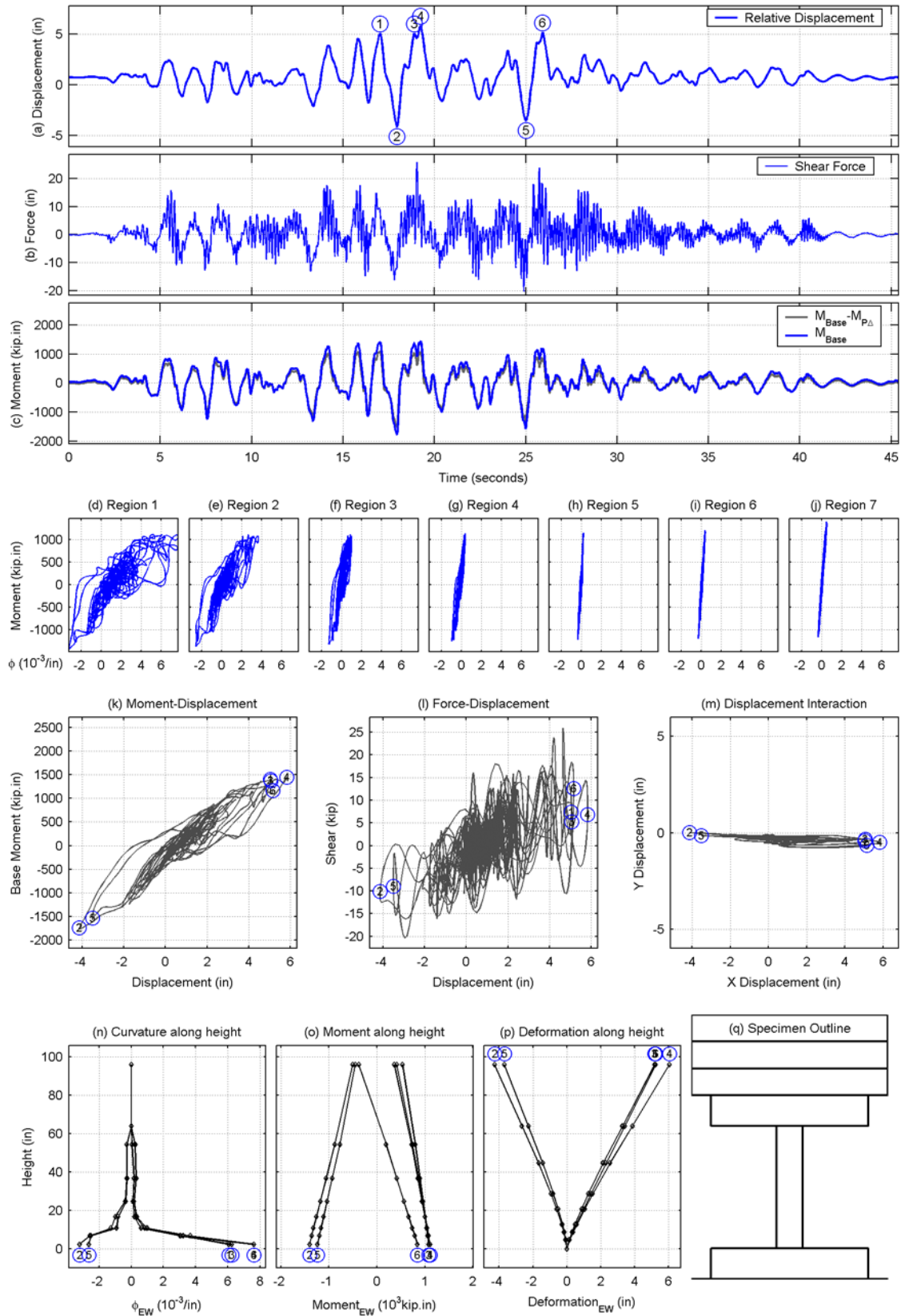
Figure D-18. Time histories and hysteresis in the longitudinal direction of Run 9 in test B1.

397
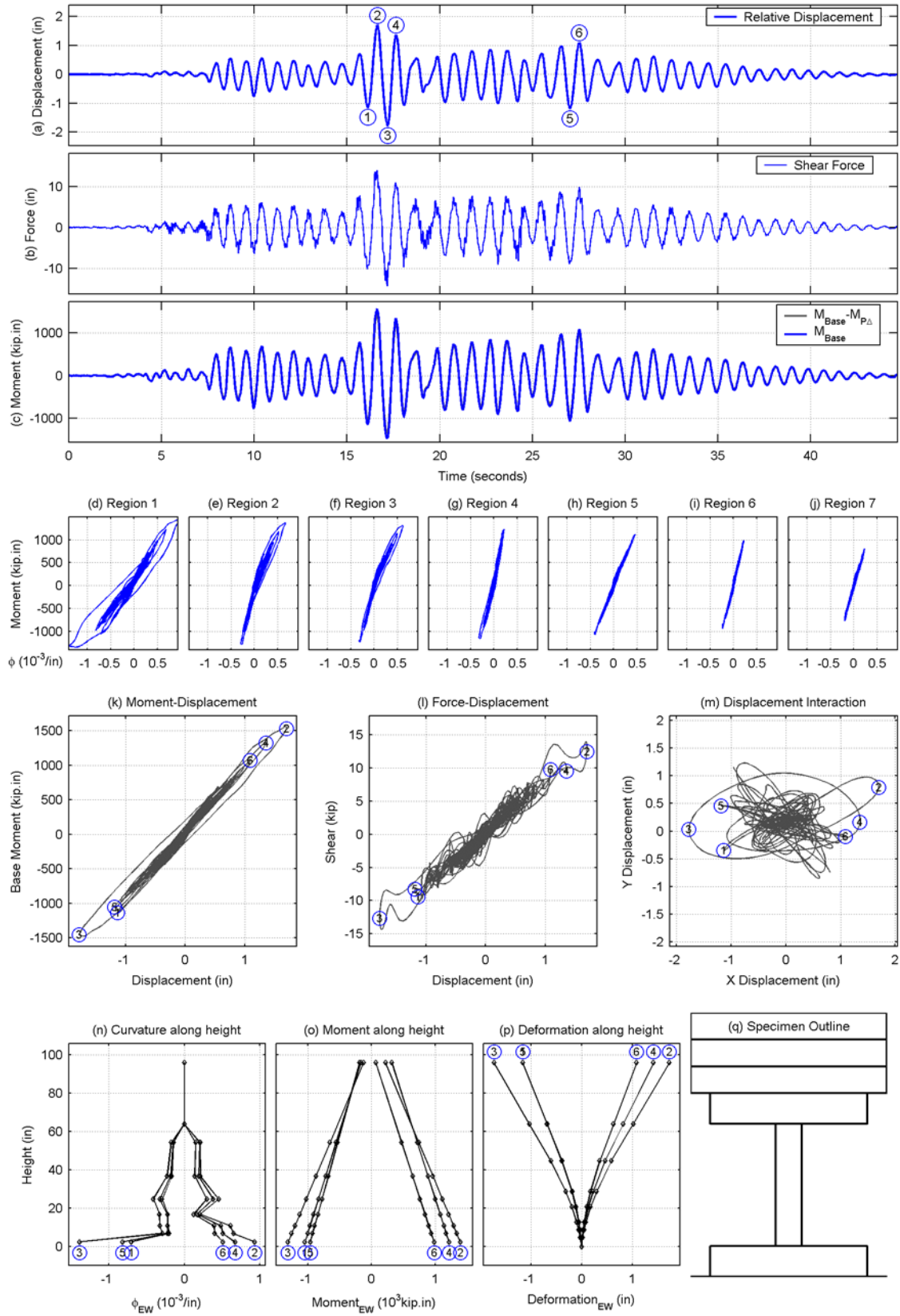
Figure D-19. Time histories and hysteresis in the longitudinal direction of Run 4 in test B2.
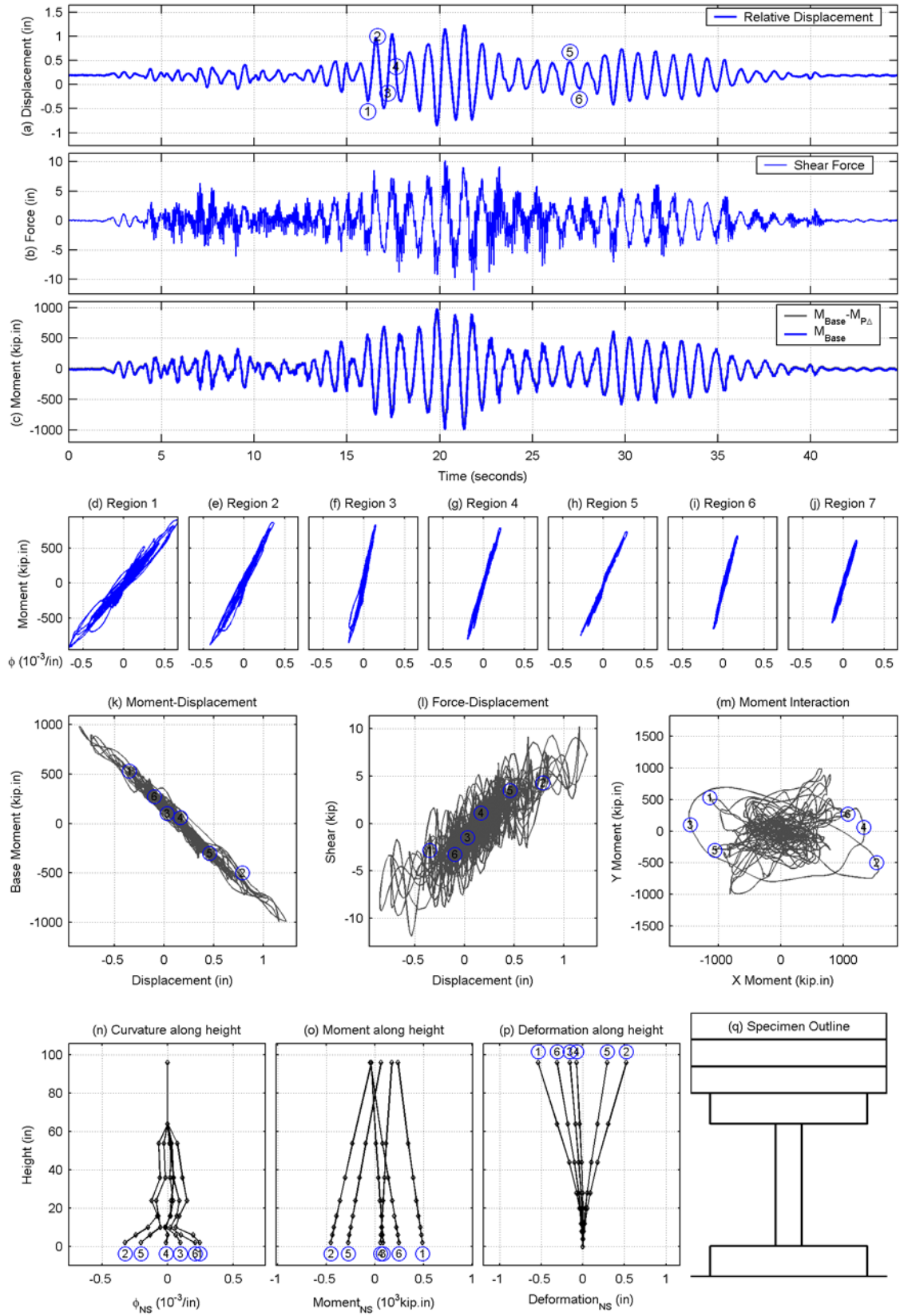
Figure D-20. Time histories and hysteresis in the lateral direction of Run 4 in test B2.

399
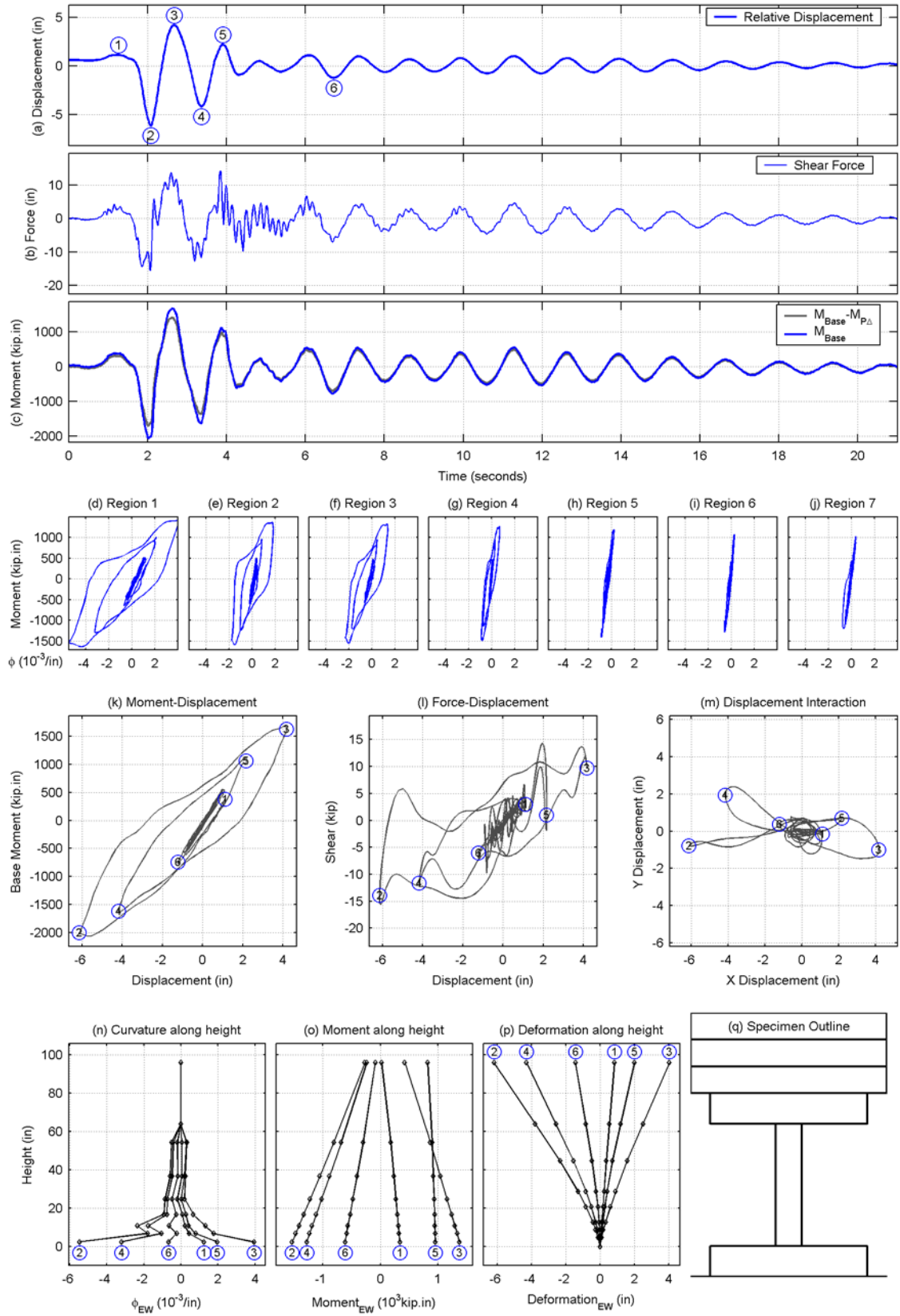
Figure D-21. Time histories and hysteresis in the longitudinal direction of Run 5 in test B2.
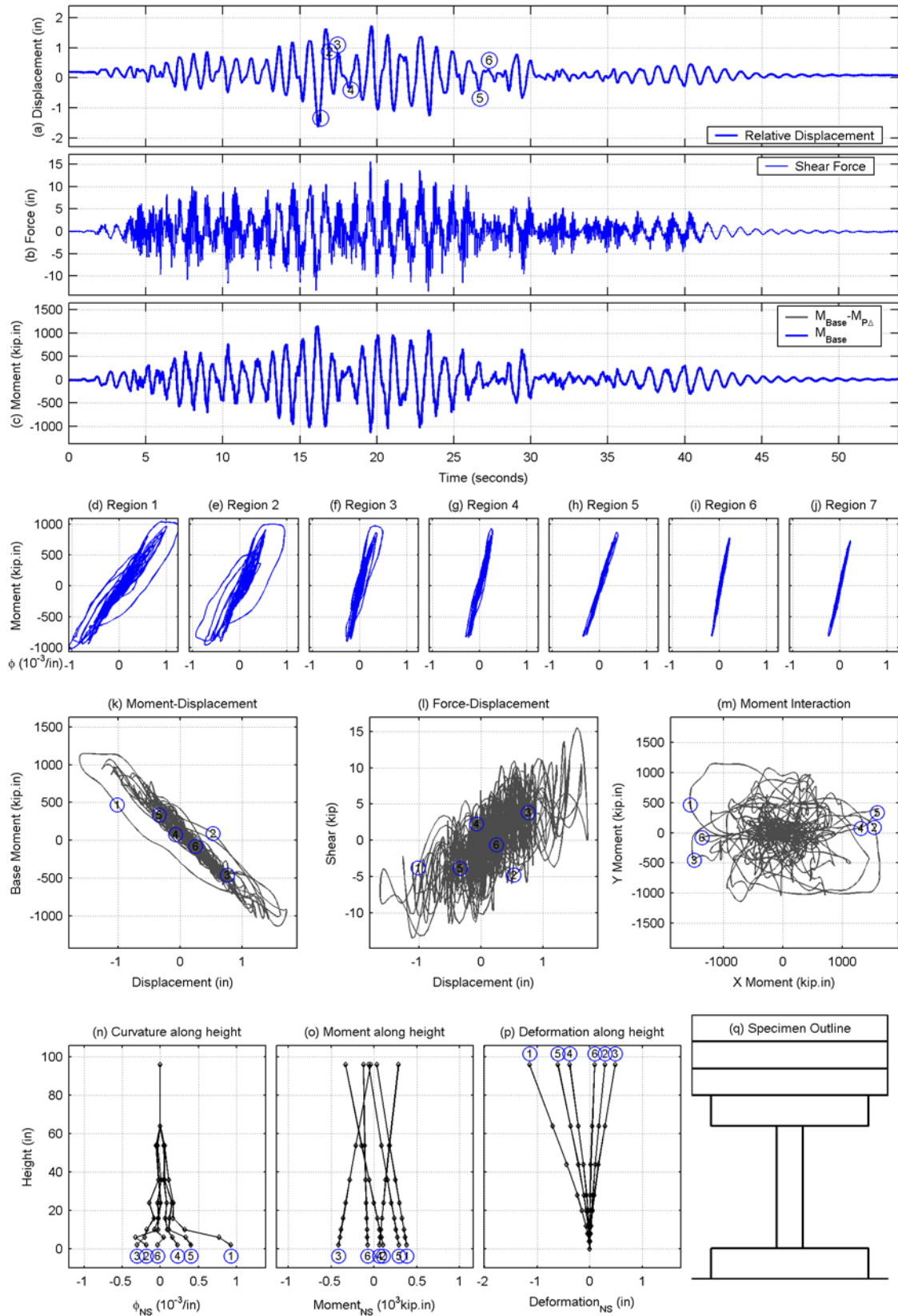
Figure D-22. Time histories and hysteresis in the lateral direction of Run 5 in test B2.
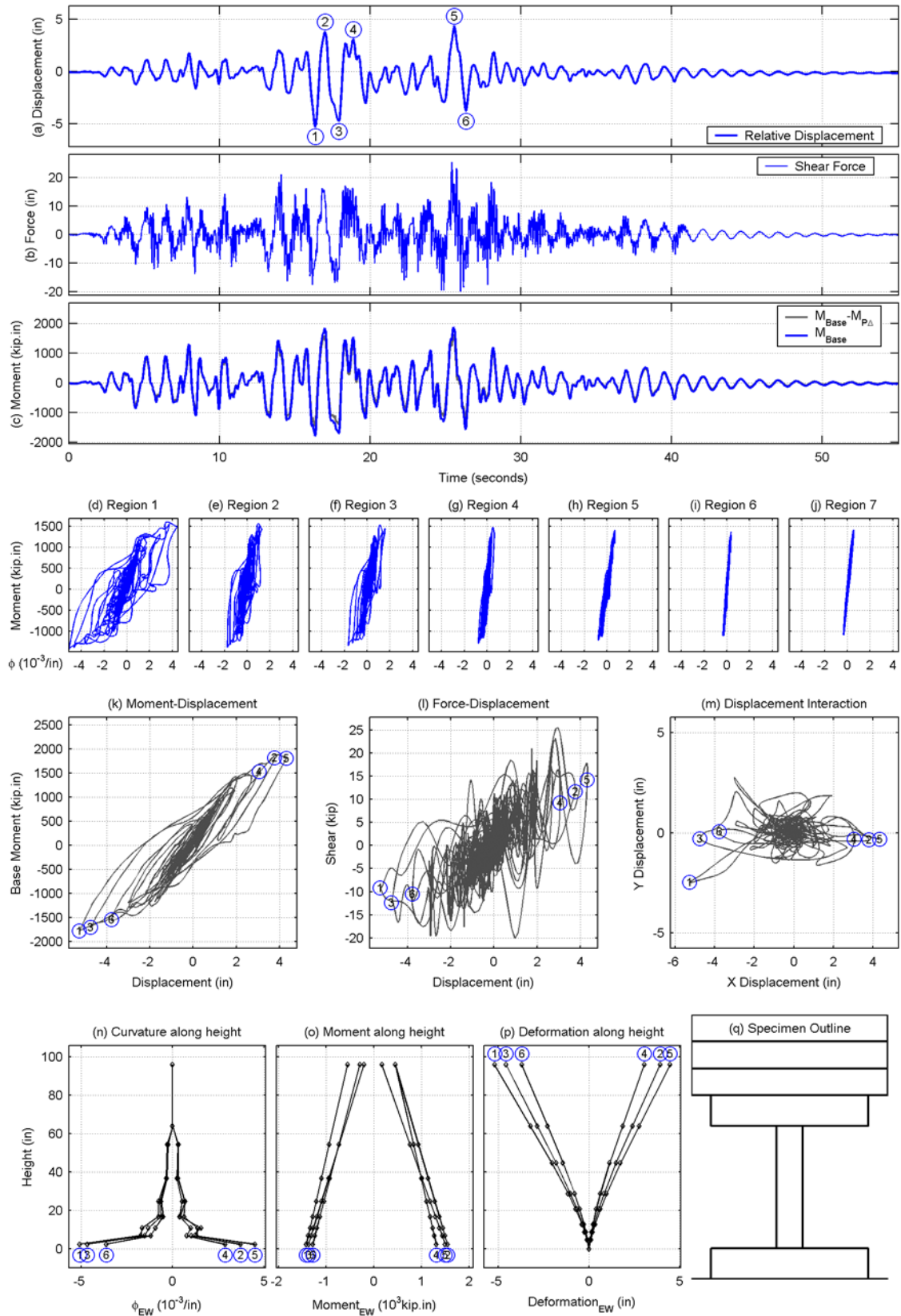
Figure D-23. Time histories and hysteresis in the longitudinal direction of Run 6 in test B2.
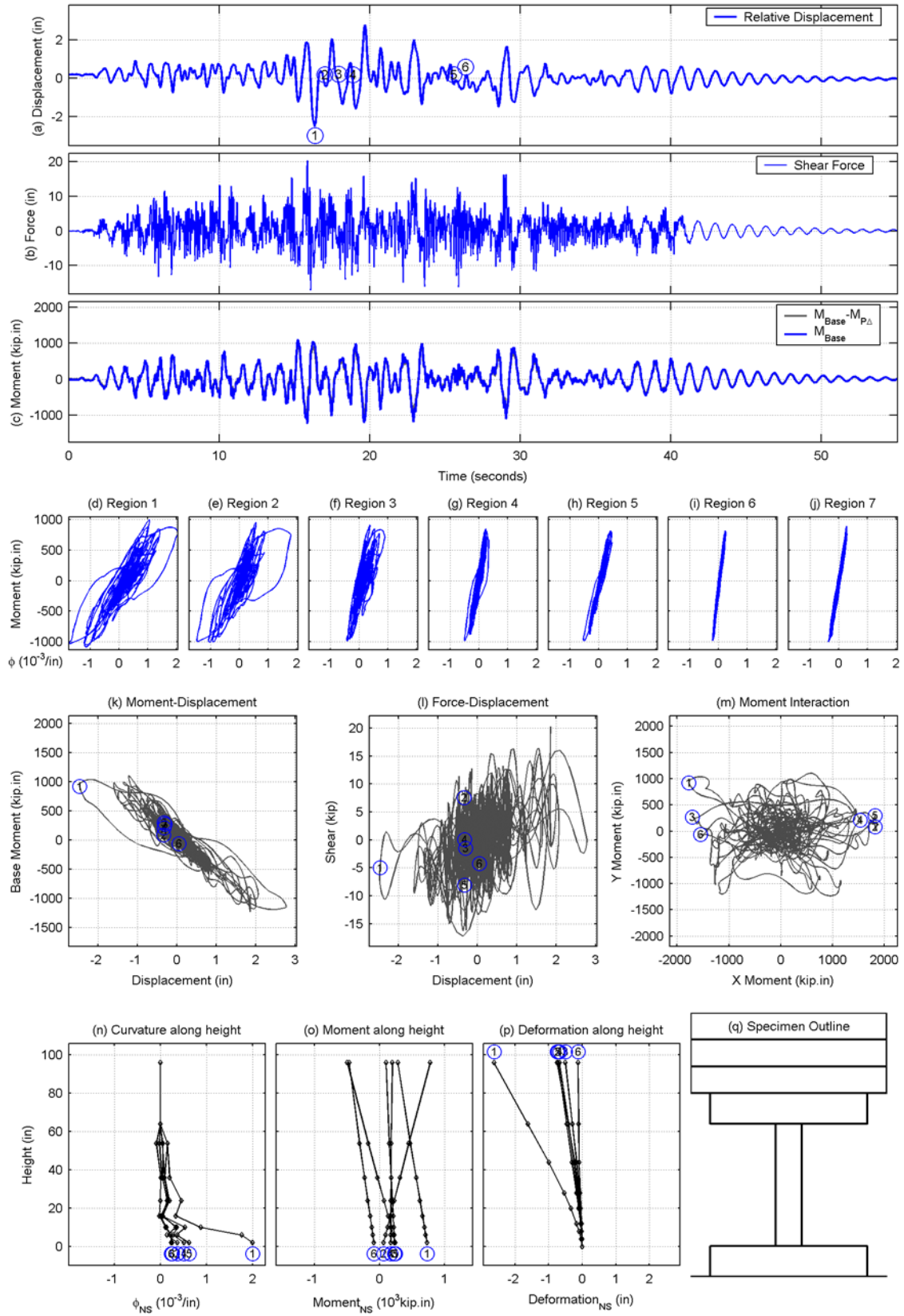
Figure D-24. Time histories and hysteresis in the lateral direction of Run 6 in test B2.
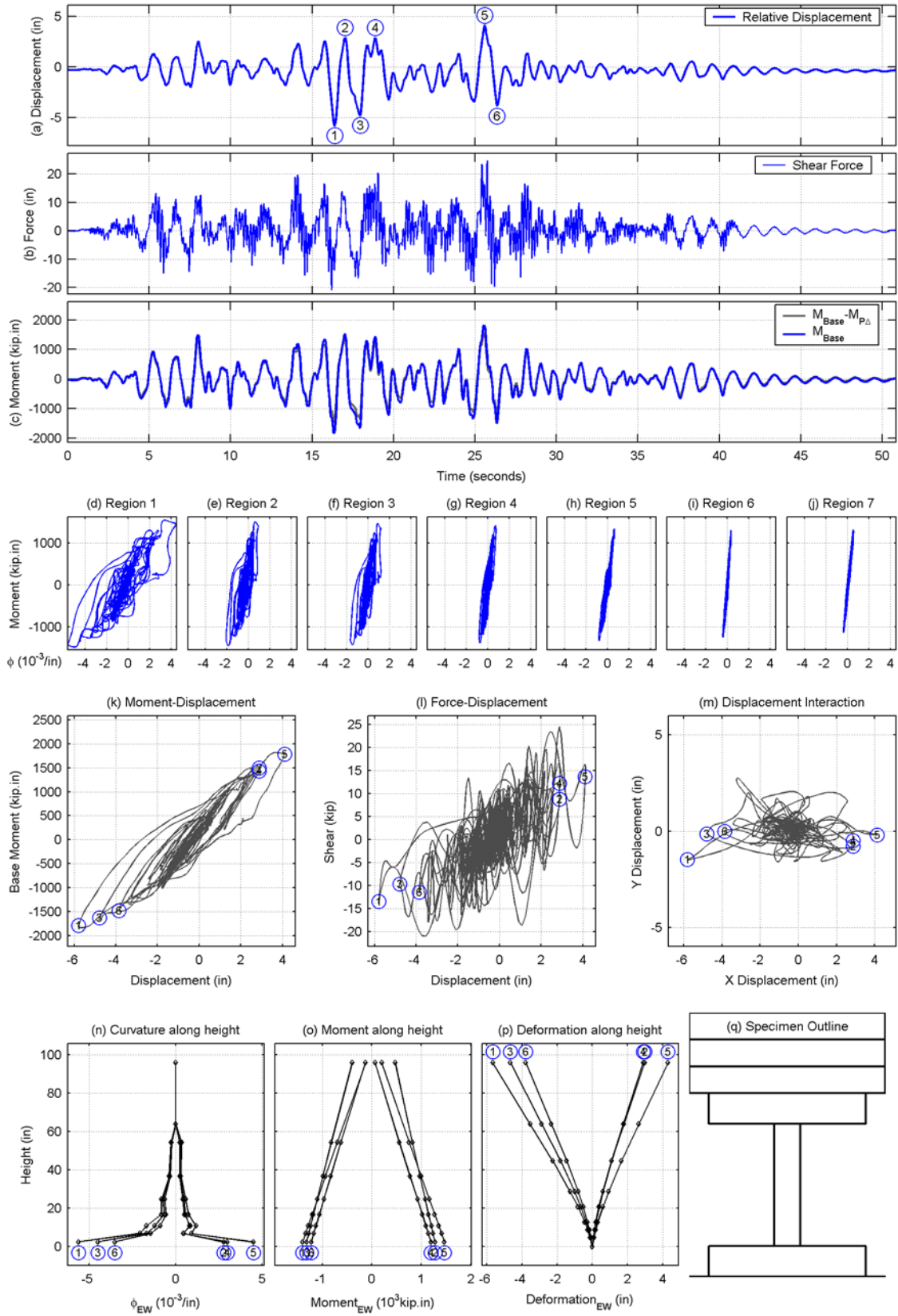
Figure D-25. Time histories and hysteresis in the longitudinal direction of Run 9 in test B2.

404
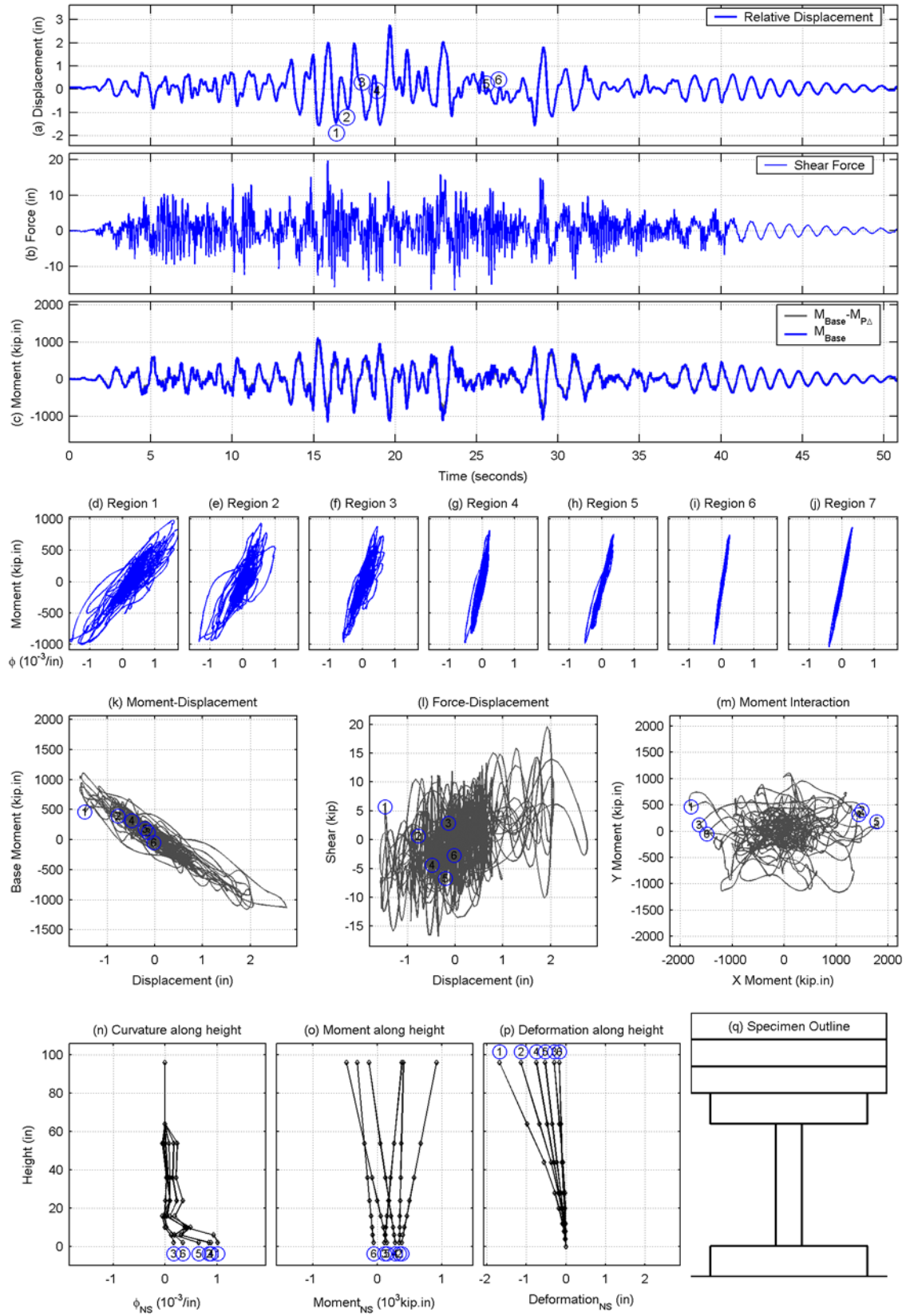
Figure D-26. Time histories and hysteresis in the lateral direction of Run 9 in test B2.
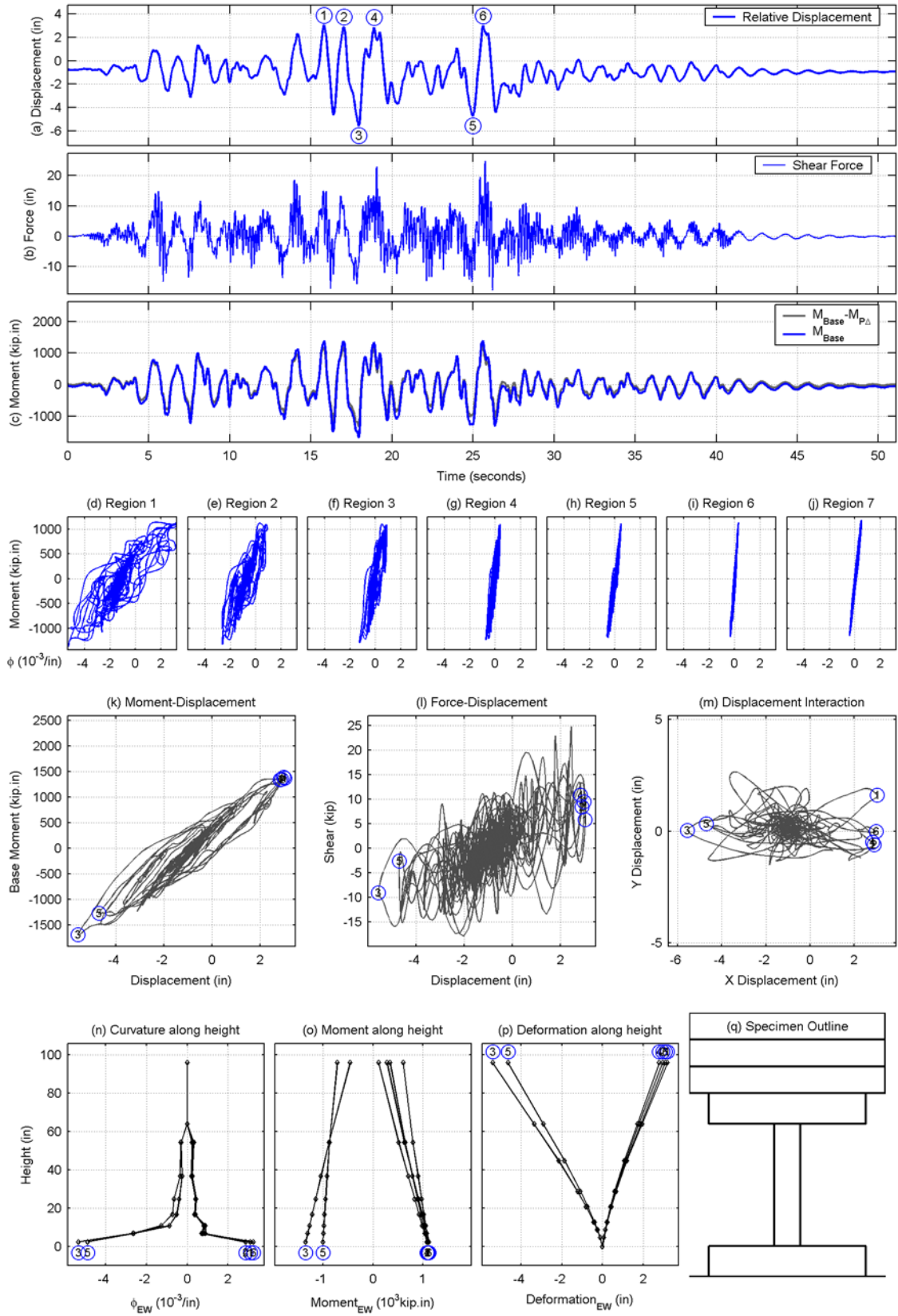
Figure D-27. Time histories and hysteresis in the longitudinal direction of Run 13 in test B2.

406
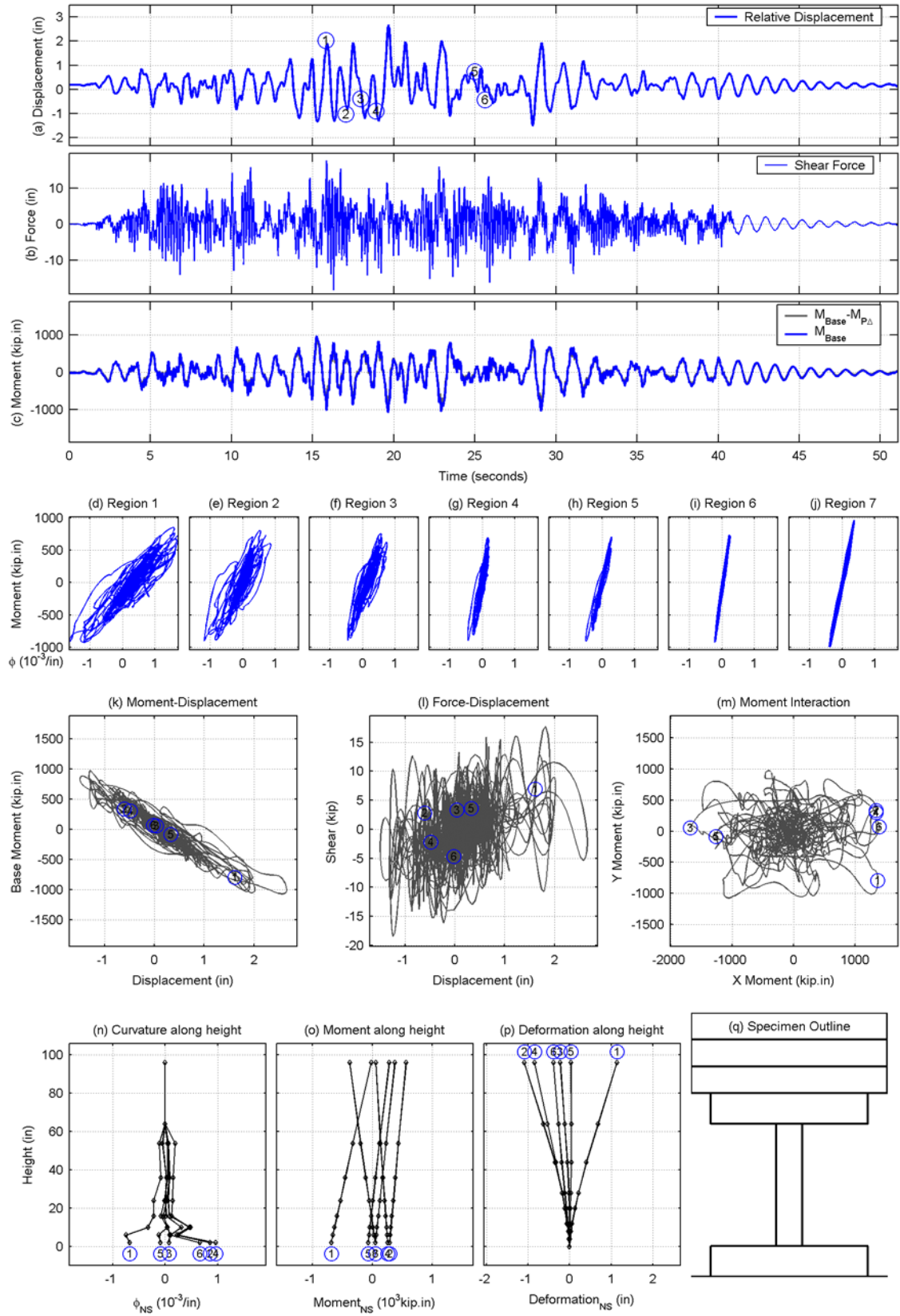
Figure D-28. Time histories and hysteresis in the lateral direction of Run 13 in test B2.

Appendix E Comparison of Experimental Data to Analytical Results for Linear and Nonlinear Models

This appendix presents comparisons of peak response quantities obtained from the different analysis models in Chapter 6 to the experimental measured results.
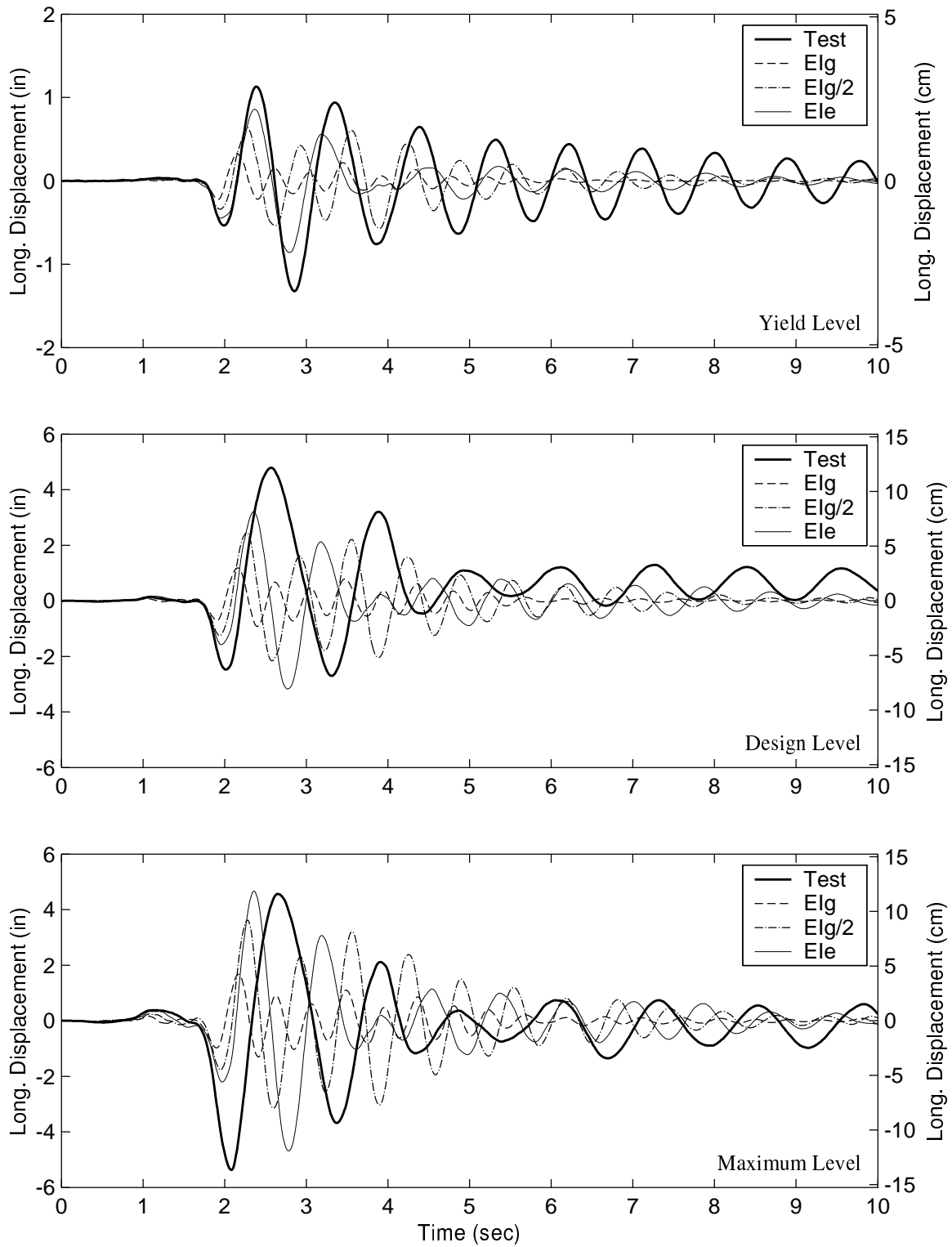
Figure E-1. Comparison of *longitudinal displacements* obtained from test results with *linear* analysis results (Specimen *A2*).

410
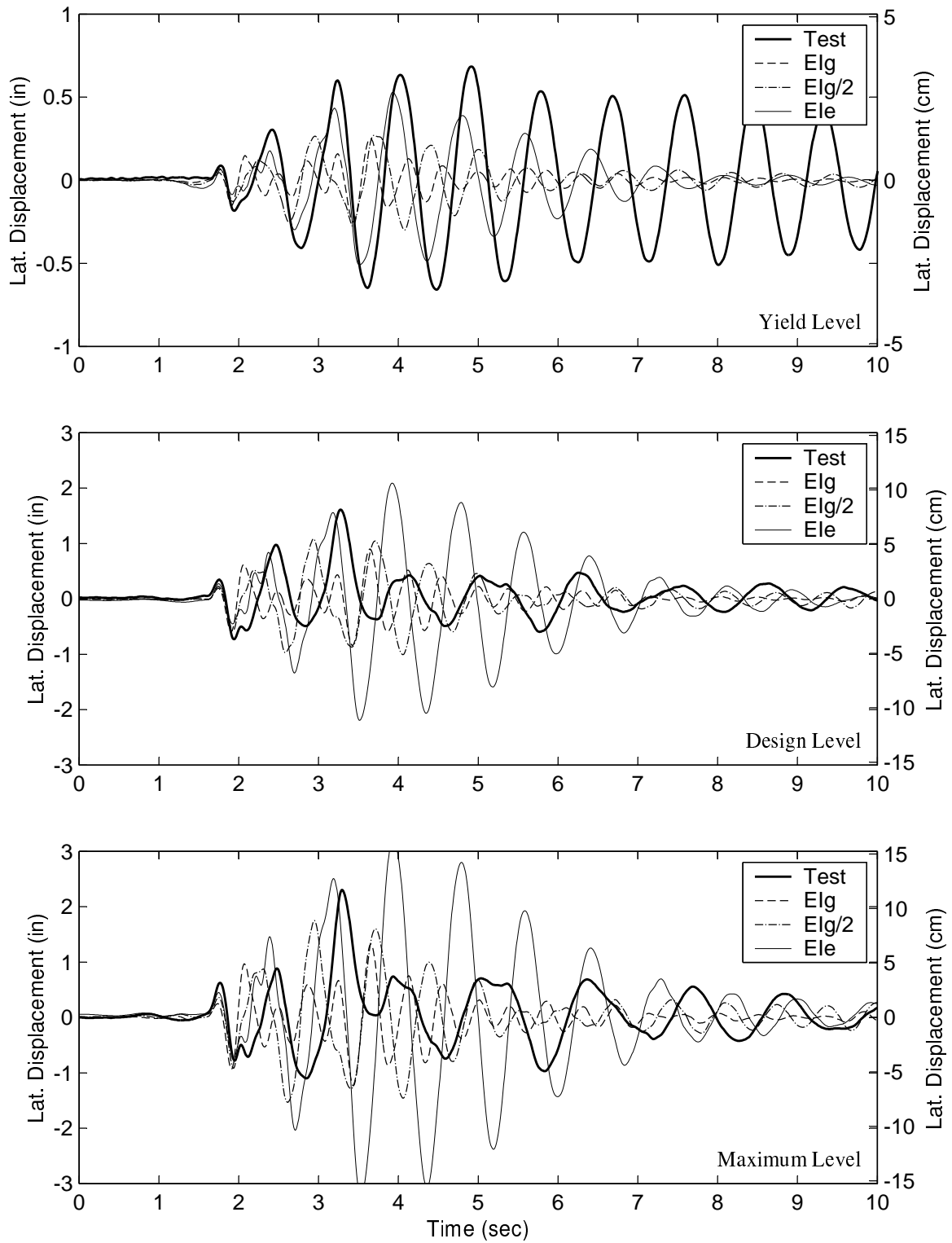
Figure E-2. Comparison of *lateral displacements* obtained from test results with *linear* analysis results (Specimen *A2*).
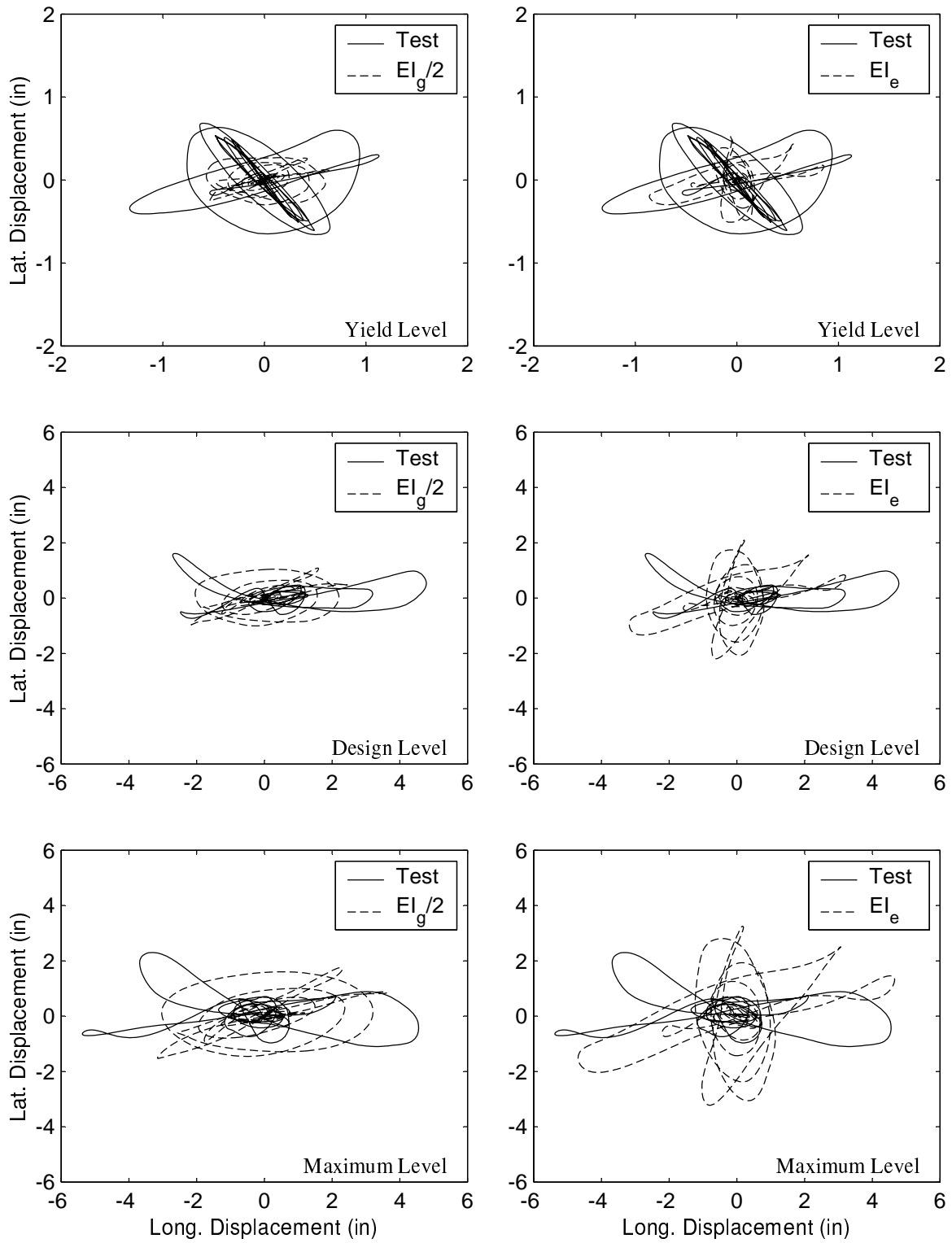
Figure E-3. Comparison of *bidirectional displacements* obtained from test results with *linear* analysis results (Specimen *A2*).

412
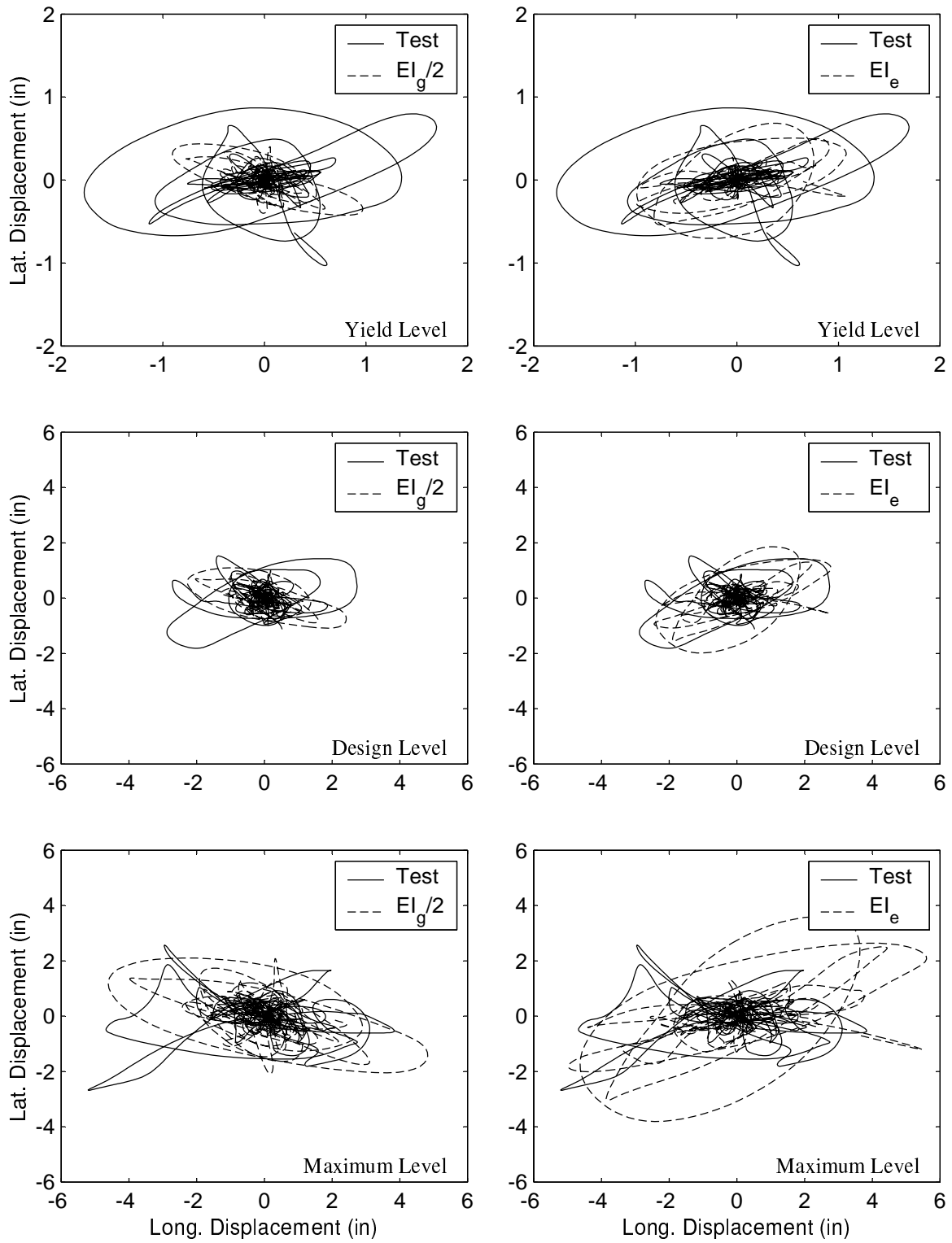
Figure E-4. Comparison of *bidirectional displacements* obtained from test results with *linear* analysis results (Specimen *B2*).

413
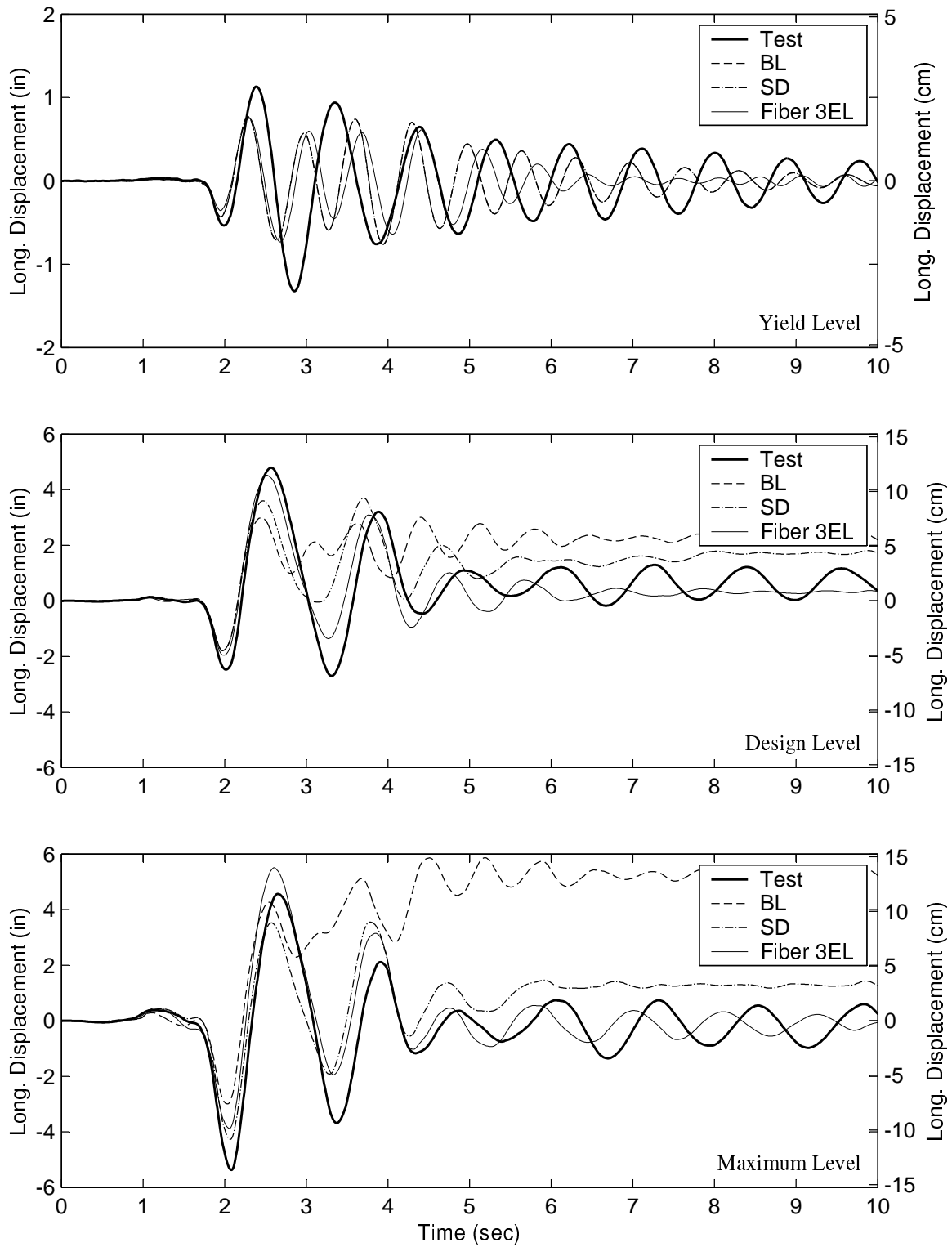
Figure E-5. Comparison of *longitudinal displacements* obtained from test results with *nonlinear* analysis results (Specimen *A2*).
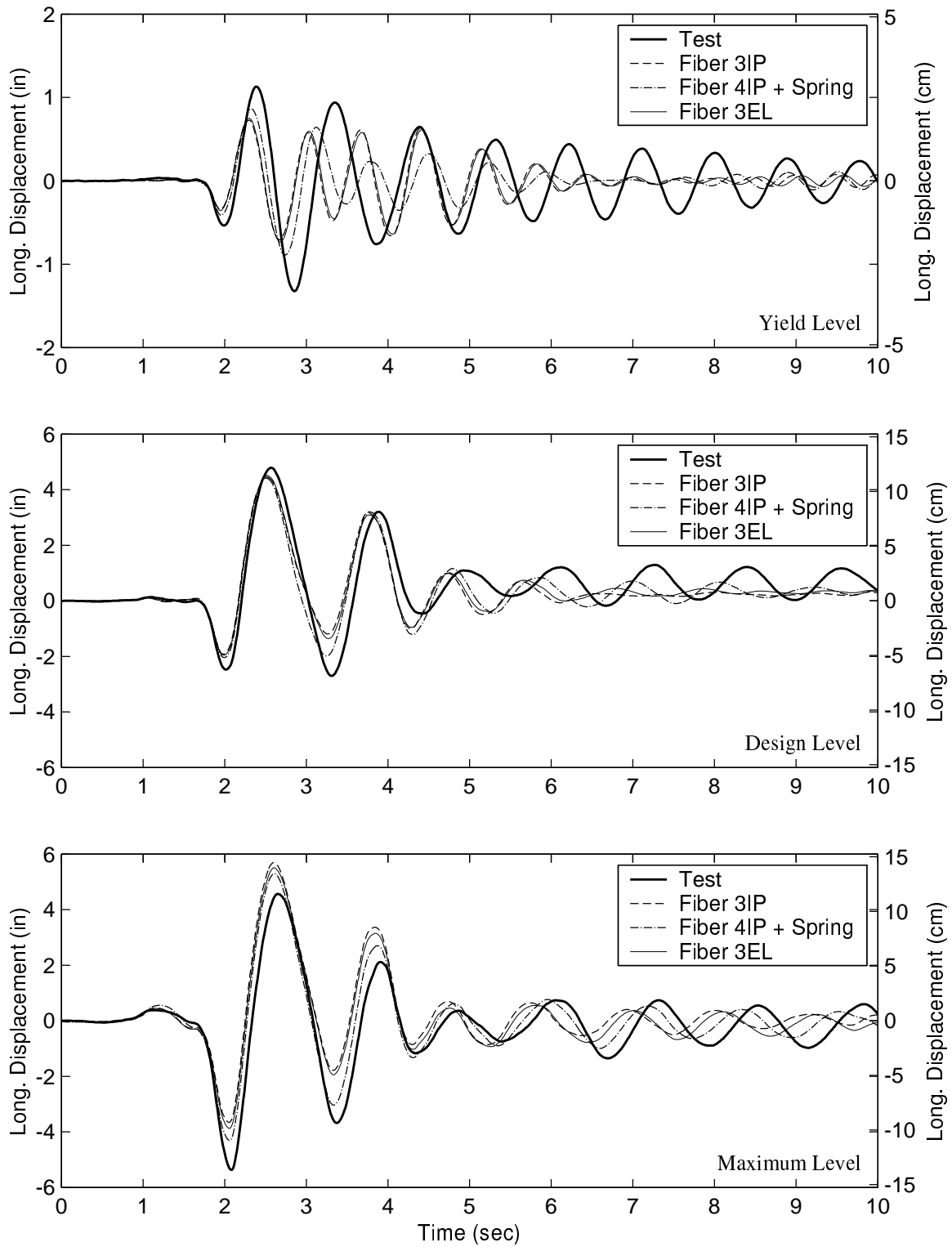
Figure E-6. Comparison of *longitudinal displacements* obtained from test results with *nonlinear* analysis results (Specimen *A2*).
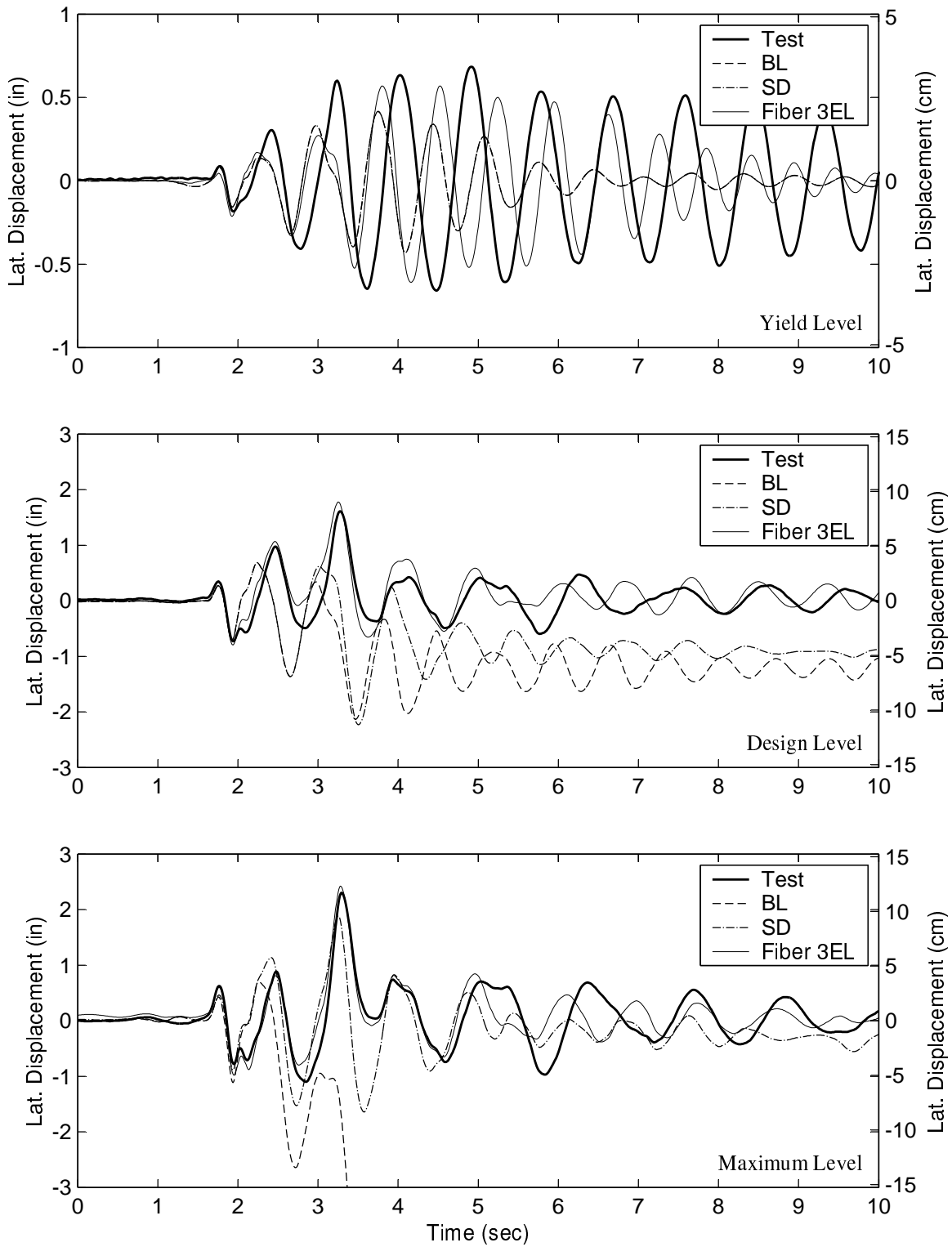
Figure E-7. Comparison of *lateral displacements* obtained from test results with *nonlinear* analysis results (Specimen *A2*).

416
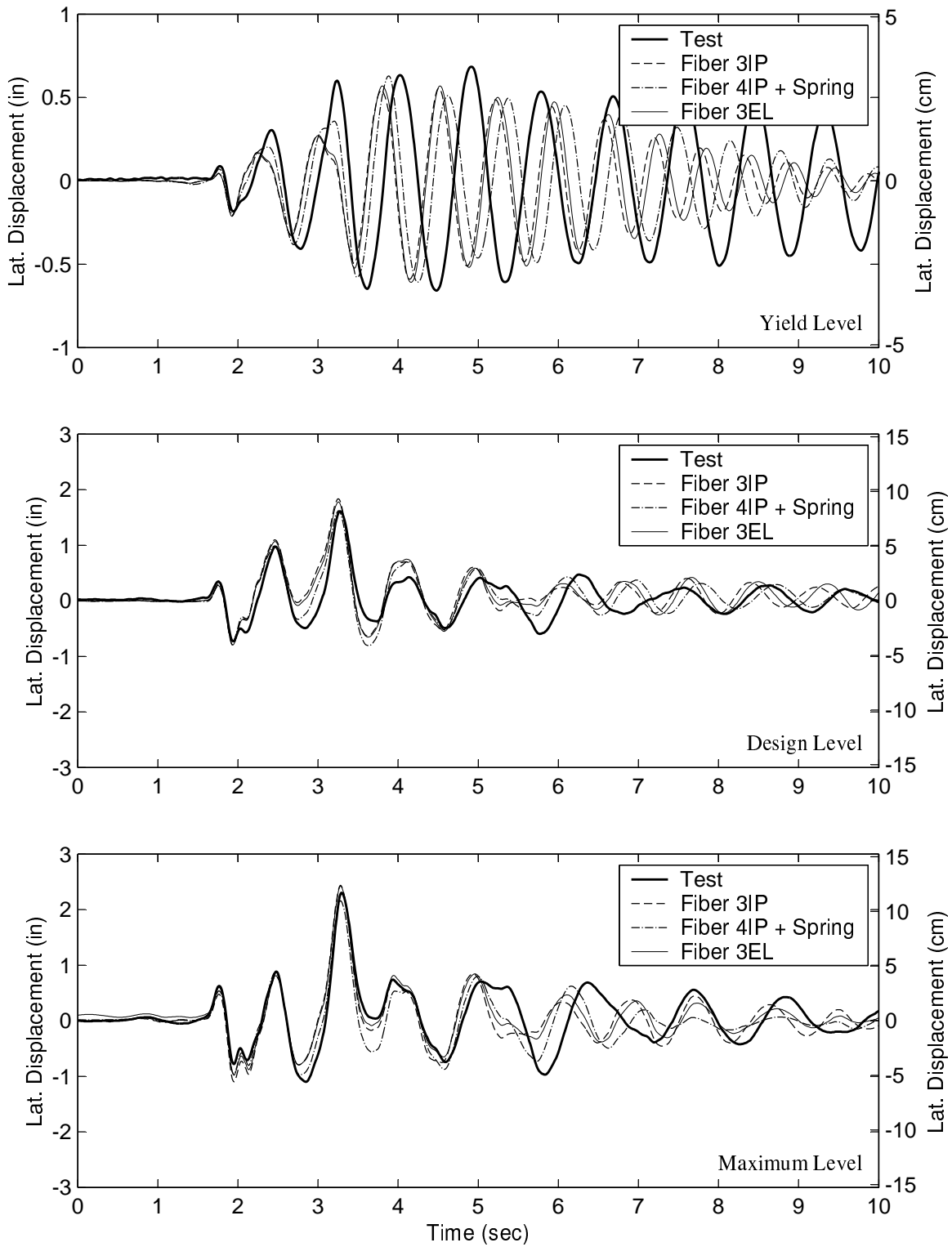
Figure E-8. Comparison of *lateral displacements* obtained from test results with *nonlinear* analysis results (Specimen *A2*).
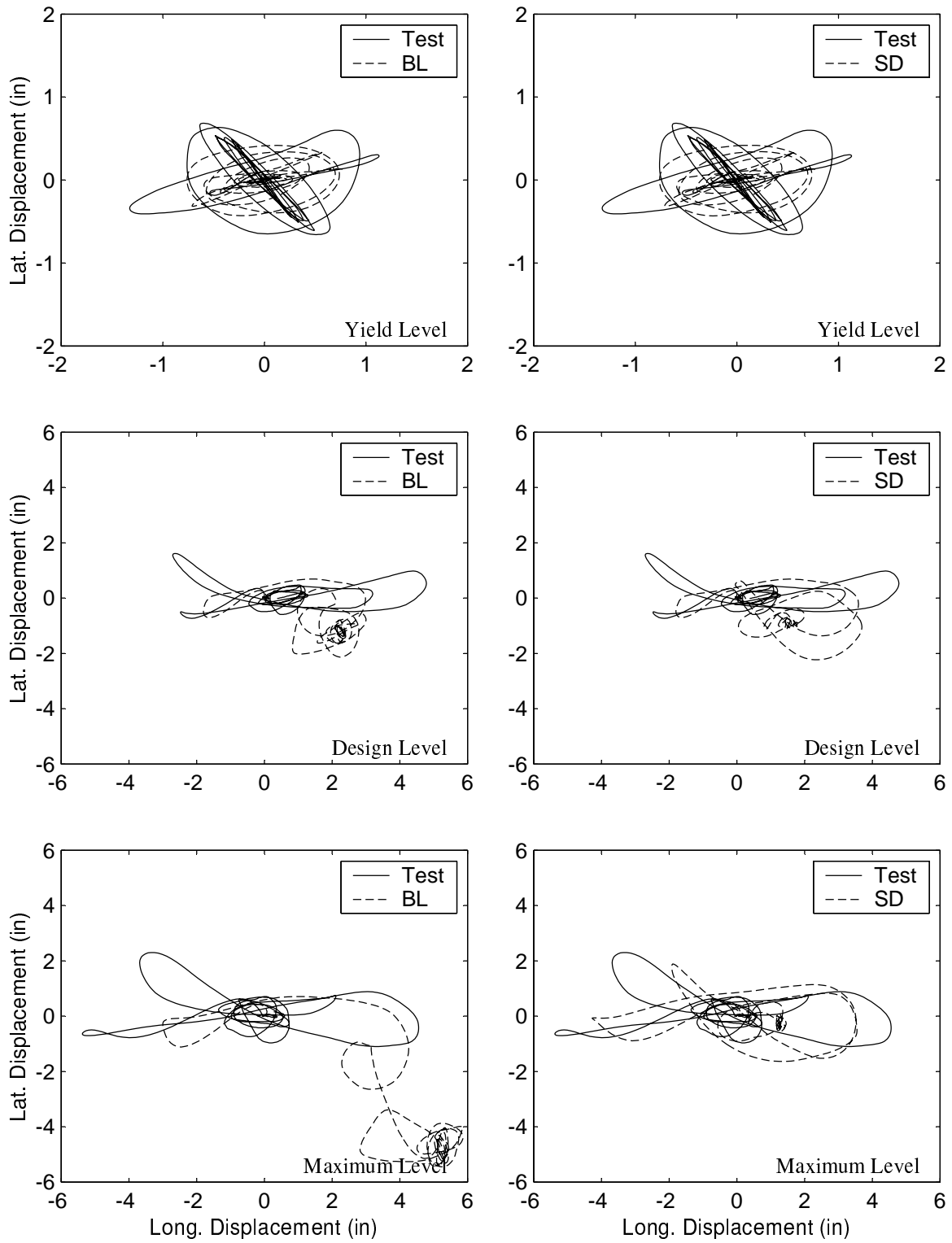
Figure E-9. Comparison of *bidirectional displacements* obtained from test results with *nonlinear* analysis results (Specimen *A2*).
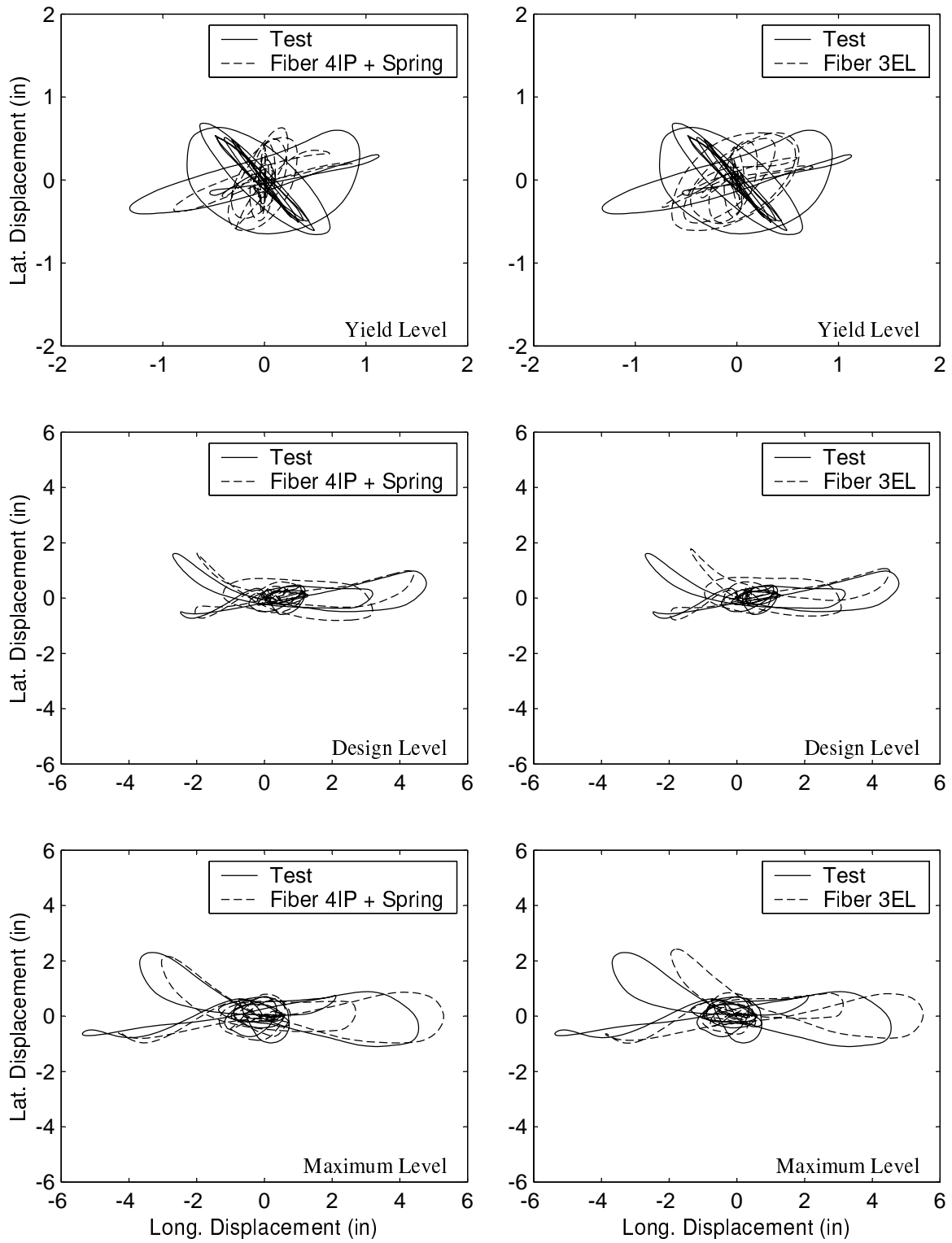
Figure E-10. Comparison of *bidirectional displacements* obtained from test results with *nonlinear* analysis results (Specimen *A2*).

419
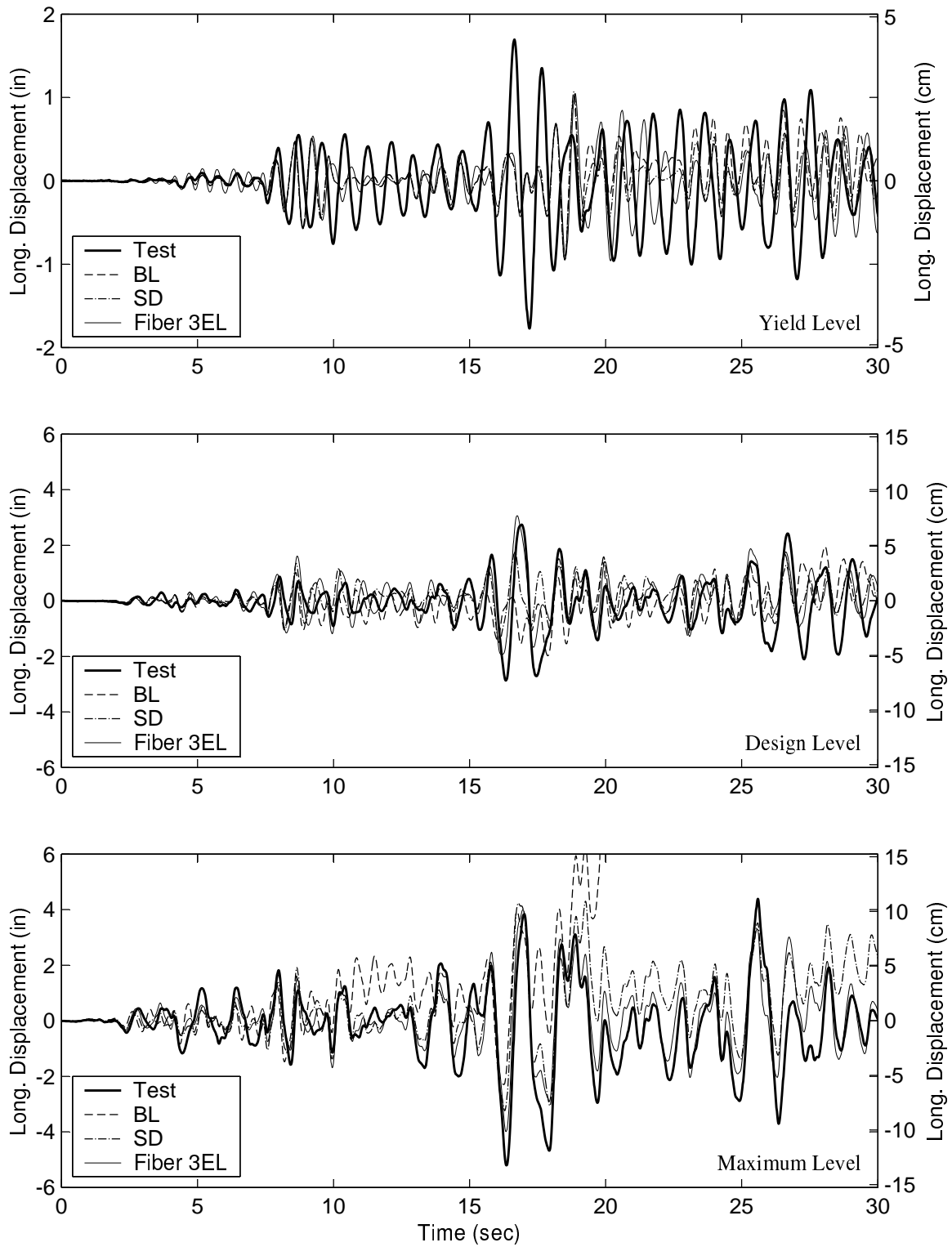
Figure E-11. Comparison of *longitudinal displacements* obtained from test results with *nonlinear* analysis results (Specimen *B2*).
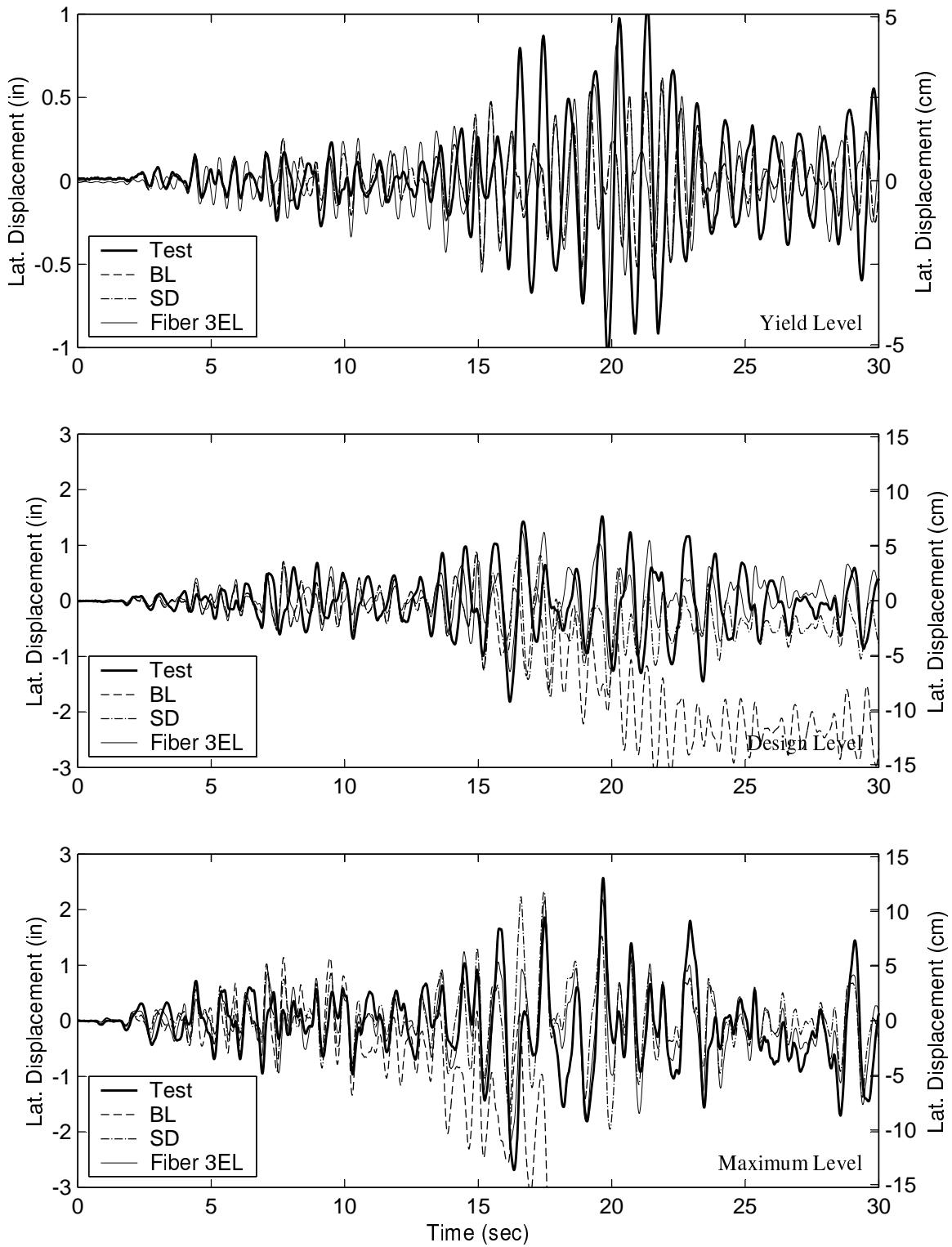
Figure E-12. Comparison of *lateral displacements* obtained from test results with *nonlinear* analysis results (Specimen *B2*).
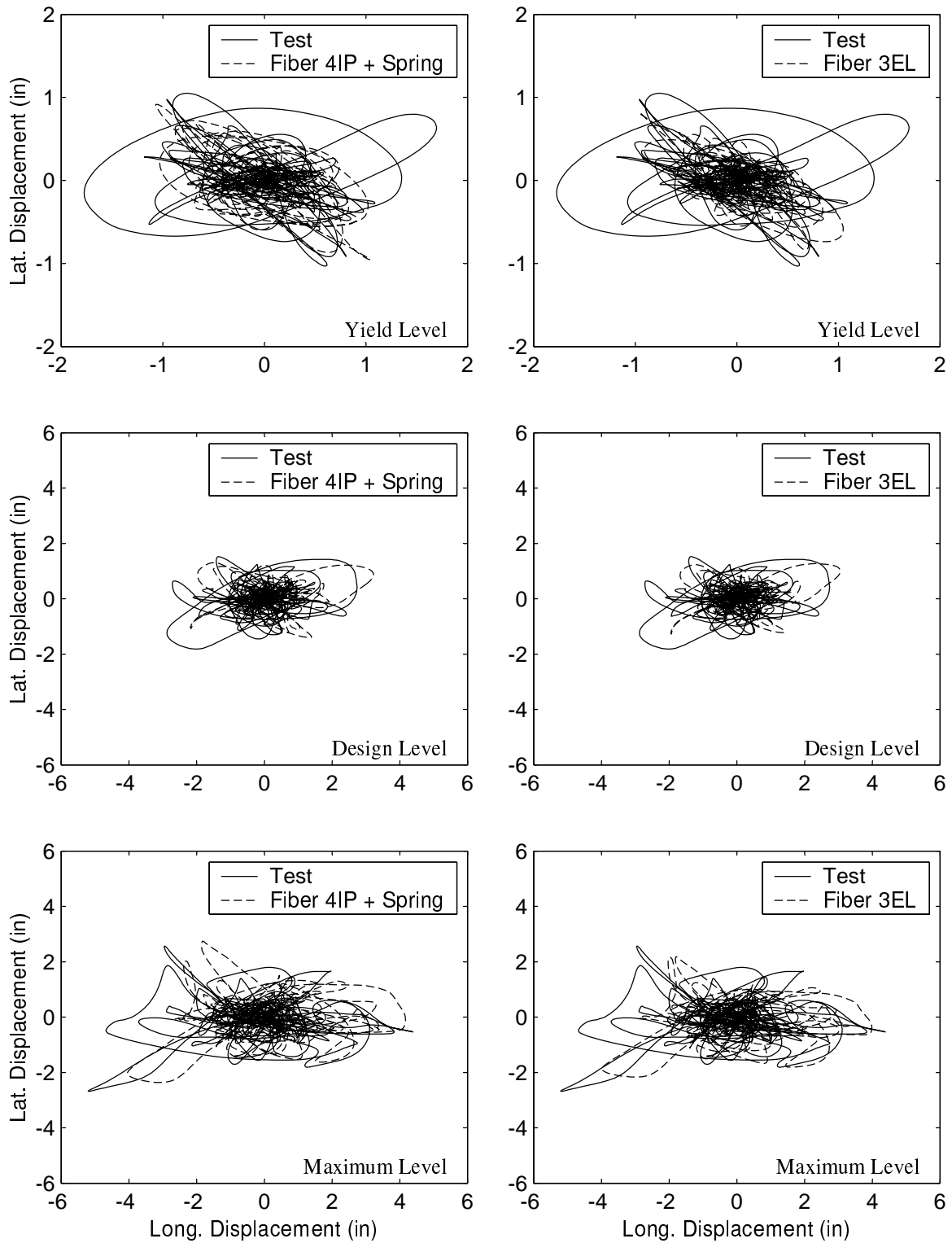
Figure E-13. Comparison of *bidirectional displacements* obtained from test results with *nonlinear* analysis results (Specimen *B2*).

422
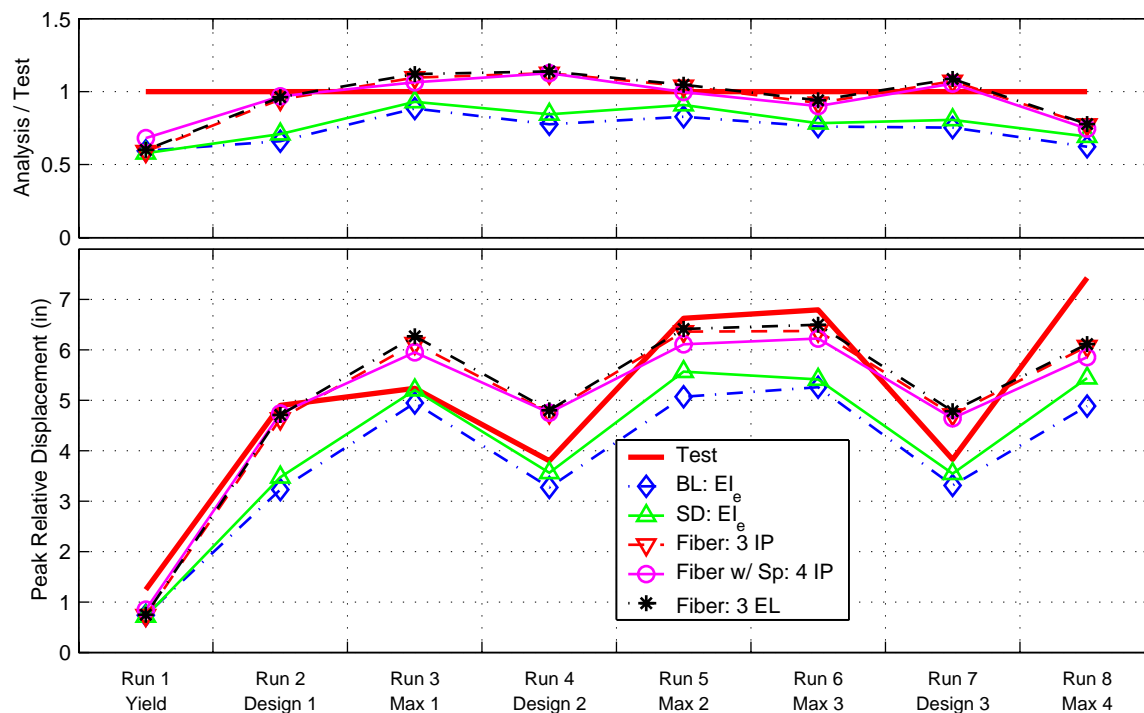
Figure E-14. Analytical and experimental *peak relative longitudinal displacements* for runs 1 to 8 of test *A1*. Each run was analyzed individually (not in sequence).
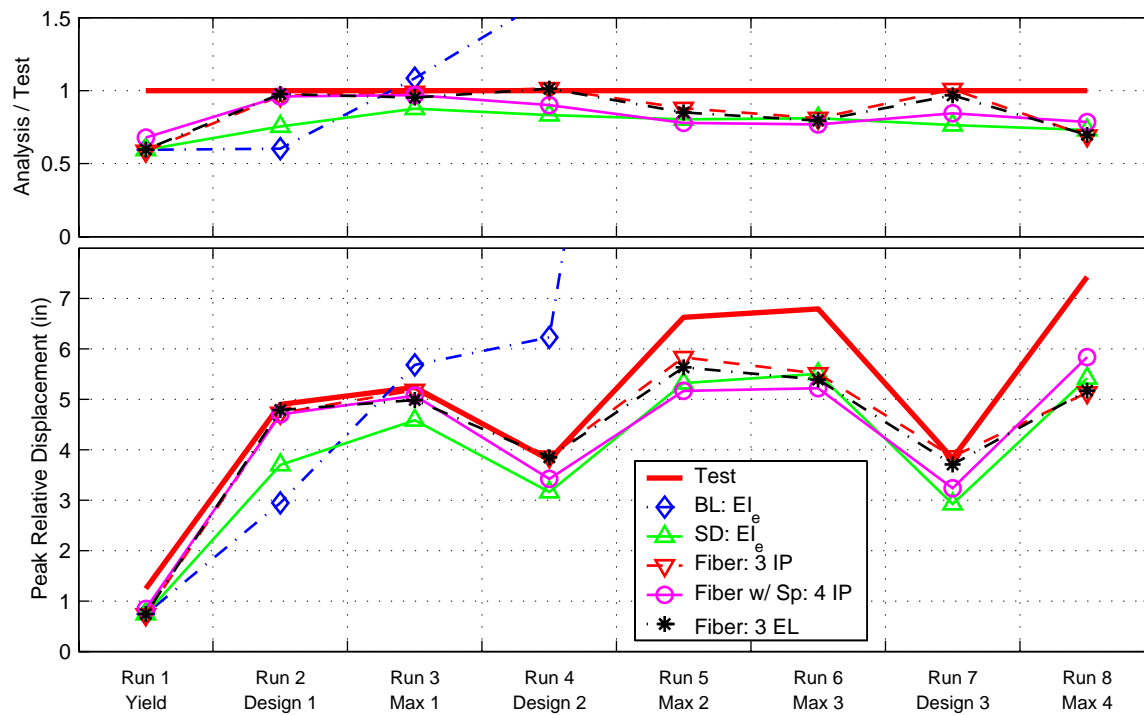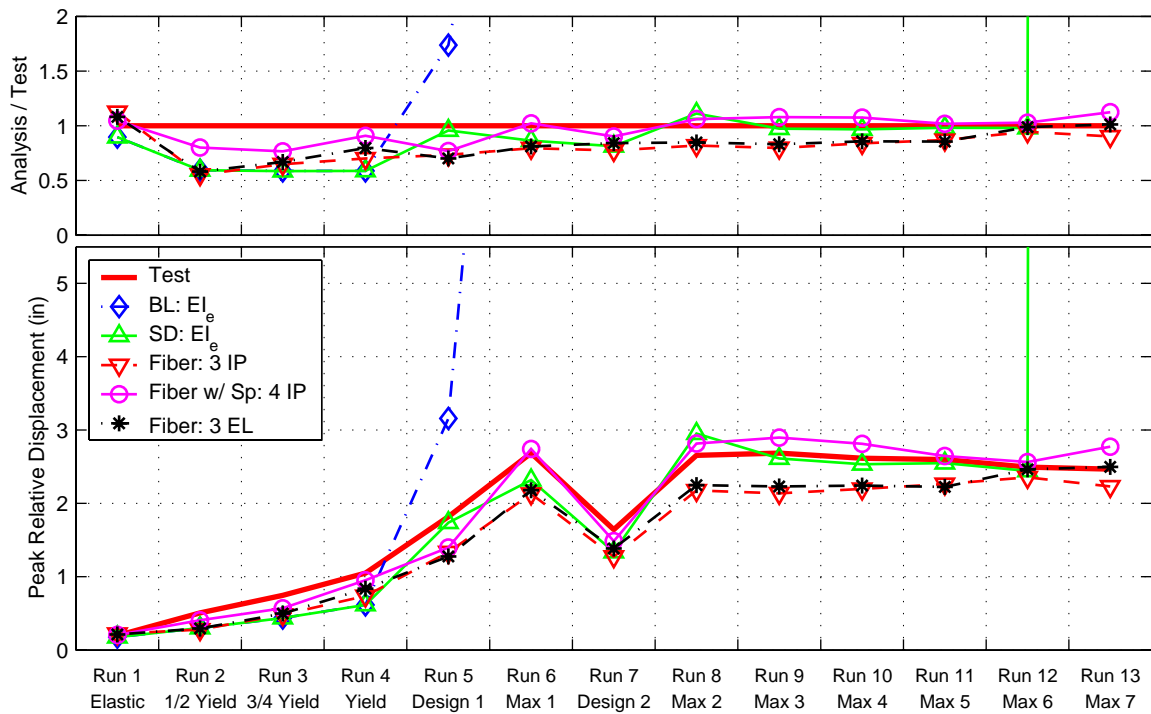

Figure E-15. Analytical and experimental *peak relative longitudinal displacements* for runs 1 to 8 of test *A1*. All runs were joined and analyzed as one long run (in sequence).[a]

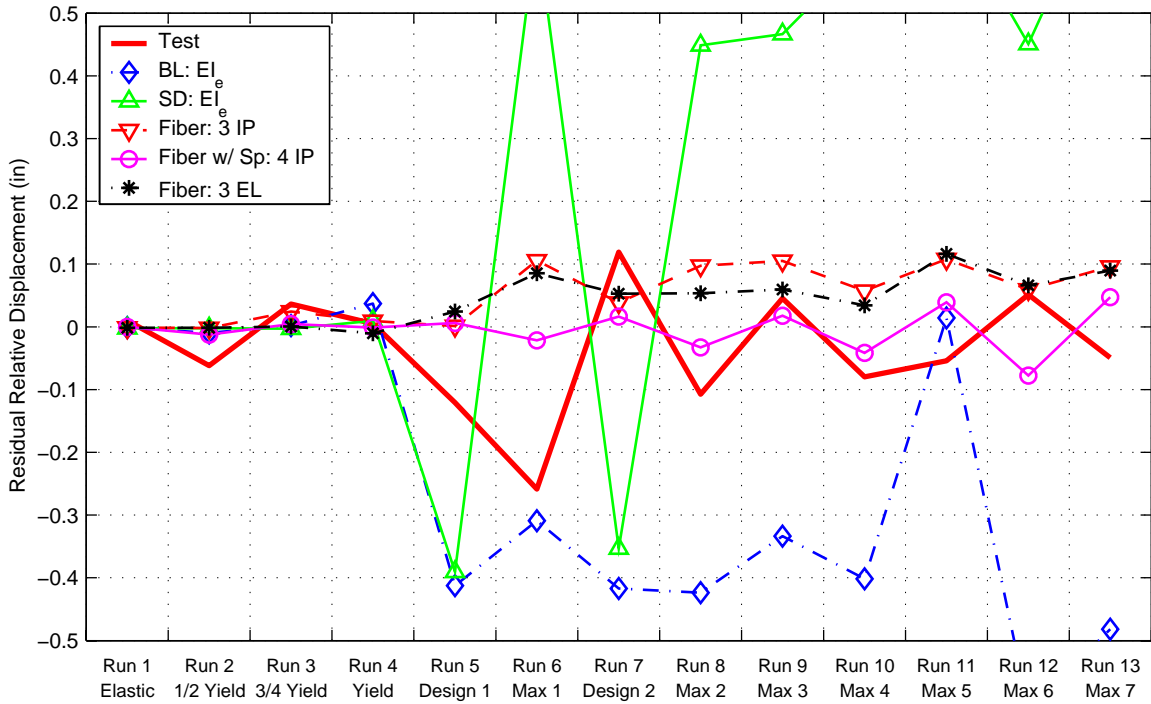a. The displacements were zeroed at the beginning of each run for both test and analysis cases.
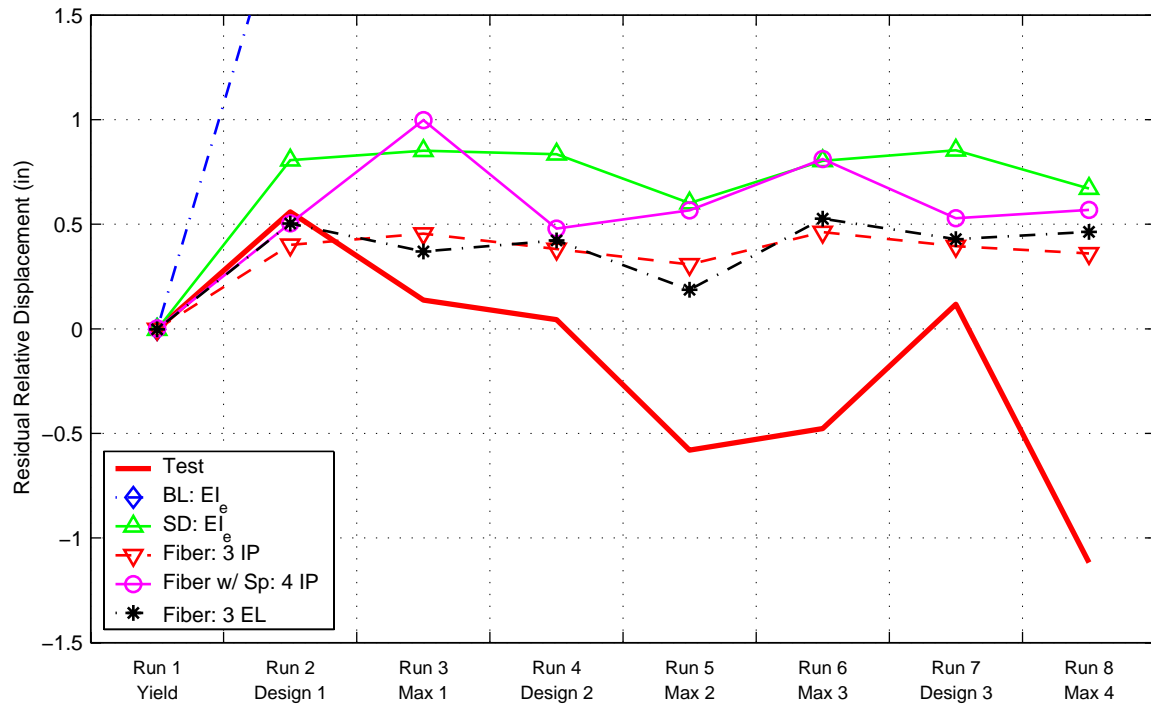
Figure E-16. Analytical and experimental *residual longitudinal displacements* for runs 1 to 8 of test *A1*. Each run was analyzed individually (not in sequence).
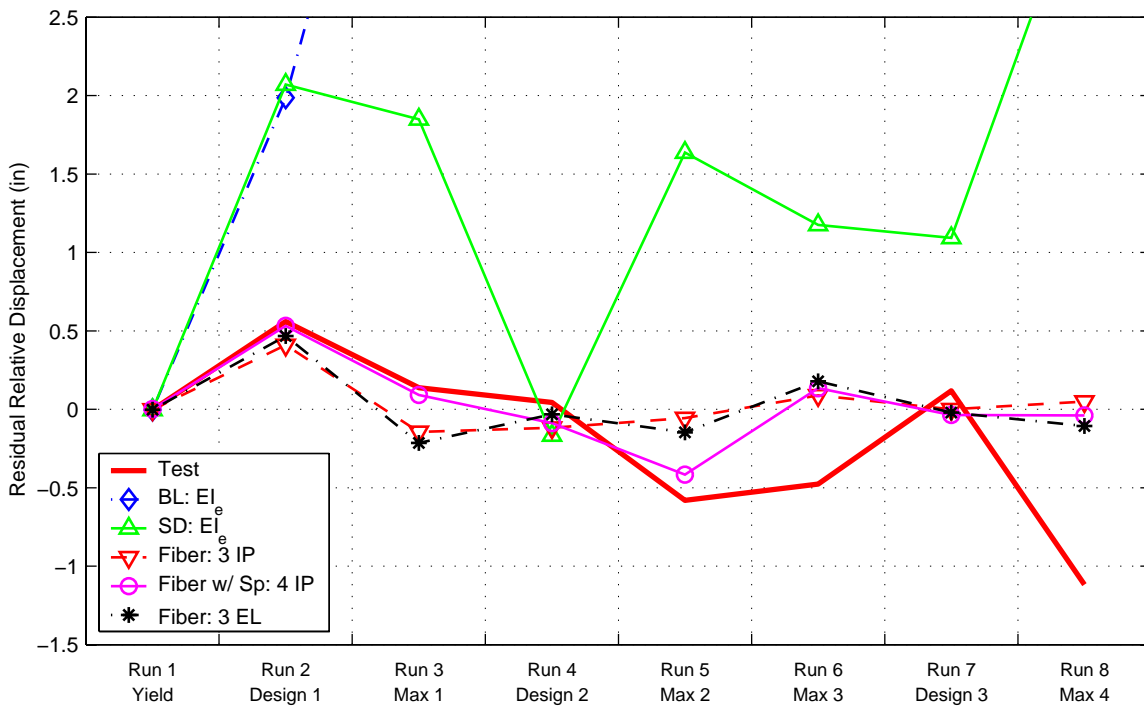
Figure E-17. Analytical and experimental *residual longitudinal displacements* for runs 1 to 8 of test *A1*. All runs were joined and analyzed as one long run (in sequence).[a]

a. The displacements were zeroed at the beginning of each run for both test and analysis cases.
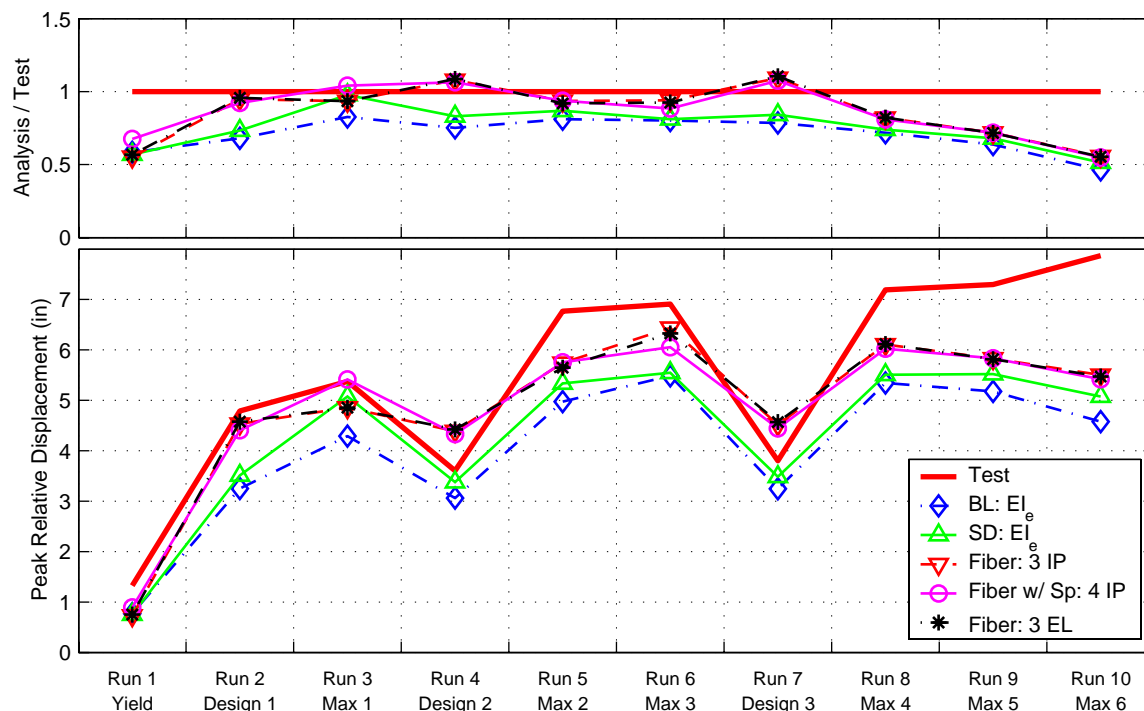
Figure E-18. Analytical and experimental *peak relative longitudinal displacements* for runs 1 to 10 of test *A2*. Each run was analyzed individually (not in sequence).
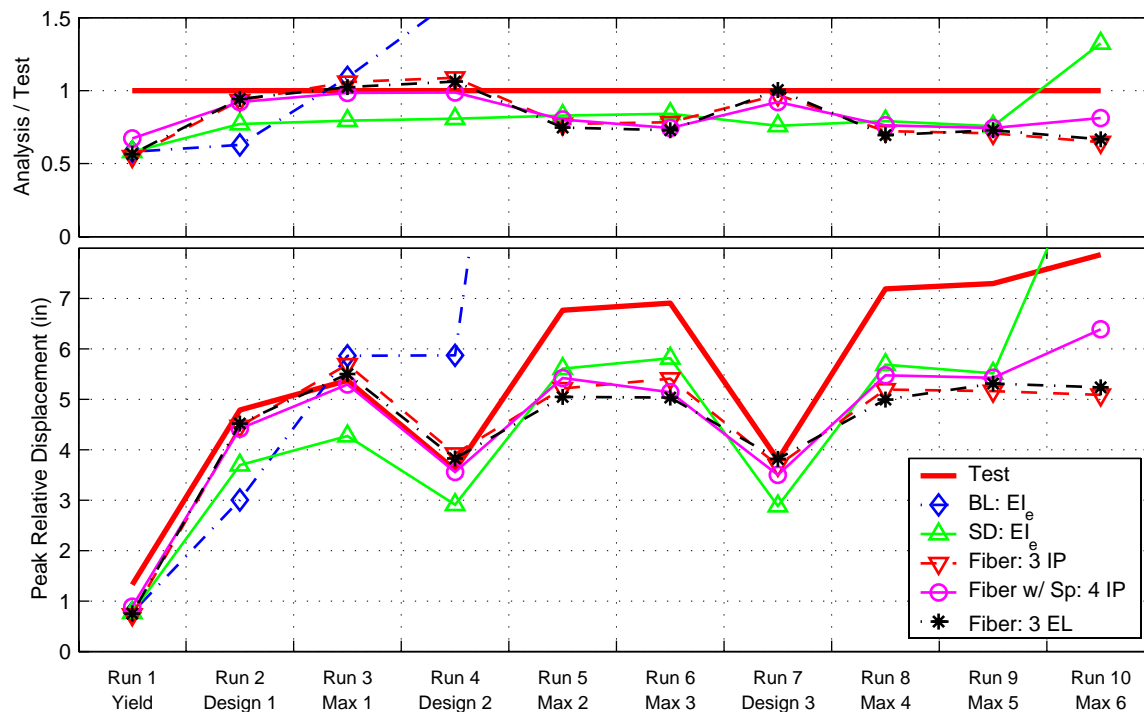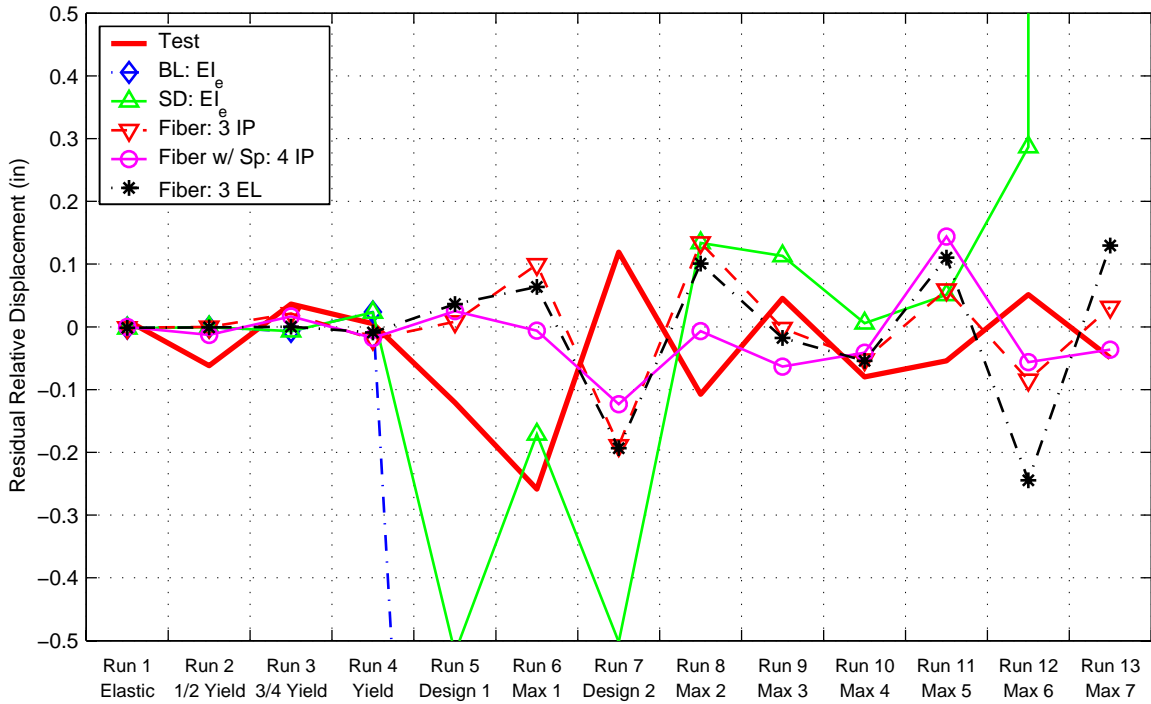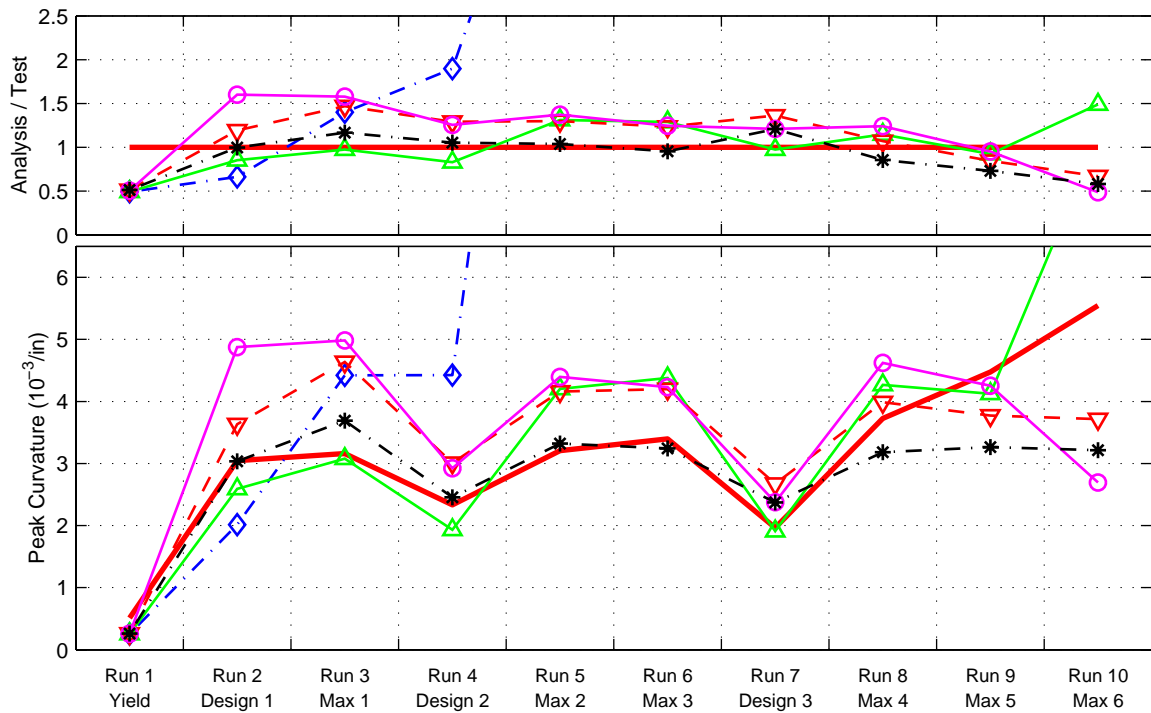

Figure E-19. Analytical and experimental *peak relative longitudinal displacements* for runs 1 to 10 of test *A2*. All runs were joined and analyzed as one long run (in sequence).[a]

a. The displacements were zeroed at the beginning of each run for both test and analysis cases.
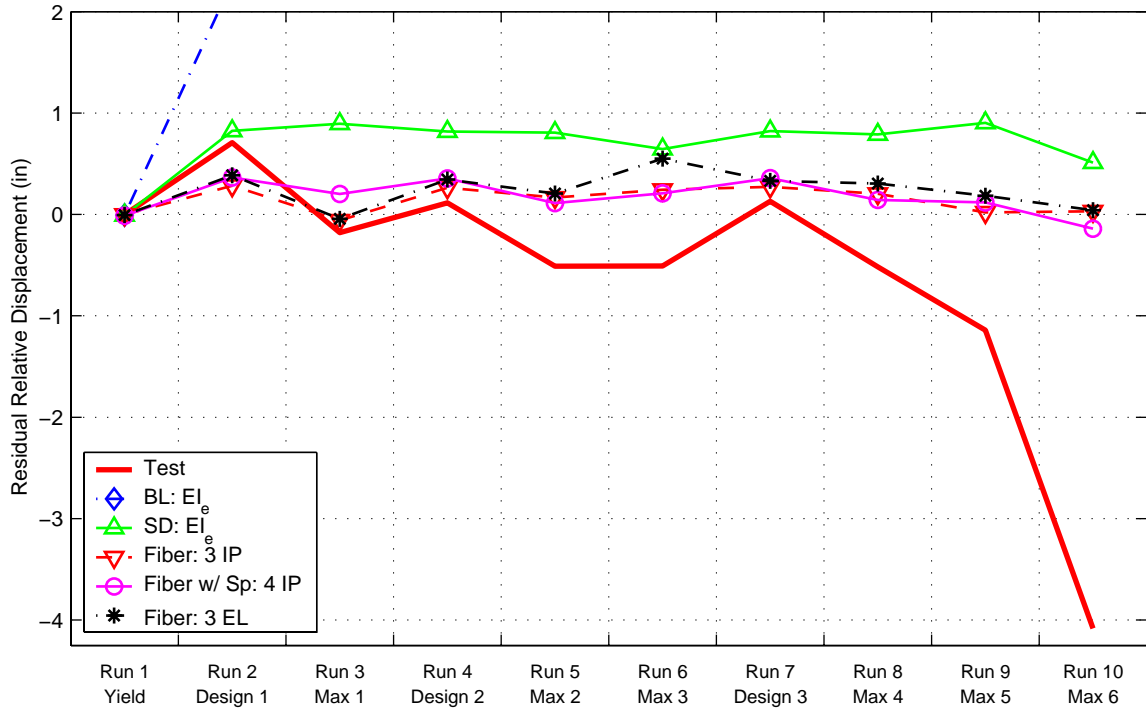
Figure E-20. Analytical and experimental *residual longitudinal displacements* for runs 1 to 10 of test *A2*. Each run was analyzed individually (not in sequence).
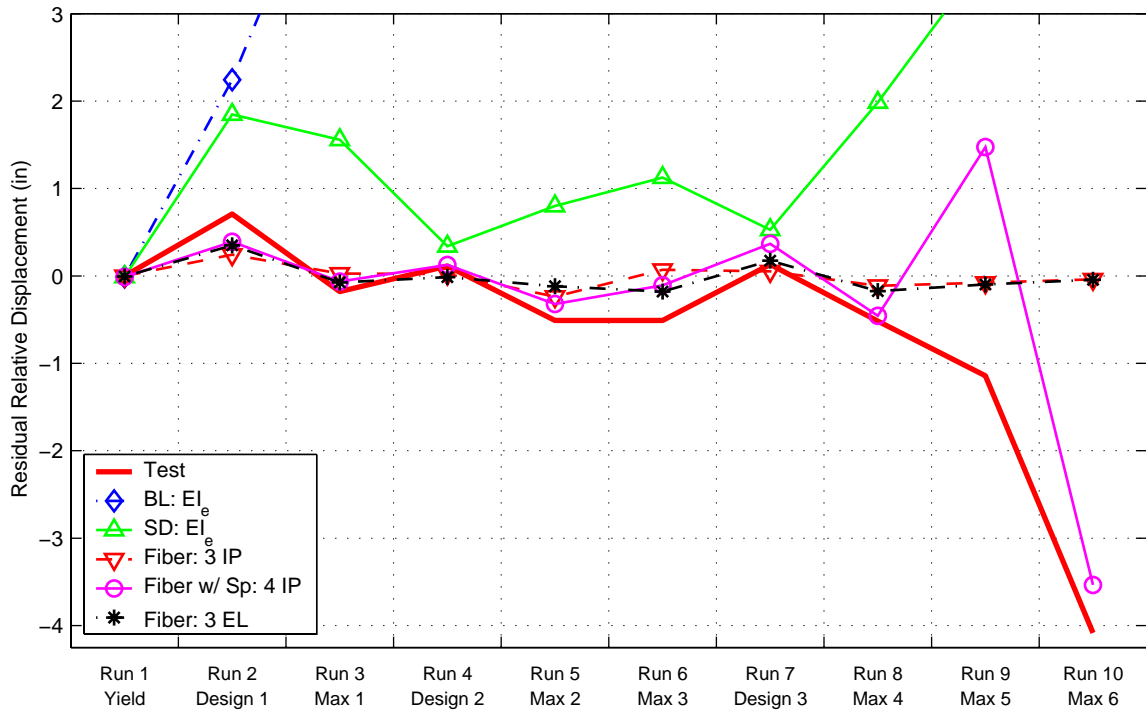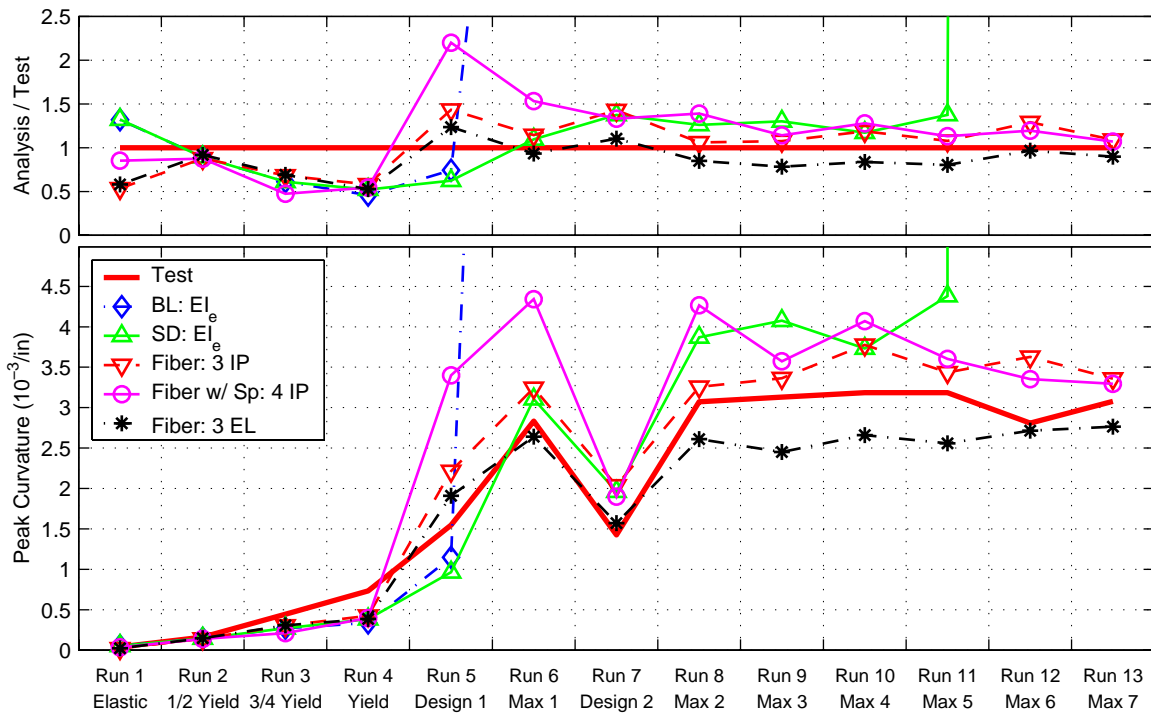

Figure E-21. Analytical and experimental *residual longitudinal displacements* for runs 1 to 10 of test *A2*. All runs were joined and analyzed as one long run (in sequence).[a]

a. The displacements were zeroed at the beginning of each run for both test and analysis cases.
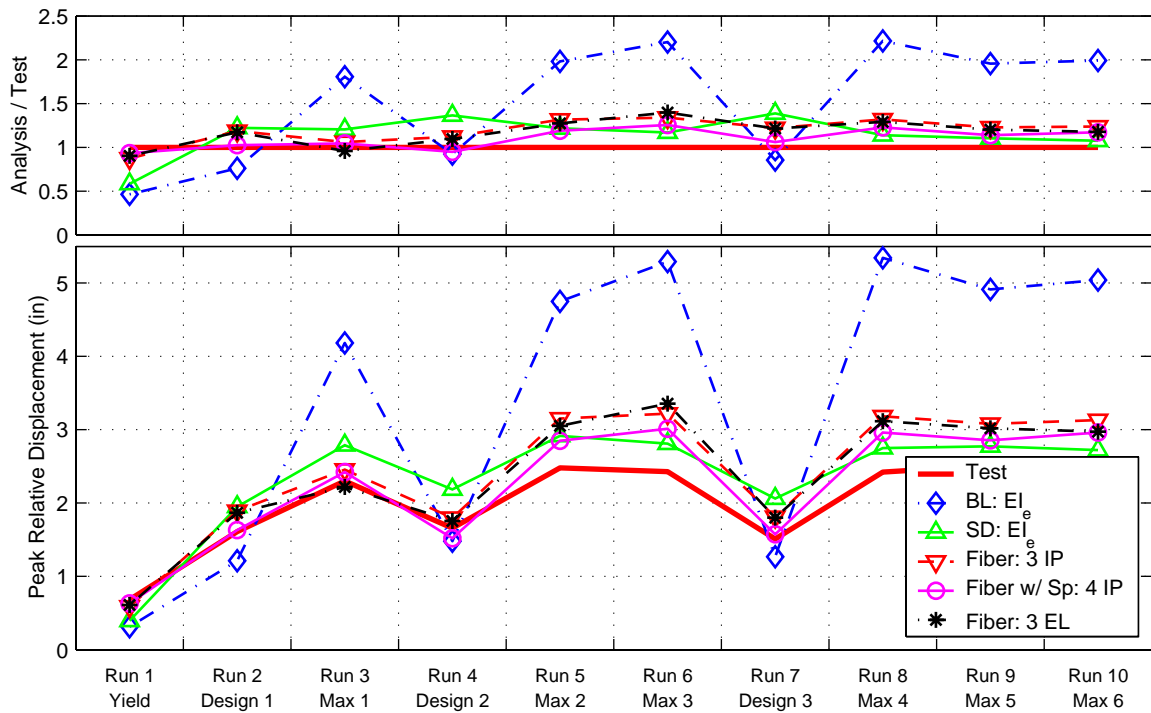
Figure E-22. Analytical and experimental *peak relative lateral displacements* for runs 1 to 10 of test *A2*. Each run was analyzed individually (not in sequence).
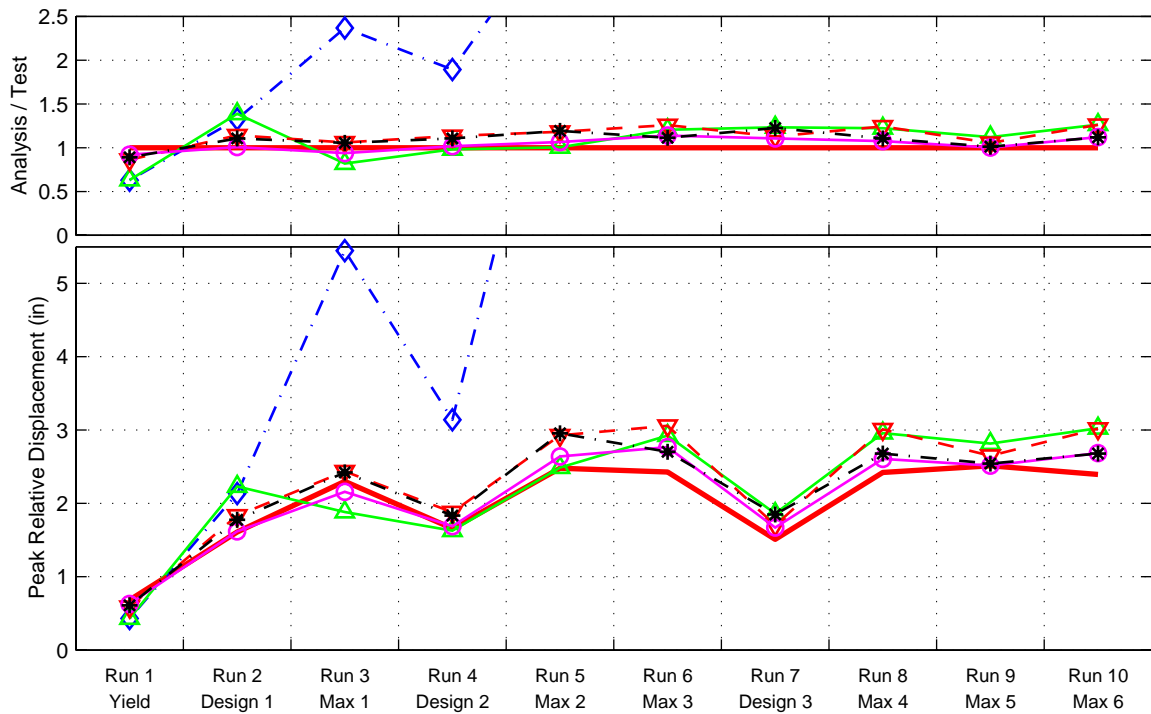
Figure E-23. Analytical and experimental *peak relative lateral displacements* for runs 1 to 10 of test *A2*. All runs were joined and analyzed as one long run (in sequence).[a]

a. The displacements were zeroed at the beginning of each run for both test and analysis cases.

427
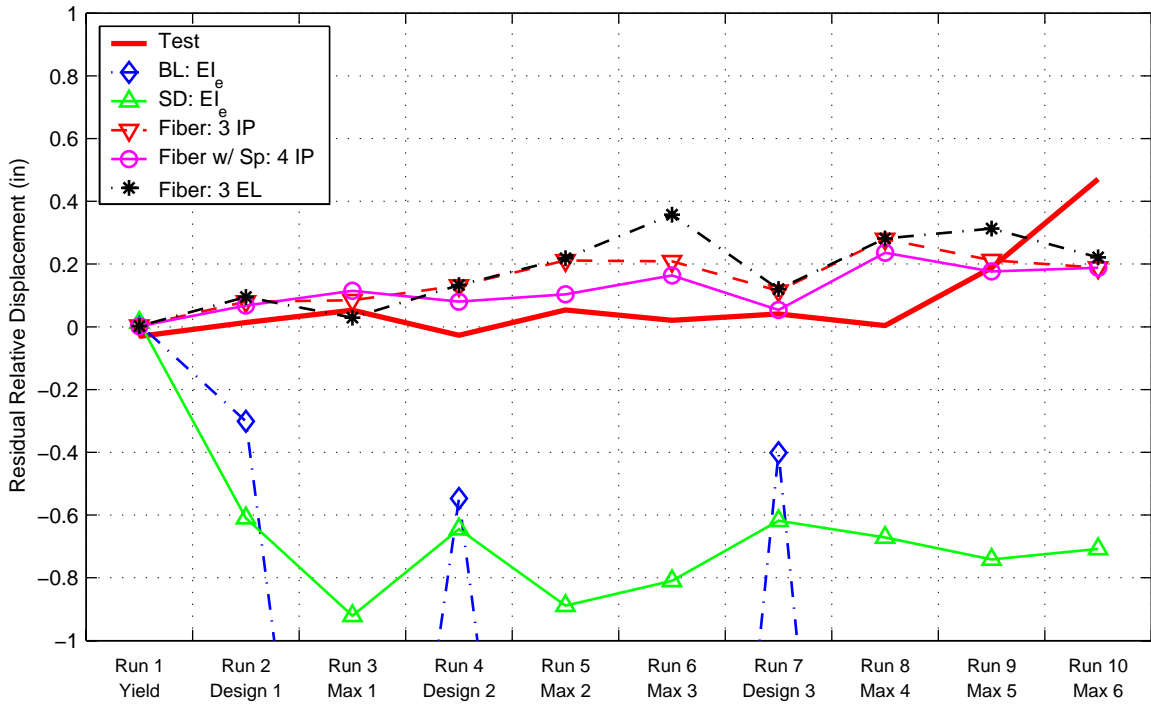
Figure E-24. Analytical and experimental *residual lateral displacements* for runs 1 to 10 of test *A2*. Each run was analyzed individually (not in sequence).
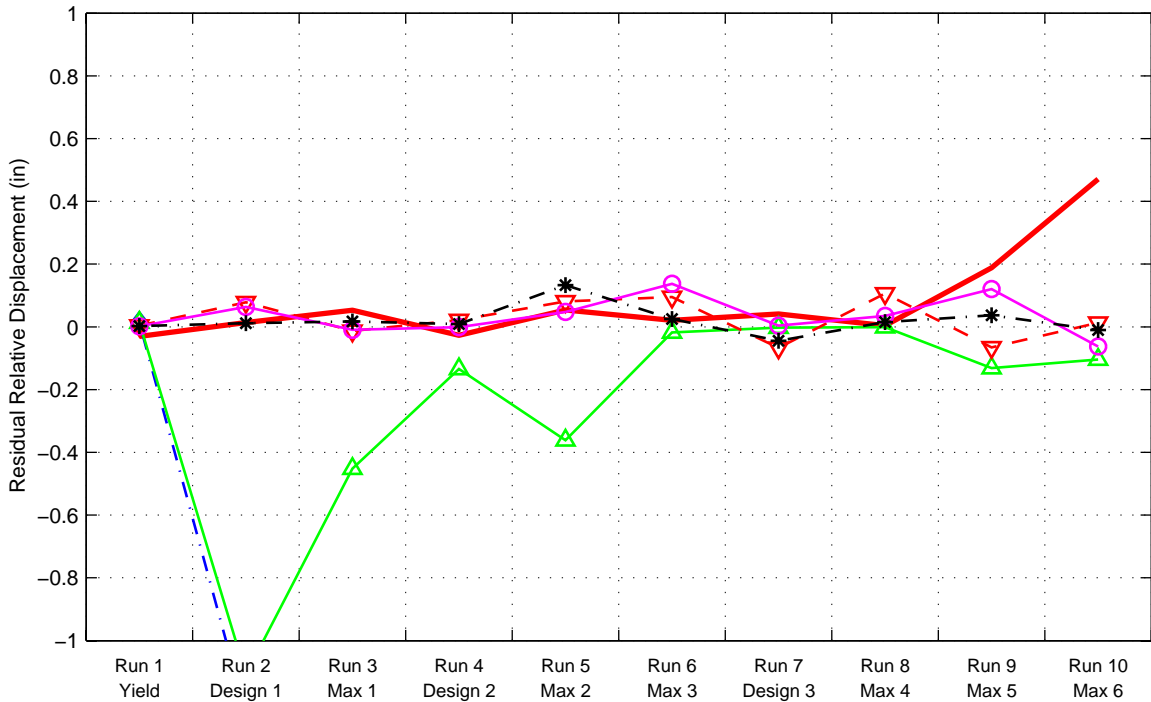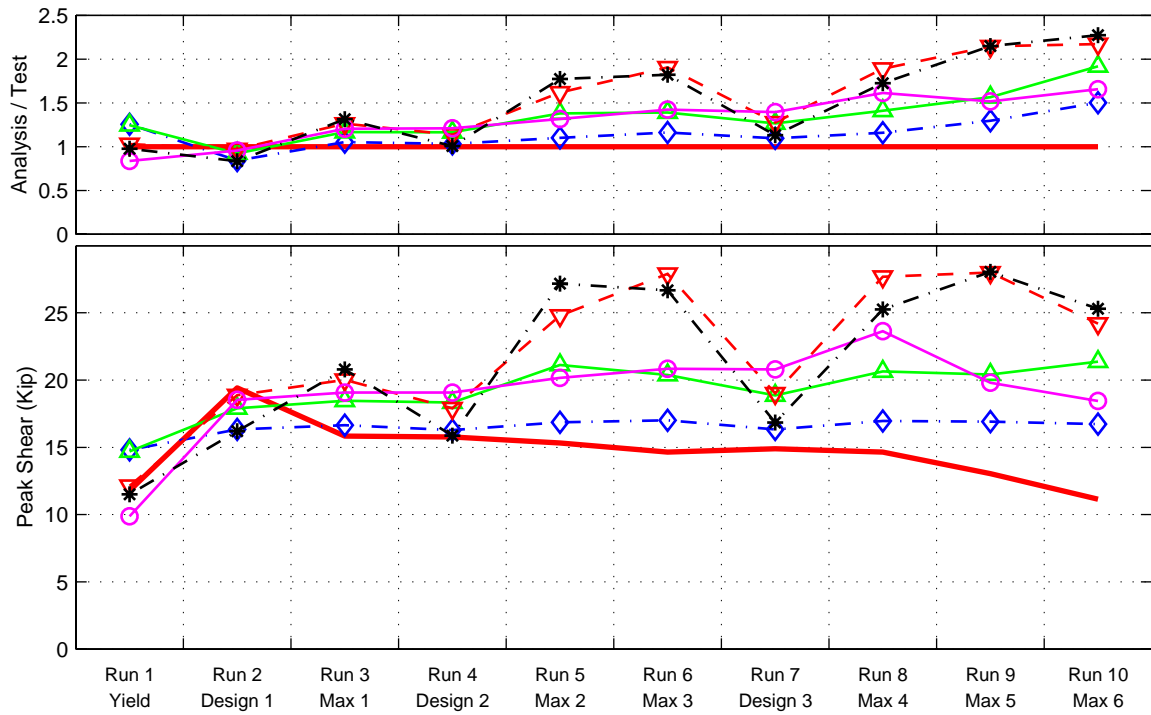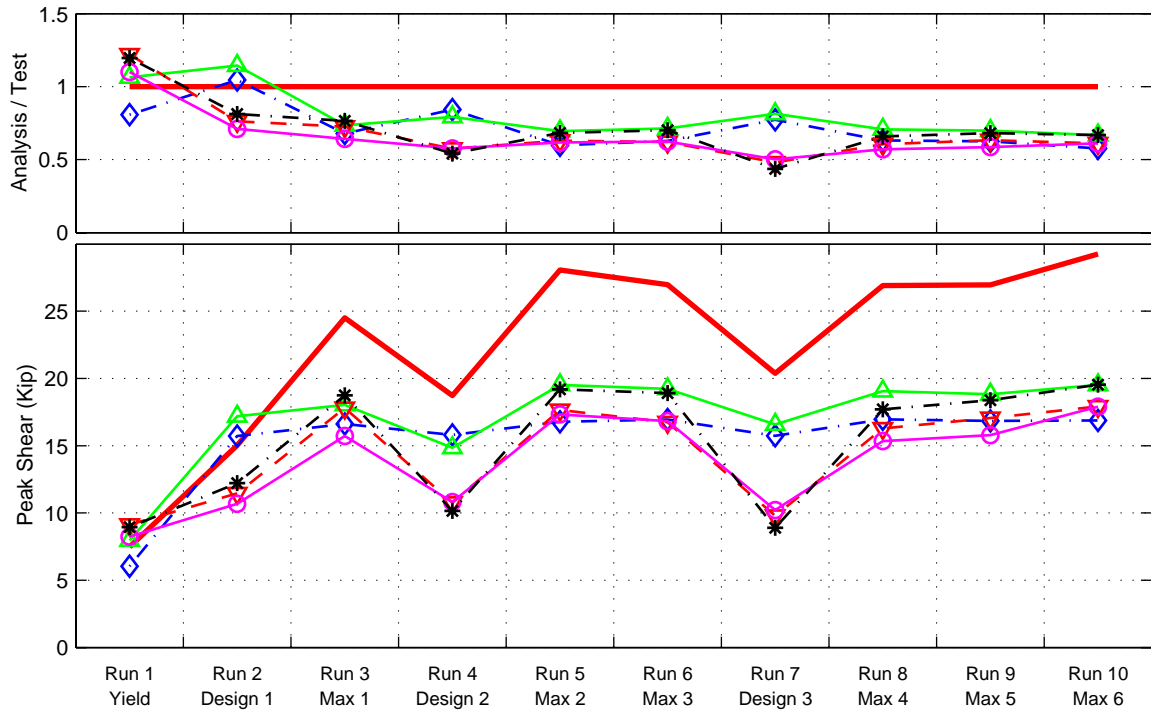

Figure E-25. Analytical and experimental *residual lateral displacements* for runs 1 to 10 of test *A2*. All runs were joined and analyzed as one long run (in sequence).[a]

a. The displacements were zeroed at the beginning of each run for both test and analysis cases.
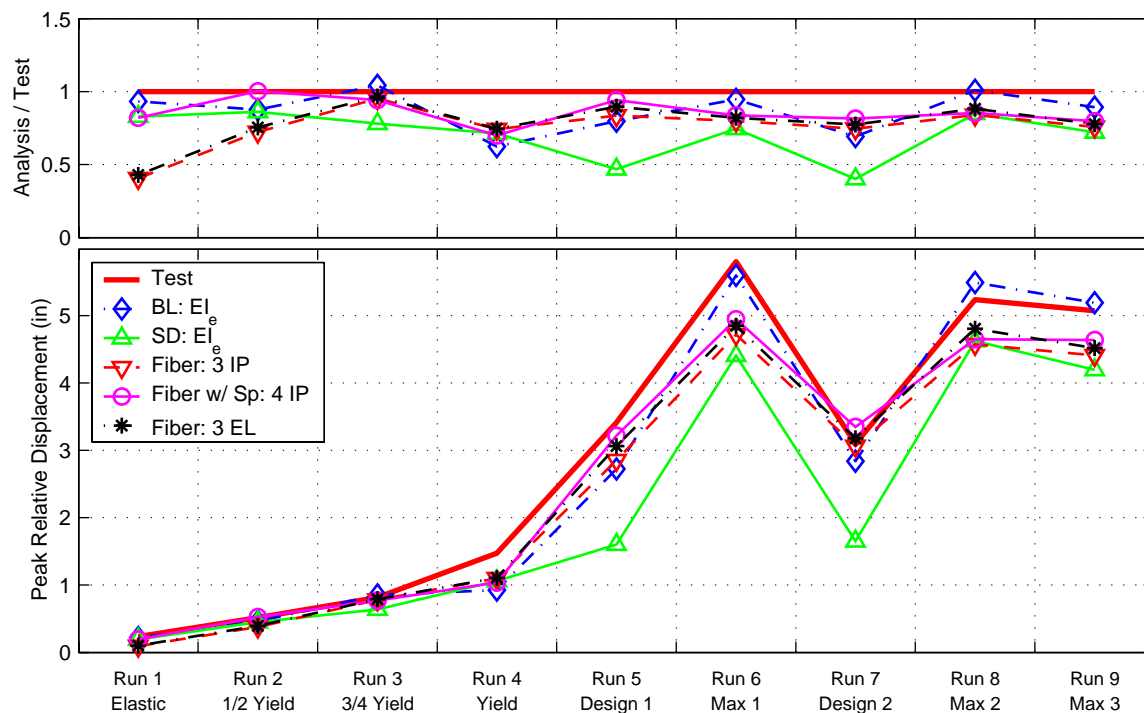
Figure E-26. Analytical and experimental *peak relative longitudinal displacements* for runs 1 to 9 of test *B1*. Each run was analyzed individually (not in sequence).
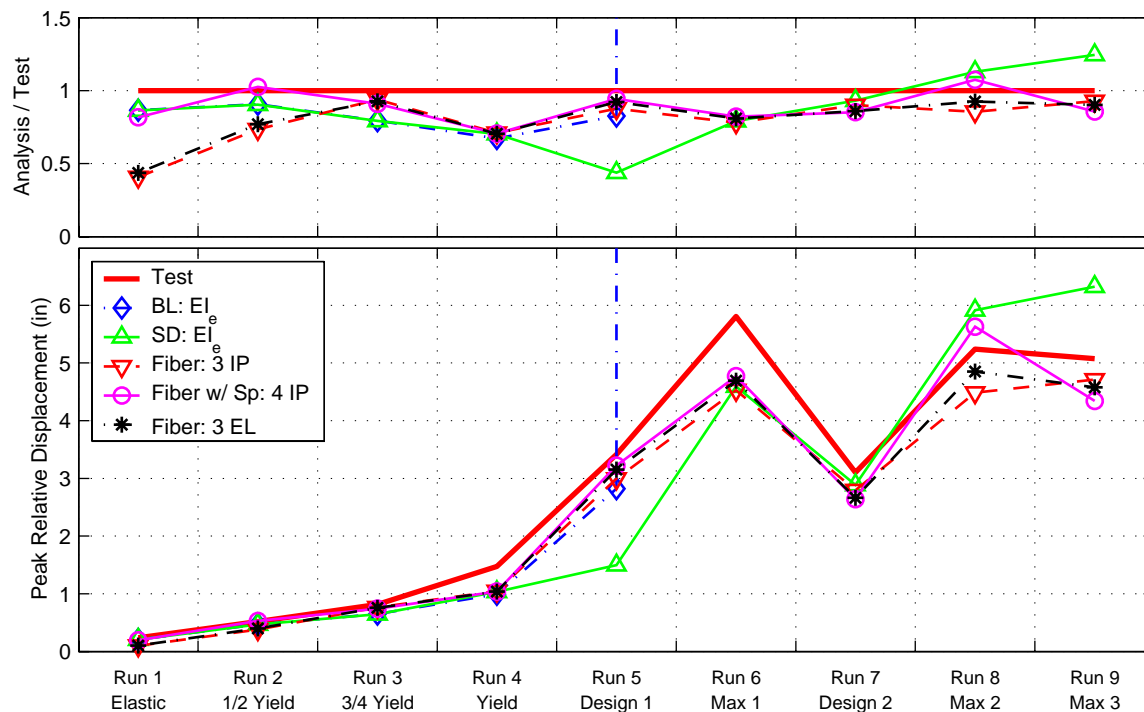
Figure E-27. Analytical and experimental *peak relative longitudinal displacements* for runs 1 to 9 of test *B1*. All runs were joined and analyzed as one long run (in sequence).[a]

a. The displacements were zeroed at the beginning of each run for both test and analysis cases.
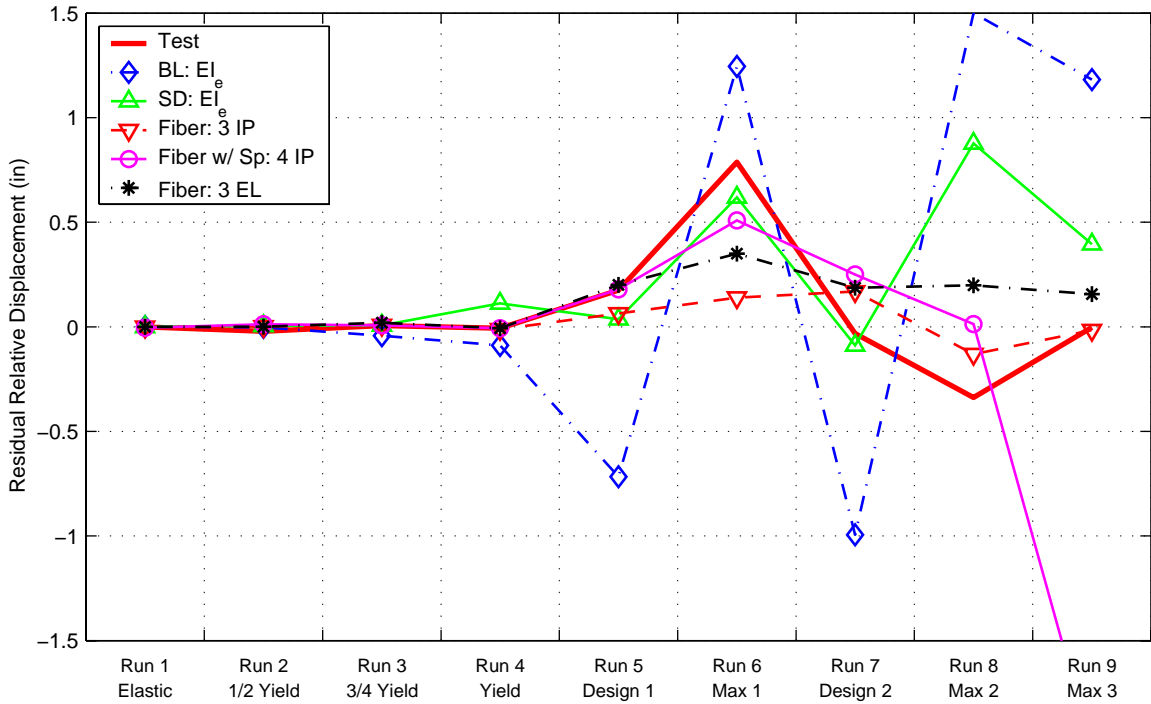
Figure E-28. Analytical and experimental *residual longitudinal displacements* for runs 1 to 9 of test *B1*. Each run was analyzed individually (not in sequence).
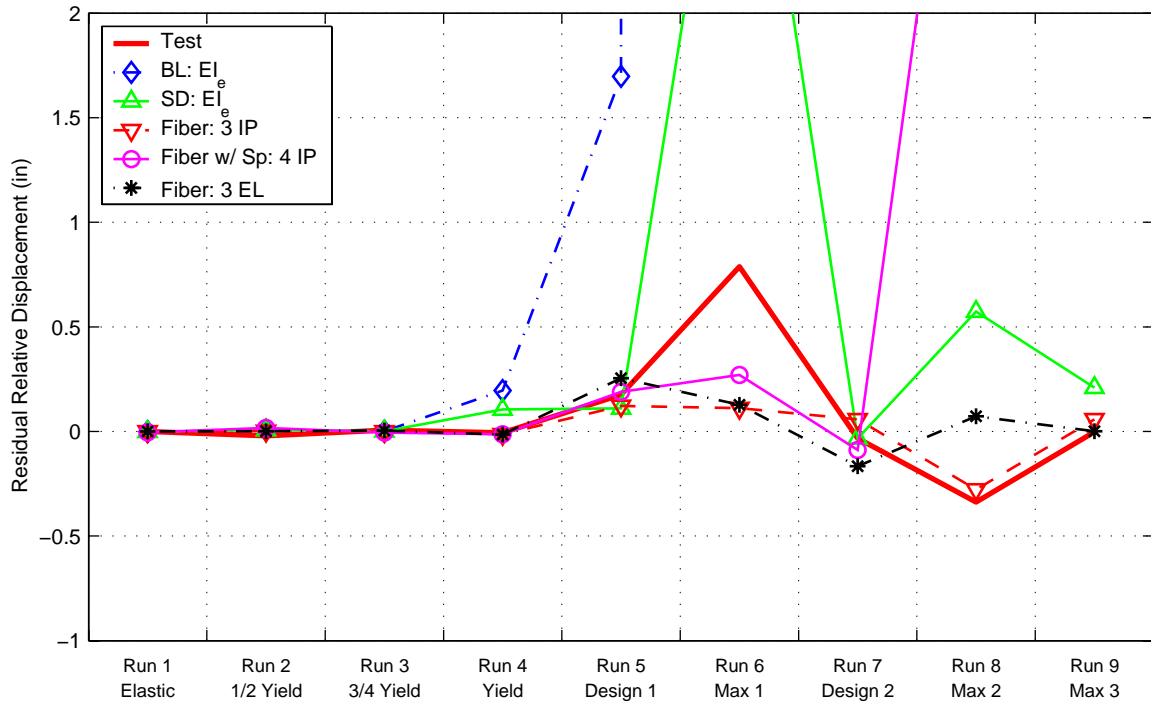
Figure E-29. Analytical and experimental *residual longitudinal displacements* for runs 1 to 9 of test *B1*. All runs were joined and analyzed as one long run (in sequence).[a]

a. The displacements were zeroed at the beginning of each run for both test and analysis cases.
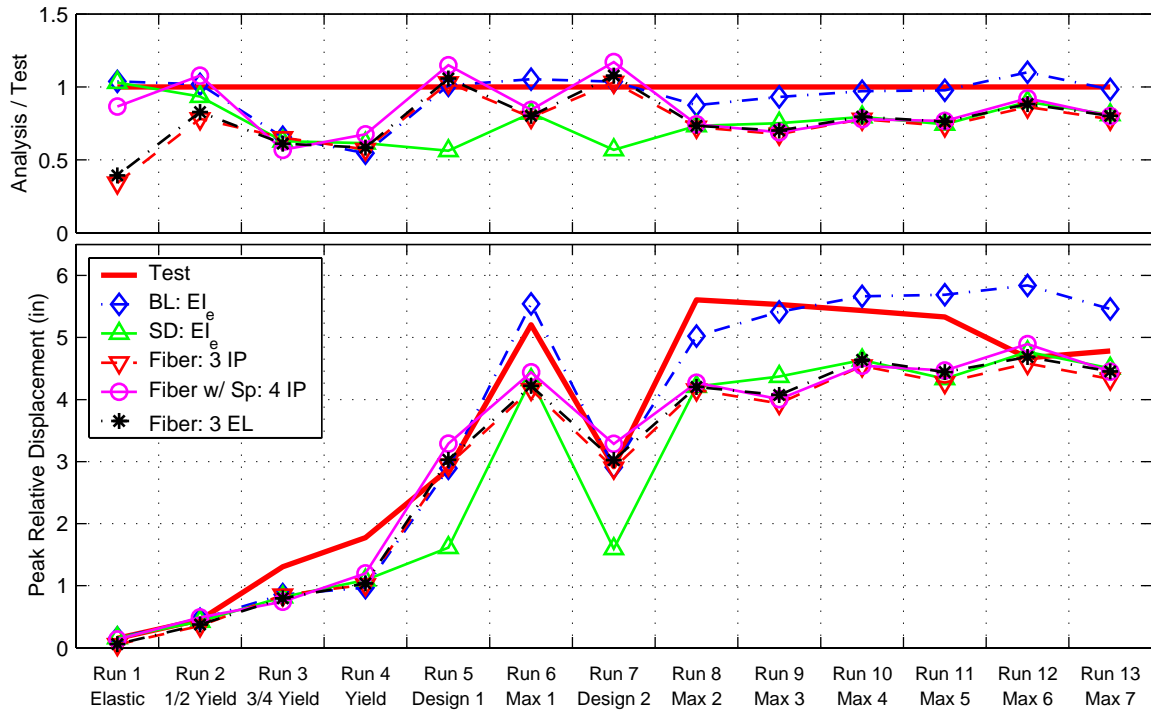
Figure E-30. Analytical and experimental *peak relative longitudinal displacements* for runs 1 to 13 of test *B2*. Each run was analyzed individually (not in sequence).
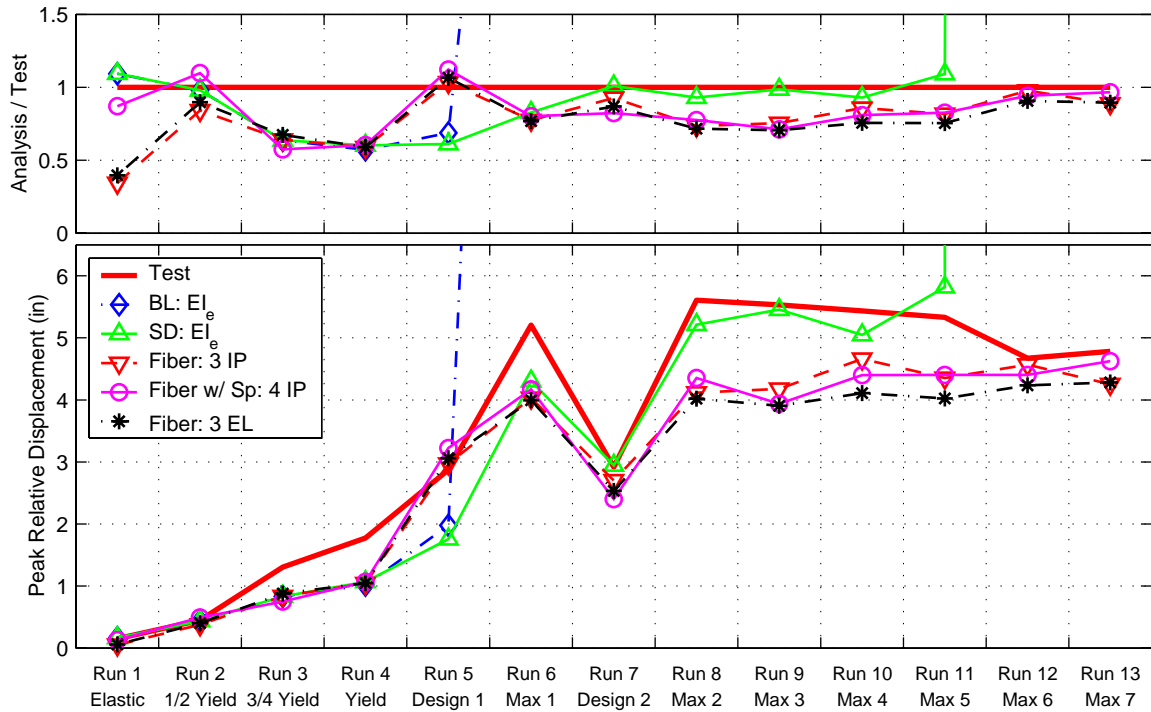
Figure E-31. Analytical and experimental *peak relative longitudinal displacements* for runs 1 to 13 of test *B2*. All runs were joined and analyzed as one long run (in sequence).[a]

a. The displacements were zeroed at the beginning of each run for both test and analysis cases.
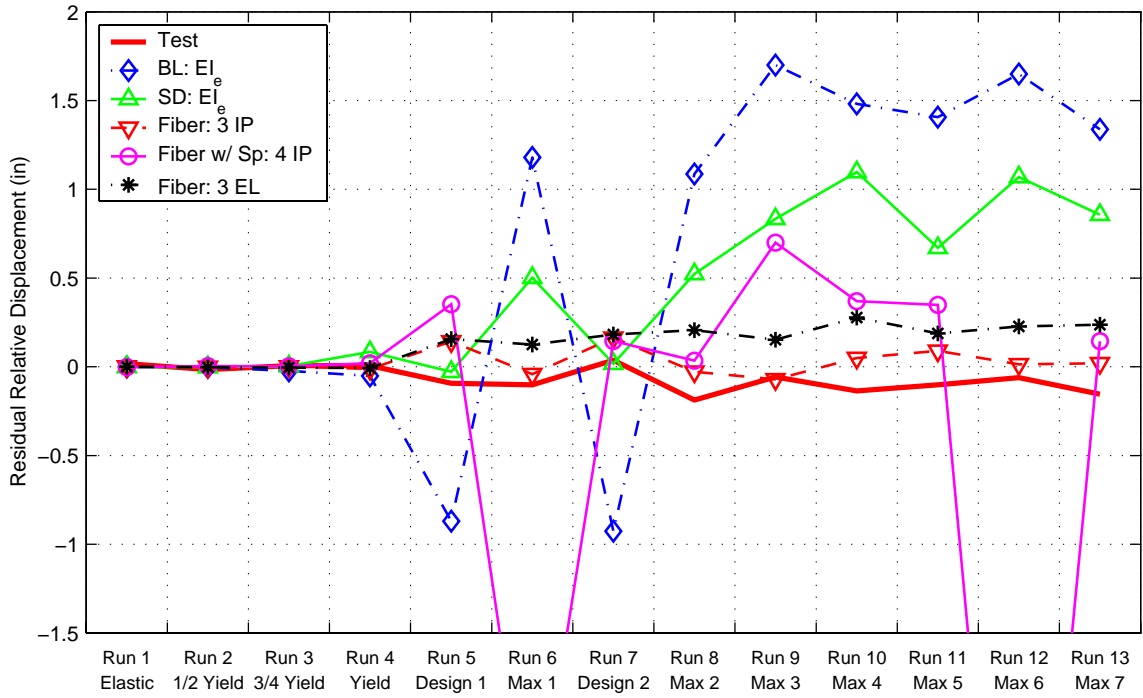
Figure E-32. Analytical and experimental *residual longitudinal displacements* for runs 1 to 13 of test *B2*. Each run was analyzed individually (not in sequence).
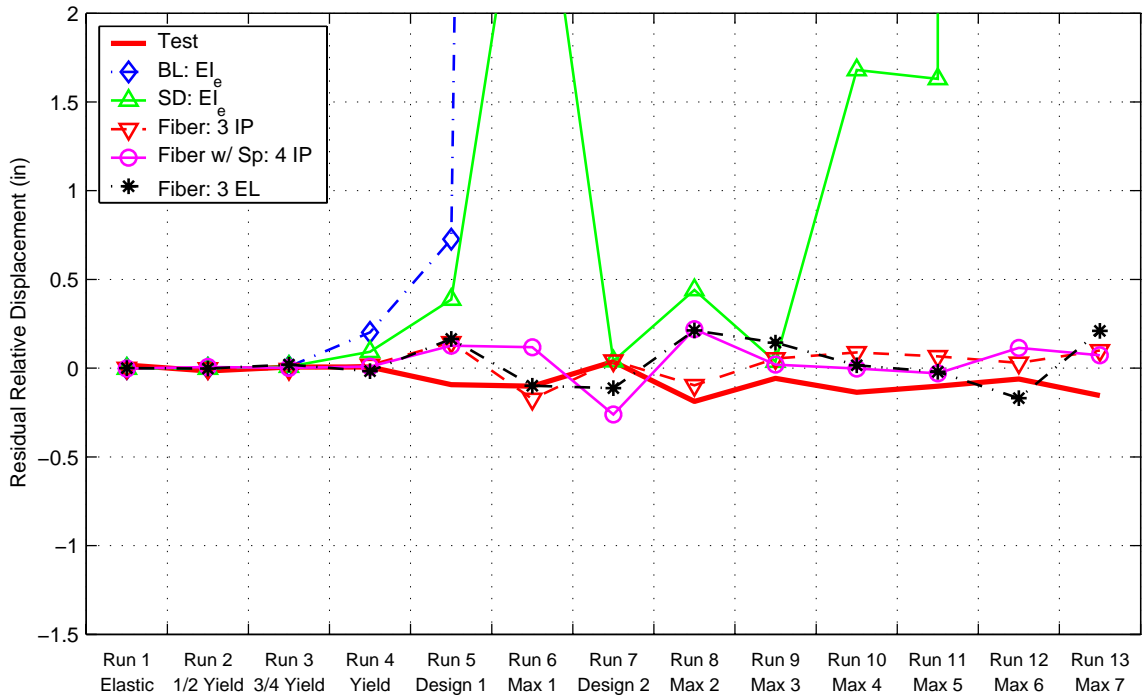
Figure E-33. Analytical and experimental *residual longitudinal displacements* for runs 1 to 13 of test *B2*. All runs were joined and analyzed as one long run (in sequence).[a]

a. The displacements were zeroed at the beginning of each run for both test and analysis cases.

432
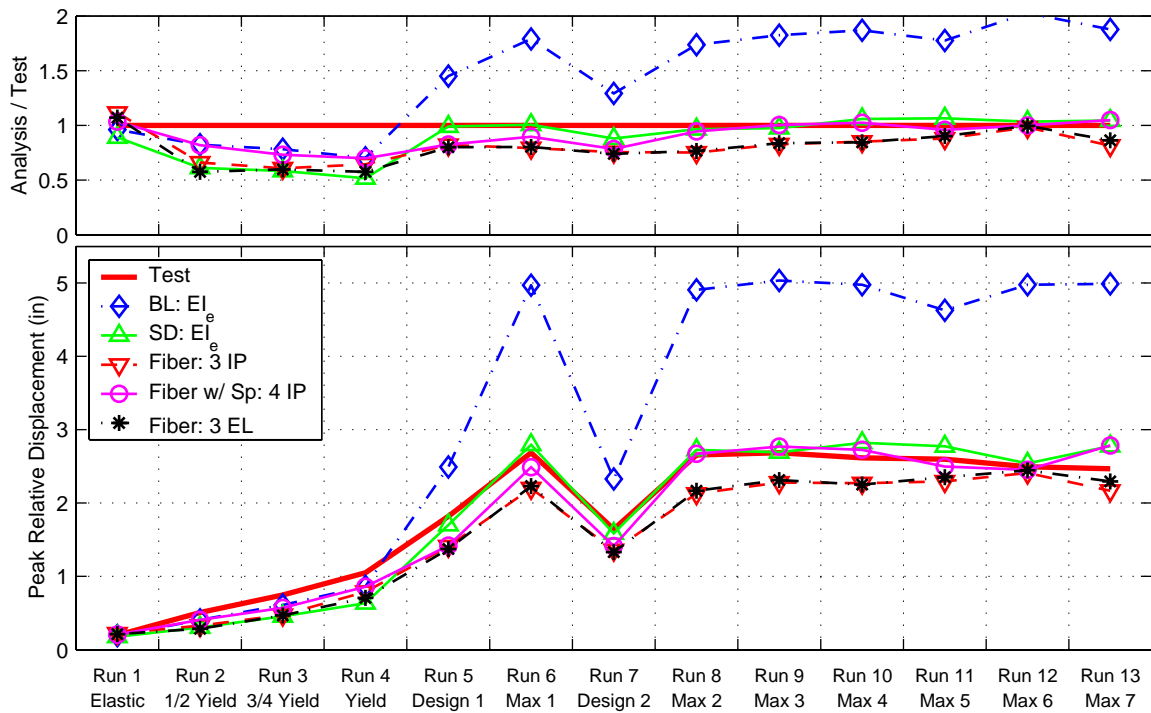
Figure E-34. Analytical and experimental *peak relative lateral displacements* for runs 1 to 13 of test *B2*. Each run was analyzed individually (not in sequence).

Figure E-35. Analytical and experimental *peak relative lateral displacements* for runs 1 to 13 of test *B2*. All runs were joined and analyzed as one long run (in sequence).[a]

a. The displacements were zeroed at the beginning of each run for both test and analysis cases.

Figure E-36. Analytical and experimental *residual lateral displacements* for runs 1 to 13 of test *B2*. Each run was analyzed individually (not in sequence).

Figure E-37. Analytical and experimental *residual lateral displacements* for runs 1 to 13 of test *B2*. All runs were joined and analyzed as one long run (in sequence).[a]

a. The displacements were zeroed at the beginning of each run for both test and analysis cases.

434

Figure E-38. Analytical and experimental *longitudinal curvatures* for runs 1 to 10 of test *A2*.[a]
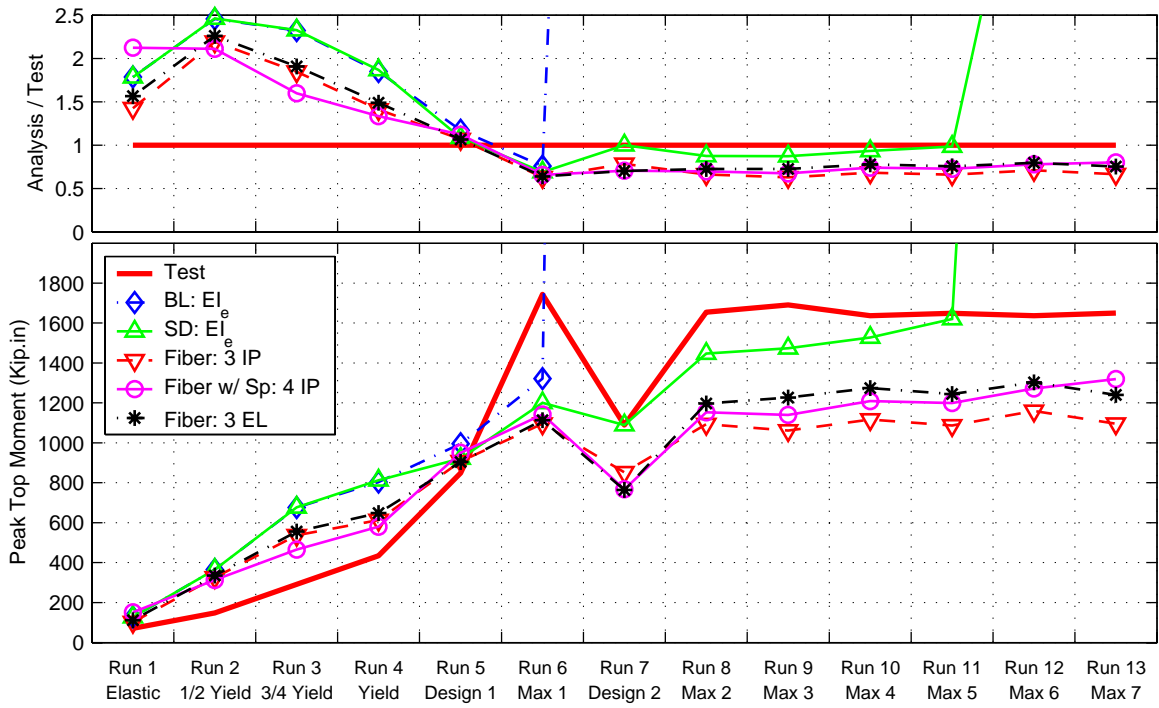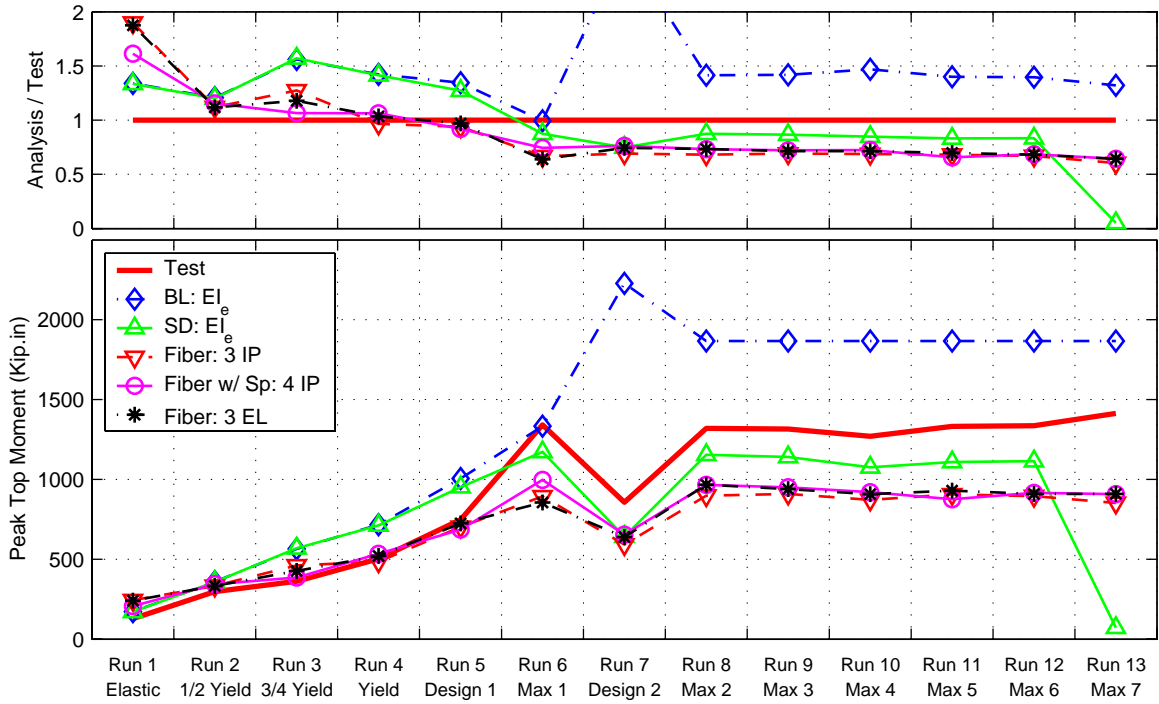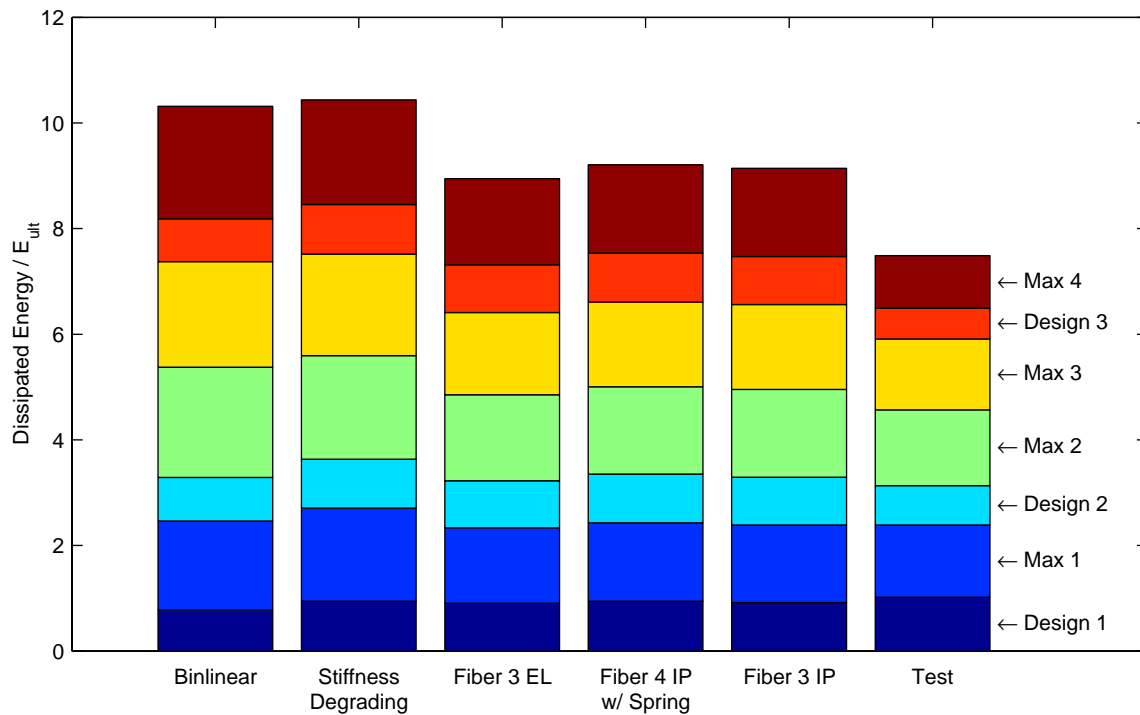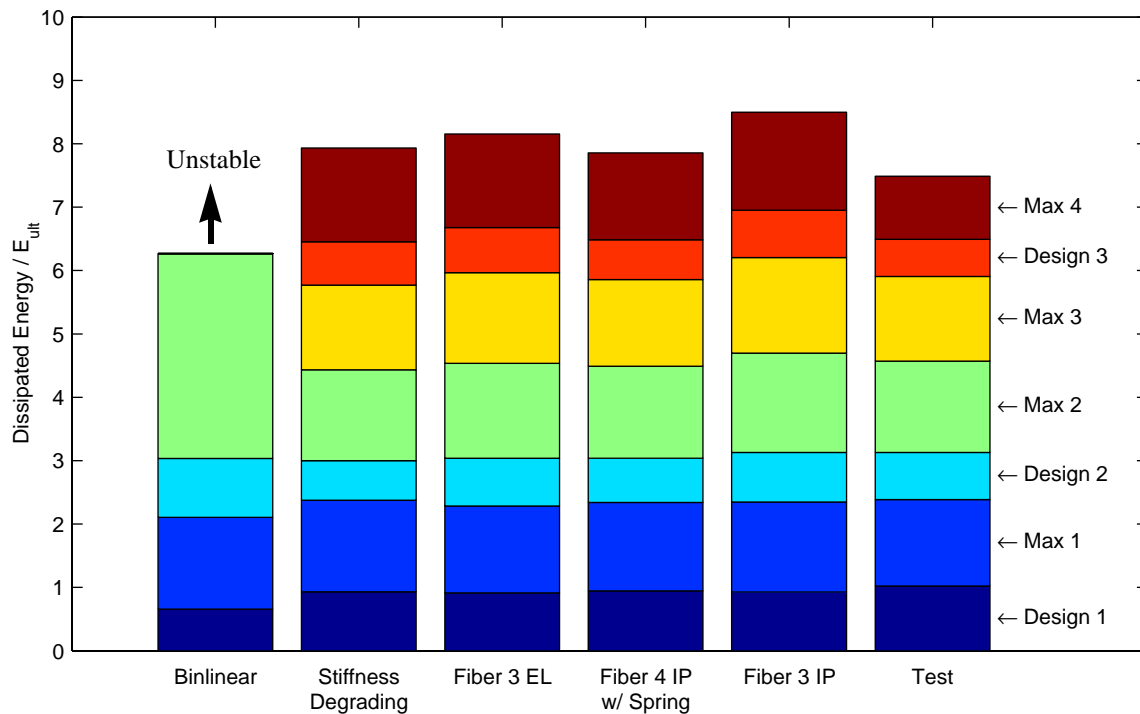

Figure E-39. Analytical and experimental *longitudinal curvatures* for runs 1 to 13 of test *B2*.[a]

a. All runs were joined and analyzed as one long run (in sequence). The curvatures were zeroed at the beginning of each run for both test and analysis cases.

435
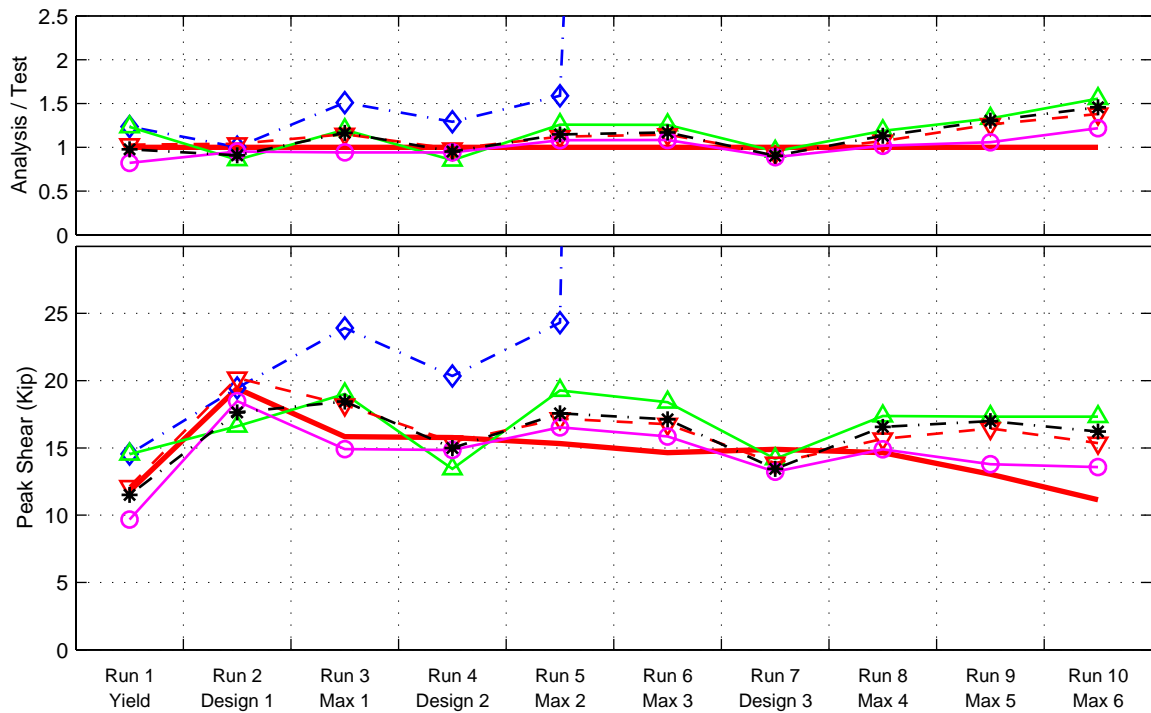
Figure E-40. Analytical and experimental *longitudinal shear force* for runs 1 to 10 of test *A2*.[a]
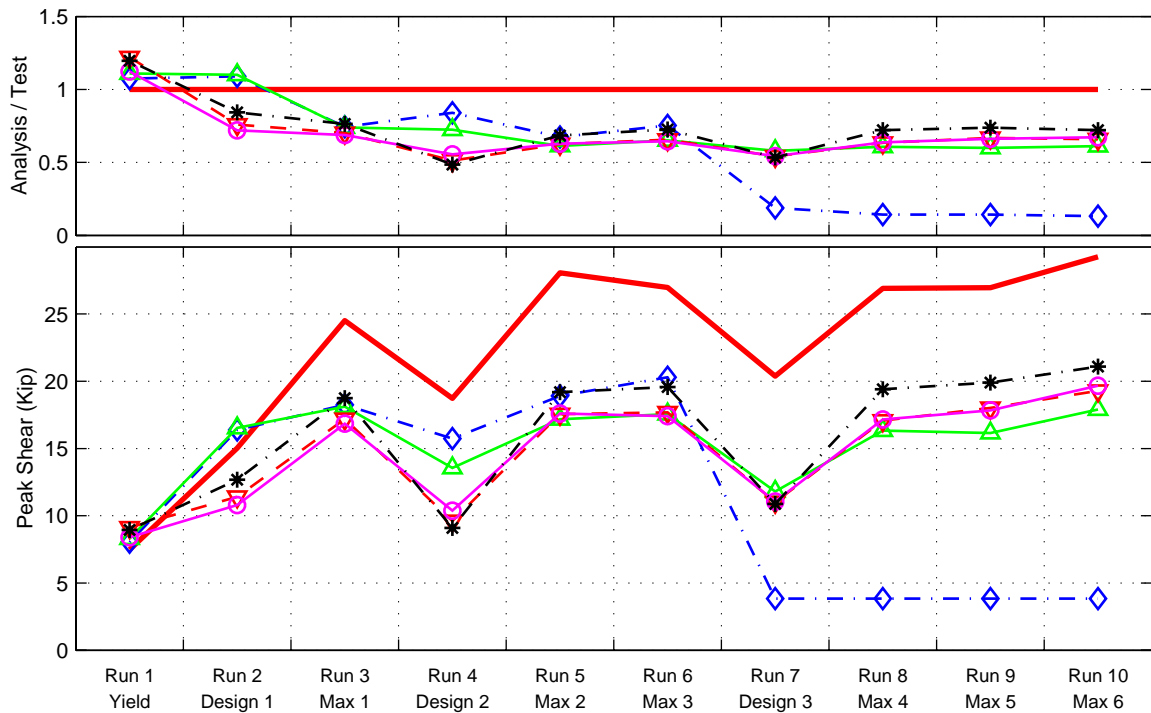
Figure E-41. Analytical and experimental *lateral shear force* for runs 1 to 10 of test *A2*.[a]

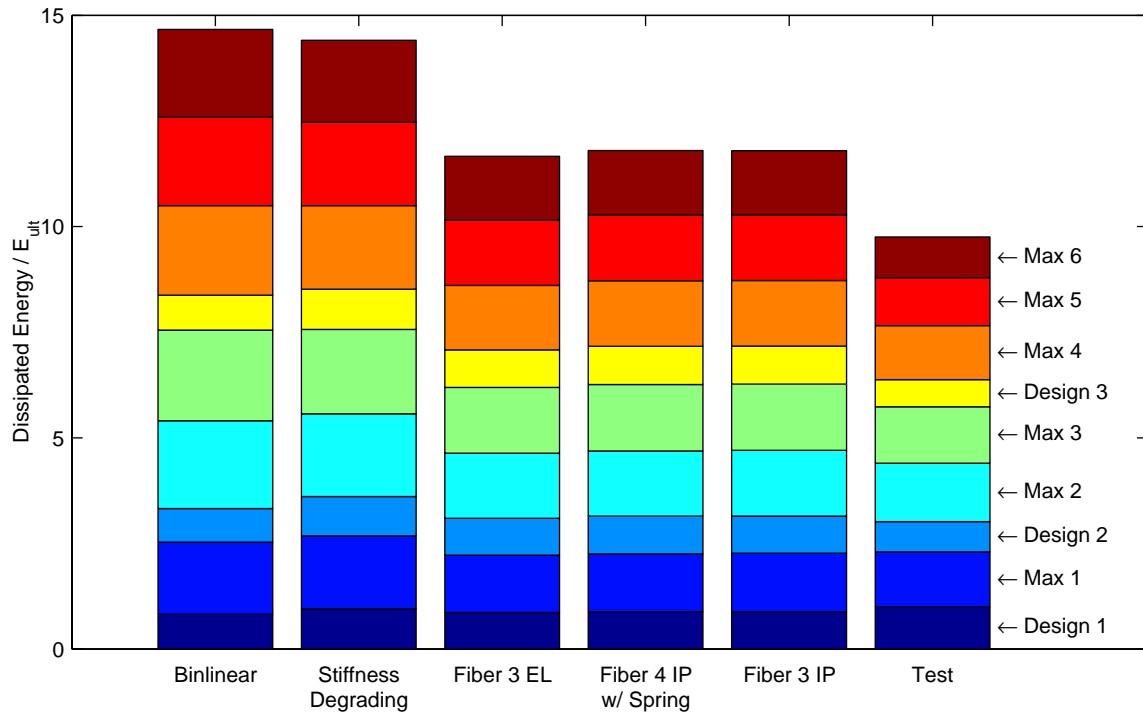a. All runs were joined and analyzed as one long run (in sequence).

Figure E-42. Analytical and experimental *longitudinal shear force* for runs 1 to 10 of test *A2*. Each run was analyzed individually (**not in sequence**).

Figure E-43. Analytical and experimental *lateral shear force* for runs 1 to 10 of test *A2*. Each run was analyzed individually (**not in sequence**).

437
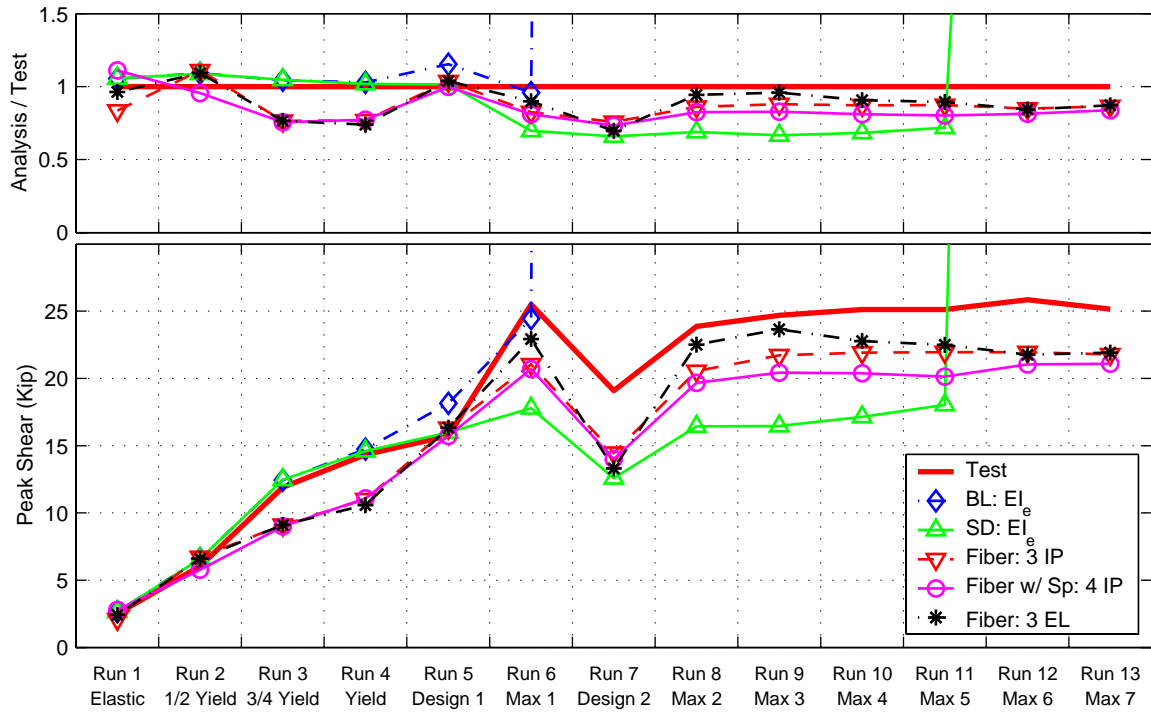
Figure E-44. Analytical and experimental *longitudinal shear force* for runs 1 to 13 of test *B2*.[a]
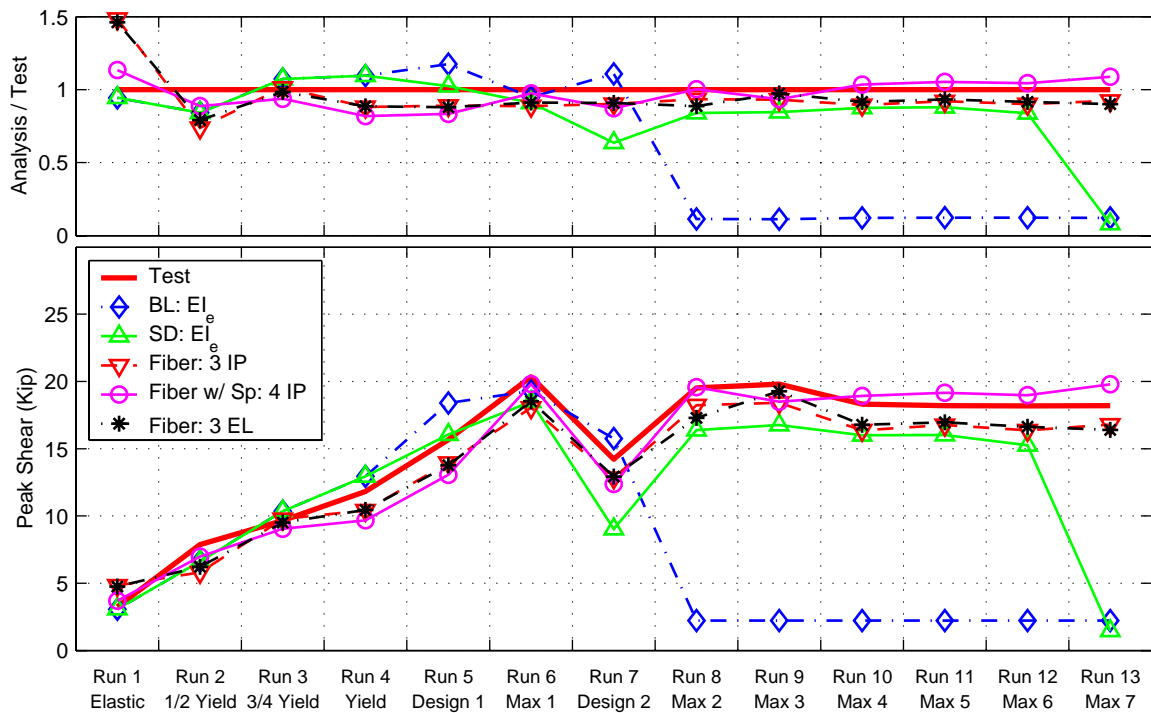
Figure E-45. Analytical and experimental *lateral shear force* for runs 1 to 13 of test *B2*.[a]

a. All runs were joined and analyzed as one long run (in sequence).
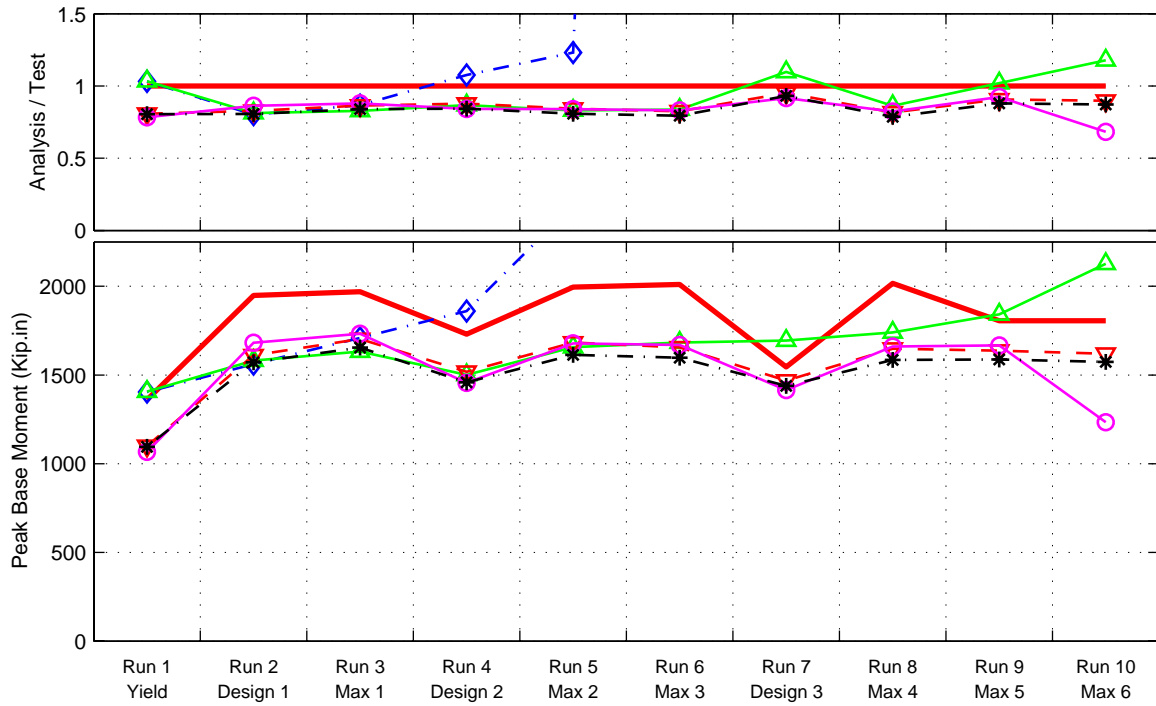
Figure E-46. Analytical and experimental *longitudinal base moment* for runs 1 to 10 of test *A2*.[a]
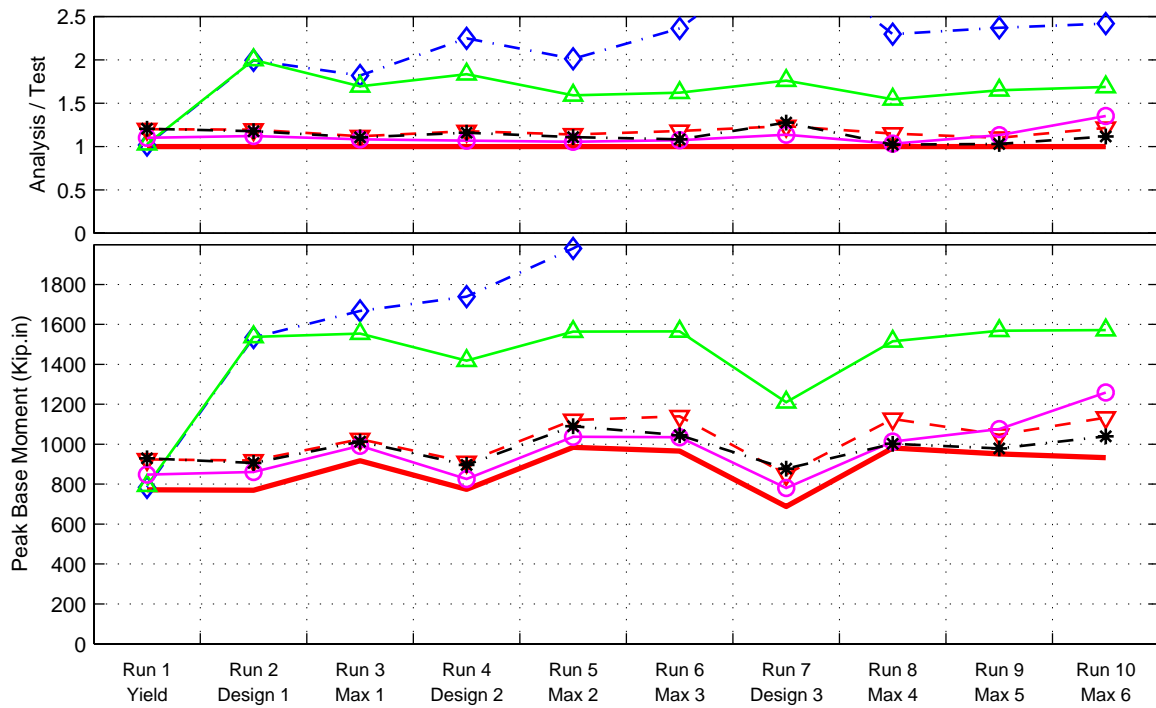
Figure E-47. Analytical and experimental *lateral base moment* for runs 1 to 10 of test *A2*.[a]

a. All runs were joined and analyzed as one long run (in sequence).

439
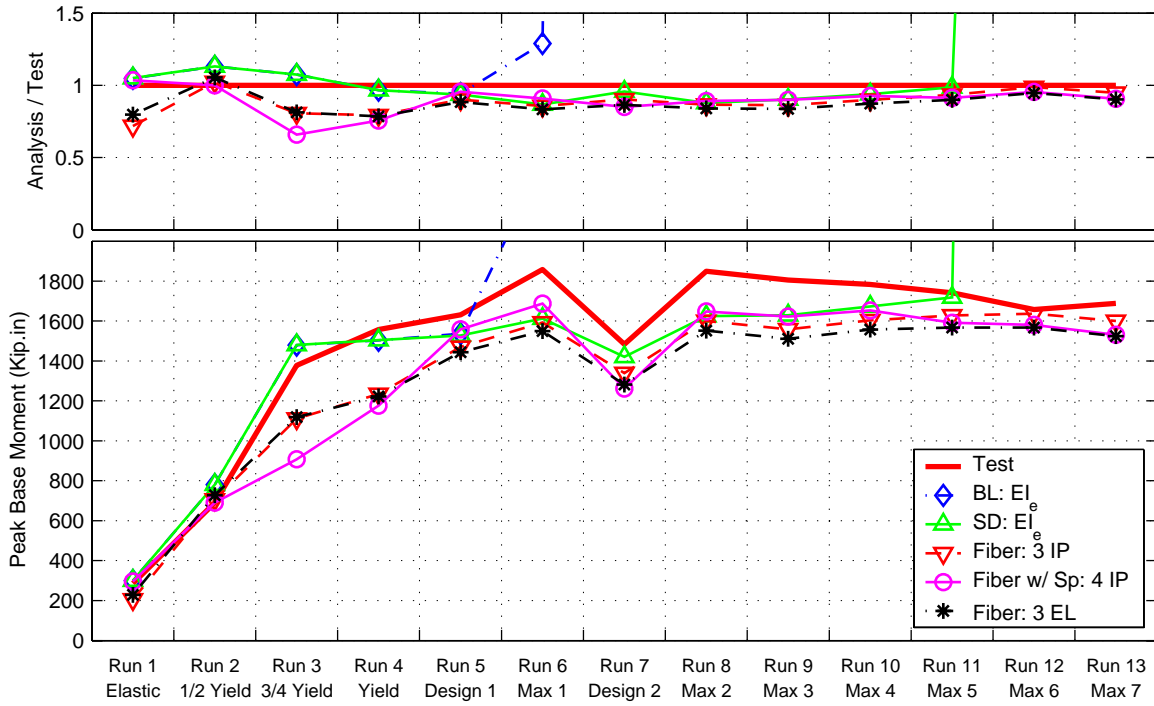
Figure E-48. Analytical and experimental *longitudinal base moment* for runs 1 to 13 of test *B2*.[a]
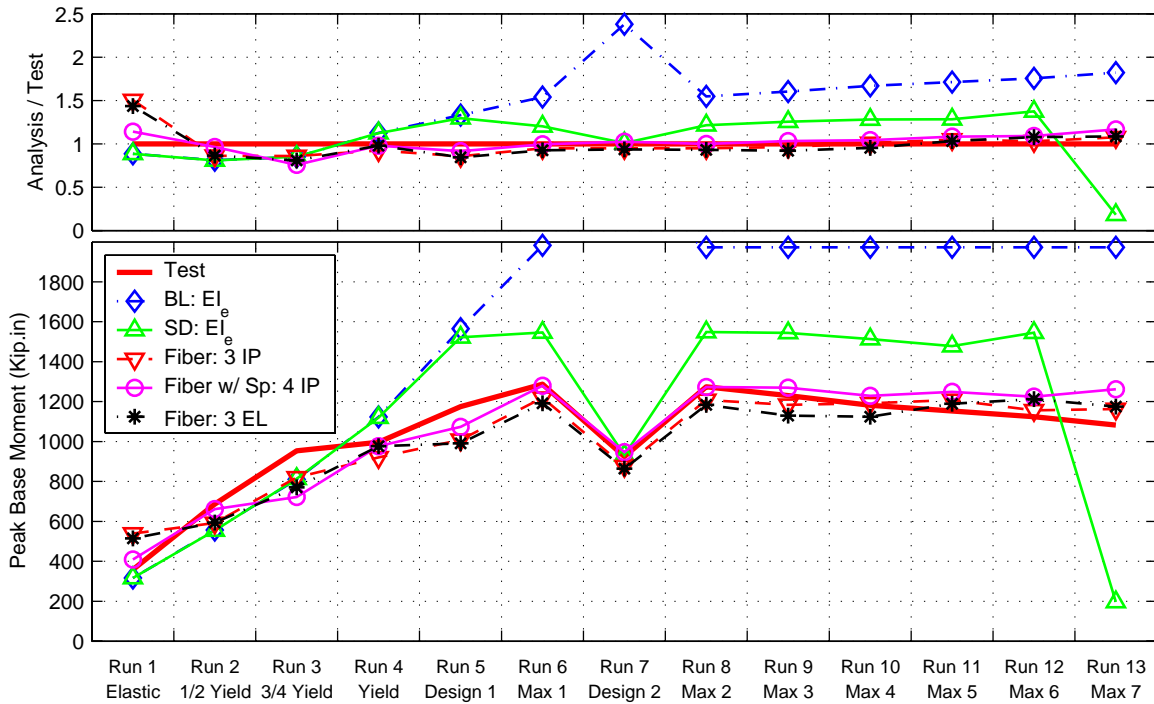
Figure E-49. Analytical and experimental *lateral base moment* for runs 1 to 13 of test *B2*.[a]

a. All runs were joined and analyzed as one long run (in sequence).
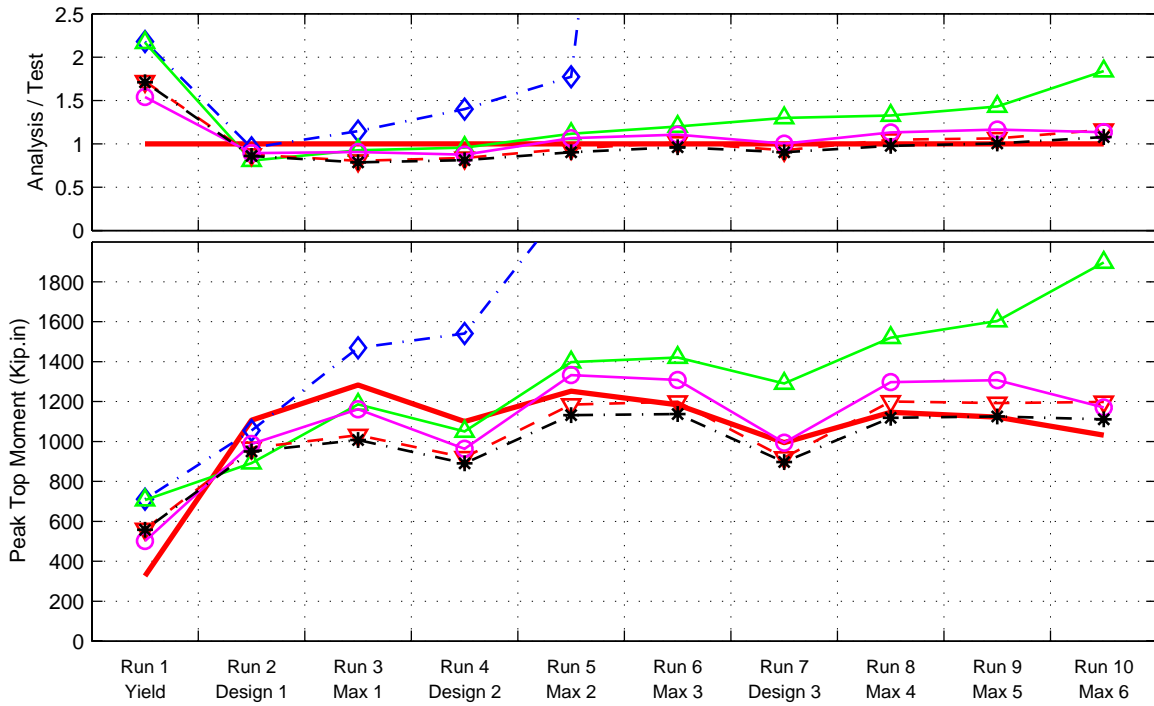
Figure E-50. Analytical and experimental *longitudinal top moment* for runs 1 to 10 of test *A2*.[a]
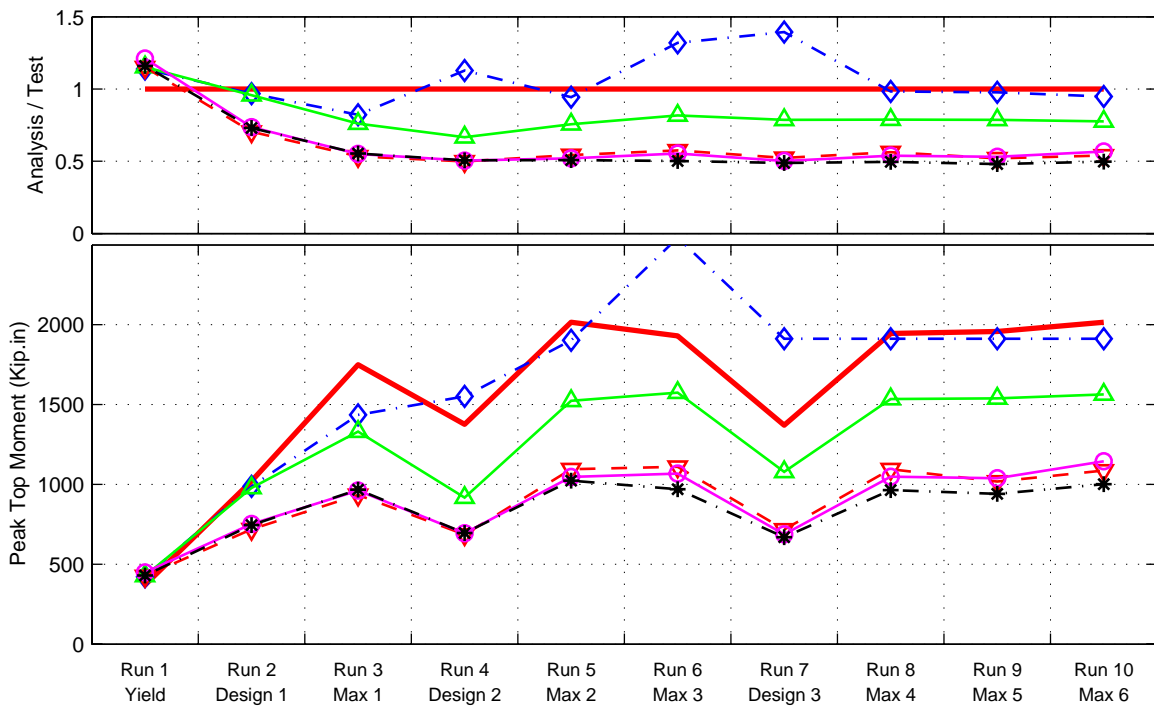
Figure E-51. Analytical and experimental *lateral top moment* for runs 1 to 10 of test *A2*.[a]

a. All runs were joined and analyzed as one long run (in sequence).

Figure E-52. Analytical and experimental *longitudinal top moment* for runs 1 to 13 of test *B2*.[a]

Figure E-53. Analytical and experimental *lateral top moment* for runs 1 to 13 of test *B2*.[a]

a. All runs were joined and analyzed as one long run (in sequence).

Figure E-54. Analytical and experimental *Energy Dissipated* in the *longitudinal* direction for runs 2 to 8 of test *A1*. Each run was analyzed individually (not in sequence).
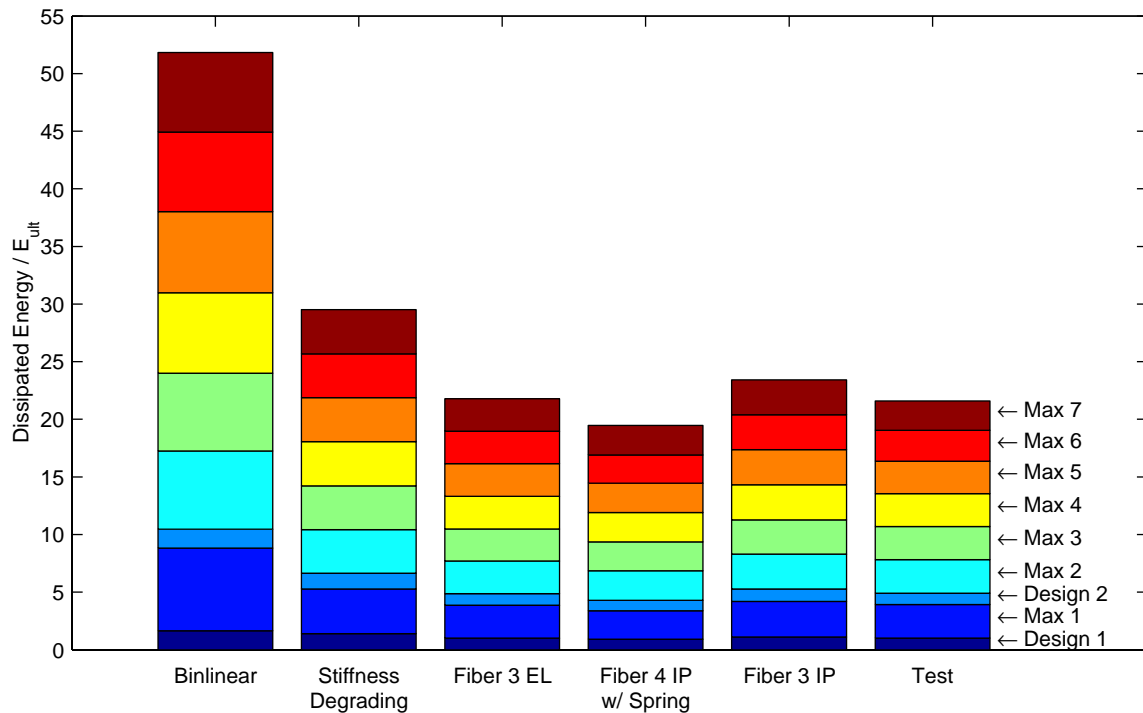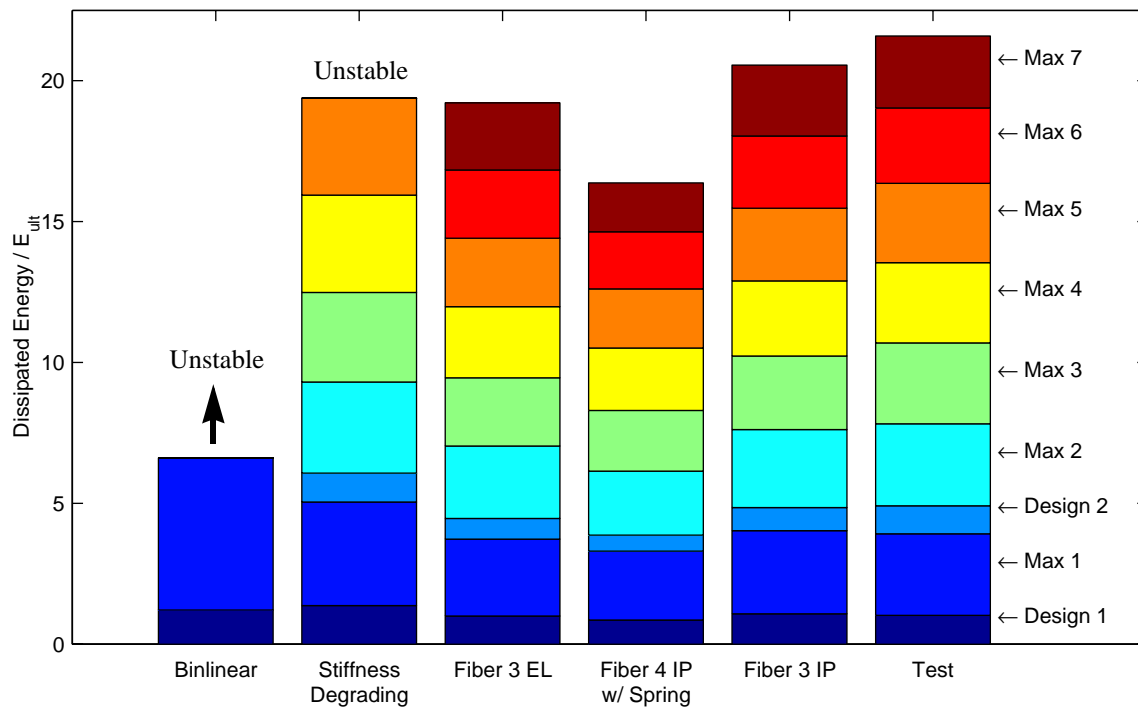

Figure E-55. Analytical and experimental *Energy Dissipated* in the *longitudinal* direction for runs 2 to 8 of test *A1*. All runs were joined and analyzed as one long run (in sequence).

Figure E-56. Analytical and experimental *Energy Dissipated* in the *longitudinal* direction for runs 2 to 10 of test *A2*. Each run was analyzed individually (not in sequence).
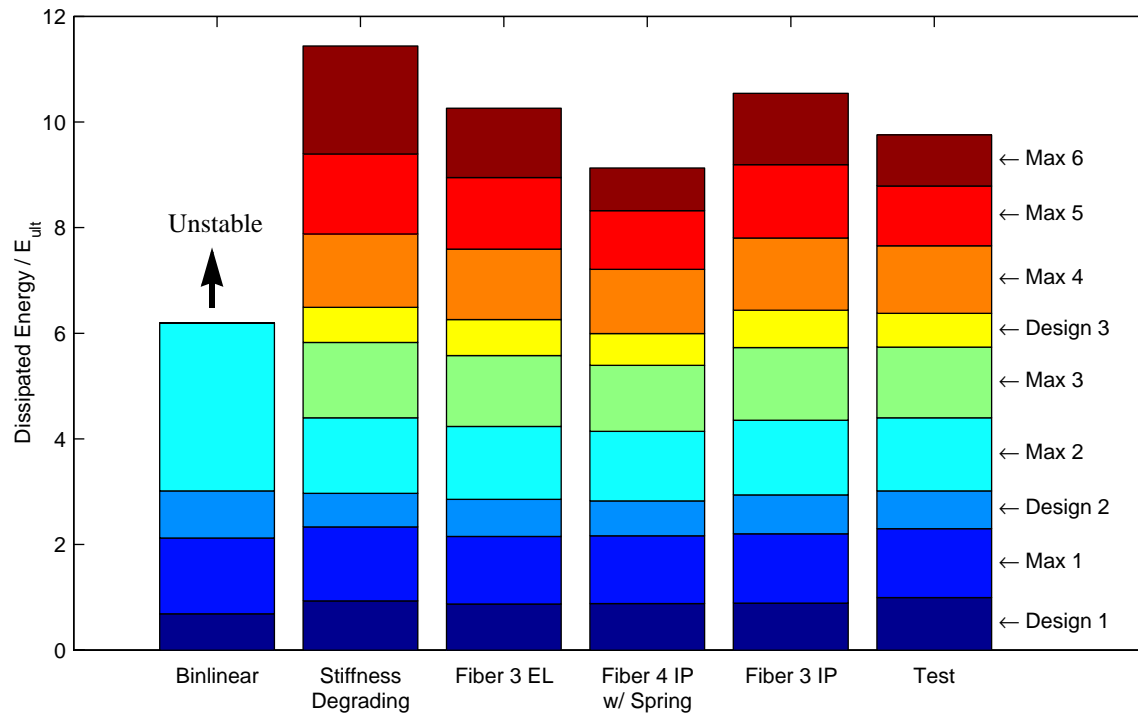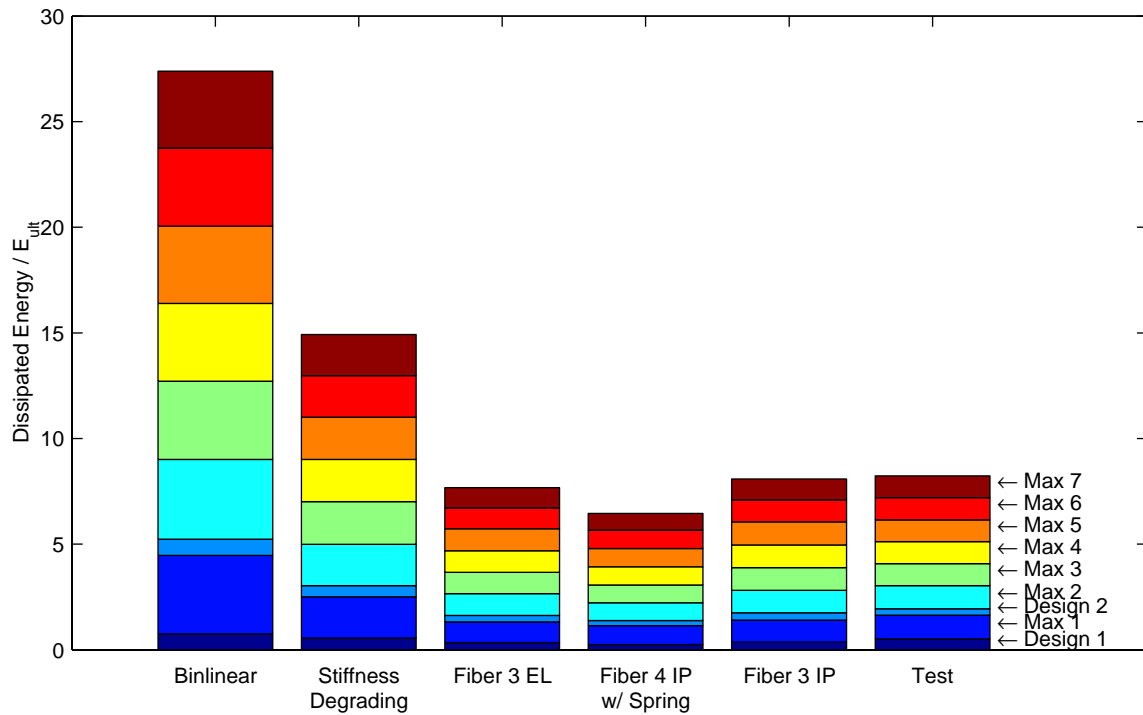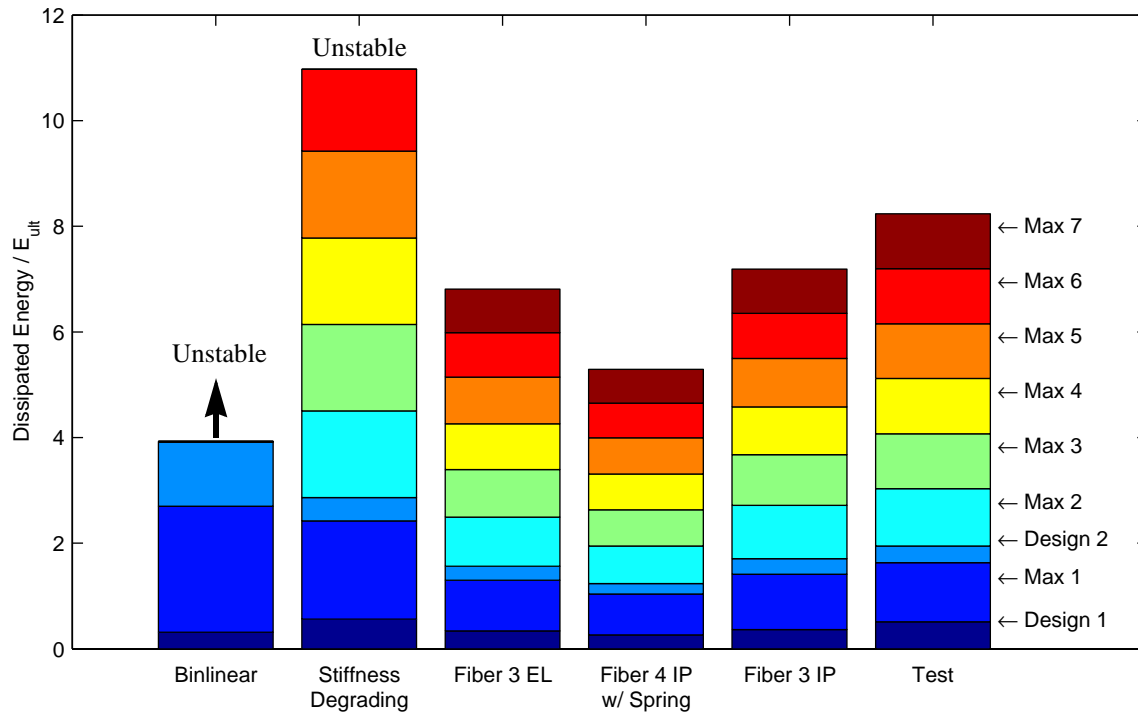

Figure E-57. Analytical and experimental *Energy Dissipated* in the *longitudinal* direction for runs 2 to 10 of test *A2*. All runs were joined and analyzed as one long run (in sequence).
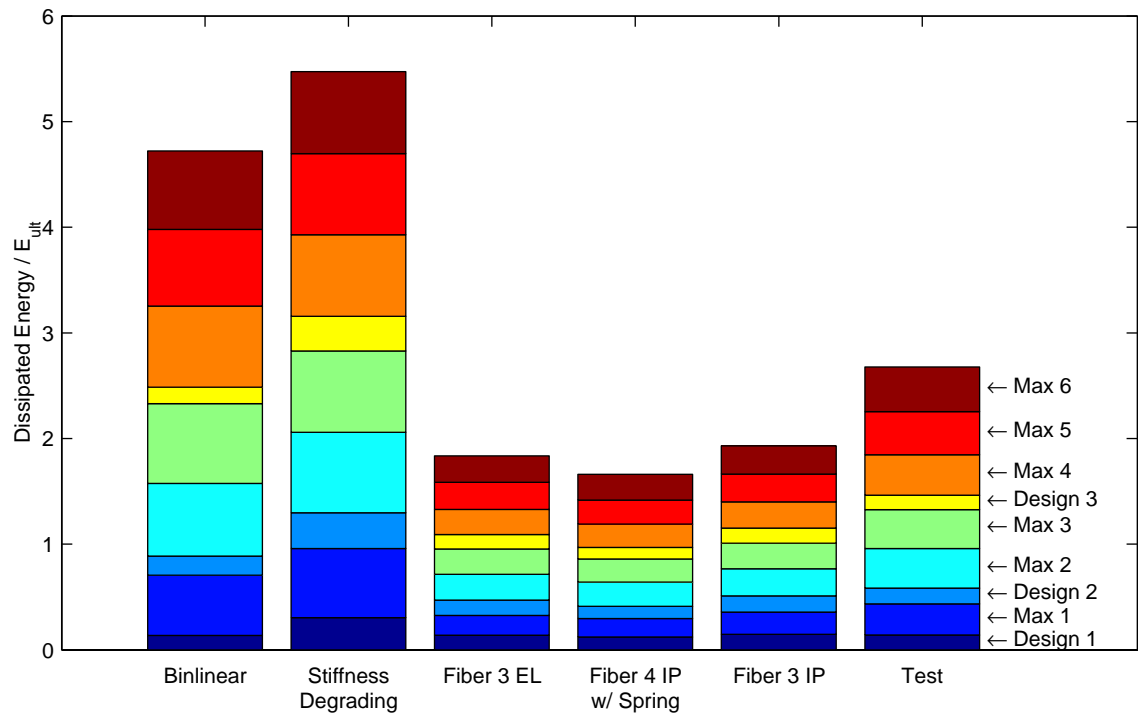
Figure E-58. Analytical and experimental *Energy Dissipated* in the *lateral* direction for runs 2 to 10 of test *A2*. Each run was analyzed individually (not in sequence).
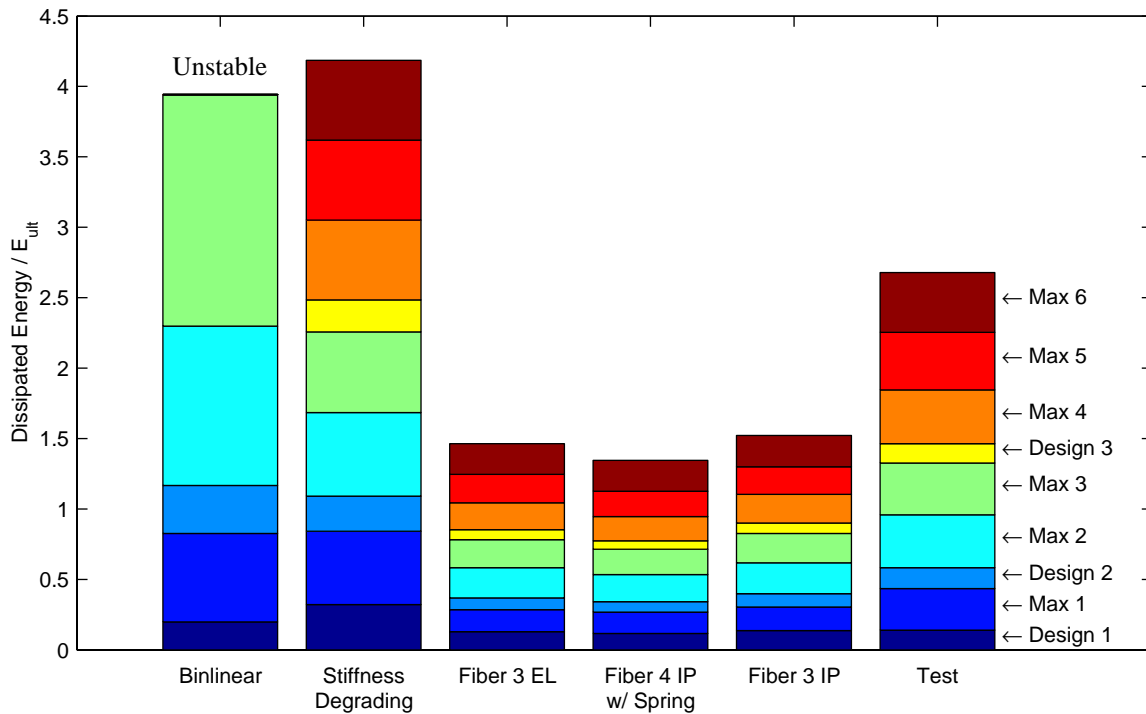
Figure E-59. Analytical and experimental *Energy Dissipated* in the *lateral* direction for runs 2 to 10 of test *A2*. All runs were joined and analyzed as one long run (in sequence).
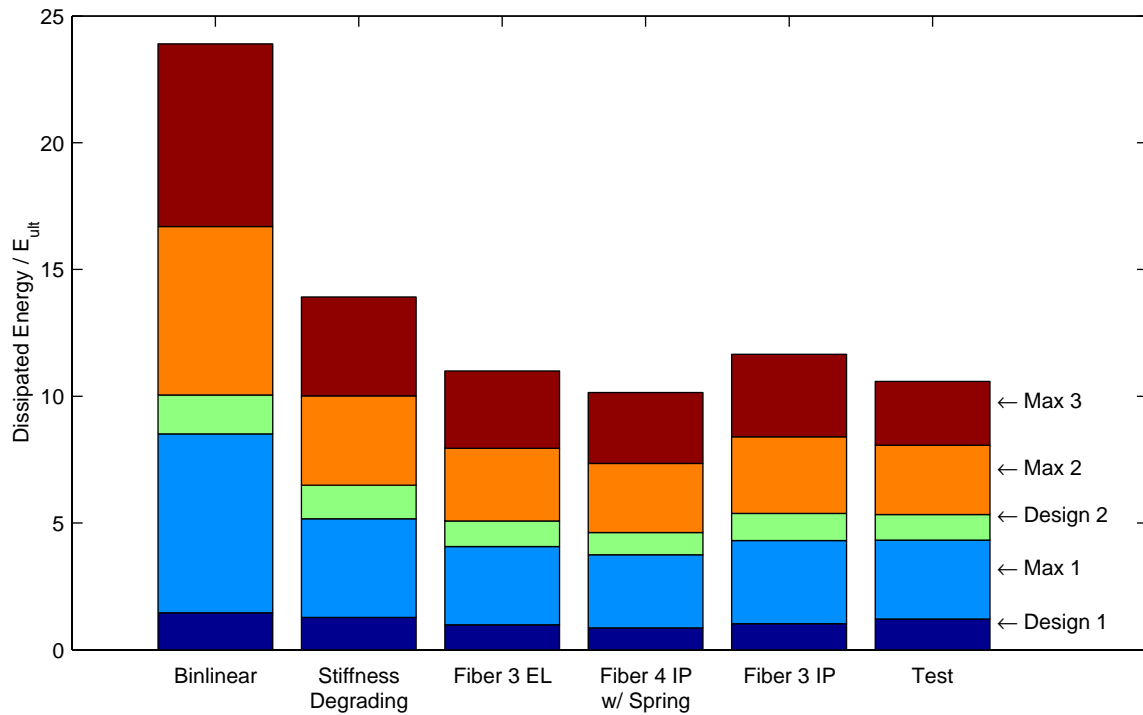
Figure E-60. Analytical and experimental *Energy Dissipated* in the *longitudinal* direction for runs 5 to 9 of test *B1*. Each run was analyzed individually (not in sequence).
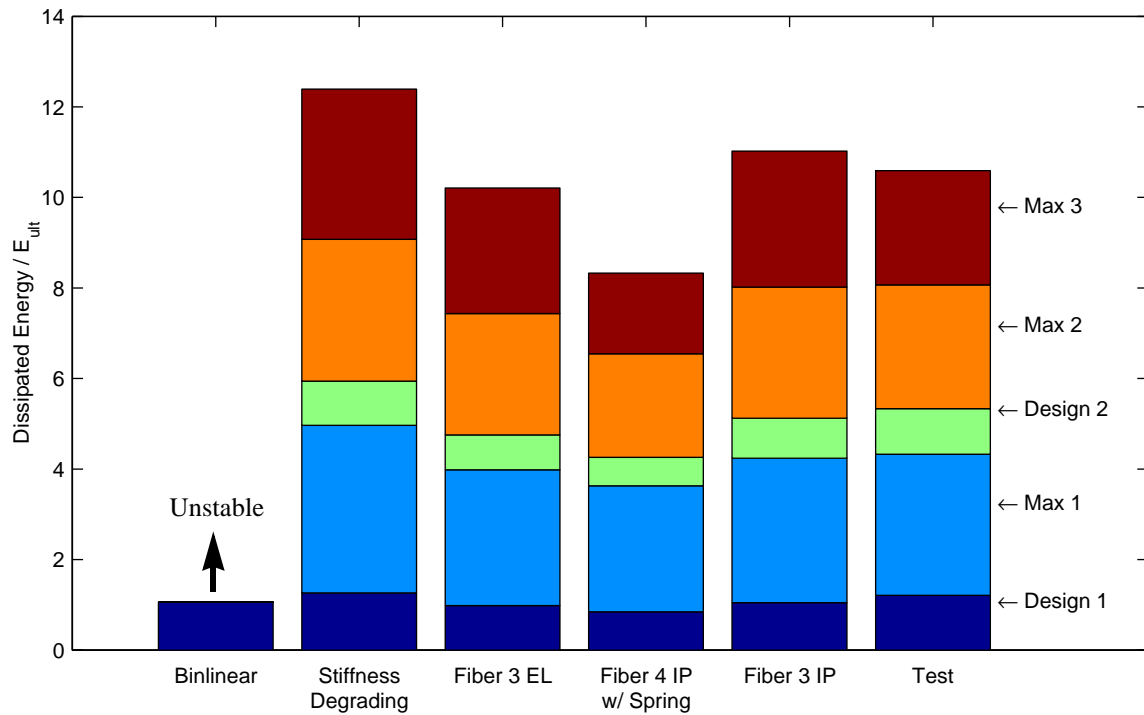
Figure E-61. Analytical and experimental *Energy Dissipated* in the *longitudinal* direction for runs 5 to 9 of test *B1*. All runs were joined and analyzed as one long run (in sequence).
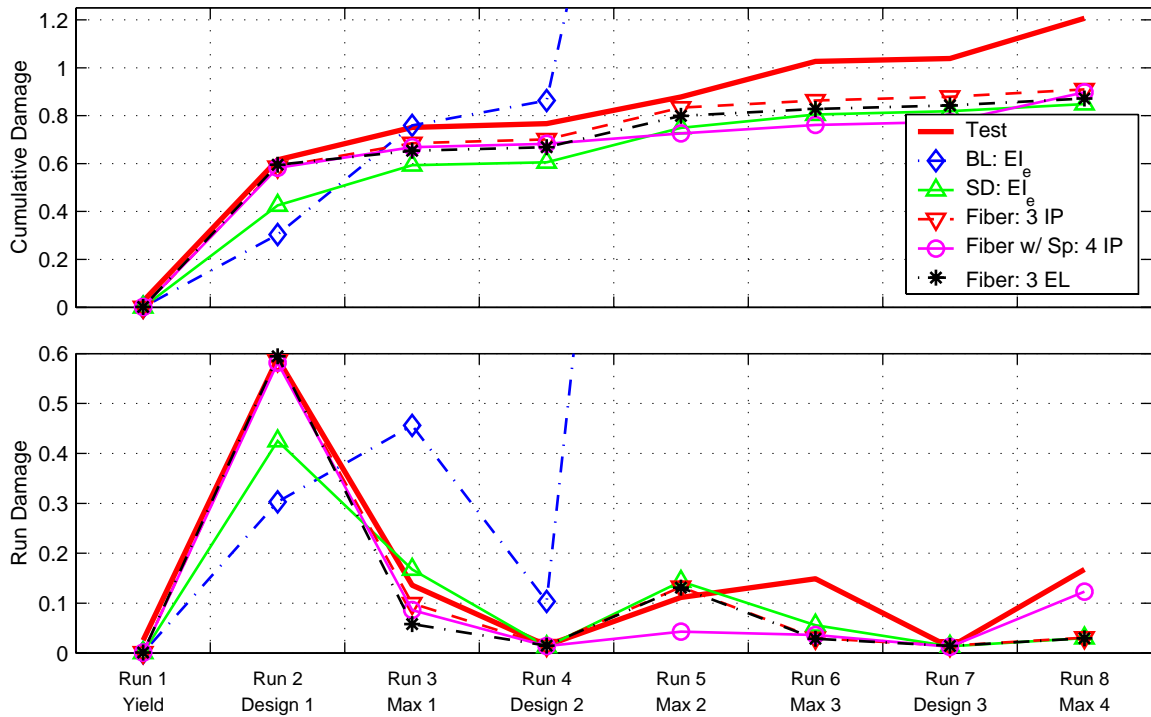
Figure E-62. Analytical and experimental *Energy Dissipated* in the *longitudinal* direction for runs 5 to 13 of test *B2*. Each run was analyzed individually (not in sequence).

Figure E-63. Analytical and experimental *Energy Dissipated* in the *longitudinal* direction for runs 5 to 13 of test *B2*. All runs were joined and analyzed as one long run (in sequence).

Figure E-64. Analytical and experimental *Energy Dissipated* in the *lateral* direction for runs 5 to 13 of test *B2*. Each run was analyzed individually (not in sequence).

Figure E-65. Analytical and experimental *Energy Dissipated* in the *lateral* direction for runs 5 to 13 of test *B2*. All runs were joined and analyzed as one long run (in sequence).

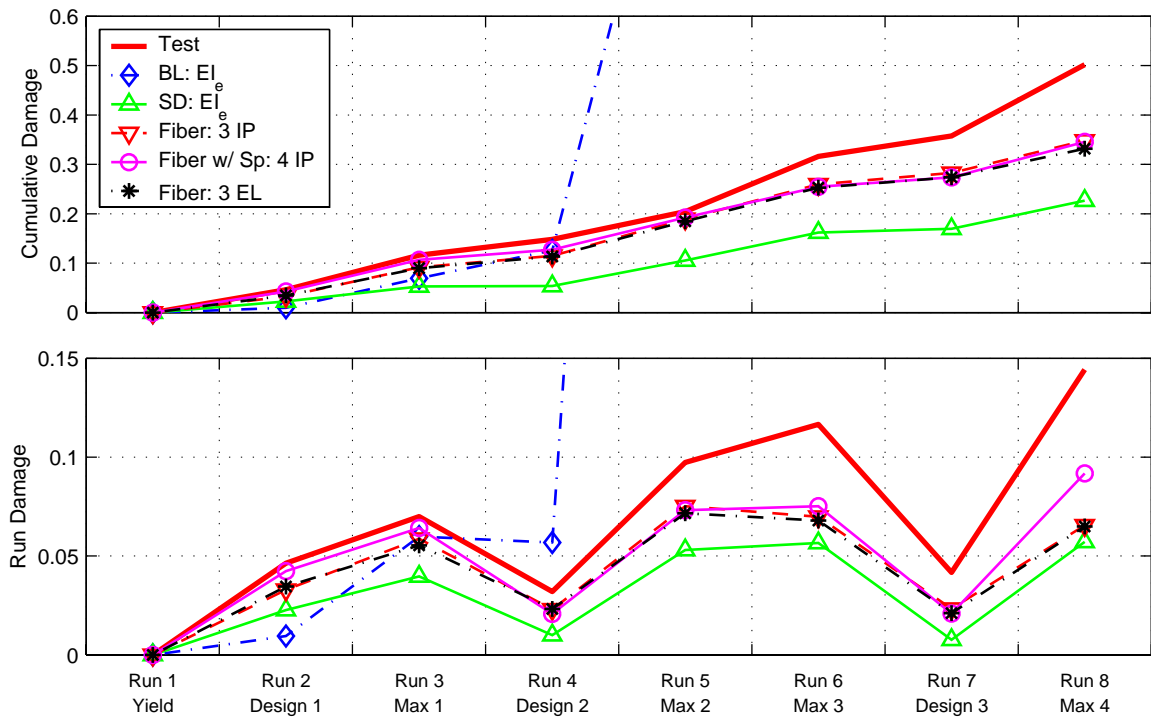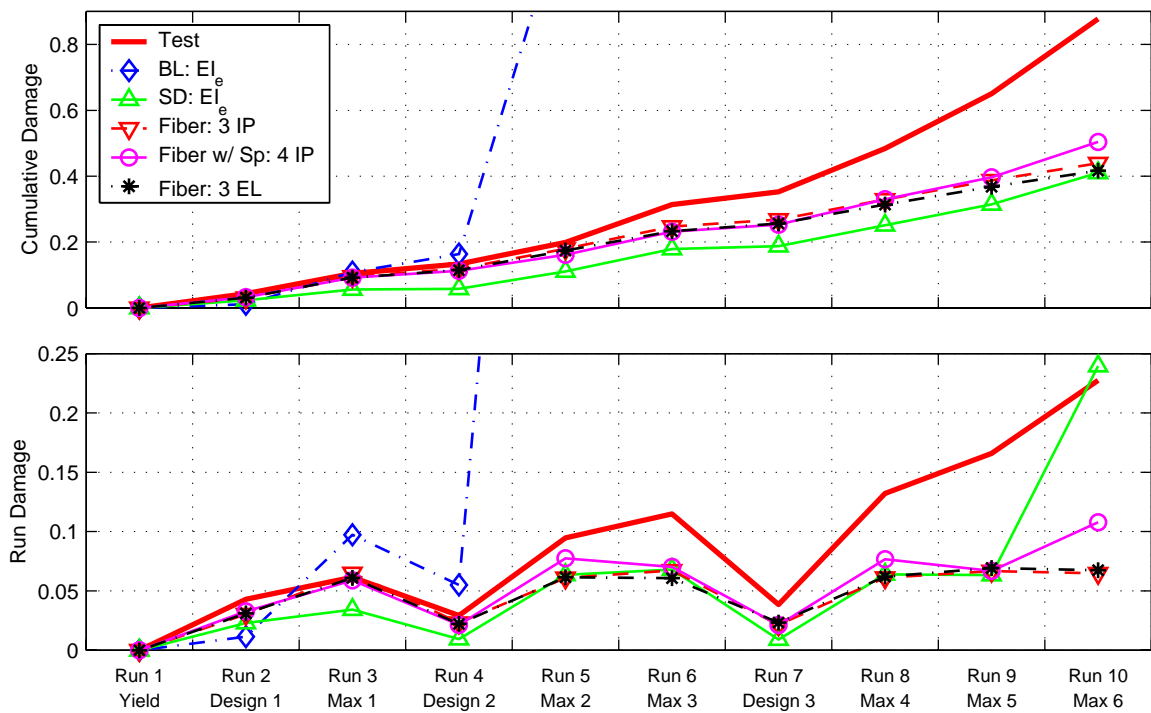**Figure E-66.** Analytical and experimental *Park Ang Damage Index* for runs 1 to 8 of test *A1*.[a]

Figure E-67. Analytical and experimental *Low Cycle Fatigue Damage Index* for runs 1 to 8 of test *A1*.[a]

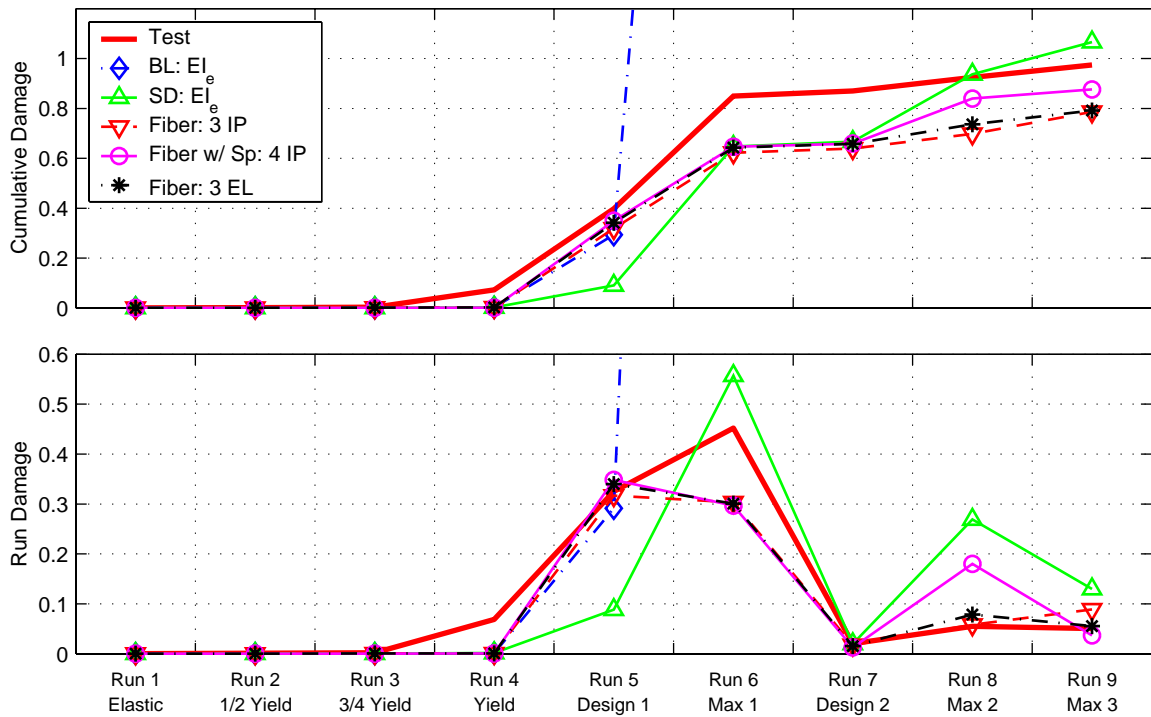a. All runs were joined and analyzed as one long run (in sequence).
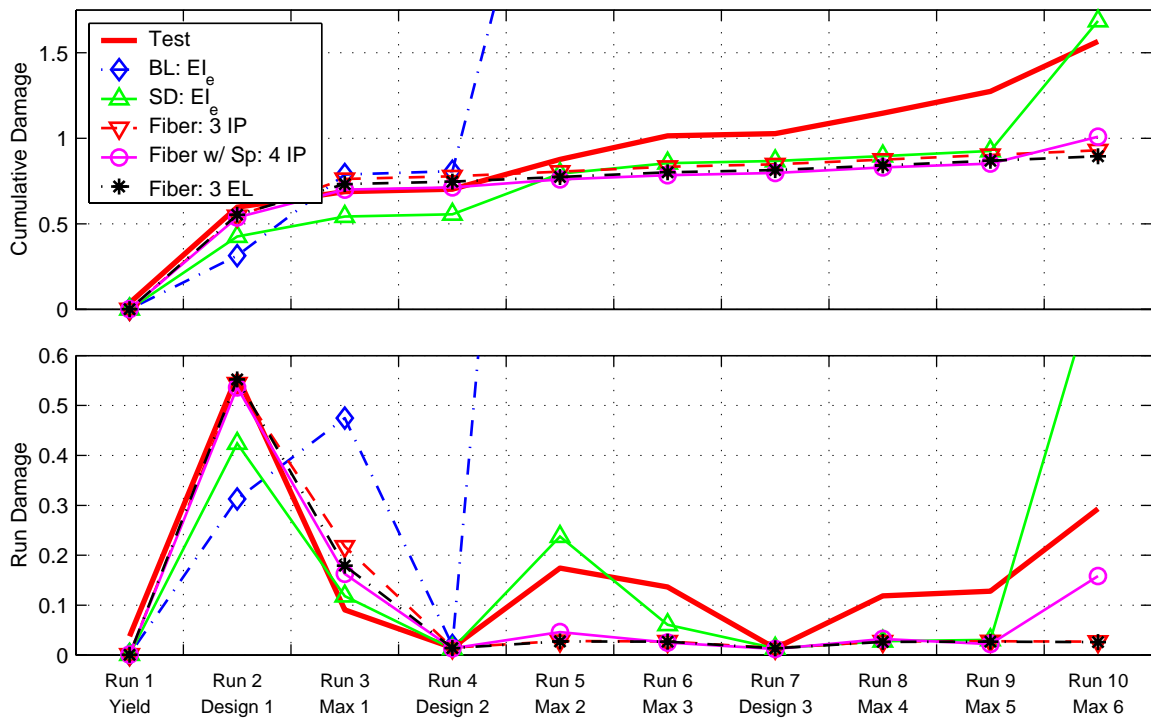
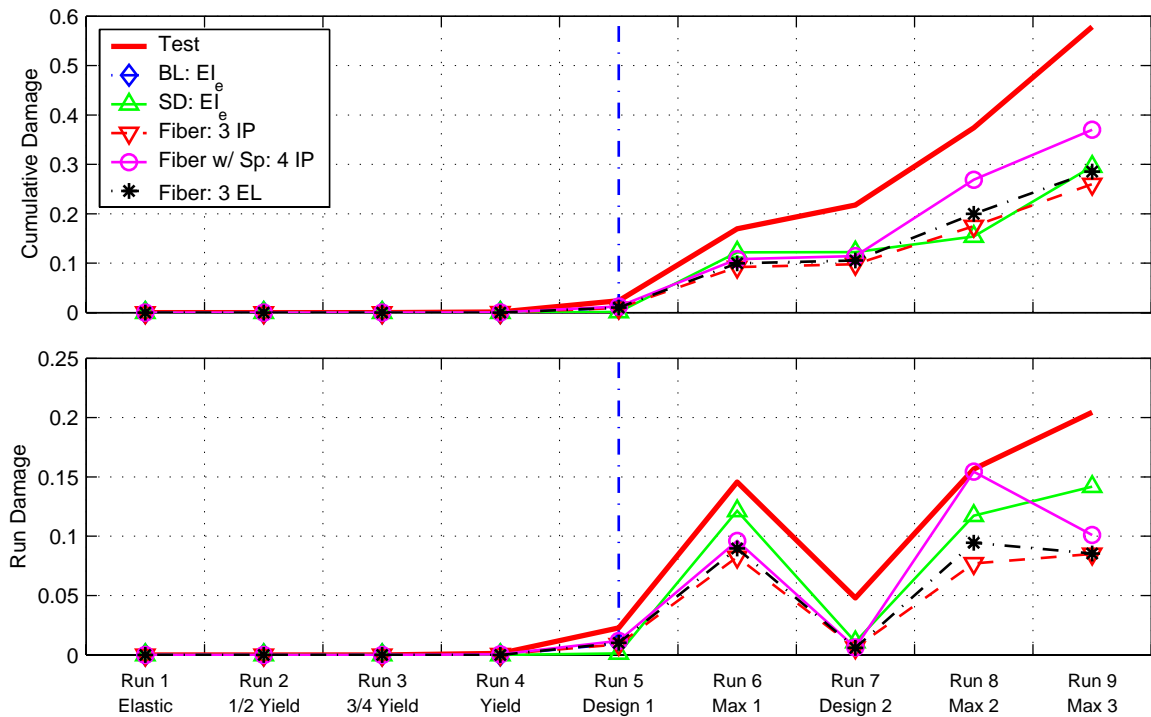**Figure E-68.** Analytical and experimental *Park Ang Damage Index* for runs 1 to 10 of test *A2*.[a]

Figure E-69. Analytical and experimental *Low Cycle Fatigue Damage Index* for runs 1 to 10 of test *A2*.[a]

---

a. All runs were joined and analyzed as one long run (in sequence).

Figure E-70. Analytical and experimental *Park Ang Damage Index* for runs 1 to 9 of test *B1*.[a]

Figure E-71. Analytical and experimental *Low Cycle Fatigue Damage Index* for runs 1 to 9 of test *B1*.[a]

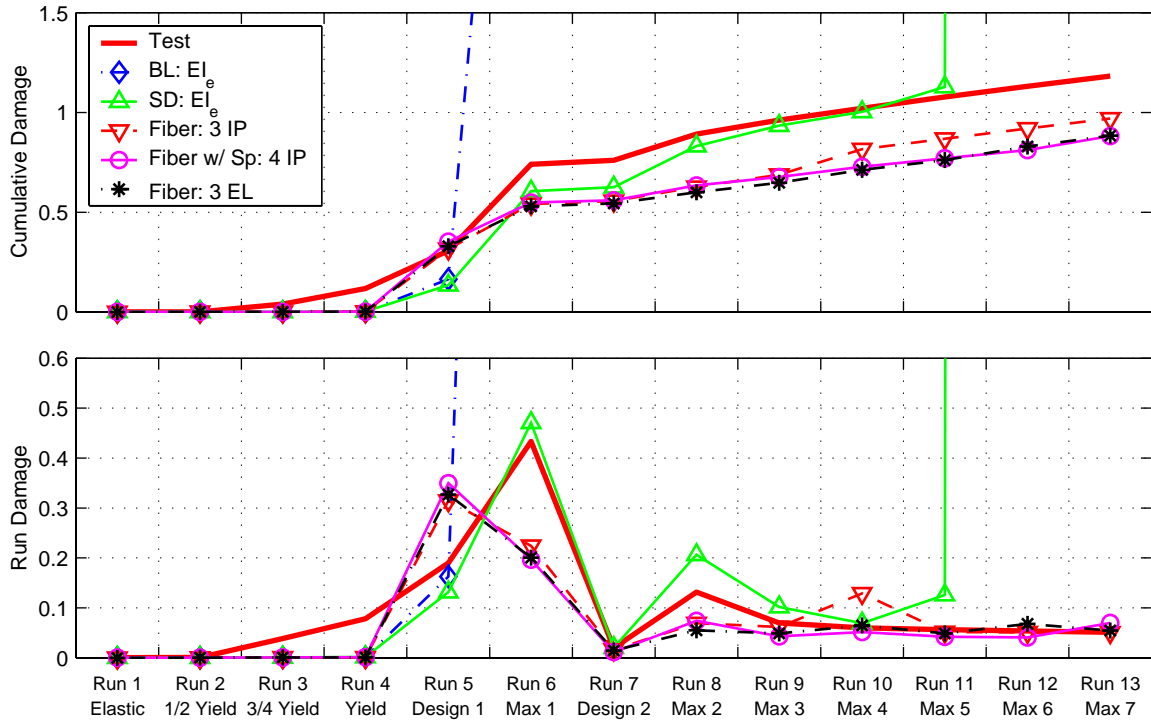a. All runs were joined and analyzed as one long run (in sequence).

Figure E-72. Analytical and experimental *Park Ang Damage Index* for runs 1 to 13 of test *B2*.[a]
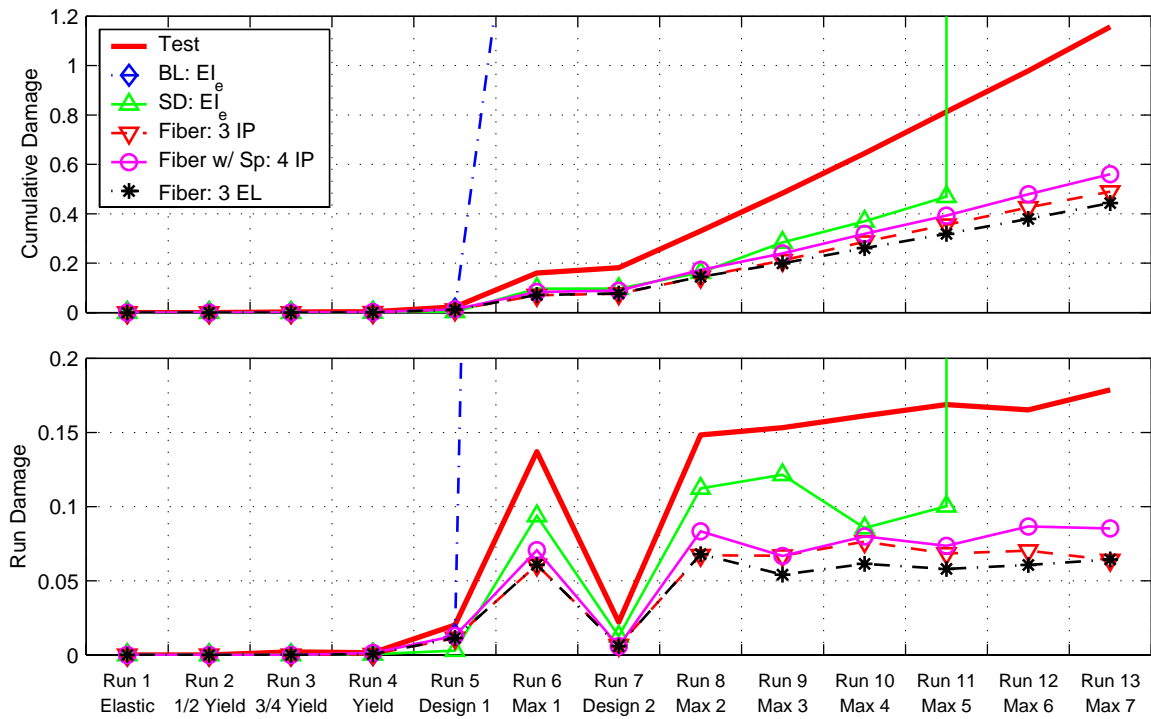

Figure E-73. Analytical and experimental *Low Cycle Fatigue Damage Index* for runs 1 to 13 of test *B2*.[a]

a. All runs were joined and analyzed as one long run (in sequence).